Journal of Heat Transfer

Published Quarterly by The American Society of Mechanical Engineers

VOLUME 121 • NUMBER 1 • FEBRUARY 1999

This journal is printed on acid-free paper, which exceeds the ANSI Z39.48-1992 specification for permanence of paper and library materials.☉ ™

♲ 85% recycled content, including 10% post-consumer fibers.

(Contents continued)

DISCUSSION

ERRATUM

ANNOUNCEMENTS AND SPECIAL NOTES

Editorial

Journal of Heat Transfer

From the Editor:

The *Journal of Heat Transfer* has traditionally published two types of technical submissions: standard papers generally of about six journal pages in length, and Technical Notes, which are on the order of one-and-one-half pages. Journal policy is to obtain a minimum of three external reviews for papers, and at least two reviews (one of which may be by an Associate Editor) for papers submitted by the author as a Technical Note.

The JHT Board of Editors has recommended a procedure to provide an outlet for more timely publication of some submissions to the Journal without compromising the Journal's noted review process. **For work submitted in the form of a Technical Note and designated by the author as a *Rapid Communication,* the Editor will strive to obtain one review by an Associate Editor and one additional review. If the reviews recommend publication, then publication will be guaranteed within six months of submittal, with possible publication on** the JHT web page upon acceptance (we are working with ASME on a policy for this). *Rapid Communications* will be strictly limited to one-and-one-half Journal pages.

Meeting the guarantee for this process will require rapid response by all concerned: assignment by the Editor to the Associate Editors, timely response by reviewers, rapid response by authors to incorporate reviewers' comments and in reading, correcting, and returning page proofs.

Authors wishing to submit a *Rapid Communication* should follow the Instructions for Authors for submissions in the form of a Technical Note, but clearly state in the cover letter that the submission is to be treated as a *Rapid Communication.* The Editorial Board will strive to make this system work as an additional method for the Journal to be of service to the heat transfer community.

John R. Howell
Technical Editor

Two Constructal Routes to Minimal Heat Flow Resistance via Greater Internal Complexity

A. Bejan

J. A. Jones Professor of
Mechanical Engineering,
Fellow ASME

N. Dan

Doctoral Candidate

Department of Mechanical Engineering
and Materials Science,
Duke University,
Durham, NC 27708-0300

This paper shows that the geometry of the heat flow path between a volume and one point can be optimized in two fundamentally different ways. In the "growth" method of the original constructal theory the structure is optimized starting from the smallest volume element of fixed size. Growth, or optimal numbers of constituents assembled into larger volumes, is one route to resistance minimization. In the "design" method the overall volume is fixed, and the designer works "inward" by optimizing the internal features of the heat flow path. The design method is new. It is shown analytically that the two methods produce comparable geometric results in which the high-conductivity channels form constructal tree networks, and where the low-conductivity material fills the interstices. For simplicity, it is assumed that the high-conductivity channels and their tributaries make 90-deg angles. In both approaches, the overall resistance decreases as the internal complexity of the conductive composite increases. In the growth method the number of constituents in each assembly can be optimized. In the design method, some of the constituent numbers cannot be optimized: these numbers assume the roles of weak parameters. The growth method is the simplest, and provides a useful approximation of the design and performance that can be achieved using the design method. Numerical solutions of the volume-to-point optimization problem confirm the results obtained analytically, and show that the geometric features of the optimal design are robust.

1 Introduction

This paper is a re-examination of the fundamental heat transfer problem of how to connect (with minimal thermal resistance) a finite-size heat-generating volume to a concentrated heat sink. This problem has many and diverse applications that go beyond the field of heat transfer, for example in physiology, river morphology, and electrical engineering. In heat transfer, where this problem was first posed (Bejan, 1997a), the main application is in miniaturized devices where cooling can be provided only by conduction. The trend toward smaller sizes and conduction-cooling at the smallest scales is illustrated in the recent reviews of the field (e.g., Aung, 1988; Peterson and Ortega, 1990; Kakac et al., 1994; Chu and Simons, 1994).

An essential aspect of the path of minimal thermal resistance between the given volume and point to that it can be optimized *geometrically.* The path can be arranged optimally in space. The geometric optimization of assemblies of heat-generating components is also an essential feature of many of the more recent contributions to the cooling of electronics (e.g., Bar-Cohen and Rohsenow, 1984; Knight et al., 1991; Anand et al., 1992). In the "constructal" optimization of the volume-to-point path for heat flow (Bejan, 1997a) it was shown that a volume subsystem of any size can have its external shape and internal details optimized such that its own volume-to-point resistance is minimal. This principle is repeated in the optimization of volumes of increasingly larger scales, where each new volume is an assembly of previously optimized smaller volumes. The construction spreads, as the assemblies cover larger spaces.

To the engineer, the result of this process is the design with minimal resistance. To the physicist, the end result is geometri-

cal form (shape, structure) *deduced* from a single deterministic principle. The visible part of the emerging structure is the tree network formed by the low-resistance portions of the medium. The invisible part—the shapeless, low-conductivity flow regime—covers the interstitial spaces and touches every point of the volume. The construction has a definite direction in time: from small to large. Shapelessness (diffusion) comes first, and structure (channels) comes later.

2 Growth as the Result of the Minimization of Flow Resistance

To see what is new in the alternate volume-to-point flow problem proposed in this paper (Section 3), it is useful to review some of the steps and conclusions of the constructal approach. We conduct this review by using an analysis that differs from that of Bejan (1997a): The present analysis emphasizes the *growth* aspect of the construction. The heat-flow geometry is two-dimensional. The low-conductivity material (k_0) generates heat volumetrically at the rate q''', which is assumed uniform. A small (fixed) amount of high-conductivity material (k_p) is to be distributed through the k_0 material.

The construction begins with the smallest volume scale (the elemental system), which is represented by the rectangular area $A_0 = H_0 L_0$. The start of this sequence of volume sizes is shown in Fig. 1. The A_0 size is known and fixed; for example, in the conduction cooling of an electronic material, A_0 is the smallest size that is allowed by manufacturing and electrical design constraints. The A_0 system is "elemental" because it has only one insert of high-conductivity material. This blade has the thickness D_0, and is positioned on the long axis of the $H_0 \times L_0$ rectangle. The heat current $q''' A_0$ is guided out of A_0 through the left end of the D_0 channel, which is the heat sink. The hot spots occur in the right-hand corners. To emphasize that the rectangular perimeter of A_0 is adiabatic except over the left extremity of the k_p channel, in Fig. 1 we stopped the right end of k_p channel short of the right boundary of the A_0 domain. This feature is

Copyright © 1999 by ASME
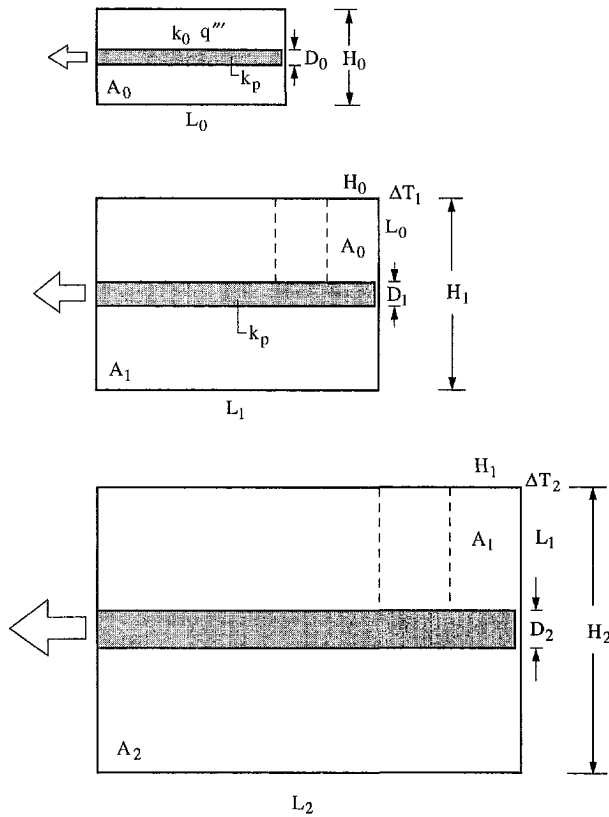
Fig. 1 Constructal growth: spatial growth through the minimization of thermal resistance

also visible in the second frame (A_1) and third frame (A_2) of Fig. 1. It will be seen even more clearly in Fig. 10, where the central (thickest) channel of the first assembly ends in the midplane of the elements that are situated the farthest from the heat sink.

The global volume-to-point resistance is the ratio $\Delta T_0/(q''' A_0)$, where ΔT_0 is the temperature difference between the hot spot and the heat sink. This measure is "global" because the heat current $q''' A_0$ is integrated over the system A_0, and the maximum temperature difference ΔT_0 is the excess temperature of the hot spot, or hot spots: The location of the hot spots is not an issue, as long as they reside inside the system. The global resistance refers to the entire system and its ability to accommodate the volume-to-point flow *without* violating the requirement that the hot spot not exceed a certain temperature ceiling. This is why in this paper we call the procedure *global* optimization, and the results *global* optima.

The composite material that fills A_0 is characterized by two dimensionless numbers, the conductivity ratio $\check{k} = k_p/k_0$, and

the volume fraction of high-conductivity material, $\phi_0 = D_0 L_0 / H_0 L_0 = D_0/H_0$. It was shown that when $\check{k} \gg 1$ and $\phi_0 \ll 1$ the volume-to-point resistance is given by the two-term expression

$$\frac{\Delta T_0 k_0}{q''' A_0} = \frac{1}{8} \cdot \frac{H_0}{L_0} + \frac{1}{2\check{k}\phi_0} \cdot \frac{L_0}{H_0}. \tag{1}$$

This resistance is minimal when the shape of A_0 is

$$(H_0/L_0)_{\mathrm{opt}} = 2(\check{k}\phi_0)^{-1/2}. \tag{2}$$

Needed later in the analysis are the optimal dimensions of the elemental rectangle, $H_{0,\mathrm{opt}} = (2A_0)^{1/2}(\check{k}\phi_0)^{-1/4}$ and $L_{0,\mathrm{opt}} = (A_0/2)^{1/2}(\check{k}\phi_0)^{1/4}$.

The construction continues with the first assembly $(A_1$, Fig. 1), which contains n_1 elemental systems, $A_1 = n_1 A_0$. The heat currents produced by the elemental systems are collected by a new high-conductivity insert of thickness D_1, the left end of which is the heat sink. The hot spot is again in one of the right-hand corners. The volume-to-point resistance is $\Delta T_1/(q''' A_1)$, where ΔT_1 is the excess temperature at the hot spot. It was shown that the resistance is given by the two-term expression

$$\frac{\Delta T_1 k_0}{q''' A_1} = \frac{H_1}{8\check{k}\phi_0 L_1} + \frac{A_1}{2\check{k} D_1 H_1} \tag{3}$$

which was later minimized with respect to the shape parameter H_1/L_1. In the present analysis we rewrite this expression in terms of n_1, to illustrate the effect of size (n_1) on the resistance of the first assembly:

$$\frac{\Delta T_1 k_0}{q''' A_1} = \frac{1}{4 n_1 (\check{k}\phi_0)^{1/2}} + \frac{n_1 A_0^{1/2}}{2^{3/2} \check{k} D_1 (\check{k}\phi_0)^{1/4}}. \tag{4}$$

The trade-off role played by n_1 is clear. In the beginning, as the size of the assembly increases from a small n_1 value, the overall resistance decreases. In other words, in the beginning resistance minimization is achieved through growth. This trend ends at a certain (optimal) value of n_1, when the second term of Eq. (4) takes over, and the resistance starts to increase. The optimal size is represented by

$$n_{1,\mathrm{opt}} = \frac{(\check{k}\tilde{D}_1)^{1/2}}{2^{1/4}(\check{k}\phi_0)^{1/8}} \tag{5}$$

where $\tilde{D}_1 = D_1/A_0^{1/2}$. The corresponding minimal value of the first-assembly resistance is

$$\left(\frac{\Delta T_1 k_0}{q''' A_1}\right)_m = \frac{1}{2^{3/4}\check{k}^{7/8}\phi_0^{3/8}\tilde{D}_1^{1/2}}. \tag{6}$$

A second minimization of this resistance is possible when the volume fraction of k_p material allocated to A_1 is fixed, $\phi_1 = A_{p1}/A_1$, where $A_{p1} = L_1 D_1 + n_1\phi_0 A_1$. This constraint is

---

Nomenclature

a, b = functions, Eqs. (33) and (34)
A = area of volume profile, m^2
A_p = area occupied by k_p material, m^2
D = thickness of k_p blade
$\tilde{D}_1$ = dimensionless thickness, $D_1/A_0^{1/2}$
$\hat{D}_i$ = dimensionless thicknesses, $D_i/A_i^{1/2}$
F = function, Eq. (45)
H = height of A domain, m
k_0 = low thermal conductivity, W/mK
k_p = high thermal conductivity, W/mK

$\check{k}$ = ratio of thermal conductivities, k_p/k_0
L = length of A domain, m
n = number of constituents in a construct
q''' = volumetric heat generation rate, W/m^3
y = variable, Eq. (43)

Greek Symbols

ΔT = peak excess temperature, K

ϵ = dimensionless group, Eq. (44)
ϕ = volume fraction occupied by k_p material

Subscripts

( )$_m$ = minimized once
( )$_{mm}$ = minimized twice
( )$_0$ = elemental
( )$_1$ = first construct
( )$_2$ = second construct
( )$_3$ = third construct

$$\phi_1 = \frac{\tilde{D}_1}{2^{1/2}(\tilde{k}\phi_0)^{1/4}} + \phi_0. \qquad (7)$$

The minimization of the resistance (6) subject to the constraint (7) yields $\phi_{0,\text{opt}} = \phi_1/2$ and $\tilde{D}_{1,\text{opt}} = 2^{-3/4}\tilde{k}^{1/4}\phi_1^{5/4}$, which can also be written as

$$\left(\frac{D_1}{D_0}\right)_{\text{opt}} = \left(\frac{\tilde{k}\phi_1}{2}\right)^{1/2} \gg 1. \qquad (8)$$

Working these results back into Eqs. (5) and (6) we obtain

$$n_{1,\text{opt}} = \left(\frac{\tilde{k}\phi_1}{2}\right)^{1/2} \gg 1 \qquad (9)$$

$$\left(\frac{\Delta T_1 k_0}{q'''A_1}\right)_{mm} = \frac{1}{\tilde{k}\phi_1}, \qquad (10)$$

where the subscript "mm" is a reminder that the resistance has been minimized twice. It can be verified that at this optimum the first-assembly shape and dimensions are exactly the same as in Bejan (1997a), namely $(H_1/L_1)_{\text{opt}} = 2$, $H_{1,\text{opt}} = (2A_1)^{1/2}$ and $L_{1,\text{opt}} = (A_1/2)^{1/2}$.

Examined from the point of view of natural sciences, Eq. (9) represents an important step: growth, assembly, or aggregation emerges for the first time as a *mechanism* of global resistance minimization. The number optimized in Eq. (9) represents *optimal* growth when the optimized geometry has been preserved (memorized) at the elemental level. Growth, assembly, or aggregation is no longer a "natural" behavior that we take for granted. It is not "self"-organization. It is not haphazard. It is a result—a consequence of the deterministic principle called constructal law—the optimization of access to internal currents, subject to global constraints (Bejan, 1997b, c; Bejan and Errera, 1997; Bejan and Tondeur, 1998; Bejan and Ledezma, 1998).

The second assembly (A_2, Fig. 1) can be optimized similarly, that is, two times: for overall size ($n_2 = A_2/A_1 \gg 1$), and for internal distribution of high-conductivity material. The second degree-of-freedom is represented by the thickness of the new central fiber (D_2), which collects the heat currents contributed by the n_2 constituents. The volume-to-point thermal resistance of the second assembly is $\Delta T_2/(q'''A_2)$, where ΔT_2 is measured between the upper right-hand corner (the hot spot) and the midpoint of the left side of the A_2 rectangle (the heat sink). The overall resistance is (Bejan, 1997a)

$$\left(\frac{\Delta T_2 k_0}{q'''A_2}\right) = \frac{H_1}{2\tilde{k}\phi_1 L_2} + \frac{A_2}{2\tilde{k}D_2 H_2} \qquad (11)$$

or, in terms of the number of constituents,

$$\left(\frac{\Delta T_2 k_0}{q'''A_2}\right) = \frac{1}{n_2\tilde{k}\phi_1} + \frac{n_2 A_1^{1/2}}{2^{3/2}\tilde{k}D_2}. \qquad (12)$$

The first minimization of this resistance is performed with respect to n_2, and the results are

$$n_{2,\text{opt}} = \frac{2^{3/4}\tilde{D}_2^{1/2}}{\phi_1^{1/2}} \qquad (13)$$

$$\left(\frac{\Delta T_2 k_0}{q'''A_2}\right)_m = \frac{2^{1/4}}{\tilde{k}\phi_1^{1/2}\tilde{D}_2^{1/2}} \qquad (14)$$

where $\tilde{D}_2 = D_2/A_1^{1/2}$. Once again, we see that optimal growth means resistance minimization. The second minimization is made with respect to $\tilde{D}_2$ when the volume fraction of k_p material is constrained: $\phi_2 = A_{p2}/A_2$, constant. The ϕ_2 constraint can also be written as

$$\phi_2 = 2^{-1/2}\tilde{D}_2 + \phi_1. \qquad (15)$$

The results of this second optimization step are $\phi_{1,\text{opt}} = \phi_2/2$ and $\tilde{D}_{2,\text{opt}} = 2^{-1/2}\phi_2$. These, in combination with the preceding results, lead to

$$\left(\frac{D_2}{D_1}\right)_{\text{opt}} = 2 \qquad (16)$$

$$n_{2,\text{opt}} = 2 \qquad (17)$$

$$\left(\frac{\Delta T_2 k_0}{q'''A_2}\right)_{mm} = \frac{2}{\tilde{k}\phi_2}. \qquad (18)$$

It can be verified that Eqs. (16)–(18) match the results reported previously (Bejan, 1997a), where the optimization was performed with respect to shape (H_2/L_2) instead of size (n_2). Equation (17) is where the integer 2 (dichotomy, bifurcation, pairing) enters the optimized architecture as a *result* of the resistance minimization principle, not as an *assumption* as in the tree network analyses of physiology and river morphology (for a review, see Bejan 1997b). Next, the pairing result $n_{2,\text{opt}} = 2$ recommends a revision—a more exact remake—of the analysis (11)–(18), because that analysis was based on the assumption that n_2 is considerably greater than 1. The revised results for the second assembly with $n_2 = 2$ can be found in Bejan (1997a).

In summary, the constructal approach reviewed in this section is one where the volume-to-point flow grows over an increasingly larger space. This growth occurs in steps (assemblies, constructs). Each step contributes external shape and internal structure, which are the results of the minimization of resistance. The size of each new assembly is such that it allows the flow to continue its outward expansion with minimal resistance.

3 Design Through the Increase in Internal Complexity

In this section we consider an entirely different way of looking at the volume-to-point flow, namely, the reverse of the "growth" reviewed in the preceding section. This time the size of the volume (A) is fixed, although its external shape may vary in order to accommodate optimally the internal structure that we will determine: the design. The volume fraction of high-conductivity material $\phi = A_p/A$ is also fixed. The design objective is to distribute this material over A such that the resistance from A to the heat sink (M) is minimal. The "design" approach described in this paper is new, especially in relation to the original constructal method (Bejan 1997a, b).

We contemplate using several designs for the internal structure of A. In Fig. 2 each is indicated by the subscript $i = 0, 1, 2, \ldots$, which represents, in order, the elemental design, the first-assembly design, the second-assembly design, etc. These designs have the same size ($A = A_0 = A_1 = A_2 = A_3$), and are indicated by the labels put in the lower-left corner of each frame. Next, we optimize the internal dimensions of each design (A_i, ϕ_i), and then see how well they perform against each other. In other words, given the system size (A) and amount of k_p-material (ϕ), which design—what degree of internal complexity—is the best for minimizing the volume-to-point flow resistance?

3.1 Elemental Design. The elemental design is represented by a single high-conductivity blade of thickness D_0, and by the external shape H_0/L_0. The resistance minimization analysis for this geometry is the same as in Bejan (1997a). The optimal external shape is given by Eq. (2) with ϕ in place of ϕ_0. This shape is independent of the size A_0. The optimal thickness of the k_p blade is $D_{0,\text{opt}} = \phi_0 H_{0,\text{opt}} = \phi_0(2A)^{1/2}(\tilde{k}\phi_0)^{-1/4}$. The minimized overall thermal resistance is
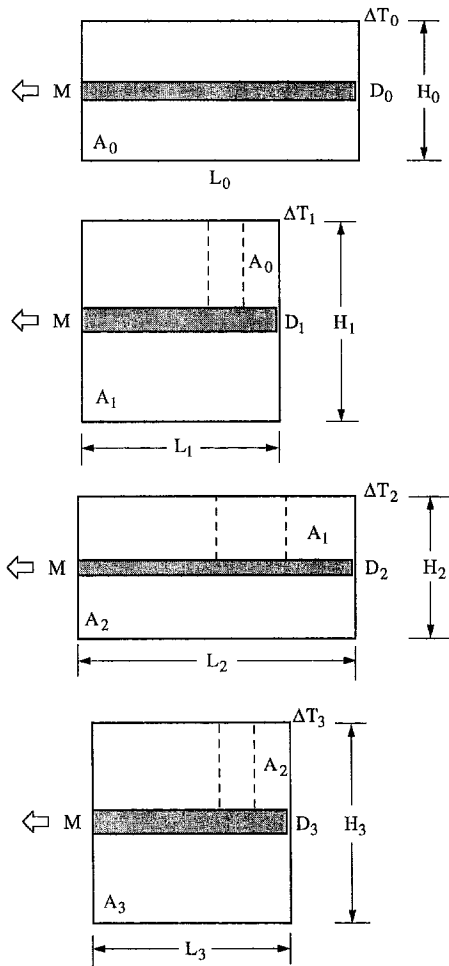
Fig. 2 Constructal design: the minimization of resistance through the increase in complexity in a volume of fixed size

$$\left(\frac{\Delta T_0 k_0}{q''' A_0}\right) = \frac{1}{2(\tilde{k}\phi_0)^{1/2}} \tag{19}$$

where ΔT_0 is the excess temperature registered in the hot-spot corners (Fig. 2).

3.2 First-Assembly Design. Consider next the design where the k_p material is distributed between one central blade (D_1, L_1) and n_1 equidistant side blades (D_0, L_0), as shown in Fig. 2. When $n_1 \gg 1$, the temperature drop along the D_1 blade is equal to $q''' H_1 L_1^2/(2 k_p D_1)$, in accordance with the analysis given in Bejan (1997a). The temperature drop from the hot-spot corner to the right end of the D_1 blade is sustained by an elemental design of size $A_0 = A_1/n_1$, and is given by Eq. (19). Adding these two temperature differences we obtain the overall resistance

$$\frac{\Delta T_1 k_0}{q''' A_1} = \frac{1}{2 n_1 (\tilde{k}\phi_0)^{1/2}} + \frac{n_1^{1/2}}{2^{3/2} \tilde{k}^{5/4} \phi_0^{1/4} \hat{D}_1} \tag{20}$$

where $\hat{D}_1 = D_1/A_1^{1/2}$ and $\phi_0 = D_0/H_0$. It is worth noting that $\hat{D}_1$ is not the same as $\tilde{D}_1$ of Eq. (5), and that Eq. (20) is not the same as Eq. (4). The main difference is that this time A_1 is fixed and A_0 varies, unlike in Eq. (4) where A_0 was fixed and A_1 (or n_1) varied. The shape of A_0 is fixed in accordance with the elemental design (Section 3.1), or Eq. (2).

The first-assembly design has two degrees-of-freedom: the number of side blades n_1 and the relative size of the two blade thicknesses. The second degree-of-freedom is represented by

either $\hat{D}_1$ or ϕ_0. By minimizing the expression (20) with respect to n_1 we find

$$n_{1,\text{opt}} = 2\tilde{k}^{1/2}\phi_0^{-1/6}\hat{D}_1^{2/3} \tag{21}$$

and the corresponding resistance minimum,

$$\left(\frac{\Delta T_1 k_0}{q''' A_1}\right)_m = \frac{3}{4\tilde{k}\phi_0^{1/3}\hat{D}_1^{2/3}} . \tag{22}$$

Next, the minimization with respect to $\hat{D}_1$ (or ϕ_0) is subjected to the k_p-material constraint $\phi_1 = A_{p1}/A_1 = $ constant, which assumes the form

$$\phi_1 = \hat{D}_1^{4/3}\phi_0^{-1/3} + \phi_0. \tag{23}$$

The results of minimizing the expression (22) with respect to this second degree-of-freedom are, in order, $\phi_{0,\text{opt}} = \phi_1/2$, $\hat{D}_{1,\text{opt}} = \phi_1/2$ and

$$\left(\frac{D_1}{D_0}\right)_{\text{opt}} = \frac{1}{2}(\tilde{k}\phi_1)^{1/2} \gg 1 \tag{24}$$

$$n_{1,\text{opt}} = (2\tilde{k}\phi_1)^{1/2} \gg 1 \tag{25}$$

$$\left(\frac{\Delta T_1 k_0}{q''' A_1}\right)_{mm} = \frac{3}{2\tilde{k}\phi_1} . \tag{26}$$

The differences between these results and their counterparts in the "growth" formulation (Eqs. (8)–(10)) are worth noting. Most obvious is the optimized external shape of A_1, which is now exactly square $(H_1/L_1)_{\text{opt}} = 1$.

When is the first-assembly design preferable to the elemental design? This question is answered by comparing the thermal resistances of the two designs on an equal basis (A, ϕ), that is by placing $A_0 = A$ and $\phi_0 = \phi$ in Eq. (19), and $A_1 = A$ and $\phi_1 = \phi$ in Eq. (26). The comparison is shown graphically in Fig. 3. The first-assembly design is preferable when $\tilde{k}\phi > 9$. The group $\tilde{k}\phi$, which accounts for the properties of the composite material, plays a critical role in the optimization of the design. As this group increases, i.e., as the k_p inserts become more conductive and/or more voluminous, there comes a point where the internal architecture makes a *transition* from one structure (A_0) to a more complex one (A_1). The transition is toward *lower resistance via higher complexity*.

3.3 Second-Assembly Design. The next question is whether a second complexity transition is possible, perhaps at a larger $\tilde{k}\phi$ value. Consider for this purpose the second-assem-
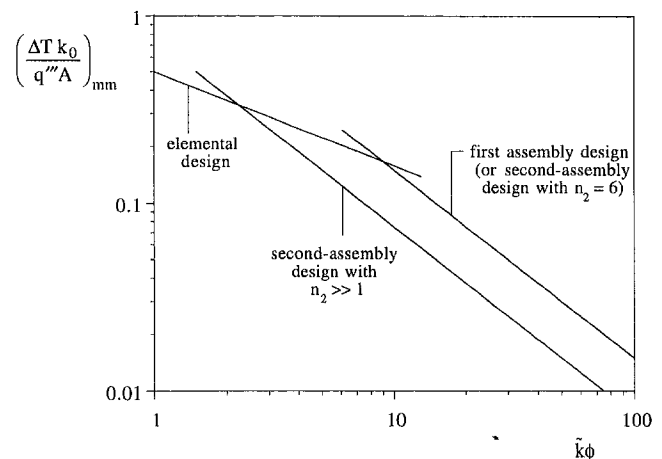
Fig. 3 The minimized thermal resistances of the elemental, first-assembly, and second-assembly designs

bly configuration shown in Fig. 2 (namely, the third frame, A_2). The new central blade (D_2, L_2) collects the heat currents contributed by n_2 blades of type (D_1, L_1). In other words, the A_2 structure is spread over a space divided into n_2 compartments such that each compartment ($A_1 = A_2/n_2$) has the external and internal shapes optimized in Section 3.2. The overall size A_2 is fixed, and the number n_2 is considerably greater than 1.

The overall resistance from A_2 to the sink M has two terms: the temperature drop along the D_2 blade, which by analogy with the start of Section 3.2 is equal to $q'''H_2L_2^2/(2k_pD_2)$, and the temperature drop sustained by the corner compartment A_1, which can be deduced from Eq. (26). The result is

$$\left(\frac{\Delta T_2 k_0}{q'''A_2}\right) = \frac{3}{2n_2\tilde{k}\phi_1} + \frac{n_2^{1/2}}{4\tilde{k}\hat{D}_2} \qquad (27)$$

where $\hat{D}_2 = D_2/A_2^{1/2}$. Minimizing the expression (27) with respect to n_2 we obtain

$$n_{2,\mathrm{opt}} = (12\hat{D}_2/\phi_1)^{2/3} \qquad (28)$$

$$\left(\frac{\Delta T_2 k_0}{q'''A_2}\right)_m = \frac{3^{4/3}}{2^{7/3}\tilde{k}\phi_1^{1/3}\hat{D}_2^{2/3}}. \qquad (29)$$

The second degree-of-freedom is with respect to the allocation of k_p material, i.e., the tradeoff between $\hat{D}_2$ and ϕ_1 subject to the $\phi_2 = A_{p2}/A_2$ constraint, which can be written as

$$\phi_2 = (2/3)^{1/3}\phi_1^{1/3}\hat{D}_2^{2/3} + \phi_1. \qquad (30)$$

We want to minimize the resistance (29) with respect to ϕ_1 subject to the constraint (30). This means that we must maximize the product $\phi_1^{1/3}\hat{D}_2^{2/3}$, which in view of the ϕ_2 constraint is equal to $(3/2)^{1/3}(\phi_2 - \phi_1)$. In conclusion, we must use the smallest ϕ_1 value possible. This corresponds to the largest n_2 that can be built, cf. Eq. (28),

$$n_2 = 6\left(\frac{\phi_2}{\phi_1} - 1\right) \qquad (31)$$

the largest $\hat{D}_2 = \phi_2 n_2^{3/2}/[2(n_2 + 6)]$, or the most slender external shape, $(H_2/L_2)_{\mathrm{opt}} = 4/n_2$. This recommendation comes also from the form of the thermal resistance expression obtained by combining these results with Eq. (29):

$$\left(\frac{\Delta T_2 k_0}{q'''A_2}\right)_m = \frac{3(n_2 + 6)}{4n_2\tilde{k}\phi_2}. \qquad (32)$$

In conclusion, in the second-assembly design the number of components (n_2) is left as a parameter constrained from above by manufacturing considerations. In the limit $n_2 \gg 1$ the resistance (32) approaches $3/[4\tilde{k}\phi_2]$. Figure 3 shows this limit on an equal basis with the other designs that are being compared (i.e., by setting $A_2 = A$ and $\phi_2 = \phi$). Once again, we see that the performance improves when the complexity of the design increases. The second-assembly design performs better than the first-assembly design when $n_2 > 6$.

3.4 Third-Assembly Design. It is instructive to consider at least one more design, that is, one more step toward higher complexity. In the third-assembly design shown in Fig. 2 (the fourth frame) the $A = A_3$ space is covered by n_3 ($\gg 1$) components of variable size A_2 ($=A_3/n_3$). The external and internal shapes (dimensionless aspect ratios) of these components have been optimized as shown in Sections 3.1–3.3. The end-to-end temperature difference sustained by the D_3 stem of the k_p tree is equal to $q'''H_3L_3^2/(2k_pD_3)$. Adding this to the temperature difference sustained by the corner component we obtain the overall resistance of the third-assembly design,
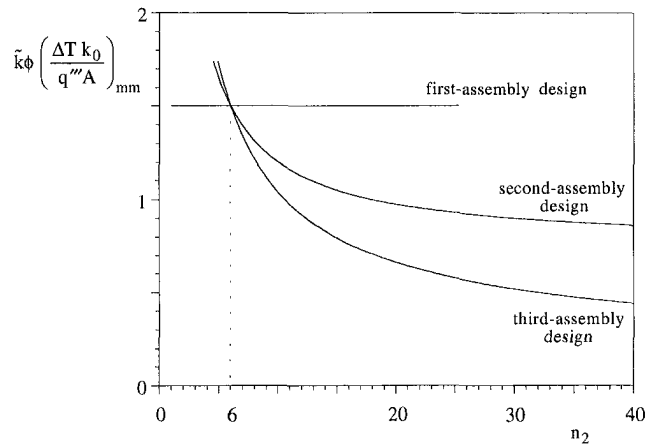
Fig. 4 The effect of n_2 on the minimized thermal resistances of the second and third-assembly designs

$$\left(\frac{\Delta T_3 k_0}{q'''A_3}\right) = \frac{3a}{4n_3\tilde{k}\phi_2} + \frac{n_3^{1/2}}{2n_2^{1/2}\tilde{k}\hat{D}_3} \qquad (33)$$

where $\hat{D}_3 = D_3/A_3^{1/2}$ and $a = (n_2 + 6)/n_2$. In this design an optimal number of components exists, and it is obtained by minimizing the expression (33) with respect to n_3

$$n_{3,\mathrm{opt}} = (3b\hat{D}_3/\phi_2)^{2/3} \qquad (34)$$

$$\left(\frac{\Delta T_3 k_0}{q'''A_3}\right)_m = \frac{3^{4/3}a^{1/3}}{4n_2^{1/3}\tilde{k}\phi_2^{1/3}\hat{D}_3^{2/3}} \qquad (35)$$

where $b = n_2^{1/2}a$. Equation (35) shows that the resistance can be minimized further by maximizing the product $\phi_2^{1/3}\hat{D}_3^{2/3}$. This second optimization is constrained by the total amount of k_p material that is allocated to the third-assembly design, namely, $\phi_3 = A_{p3}/A_3$, or

$$\phi_3 = \hat{D}_3(n_3/n_2)^{1/2} + \phi_2. \qquad (36)$$

The result of this second optimization is $\phi_{2,\mathrm{opt}} = \phi_3/2$, which can be combined with Eqs. (34), (35) to obtain, in order,

$$\hat{D}_{3,\mathrm{opt}} = \frac{n_2^{3/8}\phi_3}{2(3b)^{1/4}} \qquad (37)$$

$$\left(\frac{\Delta T_3 k_0}{q'''A_3}\right)_{mm} = \frac{3^{3/2}(n_2 + 6)^{1/2}}{2n_2\tilde{k}\phi_3} \qquad (38)$$

$$\left(\frac{H_3}{L_3}\right)_{\mathrm{opt}} = \frac{n_2}{3^{1/2}(n_2 + 6)^{1/2}} \qquad (39)$$

$$\left(\frac{D_3}{D_2}\right)_{\mathrm{opt}} = \frac{2(n_2 + 6)^{3/4}}{3^{1/4}n_2} \qquad (40)$$

$$n_{3,\mathrm{opt}} = [3(n_2 + 6)]^{1/2}. \qquad (41)$$

Several geometric features are worth noting. First, the number of constituents at the second-assembly level (n_2) continues to play the role of parameter. The ratio $(D_3/D_2)_{\mathrm{opt}}$ is of the order of 1 when n_2 is of the order of 10. The ratio $(H_3/L_3)_{\mathrm{opt}}$ is equal to 1.44 when $n_2 = 10$. The number $n_{3,\mathrm{opt}}$ is equal to 6 when $n_2 = 6$. The most important result is Eq. (38), which shows that the overall resistance continues to decrease as n_2 increases. This trend could be added to Fig. 3, but an even better comparison is provided on an equal basis by Fig. 4. In this figure we see the effect of n_2 on the best performances of the first, second, and third assemblies. The performance improves in every case

as the complexity (n_2) increases, provided n_2 is greater than 6. In other words, for the same combination of materials ($\tilde{k}\phi$), it makes sense to increase the complexity of the internal architecture of the design. The limit to this sequence of complexity increase will be dictated by manufacturing considerations.

4 First-Assembly Design With Unrestricted Elemental Features

The sequence of four designs optimized in the preceding section can be continued toward assemblies of higher order. An important feature that deserves emphasis is that in each design the constituents inherit the optimized aspect ratios of the design of preceding order. For example, in the first-assembly design of Section 3.2 we assumed that *the shape* of each constituent (elemental volume, A_0) matches the optimal value derived in Eq. (2). This choice is beneficial, because by reducing the number of degrees-of-freedom it simplifies the optimization work, but does it really lead to the best possible design?

In this section we examine this question by considering again the optimization of the first-assembly design. With reference to the second frame of Fig. 2, we write that the peak temperature difference ΔT_1 is equal to the temperature drop along the D_1 blade [namely, $q'''H_1L_1^2/(2k_pD_1)$] plus the peak temperature sustained by the upper-right element of size H_0L_0. This second contribution is provided by Eq. (1). Unlike in Section 3.2, we do not assume that H_0/L_0 is given by Eq. (2). After some algebra, it can be shown that the overall resistance of the first-assembly design is given by the dimensionless expression

$$\frac{\Delta T_1 k_0}{q'''A_1} = \frac{1}{2\tilde{k}\hat{D}_1}\left(\frac{L_1}{H_1}\right)^{1/2} + \frac{1}{2n_1^2}\frac{L_1}{H_1} + \frac{n_1^2}{8\tilde{k}\phi_0}\frac{H_1}{L_1}. \quad (42)$$

This expression shows that the first-assembly architecture is described by four dimensionless numbers: the overall aspect ratio H_1/L_1, the thickness of the central blade $\hat{D}_1$, the number of constituents n_1, and the thickness of the elemental blade ϕ_0 (or D_0/H_0). Three of these parameters are free to vary, because the amount of k_p material is constrained by Eq. (23), in which ϕ_1 is a constant. Note that in this formulation the number of degrees-of-freedom exceeds by one the corresponding number in the optimization conducted in Section 3.2.

The minimization of the thermal resistance (42) begins with eliminating $\hat{D}_1$ in favor of ϕ_0, by using the constraint (23). Taking the derivative of this resistance with respect to ϕ_0, and setting it equal to zero, we obtain

$$3y^{7/4} - y^{3/4} = \left(\frac{H_1}{L_1}\right)^{3/2} \quad (43)$$

where $y = \phi_{0,\text{opt}}/(\phi_1 - \phi_{0,\text{opt}})$. Equation (43), i.e., the selection of $\phi_{0,\text{opt}}$, completes the first resistance minimization step.

The second minimization begins with eliminating from the resistance formula (42) the ratio H_1/L_1 in favor of y, by using Eq. (43). After some algebra, the once-minimized resistance assumes the form

$$\left(\frac{\Delta T_1 k_0}{q'''A_1}\right)_m = \frac{F(y,\epsilon)}{n_1^2} \quad (44)$$

where $\epsilon = n_1^2/(2\tilde{k}\phi_1)$, and

$$F = \epsilon\frac{1+y}{y^{1/2}}\left[\frac{4}{(3y-1)^{1/3}} + (3y-1)^{2/3}\right]$$

$$+ \frac{1}{2y^{1/2}(3y-1)^{2/3}}. \quad (45)$$

The function F can be minimized with respect to y: the results
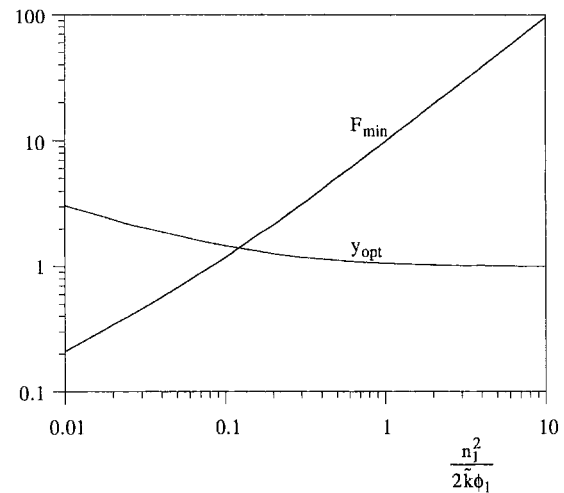
Fig. 5 Results of the double minimization of the thermal resistance of the first-assembly design with unrestricted elemental features

for y_{opt} and $F_{\text{min}} = F(y_{\text{opt}}, \epsilon)$ are reported as functions of ϵ in Fig. 5. This completes the second resistance minimization step.

The twice-minimized resistance is obtained by substituting $F = F_{\text{min}}$ in Eq. (44), namely $(\Delta T_1 k_0/q'''A_1)_{mm} = F_{\text{min}}/n_1^2$. This function depends on n_1 and the product $\tilde{k}\phi_1$, as is shown in Fig. 6. The main effect is due to $\tilde{k}\phi_1$, especially as n_1 increases: in the limit $n_1 \gg 1$, the overall thermal resistance $(\Delta T_1 k_0/q'''A_1)_{mm}$ approaches $5/\tilde{k}\phi_1$. This trend is comparable to that of Eqs. (10) and (26), which are also shown in Fig. 6. The lowest resistance estimate happens to be due to the growth method (Eq. (10), Section 2), which is by far the simplest analytical method that we have considered. The design method of Section 3.2 (Eq. (26)) leads to a higher estimate, and, finally, the design with the largest number of degrees-of-freedom—this section—leads to an even higher estimate. We discuss the relative positions of these estimates further in the next section.

Which of the three methods is the most accurate? To shed light on this issue we solved numerically the steady-state conduction problem in the heterogeneous domain A_1 shown in the second frame of Fig. 2. The heat generation rate ($q'''A_1$, fixed) was distributed only over the k_0 domain, not over the D_1 and D_0 fibers of k_p material. The length of the D_1 fiber is less than L_1, specifically, $L_1 - (H_0 - D_0)/2$. The geometry has three degrees-of-freedom: H_1/L_1, D_1/D_0 and n_1. We solved the conduction problem in many geometrical configurations, and developed the overall resistance $(\Delta T_1 k_0/q'''A_1)$ as a function of $H_1/$
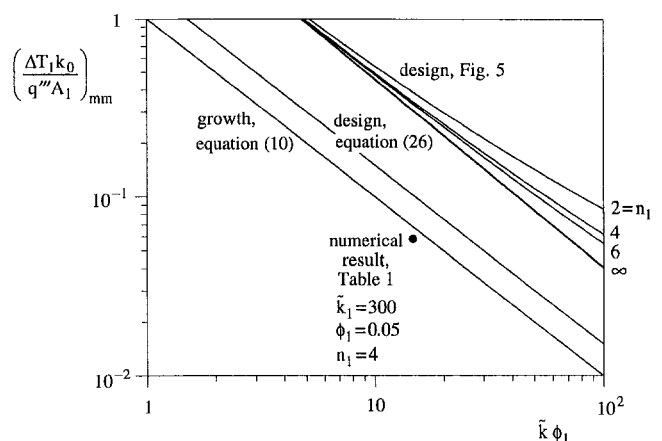
Fig. 6 The effect of n_1 and $\tilde{k}\phi_1$ on the twice minimized resistance of the first-assembly design with unrestricted elemental features

Table 1 Results of the geometric optimization of the first-assembly design, when the overall thermal resistance is determined by direct numerical simulation ($\tilde{k} = 300$, $\phi_1 = 0.05$)

n_1	$(\Delta T_1 k_0/q'''A_1)_{mm}$	$(H_1/L_1)_{opt}$	$(D_1/D_0)_{opt}$	$\phi_{0,opt}/\phi_1$
2	0.0818	3.80	3.2	0.7
4	0.0616	2.56	5	0.587
6	0.0575	2.37	6.8	0.564
8	0.0561	2.33	9	0.548

L_1, D_1/D_0 and n_1. We were able to minimize this function with respect to H_1/L_1 and D_1/D_0, but not with respect to n_1.

The numerical work was based on the finite element method. The accuracy of the code used (FIDAP, 1993) was tested in an earlier numerical study of conduction in heterogeneous dendritic media (Ledezma et al., 1997), where it was found that the results produced by the code agree within one percent with the results based on our own implementation of the finite element method. For the present work, in the code we used second-order interpolation functions and quadrilateral elements. The grid was nonuniform in both directions, with a more refined grid in the regions with larger temperature gradients. For the geometries optimized in the runs summarized in Table 1 we used 43 nodes in the y direction (i.e., the vertical direction in the second frame of Fig. 2), and between 35 and 97 nodes in the x direction. We tested the mesh convergence and found that these meshes were sufficiently fine so that the results were insensitive to further refinement.

Table 1 shows that the twice-minimized resistance decreases monotonically as n_1 increases, and that this effect becomes weak when n_1 is greater than 4 or 6. This behavior agrees with the analytical solution developed in the first part of this section and plotted in Fig. 6. Coincidental are the numerical values reported for $(\Delta T_1 k_0/q'''A_1)_{mm}$ in Table 1, which are very close to those predicted by the growth method: Note that Eq. (10) with $\tilde{k} = 300$ and $\phi_1 = 0.05$ yields $(\Delta T_1 k_0/q'''A_1)_{mm} = 0.067$. In sum, the three analytical methods anticipate the proper order of magnitude of the minimized resistance, and the effect of the group $\tilde{k}\phi_1$. The design analysis developed in this section also anticipates correctly the effect of n_1, which is weak. The closest numerical estimate for the minimized resistance happens to be provided by the growth analysis (Section 2). We discuss this aspect further in the next section.

It is worth reporting all the geometric features that accompany the twice-minimized resistance obtained in Eq. (45) and Figs. 5 and 6. The optimal external aspect ratio $(H_1/L_1)_{opt}$ emerges as a function of only $\tilde{k}\phi_1/n_1^2$, Fig. 7. For example, when $\tilde{k} = 300$, $\phi_1 = 0.05$, and $n_1 = 4$ the optimal shape is $(H_1/L_1)_{opt} = 1.86$, which agrees approximately with the numerical results shown in Table 1.

The corresponding internal ratio $(D_1/D_0)_{opt}$ is reported in Fig. 8 as a function of $\tilde{k}\phi_1/n_1^2$ and n_1. For the numerical example used in the preceding paragraph, Fig. 8 predicts $(D_1/D_0)_{opt} = 2.1$, which also verifies the order of magnitude of the numerical solution reported in Table 1. Related to the internal ratio predicted in Fig. 8 is the volume fraction ratio $\phi_{0,opt}/\phi_1$ presented in Fig. 9. This ratio is close to 0.5 when $\tilde{k} = 300$, $\phi_1 = 0.05$, and $n_1 = 4$, and increases toward 1 as $\tilde{k}\phi_1/n_1^2$ increases. The result $\phi_{0,opt}/\phi_1 \cong 0.5$ agrees with the corresponding analytical results of the growth method (listed under Eq. (7)) and the design method (listed above Eq. (24)).

5 Conclusion: The Constructal Tree Structure is Robust

In this paper we showed that in addition to the constructal "growth" method of minimizing the thermal resistance between one point and a volume, there is the "design" approach
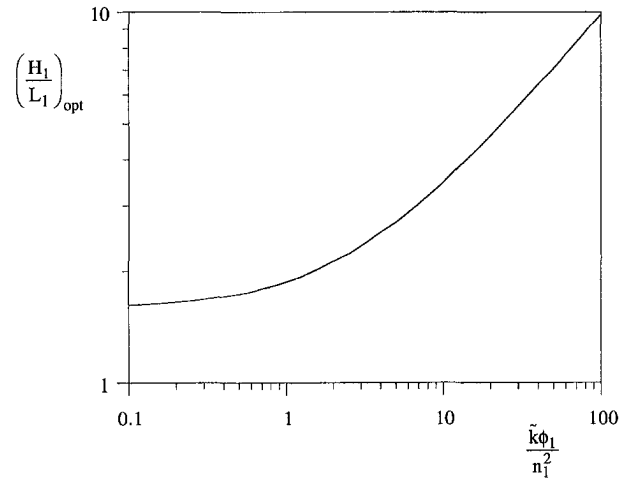
Fig. 7 The optimal external ratio $(H_1/L_1)_{opt}$ of the first-assembly design with unrestricted elemental features
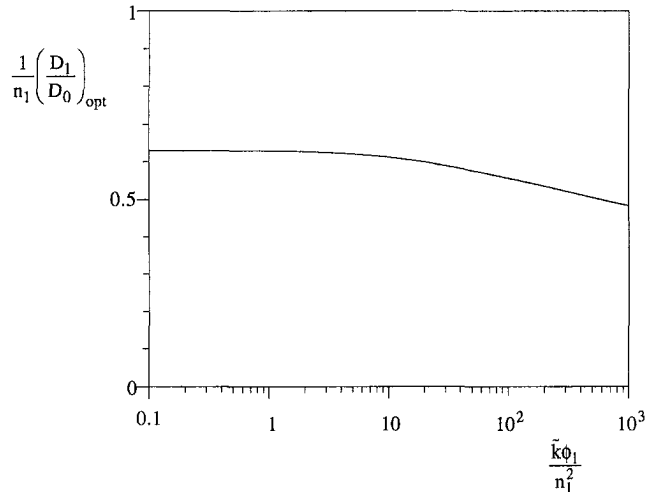
Fig. 8 The optimal internal ratio $(D_1/D_0)_{opt}$ of the first-assembly design with unrestricted elemental features
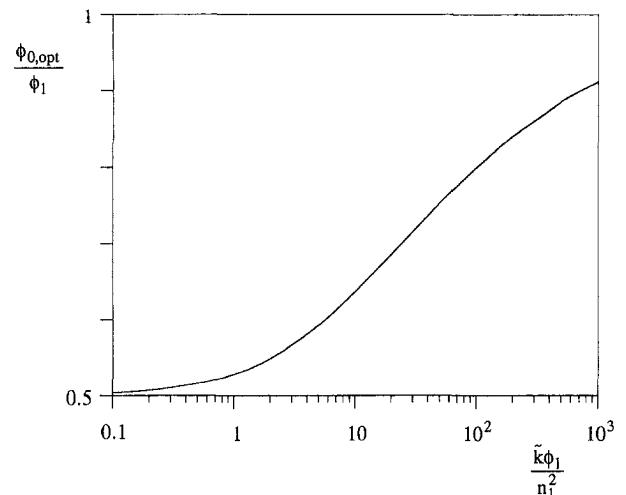
Fig. 9 The optimal k_p-volume fraction ratio $\phi_{0,opt}/\phi_1$ of the first-assembly design with unrestricted elemental features

in which the volume is fixed. In both approaches, the overall volume-to-point resistance decreases as the internal complexity of the high-conductivity path increases. In the growth method the number of constituents in each new higher-level assembly can be optimized. In the two design approaches illustrated in Sections 3 and 4 some of the number of constituents cannot be optimized, and are carried along, as parameters, on the road to higher complexity (e.g., n_2 in Fig. 4, and n_1 in Fig. 6). An important characteristic of the design method is that the effect of the number of constituents becomes weaker as that number increases (e.g., Fig. 6).

Even more important is that the growth and design approaches lead to designs that are comparable not only in overall performance but also in geometric appearance. Review, for example, the results for the overall volume-to-point resistance, as we have done in Fig. 6. Being the simplest, the growth method provides a useful shortcut to and an approximation of the architecture that would result at the end of the application of the fixed-volume design method.

In Fig. 6, the numerical value for the twice-minimized resistance of the first-assembly design with unrestricted elemental features (Table 1) is smaller than the corresponding analytical estimate (the design solution of Fig. 5). This discrepancy is explained by the fact that in the analysis of the design of Section 4 the elemental volumes were assumed to have adiabatic boundaries. When n_1 of these constituents were grouped together, the first assembly inherited $(n_1 - 1)/2$ internal adiabatic partitions, which were situated equidistantly between the D_0-thin blades. Internal partitions inhibit the free flow of heat through the volume. The first-assembly design optimized numerically in Table 1 did not have internal adiabatic partitions and, consequently, its overall resistance was lower than in the analytical solution.

To test this explanation we repeated the numerical work reported for $n_1 = 4$ in Table 1, however, this time we imposed the adiabatic-wall condition on the vertical plane situated halfway between the D_0 blades of the first assembly. The results of the double minimization of the overall resistance are $(\Delta T_1 k_0 / q''' A_1)_{mm} = 0.065$, $(H_1/L_1)_{opt} = 2.56$, $(D_1/D_0)_{opt} = 5.25$ and $\phi_{0,opt}/\phi_1 = 0.576$. These results show that, as expected, the thermal resistance is higher when the internal partitions are present. The optimized geometry, however, is practically insensitive to how the vertical midplane of the k_0 medium is modeled. This is an important conclusion, because what matters in design are the optimal dimensions of the structure that connects the volume to the point. From a design standpoint, the optimized *shapes* produced analytically are *robust*.

This conclusion is illustrated in Fig. 10, which shows side-by-side the isotherm patterns in the first-assembly design optimized numerically without (Fig. 10(a)) and with (Fig. 10(b)) internal adiabatic partitions. The curves of Fig. 10(a) and Fig. 10(b) correspond to the same isotherms, i.e., the same values of dimensionless internal temperature. The plane in which the isotherms of Fig. 10(b) are interrupted is the plane of the two adiabatic partitions. The isotherm patterns differ somewhat in the vicinity of the midplane partitions, but the external shape $(H_1/L_1)_{opt}$ and the internal shape of the two structures are nearly identical.

We are now in a position to evaluate the accuracy of the analytical growth and design results developed in Sections 2–4. We base this evaluation on the analytical first-assembly design with unrestricted elemental features (Fig. 5) in relation to the corresponding first assembly optimized numerically in Table 1. We just saw that to account for internal adiabatic partitions in the numerical solution makes very little difference in the optimized shapes of the first assembly *and* in the minimized global resistance. Then, with reference to Fig. 6, we conclude that the analytical solution ("design, Fig. 5") overestimates by a factor of order 5 the minimized global resistance of the first assembly ("numerical result, Table 1"). More important in a practical sense is the conclusion that the optimized geometry

(a)   (b)
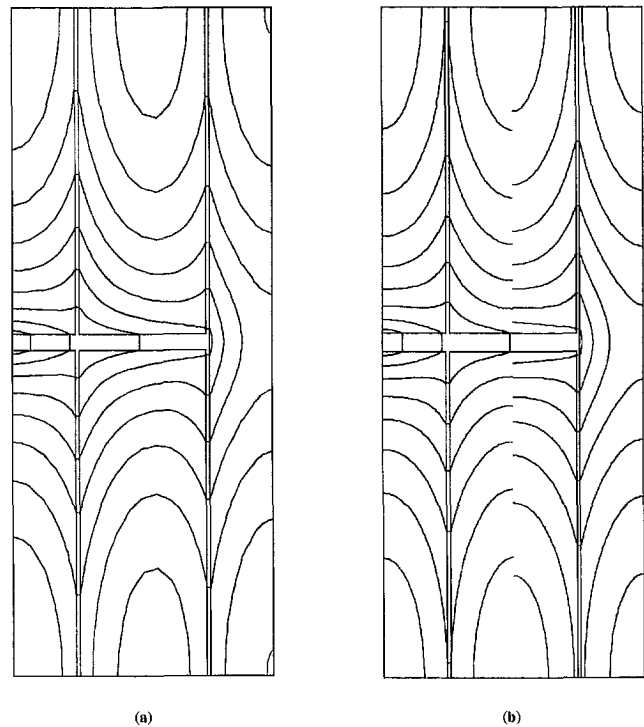
Fig. 10 The imperceptible effect of the adiabatic midplane partition on the geometry of the first assembly optimized numerically ($n_1 = 4$, $\tilde{k} = 300$, $\phi_1 = 0.05$): (a) without partition, (b) with partitions

anticipated analytically is close to the optimized geometry determined more laboriously, numerically.

Based on this test, we can expect the same degree of accuracy from the other analytical methods presented in Fig. 6, the growth method (Eq. (10)) and the design with restricted elemental features (Eq. (26)). Specifically, we can expect fairly good predictions for the geometric shapes that place the system close to the point of minimum global resistance, and only order of magnitude estimates of the minimized global resistance. It is only a coincidence that these two analytical methods predict global resistances that fall below the resistance of Fig. 5. This coincidence is responsible for the better agreement between the numerical result and the two lowest curves of Fig. 6. It is a *useful* coincidence, because if we remember Fig. 6 we may start any design of this type with the simplest method first (namely, the growth method), and expect from this first cut not only a fairly accurate image of the optimized architecture but also the least inaccurate global resistance estimate from the rough estimates that can be expected from all the analytical methods.

The correct path to the ultimate (exact) global optimum is clearly the numerical method that that led to Table 1. The number of elemental details (n_1) can be increased until costs (e.g., computation) indicate that the point of diminishing returns has been reached. Furthermore, the geometry that is being optimized can be endowed with considerably more degrees-of-freedom in order to provide additional flexibility in decreasing the global resistance. Two ways in which design flexibility can be achieved are discussed next.

Throughout this paper we used the word "optimized" quite freely. In each case, we meant that the geometry was optimized in the ways that were indicated specifically, and subject to the global constraints that were indicated specifically. We did not mean that the reported shapes are the ultimate—the absolute best—that could be conceived for minimum resistance in volume-to-point flow. The reason is that in order to keep our work simple, and to contrast the "growth" and "design" methods in the sharpest possible focus, we had to make several simplifying assumptions regarding the geometry that we were optimizing.

One example is the assumption that all the angles between a central k_p channel and its tributaries are equal to 90 deg. These angles too could have been allowed to vary, and the complexity and cost of the optimization work would have increased dramatically. We demonstrated this option in an earlier numerical study (Ledezma et al., 1997), where we discovered that when the k_p/k_0 ratio is of the order of 10^2 or larger, the optimal angles are indeed close to 90 deg. We also discovered that the global performance (overall volume-to-point resistance) of the geometry with optimized angles is practically the same as that of the geometry with assumed 90 deg angles. In other words, we discovered that certain geometric features such as the confluence angles play a very minor role, when the objective is that of *global* optimization. We discovered that the optimized geometry with 90 deg angles is *robust* with respect to such details.

Another example is the assumption that each k_p channel has constant thickness. It is possible to show analytically that if the thickness D_0 is allowed to vary with x along the k_p channel of the elemental volume, the optimal profile of the k_p channel is such that D_0 varies as $x^{1/2}$, where $x = 0$ marks the insulated (right end, Fig. 1) of the elemental k_p channel (Ledezma et al., 1997). The optimal "needles" have the familiar shape seen in nature: thick at the root and thin at the tip, with tips that are rounded (dull). The more important result is that the performance of the optimized elemental volume with optimally shaped $D_0(x)$ profile is nearly the same as that of the optimized elemental volume with constant-D_0 profile. In other words, the optimized geometry is robust with respect to the profile of each k_p channel. The channel profile and the confluence angles discussed in the preceding paragraph add themselves to the list of minor internal geometric details compiled in this paper—details that influence only in a weak way the optimized global performance of the given volume-to-point configuration.

Acknowledgment

References

Anand, N. K., Kim, S. H., and Fletcher, L. S., 1992, "The Effect of Plate Spacing on Free Convection Between Heated Parallel Plates," ASME JOURNAL OF HEAT TRANSFER, Vol. 114, pp. 515–518.

Aung, W., ed., 1988, *Cooling Technology for Electronic Equipment*, Hemisphere, New York.

Bar-Cohen, A., and Rohsenow, W. M., 1984, "Thermally Optimum Spacing of Vertical, Natural Convection Cooled, Parallel Plates," ASME JOURNAL OF HEAT TRANSFER, Vol. 106, pp. 116–123.

Bejan, A., 1997a, "Constructal-Theory Network of Conducting Paths for Cooling a Heat Generating Volume, *International Journal of Heat and Mass Transfer*, Vol. 40, pp. 799–816.

Bejan, A., 1997b, *Advanced Engineering Thermodynamics*, 2nd Ed., John Wiley and Sons, New York, Chapter 13.

Bejan, A., 1997c, "How Nature Takes Shape," *Mechanical Engineering*, Vol. 119, No. 10, pp. 90–92.

Bejan, A., and Ledezma, G. A., 1998, "Streets Tree Networks and Urban Growth: Optimal Geometry for Quickest Access between a Finite-Size Volume and One Point," *Physica A*, Vol. 255, pp. 211–217.

Bejan, A., and Errera, M. R., 1997, "Deterministic Tree Networks for Fluid Flow: Geometry for Minimal Flow Resistance between a Volume and One Point," *Fractals*, Vol. 5, pp. 687–695.

Bejan, A., and Tondeur, D., 1998, "Equipartition, Optimal Allocation, and the Constructal Approach to Predicting Organization in Nature," *Revue Générale de Thermique*, Vol. 37, pp. 165–180.

Chu, R. C., and Simons, R. E., 1994, "Cooling Technology for High performance Computers: IBM Sponsored University Research," *Cooling of Electronic Systems*, S. Kakac, H. Yüncü, and Hijikata, K., eds., Kluwer, Dordrecht, The Netherlands, pp. 97–122.

FIDAP, 1993, *Theory Manual*, v. 7, Fluid Dynamics International, Evanston, IL.

Kakac, S., Yüncü, H., and Hijikata, K., eds., 1994, *Cooling of Electronic Systems*, Kluwer, Dordrecht, The Netherlands.

Knight, R. W., Goodling, J. S., and Hall, D. J., 1991, "Optimal Thermal Design of Forced Convection Heat Sinks—Analytical," ASME *Journal of Electronic Packaging*, Vol. 113, pp. 313–321.

Ledezma, G. A., Bejan, A., and Errera, M. R., 1997, "Constructal Tree Networks for Heat Transfer," *Journal of Applied Physics*, vol. 82, pp. 89–100.

Peterson, G. P., and Ortega, A., 1990, "Thermal Control of Electronic Equipment and Devices," *Advances in Heat Transfer*, Vol. 20, pp. 181–314.

R. L. McMasters
e-mail: mcmaster@pp.msu.edu

J. V. Beck
Fellow ASME

Department of Mechanical Engineering,
Michigan State University,
East Lansing, MI 48824

R. B. Dinwiddie

H. Wang

High Temperature Materials Laboratory,
Oak Ridge, TN 37831-6062

Accounting for Penetration of Laser Heating in Flash Thermal Diffusivity Experiments

Since the early 1960s, the laser flash method of thermal diffusivity measurement has been used on a large variety of materials. Several parameter estimation methods have also been used in analyzing such experiments, employing various levels of sophistication. Estimation of thermal parameters, using the models developed as part of this research, is performed on experimental data from the Oak Ridge National Laboratory in Oak Ridge, TN. The material used is carbon bonded carbon fiber (CBCF) which is designed as an insulating material for atmosphere re-entry applications. Ambient temperatures in the experiments range from 800°C to 1200°C. The approximate thermal diffusivity of the material is 0.3 mm²/sec. This research investigates the penetration of the laser flash beyond the surface of the material being heated. Three heat transfer models are presented, each with different assumptions about the initial temperature distribution inside the material. An evaluation is made of the response of the methods to factors which may enter into the experimental process. This is done in quantitative terms so as to assess the adequacy of the models in comparison to one another.

1 Introduction

Prior to the widespread availability of high-speed computers for use in parameter estimation, simplified methods were utilized to facilitate rapid parameter estimate computation. When the procedure of laser flash diffusivity measurement was introduced in 1961, the primary means by which diffusivity was calculated involved the principle of "half-rise time." This pioneering work is described in Parker et al. (1961). Early models assumed a pulse heat addition to the incident side of the sample, and insulated conditions otherwise. Using these assumptions, the nondimensional time corresponding to the point where measured surface temperature on the nonheated side reaches half of its maximum, or equilibrium, temperature is 1.38 nondimensional time units. Based on this correlation, the relationship was established,

$$\alpha = \frac{1.38L^2}{\pi^2 t_{1/2}},$$ (1)

where L is the sample thickness and $t_{1/2}$ is the time corresponding to that at which measured temperature reaches half of the final, or equilibrium, temperature.

Numerous revisions to this method have been presented in the literature in subsequent years. Cowan (1963) provided accommodation for radiative heat losses from the sample surfaces. This modification required the analyst to enter correction charts with parameters such as ambient temperature, maximum sample temperature, and surface emissivity. The correction factors are then applied to the half-rise-time method described above. A similar method accounting for heat losses from the sample circumference is examined by Clark and Taylor (1975). Several test cases comparing this method with the Cowan method are examined by Clark and Taylor as well.

Later work incorporated the minimization of least-squares error as a means of estimating diffusivity and heat loss coeffi-

cient simultaneously. Early work in this area was performed by Koski (1981) and includes discussion on the conformance of the mathematical model to the laboratory measured data. Taylor (1979) also examines conformance of the mathematical model to the measured data for surface cases involving surface heat loss and finite pulse duration and shape. This effect has to do with the time duration of the flash. This paper by Taylor examines the residuals in various experiments, that is, the difference between the measured data and the mathematical model.

Further investigation into aspects of this experiment is made by Raynaud et al. (1989) in regard to the adequacy of various models. This discussion not only includes an examination of the residuals, but of the sequential estimates as well. More recently, the method of nonlinear regression using ordinary least squares has been applied to the flash diffusivity experiment by Beck and Dinwiddie (1996). This method has the advantage of allowing model flexibility to account for various phenomena by simultaneously calculating multiple parameters. Even more recently presented is the logarithmic method by Thermitus and Laurent (1997). This method approximates the direct solution to the heat transfer problem in logarithmic form and fits the data to this model to find parameters.

The present research work is based on the method of least squares and compares the measured data to the mathematical model by examining residuals. The foundational model includes three parameters: diffusivity, heat flux and Biot number. The standard deviation of the residuals in many of the experiments conducted with carbon bonded carbon fiber (CBCF) is noticeably higher than that of the anticipated measurement errors, pointing to some unresolved inadequacy in the model. Although large improvements are made in model conformance through simultaneous calculation of heat loss and diffusivity, a characteristic signature is evident in the residuals with the analysis of experiments for some materials. The shape of the signature generated from these models suggests that the "wave" of heat diffusing through the solid material arrives earlier than that predicted by conventional kinetic conduction. This implies that another mechanism is at work in these experiments, such as internal radiation or a penetration of the laser flash beyond the surface of the material.

The inadequacies of the three parameter model, which includes only diffusivity, heat flux and Biot number, do not seem

to be rectified by the inclusion of internal radiation as a mode of heat transfer in the model. This was investigated through extensive testing of a direct solution which modeled internal radiation as a diffusive process, a model suitable for optically thick materials like CBCF. Better results were obtained when the assumed time of the flash was considered to have occurred prior to time zero. This indicates that the initial temperature distribution caused by the flash can be approximated as a time shift. The time interval between the flash and time zero in this model is treated as a parameter. Also investigated were various forms of internal deposition of the flash which are treated as initial condition temperature distributions. The form of deposition which emerged with the most successful conformance to the measured data was an initial temperature distribution of exponential shape with the highest temperature on the incident face of the sample.

2 Mathematical Formulation

Assuming constant conductivity with respect to temperature, the one-dimensional differential equation for this problem is

$$\rho c_p \frac{\partial T}{\partial t} = k \frac{\partial^2 T}{\partial x^2} . \qquad (2)$$

The boundary conditions are

$$-k\left[\frac{\partial T}{\partial x}\right]_{x=0} = q_0 \delta(t) + h(T_\infty - T_{x=0}) \qquad (3)$$

$$-k\left[\frac{\partial T}{\partial x}\right]_{x=L} = h(T_{x=L} - T_\infty). \qquad (4)$$

In these equations, ρ is the density, c_p is the specific heat, T is temperature, t is time, k is thermal conductivity, q_0 is the magnitude of the heat pulse, typically expressed in joules per square mm, $\delta(t)$ is the Delta Dirac function, h is the heat transfer coefficient, L is the sample thickness, and x is the spacial dimension. Prior to the initiation of the flash at $t = 0$, the sample is assumed to be at ambient temperature, T_∞. The Green's function solution equation given in Beck et al. (1992) is

$$T(x, t) = T_\infty + \frac{\alpha}{k} \int_{\tau=0}^t G_{X33}(x, x' | t, \tau) q_0 \delta(\tau) d\tau \qquad (5)$$

where the Green's function for X33, that is a one-dimensional conduction problem with convection on both surfaces, is given as

$$G_{X33}(x, x' | t, \tau) = \frac{2}{L} \sum_{m=1}^\infty e^{-\beta_m^2 \alpha(t-\tau)/L^2} \frac{\eta_m(x)\eta_m(x')}{N_m} \qquad (6)$$

where

$$N_m(x) = (\beta_m^2 + \text{Bi}_1^2)\left[1 + \frac{\text{Bi}_2}{\beta_m^2 + \text{Bi}_2^2}\right] + \text{Bi}_1 \qquad (7)$$

$$\eta_m(x) = \beta_m \cos\left(\beta_m \frac{x}{L}\right) + \text{Bi}_1 \sin\left(\beta_m \frac{x}{L}\right). \qquad (8)$$

In these equations, Bi_1 and Bi_2 refer to the Biot numbers on the right and left-hand sides of the specimen, respectively. Since the temperature measuring instrument used in the flash diffusivity experiments reports voltage proportional to temperature rise above the experimental ambient temperature, it is convenient to set $T_\infty = 0$ in the solution. Since the same medium exists on both sides of the sample at approximately the same temperature, it is also reasonable to set $\text{Bi}_1 = \text{Bi}_2$. The solution now becomes

$$T(L, t) = \frac{\alpha q_0}{k} \int_{\tau=0}^t \frac{2}{L} \sum_{m=1}^\infty e^{-\beta_m^2 \alpha(t-\tau)/L^2} A_m \delta(\tau) d\tau \qquad (9)$$

where

$$A_m = \frac{\beta_m[\beta_m \cos(\beta_m) + \text{Bi} \sin(\beta_m)]}{\beta_m^2 + \text{Bi}^2 + 2\text{Bi}} . \qquad (10)$$

Integrating and nondimensionalizing, we have

$$T^+(L, t) = \frac{T(L, t)kL}{\alpha q_0} = 2 \sum_{m=1}^\infty e^{-\beta_m^2 \alpha t/L^2} A_m. \qquad (11)$$

The eigenvalues, β_m, are calculated by satisfying the following eigen condition:

$$\tan(\beta_m) = \frac{2\beta_m \text{Bi}}{\beta_m^2 - \text{Bi}^2} . \qquad (12)$$

This solution was used to analyze data measured at Oak Ridge National Laboratory using CBCF material. The three parameters simultaneously estimated were

1 thermal diffusivity, α (mm^2/sec),
2 flash heat flux, q_o (joules/mm^2), and
3 Biot number, $\text{Bi} = hk/L$, dimensionless.

These parameter estimates were found, through the method of ordinary least squares, by minimizing the following expression:

$$S = \sum_{i=1}^n (Y_i - T_i)^2, \qquad (13)$$

where Y_i represents the temperature measurements, T_i represents the calculated temperatures, and n is the number of measurements.

The parameter estimation results using this method were approximately the same as those obtained from the simpler methods discussed in the Introduction, such as the methods of Parker, Cowan, Clark, and Taylor. A systematic disparity was found between the calculated temperatures and the measured temperatures which indicates that the model is not fully accounting for all of the aspects of the physics of the problem. This disparity is most easily observed when plotting the residuals, that is, the difference between measured and calculated temperatures as a function of time.

Nomenclature

a = penetration coefficient (mean free path of a photon)
Bi = Biot number (hL/k)
c_p = specific heat
e_i = residual
$G_{X33}(x, x', t, \tau)$ = Green's function for the X33 case
h = convective heat transfer coefficient

k = thermal conductivity
k_r = radiative conductivity
n = number of measurements
L = sample thickness
q_0 = magnitude of the laser pulse
t = time
t^+ = nondimensional time ($\alpha t/L^2$)
$t_{1/2}$ = half-rise time
T = temperature

T_∞ = experiment ambient temperature
x = spacial dimension
Y_i = temperature measured at time step i
α = thermal diffusivity
κ = extinction coefficient
ρ = density
σ_b = Stefan-Boltzmann constant
σ_r = standard deviation of residuals

Table 1 Parameter estimation using the Model 1 procedure on a Model 2 direct solution

	Diffusivity	Heat flux	Biot number	Δt
Actual Values	1	1	1	0.01
Estimated Values	1.144	0.9102	0.8314	N/A

A simple attempt at more accurately modeling the Oak Ridge National Laboratory measured data was pursued by shifting the time scale of the measured data by an amount, designated as Δt, from the given "time zero" of the experiment. In this case, an exact solution was used of the differential equation as given above and was simply offset by a predetermined Δt. This time shift served to effectively advance the time of the heating pulse prior to time zero. In order to estimate an accurate effective time shift of the heating pulse, the quantity Δt was treated as a parameter. For future reference, the initial model presented here with no time shift is designated as Model 1 and the time shift model is designated as Model 2.

Another way of considering the time-shift model is to think of it as an initial condition of penetrated heating. This initial temperature distribution happens to have a form which is somewhat similar to an exponential temperature distribution. As a simulated experiment, a direct solution generated using Model 2 was analyzed by the three-parameter model, Model 1. Table 1 shows the direct solution parameters and the estimated parameters for this problem. A considerable error of 14 percent arises in the estimated value for diffusivity due to the introduction of the time offset of .01 units of nondimensional time. The time shift toward early heating seems to be a phenomenon by which the more rapid initial heat transfer could be manifest in the actual laboratory experiment.

The actual laboratory data from Oak Ridge National Laboratory was also analyzed using Model 2. The standard deviation of these residuals is 0.009935, which is extremely small in comparison with the peak temperature measurement, which is typically on the order of 6 in this set of experiments. By comparison, the estimated standard deviation of the residuals generated from using Model 1 as the mathematical model is approximately 0.04, over four times the magnitude generated using Model 2.

The most significant aspect of this analysis is that the estimates of the parameters of interest are substantially altered between Model 1 and Model 2. The estimate for diffusivity is 26 percent lower and Biot number is 65 percent higher using Model 2 as opposed to Model 1. As can be seen from the residuals, the estimates using Model 2 appear to be more valid than those obtained using Model 1. Since there is no reason to assume that the Oak Ridge National Laboratory data were recorded inaccurately and since there is no time shift between the measurement time scale and the true time scale, a logical physical explanation for the apparent time shift is radiation penetration.

Since the flash method of thermal diffusivity measurement has been in use for several decades, equipment designed for conducting flash diffusivity experiments is available for purchase in the form of premanufactured systems. Two companies which sell such equipment are Holometrix, Inc. of Bedford, MA and Anter Corporation of Pittsburgh, PA. Measurements were made as part of this research by equipment made from both these manufacturers. A majority of the sample measurements, however, were made using the Anter system at Oak Ridge National Laboratory. In this system, the sample is held horizontally and the laser flash is introduced vertically, incident on the top of the sample. The module used for the experiments in this research was the 500°C to 2500°C graphite furnace.

Samples held at high ambient temperatures in a furnace are typically in a vacuum or an inert gas in order to minimize chemical interaction with the surroundings. The laser flash is generated on the outside of the furnace and passes through a spectrally neutral neodymium-glass window in order to reach the sample. Since the sample is small, the laser flash is able to cover the entire surface to promote even heating. The laser has a wavelength of 1.06 microns. The laser has a maximum pulse energy of 35 joules and typically has a duration of 0.8–1.0 milliseconds. The pulse in this system, as a function of time, is triangular in shape. This pulse magnitude is adjustable and is established based on an initial operator-assigned maximum. Subsequent laser flashes for a given experiment are adjusted through a trial and error process, facilitated by the computer control system, after the initial flash.

The infrared temperature sensor used in the experiment is also physically located outside the sample furnace and takes readings through a spectrally noninteractive glass window at the bottom of the furnace. The measured signal is passed through a fiber optic cable to the actual detector unit. The detector unit includes a pre-amplifier, which allows several furnaces to be served by the same infrared temperature detector without moving the detector itself. Additionally, the sensitive electronic components of the detector are protected from the high temperatures of the furnace by the physical separation. The Oak Ridge machine uses two detectors: a silicon photodiode detector for high-temperature applications and cryogenically cooled indium-antimony detector for low-temperature applications.

The output of the detector is usually expressed in terms of volts, which are directly proportional to temperature. The detector is normally calibrated to read zero for each experiment at furnace temperature. The final signal recorded in the data acquisition equipment is an expression of a signal proportional to temperature rise above furnace ambient temperature.

The temperature-measuring instruments tend to perform better in higher temperature experiments due to the more distinctive spectral signal emitted at high temperatures. An additional requirement for low-temperature experiments is that liquid nitrogen must be used to provide a cryogenic environment for the detector. This is necessary so as to minimize background radiation not related to the temperature measurement of the sample. In spite of this precaution, more background noise typically exists in measurements taken below 600°C than is exhibited above that temperature.

A significant amount of investigation was performed as part of this research on the possibility of heat transfer by internal radiation through the solid material as a participative medium. The equation governing this type of transport as given by Siegel and Howell is

$$\rho c_p \frac{\partial T}{\partial t} = \frac{\partial T}{\partial x}\left(k \frac{\partial T}{\partial x} - q_r\right) \qquad (14)$$

where

$$q_r = -k_r \nabla T \quad \text{and} \quad k_r = \frac{16\sigma_b T^3}{3\kappa}. \qquad (15)$$

In this context, k_r can be thought of as the "radiative conductivity." The κ term is known as the "extinction coefficient" which is the sum of the absorption coefficient and the scattering coefficient, each having units of inverse length. The reciprocal of the extinction coefficient represents the mean free path of a photon in the material, or the mean distance traveled without an absorption or scattering interaction. The term σ_b represents the Stefan-Boltzmann constant.

This equation was solved numerically and families of direct solutions were generated. These direct solutions were in turn analyzed as simulated experiments in order to determine the extent to which internal radiation might have been responsible for the systematic signature observed in the residuals. The residual curves generated from these tests were mirror images of the residual curves generated from the laboratory data, demonstra-

ting that some other mechanism was causing the signature in the residuals in the laboratory data.

Even though there seems to be no evidence of internal radiation as a heat transfer mechanism subsequent to the flash, it is still possible that the radiation wavelength of the flash itself is such that a non-negligible mean free path exists inside the material for photons of that energy. The manifestation of this phenomenon would be best modeled as an initial condition since the flash takes place over such a short period of time. This model is very similar to Model 2 in terms of a nonuniform initial temperature distribution, but is based on a more reasonable physical explanation as to its origin.

For Model 3, an exponential temperature distribution was chosen since this most closely corresponds to the principle embodied in Bouger's Law, as discussed in Siegel and Howell (1981). In order to calculate the direct solution for this model, a Green's function solution was chosen for convective conditions at both boundaries and zero ambient temperature. The Green's function solution equation for this problem reduces to a single integral for the initial condition

$$T(x, t) = \int_{x'=0}^{L} G_{X33}(x, t | x', 0) F(x') dx' \qquad (16)$$

where $F(x')$ is the initial temperature distribution in the material, or in this case

$$F(x') = \frac{q_0 e^{-x'/a}}{\rho c_p a (1 - e^{-L/a})} \qquad (17)$$

where a is a measure of the penetration of the flash, the mean free path of a photon in the material. The reciprocal of this term is the extinction coefficient, κ. The denominator of Eq. (15) is obtained by normalizing the exponential temperature distribution to the magnitude of the heating that brought about the temperature rise. In this case

$$q_0 = \rho c_p \int_{x=0}^{L} F(x) dx. \qquad (18)$$

The $F(x)$ defined above satisfies this equation. The Green's function for X33 given by Eq. (6) in Eq. (13) gives

$$T(L, t) = \frac{2q_0 \alpha}{kL(1 - e^{-L/a})} \sum_{m=1}^{\infty} e^{-\beta_m^2 \alpha t/L^2} \frac{A_m C_m}{1 + \left(\frac{\beta_m a}{L}\right)^2} \qquad (19)$$

where

$$C_m = \left(\frac{a\beta_m^2}{L} - \mathrm{Bi}\right) e^{-L/a} \sin(\beta_m)$$

$$- \left(\beta_m + \frac{a\beta_m \mathrm{Bi}}{L}\right) (e^{-L/a} \cos(\beta_m) - 1). \qquad (20)$$

3 Model Evaluation

Figure 1 displays the sensitivity coefficients for the exponential penetration model, Model 3. These are obtained by differentiating the direct temperature solution with respect to each parameter. The plots shown in Fig. 1 are of the "modified" sensitivity coefficients which are the derivatives mentioned above multiplied by the applicable parameter. In general,

$$X_n = p_n \frac{\partial T}{\partial p_n}, \qquad (21)$$

where X_n is the sensitivity coefficient and p_n is the applicable parameter. The magnitudes of these sensitivity coefficients can be compared directly since they all have units of temperature. Sensitivity coefficients in a well-designed experiment are large

and uncorrelated. Uncorrelated sensitivity coefficients have shapes which are different from one another. If one is positive and the other negative, they may be correlated if their ratio for the duration of the experiment is approximately constant.

Since there are four parameters in the penetration model, there are four sensitivity coefficients. Each one is graphed as a function of time in Fig. 1. The sensitivity coefficient for the penetration parameter, a, appears to be somewhat correlated with the heat flux sensitivity coefficient. Experience has shown, however, that it is unique enough to allow independent estimation of the four parameters. In spite of the apparent correlation between diffusivity and a, and between heat flux and Biot number, the parameter estimates converged, normally in five iterations.

Next, Models 1, 2, and 3 were tested on CBCF data measured at 700°C at Oak Ridge National Laboratory. In contrast to the first three models, the standard deviation of the residuals for Model 2, which treats the time-shift of the heating pulse as a parameter, gives significantly improved results over each of the other models. Table 2 shows the parameters obtained by each method. The column entitled "Δt or a" refers to the time shift, in seconds, or the penetration distance, in mm, as applicable for the model. The column entitled "Resid" refers to the estimated standard deviation of the residuals, which are in units of voltage which is proportional to temperature. A large reduction in residuals is gained in implementing the time-shift model, Model 2, over the simple three-parameter model. Additional gains are realized when utilizing the exponential penetration feature of Model 3. The results using Models 2 and 3 are somewhat similar in that both return lower values for diffusivity than the simpler Model 1. The estimated Biot number is also higher in each of these cases than that calculated by Model 1. These factors suggest that both models are, to some extent, accomplishing the same thing through different means. That is, they both model a more rapid heat transport in the early time steps of the experiment than would be predicted by the conventional Model 1 assumptions.

In comparing Models 1 and 3 on actual laboratory data, Fig. 2 shows residuals for the Oak Ridge National Laboratory data. This figure shows a near-elimination of the signature associated with Model 1 when using Model 3. The signature, generated from the Model 1 analysis of the laboratory data, is evidently caused by some manner of penetration of the flash into the material at the instant of heating.

Tables 3 and 4 present the results of Models 1 and 3, respectively, in analyzing samples of varying thickness. Two samples were tested of each of two thicknesses of the CBCF material, for a total of four samples. The sample thicknesses tested were 1.0 mm and 1.2 mm and the samples of these thicknesses are differentiated by the designations (a) and (b). Due to variations in the manufacturing process, there are considerable differences in diffusivity between samples, even of the same thickness. The standard deviation of the residuals in these tables is lower in each experiment when analyzed using Model 3. Additional validation of the penetration model is provided by the consistence between the penetration depth parameter estimates obtained from samples of different thickness. The value for this parameter seems to be nominally 80 microns in each case. Finally, validation is provided in that the diffusivity values found for the various samples are closer to one another when using Model 3 than are the values obtained using Model 1.

4 Additional Considerations

Other methods by which competing models are evaluated include comparison of sequential estimates and confidence regions. The sequential estimates are arrived at by estimating parameters at each time step by adding one measurement at a time to the sum of squares expression given in Eq. (13). When the experiment is approximately half over, the estimates should
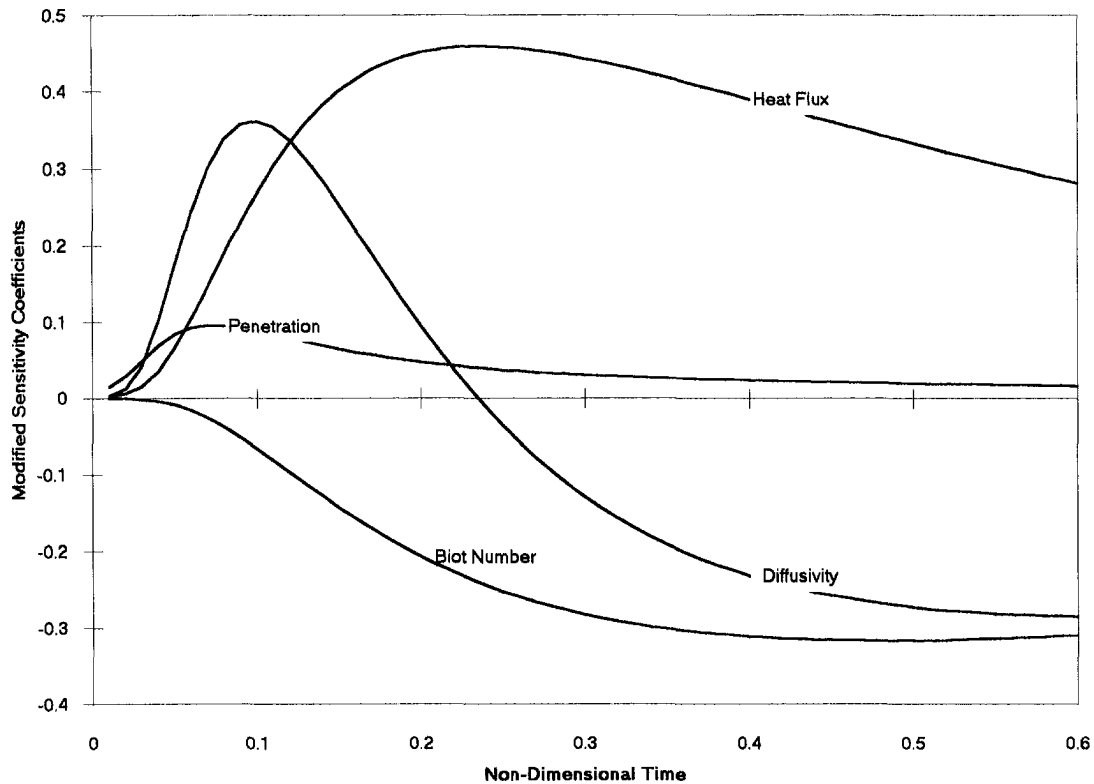
Fig. 1 Modified sensitivity coefficients for model 3 ($\alpha = 1$, $q_0 = 1$, Bi = 1, and $a = 0.1$)

not change significantly with the addition of measurement data. Parameter estimates which waver significantly in the last half of the experiment usually indicate a model which is not well suited to the physics of the experiment. Additionally, models which have a larger number of parameters tend to be inherently less stable than simpler models. In the present case, the sequential estimates generated with Model 3 are not superior to those of Model 1.

A similar evaluation means is the comparison of confidence intervals for the parameters. The confidence intervals can be arrived at by approximating the covariance matrix as the product of the variance of the measurement errors and the identity matrix.

$$\psi = \sigma^2 \mathbf{I} \tag{22}$$

With this assumption, the confidence interval for the parameter of interest can be found by multiplying the corresponding term in the $(\mathbf{X}^T \mathbf{X})^{-1}$ matrix by the variance and the t statistic for the desired confidence region. As with the comparison of sequential estimates, the confidence regions tend to become wider for models using more parameters, due to the inherent instability of solving a larger number of simultaneous equations. The confidence regions for Model 3 are not an improvement over those of Model 1.

As experiments are performed over a range of temperatures, individual values of the parameters are normally reported at each temperature. Polynomial curves can be approximated using

Table 2 Parameter estimation comparing Models 1, 2, and 3 on actual data taken at 700°C

Model	Diffusivity	Heat flux	Biot number	Δt or a	Resid
1	0.3400	19.138	1.2765	N/A	0.03202
2	0.3027	22.203	1.5550	0.0121	0.01212
3	0.3066	19.753	1.5178	0.0682	0.01098

these points, in order to express the value of these parameters as functions of temperature. An alternative to using the individual experimental results to construct the polynomial relationships is to analyze individual experiments sequentially in a collaborative fashion to obtain the temperature dependence as discussed in Beck and Osman. One advantage of this method is that individual experiments are automatically weighted in comparison with one another based on the number of data points collected in each experiment. Moreover, the experiments can each be assigned weighting factors in proportion to the degree of reliability of each experiment.

Estimation of the first three parameters, as in previous cases, is accomplished by approximately minimizing the following expression:

$$S_1 = \sum_{j=1}^{M} \sum_{i=1}^{N} (Y_i - T_i)_j^2 \tag{23}$$

where the index j refers to the individual experiment and the index I refers to each individual measurement within the applicable experiment.

Table 5 compares the estimates arrived at for diffusivity and Biot Number using three methods. These are

1 individual experiment results averaged for each temperature at which more than one experiment was performed.
2 fitting a least-squares parabola through the individual experimental results.
3 using all of the experiments in a sequential estimation scheme as described above.

As shown in the table, the results are very close between all of the methods. In the case of these particular experiments from Oak Ridge National Laboratory, the number of measurements for each experiment was approximately the same. Had this not been the case, or if one experiment had been weighted more heavily than another, the results may not have been this close.

Figure 3 shows the results from this table in graphical form. Superimposed on the sequential results are the results from
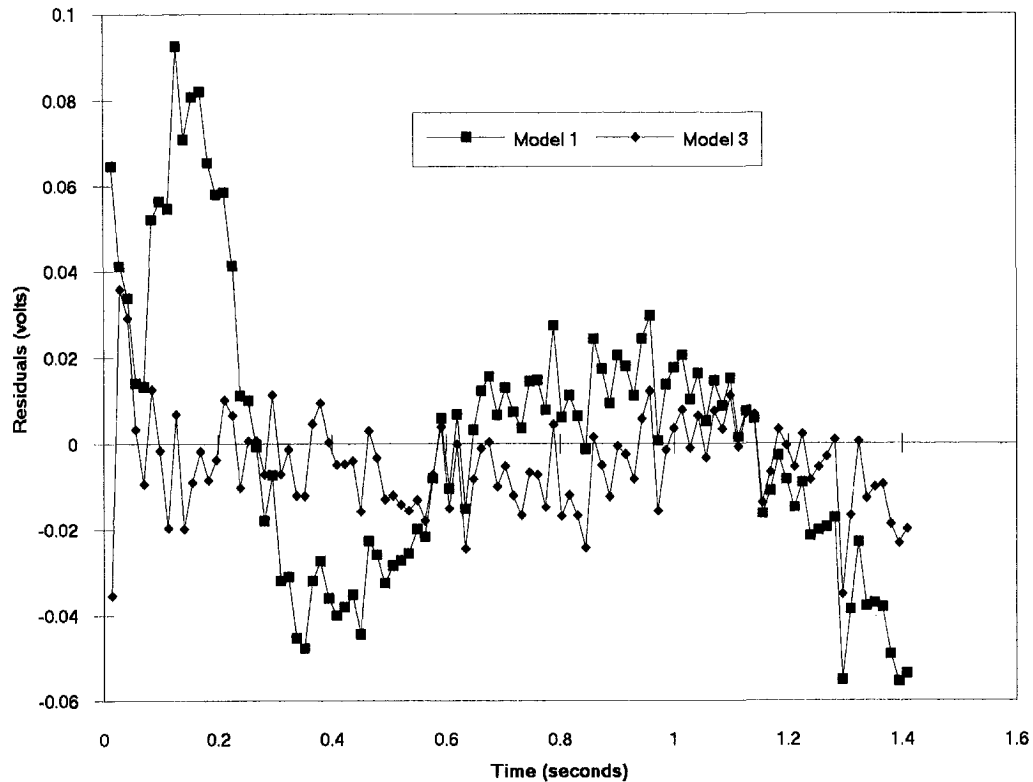
Fig. 2 Residuals from CBCF samples at 700°C comparing Models 1 and 3

Table 3 CBCF samples measured at ORNL 800°C using the nonpenetrating model (Model 1)

Sample	Shot	Diffusivity	Biot number	Residual standard deviation
1.0 mm (a)	1	0.29372	2.16129	0.01743
1.0 mm (a)	2	0.29521	2.16418	0.01773
1.0 mm (a)	3	0.29474	2.18856	0.01827
1.0 mm (b)	1	0.26229	2.44981	0.01483
1.0 mm (b)	2	0.26362	2.43437	0.01448
1.0 mm (b)	3	0.26386	2.44566	0.01520
		(0.276 ave)		
1.2 mm (a)	1	0.35628	2.10463	0.01726
1.2 mm (a)	2	0.35028	2.39603	0.01865
1.2 mm (a)	3	0.35182	2.3996	0.01989
1.2 mm (b)	1	0.31311	2.7485	0.01251
1.2 mm (b)	2	0.31985	2.64612	0.01323
1.2 mm (b)	3	0.31887	2.72847	0.01379
		(0.332 ave)		

Table 4 CBCF samples measured at ORNL at 800°C using the penetrating model (Model 3)

Sample	Shot	Diffusivity	Biot number	Penetration	Residual standard deviation
1.0 mm (a)	1	0.25193	2.99722	0.08086	0.00955
1.0 mm (a)	2	0.25389	2.98195	0.08028	0.009624
1.0 mm (a)	3	0.25335	3.0202	0.0803	0.009908
1.0 mm (b)	1	0.22765	3.3298	0.0773	0.013172
1.0 mm (b)	2	0.22959	3.28179	0.07658	0.01307
1.0 mm (b)	3	0.22935	3.31184	0.07701	0.013565
		(0.240 ave)			
1.2 mm (a)	1	0.31202	2.82292	0.08832	0.006764
1.2 mm (a)	2	0.31327	3.02372	0.08372	0.006259
1.2 mm (a)	3	0.31443	3.03208	0.08401	0.006966
1.2 mm (b)	1	0.284	3.39654	0.07632	0.009332
1.2 mm (b)	2	0.29128	3.23404	0.07545	0.008824
1.2 mm (b)	3	0.28988	3.35047	0.07584	0.009762
		(0.300 ave)			

Table 5 Sequential versus individual estimation

Ambient temperature	Average individual	Least squares curve fit	Sequential method
Diffusivity			
100	.32461	.32447	.32748
400	.31351	.31154	.31288
500	.31184	.31517	.31785
600	.32691	.32277	.32775
700	.33277	.33434	.34257
Biot number			
100	.15379	.15874	.14343
400	.53483	.52030	.50472
500	.74180	.70679	.69697
600	.86154	.92627	.92513
700	1.20691	1.17873	1.18921

analyzing experiments individually. The results from the sequential experiment method basically conform to the parameter values obtained by analyzing the experiments individually. One area of exception is in the region of the three highest temperatures at which the experiments were conducted.

Particularly, the results for Biot Number taken at 600°C are not in conformance with the assumed parabolic temperature dependency used in the sequential experiment method.

Diffusivity, the parameter of interest, is remarkably constant throughout the temperature range in which these experiments were conducted. This has proven true in both the sequential and individual experiment analysis cases.

5 Conclusions

When undertaking a parameter estimation problem, it is important to examine the residuals in order to determine the adequacy of the model used. A least-squares or maximum likelihood approach can yield substantial improvements over more simplified methods because of the flexibility available in selecting appropriate direct solutions. When using a least-squares
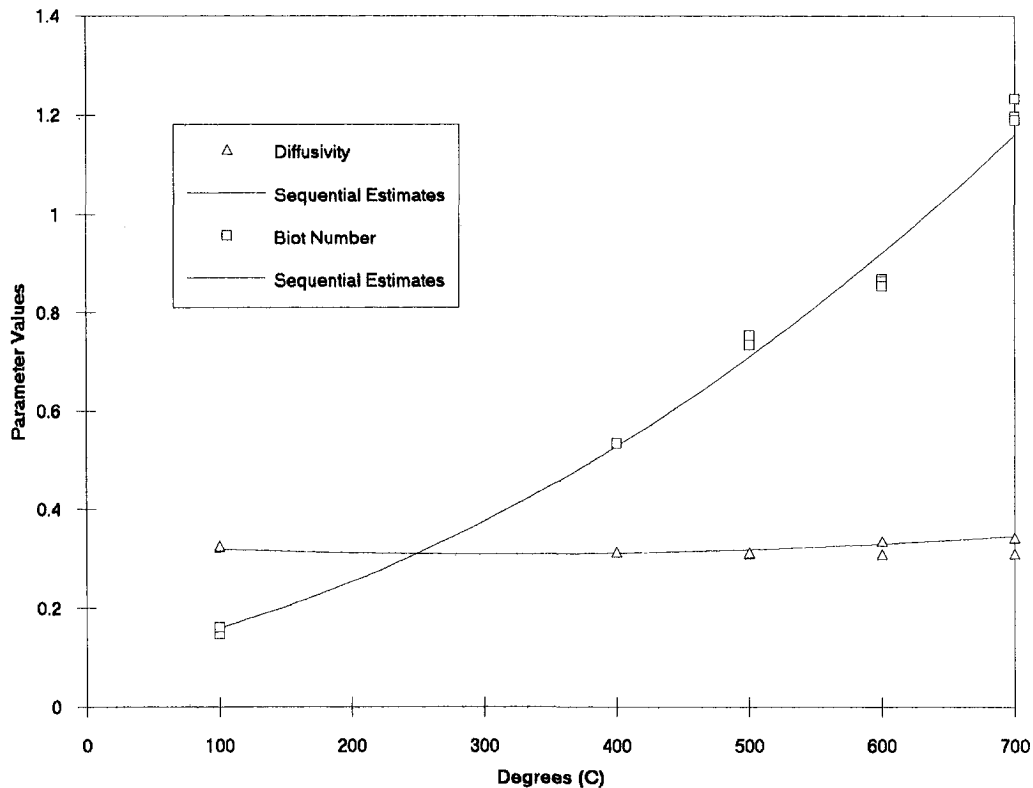
Fig. 3 Parabolic fit for parameter using simultaneous experiment analysis

approach, the choice of a direct solution model can have a significant impact on the value of the estimated parameter.

Of the models presented here, Model 1 seems most appropriate for samples which are either completely opaque or are well coated such that no penetration is made by the flash. If neither Model 2 nor 3 shows any improvement over Model 1 for a given experiment, it can be reasonably assured that no type of flash penetration is present.

Models 2 and 3, which account for flash penetration, produced values for diffusivity which were substantially lower than those produced by Model 1. This is also to be expected since, with flash penetration, the temperature rise on the measured surface comes more quickly than with no penetration. A model which does not account for penetration would interpret this early rise as a higher diffusivity.

For cases where little or no penetration occurs, there is no advantage to utilizing the advanced models since the parameters measuring penetration are estimated as being very small in magnitude and the confidence regions for these parameters are extremely large. Moreover, the values estimated by the advanced models for diffusivity were virtually unchanged from those estimated using Model 1, with no improvement in the residuals when analyzing opaque materials. In these cases, the advanced models prove to be more of a liability than an asset.

Although the values estimated for diffusivity using the penetration models for cases exhibiting penetration were not radically different from those estimated using Model 1, there is a higher degree of confidence in the accuracy of the estimates. More importantly, the differences in estimated diffusivity are large enough to affect design considerations for applications of re-entry heat shields. The basis of the higher degree of confidence is the removal of a characteristic signature in the residu-

als, the lower standard deviation of the residuals and the consistent estimates for flash penetration depth between samples of varying thicknesses. These models achieve a higher level of agreement with the measured data.

References

Beck, J., and Osman, A., 1991, "Sequential Estimation of Temperature Dependent Thermal Properties," High Temperatures–High Pressures, Vol. 23.

Beck, J., Cole, K., Haji-Sheikh, A., and Litkouhi, B., 1992, Heat Conduction Using Green's Functions, Hemisphere Publishing, Washington DC.

Beck, J., and Dinwiddie, R., 1996, "Parameter Estimation Method for Flash Thermal Diffusivity with Two Different Heat Transfer Coefficients," Proceedings from 23rd Thermal Conductivity Conference, Technomic Publishing, Lancaster, PA.

Beck, J., 1998, "Parameter Estimation Concepts and Flash Diffusivity Application," Proceedings of the Second International Conference on inverse problems in Engineering: Theory and Practice, Le Croisic, France, to be published.

Beck, J., 1999, "Inverse Problems in Heat Transfer," Proceedings of the Institute of Mathematics and its Applications Conference, Bradford England, to be published.

Clark, L., and Taylor, R., 1975, "Radiation Loss in the Flash Method for Thermal Diffusivity," Journal of Applied Physics, Vol. 26, No. 2, pp. 714–719.

Cowan, R., 1963, "Pulse Method of Measuring Thermal Diffusivity at High Temperature," Journal of Applied Physics, Vol. 34, No. 4, pp. 926–927.

Koski, J., 1981, Improved Data Reduction Methods for Laser Pulse Diffusivity Determination with the use of Minicomputers, National Technical Information Service, Springfield Va.

Parker, W., Jenkins, Butler, C., and Abbott, G., 1961, "Flash Method of Determining Thermal Diffusivity, Heat Capacity and Thermal Conductivity," Journal of Applied Physics, Vol. 32, No. 9, pp. 1679–1684.

Raynaud, M., Beck, J., Shoemaker, R., and Taylor, R., 1989, "Sequential Estimation of Thermal Diffusivity for Flash Tests," Proceedings from 20th Thermal Conductivity Conference, Plenum Publishing, pp. 305–321.

Siegel, R., and Howell, J., 1981, Thermal Radiation Heat Transfer, Hemisphere, New York.

Taylor, R., 1979, "Heat Pulse Thermal Diffusivity Measurements," High Temperatures–High Pressures, Vol. 11, pp. 43–58.

Thermitus, M., and Laurent, M., 1997, "New Logarithmic Technique in the Flash Method," International Journal of Heat and Mass Transfer, Vol. 40, No. 17.

The Effect of Periodic Unsteady Flow on Aerodynamics and Heat Transfer on a Curved Surface

L. Wright

M. T. Schobeiri
e-mail: tschobeiri@mengr.tamu.edu

Turbomachinery Performance Laboratory,
Texas A&M University,
College Station, TX 77843-3123

Aerodynamic and heat transfer investigations were performed on a constant curvature curved plate in a subsonic wind tunnel facility for various wake passing frequencies under zero pressure gradient conditions. Steady and unsteady boundary layer transition measurements were taken on the concave surface at different wake passing frequencies in which a rotating squirrel cage was used to generate the unsteady wake flow. The data were analyzed using time-averaged and ensemble averaged techniques to provide insight into the growth of the boundary layer and transition. Ensemble averaged turbulence intensity contours in the temporal spatial domain showed that transition was induced for increasing wake passing frequency and structure. The local heat transfer coefficient distributions for the concave and convex surfaces were determined for each wake passing frequency using a liquid crystal heat transfer measurement technique. Aerodynamic and heat transfer investigations showed that higher wake passing frequencies caused earlier transition on the concave surface. Local Stanton numbers were calculated on the concave surface and compared to Stanton numbers predicted using a boundary layer and heat transfer calculation method. On the convex side, no effect of wake passing on heat transfer was observed, due to a separation bubble that induced transition.

1 Introduction

The flow within a gas turbine component is characterized as periodic unsteady wake flow due to the interaction between the rotor and stator. The unsteady wakes, which are the result of a velocity defect that occurs at the trailing edge of each turbine blade, pass through the following blade rows altering the natural boundary layer development, the boundary layer transition region, the efficiency of the blade rows, and the heat transfer characteristics of each cascade. From a thermal design point, knowledge of the state of the boundary layer is crucial for design of cooling schemes. These schemes allow turbines to operate reliably at higher temperatures which result in increased thermal efficiency and higher specific power. Successful prediction of boundary layer transition enables designers to reliably determine the turbine stage efficiency and heat transfer characteristics. However, partially due to a lack of understanding of the interaction of the unsteady wakes, boundary layer transition has not been predicted reliably. This investigation focuses on the effect that periodic unsteady wakes have upon boundary layer transition and convective heat transfer characteristics of a curved plate which simulates the pressure surface of a turbine blade. This is one of the few experiments where heat transfer on a curved surface under the influence of unsteady wakes has been investigated. The data presented in this paper can be used for further testing of CFD codes. Also, through proper digital signal processing techniques for intermittency, a transition model under unsteady wake flow conditions can be developed from the aerodynamic data. The intermittency analysis is explained in a separate paper by Chakka and Schobeiri (1997).

Experimental investigations on the effect of periodic unsteady flow on a concave surface were performed by Schobeiri and Pardivala (1992), Schobeiri and Radke (1994), and Schobeiri et al. (1995a, b). Schobeiri and Radke observed that the wake flow affects boundary layer transition leading to the formation

of a *primary* boundary layer that possesses a quasi-steady characteristic and a periodic unsteady *secondary* boundary layer resulting from the interaction of the wake strips and the surface of the curved plate. The secondary boundary layer was found to undergo a periodic transition process and convect towards the primary boundary layer leaving becalmed quasi-laminar regions. This work was continued by Schobeiri et al. (1995a) who studied the effects of wake passing on boundary layer transition on a curved plate with zero streamwise pressure gradient. It was found that an increase in frequency results in a shift of transition towards the leading edge due to increased turbulence.

The wake effect has been studied in a single stage turbine by Hodson (1984) and Addison and Hodson (1990a, b) and in a linear turbine cascade facility by LaGraff et al. (1989), Ashworth et al. (1989), Liu and Rodi (1992), and Schobeiri et al. (1995b). Boundary layer transition models for wake induced transition have been developed by Walker (1974), Doorly (1988), Sharma et al. (1988), Addison and Hodson (1990a, b), Mayle and Dullenkopf (1989), and Mayle (1991) but none are applicable to an unsteady flow situation. Investigations by Gaugler (1985) and Schobeiri et al. (1991) have proven that existing correlations for external aerodynamics applications are not capable of predicting unsteady transition on gas turbine blades. Thus, more research is needed.

The effect that periodic unsteady wakes have upon heat transfer has been investigated by Dunn (1986), Dring et al. (1986), Wittig et al. (1988), Dullenkopf et al. (1991), Liu and Rodi (1992), and Han et al. (1993). Liu and Rodi used a rotating *squirrel cage* wake generator while Wittig et al., Dullenkopf et al., and Han et al. used a spoked wheel. Heat transfer coefficients have been determined with quick-response sensors to detect the real-time variation on blade surface heat transfer induced by unsteady wakes by Dunn et al. (1986) and Doorly et al. (1985), while Liu and Rodi, Wittig et al., Blair et al., and Dullenkopf et al. used thermocouples to measure the time-averaged heat transfer coefficient. The investigations have shown that periodic unsteady wakes increase mean heat transfer. Dullenkopf et al. and Han et al. found that higher wake passing
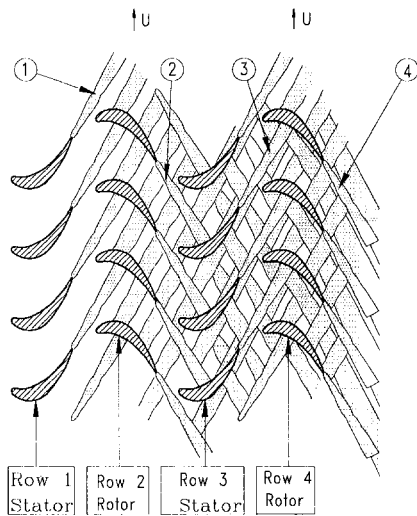
Fig. 1 Stator-rotor wake interaction in a multistage environment, ① **absolute wake from row 1 (stator),** ② **relative wake from row 2 (rotor),** ③ **absolute wake from row 1 (stator),** ④ **relative wake from row 2 (rotor)**

frequencies significantly enhance heat transfer on both suction and pressure surfaces of a turbine blade due to increased background turbulence. Also, suction surface average heat transfer coefficients are higher than pressure surface.

A schematic picture of the wake flow within a multistage turbine in an absolute and relative frame of reference is shown in Fig. 1. The structure of the unsteady turbulent flow changes as it passes through the stator and rotor rows. Leaving the first stator blade row, the wake flow impinges on the second blade row (rotor) with a spatial frequency that corresponds to the spacing of the preceding stator blades. The second cascade is exposed to a periodic unsteady turbulent flow that affects the boundary layer flow, velocity, turbulence, and losses. The third row (second stator) is subjected to two sets of unsteady wakes that originate from the first two rows. These wakes impinge and convect with different velocities, phase displacements, and turbulence structures. At the exit of the third row, the periodic unsteady flow is, to some extent, degenerated into a more sto-

chastic one. From this point on, the downstream rows are subjected to a highly turbulent flow. This indicates that boundary layer transition of each row within a multistage arrangement is subjected to distinctively different unsteady flow structures.

The present investigation includes aerodynamic and heat transfer experiments. Unsteady boundary layer experiments on the concave surface using hot-wire anemometry show the impact of unsteady wake flow on boundary layer transition. Likewise, liquid crystal measurements determine the heat transfer behavior under steady and unsteady conditions. Finally, a comparison between experimental results and theory concludes the paper.

2 Experimental Research

The data in this paper were acquired using a subsonic wind tunnel. A complete description can be found in Schobeiri and Radke (1994) and as a result, only a brief description is given here. The facility consists of a centrifugal fan, settling chamber, nozzle, wake generator, and curved test section. Through the use of a throttle mechanism at the exit of the fan, the velocity at the inlet of the test section was set at 12 m/s. The rest of the inlet flow conditions are in Table 1. Downstream of the diffuser is the settling chamber. Four stainless steel screens and one honeycomb flow straightener are located throughout the chamber to control the turbulence and flow uniformity. A nozzle with a 4:1 area ratio is at the exit of the settling chamber. This configuration produces an inlet freestream turbulence intensity of approximately 1.2 percent.

The *squirrel cage* wake generator, run at a constant 300 rpm for every unsteady test, consists of two parallel, rotating, circular disks in which circular rods or cylinders are arranged circumferentially. The wake spacing is varied by changing the number of rods which results in a change in frequency of the impinging wakes and freestream turbulence. This method reasonably simulates the multistage turbine flow environment previously described. The disks are covered by stationary disks to eliminate the undesirable secondary shear flows generated by the rotating disks.

Each rod generates a primary and a secondary wake per revolution at a given height above the plate. Primary wakes are generated by rods closest to the plate and secondary wakes are generated by rods farthest from the plate. The primary wake is

Nomenclature

A_{foil} = total heat surface area of Inconel foil
C_D = wake drag coefficient
d = lateral distance above the plate surface, $d = 10$ mm
d_R = rod diameter (mm)
h = heat transfer coefficient (W/m² K)
h_n = nozzle exit height (mm)
I = measured current of foil circuit
n_R = number of rods
Nu = Nusselt number
Q_{cond} = conductive heat flux
Q_{conv} = convective heat flux
Q_{rad} = radiation heat flux
Q_{foil} = heat flux of Inconel foil
Re_h = nozzel exit Reynolds number, $Re_h = \rho \bar{U}_{in} h_n / \mu$
$r_0 - r$ = lateral distance in test section
s = streamwise position (mm)

s_0 = arc length of concave surface of curved plate, $s_0 = 690$ mm
s_R = rod spacing
St = Stanton number
t = time
T_∞ = freestream air temperature
Tu_{in} = inlet turbulence intensity
Tu = reference turbulence intensity
Tu_{loc} = local turbulence intensity
$\langle Tu \rangle$ = ensemble-averaged reference turbulence intensity
T_{yl} = yellow line temperature
u = turbulent fluctuation component
u_τ = shear stress velocity
$\langle u \rangle$ = ensemble-averaged fluctuation velocity
U = instantaneous velocity
$\bar{U}$ = time-averaged velocity
$\bar{U}_{in}$ = time-averaged inlet velocity
$\bar{U}w$ = circumferential velocity of wake generator
U_{ref} = reference local velocity at a distance of $d = 10$ mm

$\langle U \rangle$ = ensemble-avearged velocity
V = voltage applied to Inconel foil
w = nozzle exit width
X_{Ple} = distance between the rod and the plate's leading edge
y = lateral distance from plate surface
$y+$ = nondimensional wall distance, $y+ = u_\tau y / \nu$
α = flow angle with respect to horizontal
β = flow angle with respect to probe coordinates
ϵ = emisivity
σ = Stefan-Boltzmann constant
τ = one wake passing period
Θ_l = angle at which leading edge is from vertical, $\Theta_l = 14$ deg
Θ_P = angle at which X-probe is from vertical, $\Theta_P = 13$ deg
μ = absolute viscosity
ν = kinematic viscosity of air
Ω = unsteady flow parameter, $\Omega = C_D s_0 \bar{U}_w / s_R \bar{U}_{in}$

Table 1 Specifications of inlet flow and wake generator characteristics

Parameters	Values	Parameters	Value
Curved plate arc length	$s_0 = 690$ mm	Nozzle exit turbulent intensity	$Tu = 1.20$ percent
Nozzle exit height	$h_n = 420.00$ mm	Nozzle exit width	$w = 593.00$ mm
Plate Reynolds number	$Re_{s0} = 0.56 \times 10^6$	Rod diameter	$d_R = 2$ mm
Steady reference (no rods)	$s_R = \infty$ mm	Ω—parameter steady case	$\Omega = 0.0$
Set 1 rod spacing	$s_R = 314.0$ mm	Ω—parameter for set 1	$\Omega = 1.033$
Set 2 rod spacing	$s_R = 188.4$ mm	Ω—parameter for set 2	$\Omega = 1.725$
Set 3 rod spacing	$s_R = 94.2$ mm	Ω—parameter for set 3	$\Omega = 3.443$
Set 4 rod spacing	$s_R = 62.8$ mm	Ω—parameter for set 4	$\Omega = 5.166$
No. of rods in set 1	$n_R = 3$	No. of rods in set 2	$n_R = 5$
No. of rods in set 3	$n_R = 15$	No. of rods in set 4	$n_R = 10$
Distance between the rod and the plate leading edge	$x_{Ple} = 252.9$ mm	Distance/rod diameter ratio	$x_{Ple}/d_R = 126.5$

responsible for generating the periodic unsteady flow, whereas the secondary wake serves as a background turbulence generator because it has sufficiently decayed before reaching the primary wake. The generator was run with five different rod sets (see Table 1). The unsteady character of the wake flow produced by the wake generator is appropriately characterized by the unsteady parameter $\Omega = C_D s_0 U_w / s_R U_{in}$ which is related to the Strouhal number introduced by Speidel (1957). However, the Strouhal number does not account for turbomachinery stage characteristics and the wake decay process which is characterized by the drag coefficient C_D. Investigations by Schobeiri et al. (1996) show that for a distance/diameter ratio of $x_{Ple}/d_R = 126.5$ (see Table 1), the wake drag coefficient is approximated as $C_D \cong 1.0$. The values of Ω are listed in Table 1 cover a range that is typical of a turbomachine.

The test section, shown in Fig. 2, consists of a top convex wall, a lower concave wall, and two vertical, Plexiglass side walls. The top convex wall supports a linear traversing system and can rotate about its center of curvature which permits the streamwise and radial positioning of the hot-wire probes and thermocouple. The curved plate is mounted between the two

plexiglas side walls, where its axial and angular position can be varied by a positioning system. This positioning system allows variation of the pressure gradient and the adjustment of the leading edge position to avoid the inception of separation bubbles. The plate was positioned for a zero streamwise pressure gradient.

Two curved plates which simulate the pressure surface of a turbine blade were utilized. The aluminum plate, shown in Fig. 2, and the heat transfer plate, shown in Fig. 3, have the same concave dimensions. Boundary layer measurements were taken on the aluminum and heat transfer plates (concave surface only), and heat transfer measurement were taken on both surfaces of the latter. The aluminum plate is 593.0 mm wide, has an arc length of 690.0 mm, a radius of curvature of 702.5 mm, a leading edge radius of 1.0 mm, and a thickness of 15.0 mm.

Like the aluminum curved plate, the heat transfer plate was positioned mid-height in the test section and was angled so that the concave surface was exposed to a zero pressure gradient. The heat transfer plate has the same dimensions as the aluminum plate with the only exception being the leading edge radius which is 5 mm and the radius of curvature for the first three
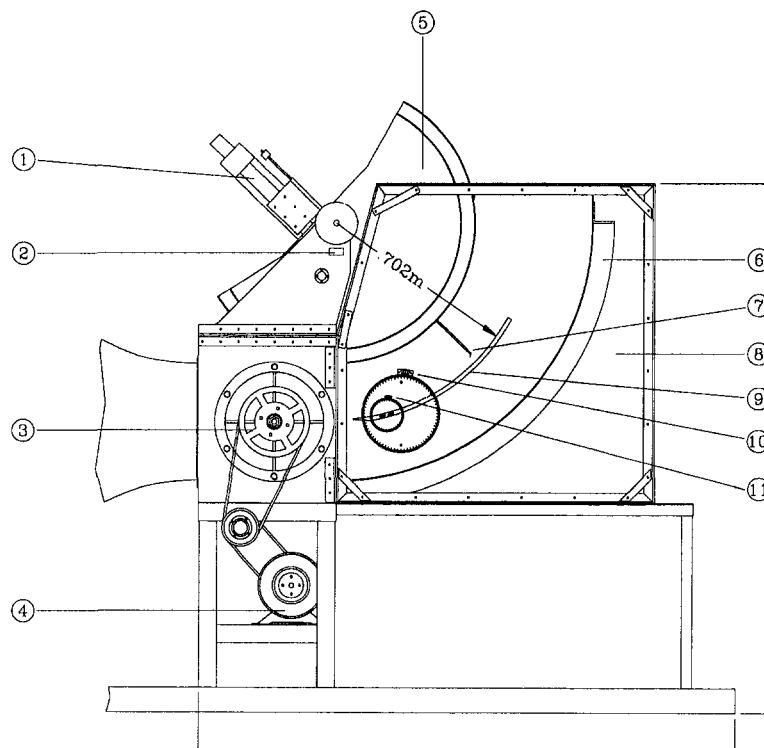

Fig. 2 Test section: (1) traversing system, (2) nozzle, (3) wake generator, (4) electric motor, (5) convex wall, (6) concave wall, (7) hot-wire probe, (8) plexiglass wall, (9) curved plate, (10) small vernier, (11) large vernier
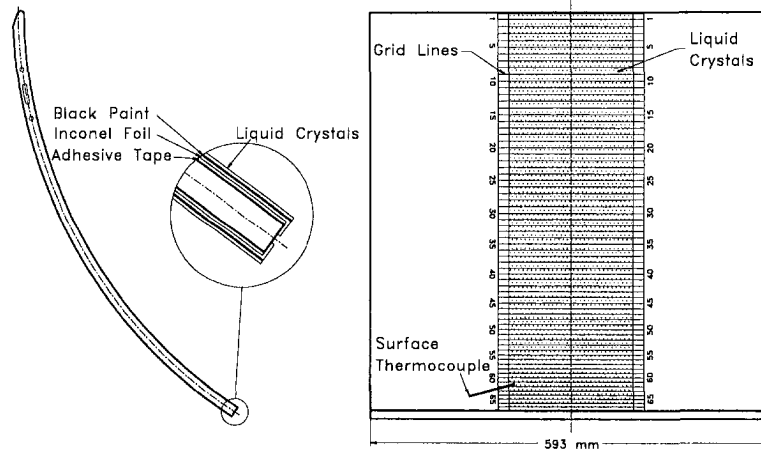
Fig. 3 External view of the heat transfer curved plate showing grid lines, liquid crystals, and surface thermocouple

percent of the convex surface. These difference are due to different construction techniques. The heat transfer plate is constructed of 1-mm thick Bakelite sheets laid over several Bakelite ribs. High resistant insulation is used to fill the air pockets between the ribs to minimize the heat loss. Two copper bus bars located long-wise at the trailing edge of the curved plate are connected to 10-gauge copper wire that is attached to a DC power supply. The external surface of the plate is shown in Fig. 3. A double-sided acrylic-based high-temperature adhesive sheet with a 0.1-mm thickness and 183-mm width is applied to the Bakelite surface from the concave surface trailing edge to the convex surface trailing edge. On top of that, a 0.0254-mm thick sheet of Inconel 600 foil is attached and tach welded to the copper bus bars at the trailing edge. Applied to the surface of the foil is a thin coat of black paint which absorbs the incoming radiation and minimizes its refraction and allows the liquid crystals to achieve maximum brilliance. The final layer is a thin coat of cholesteric liquid crystals.

3 Instrumentation, Data Acquisition, and Reduction

3.1 Boundary Layer Measurements. Data acquisition is controlled by a 386, 40 MHZ personal computer that is connected to a 12 bit, 16 channel A/D board with simultaneous sample and hold. A constant-temperature hot-wire anemometer system (TSI-IFA 100) connected to the first channel of the A/D board supplies the instantaneous velocity signal. A single-wire probe with a 4 μm tungsten filament was used for boundary layer measurements. Inlet velocity information was collected with an X-wire probe. These probes were calibrated with the method described in John and Schobeiri (1993). A T-type thermocouple is mounted on the side of the test section to determine the air temperature. The instantaneous flow velocity is defined as

$$U = \bar{U} + u. \tag{1}$$

The root mean square value of the turbulent velocity fluctuation is obtained from the instantaneous and time-averaged velocity by

$$u = \sqrt{\frac{1}{N} \sum_{j=1}^{N} (U_j - \bar{U})^2} \tag{2}$$

and the local turbulence intensity is defined as

$$Tu_{\text{loc}} = \frac{u}{\bar{U}} \times 100 = \frac{1}{\bar{U}} \sqrt{\frac{1}{N} \sum_{j=1}^{N} (U_j - \bar{U})^2} \times 100. \tag{3}$$

Reference turbulence intensity can be determined by replacing $\bar{U}$ with U_{ref} in Eq. (3).

In addition to time-averaged results, the unsteady data are ensemble-averaged with respect to the rotation period of the wake generator. Thus, the ensemble-averaged results calculated over the 300 revolutions show primary wake passes equal to the number of rods. A series of preliminary experimental investigations with different wake generator revolutions showed that 300 revolutions are sufficient to capture the details necessary for reproducing ensemble-averaged velocity profiles. The ensemble-averaged velocity, fluctuation velocity, and turbulence intensity are given by

$$\langle U_i(t_i) \rangle = \frac{1}{N} \sum_{j=1}^{N} U_{ij}(t_i) \tag{4}$$

$$\langle u_i(t_i) \rangle = \sqrt{\frac{1}{N} \sum_{j=1}^{N} (U_{ij}(t_i) - \langle U_i(t_i) \rangle)^2} \tag{5}$$

$$\langle Tu_i(t_i) \rangle = \frac{\langle u_i(t_i) \rangle}{U_{\text{ref}}} \times 100 \tag{6}$$

where $j = 1, 2, \ldots, N$, and N is the total number of periods ($N = 300$) and $I = 1, 2, \ldots, M$ where M is the number of samples taken per period ($M = 2048$).

Boundary layer measurements were taken on the concave surface of the aluminum plate for $\Omega = 0.0, 1.725, 3.443$, and $\Omega = 5.166$ utilizing a TSI single-wire probe. To capture the major portion of the transition onset, the plate was traversed in the longitudinal direction in steps of 2 deg until 50 percent of the plate was reached. The next 25 percent of the plate was traversed in increments of 3 deg and the last quarter was traversed in increments of 5 deg. For each streamwise position, the boundary layer measurements were started 0.1 mm above the surface of the plate and terminated 10.0 mm above the curved plate. The same procedure was used to take aerodynamic measurements on the heat transfer plate. Measurements were taken to ensure that the new plate provided a similar response so that a comparison could be made between the aerodynamic and heat transfer measurements. A comparison of steady flow results showed that the responses was similar, and as a result, a 3-rod case, $\Omega = 1.033$, was performed on the heat transfer plate to acquire more data on the effect of wake passing frequency.

Steady X-wire measurements were performed at an angular distance of 1 deg (12.25 mm) directly upstream of the heat transfer plate to determine the inlet flow turbulence intensity, velocity components, and flow angles. Measurements were taken using 16,384 samples per wire per radial location. The traverse started 50 mm above the bottom concave wall and stopped 50 mm below the top convex wall. The time-averaged
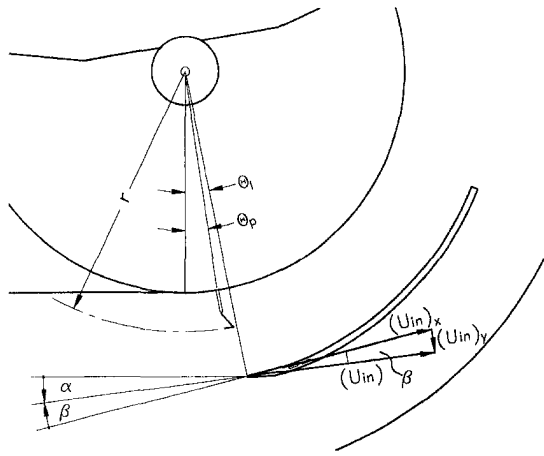
Fig. 4 Representation of inlet velocity with respect to probe coordinate and Cartesian coordinates

results were used to calculate the flow angle with respect to probe coordinates, β. This flow angle, due to the X-wire probe being aligned normal and 1 deg in front of the leading edge of the curved plate, also approximates the flow angle that is with respect to the curved plate. α is the flow angle with respect to horizontal. All of the aforementioned coordinates and angles are clearly defined in Fig. 4. The equations to calculate these entities can be found in Wright (1996).

3.2 Heat Transfer Measurements. The liquid crystal technique used in this investigation has been used by several researchers (Simonich and Moffat, 1984; Crane and Sabzvari, 1989; You et al., 1989; Schobeiri et al., 1991) but none have used the scheme in conjunction with unsteady wakes. Hippensteele et al. (1983) applied the use of liquid crystals to turbomachinery by developing a convenient method of using liquid crystals with a composite heater sheet to determine the local heat transfer coefficient distribution on both sides of a turbine blade. The original heater sheet consisted of a plastic with a carbon impregnated coating which gave a heat transfer coefficient error of ± 6.2 percent. You et al. and Schobeiri et al. used Inconel 600 foil as the heater sheet, and Russell et al. (1993) proved that the Inconel 600 foil was a more uniform heater sheet by determining that the error for the heat transfer coefficient was approximately ± 3.7 percent. For this reason, the heater sheet in this investigation is Inconel 600. The benefit of liquid crystals is that they allow for the continuous visualization of present thermal pattern.

The heating of the heat transfer plate is accomplished with a Sorenson DC40-70 power supply which is capable of 40 volts at 70 amps. Voltage and current are recorded using a Fluke 87 multimeter. The freestream air temperature is recorded with an E-type thermocouple that fits in the probe traversing system. The thermocouple is positioned high enough from the curved plate that it is not affected by the velocity or thermal boundary layer. Another E-type thermocouple mounted on the surface of the heat transfer plate is used to calibrate the color of the liquid crystals under no flow conditions.

At the beginning of each test, the yellow band of the liquid crystal is calibrated for temperature. The yellow band is used for measurements because it occurs over the narrowest temperature band and has good uniformity (Hippensteele et al., 1985). Calibration consists of adjusting the power from the power supply until the yellow band is directly on top of the surface mounted thermocouple. Once steady state has been reached, the temperature is recorded. This calibration is performed under no flow conditions and repeated several times. The yellow band temperature was found to be approximately 47.5°C for each calibration performed. Following calibration, the wind tunnel is started, the

wake generator is set, and the power supply is adjusted so that the yellow band is located at the leading edge of the curved plate. The facility, in this configuration, is run for two hours so that the temperature inside the curved plate can reach equilibrium. This helps reduce the losses due to conduction and allows the location of the yellow band to be accurately determined. To check whether steady state has been reached, the surface thermocouple is constantly monitored to ensure that the foil temperature is not fluctuating.

After two hours, the voltage and current supplied to the Inconel foil are obtained from the multimeters and recorded. The location of the yellow band at the centerline of the curved plate on the convex and concave surface is read from the appropriate set of grid lines as shown in Fig. 3. These values, along with freestream air temperature, atmospheric pressure, rpm, number of rods, and foil temperature are recorded. The power is then reduced to move the yellow band away from the leading edge in 10-mm increments, and a period of 30 minutes is allowed for steady-state operation to be achieved before the aforementioned quantities are recorded. This process is continued until the full longitudinal length of the plate for both surfaces is completely mapped. This process is the same for all wake passing frequencies.

The collected data are reduced based upon a heat flux analysis which entails determining all the energy losses on a flux basis and subtracting them from the heat flux of the Inconel foil. This leaves the convective portion of the energy equation, and from this, the heat transfer coefficient can be obtained with the following equation:

$$h = \frac{Q_{\text{conv}}}{(T_{yl} - T_\infty)} . \tag{7}$$

Q_{conv} is the convective portion of the energy equation per unit area and is defined by

$$Q_{\text{conv}} = Q_{\text{foil}} - Q_{\text{rad}} - Q_{\text{cond}} \tag{8}$$

where Q_{foil} is the heat flux of the Inconel foil and Q_{rad} is the radiation heat flux emitting from the surface of the liquid crystals. These two quantities are given by

$$Q_{\text{foil}} = \frac{VI}{A_{\text{foil}}} \tag{9}$$

and

$$Q_{\text{rad}} = \epsilon\sigma(T_{yl}^4 - T_\infty^4). \tag{10}$$

The emissivity of the liquid crystals has a value of 0.85. The amount of radiation reflected back from the top aluminum wall was found to be less than two percent of the input power and as a result was neglected. The third loss, the conduction losses, were found to be negligible based upon a two-dimensional finite difference nodal analysis method on a slice of the curved heat transfer plate.

4 Results and Discussion

4.1 Aerodynamics.

Channel and Inlet Velocity Conditions: Figure 5 shows the nondimensional time-averaged freestream velocity above the surface of the heat transfer plate. It is evident that there is a zero pressure gradient over most of the curved plate and that the rise in freestream velocity at the trailing edge is due to the boundary layer on the curved plate and on the plexiglass side walls blocking the exit cross sectional area.

The lateral traverse of the inlet using the X-wire probe under steady flow conditions at an angular distance of 1 deg (12.25 mm) in front of the heat transfer plate showed that the inlet flow has a small nonzero incidence angle with respect to the curved plate at any r_0-r location. On the concave side of the
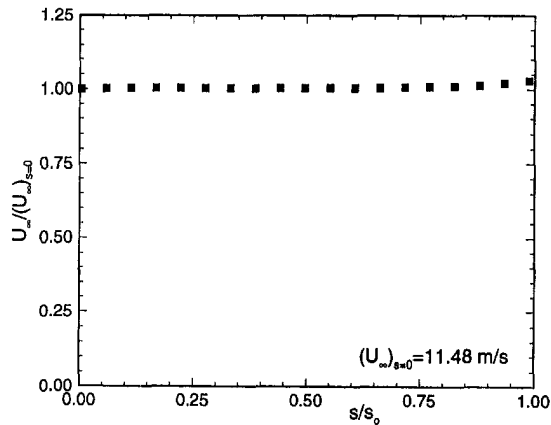
Fig. 5 Nondimensional time-averaged freestream velocity at $y = 25.0$ mm above the surface of the heat transfer plate

plate, this incidence angle prevents the inception of a leading edge separation bubble. However, on the convex side of the plate this incidence angle causes a separation bubble at the plate's leading edge which will be discussed later. At the leading edge, the flow has an incidence angle of $\beta = -8$ deg with respect to the curved plate and an incidence angle of $\alpha = +6.0$ deg with respect to horizontal. These angles are defined in Fig. 4. The overall inlet turbulent intensity and its x-component were also measured. Above and below the plate, the inlet turbulence intensity was approximately 2.2 percent, and 2.4 percent directly in front of the plate. The rise in turbulence intensity is due to increased mixing that occurs in the stagnation region in front of the plate. $(Tu_{in})_x$ behaves in a similar fashion but has a lower magnitude with an average of 1.2 percent and a maximum of 1.4 percent at the leading edge.

Time-Averaged nondimensional Mean Velocity: The nondimensional time-averaged velocity distributions are presented in Figs. 6(a, b, c) for $\Omega = 0$, 1.033, and 3.443. For all cases, a wall correction scheme developed by Zemskaya et al. (1979) was implemented for $y^+ < 6$ which is necessary when measuring with a hot-wire probe in the near wall region. In Fig. 6(a) at $s/s_0 = 0.15$ for $\Omega = 0.0$, the nondimensional velocity diagram shows the edge of the boundary layer to be around $y/d = 0.06$, where $d = 10$ mm for different streamwise position. The high-velocity gradient and small boundary layer thickness suggest that the state of the boundary layer is laminar. Further downstream at $s/s_0 = 0.37$, the velocity profile indicates a transitional character. At this location, the edge of the boundary layer is around $y/d = 0.25$. Towards the trailing edge of the plate, $s/s_0 = 0.88$, the shape of the nondimensional velocity profile approaches almost a typical turbulent shape with an increased turbulence activity inside the boundary layer. At this point, the boundary layer has grown considerably indicating that the boundary layer tends to become fully turbulent. These profiles clearly show that the boundary layer is undergoing a transition process. Even though these profiles give a good description of the boundary layer development, they are not descriptive enough to give the state of the boundary layer. The nondimensional velocity distributions for $\Omega = 1.033$ (3 rods), and 3.443 (10 rods) can be found in Figs. 6(b) and 6(c), respectively. These figures show the same behavior as the steady case, but it was found that the boundary layer thickness grows faster for higher values of Ω which is an indication that transition occurs sooner for increasing wake passing frequency. Besides showing the fact that the velocity distribution changes during the transition process and that the location of the transition region is dependent upon the wake passing frequency, the time-averaged velocity distributions do not show any further details regarding the effect of the wakes upon the boundary layer. Detailed insight

into the boundary layer transition process is provided by the following unsteady flow investigations.

Instantaneous Velocity Traces: Instantaneous velocity, U, as a function of time is plotted in Figs. 7(a, b, c, d) for $\Omega = 0.0$, 1.725, 3.443, and 5.166 at $y = 0.3$ mm above the concave surface of the curved plate for four different streamwise locations. The total time of 200 ms is one revolution of the wake generator at 300 rpm. For $\Omega = 0.000$ (Fig. 7(a)), the velocity at $s/s_0 = 0.04$ is smooth and has a magnitude around 10 m/s which indicates that the boundary layer is thin since the velocity is close to the potential flow velocity. Further downstream, small disturbances appear in the form of two-dimensional Tollmien-Schlichting (TS) waves. These disturbances continue to
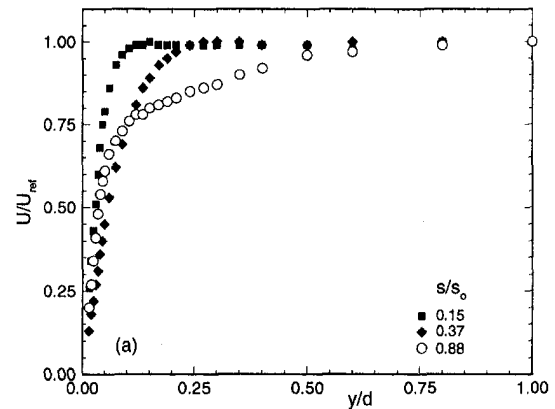

Fig. 6(a) Nondimensional mean velocity at three different s/s_0 locations for $\Omega = 0.000$
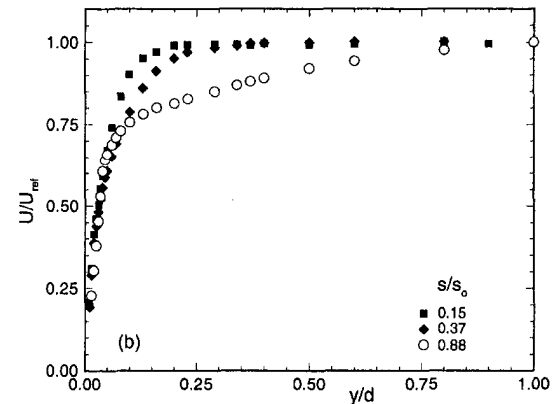

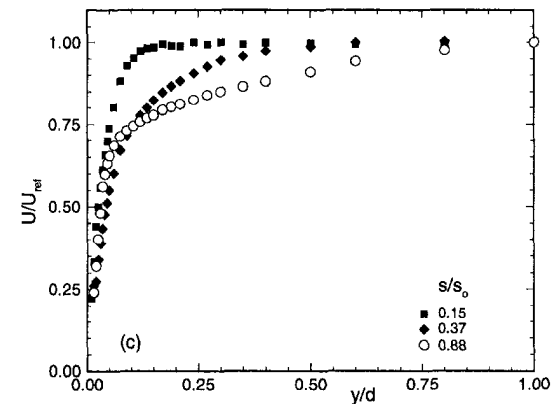**Fig. 6(b)** Nondimensional mean velocity at three different s/s_0 locations for $\Omega = 1.033$

Fig. 6(c) Nondimensional mean velocity at three different s/s_0 locations for $\Omega = 3.443$

Journal of Heat Transfer
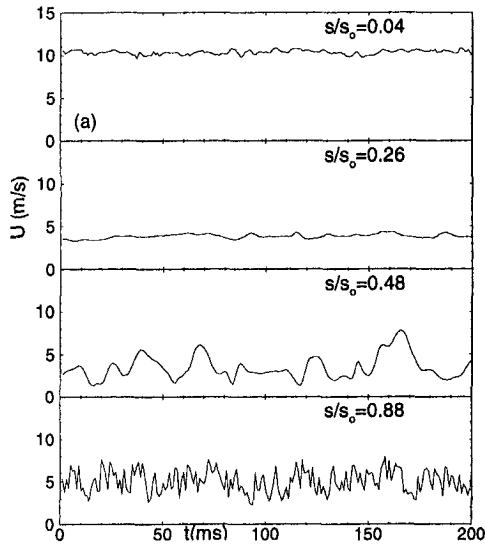
Fig. 7(a) Instantaneous velocity traces for four different s/s_0 locations for $\Omega = 0.000$ at $y = 0.3$ mm
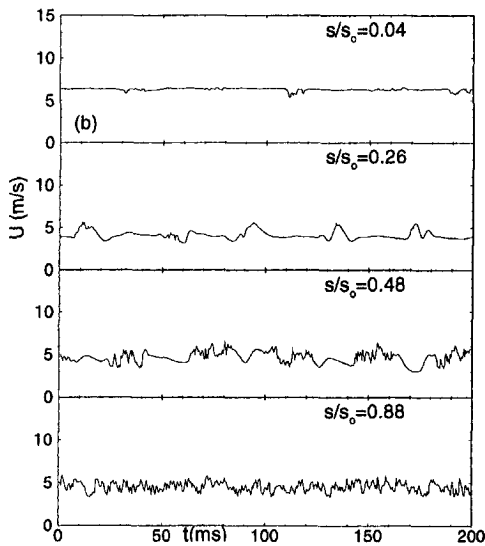
Fig. 7(b) Instantaneous velocity traces for four different s/s_0 locations for $\Omega = 1.725$ at $y = 0.3$ mm
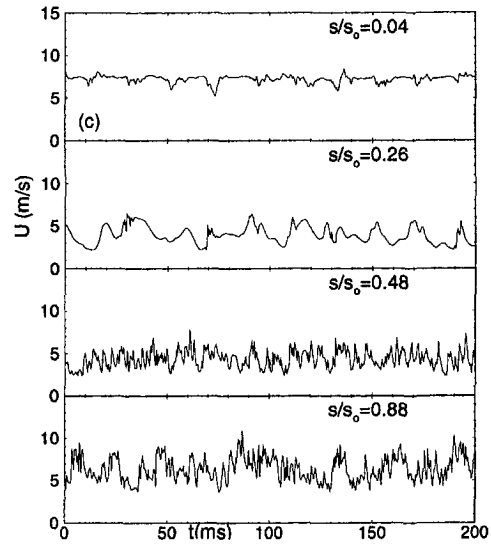
Fig. 7(c) Instantaneous velocity traces for four different s/s_0 locations for $\Omega = 3.443$ at $y = 0.3$ mm
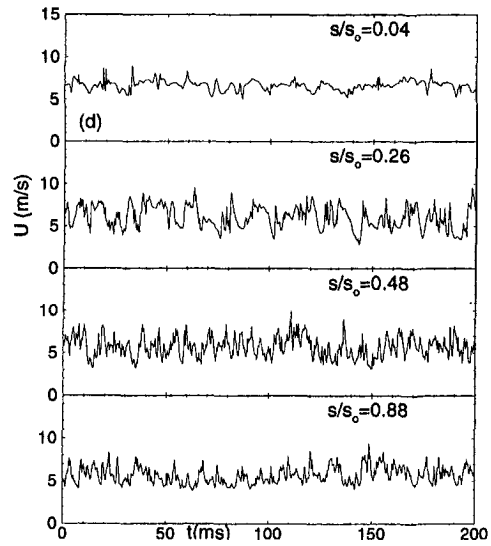
Fig. 7(d) Instantaneous velocity traces for four different s/s_0 locations for $\Omega = 5.166$ at $y = 0.3$ mm

amplify into large amplitude fluctuations ($s/s_0 = 0.48$) and finally develop into turbulent spots somewhere between $s/s_0 = 0.48$ and $s/s_0 = 0.88$. The turbulent spots continue to grow and convect downstream where they coalesce into a fully stochastic developed turbulent boundary layer as exhibited at $s/s_0 = 0.88$. As this process is occurring, the velocity is continually decreasing, as shown by the traces, which is the result of the boundary layer growth. The streamwise location where the turbulent spots start to develop is taken as the start of boundary layer transition.

Figure 7(b) shows the instantaneous velocity traces for $\Omega = 1.725$. As shown, five primary wakes are present. At $s/s_0 = 0.04$, the velocity is very smooth in between the wakes which is characteristic of a laminar boundary layer. As with the steady case, small disturbances in the form of TS waves appear ($s/s_0 = 0.26$) and continue to grow to form turbulent spots downstream ($s/s_0 = 0.48$). At $s/s_0 = 0.88$, the turbulent spots have coalesced together generating a fully turbulent boundary layer in which no wakes are distinguishable. For $\Omega = 3.443$ (Fig. 7(c)), a similar, but quicker, trend is observed.

The $\Omega = 5.166$ case reveals a different flow picture than the lower wake passing frequencies and the velocity traces for this case can be found in Fig. 7(d). At $s/s_0 = 0.04$, the wakes are

not visible due to a strong wake interaction. Further downstream at $s/s_0 = 0.26$, turbulent spots are present which coalesce to form a fully turbulent boundary layer. At $s/s_0 = 0.48$ the flow is completely turbulent. Due to the small wake spacing and intense mixing of the wakes, it appears that the TS mode of instability has been completely bypassed. For a discussion of bypass transition refer to Mayle (1991). It is evident from these traces that the combined effect of increased wake passing frequency and wake mixing increases the freestream turbulence causing an intense turbulent activity within the boundary layer towards the leading edge of the curved plate. This means that the onset of transition has shifted towards the leading edge of the curved plate.

Time-Averaged Turbulence Intensity Contours: Further details on boundary layer transition and development can be obtained from the time-averaged reference turbulence intensity contours presented in Figs. 8(a, b, c, d, e). For each wake passing frequency, the turbulence intensity was time-averaged in the lateral direction, y/d, where $d = 10$ mm for different streamwise position. As shown in Fig. 8(a) for $\Omega = 0.000$, there is a high turbulent intensity core (>15 percent) in the near wall region over 75 percent of the plate with its center
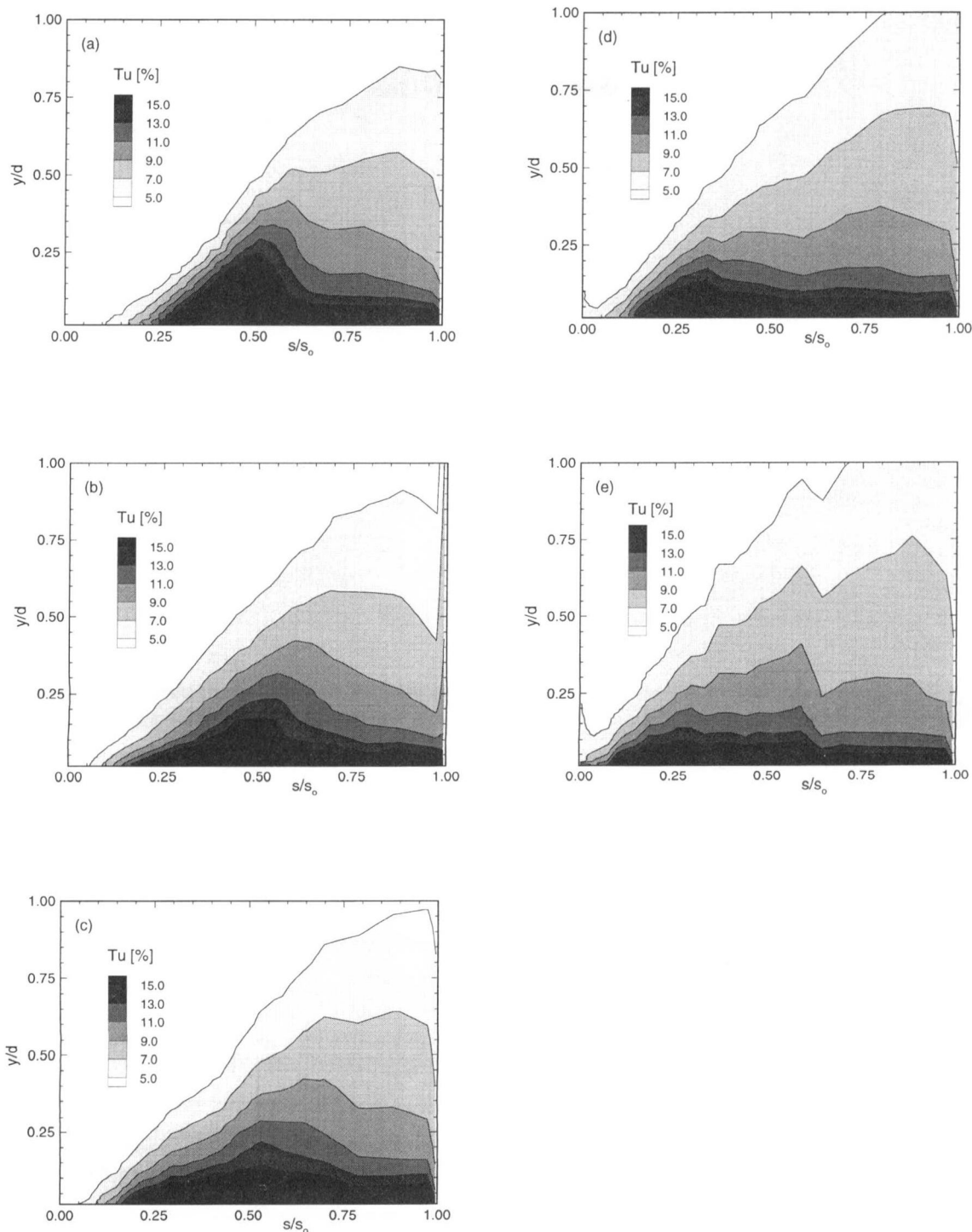
Fig. 8   Time-averaged turbulence intensity contours for (a) $\Omega = 0.000$, (b) $\Omega = 1.033$, (c) $\Omega = 1.725$, (d) $\Omega = 3.443$, and (e) $\Omega = 5.166$

located around $s/s_0 = 0.51$ and has a lateral extension of y/d = 0.25. At $\Omega = 1.033$, the core shifts toward the leading edge indicating an earlier transition, and the lateral extension reduces to $y/d = 0.17$. This reduction is due to the calming effect caused by wake impingement on the boundary layer flow. This phenomenon was discussed extensively by Schobeiri and Radke (1994), Orth (1992), and Pfeil and Herbst (1979). Further increasing the wake passing frequency to $\Omega = 3.443$, Fig. 8(d), the high turbulent intensity core has moved towards the leading edge and further extends the becalmed regions. For $\Omega = 5.166$,

Fig. 8(e), the lateral extension of the core has diminished to $y/d = 0.08$ and the start of the turbulent core is at $s/s_0 = 0.08$ revealing the effect of unsteadiness as to cause earlier transition. Liu and Rodi (1992) also observed this trend. The shift in transition toward the leading edge of the curved plate due to the increase of unsteady wake parameter Ω has two causes. The first is that a higher impinging frequency precipitates increased energy transfer to the boundary layer, and the second is that the earlier mixing of the secondary wakes causes a rise in the freestream turbulence intensity (see Schobeiri et al., 1995a).
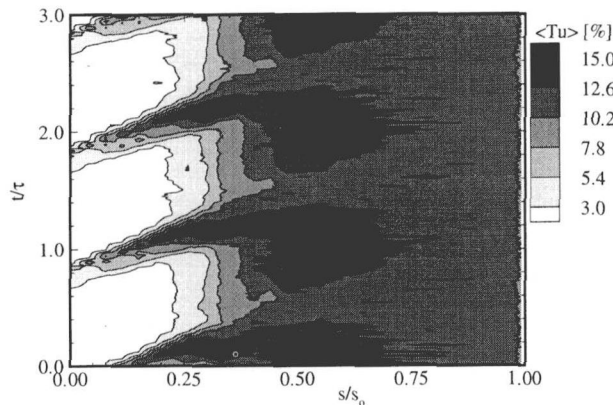
Fig. 9(a) Ensemble-averaged reference turbulence intensity in the temporal-spatial domain at $y = 0.3$ mm above the plate for $\Omega = 1.033$
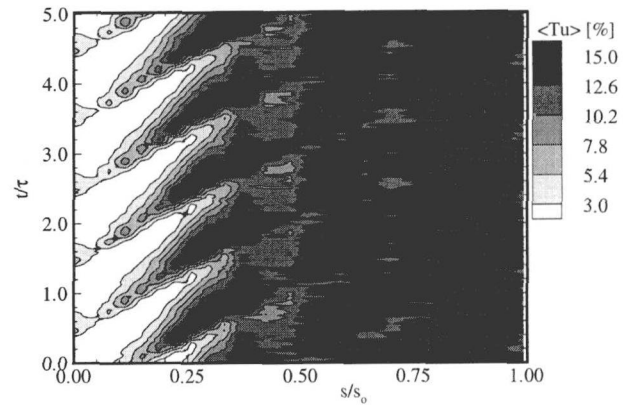
Fig. 9(c) Ensemble-averaged reference turbulence intensity in the temporal-spatial domain at $y = 0.3$ mm above the plate for $\Omega = 3.443$
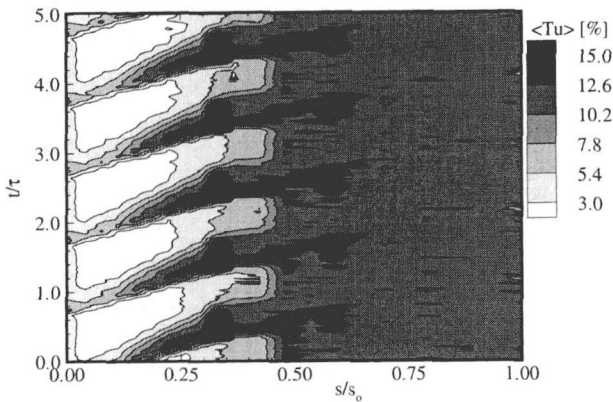
Fig. 9(b) Ensemble-averaged reference turbulence intensity in the temporal-spatial domain at $y = 0.3$ mm above the plate for $\Omega = 1.725$
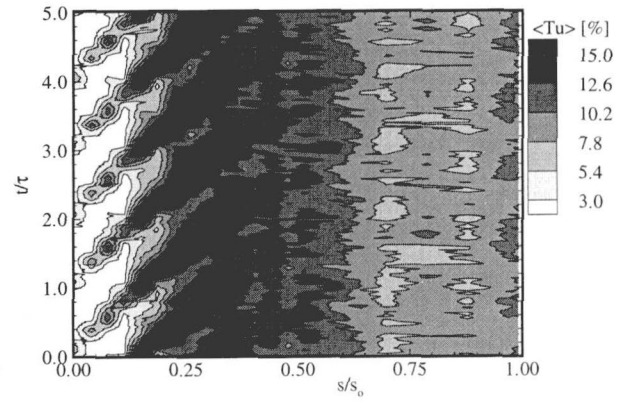
Fig. 9(d) Ensemble-averaged reference turbulence intensity in the temporal-spatial domain at $y = 0.3$ mm above the plate for $\Omega = 5.166$

The time-averaged data presented above give a reasonably good picture of how the transition process occurs under the influence of periodic unsteady wakes.

Ensemble-Averaged Turbulence Intensity: To obtain a detailed picture that reflects the physics of the unsteady boundary layer process, the ensemble-averaged reference turbulence intensity contours in the temporal-spatial domain at a wall distance of $y = 0.3$ mm for each Ω-case are presented in the Figs. $9(a, b, c, d)$. The reference velocity is equal to the velocity at 10 mm above the plate's surface for each streamwise position, and the data have been ensemble averaged for 300 revolutions of the wake generator. As shown in Fig. $9(a)$ ($\Omega = 1.033$), three wakes are present which periodically disturb the boundary layer and produce high turbulence intensity cores (up to 15 percent) and extended becalmed regions (less than one percent). Compared to the steady case shown in Fig. $8(a)$, these extended becalmed regions start at $s/s_0 = 0.0$ and extend to $s/s_0 = 0.23$.

By increasing Ω to 1.725 and 3.443 (Figs. $9(b)$ and $9(c)$), the becalmed regions become narrower due to the increase in wake passing frequency and earlier mixing of the wakes. The high turbulent intensity core shifts forward indicating earlier transition, and the turbulent intensity of the last 50 percent of the plate is extremely high around 13 percent due to increased wake impingement and interaction. At $\Omega = 5.166$, Fig. $9(d)$, the becalmed regions become shorter and now extend from $s/s_0 = 0.0$ to $s/s_0 = 0.15$. They also shift towards the leading edge and now start around $s/s_0 = 0.20$. Unlike the $\Omega = 3.443$ case, the turbulent intensity of the last 40 percent of the curved plate is only around 8 percent instead of 13 percent. The reason for this is that the wakes have mixed thoroughly and there are less instabilities in the flow. Figures $9(a, b, c, d)$ present a

clear picture about the effect of periodic unsteady wakes on boundary layer transition. As previously mentioned, the shifting of the transition process towards the leading edge of the plate is a result of two effects. The first is an increase in the impinging frequency of the primary wakes. As the wakes convect downstream, the individual wake widths continually increase until they have reached approximately the size of the rod spacing. At this location, there is a mixing of the wake and the flow which causes a highly turbulent flow with a turbulent intensity around 15 percent. As the wake passing frequency increases, the wake interaction occurs earlier which introduces an excessive turbulent kinetic energy transport to the boundary layer causing a shift of transition towards the leading edge (see Schobeiri et al., 1995a). The second cause is an earlier mixing of wakes due to the reduction of the wake spacing causing a higher freestream turbulent intensity which has been proven to contribute to the onset of boundary layer transition. A combination of these two factors determines the transition process as presented above.

4.2 Heat Transfer.

Local Heat Transfer Coefficient Distribution on Concave Surface: Figures 10 and 11 show the Nusselt number distribution on the concave and convex surface along the longitudinal length of the plate for $\Omega = 0.000, 1.033, 1.725, 3.443,$ and 5.166. For the concave side of the curved plate, the effect of the wakes on the Nusselt number can clearly be seen. As shown in Fig. 10, the start and end of transition shifts towards the leading edge as the wake passing increases. The beginning of transition occurs for $\Omega = 0.0, 1.033, 1.725, 3.443,$ and 5.166 around $s/s_0 = 0.35, 0.27, 0.26, 0.21,$ and 0.17, respectively. For the aforementioned values of Ω, the end of transition occurs around $s/s_0 = 0.63, 0.60, 0.58, 0.38,$ and 0.34, respectively. Elevated

Fig. 10 Nusselt number distribution on the concave surface of the heat transfer plate for Ω = 0.000, 1.033, 1.725, 3.443, and 5.166

average heat transfer coefficient occurs for higher values of Ω mainly due to a higher freestream turbulence level generated by stronger wake mixing and 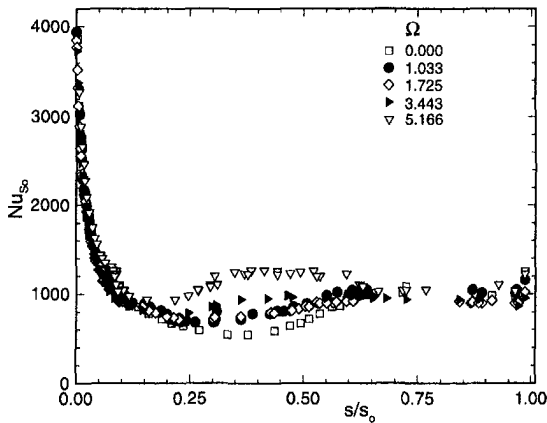turbulent activities inside the boundary layer. In full accord with the aerodynamic picture of the boundary layer transition discussed previously, the heat transfer is predominantly dictated by freestream turbulence. This is in agreement with Han et al. (1993), Liu and Rodi (1989), and Wang and Simon (1987). This data also seems to support the work of Simonich and Moffat (1984) and Kestoras and Simon (1993). These researchers found that the time-averaged overall heat transfer coefficient was higher for a concave surface than a flat plate under zero pressure gradient. By comparing the Ω = 5.166 case to Liu and Rodi's flat plate investigation, which was run under similar flow conditions, it is found that the heat transfer coefficient is about ten percent greater for the curved plate. This increase may be attributed to the Görtler vortices and/or the effect of curvature. The aerodynamic measurements by Schobeiri and Radke (1994) as well as the present heat transfer investigation do not indicate the existence of these vortices.

Local Heat Transfer Coefficient Distribution on Convex Surface: For the convex side, Fig. 11, the shape of the Nusselt number distribution remains constant for all values of Ω (positive and negative, i.e., counterclockwise and clockwise rotation of the wake generator). The reason for this is a separation bubble that occurs just downstream of the leading edge of the curved plate. As previously discussed, a flow separation on the convex side of the plate was expected to occur due to an incidence angle of $\beta = -8$ deg relative to the convex surface. This caused a separation bubble to form $s/s_0 = 0.075$. Once the flow finally reattaches at $s/s_0 = 0.125$, it is fully turbulent which is evident by the increased heat transfer after reattachment. Thus, the mode of transition is separated flow in which a laminar-separation/turbulent reattachment bubble is formed as described by Mayle (1991).

Comparison Between Experimental Results and TEXSTAN: To help corroborate the results of the liquid crystal technique, the experimental results were compared to numerical results generated by TEXSTAN, a computer code written by Crawford and Kays (1976) which solves steady flow boundary layer equations that govern two-dimensional boundary layer flows.

Mayle's (1991) intermittency model, which incorporates unsteady wake flow into a steady-flow analysis by introducing a time-averaged intermittency function, was the chosen turbulence model. Mayle showed that the time-averaged heat transfer distribution on an airfoil surface can be obtained using the time-averaged turbulence intermittency function. Since unsteady flow was an integral part of the heat transfer investigation, this model

was chosen to calculate the start and end of transition. The necessary input for this model is inlet freestream turbulence intensity and inlet velocity which were taken from the boundary layer data of the heat transfer and aluminum curved plates. However, the best results were achieved when the freestream turbulence intensity (at d = 10 mm above the surface) for each boundary layer traverse was averaged for each rod case and substituted for the inlet turbulence intensity. This could be important information in the development of CFD models.

For a more detailed description of Mayle's intermittency model, refer to Mayle (1991). In addition to Mayle's model as an input, the geometry of the heat transfer plate, the heat flux boundary conditions, the air properties, and the mode of transition were other major inputs. The chosen turbulence models were ktmu = 5 and ktme = 3. Refer to Crawford and Keyes (1976) for a description of these models.

For the TEXSTAN comparison, turbulent intensities of 1.4, 2.5, 2.7, 3.8, and 4.5 percent which correspond to Ω = 0.0, 1.033 (3 rods), 1.725 (5 rods), 3.443 (10 rods), and 5.166 (15 rods), respectively, were used in the constant heat flux simulation. As shown by Fig. 12, there was good agreement between the experimental data and TEXSTAN for Ω = 1.033, 1.725, 3.443, and 5.166. Mixed results were found for the steady case. For the steady case, good agreement was observed up to $Re_s = 1.75 \times 10^5$, which is the start of transition measured experimentally, then the numerical result deviates from the experimental results. For this case, TEXSTAN overpredicts the start of transition. This disagreement is primarily due to the curve-fit correlations for the spot production rate and the momentum thickness Reynolds number. Both have a large curve-fit error at low turbulent intensities (<1.5 percent) due to the nonlinearity in the curve-fit data at low turbulent intensities (see Mayle, 1991).

When the Stanton number distribution is compared to other heat transfer investigations involving a concave surface, there is generally good agreement. The magnitude of the Stanton number in the turbulent region compares favorably with the results of Mayle et al. (1979) in which the heat transfer of a turbulent boundary layer on a concave surface was investigated. Both the transition and turbulent regions of the steady case compare well in terms of magnitude and trend to the results of Kestoras and Simon (1993). Kestoras and Simon had a similar inlet velocity but a lower turbulence intensity (Tu = 0.68 percent) as opposed to the 1.2 percent for the steady case in this investigation. The curved plate, however, was different. Kestoras and Simon had a longer curved plate with slightly less curvature. Due to the lower turbulence intensity, the rise in Stanton number in the transition region was greater but peaked at about the same magnitude as found in this investigation. Simonich and Moffat (1984) also studied the effects of concave
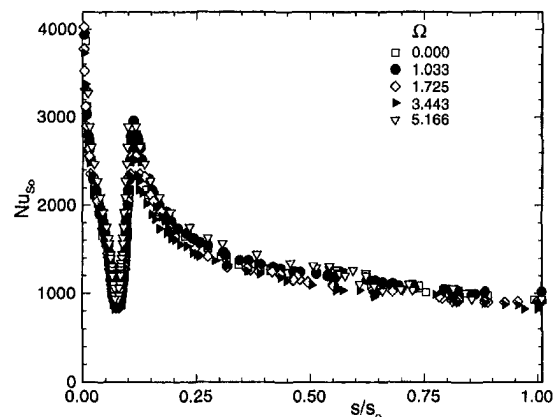

Fig. 11 Nusselt number distribution on the convex surface of the heat transfer plate for Ω = 0.000, 1.033, 1.725, 3.443, and 5.166
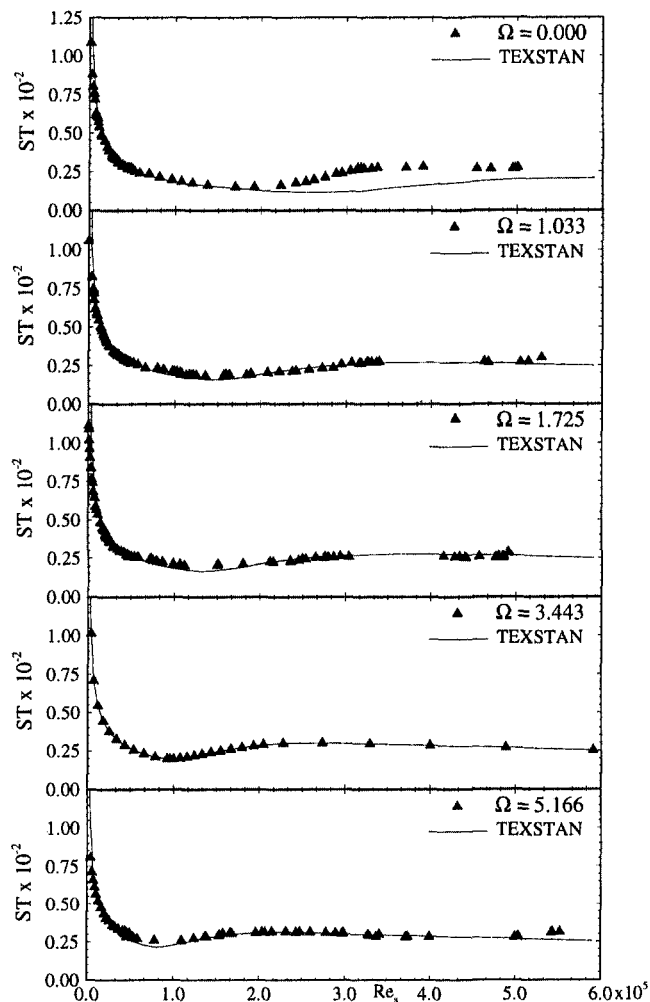
Fig. 12 Stanton number versus local Reynolds number on the concave surface of the heat transfer plate for all values of Ω

curvature on turbulent boundary layers. They found Stanton numbers in the turbulent region to be about 50 percent less than those found in this investigation. The discrepancy is most likely due to their radius of curvature being twice that of the radius of curvature of the heat transfer plate and their different inlet conditions.

5 Uncertainty Analysis

The Kline and McClintock (1953) uncertainty analysis method was used to determine the uncertainty in velocity after calibration and data reduction for the single-wire probe. In addition, the uncertainty in the heat transfer measurements was also determined. The Kline and McClintock method determines the uncertainty for a 95 percent confidence level. The uncertainty in velocity for the single-wire probe after data reduction is given in Table 2.

As shown, the uncertainty in velocity increases as the flow velocity decreases. This is due to the pneumatic pressure transducer having a large uncertainty during calibration. The maximum uncertainty in the local heat transfer coefficient for all the

Table 2 Uncertainty in velocity measurement for hot-wire probe

$\bar{U}$ (m/s)	3	5	12
$\omega \bar{U}/\bar{U}$ (%)$_{\text{red}}$	5.78	2.41	1.40

rod cases was approximately ± 5.87 W/m²K. With regard to position, there is a ± 1.0 mm uncertainty in the determination of the yellow band region.

6 Conclusions

The effect of periodic unsteady wakes on boundary layer transition on the concave side of a constant curvature curved plate under zero pressure gradient was experimentally investigated in a subsonic wind tunnel test facility. In addition, the effect that these wakes have upon heat transfer on the concave and convex surfaces was experimentally investigated in the same test facility. For both experiments, the same wake passing frequency was utilized so a comparison could be made between the aerodynamic and heat transfer data. From this investigation, the following conclusions were drawn:

1 Increasing wake passing frequency results in earlier transition and approximately equal transition zones. At $\Omega = 1.033$ (3 rods) and $\Omega = 1.725$ (5 rods), the isolated unsteady wakes shed no visible interaction with each other. Visible wake interaction is present at $\Omega = 3.443$ (10 rods) and $\Omega = 5.166$ (15 rods) simulating the flow through the third and fourth row of a multistage turbine. This shows that the research is applicable to actual turbomachines.

2 Higher turbulence intensity occurs for increasing the unsteady parameter Ω due to the intense mixing of the primary and secondary wakes at higher values of Ω, and at higher turbulence levels, the start of transition is closer to the leading edge of the curved plate.

3 On the concave surface of the heat transfer plate, increasing the unsteady parameter Ω results in earlier transition and a higher average heat transfer coefficient.

4 Increasing the unsteady parameter Ω has no effect upon a laminar separation/turbulent reattachment bubble on the convex surface at turbulent intensities (x-component) less than five percent.

5 Considering the transition onset, the hot-wire and heat transfer data were in good agreement with each other which says that the liquid crystal techniques delivers accurate and dependable results. In addition, the time-averaged heat transfer results are predicted well by TEXSTAN using Mayle's time-averaged intermittency correlations.

Acknowledgments

References

Addison, J. S., and Hodson, H. P., 1990a, "Unsteady Transition in an Axial-Flow Turbine, Part 1: Measurements on the Turbine Rotor," ASME *Journal of Turbomachinery*, Vol. 112, pp. 206–214.

Addison, J. S., and Hodson, H. P., 1990b, "Unsteady Transition in an Axial-Flow Turbine, Part 2: Cascade Measurements and Modeling," ASME *Journal of Turbomachinery*, Vol. 112, pp. 215–221.

Ashworth, D. A., LaGraff, J. E., and Schultz, D. L., 1989, "Unsteady Interaction Effects on a Transitional Turbine Blade Boundary Layer," ASME *Journal of Turbomachinery*, Vol. 111, pp. 162–168.

Chakka, P., and Schobeiri, T., 1997, "Modeling Unsteady Boundary Layer Transition on a Curved Plate Under Periodic Unsteady Flow Conditions: Aerodynamic and Heat Transfer Investigations," ASME Paper No. 97-GT-399.

Crane, R. I., and Sabzvari, J., 1989, "Heat Transfer Visualization and Measurement in Unstable Concave-Wall Laminar Boundary Layers," ASME *Journal of Turbomachinery*, Vol. 111, pp. 51–56.

Crawford, M. E., and Kays, W. M., 1976, "STAN5 (TEXSTAN version)—A Program for Numerical Computation of Two Dimensional Internal and External Boundary Layer Flow," NASA CR-2742.

Doorly, D. J., Oldfield, M. L. G., and Scrivener, C. T. J., 1985, "Wake-Passing in a Turbine Rotor Cascade," Heat Transfer and Cooling in Gas Turbines, AGARD-DP-390, pp. 7-1–7-18.

Doorly, D. J., 1988, "Modeling the Unsteady Flow in a Turbine Rotor Passage," ASME Journal of Turbomachinery, Vol. 110, pp. 27–37.

Dring, R. P., Blair, M. F., Joslyn, H. D., Power, G. D., and Verdon, J. M., 1986, "The Effect of Inlet Turbulence and Rotor/Stator Interactions on the Aerodynamics and Heat Transfer of a Large Scale Rotating Turbine Model," NASA CR 4079.

Dullenkopf, K., Schulz, A., and Wittig, S., 1991, "The Effect of Incident Wake Conditions on The Mean Heat Transfer of An Airfoil," ASME Journal of Turbomachinery, Vol. 113, pp. 412–418.

Dunn, M. G., 1986, "Heat Flux Measurements for the Rotor of a Full-Stage Turbine: Part I—Time Averaged Results," ASME Journal of Turbomachinery, Vol. 108, pp. 90–97.

Gaugler, R., 1985, "A Review and Analysis of Boundary layer Transition Data for Turbine Application," ASME Paper No. 85-GT-83.

Han, J. C., Zhang, L., and Ou, S., 1993, "Influence of Unsteady Wake on Heat Transfer Coefficient From A Gas Turbine Blade," ASME JOURNAL OF HEAT TRANSFER, Vol. 115, pp. 904–911.

Hippensteele, S. A., Russell, L. M., and Stepka, F. S., 1983, "Evaluation of a Method for Heat Transfer Measurements and Thermal Visualization Using a Composite of a Heater Element and Liquid Crystals," ASME JOURNAL OF HEAT TRANSFER, Vol. 105, pp. 184–189.

Hippensteele, S. A., Russell, L. M., and Torres, F. J., 1985, "Local Heat Transfer Measurements on A Large, Scale-Model Turbine Blade Airfoil Using A Composite of A Heater Element and Liquid Crystals," NASA TM-86900.

Hodson, H. P., 1984, "Measurement of Wake-Generated Unsteadiness in the Rotor Passage of Axial Flow Turbines," ASME Paper No. 84-GT-189.

John, J., and Schobeiri, T., 1993, "A Simple and Accurate Method of Calibrating X-Probes," ASME Journal of Fluids Engineering, Vol. 115, pp. 148–152.

Kestoras, M. D., and Simon, T., 1993, "Combined Effects of Concave Curvature and High Free-Stream Turbulence Intensity of Boundary Layer Heat and Momentum Transport," ASME Paper No. 93-WA/HT-56.

Kline, S. J., and McKlintock, F. A., 1953, "Describing Uncertainties in Single-Sample Experiments," Mechanical Engineering, Vol. 75, Jan. pp. 3–8.

LaGraff, J. E., Ashworth, D. A., and Schultz, D. L., 1989, "Measurement and Modeling of the Gas Turbine Blade Transition Process as Disturbed by Wakes," ASME Journal of Turbomachinery, Vol. 111, pp. 315–322.

Liu, X., and Rodi, W., 1989, "Measurement of Unsteady flow Over and Heat Transfer From a Flat Plate," ASME Paper No. 89-GT-2.

Liu, X., and Rodi, W., 1992, "Measurement of Unsteady Flow and Heat Transfer in A Linear Turbine Cascade," ASME Paper No. 92-GT-323.

Mayle, R. E., Blair, M. F., and Kopper, F. C., 1979, "Turbulent boundary Layer Heat Transfer on Curved Surfaces," ASME JOURNAL OF HEAT TRANSFER, Vol. 101, pp. 521–525.

Mayle, R. E., and Dullenkopf, K., 1989, "A Theory for Wake-Induced Transition," ASME Journal of Turbomachinery, Vol. 112, pp. 188–195.

Mayle, R. E., 1991, "The Role of Laminar-Turbulent Transition in Gas Turbine Engines," ASME Journal of Turbomachinery, Vol. 113, pp. 509–537.

Orth, U., 1992, "Unsteady Boundary-Layer Transition in Flow Periodically Disturbed by Wakes," ASME Paper No. 92-GT-283.

Pfeil, H., and Herbst, R., 1979, "Transition Procedure of Instationary Boundary Layers," ASME Paper No. 79-GT-128.

Russell, L. M., Hippensteele, S. A., and Poinsatte, P. E., 1993, "Measurements and Computational Analysis of Heat Transfer and Flow in A Simulated Turbine Blade Internal Cooling Passage," NASA TM-106189.

Schobeiri, M. T., McFarland, E., Yeh, F., 1991, "Aerodynamic and Heat Transfer Investigations on a High Reynolds Number Turbine Cascade," ASME Paper No. 91-GT-157.

Schobeiri, T., and Pardivala, D., 1992, "Development of A Subsonic Flow Research Facility for Simulating The Turbomachinery Flow and Investigating its Effects on boundary layer Transition, Wake Development and heat Transfer," Fourth International Symposium on Transport Phenomena and Dynamics of Rotating Machinery, Washington, DC, pp. 98–114.

Schobeiri, T., and Radke, R., 1994, "Effects of Periodic Unsteady Wake Flow and Pressure Gradient on Boundary Layer Transition Along The Concave Surface of A Curved Plate," ASME Paper No. 94-GT-327.

Schobeiri, T., Read, K., and Lewalle, J., 1995a, "Effect of Unsteady Wake Passing Frequency on Boundary Llayer Transition, Experimental Investigation and Wavelet Analysis," ASME Paper No. 95-GT-437.

Schobeiri, T., Pappu, K., and Wright, L., 1995b, "Experimental Study of the Unsteady boundary Layer Behavior on A Turbine Cascade," ASME Paper No. 95-GT-435.

Schobeiri, M. T., John, J., and Pappu, K., 1996, "Development of Two-Dimensional Wakes Within Curved Channels, Theoretical Framework and Experimental Investigation," ASME Journal of Turbomachinery, Vol. 118, pp. 506–518.

Sharma, O. P., Renaud, E., Butler, T. L., Milsaps, K., Jr., Dring, R. P., and Joslyn, H. D., 1988, "Rotor-Stator Interaction in Axial-Flow Turbines," AIAA Paper No. 88-3013.

Simonich, J. C., and Moffat, R. J., 1984, "Liquid Crystal Visualization of Surface Heat Transfer on A Concavely Curved Turbulent Boundary Layer," ASME Journal of Engineering for Gas Turbines and Power, Vol. 106, pp. 619–627.

Walker, G. J., 1974, "The Unsteady Nature of Boundary Layer Transition on an Axial-Flow Compressor Blade," ASME Paper No. 74-GT-135.

Wang, T., and Simon, T. W., 1987, "Heat Transfer and Fluid Mechanics Measurements in Transitional Boundary Layers on Convex-Curved Surfaces," ASME Journal of Turbomachinery, Vol. 109, pp. 443–451.

Wittig, S., Schultz, A., Dullenkopf, K., and Fairbank, J., 1988, "Effects of Free-Stream Turbulence and Wake Characteristics on the Heat Transfer Along a Cooled Gas Turbine Blade," ASME Paper No. 88-GT-179.

Wright, L., 1996, "The Effect of Periodic Unsteady Wakes on Boundary Layer Transition and Heat Transfer on a Curved Surface," thesis, Texas A&M University, College Station, TX.

You, S. M., Simon, T. W., and Kim, J., 1989, "Free-Stream Turbulence Effects on Convex-Curved Turbulent boundary Layers," ASME JOURNAL OF HEAT TRANSFER, Vol. 111, pp. 66–76.

Zemskaya, A., Levitsky, V., Repik, Y., and Sosedko, Y., 1979, "Effect of the Proximity of the Wall on Hot-Wire Readings in Laminar and Turbulent Boundary Layers," Fluid Mechanics-Soviet Research, Vol. 8, No. 1, pp. 133–141.

Experimental and Numerical Investigation of Forced Convective Characteristics of Arrays of Channel Mounted Obstacles

T. J. Young

K. Vafai[1]
e-mail: vafai.1@osu.edu
Fellow ASME

Department of Mechanical Engineering,
The Ohio State University,
206 W. 18th Avenue,
Columbus, OH 43210

An experimental investigation of the forced convective heat transfer of individual and arrays of multiple two-dimensional obstacles is reported. The airflow rate was varied from $800 \leq Re_{D_h} \leq 13000$. The effects upon the Nusselt numbers and obstacle temperature differences of parametric changes in the Reynolds number, channel height, array configuration, and input heat flux are established. The input heat fluxes to the obstacles ranged from $950 \leq q'' \leq 20200 \ W/m^2$, which significantly extends beyond that seen in the open literature for forced convective air cooling of simulated electronic components. Comparisons of the obstacle mean Nusselt numbers are made with a two-dimensional laminar numerical model employing the Navier-Stokes equations. A set of correlations characterizing the heat transfer from the protruding heat sources within the channel is obtained. It was found that the obstacle temperature, the critical measure for electronic device failure, must be shown along with the corresponding Nusselt number to fully characterize the thermal state of the heated obstacle as the ratio definition of the Nusselt number can obscure large temperature increases. The results find that the proper placement of geometrically dissimilar obstacles, such as a taller obstacle, can be used to passively enhance the heat transfer in its vicinity. This effect would be dependent upon the flow rate and geometries in order to control the reattachment zones and their subsequent convective augmentation. The experimental results are found to be in good agreement with the results from the numerical simulation. Finally, a set of pertinent correlations for the arrays of channel mounted obstacles is given.

Introduction

The canonical model for the cooling of electronic devices, convective heat transfer from discrete heated obstacles in a channel, has been of interest for several decades (Peterson and Ortega, 1990). With each new generation of electronic devices that are further miniaturized and, concurrently, required to handle and dissipate larger energy loads, thermal management becomes the limiting operational factor (Mahefkey, 1995). In order to reduce localized hot spots, increase energy throughput, and reduce the failure rate, which is proportional to the exponential of the device junction temperature (U. S. DoD, 1991), thermal design of electronic components must necessarily be improved.

The forced convective cooling of flush-mounted and protruding two-dimensional heated obstacles in a channel was experimentally investigated by McEntire and Webb (1990). For an airflow range of $10^3 \leq Re \leq 10^4$ and heat fluxes of 850 W/ m^2, protruding heat sources were found to enhance the heat transfer compared with the flush sources. The characterization of turbulent flow and convective heat transport of single isolated two and three-dimensional obstacles in a channel was performed by Roeller et al. (1991). Larger obstacle widths increase the flow acceleration by blocking more channel flow area while

smaller widths have more intense three-dimensional transport effects.

The two-dimensional conjugate heat transfer problem for laminar flow over an array of three obstacles was solved, utilizing a control volume formulation, by Davalath and Bayazitoglu (1987). Their obstacles had uniform conductivity and were volumetrically heated. The spacing between the obstacles was varied from one to two times the obstacle width. Their analysis included the effects of obstacle spacing on the maximum temperature attained within the obstacles and the development of overall mean Nusselt number correlations of the form $\overline{Nu}_m = a \ Re^b \ Pr^c$ for the obstacles.

The use of an odd-sized rectangular obstacle within a three-dimensional array of square obstacles, with maximum heat fluxes of 6700 W/m^2, was found to enhance the heat transfer up to 40 percent by Jubran et al. (1996). Jubran and Al-Salaymeh (1996), using a similar experimental apparatus added spanwise ribs and spanwise "film cooling" to the obstacle array in order to enhance heat transfer up to 50 percent. Pressure drops were found to increase by nearly 70 percent when utilizing these techniques. Sparrow et al. (1984) also investigated the effects of height differences within three-dimensional arrays of square obstacles and found, using the naphthalene sublimation technique, heat transfer enhancements of up to 80 percent compared with an array of uniform height. A comprehensive experimental study of heat transfer in the entrance region of an array of rectangular heated blocks was presented in Molki et al. (1995).

In the previous studies, the periodicity within the ten obstacle array has been shown at the five percent difference level and at the less restrictive ten percent level. The mean Nusselt number,

---

Copyright © 1999 by ASME

which reflects both fluid and thermal conditions, for eight and seventh obstacles were within five percent and ten percent, respectively, of the value found at the ninth obstacle. The local values of the velocity components and temperature at the "periodic" boundaries clarify and support the use of periodic boundary conditions for obstacles that are assumed to be located away from the entrance. Comparisons with experimental work shows similar results. Lehmann and Pembroke (1991) reported Nu_m being constant, within experimental uncertainty, for rows six to ten. Garimella and Eibeck (1990) reported that the heat transfer coefficient was asymptotic by the fourth row in their experiments.

This work presents a systematic and thorough investigation of forced convective cooling of a two-dimensional array of multiple heated obstacles located upon one wall of an insulated channel. Experiments were performed for a generic set of obstacles representative of an electronics cooling configuration over a range of geometries, input thermal energies, and airflow rates. The experiments were carried out over a range of Reynolds numbers, $800 \leq Re_{D_h} \leq 13000$, typical of forced air cooled electronics. The input heat flux to the test articles mounted within the channel ranged from $950 \leq q'' \leq 20200$ W/m^2. This input heat flux range significantly extends that seen in the open literature for forced air cooling experiments of heated obstacles. The influences of parametric changes in the obstacle geometry, spacing, number, thermal conductivity, and heating method, at various flow rates, upon the flow and heat transfer were examined prior to experimentation to isolate the important criteria for performing the tests. The dependence of the streamlines, isotherms, and Nusselt numbers on the governing parameters was studied. The different geometric arrangements that were employed to study the effects upon the heat transfer include changes in the channel height and the use of an individual obstacle or an array of five similar obstacles. The effect of the position of a taller obstacle within an array was also investigated. It is shown that very large heat fluxes approach the limits for sensible heat convective transport while substantially increasing the obstacle to coolant temperature difference. The use of a taller obstacle in an array was found to provide heat transfer enhancement downstream as the core flow expands, providing a method to tune thermal transport at specific positions.

Experimental Apparatus and Procedure

The test channel which was constructed to study the forced convective heat transfer of the heated test articles, including the entrance and outlet plenums and the related test and measurement equipment, is shown in Fig. 1. The setup was designed for accurate measurements as well as enabling a wide range of adjustments in the relevant parameters, such as Reynolds number, channel height, and obstacle number and spacing. The purpose of the experiments is to obtain the temperatures and con-

vective heat transfer coefficients at the obstacle surfaces for various coolant rates and obstacle arrangements.

As shown in Fig. 2, the channel walls, floor, and base were constructed of 12.7-mm-thick clear acrylic ($k \approx 0.2$ W/m·K) while the ceiling was 6.4-mm-thick clear acrylic. The test channel has a length of 2.5 m with approximately 1.7 m between the entrance and test section. Slots in the vertical walls permit ceiling assembly adjustments to be made that allow a channel height range of about $H = 10$ to 90 mm. The channel width was fixed at $W = 305$ mm to reduce end effects upon the measurements made along the channel spanwise centerline. Roeller et al. (1991) found, for a similar channel arrangement, that the end wall effects were limited to ten percent of the channel width. All joints were sealed with silicone rubber sealant or vinyl tape to ensure that no air leakage occurred. At the channel entrance, isolation from the ambient environment is achieved using a large cubical plenum (0.8 m each side) with multiple screens positioned at the inlet. A honeycomb structure assures smooth airflow transition into the test channel. At the channel outlet, a 0.4-m-long plenum with a gradual rectangular to circular transition employs several layers of fine mesh to isolate the test channel from downstream influences.

A regenerative blower, rated at 4 to 80 SCFM and operating in suction mode to reduce airflow disturbances within the test channel, drew air through the test channel and to the appropriate orifice plate bypass flow meter (AquaMatic FLT series) depending upon the desired flow rate. The factor calibration of the flow meters showed accuracy of better than two percent. The recommended lengths of straight pipe were installed before and after the orifice plates to ensure accurate measurements. The exhaust air was routed away from the experimental apparatus to avoid tainting the inlet air or measurement of ambient conditions.

The test articles that were mounted within the flow channel were machined from solid 6061-T6 aluminum alloy ($k = 165$ W/m·K). As shown in the details of Fig. 2, a 3.2-mm-deep cavity for the heater was machined into the obstacle base in order to provide an insulative air gap between the obstacle and the channel floor. The contact areas between the obstacle base and the channel floor are only 1.6 mm wide across nearly the entire channel width in order to reduce conductive losses to the channel floor. The exposed obstacle surfaces were polished with very fine steel wool prior to testing. The obstacles were firmly affixed to horizontal slots in the test section vertical walls. This arrangement allowed the obstacle number and spacing within the test section to be varied. Two different obstacle sizes were employed in this work: 28.6_25.4_305 mm and 28.6_12.7_305 mm (streamwise length, height, and spanwise width, respectively).

The constant heat flux at the base of the test articles was applied using thin-film etched foil heaters (Watlow Electric)

Nomenclature

A, B, C, D = obstacle corners
D_h = channel hydraulic diameter, m
h = obstacle height, m
h_c = convective heat transfer coefficient, W/(m^2·K)
H = channel height, m
k = thermal conductivity, W/(m·K)
L = obstacle streamwise length, m
Nu = Nusselt number, $h_c H/k_f$
Pe_H = Péclet number, $\rho_f c_{p_f} u_m H/k_f$

q = heat transfer rate, W
q'' = heat flux, W/m^2
Re_{D_h} = Reynolds number, $\rho_f u_m D_h/\mu_f$
s = obstacle spacing, m
T = temperature, °C
u = velocity, m/s
W = channel width, m
μ = dynamic viscosity, (N·s)/m^2
ρ = density, kg/m^3
Θ = dimensionless temperature, $(T - T_e)/(q''H/k_f)$

Subscripts

e = entrance
elec = electrical
f = fluid
m = mean
s = solid
w = wall
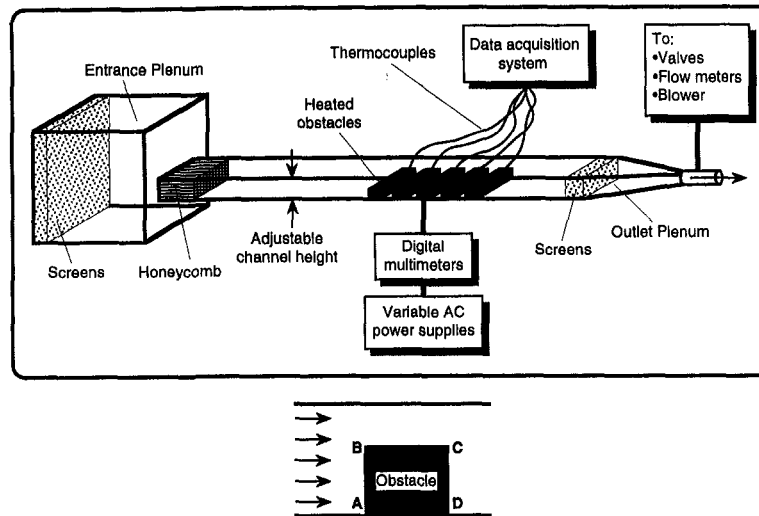
Fig. 1 Schematic diagrams of the experimental apparatus and heated obstacle edge view
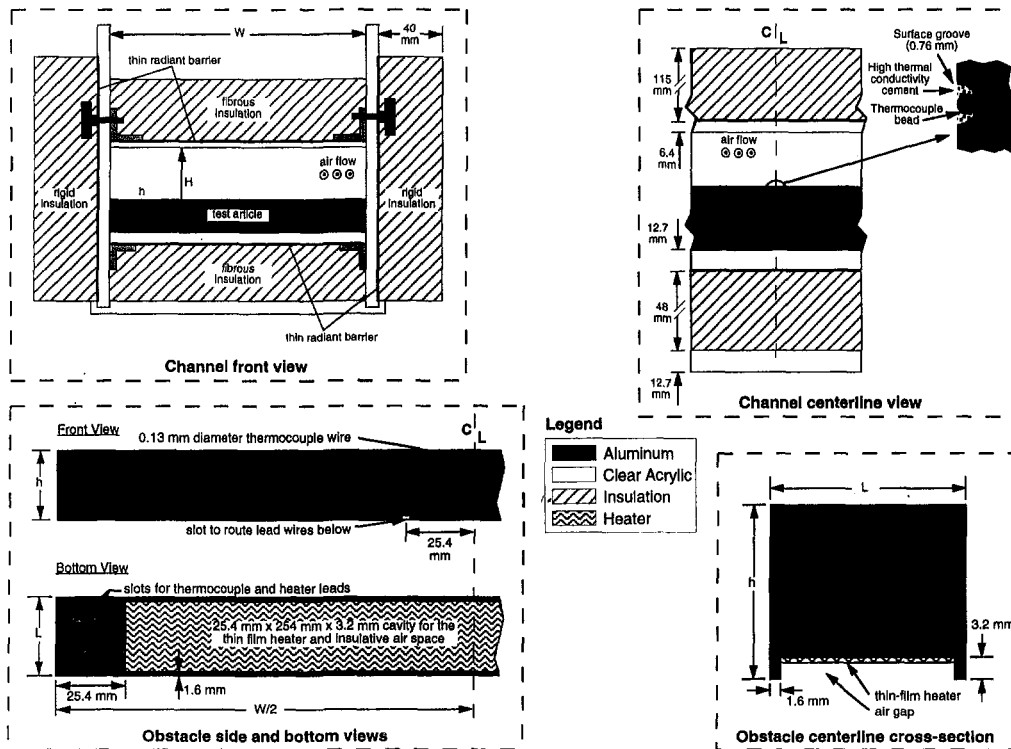
Fig. 2 Details of the experimental test channel and test articles

rated at 100 watts with length 254 mm and width 25.4 mm. An unheated spanwise length of 25.4 mm was situated adjacent to the obstacle attachment points. The heaters were attached to the obstacles by means of a pressure-sensitive adhesive capable of providing good thermal contact. To reduce radiative losses, the downward-facing exposed heater surface was coated with a reflective low-loss coating while a thin reflective barrier was applied immediately outside the four channel walls. Conductive losses from the channel were reduced through the use of fibrous insulation ($k \approx 0.04$ W/m·K) at the channel top (115 mm thick) and bottom (48-mm-thick) surfaces and expanded polystyrene insulation ($k \approx 0.07$ W/m·K), 40 mm thick, along the vertical channel surfaces.

In order to accurately measure the temperature of the wetted surfaces, the aluminum obstacles were instrumented by embedding thin (36 AWG) Type-E thermocouples in very small (0.76 mm) surface grooves designed to minimize flow disturbances (Fig. 2). The thermocouple beads were located along the spanwise obstacle centerline ($W/2$). The lead wires were led away from the centerline in the grooves and routed underneath the obstacle to avoid disturbing the airflow. High thermal conductivity cement (Omega OB-400) was used to hold the thermocouples in place and completely fill the grooves in order to minimize the effects of removing material from the obstacles. The taller obstacles employed ten thermocouples: four on the top surface (**BC**) and three each on the up (**AB**) and down-

stream (**CD**) surfaces. The shorter obstacles had eight thermocouples: four on the top surface (**BC**) and two each on the vertical (**AB** and **CD**) surfaces. One thermocouple was employed outside the test channel to measure the ambient air temperature.

The electrical power to each heater under test was supplied by a separate a-c autotransformer. The variable output of the autotransformers allowed precise and individual control of up to 140 VAC (at ±0.5 percent or better) to be furnished to the heaters. The RMS voltages and currents were measured using calibrated digital multimeters. The thermocouple signals were amplified, filtered, and multiplexed near the test section to reduce noise corruption and signal errors.

The experimental site was a very large volume room capable of absorbing the warm airflow output from the blower without affecting the ambient conditions. The experiments were performed meticulously, for example, through verifications of adjusted dimensions with digital calipers, thorough cleanings of the test channel interior, and regular observations of the flow rate and the heater input powers. To begin the experiments the blower was first metered to the desired flow rate. The required input power to the heaters was then supplied by the autotransformers while the voltage and current were recorded for heat flux calculations. The obstacle temperatures were continuously monitored until steady-state conditions were reached (approximately 45 to 300 minutes, depending upon airflow rate and heater power). A data acquisition system was used to gather and process the thermocouple signals and perform data reduction. To verify the attainment of steady conditions, several experiments were run after the steady-state conditions were attained to supply additional data for comparison. Duplicate experimental runs were performed at each test, and on different days, to verify the repeatability of the results.

Data Reduction. The local convective heat transfer coefficient on the obstacle surface was defined as

$$h_c = \frac{q}{A_c(T - T_e)} \quad (1)$$

where the convective heat transfer, q, was calculated from

$$q = q_{\text{elec}} - (q_{\text{cond}} + q_{\text{rad}} + q_{lw}). \quad (2)$$

In the above expressions A_c is the test article wetted surface area, T and T_e are the local surface and ambient temperatures, respectively, $q_{\text{elec}} = EI$ is the total electrical power input to the heater, and q_{cond}, q_{rad}, and q_{lw} are the heat losses due to conduction, radiation, and lead wire conduction, respectively. The conduction heat loss was estimated at four percent using measurements of the temperature drop across the channel walls and through use of a miniature heat flux sensor (Concept Engineering) located beneath the channel floor. The radiation loss was estimated at two percent while a one-dimensional conduction analysis found the heater lead wire loss to be less than one percent and was combined into the conduction loss estimate. Each temperature value (T, T_e) gathered was the mean of 100 readings. The standard deviation for these sets of temperatures was found to vary between 0.005 and 0.15°C.

The local Nusselt number was defined as $\text{Nu} = h_c H/k_f$. The mean Nusselt number was found as the average of the local values,

$$\text{Nu}_m = \frac{\int_{A_c} \text{Nu} \, dx}{A_c}. \quad (3)$$

The Reynolds number was defined as $\text{Re}_{D_h} = \rho_f u_m D_h / \mu_f$, where the mean fluid velocity, u_m, was found from the volumetric flow rate within the channel and the channel hydraulic diameter is $D_h = 2WH/(W + H)$. All thermophysical properties of the air were evaluated at the entrance temperature.

Experimental Uncertainty. An error analysis utilizing the method of Kline and McClintock (1953), as extended by Moffat (1988), was performed to evaluate the uncertainty in the experimental data. The relative uncertainty of dependent variable $R = f(\lambda_i)$ was obtained using

$$\frac{\delta R}{R} = \left[\sum_{i=1}^{N} \left(\frac{\delta \lambda_i}{\lambda_i} \right)^2 \right]^{1/2}. \quad (4)$$

Best and worst-case values were assessed for the uncertainties in the relevant independent variables. The Nth-order uncertainty in the Nusselt numbers obtained was calculated to lie between 4.3 and 8.5 percent whereas that in the Reynolds numbers was between 3.5 and 7.7 percent. A first-order uncertainty estimate of the data scatter (Moffat, 1988) found that, in 25 repeated trials, the standard deviation of the measured temperature difference $T - T_e$ for the ten thermocouples on an individual obstacle was less than one percent.

Numerical Analysis and Procedure

A numerical model for the convective cooling of heated obstacle arrays located in a two-dimensional insulated wall channel was developed and utilized for comparative purposes. The Navier-Stokes equations for the laminar flow of a steady incompressible Newtonian fluid with constant thermophysical properties were solved, fully accounting for the conductive energy flow through the solid obstacles. The governing conservation equations are

Mass

$$\frac{\partial u_i}{\partial x_i} = 0. \quad (5)$$

Momentum

$$\text{Re}_H \left(u_k \frac{\partial u_j}{\partial x_k} \right) = -\frac{\partial p}{\partial x_j} + \frac{\partial^2 u_j}{\partial x_i \partial x_i}. \quad (6)$$

Energy (fluid)

$$\text{Pe}_H \left(u_j \frac{\partial \Theta_f}{\partial x_j} \right) = \frac{\partial^2 \Theta_f}{\partial x_i \partial x_i}. \quad (7)$$

Energy (solid)

$$\frac{\partial^2 \Theta_s}{\partial x_i \partial x_i} = 0. \quad (8)$$

Boundary conditions were specified along the entire solution domain due to the elliptic nature of the governing equations. At the obstacle bases, a constant surface heat flux was applied.

Entrance

$$u = 6y(1 - y), \quad v = 0, \quad \Theta_f = 0. \quad (9)$$

Outlet

$$\frac{\partial u}{\partial x} = 0, \quad \frac{\partial v}{\partial x} = 0, \quad \frac{\partial \Theta_f}{\partial x} = 0. \quad (10)$$

Fluid/solid interfaces

$$u = 0, \quad v = 0, \quad \Theta_f = \Theta_s, \quad k_f \frac{\partial \Theta_f}{\partial \mathbf{n}} = k_s \frac{\partial \Theta_s}{\partial \mathbf{n}}. \quad (11)$$

Channel walls

$$u = 0, \quad v = 0, \quad \frac{\partial \Theta_f}{\partial y} = 0. \quad (12)$$

The system of equations that are being solved as well as the boundary conditions are of the elliptic form. The reason that the boundary conditions at the right-hand side of the domain are not explicitly specified is explained in what follows (this is already partly discussed in the text but in the revised manuscript this discussion has been expanded). The fact that needs to be mentioned in here is, through extensive numerical experimentation, it was discovered that the boundary conditions on the right-hand side of the computational domain have a limited effect on the upstream results. In fact, this influence was usually not more than ten grid points upstream due to the strong parabolic nature of the problem. Hence, the type of boundary condition specification on the right-hand side of the computational domain did not have much influence on the physical domain. Therefore, by using an extended computational domain, very accurate results for our physical domain were performed. That is, the computational domain was always chosen to be larger than the physical domain. Extensive tests on the effect of varying the size of the computational domain were run, and its effects on the physical domain were observed to ensure that the boundary conditions on the downstream side of the computational domain (the right-hand side) had no influence on the results. In our work, for simplicity, the conditions at the last interior grid points from the outflow boundary condition in the previous iteration were used and it yielded the same solution for the domain of interest except for the region very close (this is the region which was part of our computational domain but not the physical domain) to the downstream boundary as when the other conditions were used.

Indeed, this mesh was designed to capture the critical features near the obstacle region and to provide sufficient mesh density, with minimal element distortion, at the obstacle surfaces. Extensive tests, involving mesh densities and gradings, were performed to confirm the grid independence of the model until further refinement showed less than a one-percent difference in the results. To eliminate the influences of the entrance and outlet upon the solution near the obstacle region, as described by Vafai and Kim (1990), additional tests were performed by individually increasing the lengths of the channel before and after the obstacle array. Entrance effects were found to be effectively isolated with $L_e = 2$. An outlet length of $L_o = 8$ ensured that the large downstream recirculation zone was well ahead of the outlet and that the fluid exited in a parabolic profile. Therefore, the problem was solved without making any assumptions regarding a periodic boundary condition and as such the solution is more accurate.

The local Nusselt numbers, found from $\mathrm{Nu} = h_c H / k_f = -\Theta_w^{-1}(\partial \Theta_f / \partial n)$, where n is the surface normal, were averaged to obtain the mean obstacle Nusselt numbers. Because of the geometric differences between the experimental flow channel and the two-dimensional model, a geometric factor was utilized to allow comparison between the Reynolds numbers. The mean fluid velocities (u_m) in the Reynolds number definitions for the numerical and experimental methods were equalized, which resulted in the ratio $\mathrm{Re}_{\mathrm{exp}}/\mathrm{Re}_{\mathrm{num}} = W/(W + H)$, allowing the numerical results to be compared with the experimental data.

To validate the numerical scheme used in the present investigation, comparisons with previous studies were performed. This was achieved through adjustments to the model to match the geometric, hydrodynamic, and thermal conditions of the related works. First, comparisons were made with the analytical solutions of Cess and Shaffer (1959a, b) with respect to the problems of thermal entry length in a channel with constant wall temperature or heat flux. Calculated entrance region and fully developed Nusselt numbers showed excellent agreement. Next, a hydrodynamic comparison with the single obstacle case of Zebib and Wo (1989) was made. Thermal comparisons were not made due to lack of information for their multiconductivity obstacle and the multilayer channel walls with a constant con-

vective coefficient beneath the bottom surface. Their three inlet velocities correspond to $\mathrm{Re}_{D_h} = 806$, 1772, and 3222. A comparison of the recirculation zone and reattachment length behind the obstacle was within ~2 percent for the lowest two Reynolds numbers and within ~8 percent for the highest (run as laminar flow even though the Reynolds number was well within the transition regime).

The solution to the governing equations was found through the Galerkin finite element method (FIDAP, 1993). A highly variable mesh was employed to capture the critical features near the obstacle regions and to provide sufficient mesh density, with minimal element distortion, at the obstacle surfaces. Extensive tests, involving mesh densities and gradings, were performed to confirm the grid independence of the model. Complete details of the solution scheme and the extensive validation studies can be found in Young and Vafai (1998a, b) and will not be presented for brevity.

Results

The experiments reported here fall into three distinct classes based upon the number and geometry of the test articles located within the channel: an individual obstacle, an array of five, similar obstacles, and an array of four obstacles incorporating one taller obstacle. The study included the effects of changes in the Reynolds number, Re_{D_h}, input electrical power to the heaters, q_{elec}, and channel height, H, upon the heat transfer, characterized by the Nusselt number. The Reynolds number ranged from $800 \leq \mathrm{Re}_{D_h} \leq 13000$ while the input electrical power imposed upon the heaters, $q_{\mathrm{elec}} = EI$, ranged from 6.1 to 130.2 W ($950 \leq q''_{\mathrm{elec}} \leq 20200$ W/m^2, where $q''_{\mathrm{elec}} = q_{\mathrm{elec}}/A_h$ and A_h is the heater-obstacle contact area). Measured temperature differences ranged from $3 \leq T_m - T_e \leq 148$°C. The streamwise length of the obstacles, L, was chosen to nondimensionalize the geometric data as it remained constant at $L = 28.6$ mm. Two obstacle heights were thus employed, $h/L = 0.44$ and 0.89, while the channel height varied in the range of $1.22 \leq H/L \leq 3.11$.

Single Obstacle. For these experiments a single obstacle was placed within the test channel. Numerical results corresponding to some experimental runs were obtained using the method described above. Presented in Fig. 3(a) are comparisons between the experimentally and numerically obtained mean Nusselt numbers for an individual heated obstacle of height $h/L = 0.89$ in a channel of height $H/L = 3.11$. The numerical model is seen to slightly over predict the Nusselt number as the Reynolds number increases, from 3.6 percent at Re = 770 to 13.6 percent at Re = 1530. Overall, the agreement is very good and it was observed that the experimental and numerical results display the same trends in the Nusselt number with changes in the airflow rate. Similar comparative results between the experimental and numerical data are shown in Fig. 3(b) for an individual obstacle of height $h/L = 0.44$ within the channel of height $H/L = 3.11$ in the laminar regime.

To provide a baseline for the parametric analyses and for further comparison, a single obstacle of height $h/L = 0.89$ was placed within the test channel of height $H/L = 1.57$. The mean Nusselt numbers of the single obstacle, for $800 \leq \mathrm{Re}_{D_h} \leq 13000$, and an input power of $q_{\mathrm{elec}} = 54.6$ W ($q''_{\mathrm{elec}} = 8500$ W/m^2), were found and compared with the composite correlation of Roeller et al. (1991) developed for a range of obstacle geometries. Figure 4 shows the experimental mean Nusselt number data for the parameters given above and two correlations. The first is the least-squares correlation developed for the experimental data,

$$\mathrm{Nu}_m = 0.4472\,\mathrm{Re}_{D_h}^{0.5618}, \tag{13}$$
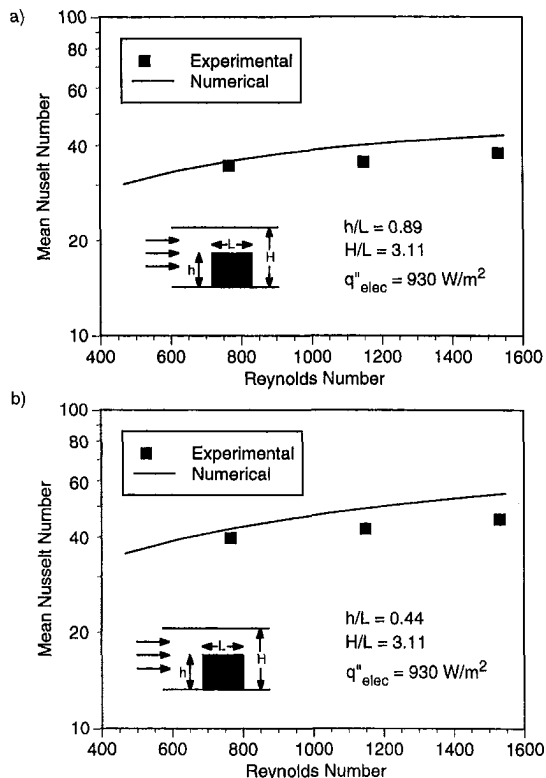
with $R^2 = 0.96$, for the wide range of Reynolds numbers, 800

Fig. 3 Mean Nusselt number comparison between the experimental and numerical analyses for h/L = 0.89, H/L = 3.11, and q''_{elec} = 930 W/m²

Fig. 5 Mean Nusselt number comparisons, and corresponding temperature differences, between the single obstacle baseline case (Nu_{m0} = 105.7) and cases with parametric variations in (a) Reynolds number, (b) input electrical power to the heater, and (c) channel height

$\leq Re_{D_h} \leq 13000$. The second curve is the composite correlation recommended by Roeller et al. (1991), $Nu_m = 0.454\, Re_{D_h}^{0.555}$, for the given geometries. The experimental data of Fig. 3 is matched fairly well by either correlation, with the correlation of Roeller et al. (1991), thereby corroborating the current results.

The mean Nusselt number at Re_{D_h} = 13000 in Fig. 4, considered as the baseline single-obstacle case (Nu_{m0} = 105.7), was used to normalize the mean Nusselt numbers presented in the parametric results of Fig. 5. An increase in mean Nusselt number with increased Reynolds number, for fixed geometry and input electrical power, is shown in Fig. 5(a). As the flow rate, and consequently the convective heat transfer was increased, the average surface temperature difference decreased from about 147°C to 32°C. With this large imposed heat flux, large

Fig. 4 Comparison of the experimental data for h/L = 0.89, H/L = 1.57, and q''_{elec} = 8500 W/m² with the correlation developed by Roeller et al. (1991)

airflow rates are required to keep the obstacle temperatures, and corresponding electronic device failure rates, low. Figure 5(b) reports the results found when at a fixed geometry (h/L = 0.89, H/L = 1.57) and airflow rate (Re_{D_h} = 13000), the electrical power input to the heater is parametrically varied from 6 W to 130 W (950 $\leq q''_{elec} \leq$ 20200 W/m²). The Nusselt numbers are roughly grouped into two regions. At the lower heat fluxes the Nusselt numbers are within ±5 percent of that of the baseline. At the larger heat fluxes the trend is for the Nusselt numbers to decrease with increasing heat flux. Though the decrease in Nusselt numbers is small as the input heat flux increases from about 15 to 20 kW/m², the temperature difference increases considerably. Such temperature increases have the potential to destroy electronic devices, though this is not immediately apparent when consulting the dimensionless parameters because the $q/(T - T_e)$ ratio in the Nusselt number definition (Eq. (1)) decreases slightly as the heater input power is increased. The general decrease in mean Nusselt numbers at greater heater input powers suggests that the forced convective heat transfer limit for direct air cooling is being approached (Peterson and Ortega, 1990).

The effect that a change in channel height (1.22 $\leq H/L \leq$ 2.97) for fixed-obstacle size, airflow rate, and input heater power has upon the mean heat transfer is shown in Fig. 5(c). The Reynolds number, for fixed airflow rate, changes about 15 percent due to the channel height variation. When the channel height is at its lowest value, the airflow velocity through the bypass region increases, causing an increase in the convective heat transfer and a corresponding reduction in obstacle temperature compared with the baseline case. The Nusselt number for the largest channel height (H/L = 2.97) was found to be about five percent greater than for H/L = 2.27, though the larger channel height case has a surface temperature difference of about 14°C greater than that for H/L = 2.27. Again, due to the exponential dependence of electronic device failure on temperature (U. S. DoD, 1991), hidden temperature increases, such as these, need to be accounted for. A local minimum in the Nusselt number versus channel height curve is expected as this curve should have positive concavity. Consider the mean Nusselt number definition $Nu_m = (h_c)_m H/k_f \propto H/(T_m - T_e)$. At the

Fig. 6 Mean Nusselt number comparisons between the experimental and numerical results for a three obstacle array with $h/L = 0.44$, $s/L = 0.44$, $H/L = 3.11$, and $q''_{elec} = 930$ W/m^2

tion of the numerical model to include three dimensions and low Reynolds number turbulence modeling, for example.

For the set of multiple obstacle array experiments, two different test article geometries were considered. In the first case, five identical obstacles of height $h/L = 0.89$ and inter-obstacle spacing $s/L = 1.0$ were placed within the channel of height $H/L = 1.57$. In the second case, four obstacles of identical streamwise length and spacing ($s/L = 0.72$) were utilized, but three obstacles were of height $h_2/L = 0.44$ while one was $h/L = 0.89$. The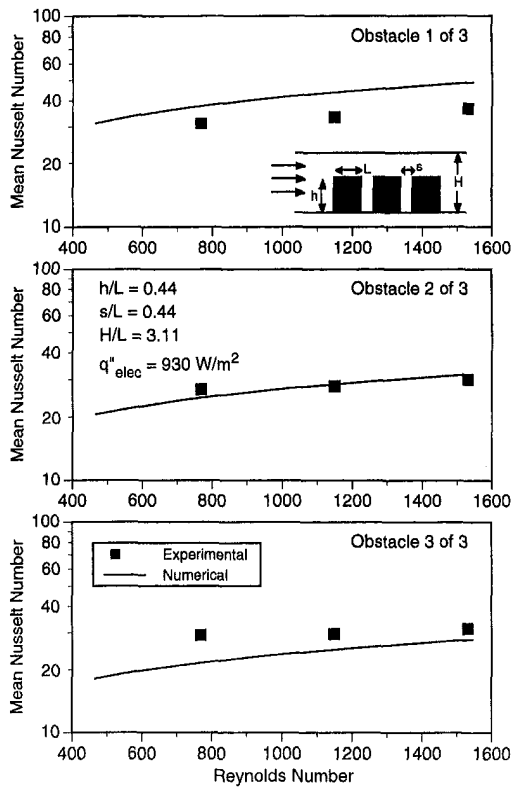 taller obstacle was systematically positioned in all four possible locations within this array configuration to investigate its effect upon the convective heat transfer.

The experimental mean Nusselt numbers for the five obstacle array at $2500 \leq \mathrm{Re}_{D_h} \leq 13000$ and $q''_{elec} = 3750$ W/m^2 are shown in Fig. 8. An effort was made to compare this Nusselt number data for the five heated obstacles with other experimental works. McEntire and Webb (1990) tested an array of four two-dimensional surface-heated-only thermally insulative obstacles. Their composite relation for the mean convective heat transport considering all four obstacles in their array, over the range $1850 \leq \mathrm{Re}_{D_h} \leq 9300$, was $\mathrm{Nu}_m \propto \mathrm{Re}^{0.61}$. As shown in Fig. 8, this composite correlation over predicts the data generated in the current experimental apparatus, which is to be expected as the insulative obstacles employed by McEntire and Webb (1990) eliminate the reduced convective transport from the vertical obstacle surfaces. The mean Nusselt numbers shown in Fig. 8 do account for the reduced convective behavior along the vertical surfaces of the conducting obstacles and, as a result, show lower Nusselt numbers than the composite correlation of McEntire and Webb (1990). However, the least-squares corre-

smallest channel heights (H), with the resulting greater mean channel airflow velocities (u_m), the reduced obstacle temperature difference dominates the Nusselt number. As the channel height increases, the mean airflow velocity decreases, reducing the convective transport at the obstacle and increasing its temperature. Near the local minimum neither H nor ($T_m - T_e$) dominates the Nusselt number. However, as the channel height increases beyond the local minimum, its increases are greater than the resulting increases in temperature difference, causing the ratio $H/(T_m - T_e)$, and, hence, the Nusselt number, to increase. Consider dramatic increases in channel height (beyond the heights given in the current experimental apparatus) where the changes in temperature would be small compared with the increases in H, resulting in an "artificial" increase in Nusselt number.

Multiple Obstacle Arrays. The numerical analysis was utilized to compare the mean convective heat transfer behavior for the system-like configuration of an array of three heated obstacles of height $h/L = 0.44$ and inter-obstacle spacing $s/L = 0.44$ within a channel of height $H/L = 3.11$. For the experiments the input heat flux was $q''_{elec} = 930$ W/m^2 while the airflow was kept within the laminar regime. Figure 6 shows, for the three obstacles, the mean Nusselt number comparison between the experimental and numerical analyses. Both analyses show the trends of increased Nusselt number with increases in Reynolds number and decreased convective heat transfer with downstream obstacle position. For each of these trends, the numerical analysis, however, shows differences, such as a greater Nusselt number increase with increased flow rate and larger Nusselt number decreases with downstream position. A similar comparison for an array of five obstacles with the geometry $h/L = 0.89$, $s/L = 1.0$, and $H/L = 3.11$, is shown in Fig. 7. A reduction in the disparities between the experimental and numerical results could come with an increase in the sophistica-
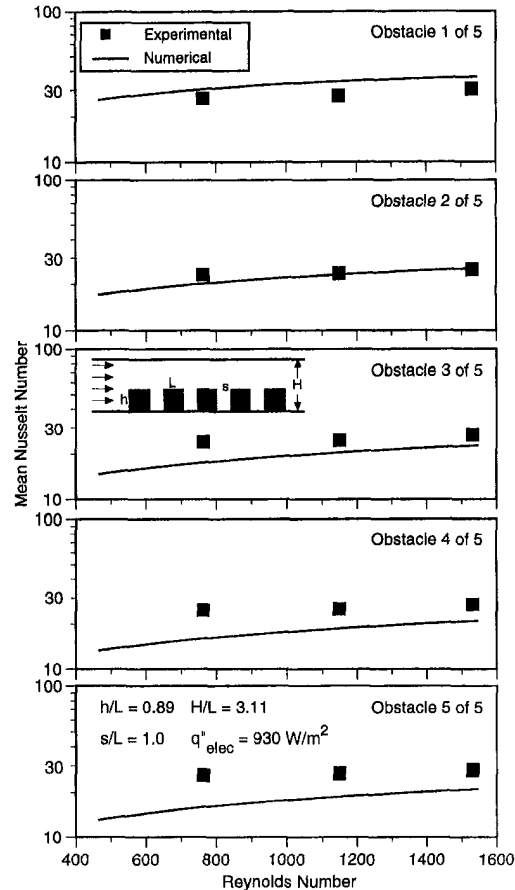

Fig. 7 Mean Nusselt number comparisons between the experimental and numerical results for a three obstacle array with $h/L = 0.89$, $s/L = 1.0$, $H/L = 3.11$, and $q''_{elec} = 930$ W/m^2
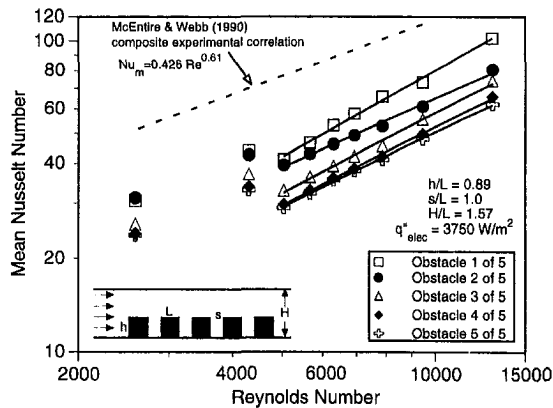
Fig. 8 Mean Nusselt numbers for the array of five identical obstacles with $h/L = 0.89$, $s/L = 1.0$, $H/L = 1.57$, and $q''_{elec} = 3750$ W/m^2

Fig. 9 Mean Nusselt numbers for the four obstacle array with one taller obstacle ($h/L = 0.89$) systematically positioned in an array of obstacles with height $h_2/L = 0.44$ ($s/L = 0.72$, $H/L = 1.57$, $Re_{D_h} = 9450$, $q''_{elec} = 3750$ W/m^2)

lation for the experimental data of Fig. 8, considering all five obstacles in the array

$$\mathrm{Nu}_m = 0.186\ \mathrm{Re}_{D_h}^{0.61} \tag{14}$$

($2500 \le \mathrm{Re}_{D_h} \le 13000$), does exhibit nearly the same Reynolds number dependency.

The general trends in the obstacle mean Nusselt numbers are an increase with increased Reynolds numbers and a decrease with downstream obstacle position. At a Reynolds number of about 4500, however, the relationship between the Nusselt and Reynolds numbers changes. Dividing the data at this point and applying least-squares correlations using the equation

$$\mathrm{Nu}_m = A\ \mathrm{Re}_{D_h}^{B} \tag{15}$$

(with correlation coefficients greater than 0.99) shows a considerable difference in the Reynolds number exponents (B), as shown in Table 1. This is perhaps attributable to the change in the flowfield from transitional to fully turbulent, though velocity surveys would be required to corroborate this point. The channel mean velocity at this flow rate is about 0.9 m/s. Arvizu and Moffat (1981) found that, in the fully developed regime of an array of obstacles, $\mathrm{Nu}_m \propto \mathrm{Re}^{0.75}$, which is similar to that reported here for downstream obstacles 2–5. The first obstacle in the array was found to have a greater Reynolds number exponent. This is due to the greater heat transfer along the upstream vertical face (**AB**) caused by core flow impingement. The downstream obstacles do not experience this heat transfer along their vertical faces because the core flow does not expand substantially into the interobstacle cavities and interact strongly with this fluid when the obstacles are moderately spaced ($s/L = 1.0$).

Table 1 Mean Nusselt number correlation parameters for the five identical obstacle array with $h/L = 0.89$, $s/L = 1.0$, $H/L = 1.57$, and $q''_{elec} = 3750$ W/m^2

Obstacle Number	Re_{D_h} Range	A	B
1	2600 - 4300	0.1262	0.699
	5000 - 13000	0.0140	0.940
2	2600 - 4300	0.2701	0.605
	5000 - 13000	0.0672	0.746
3	2600 - 4300	0.1028	0.703
	5000 - 13000	0.0212	0.860
4	2600 - 4300	0.1339	0.661
	5000 - 13000	0.0244	0.833
5	2600 - 4300	0.1661	0.632
	5000 - 13000	0.0338	0.794

$$\mathrm{Nu}_m = A\,\mathrm{Re}_{D_h}^{B}$$

$h/L = 0.89$, $s/L = 1.0$, $H/L = 1.57$, $q''_{elec} = 3750\,\mathrm{W/m^2}$
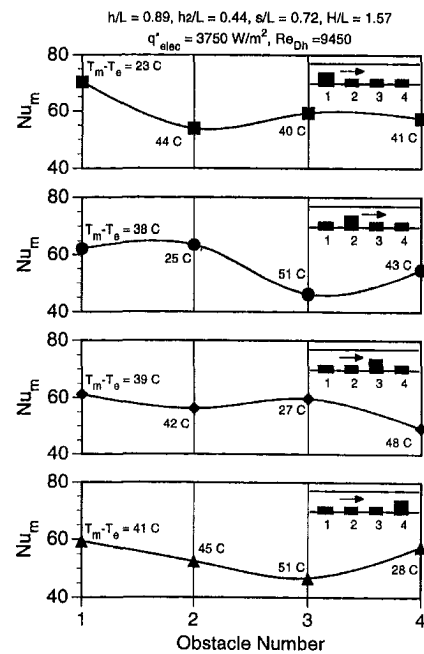
In order to quantify the effects caused by a taller obstacle upon the heat transfer from the remaining shorter obstacles in the array, in the thermal development region, experiments were performed for four ordered configurations. In these four cases the taller obstacle ($h/L = 0.89$) was systematically located in the first through fourth positions in the array while the remaining three positions were populated with obstacles of height $h_2/L = 0.44$. All four of the obstacles were of the same length, L, the interobstacle spacing was maintained at $s/L = 0.72$, and the channel height was $H/L = 1.57$. The airflow rate was held at $Re_{D_h} = 9450$ while the input electrical power to the heaters yielded $q''_{elec} = 3750$ W/m^2.

When compared with the shorter obstacles in the array, the introduction of the taller obstacle into the array reduces the bypass area, causing the air flow rate to increase as it is diverted upwards away from the channel floor into the bypass region. Beyond the taller obstacle the core flow expands which, in the absence of further obstructions, would produce a large recirculation, with corresponding low fluid velocities, that would reattach to the channel floor downstream. The effect found here was, as expected, that the shorter obstacle immediately behind the taller obstacle always showed a decrease in mean Nusselt number, as shown in Fig. 9, and an increase in temperature difference ($T_m - T_e$). It should be noted that the curves in Fig. 9 are for illustrative purposes to elucidate the trends in the mean Nusselt numbers for each of the obstacles in the arrays. The shorter obstacles further downstream, however, show an increase in Nusselt numbers. This increase is due to the reattachment of the expanding core flow, causing increased mixing and flow impingement upon these downstream obstacles.

The mean Nusselt numbers of the taller obstacle, at each position in the array, form an envelope under which the Nusselt numbers for the shorter obstacles remain below. The downstream obstacles with heat transfer enhancement due to flow impingement do, though, draw near to these values. The temperatures of the shorter obstacles, however, are always larger than that of the taller obstacle due to their reduced convective surface area. This result suggests that the proper placement of geometrically dissimilar obstacles, in this case a taller obstacle, can be

used to passively enhance the heat transfer for critical components in its vicinity, though, again, the temperature must be found to characterize the thermal state of the component. The proper tuning of such a system would be dependent upon the flow rate and geometries in order to control the reattachment zones and their subsequent convective augmentation. Since the current experimental configuration emphasizes the spanwise obstacle formation, the effect of the flow recirculation immediately behind the taller obstacle is further pronounced. Without streamwise flow passages between obstacles, there is no suction influence to draw the fluid in this low-velocity/high-pressure region away. The result is the heat transfer decrease immediately behind the taller obstacle.

Conclusions

An experimental investigation was performed to determine the thermal effects of parametric changes to a modular airflow channel containing individual and arrays of heated two-dimensional obstacles. The effects of changes in the channel height, input heater power, and airflow rate upon the mean Nusselt numbers and surface temperature differences were documented for an individual as well as an array of obstacles within the channel. As expected, low flow rates were found to significantly increase the temperature of the obstacle due to reduced convective coefficients. Very large heater powers were also found to increase the obstacle temperature as the limits for sensible heat convective transport for air are approached. Large-obstacle temperature increases, the critical measure for electronic device failure, were explicitly detailed as they were found to be obscured by the Nusselt number due to its definition as a ratio. The experimental mean Nusselt numbers for individual and multiple obstacle arrays were found to be in good agreement with the numerical model. The mean heat transfer from individual and arrays of protruding heat sources within the channel was correlated with the airflow Reynolds number. For the individual obstacle, with $h/L = 0.89$, $H/L = 1.57$, and $q''_{\text{elec}} = 8500$ W/m^2, the correlation obtained was

$$\text{Nu}_m = 0.4472 \, \text{Re}_{D_h}^{0.5618}(800 \leq \text{Re}_{D_h} \leq 13000).$$

For the obstacle array with geometry $h/L = 0.89$, $s/L = 1.0$, $H/L = 1.57$, and $q''_{\text{elec}} = 3750$ W/m^2, correlations of the form $\text{Nu}_m = A \, \text{Re}_{D_h}^B(2600 \leq \text{Re}_{D_h} \leq 13000)$ were obtained for all five of the obstacles within the array, where A and B are given in Table 1. The position of a taller obstacle in an array was found to reduce the heat transport from the obstacle immediately behind it, though it also enhanced the thermal transport from obstacles further downstream that benefit from increased mixing and impingement as the core flow expands and reattaches. This passive heat transfer augmentation effect would require the synchronization of the airflow rate with the channel and obstacle geometries to control the reattachment region and its subsequent convective augmentation.

Acknowledgments

References

Arvizu, D. E., and Moffat, R. J., 1981, "Experimental heat transfer from an array of heated cubical elements on an adiabatic channel wall," Report HMT-33, Thermosciences Division, Department of Mechanical Engineering, Stanford University, Stanford, CA.

Cess, R. D., and Shaffer, E. C., 1959a, "Heat Transfer to Laminar Flow Between Parallel Plates with a Prescribed Wall Heat Flux," *Applied Scientific Research*, Vol. A8, pp. 339–344.

Cess, R. D., and Shaffer, E. C., 1959b, "Summary of Laminar Heat Transfer Between Parallel Plates with Unsymmetrical Wall Temperatures," *J. Aero Space Sciences*, Vol. 26, p. 538.

Davalath, J., and Bayazitoglu, Y., 1987, Forced Convection Cooling Across Rectangular Blocks, ASME JOURNAL OF HEAT TRANSFER, Vol. 109, pp. 321–328.

FIDAP, 1993, *Theory Manual*, Fluid Dynamics International, Evanston, IL.

Garimella, S. V., and Eibeck, P. A., 1990, Heat Transfer Characteristics of an Array of Protruding Elements in Single-Phase Forced Convection, *Int. J. Heat Mass Transfer*, Vol. 33, pp. 2659–2669.

Jubran, B. A., Swiety, S. A., and Hamdan, M. A., 1996, "Convective heat transfer and pressure drop characteristics of various array configurations to simulate the cooling of electronic modules," *Int. J. Heat and Mass Transfer*, Vol. 39, pp. 3519–3529.

Jubran, B. A., and Al-Salaymeh, A. S., 1996, "Heat transfer enhancement in electronic modules using ribs and 'film-cooling-like' techniques," *Int. J. of Heat and Fluid Flow*, Vol. 17, pp. 148–154.

Kline, S. J., and McClintock, F. A., 1953, "Describing uncertainties in single-sample experiments," *Mechanical Engineering*, Jan., pp. 3–8.

Lehmann, G. L., and Pembroke, J., 1991, Forced Convection Air Cooling of Simulated Low Profile Electronic Components: Part 1—Base Case, ASME *Journal of Electronic Packaging*, Vol. 113, pp. 21–26.

Mahefkey, E. T., 1995, "High temperature (500–600 K) power electronics thermal management," *Proc. 12th Symposium on Space Nuclear Power and Propulsion*, American Institute of Physics, New York, pp. 917–929.

McEntire, A. B., and Webb, B. W., 1990, "Local forced convective heat transfer from protruding and flush-mounted two-dimensional discrete heat sources," *Int. J. Heat and Mass Transfer*, Vol. 33, pp. 1521–1533.

Moffat, R. J., 1988, "Describing the uncertainties in experimental results," *Experimental Thermal and Fluid Science*, Vol. 1, pp. 3–17.

Molki, M., Faghri, M., and Ozbay, O., 1995, "A Correlation for Heat Transfer and Wake Effect in the Entrance Region of an In-Line Array of Rectangular Blocks Simulating Electronic Components," ASME JOURNAL OF HEAT TRANSFER, Vol. 117, pp. 40–46.

Peterson, G. P., and Ortega, A., 1990, "Thermal control of electronic equipment and devices," *Advances in Heat Transfer*, Vol. 20, J. P. Hartnett and T. F. Irvine, eds., Academic Press, San Diego, pp. 181–314.

Roeller, P. T., Stevens, J., and Webb, B. W., 1991, "Heat Transfer and Turbulent Flow Characteristics of Isolated Three-Dimensional Protrusions in Channels," ASME JOURNAL OF HEAT TRANSFER, Vol. 113, pp. 597–603.

Sparrow, E. M., Yanezmoreno, A. A., and Otis, D. R., 1984, "Convective heat transfer response to height differences in an array of block-like electronic components," *Int. J. Heat and Mass Transfer*, Vol. 27, pp. 469–473.

U. S. Department of Defense, 1991, "Reliability Prediction of Electronic Equipment," Military Handbook MIL-HDBK-217F, Washington, DC, Chapter 6.

Vafai, K., and Kim, S. J., 1990, Analysis of Surface Enhancement by a Porous Substrate," ASME JOURNAL OF HEAT TRANSFER, Vol. 112, pp. 700–705.

Young, T. J., and Vafai, K., 1998a, "Convective Cooling of a Heated Obstacle in a Channel," *Int. J. Heat Mass Transfer*, Vol. 41, pp. 3131–3148.

Young, T. J., and Vafai, K., 1998b, "Convective flow and heat transfer in a channel containing multiple heated obstacles," *Int. J. Heat Mass Transfer*, Vol. 41, pp. 3279–3298.

Zebib, A., and Wo, Y. K., 1989, A Two-Dimensional Conjugate Heat Transfer Model for Forced Air Cooling of an Electronic Device, ASME *Journal of Electronic Packaging*, Vol. 111, pp. 41–45.

S. Parneix

M. Behnia

Center for Turbulence Research,
Stanford University,
Stanford, CA 94305-3030

P. A. Durbin

Mechanical Engineering Department,
Stanford University,
Stanford, CA 94305-3030

Predictions of Turbulent Heat Transfer in an Axisymmetric Jet Impinging on a Heated Pedestal

Cooling or heating of a flat plate by an impinging jet, due to its many applications, has been widely studied. Recent experimental data concerning more complex geometries has become available. In this study, the cooling of a heated pedestal mounted on a flat plate, a configuration which is closer to the one met in some engineering applications (e.g., cooling of electronic components), has been numerically simulated. The normal velocity relaxation turbulence model (V2F model) in an axisymmetric geometry has been adopted. Results have been obtained for a range of jet Reynolds numbers and jet-to-pedestal distances. Comparison of the predicted heat transfer coefficient with experiments has shown a very good agreement. For comparison, results have also been obtained with the widely used k–ε turbulence model and the agreement with the data is poor.

1 Introduction

Jet impingement is an effective mean of localized heating or cooling. In many engineering and industrial applications, this process is used to achieve high heat fluxes (Nakayama, 1995). In such applications, a turbulent jet of gas or liquid is directed onto the target area of interest. There are a number of parameters to be considered in the design of such systems: the jet-to-target distance, the flow rate, jet diameter, the overall geometry of the system. However, the impinging flow produces a nonuniform temperature field on the surface, which makes it impossible to characterize heat transfer by a single coefficient. A detailed knowledge of the temperature distribution (including the local wall heat transfer coefficient) is required in order to understand the process. To this end, the flow and thermal fields must be accurately and economically computed.

In the last two decades, a number of comprehensive literature reviews citing numerous jet impingement studies has been published (e.g., Martin, 1977; Downs and James, 1987; Viskanta, 1993). Most of these studies have been concerned with either free or confined jets impinging on flat surfaces. They have determined the influence of many parameters of importance on the heat transfer rate.

Due to the complexity of the flow field, the impinging jet is also a challenging test case for validation of turbulence models; a number of investigators have gauged the success of their models on this flow. The complex features of turbulent impinging jets include entrainment, stagnation, change of flow direction, and streamline curvature. Most turbulence models have been developed using flows parallel to the wall; they can encounter difficulties with impingment flows. In commercial CFD codes, heat transfer is usually predicted with standard or modified versions of the $k–\epsilon$ turbulence model. Recent computations with this model have shown a 100 percent overprediction of heat transfer in the stagnation region of an impinging jet (Craft et al., 1993). Although a high range of variability has been sometimes reported by different experimentalists, some recent experiments (Baughn and Shimizu 1989; Baughn et al., 1991; Yan, 1993; Lytle and Webb, 1994), using rigorously identical jet flow conditions (fully developed pipe flows at the jet exit),

only showed a 20 percent scatter: Turbulence modeling was clearly responsible for the major part of this overestimation. The $V2F$ turbulence model (Durbin, 1995) has been indeed successfully used for flat-plate impingment, giving much better predictions, with improved numerical stability (Behnia et al., 1998).

The objective of the present work was to accurately compute the flow and thermal fields in an axisymmetric isothermal jet perpendicular to a heated pedestal mounted on a flat plate. The geometry resembles that of an electronic component. Very little experimental and computational work has been done previously on impinging flows in geometries other than flat plates. To our knowledge, only concave (Lee et al., 1997) and convex (Mesbah, 1996) circular impinging surfaces have been studied experimentally, and no computations have been compared to these "complex" configurations. Recently, Mesbah (1996) has measured the local heat transfer coefficient on a heated pedestal. He used the preheated-wall transient technique in conjunction with surfaces coated by thermochromic liquid crystals. For comparison purposes we adopted the same geometry. We solved the axisymmetric incompressible Navier-Stokes, the turbulent kinetic energy (k) and dissipation (ϵ) equations in conjunction with the v^2 transport and the f elliptic relaxation equations (hence the acronym $V2F$ model) on a nonuniform, orthogonal, cylindrical grid. In addition, computations were performed using the standard $k–\epsilon$ turbulence model with wall damping.

2 Turbulence Model

The concept of the $V2F$ turbulence model, used in the following computations, involves some new elements: We defer to the references for lengthy discussion (Durbin, 1991; Durbin, 1993a, b, 1995, 1996; Behnia et al., 1998) and to the Appendix for the whole set of equations of the model. In summary, it is a general model, using a linear eddy viscosity assumption (Eq. (1) which keeps excellent stability properties); it is valid up to the solid wall. There is no need to use wall functions, i.e., the "log-law," whose universality is questionable, especially in impinging flows. The usual alternative to wall functions is to introduce some form of damping function in an attempt to represent the effects of a proximate wall on the turbulence (e.g., Craft et al., 1993). Damping functions often involve the "ill-behaved" normalized distance to the wall; this can be problematic in complex configurations. Some damping functions can also be highly nonlinear and numerically stiff.

What is desired is a more physically based approach. All engineering models use a single-point formulation and cannot represent the nonlocal effects of pressure reflection, which occur near solid boundaries. In part, $V2F$ is an attempt to approximate such effects within the confines of single-point closure; this part of the model is the elliptic-relaxation equation for f (Eq. (6)); f is analogous to the pressure-strain correlation in Reynolds stress transport closures (cf. Durbin, 1993a).

A new velocity scale, $\overline{v^2}$, is used to evaluate the turbulent viscosity; in some cases this might be regarded loosely as the velocity fluctuation normal to streamlines, it becomes the velocity fluctuation normal to a solid surface, irrespective to the direction of this surface. Launder (1986) and Durbin (1991) noted that $\overline{v^2}$, and not k, was the appropriate scaling for evaluating turbulent transport near the wall. Indeed, this new scale drastically improves the evaluation of turbulence near solid boundaries, especially, it allows to represent better the anisotropy of near-wall turbulence.

Further, the more physical Kolmogorov time scale—respectively, length scale—is used instead of the traditional k/ϵ— $k^{3/2}/\epsilon$—in the viscous sublayer near the wall (Durbin, 1991). Finally, some constraints have been added in order to prevent nonrealizability of the solution, especially in the stagnation region (Durbin, 1996); this imposes some maxima limits on the turbulence scales (see Eqs. (8) and (9)). The equations of the model are outlined in the Appendix. Note that the distance to the closest wall, δ, is still used in the definition of the coefficient C'_{ϵ_1} (making it to vary from 1.3 to 1.55), but it does not present the same kind of restrictions as using δ directly in a damping function.

The temperature field is computed by a standard eddy diffusivity approximation. In a previous study on jet impingment (Behnia et al., 1998), several Pr_t formula were considered. The Kays and Crawford formulation (1993) was chosen, since it gave a more physical representation near the wall and yielded somewhat better agreement in the impingement region. However, the improvement over using a constant Pr_t was only of the order of ten percent. It is inescapable that the flow and the turbulent fields have to be accurately modeled to obtain good heat transfer predictions.

3 Configuration

The problem is the cooling of a heated pedestal, mounted on a heated flat plate. Most impinging jet computations have been conducted with a single flat plate. The present configuration is more characteristic of an electronic component being cooled by a jet. Recently, experiments in this geometry were performed by Mesbah (1996). He adopted the preheated-wall transient liquid crystal method, developed and validated by Yan (1993) and Baughn et al. (1993).

Figure 1 is a sketch of the computational domain. The geometry is axisymmetric, so our computations were on a cylindrical mesh. The jet issues from a very long pipe, such that the nozzle-exit turbulent profiles are fully developed. The cylindrical pedestal diameter and height, d, are both equal to $D/1.06$ (D is the diameter of the jet pipe). On top of the pedestal, in the
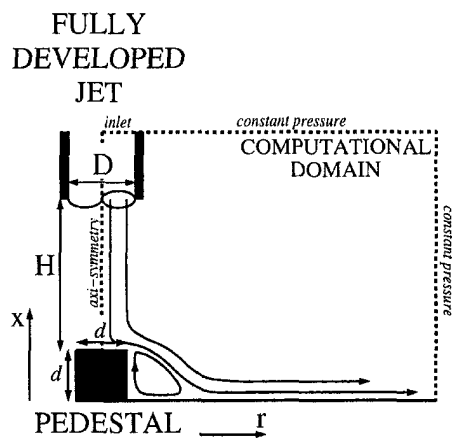

Fig. 1 Schematic of the geometry and computational domain

impingement region, the mean flow is perpendicular to the wall. It then turns sharply and follows the upper surface of the pedestal. The flow separates at the corner of the body and reattaches downstream on the flat plate. A recirculation zone adjacent to the pedestal was observed in the experiments. Beyond the reattachment point, a wall jet develops.

Profiles at the inlet were created by solving a fully developed turbulent pipe flow on a very fine grid. To ensure high accuracy inlet data, at least five points were placed in the region where $y^+ \leq 5$, in the laminar layer. These high-accuracy profiles were interpolated onto each grid used for the pedestal geometry. The full computation did not use, or require the degree of resolution used to generate the inlet data.

As for previous flat-plate calculations (Craft et al., 1993; Behnia et al., 1998), we included part of the pipe in the computational domain, mainly for stability and accuracy of the numerical simulations. The upper boundary of the domain was placed far from the pedestal and a constant static pressure condition was specified there. This pressure was set equal to the constant pressure imposed on the right outlet boundary of the domain (cf. Fig. 1). The thickness of the pipe wall was $0.112D$.

Computations were performed at various jet Reynolds numbers ($U_{jet}D/\nu$) and various aspect ratios ($1 \leq H/D \leq 8$) corresponding to the experiments. All simulations used a generalized coordinate, finite difference code (Rogers and Kwak, 1990). The spatial discretization of convective terms was via a third-order flux-difference splitting scheme in all the equations. Each computation required several minutes on a Cray C90 for complete convergence. The code uses the artificial compressibility method to solve the incompressible RANS equations; for this method the most stringent convergence criterion is placed on the flow divergence; we used max ($\nabla \cdot U$) $\leq 10^{-4}$. The latter condition has been tested to be sufficient for ensuring a complete convergence, giving an average residual of about 10^{-6} for all the equations of the model.

For the $k-\epsilon$ model, we used the same k and ϵ equations as for $V2F$, but included a damping function for the eddy viscosity

———— Nomenclature ————

C_p = specific heat
D = diameter of the jet
H = nozzle-to-pedestal distance
Nu = Nusselt number Nu = hD/κ
Pr = Prandtl number Pr = $\mu C_p/\kappa$
Pr_t = turbulent Prandtl number
Re = Reynolds number Re = $U_{jet}D/\nu$
U = mean velocity
U_{jet} = jet bulk velocity

d = diameter and height of the pedestal
f = variable related to energy redistribution
h = wall heat transfer coefficient $h = q/(\Theta_{wall} - \Theta_{in})$
k = turbulent kinetic energy
q = local surface heat flux on the wall
$\overline{v^2}$ = velocity scale for turbulent transport
x_n = normal distance to the wall

Θ = temperature
Θ_{in} = inlet temperature
Θ_{wall} = constant temperature at the wall
δ = distance to the closest boundary
ϵ = dissipation rate of turbulence
κ = thermal conductivity
μ = fluid dynamic viscosity
ν = fluid kinematic viscosity
ν_t = turbulent kinematic viscosity

of the form $\nu_t = 0.09kT[1 - \exp(-0.01|kT/\nu|)]$, instead of using $\overline{v^2}$. This yields results similar to the Launder and Sharma model (Craft et al., 1993) for the case of jet impingement on a flat plate (see Behnia et al., 1998). This version was chosen in order to keep the tested model as close as possible to the $V2F$ set of equations. The impact of the new scaling $\overline{v^2}$ and the elliptic equation for representing nonlocal effects of near-wall turbulence, can be assessed better.

4 Preliminary Computations

The flow around the pedestal is far more complex than for the single flat impingment plate. A very thin boundary layer approaches the corner of the pedestal, where separation occurs. A thin, curved, highly turbulent region develops along the separated shear layer, then reattaches to the base plate at the side of the pedestal. This reattachment region requires a high density of discretization nodes. The presence of the jet makes the streamline curvature stronger in this region than in a classical backward-facing step. The chosen mesh has 300 nodes in the axial direction, with half of them placed between the top of the pedestal and the base plate, and 165 nodes in the radial direction, with half of them placed in the recirculation and reattachment region. Note that a smaller number of nodes would have been obtained with a non-Cartesian mesh.

Grid sensitivity has been studied by doubling the number of grid points in both directions. The computed Nusselt number is presented in Fig. 2. The difference between the two computations is less than one percent everywhere, except in the reattachment location where the difference is less than two percent. Since the local heat transfer coefficient is extremely sensitive to variations in the mean flow or temperature solution, the 300 $\times$ 165 mesh is deemed accurate and has been used for all the following simulations.

The preheated-wall transient technique used in the experiment presents a difficulty in deciding the heat transfer boundary condition. In the experimental technique, the local heat transfer coefficient is determined from a difference between two measurements of the surface temperature difference at two different times. The boundary condition is not exactly constant wall temperature. In addition to temporal variation of the surface temperature, horizontal variations occur as well, especially near the corners of the pedestal. To examine the effect of this uncertainty, we compared solutions for isothermal and constant heat flux boundary. Fortunately, the overall distribution of Nusselt number was rather insensitive to this boundary condition, especially on top of the pedestal. Differences were all well below other sources of experimental uncertainty. This is consistent with previous results on the flat-plate configuration. All computations have been performed with a constant wall temperature.

Fig. 3 Streamlines for $H/D = 2$ and Re = 23,000

5 The Turbulent Flow Field at Re = 23,000

Contours of Stokes streamlines are shown in Figs. 3 and 4 for $H/D = 2$ and 6, respectively. Only a qualitative analysis will be done since no flow measurements are available. Both cases show similar features. The flow is parallel to the jet axis at the nozzle exit, develops into a free jet, and decelerates as it impinges on top of the pedestal. Then, it turns sharply and starts to form a radial wall jet along the upper surface of the pedestal. At the corner, the flow separates, reattaching downstream on the base plate. The recirculation zone that forms at the side of the pedestal has a significant effect on wall heat transfer. The length of this recirculation, L, varies slightly with the nozzle-to-pedestal distance: $L/d \simeq 1.33$ for $H/D = 2$ and $L/d \simeq 1.22$ for $H/D = 6$. This zone is much shorter than can be found downstream of a backward-facing step, where typical lengths are $L/d \simeq 5 - 8$. After reattachment, the flow develops into a wall jet along the flat plate.

Ambient fluid is entrained into the core of the jet prior to impingement. This entrainment is shown by the curvature of the ambient streamlines towards the symmetry axis. It leads to the small recirculation zone at the exit of the pipe. Resolution of the recirculation zones requires sufficient gridding in these regions and provides a further demonstration of the adequacy of the present grid.

Values or turbulent kinetic energy, obtained from both $V2F$ and $k-\epsilon$ computations, are contrasted in Fig. 5. The fields of

Fig. 2 Grid sensitivity (Re = 23,000, $H/D = 6$)
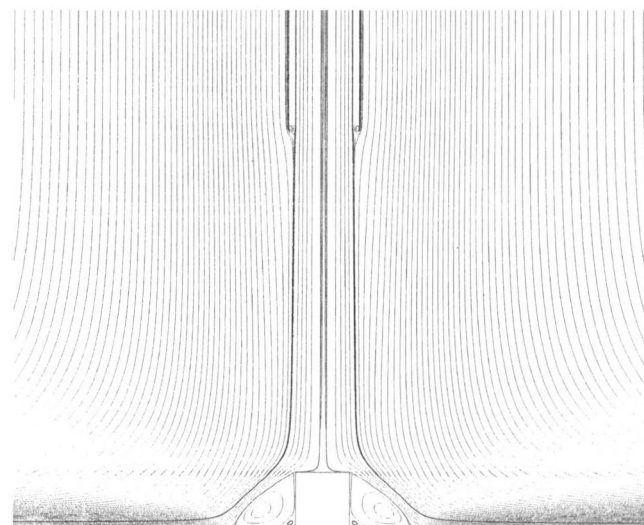
Fig. 4 Streamlines for $H/D = 6$ and Re = 23,000
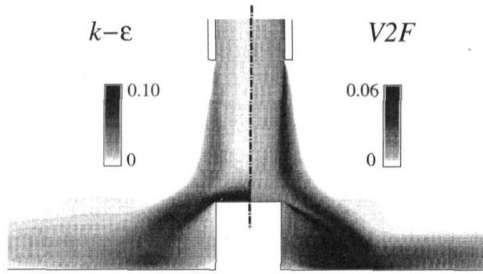
Fig. 5 Shaded contours of *k* for *H/D* = 2 and Re = 23,000

the turbulent kinetic energy are rather different in these two computations: $k-\epsilon$ predicts the highest values of k on top of the pedestal and in part of the shear layer above the recirculation zone; $V2F$ shows that the highest values are in the whole shear layer and around the reattachment on the flat plate, the turbulence being damped in the stagnation region on the upper surface of the pedestal. The maximum value of k computed with the $k-\epsilon$ model is about 70 percent higher than the $V2F$ model. This high level of turbulent kinetic energy on top of the pedestal is believed to be responsible for the overprediction of heat transfer by $k-\epsilon$ in the whole domain.

6 Heat Transfer Predictions at Re = 23,000

After computing the fluid flow, the temperature equation was solved with an isothermal boundary condition along the upper surface of the pedestal, its side and the base plate. For all nozzle-to-pedestal distances computed, a general trend was observed: the heat transfer coefficient has a local minimum on the stagnation line on top of the pedestal. The Nu number is nearly constant in the vicinity of the stagnation point and then increases sharply as the corner is approached. The sharp increase of the heat transfer coefficient at the corner is due to the strong flow convergence. It occurs too close to the edge of the pedestal to be resolved by the experiment. Also, standard boundary conditions (constant heat flux or constant temperature) might not be valid any more and may explain the smoother distribution of the experimental profiles.

The value of stagnation Nusselt number is similar to that of a jet impinging on a flat plate. However, the local Nusselt number distribution is radically different. On the flat wall, the stagnation Nusselt number is a local maximum (Behnia et al., 1998). Hence, the flat plate results are not suitable for complex geometries. Figures 6 and 7 show that the $V2F$ model reproduces the local minimum at the symmetry line, whereas the k–
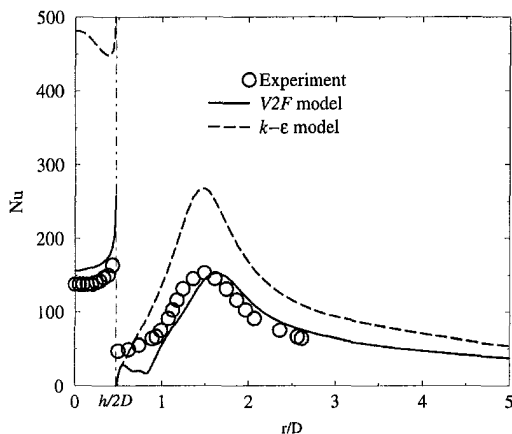

Fig. 6 The local wall heat transfer coefficient for *H/D* = 2 and Re = 23,000 on top of the pedestal (left of – · –) and downstream of pedestal on the flat plate (right of – · –)
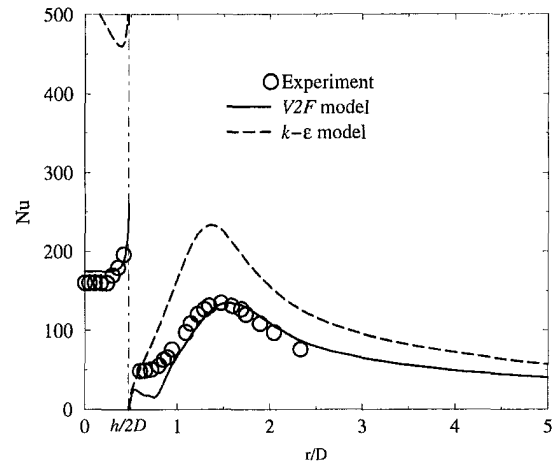
Fig. 7 The local wall heat transfer coefficient for *H/D* = 6 and Re = 23,000 on top of the pedestal (left of – · –) and downstream of pedestal on the flat plate (right of – · –)

ϵ predictions show a local maximum and a sharp decrease of Nu for all values of H/D.

Quantitatively, $k-\epsilon$ predictions overestimate the wall heat transfer above the whole pedestal upper surface by more than 150 percent. This overprediction is believed to be due to the overprediction of turbulent kinetic energy in that region. The $V2F$ computations are much more realistic with only 5 to 15 percent overprediction. For the impinging jet on a flat plate, the set of available experiments shows a 20 percent data scatter (Behnia et al., 1998).

Along the plate, a local maximum wall heat transfer point is created in the reattachment region, about one diameter downstream of the pedestal and slightly upstream of the reattachment point. The $V2F$ model predicts both the location and magnitude of this peak accurately; $k-\epsilon$ predictions show almost 100 percent overprediction. This may be due to transport of the heat transfer overprediction on top of the pedestal, rather than to an overprediction of turbulence production in the reattachment area: The angle of impingement is much smaller in the reattachment region than near the symmetry axis. Finally, the $V2F$ simulations show a plateau with a secondary peak at the foot of the pedestal. This phenomenon is believed to be due to the existence of a secondary recirculation. The plateau is present in the experiment, but without any secondary maximum. In the experiment, longitudinal heat transfer in the solid near the corner of the pedestal may have affected the data (it acts as smoothing the heat transfer coefficient). Long measurement times were also required in this region; added to the fact that a local one-dimensional approximation is used in the experimental methodology, this may make the transient technique inaccurate (see Mesbah, 1996). Too much uncertainty does exist in the dataset to really assess the performances of the models.

Local heat transfer coefficients were also measured on the side of the pedestal. Figure 8 presents the corresponding values obtained by both $V2F$ and $k-\epsilon$ models for $H/D = 6$. There are two local extrema, which indicate complex flow features downstream of the pedestal (at least one recirculation cell). These extrema are captured by both models. The $V2F$ computations fit with the experimental data in the upper half of the pedestal, and $k-\epsilon$ shows a better agreement in the lower half. The variation of heat transfer along the vertical wall of the pedestal seems to be more pronounced in the experiment than in either computation. This local disagreement between the $V2F$ predictions and the experiment may appear surprising at first sight, since the rest of the domain shows very good agreement. However, these side walls are also in the recirculation region, where the measurements are subject to considerable uncertainty, as stated previously.

Fig. 8 The local wall heat transfer coefficient on the side of the pedestal for Re = 23,000 and H/D = 6

Fig. 10 Effect of the nozzle-to-pedestal distance on the maximum heat transfer coefficient downstream of the pedestal for Re = 23,000

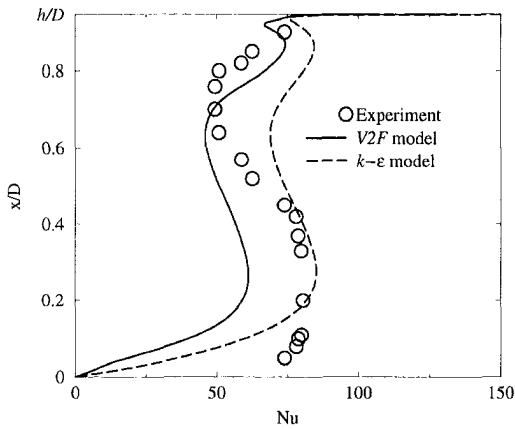Simulations have been carried out for a Reynolds number of 23,000 and a wide range of jet-to-pedestal distances in order to determine the dependence upon H/D of the stagnation Nusselt number, on top of the pedestal, and the maximum Nusselt number on the plate. Figures 9 and 10 show values computed with both the $V2F$ and $k-\epsilon$ models. The $V2F$ computations show very good agreement with Mesbah's experiment. The transient technique yielded results in the lower band of flat-plate experimental data (Behnia et al., 1998), so the 5 to 15 percent overprediction may be considered as quite accurate. Moreover, the parametric dependence of stagnation Nusselt number on H/D is very well reproduced. The $V2F$ computations show a slight maximum in the range $6 < H/D < 7.5$. This cannot be compared to Mesbah's experiment, since H/D = 6 was the highest aspect ratio studied, but this corresponds to the behavior for the flat plate (see Yan, 1993; Behnia et al., 1998).

The $k-\epsilon$ model fails to reproduce the experimental trends, quantitatively or qualitatively. The latter may be more critical than the former from a practical point of view. Both models produce a constant decrease with H/D of the maximum Nusselt number downstream of the pedestal (Fig. 10). However, the $k-\epsilon$ computations yield almost a 100 percent overestimating, whereas $V2F$ simulations are close to the experiment.

7 Influence of Re Number

All the above simulations have been performed at a single Reynolds number of 23,000. The accuracy of the model at different Reynolds numbers has to be checked. Previous compu-

tations of an impinging jet on a flat plate (Behnia et al., 1998) have shown the ability of the model to reproduce the influence of Re. Mesbah (1996) performed two additional sets of experiments at Re = 50,000 and 70,000. These were also simulated and the results are presented here.

Figures 11 and 12 are a comparison of the heat transfer coefficient on top of the pedestal and on the plate for the three Reynolds numbers at two nozzle-to-pedestal distances (H/D = 2 and 6). Qualitatively and quantitatively, the predicted influence of Re is largely in agreement with the data. The primary discrepancy occurs on the plate, in the region close to the pedestal. Here a strong underprediction is noted. This may be due to the effect of the thermal boundary condition or the inaccuracy of the data, as mentioned previously.

The computational results have been used to determine the exponent of the Reynolds number in the Nusselt number relationship Nu $\propto$ (Re)$^\gamma$. This was done both for the stagnation area on top of the pedestal and for the maximum of local heat transfer on the plate. The respective γ have been computed only with three points, so they are subject to high uncertainty, but the $V2F$ simulations have been seen to follow similar trends to the experiment. The "laminar-like" exponent of 0.5 on top of the pedestal, widely cited in the literature (Yan, 1993; Lee et al., 1995), is well predicted by the model: γ evaluated by the $V2F$ is 0.51 for H/D = 2 and 0.55 for H/D = 6; the experimental values (again, based on only three points) were 0.60 for H/D = 2 and 0.65 for H/D = 6. On the flat plate, the maximum Nusselt number does not follow the Re$^{0.5}$ trend;
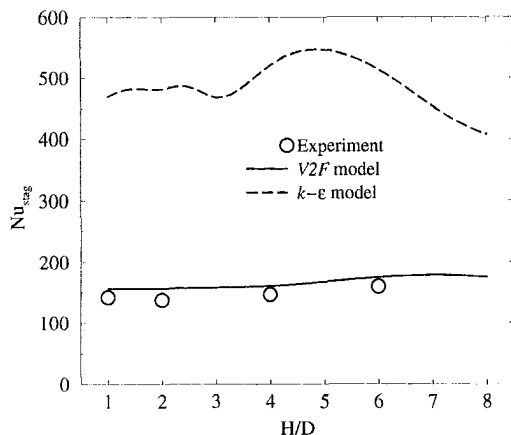

Fig. 9 Effect of the nozzle-to-pedestal distance on the stagnation heat transfer coefficient on top of a pedestal for Re = 23,000

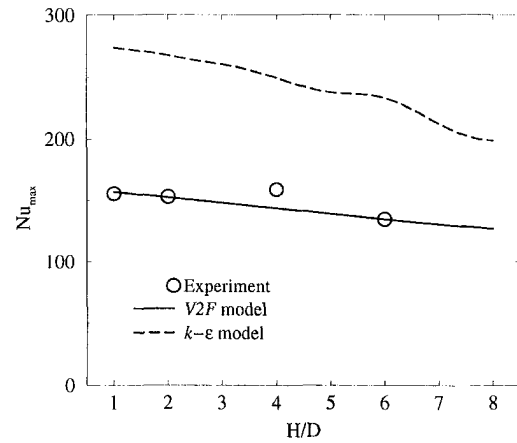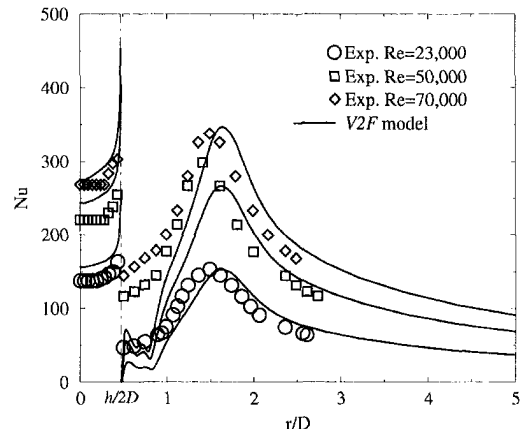**Fig. 11** Effect of Reynolds number on the stagnation Nusselt number on top of the pedestal and on the maximum Nusselt number downstream of the pedestal for H/D = 2
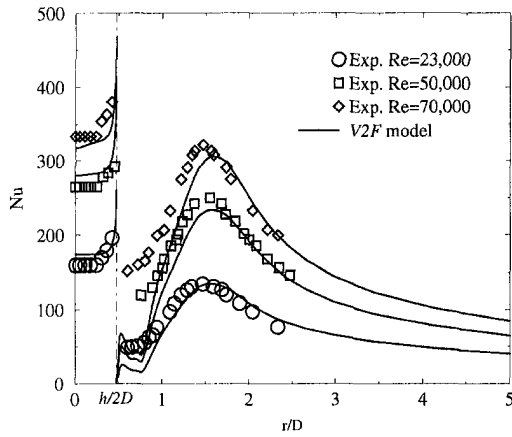
Fig. 12 Effect of Reynolds number on the stagnation Nusselt number on top of the pedestal and on the maximum Nusselt number on the plate for $H/D = 6$

higher values of γ are obtained, consistent with classical turbulent correlations. The model gave an exponent of 0.73 for both $H/D = 2$ and $H/D = 6$, in good agreement with experimental values of 0.78 for $H/D = 2$ and 0.74 for $H/D = 6$.

8 Concluding Remarks

The aim of this research has been to accurately and economically predict the heat transfer rate in a jet impinging on a wall-mounted protuberance. To this end, the $V2F$ model was tested. The computed results were shown to accurately predict the local heat transfer coefficients over most of the impingment surface. Also, these accurate computations contributed to the understanding of the heat transfer characteristics in such a complex flow.

The local heat transfer coefficient exhibits a minimum in the stagnation region, which is rather different from the behavior of an impinging jet on a flat plate. Complex features like separation and reattachment on the plate strongly influence the wall temperature distribution and heat transfer coefficient.

For comparison, computations were also performed with the widely used $k-\epsilon$ model. It has been shown that this model does not properly represent the flow features, overpredicts the rate of heat transfer, and yields physically unrealistic behavior for the turbulent kinetic energy. Computations not reported here show that using the "RNG" coefficients produces results quite similar to those of the $k-\epsilon$ model. In particular, the excessive production of turbulence in the stagnation region is not alleviated by the altered set of coefficients.

Acknowledgments

References

Baughn, J., Mesbah, M., and Yan, X., 1993, "Measurements of local heat transfer for an impinging jet on a cylindrical pedestal," ASME HTD-Vol. 239, pp. 57–62.

Baughn, J., and Shimizu, S., 1989, "Heat Transfer Measurements From a Surface With Uniform Heat Flux and an Impinging Jet," ASME JOURNAL OF HEAT TRANSFER, Vol. 111, pp. 1096–1098.

Baughn, J., Hechanova, A., and Yan, X., 1991, "An Experimental Study of Entrainment Effects on the Heat Transfer From a Flat Surface to a Heated Circular Impinging Jet," ASME JOURNAL OF HEAT TRANSFER, Vol. 113, pp. 1023–1025.

Behnia, M., Parneix, S., and Durbin, P., 1998, "Prediction of Heat Transfer in and Axisymmetric Turbulent Jet Impinging on a Flat Plate, *Int. J. Heat Mass Transfer,* Vol. 41, pp. 1845–1855.

Craft, T., Graham, L., and Launder, B., 1993, "Impinging jet studies for turbulence model assessment-II. An examination of the performance of four turbulence models," *Int. J. Heat Mass Transfer,* Vol. 36, No. 10, pp. 2685–2697.

Downs, S. J., and James, E. H., 1987, "Jet impingement heat transfer—A literature survey," ASME Paper No. 87-HT-35.

Durbin, P., 1991, "Near-wall turbulence closure without damping functions," *Theoretical and Computational Fluid Dynamics,* Vol. 3, No. 1, pp. 1–13.

Durbin, P., 1993a, "A Reynolds-stress model for near-wall turbulence," *Journal of Fluid Mechanics,* Vol. 249, pp. 465–498.

Durbin, P., 1993b, "Application of a near-wall turbulence model to boundary layers and heat transfer," *Int. J. Heat and Fluid Flow,* Vol. 14, No. 4, pp. 316–323.

Durbin, P., 1995, "Separated flow computations with the $k - \epsilon - \overline{v}^2$ model," *AIAA Journal,* Vol. 33, No. 4, pp. 659–664.

Durbin, P., 1996, "On the $k-\epsilon$ stagnation point anomaly," *Int. J. Heat and Fluid Flow,* Vol. 17, pp. 89–90.

Kays, W. M., and Crawford, M. E., 1993, *Convective heat and mass transfer,* 3rd Ed., McGraw-Hill, New York.

Launder, B. E., 1986, "Low Reynolds number turbulence near walls," UMIST Mechanical Engineering Department Report TFD/86/4, University of Manchester, England, UK.

Lee, D., Greif, R., Lee, S., and Lee, J., 1995, "Heat Transfer From a Flat Plate to a Fully Developed Axisymmetric Impinging Jet," ASME JOURNAL OF HEAT TRANSFER, Vol. 117, pp. 772–776.

Lee, D. H., Chung, Y. S., and Kim, D. S., 1997, "Turbulent flow and heat transfer measurements on a curved surface with a fully developed round impinging jet," *Int. J. Heat and Fluid Flow,* Vol. 18, pp. 160–169.

Lytle, D., and Webb, B., 1994, "Air jet impingement heat transfer at low nozzle-plate spacings," *International Journal of Heat and Mass Transfer,* Vol. 37, pp. 1687–1697.

Martin, H., 1977, "Heat and mass transfer between impinging gas jets and solid surfaces," *Advances in Heat Transfer,* Vol. 13, pp. 1–60.

Mesbah, M., 1996, "An experimental study of local heat transfer to an impinging jet on nonflat surfaces: a cylindrical pedestal and a hemispherically concave surface," Ph.D. thesis, University of California, Davis, CA.

Nakayama, W., 1995, "Heat transfer engineering in systems integration: outlook for closer coupling of thermal and electrical designs of computers," *IEEE Trans. on Components, Packaging, and Manufacturing Tech.—Part A,* Vol. 18, No. 8, pp. 818–826.

Rogers, S., and Kwak, D., 1990, "Upwind differencing scheme for the time-accurate incompressible Navier-Stokes equations," *AIAA Journal,* Vol. 28, pp. 253–262.

Viskanta, R., 1993, "Heat transfer to impinging isothermal gas and flame jets," *Exp. Thermal Fluid Sci.,* Vol. 6, pp. 111–134.

Vogel, J. C., and Eaton, J. K., 1985, "Combined Heat Transfer and Fluid Dynamic Measurements Downstream of a Backward-Facing Step," ASME JOURNAL OF HEAT TRANSFER, Vol. 107, pp. 922–929.

Yan, X., 1993, "A preheated-wall transient method using liquid crystals for the measurement of heat transfer on external surfaces and in ducts," Ph.D. thesis, University of California, Davis, CA.

APPENDIX

The equations of the $V2F$ model are briefly summarized below. The standard $k-\epsilon$ type notation is used.

$$D_t U = -\nabla P + \nabla \cdot ((\nu + \nu_t)(\nabla U + \nabla' U)) \qquad (1)$$

$$\nabla \cdot U = 0 \qquad (2)$$

$$D_t k = P - \epsilon + \nabla \cdot ((\nu + \nu_t)\nabla k) \qquad (3)$$

$$D_t \epsilon = \frac{C'_{\epsilon_1} P - C_{\epsilon_2}\epsilon}{T} + \nabla \cdot \left(\left(\nu + \frac{\nu_t}{\sigma_\epsilon} \right) \nabla \epsilon \right) \qquad (4)$$

$$D_t \overline{v^2} = kf - \frac{\overline{v^2}}{k}\epsilon + \nabla \cdot \left((\nu + \nu_t)\nabla \overline{v^2} \right) \qquad (5)$$

$$f - L^2 \nabla^2 f = (C_1 - 1)\frac{(2/3 - \overline{v^2}/k)}{T} + C_2 \frac{P}{k} \qquad (6)$$

in which

$$\nu_t = C_\mu \overline{v^2} T; \quad P = 2\nu_t S^2; \quad S^2 \equiv S_{ij} S_{ij};$$

$$S_{ij} = \frac{1}{2}\left(\frac{\partial U_i}{\partial x_j} + \frac{\partial U_j}{\partial x_i} \right) \qquad (7)$$

and the length and time scales are

$$T' = \max \left(\frac{k}{\epsilon} ; \quad 6 \left(\frac{\nu}{\epsilon} \right)^{1/2} \right)$$

$$T = \min \left(T' ; \quad \frac{\alpha}{\sqrt{3}} \frac{k}{\overline{v^2} C_\mu \sqrt{2S^2}} \right) \tag{8}$$

$$L' = \min \left(\frac{k^{3/2}}{\epsilon} ; \quad \frac{1}{\sqrt{3}} \frac{k^{3/2}}{\overline{v^2} C_\mu \sqrt{2S^2}} \right)$$

$$L = C_L \max \left(L' ; \quad C_\eta \left(\frac{\nu^3}{\epsilon} \right)^{1/4} \right) . \tag{9}$$

The solid wall no-slip boundary conditions are: $U = 0$, $k = \partial_n k = 0$, $\overline{v^2} = 0$ and $\overline{v^2} = O(x_n^4)$, x_n being the axis normal to the wall. The $V2F$ constants are the following, δ being the distance to the closest boundary:

$$C'_{\epsilon_1} = 1.3 + 0.25/[1 + (\delta/2l)^2]^4, \quad l = L/C_L$$

$$C_\mu = 0.19, \quad C_L = 0.3, \quad C_\eta = 70.0, \quad \alpha = 0.6$$

$$C_1 = 1.4, \quad C_2 = 0.3, \quad C_{\epsilon_2} = 1.9, \quad \sigma_\epsilon = 1.3.$$

The mean temperature equation is

$$D_t \Theta = \nabla \cdot \left(\left(\frac{\nu}{\text{Pr}} + \frac{\nu_t}{\text{Pr}_t} \right) \nabla \Theta \right) \tag{10}$$

with

$$\text{Pr}_t = \frac{1}{0.5882 + 0.228(\nu_t/\nu) - 0.0441(\nu_t/\nu)^2 \left[1 - \exp\left(\frac{-5.165}{(\nu_t/\nu)} \right) \right]} .$$

Three-Dimensional Simulation of Laminar Rectangular Impinging Jets, Flow Structure, and Heat Transfer

I. Sezai

A. A. Mohamad
Assoc. Mem. ASME

Mechanical Engineering Department,
Eastern Mediterranean University,
Magosa, Mersin 10, Turkey

The flow and heat transfer characteristics of impinging laminar jets issuing from rectangular slots of different aspect ratios have been investigated numerically through the solution of three-dimensional Navier-Stokes and energy equations in steady state. The three-dimensional simulation reveals the existence of pronounced streamwise velocity off-center peaks near the impingement plate. Furthermore, the effect of these off-center velocity peaks on the Nusselt number distribution is also investigated. Interesting three-dimensional flow structures are detected which cannot be predicted by two-dimensional simulations.

Introduction

Impinging jets are commonly used in many industrial applications to enhance heat or mass transfer from the impingement surface. Typical applications include tempering of glass, annealing of materials, cooling of turbine blades and drying of paper. However, in most applications the flows are turbulent, and consequently most of the work in this area is concerned with turbulent jets, although some studies on laminar jets are also available.

The jets discharge from round or rectangular slots and often bank of such jets are used in the applications. The use of a single circular jet results in a localized high heat transfer rate at the point of jet impingement. Multiple jets produce a more uniform cooling. Nevertheless multiple jets complicate the fluid distribution downstream, where the chips require ease of fluid introduction and rejection from the smallest volume possible. The study of Wadsworth and Mudawar (1990) found that use of a slot jet, in place of a round jet, provided a larger impingement zone and ensured uniform coolant rejection. Therefore rectangular jet impingement offers some beneficial features, such as cooling uniformity and effectiveness.

Most of the effort so far has been devoted to the study of the circular jet. The experimental and theoretical investigations on rectangular jets are mostly related with turbulent jets. The various factors affecting the local heat transfer behavior of the impinging laminar rectangular jets have not been systematically investigated.

An early and detailed measurements of heat transfer coefficients between a flat plate and impinging two-dimensional slot jets was carried out by Gardon and Akfirat (1966). Gossman et al. (1969) investigated numerically the impinging jet on a heated wall, using the vorticity and stream function method and solved the laminar and turbulent flow cases for different Prandtl numbers. The effects of nozzle exit velocity profile on the flow and heat transfer characteristics of a semi-confined laminar impinging slot-jet was investigated by Heiningen et al. (1976) using a similar computational procedure.

A two-dimensional numerical model is used by Al-Sanea (1992) for calculating the steady flow and heat transfer charac-

teristics of a laminar slot-jet impinging on an isothermal flat surface, including the cross-flow effects. The presence of cross flow has been found to degrade the favorable characteristics of laminar impinging jets. Also, it has been found that a fully developed parabolic velocity profile enhances the rate of heat transfer at the impingement region, well above those produced by a uniform velocity profile. The free and semi-confined jet impingements show practically identical results at and near the impingement plate. Two-dimensional, incompressible, laminar slot-jet impingement on a isothermally heated surface has been studied numerically by Chou and Hung (1994) in the Reynolds number range of 100–400. Local Nusselt number correlations in the wall region of confined slot-jet flow under different jet-exit velocity profiles are postulated. An experimental study on heat transfer behaviors of a confined slot jet impingement has been performed by Lin et al. (1997), in the Reynolds number range of 190–1537. For the cases of Re < 1226, the turbulence intensities are found to be less than five percent at nozzle exit and the jet is regarded as in an initially laminar flow. The Nusselt number is found to be significantly affected by the jet Reynolds number, while it is rather insensitive to jet separation distance. Other laminar slot-jet impingement studies include the work of Miyazaki and Silberman (1972), Mikhail et al. (1982), Yuan et al. (1988), Garg and Jayaraj (1988), and Schafer et al. (1992).

It is well established that, depending on the distance between the jet and the impingement plate, the flow remains steady up to a critical Reynolds number Re_c. As Re exceeds Re_c, the flow becomes unsteady. At even higher Re the flow becomes turbulent. The numerical investigation of Potthast et al. (1994) gives values of the critical Reynolds numbers as 980 and 625 for impinging axial and radial jets, respectively, issuing from a circular cross section. For the impinging rectangular jets in this study, the maximum Reynolds number used is 500.

A literature survey indicates that most of the analysis on the jet impingement cooling is based on the assumption that the jet is either axisymmetric or two-dimensional. However, the jets issuing from rectangular nozzles are not necessarily two-dimensional. Three-dimensional physics of the impinging jets coming from rectangular nozzles are far from being fully understood. The present work deals with laminar, three-dimensional, numerical analysis of a rectangular submerged jet, impinging on a heated flat surface (Fig. 1). The three-dimensional model enabled us to detect the formation of two and four off-center velocity peaks in the jet and the resulting effect on Nusselt
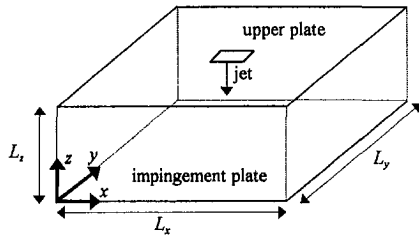
Copyright © 1999 by ASME

Fig. 1 Schematic diagram and the coordinate system

number which would have been impossible with a two-dimensional model. The explanation of the mechanism by which these off-center velocity peaks form, is also attempted. It should be mentioned that previous work have attributed the off-center velocity peaks to turbulence or nozzle outlet effects. Our results show that off-center velocity peaks form even in laminar jets near the impinging plate, with resulting off-center maximum heat transfer rates.

Computation Scheme

The steady-state three-dimensional Navier-Stokes and energy equations for incompressible flows are used in Cartesian coordinates. The flow is assumed to be laminar with constant properties. The velocity and length are normalized with jet-exit velocity and hydraulic diameter, respectively. The buoyancy effect has been neglected in this study. The authors are aware that for low Reynolds number, or more precisely, for Richardson number, Ri, in the order of unity and above, the effect of buoyancy can not be neglected. However, as a first analysis and to separate the effect of different parameters, it is decided to neglect buoyancy. Hence this analysis is valid for $Ri < 1$. The continuity, momentum, and energy equations in nondimensional form can be written as

$$\frac{\partial U}{\partial X} + \frac{\partial V}{\partial Y} + \frac{\partial W}{\partial Z} = 0, \tag{1}$$

$$U\frac{\partial U}{\partial X} + V\frac{\partial U}{\partial Y} + W\frac{\partial U}{\partial Z} = -\frac{\partial P}{\partial X} + \frac{1}{Re}\nabla^2 U, \tag{2}$$

$$U\frac{\partial V}{\partial X} + V\frac{\partial V}{\partial Y} + W\frac{\partial V}{\partial Z} = -\frac{\partial P}{\partial Y} + \frac{1}{Re}\nabla^2 V, \tag{3}$$

$$U\frac{\partial W}{\partial X} + V\frac{\partial W}{\partial Y} + W\frac{\partial W}{\partial Z} = -\frac{\partial P}{\partial Z} + \frac{1}{Re}\nabla^2 W, \tag{4}$$

$$U\frac{\partial T}{\partial X} + V\frac{\partial T}{\partial Y} + W\frac{\partial T}{\partial Z} = \frac{1}{Re\ Pr}\nabla^2 T. \tag{5}$$

Boundary conditions for velocities are as follows:

$$\frac{\partial U}{\partial X} = \frac{\partial V}{\partial X} = \frac{\partial W}{\partial X} = 0 \quad \text{at } X = 0, X = A_x \tag{6a}$$

$$\frac{\partial U}{\partial Y} = \frac{\partial V}{\partial Y} = \frac{\partial W}{\partial Y} = 0 \quad \text{at } Y = 0, Y = A_y \tag{6b}$$

$$U = V = W = 0 \quad \text{at } Z = 0, Z = A_z$$

$$\text{(except at nozzle exit)}$$

$$U = V = 0, W = -1 \quad \text{at } Z = A_z \text{ (at nozzle exit).} \tag{6c}$$

Boundary conditions for temperature are

$$\text{at } X = 0 \quad \begin{array}{l} \dfrac{\partial T}{\partial X} = 0 \text{ for } U < 0 \\[6pt] T = 0 \text{ for } U > 0 \end{array} \tag{7a}$$

$$\text{at } X = A_x \quad \begin{array}{l} \dfrac{\partial T}{\partial X} = 0 \text{ for } U > 0 \\[6pt] T = 0 \text{ for } U < 0 \end{array} \tag{7b}$$

$$\text{at } Y = 0 \quad \begin{array}{l} \dfrac{\partial T}{\partial Y} = 0 \text{ for } V < 0 \\[6pt] T = 0 \text{ for } V > 0 \end{array} \tag{7c}$$

$$\text{at } Y = A_y \quad \begin{array}{l} \dfrac{\partial T}{\partial Y} = 0 \text{ for } V > 0 \\[6pt] T = 0 \text{ for } V < 0 \end{array} \tag{7d}$$

$$\text{at } Z = A_z \quad \begin{array}{l} \dfrac{\partial T}{\partial Z} = 0 \text{ (except at nozzle exit)} \\[6pt] T = 1 \text{ (at nozzle exit)} \end{array} \tag{7e}$$

$$\text{at } Z = 0 \quad T = 0. \tag{7f}$$

Method of Solution

The governing equations are discretized using the finite volume method in staggered nonuniform grids. The grids are generated such that denser grid clustering is obtained at the edges of the jet-exit cross section. The equation used for such a distribution is (Hoffmann and Chiang, 1995)

--- **Nomenclature** ---

A_x, A_y, A_z = aspect ratios in x, y, and z direction, L_x/D_h, L_y/D_h, L_z/D_h

a = nozzle length
b = nozzle width
D_h = hydraulic diameter of jet
h = convection heat transfer coefficient
L_z = distance between nozzle exit and impinging plate
Nu = local Nusselt number, hD_h/k
P = nondimensional pressure, $p/\rho u_j^2$
p = pressure
Pr = Prandtl number, ν/α

q_w'' = local convective heat flux
Re = Reynolds number, $u_j D_h/\nu$
T = nondimensional temperature, $(t - t_j)/(t_w - t_j)$
t = temperature
U, V, W = nondimensional Cartesian velocities u/u_j, v/u_j, w/u_j, respectively
u, v, w = Cartesian velocities
u_j = jet exit velocity
X, Y, Z = nondimensional Cartesian coordinates, x/D_h, y/D_h, z/D_h, respectively
x, y, z = Cartesian coordinates
α = thermal diffusivity

ϕ = U, V, W, P, or T field
ν = kinematic viscosity
ρ = density

Superscripts

Q = QUICK
U = UPWIND

Subscripts

f = cell face value
j = jet exit
w = wall

$$x_i = B\left\{1 + \frac{\sinh\left[\beta(i/n - C)\right]}{\sinh(\beta C)}\right\} \qquad (8)$$

where

$$C = \frac{1}{2\beta}\ln\left[\frac{1 + (e^\beta - 1)(B/L)}{1 + (e^{-\beta} - 1)(B/L)}\right]. \qquad (9)$$

n is the total number of grid points, L is the length of the domain to be divided, β is the clustering parameter in the range of $0 < \beta < \infty$, and B is the x coordinate where clustering is desired. For $\beta = 0$, no clustering is enforced, while a denser clustering of grid points near $x = B$ is produced for larger values of β. For cases of $A_z = 2.5$ the solution domain has $L_x = L_y = 20D_h$ where $51 \times 51 \times 51$ grids are used and $\beta = 3.0$ is adapted for the grid distributions in x and y directions. For $A_z = 10$ the solution domain in x and y directions is extended to $100D_h$ in order to eliminate the effect of domain size on the results. To have similar grid distribution in the jet region $101 \times 101 \times 51$ grids were used, with $\beta = 6$ for grid distributions in x and y directions for $A_z = 10$. Sine function distribution is employed for grids in the z direction, which yields denser grids near the top and the impingement plate.

In order to insure that the results are grid-size independent, tests were performed by doubling the grid sizes in z direction. The maximum difference between the local Nusselt numbers obtained by the two different grid systems is less than 1.5 percent. This difference decreases sharply away from the jet axis. The corresponding jet velocity profiles at the vertical mid-plane are almost coincident for the two grid systems.

The convection of a scalar ϕ at a control volume face is calculated by QUICK (Leonard, 1979) scheme using the ULTRA-SHARP (Leonard and Mokhtari, 1990; Leonard and Drummond, 1995) flux limiting strategy. The value of a scalar at the east face of a control volume in QUICK scheme is formulated in compact form as

$$\phi_{f_i}^Q = \phi_i + \alpha_i(\phi_{i+1} - \phi_i) + \gamma_i[\phi_{i+M} - \phi_{i+1-M}$$
$$+ \xi_i(\phi_{i+2-3M} - \phi_{i+1-M})] \qquad (10)$$

where

$$\alpha_i = \frac{\delta x_i}{\Delta x_i}, \quad \xi_i = \frac{\Delta x_i}{\Delta x_{i+1-2M}}, \quad \gamma_i = \alpha_i\xi_i\frac{\alpha_i - 1}{\xi_i + 1}.$$

$M = 1$ for $u_{f_i} > 0$, $M = 0$ for $u_{f_i} < 0$. Δx_i is the distance between nodal points i and $i + 1$, δx_i is the distance between the nodal point i and the control volume face at east of i.

Instead of casting the extra neighboring points resulting from QUICK scheme into the source term, the deferred correction method (Leonard and Drummond, 1995) is employed, which is based on replacing the face value ϕ_f in terms of the first-order upwind face value plus a correction term involving the values from previous iteration,

$$\phi_{f_i} = \phi_{f_i}^U + \phi_{f_i}^Q(\text{old}) - \phi_{f_i}^U(\text{old}), \qquad (11)$$

where the superscript Q stands for QUICK and U for first-order upwind. By adding the $\phi_{f_i}(\text{old})$ terms to the source term, the numerical stability is increased while keeping the seven diagonal structure of the coefficient matrix.

The Bi-CGSTAB (Van der Vorst, 1989) iterative method with SSOR preconditioning (Saad, 1996) is applied to the pressure and energy equations in the sequential procedure of the SIMPLE (Patankar, 1980) algorithm. An under relaxation factor of 0.7 is used for momentum and energy equations in all calculations. Iterations are continued until the second norm of the residuals for all equations reduced below 10^{-6}. It takes about 2000 iterations to achieve this condition for the $101 \times 101 \times 51$ grid system. Also, prescribed values of U, V, W, and
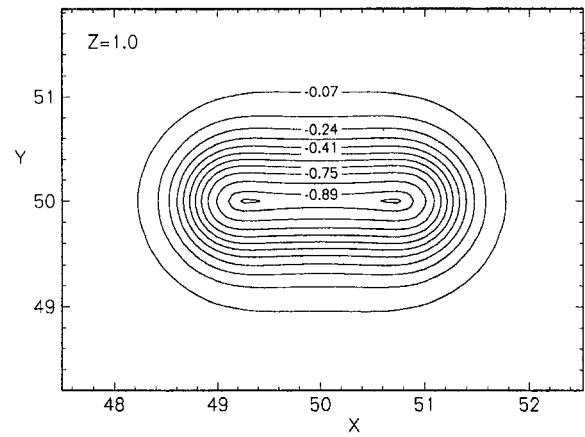
Fig. 2(a)
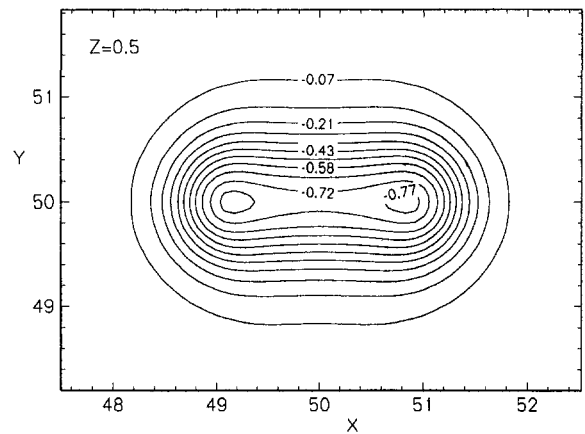
Fig. 2(b)

Fig. 2 *W* velocity contours at (*a*) $Z = 1.0$ and (*b*) $Z = 0.5$ (Re = 500, A_z = 10, a/b = 3.9)

P are monitored and no significant variations observed at this residual level.

Results and Discussions

Air is used as the working fluid having a Prandtl number of 0.71. The analysis is performed for the following aspect ratios of the rectangular jet at the exit of the slot: 1.0, 1.5, 2.0, 3.9, and 8.1. Noninteger ratios were used to avoid the complications of grid adjustment at nozzle edges.

Flow Structure. The jet velocity at the exit of the nozzle is assumed to have a flat profile. After the nozzle exit the jet velocity decays away from the center line attaining a nonuniform profile with maximum velocity at the center. For a square jet this nonuniform velocity profile with a single peak at the center line has been found to persist down to the impinging plate. However, for a rectangular nozzle two off-center velocity peaks are observed near the impingement plate. Figure 2 illustrates the contour plots of W velocity at Re = 500 for a nozzle with $a/b = 3.9$ and $A_z = 10$, where jet exit plane is located at $Z = 10$. At $Z = 1.0$ the two off-center velocity peaks start forming which are barely noticeable and become more distinct for distances closer to the impinging plate (Fig. 2(b)). The two off-center velocity peaks are an indication of a "saddle-backed" spanwise profile of the jet velocity shown in Fig. 3. The off-center peaks of the jet velocity have also been observed in incompressible turbulent unbounded jet flows issuing from rectangular nozzles by Sfeir (1979), Masters (1981), Tsuchiya et al. (1986), and Quinn (1991). Although this peculiar feature of turbulent jets has been the subject of some discussion, it

Fig. 3 Jet velocity profile near the impinging plate

$$\Omega_z = \frac{\partial V}{\partial X} - \frac{\partial U}{\partial Y} \qquad (12)$$

and that positive and negative Ω_z indicate counterclockwise and

Fig. 4(a)

Fig. 4(b)

Fig. 4(c)

Fig. 4(d)

Fig. 4 Stream trace plots around jet for $A_z = 10$, $a/b = 3.9$, and Re = 500, at horizontal cross sections of (a) $Z = 9.0$, (b) $Z = 2.0$, (c) $Z = 1.0$ and (d) $Z = 0.5$

appears that the mechanism which produces these distributions is not clear yet. Sfeir (1979) has taken up the encircling vortex hypothesis in explaining the two off-center velocity peaks in unbounded turbulent jets but his proposals are less than conclusive. Marsters (1981) points out that the pressure field may induce secondary flows, which in turn results in velocity peaks at the ends of the jet flow. According to Quinn and Militzer (1988), the off-center peaks are the result of upstream flow conditions where the flow contracts from a large cross section into a rectangular slot producing strong curvature of the streamlines. They suggested that this particular velocity profile i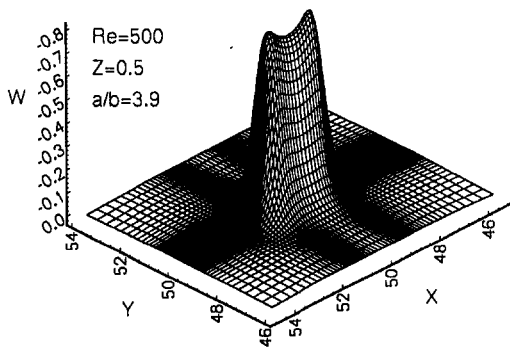s the result of secondary flow of the Prandtl first kind, which is pressure driven, generated by streamline curvature and the attendant centrifugal effects. On the other hand for partially bounded turbulent jet flows from low-aspect ratio rectangular slots vortex stretching hyphotesis have been postulated (Rockwell, 1977) to explain the existence of mean streamwise velocity off-center peaks. However, the physics of laminar flows is different than that of turbulent flows. The off-center peaks observed in the rather low Reynolds number flow studied here cannot be attributed to secondary flows generated by turbulence near the nozzle corners. The upstream flow conditions are also not responsible as uniform velocity profile is assumed at the nozzle discharge. The stream trace plots on different x-y planes around the jet are shown in Fig. 4 which are obtained from the U-V data on the corresponding horizontal planes using the commercial plotting package, Tecplot. As soon as the fluid exits from the nozzle a negative pressure is induced around the jet cross section which drags fluid both from the surroundings as well as the jet core itself (Fig. 4(a)). The negative static pressure around the jet near the nozzle exit is evident in the three-dimensional plot of nondimensional pressure in Fig. 5(a). The jet starts evolving into an elliptical cross section and at $Z = 2.0$, the flow is directed towards two points, which are located at the ends of the minor axis of the jet (Fig. 4(b)). Further downstream, at $Z = 1.0$, wall jet forms in y direction (Fig. 4(c)) as a result of jet impingement on the bottom plate and fluid flows away from jet core along y direction while the flow is towards jet core along x direction. It is at this plane where the two off-center velocity peaks first appear. At $Z = 0.5$ (Fig. 4(d)) the whole jet core is transformed into a wall jet with a resulting flow from center towards sides in all directions. The off-center velocity peaks prominent in Fig. 2(b) correspond to this plane. An examination of Fig. 5(b), illustrating the pressure distribution at this particular cross section, clearly shows that the velocity peaks cannot be induced by the pressure field either. This assesses the idea that the off-center velocity peaks are related with the interaction of jet with the impingement plate where wall jet formation takes place.

The contour plots of the streamwise vorticity, Ω_z, near the impingement plate are shown in Fig. 6. Note that vorticity is defined as
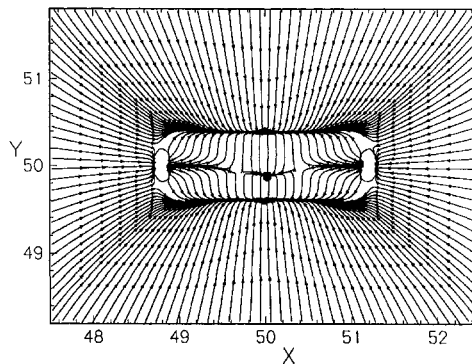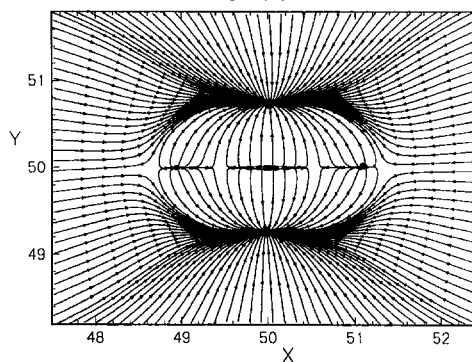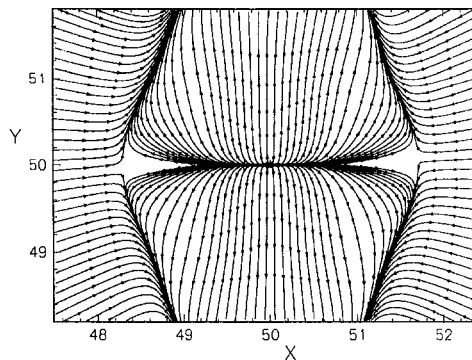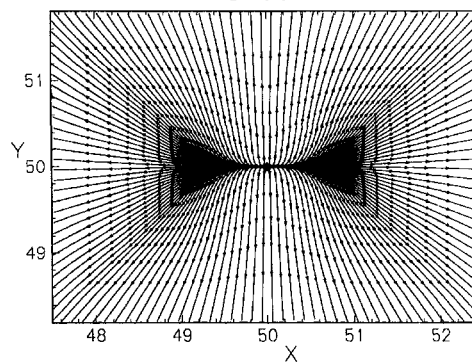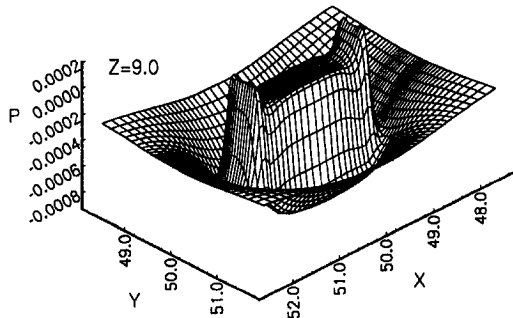
Fig. 5(a)
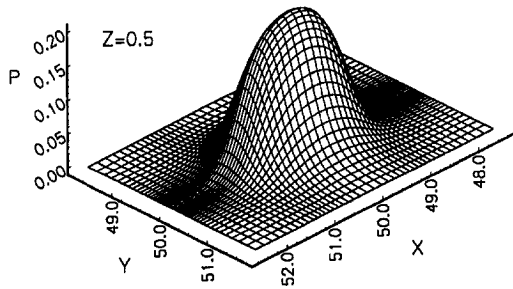
Fig. 5(b)

Fig. 5 Pressure distribution around jet for $A_z = 10$, $a/b = 3.9$ and Re = 500 at (a) $Z = 9.0$ and (b) $Z = 0.5$

clockwise rotation, respectively. The four vortex rings shown in Fig. 6(a) are weak in strength and correspond to the plane where the off-center velocity peaks first appear. At this plane,
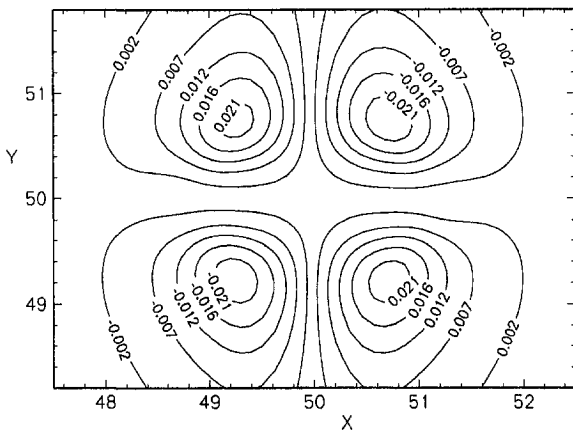
Fig. 6(a)
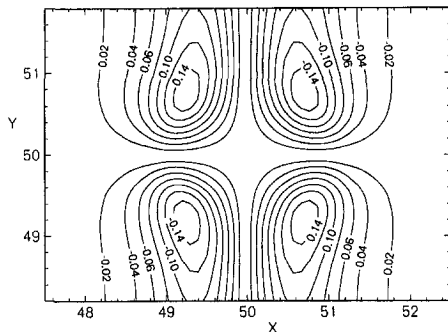
Fig. 6(b)

Fig. 6 Streamwise vorticity, Ω_z, contours at (a) $Z = 1.0$ and (b) $Z = 0.5$ (Re = 500, $A_z = 10$, $a/b = 3.9$)
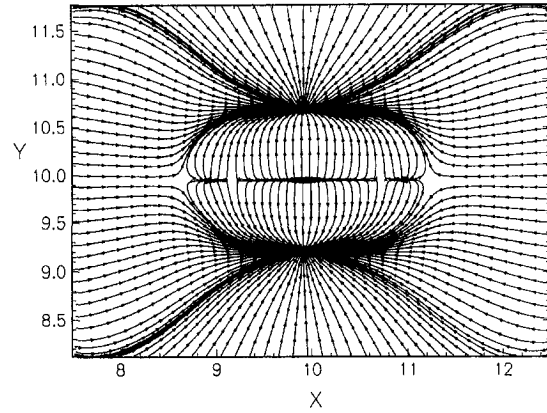
Fig. 7(a)
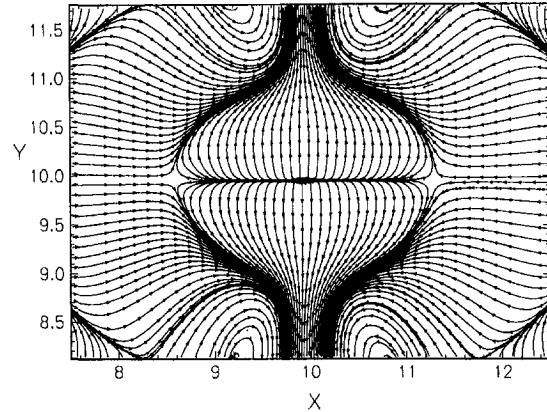
Fig. 7(b)
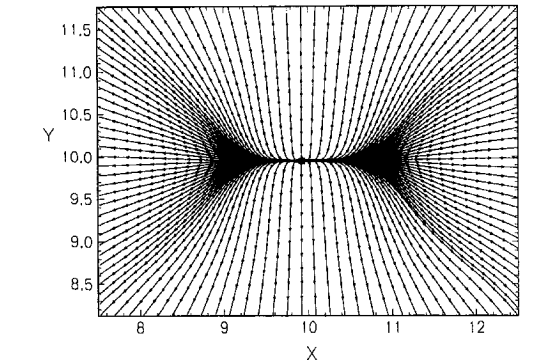
Fig. 7(c)

Fig. 7 Stream trace plots around jet for $A_z = 2.5$, $a/b = 3.9$ and Re = 100, at horizontal cross sections of (a) $Z = 1.25$ (b) $Z = 1.0$ and (c) $Z = 0.5$

($Z = 1.0$) wall jet forms along y-direction whereas no wall jet has yet evolved along x direction. As a result V velocities are maximum at central X position ($X = 50$) decreasing away from the central axis. This produces negative $\partial V/\partial X$ values in the upper-right quadrant and positive $\partial V/\partial X$ values at upper-left quadrant of Fig. 6(a). contributing to negative and positive streamwise vorticities in these quadrants. Bearing in mind that V velocities are negative in the lower half of the figure, the variation of the V velocity along x-axis produces positive Ω_z in the lower-right quadrant and negative Ω_z in the left quadrant. At $Z = 0.5$ a similar vortex structure prevails with vorticity lines being stretched along the wall jet in y-direction and the streamwise vorticities are stronger as shown in Fig. 6(b). At this plane wall jet forms in all directions as seen from Fig. 4(d) but the wall jet velocities along y direction are larger than the
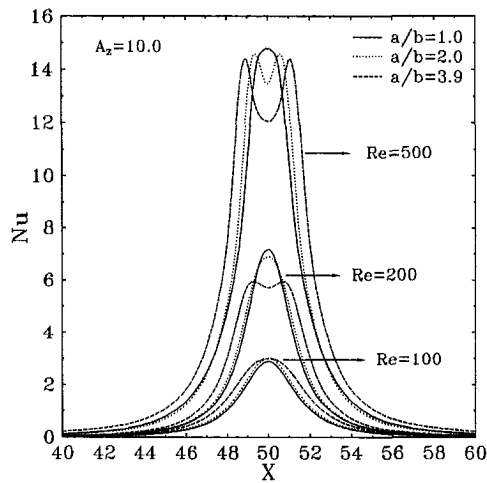
Fig. 8 Effect of nozzle aspect ratio on Nusselt number variation in x direction for A_z = 10.0 and Y = 0

jet velocities along x-direction yielding V velocity gradients, $\partial V/\partial X$, and resulting streamwise vorticities as before. The stronger vorticity values are a result of higher wall jet velocity gradients, as this plane is closer to the wall jet center line. The observed streamwise velocity off-center peaks may be the result of the self-induction of the counter-rotating streamwise vortices.

For A_z = 10 off-center velocity peaks do not form for Reynolds number below about 200. As the nozzle plate distance gets smaller the off-center velocity peaks form at smaller Reynolds numbers. Figure 7 shows the stream trace plots for jet of L_z/D_h = 2.5 and a/b = 3.9 at different horizontal planes for Re = 100. For this rather low Reynolds number wall jet formation in y direction starts at Z = 1.0 (Fig. 7(b)) where the off-center velocity peaks first appear before impingement. Near the plate the wall jet forms and the flow is directed from center to sides (Fig. 7(c)).

Heat Transfer. The velocity profile with off-center peaks near the impingement plate is expected to effect the local heat transfer mechanism. The local convection heat transfer coefficient is expressed as
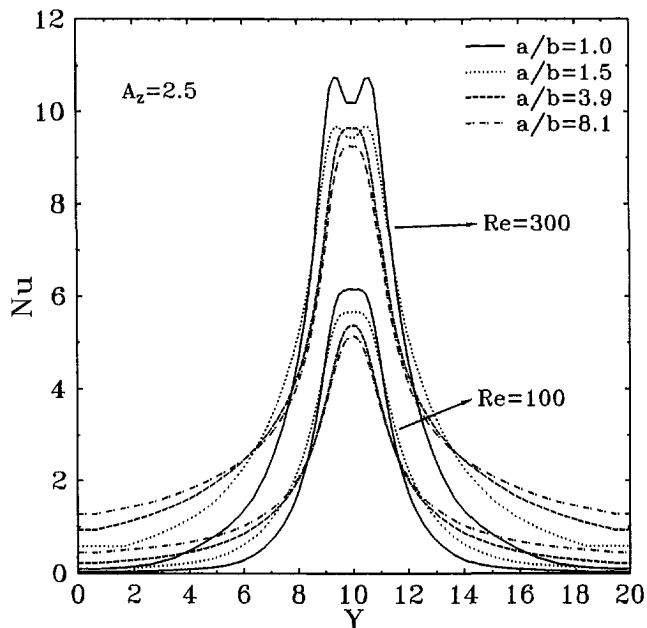
Fig. 9 Effect of nozzle aspect ratio on Nusselt number variation in y direction for A_z = 2.5 and X = 0
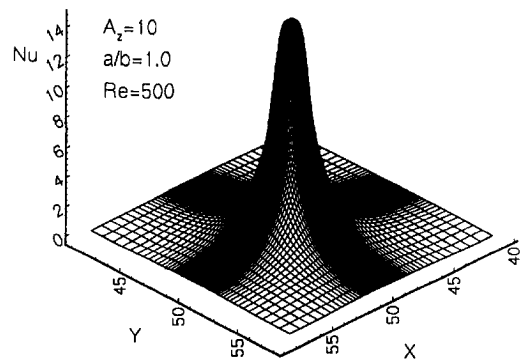
Fig. 10(a)
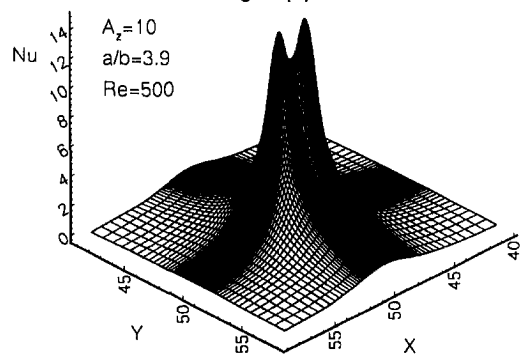
Fig. 10(b)

Fig. 10 The three-dimensional plots of the Nusselt Number for Re = 500, A_z = 10 and nozzle aspect ratios of (a) a/b = 1.0 and (b) a/b = 3.9

$$h = \frac{q_w''}{t_w - t_j} \tag{13}$$

and the local Nusselt number is defined in terms of the hydraulic diameter of the jet as

$$Nu = \frac{hD_h}{k} \tag{14}$$

where it is also equal to the nondimensional heat flux and calculated from $Nu = \partial T/\partial Z$. The variation of the local Nusselt number with X distance at the midplane is shown in Fig. 8 for A_z = 10. At a rather low Reynolds number of 100 the maximum Nusselt number is at the stagnation point for all nozzle aspect ratios. For Re = 200 the position of the maximum Nusselt number shifts towards the edges of the jet core for the nozzle with a/b = 3.9. At a higher Reynolds number of 500 two off-center peaks of the Nusselt is observed for jets issuing from rectangular nozzles whereas the Nusselt number resulting from square nozzles has a single peak at all Re investigated. The positions of the maximum Nusselt number correspond to the positions of the off-center streamwise velocity peaks discussed earlier, indicating that the off-center peaks of the Nusselt number is the result of the jet velocity profile near the impinging plate. The variation of the Nusselt number in y direction is exemplified in Fig. 9 for A_z = 2.5 and for different nozzle aspect ratios. The drop in Nusselt number is more gradual for jets with higher nozzle aspect ratios but decreases sharply for square nozzles. (This is consistent with the jet velocity profile shown in Fig. 4, where the maximum jet velocity is at the center.)

Three-dimensional plots of the Nusselt number for A_z = 10 are shown in Fig. 10. The two off-center peaks of Nusselt number observed in Fig. 10(b) is consistent with the jet velocity profile shown in Fig. 3. The three-dimensional plots of the Nusselt number for A_z = 2.5 and Re = 300 are shown in Fig.
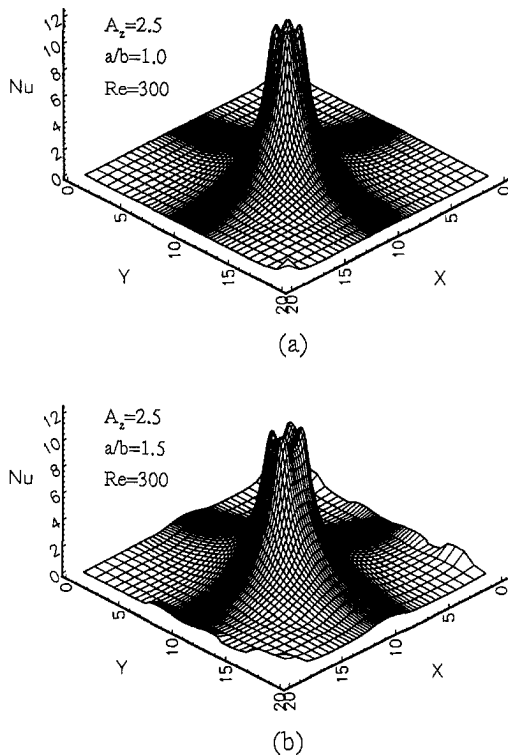
Fig. 11 The three-dimensional plots of the Nusselt number for Re = 300, A_z = 2.5, and nozzle aspect ratios of (a) a/b = 1.0, (b) a/b = 1.5

11. For nozzle aspect ratios of 1.0 and 2.5, four peaks are observed in a region corresponding to the corners of the nozzle exit cross section, while the number of the peaks reduces to two for higher nozzle aspect ratios. The positions of the peak Nusselt numbers correspond to the positions of the streamwise velocity peaks observed near the plate, not shown here. However, no such off-center peaks of Nu appear for A_z = 10 for a square nozzle in the range of the Reynolds numbers investigated.

Conclusions

The off-center streamwise jet velocity peaks observed in incompressible turbulent unbounded jet flows (Sfeir, 1979; Masters, 1981; Tsuchiya et al., 1986; Quinn and Millitzer, 1988; Quinn, 1991), issuing from rectangular nozzles has been found to exist in the laminar jets, at a height where wall jet formation starts. The explanation put forward for the turbulent free jets that the off-center velocity peaks are the result of turbulence generated secondary flows are not applicable for laminar rectangular jets. The pressure distribution on different horizontal planes indicates that the off-center velocity peaks of the jet cannot be explained by pressure effects either. These peaks have been found to form at an elevation where wall jet formation starts along the minor axis of the jet accompanied by four counter rotating vortex rings. The off-center velocity peaks are formed by the diffusion of vorticity along wall jet, as jet impinges on the plate.

The off-center velocity peaks in the jet results in the formation of the off-center Nusselt number peaks on the impingement

plate. The Nusselt number is higher in the direction of the minor axis of the jet as the flow velocities are higher in that direction.

The effect of buoyancy on three-dimensional rectangular jet impingement is currently under investigation.

References

Al-Sanea, S., 1992, "A Numerical Study of the Flow and Heat Transfer Characteristics of an Impinging Laminar Slot-jet Including Crossflow Effects," *Int. J. Heat Mass Transfer*, Vol. 35, pp. 2501–2513.

Chou, Y. J., and Hung, Y. H., 1994, "Impingement Cooling of an Isothermally Heated Surface with a Confined Slot Jet," ASME JOURNAL OF HEAT TRANSFER, Vol. 116, pp. 479–482.

Gardon, R., and Akfirat, J. C., 1966, "Heat Transfer Characteristics of Impinging Two-Dimensional Air Jets," ASME JOURNAL OF HEAT TRANSFER, Vol. 88, pp. 101–108.

Garg, V. K., and Jayaraj, S., 1988, "Boundary Layer Analysis for Two-Dimensional Slot Jet Impingement on Inclined Plates," ASME JOURNAL OF HEAT TRANSFER, Vol. 110, pp. 577–582.

Gosman, D., Pun, W. M., Runchal, A. K., Spalding, D. B., and Wolfshtein, M., 1969, *Heat and Mass Transfer in Recirculating flows*, Academic Press, London.

Heiningen, A. R. P. V., Majumdar, A. S., and Douglas, W. J. M., 1976, "Numerical Prediction of the Flow Field and Impinging Heat Transfer Caused by a Laminar Slot Jet," ASME JOURNAL OF HEAT TRANSFER, Vol. 98, pp. 654–658.

Hoffmann, K. A., and Chiang, S. T., 1995, *Computational Fluid Dynamics for Engineers*, Vol. 1, Engineering Education System Publications, Wichita, KS.

Leonard, B. P., 1979, "A Stable and Accurate Convective Modelling Procedure Based on Quadratic Upstream Interpolation," *Comput. Methods Appl. Mech. Engng.*, Vol. 19, pp. 59–98.

Leonard, B. P., and Mokhtari, S., 1990, "Beyond First Order Upwinding: The ULTRA-SHARP Alternative for Nonoscillatory Steady-State Simulation of Convection," *Int. J. Numer. Methods Eng.*, Vol. 30, pp. 729–766.

Leonard, B. P., and Drummond, J. E., 1995, "Why You Should Not Use 'Hybrid,' 'Power Law' or Related Exponential Schemes for Convective Modelling—There are Much Better Alternatives," *Int. J. Numer. Meth. Fluids*, Vol. 20, pp. 421–442.

Lin, Z. H., Chou, Y. J., and Hung, Y. H., 1997, "Heat Transfer Behaviors of a Confined Slot Jet Impingement," *Int. J. Heat Mass Transfer*, Vol. 40, pp. 1095–1107.

Masters, G. F., 1981, "Spanwise Velocity Distributions in Jets from Rectangular Slots," *AIAA J.*, Vol. 19, pp. 148–152.

Mikhail, S., Morcos, S. M., Abou-Ellail, M. M. M., and Ghaly, W. S., 1982, "Numerical Prediction of Flow Field and Heat Transfer from a Row of Laminar Slot Jets Impinging on a Flat Plate," *Proc. 7th Int. Heat Transfer Conf.*, Vol. 3, pp. 377–382.

Miyazaki, H., and Silberman, E., 1972, "Flow and Heat Transfer on a Flat Plate Normal to a Two-dimensional Laminar Jet Issuing from a Nozzle of Finite Height," *Int. J. Heat Mass Transfer*, Vol. 15, pp. 2097–2107.

Patankar, S. V., 1980, *Numerical Heat Transfer and Fluid Flow*, Hemisphere, New York.

Potthast, F., Laschefski, H., and Mitra, N. K., 1994, "Numerical Investigation of Flow Structure and Mixed Convection Heat Transfer of Impinging Radial and Axial Jets," *Numer. Heat Transfer, Part A*, Vol. 26, pp. 123–140.

Quinn, W. R., 1991, "Passive Near-Field Mixing Enhancement in Rectangular Jet Flows," *AIAA J.*, Vol. 29, pp. 515–519.

Quinn, W. R., and Millitzer, J., 1988, "Experimental and Numerical Study of a Turbulent Free Square Jet," *Physics of Fluids*, Vol. 31, pp. 1017–1025.

Rockwell, D. O., 1977, "Vortex Stretching Due to Shear Layer Instability," *J. Fluids Eng.*, Vol. 99, pp. 240–244.

Saad, Y., 1996, *Iterative Methods for Sparse Linear Systems*, PSW Publ. Co., Boston.

Schafer, D. M., Incropera, F. P., and Ramadhyani, S., 1992, "Numerical Simulation of Laminar Convection Heat Transfer from an In-line Array of Disscrete Sources to a Confined Rectangular Jet," *Numer. Heat Transfer, Part A*, Vol. 22, pp. 121–141.

Sfeir, A., 1979, "Investigation of Three-Dimensional Turbulent Rectangular Jets," *AIAA J.*, Vol. 17, pp. 1055–1060.

Tsuchiya, Y., Horikoshi, C., and Sato, T., 1986, "On the Spread of Rectangular Jets," *Exp. Fluids*, Vol. 4, pp. 1197–204.

Van der Vorst, H. A. V., 1989, "BiCGSTAB: A Fast and Smoothly Converging Variant of Bi-CG for the Solution of Non-Symmetric Linear Systems," *SIAM J. Sci. Statist. Comput.*, Vol. 10, pp. 1174–1185.

Wadsworth, D. C., and Mudawar, I., 1990, "Cooling of a Multichip Electronic Module by Means of Confined Two-Dimensional Jets of Liquids," ASME JOURNAL OF HEAT TRANSFER, Vol. 112, pp. 891–898.

Yuan, T. D., Liburdy, J. A., and Wang, T., 1988, "Buoyancy Effects on Laminar Impinging Jets," *Int. J. Heat Mass Transfer*, Vol. 31, pp. 2137–2145.

A. F. Emery[1]

Department of Mechanical Engineering,
University of Washington,
Box 352600,
Seattle, WA 98195-2600

J. W. Lee

Institute for Advanced Engineering,
Yongin P. O. Box 25,
Yongin, Kyonggi-do, Korea

The Effects of Property Variations on Natural Convection in a Square Enclosure

Natural convection in a square enclosure with heated vertical walls and temperature-dependent conductivity and viscosity was simulated for Prandtl numbers ranging from 0.01 to 1.0 and Ra $\leq 10^6$. Although the variable properties produced observable changes in the the temperatures and velocities, the overall heat transfer, as represented by the Nusselt number, was found to be unaffected and was accurately correlated in terms of the Rayleigh and Prandtl numbers using Nu = 0.185 $Ra_0^{0.278}$ $Pr_0^{0.089}$ with properties evaluated at the average temperature. This correlation applies to both isothermal and constant heat flux hot walls.

1 Introduction

In natural convection flows, the fluid velocities are highly dependent on the thermal field and variable properties can have strong effects on both the velocities and the temperature. The basic effects of the properties are embedded in the dimensionless groups, the Rayleigh and Prandtl numbers. It is common to assume that for temperature-dependent properties the viscosity and conductivity vary in such a way that the Prandtl number remains constant or that average properties can be used in evaluating Pr and Ra. In this study, we are particularly interested in the interplay between the viscosity and the conductivity in natural convection heat transfer in a two-dimensional square region when both properties vary strongly with temperature.

The effect of the variation of viscosity with temperature has been widely studied (Yamasaki and Irvine, 1984; Hyun and Lee, 1988). Although the free-convection-induced velocities are strongly affected by the varying viscosity, the overall heat transfer has been found to be nearly constant if the properties are evaluated at the average temperature for a variety of configurations for ratios of maximum to minimum viscosity in the order of 10 or less (Hyun and Lee, 1988; Booker, 1976). However, the effect of temperature-dependent conductivity, which can significantly affect the thermal field, has received little attention, particularly in conjunction with a simultaneous variation in the viscosity. Chenoweth and Paolucci (1986) studied the natural convection of an ideal gas where both the conductivity and viscosity followed Sutherland's law, but only for $Pr_0 = 0.71$. We have conducted a comprehensive set of numerical solutions to demonstrate the effects of temperature-dependent conductivity and viscosity over a wide range of Prandtl number. Since the effect of Pr is small for Pr > 1 (Incropera and DeWitt, 1996), we present the results here only for 0.01 ≤ Pr ≤ 1. which is representative of liquid metals and gases. All other properties (β, ρ, and c_p) are taken as constant.

2 Mathematical Formulation

A square enclosure is filled with an incompressible viscous fluid and the flow and thermal fields are represented by the nondimensional Navier-Stokes equations using the Boussinesq approximation. (Chenoweth and Paolucci (1986) have shown that the Boussinesq approximation leads to accurate computa-

tions of the overall heat transfer for 0 < $\Delta T/T_0$ < 0.6. However, the approximation can lead to significant errors in the velocity and temperature fields if $\Delta T/T_0$ is large, i.e., >0.2.) The appropriate nondimensional equations are

$$\frac{\partial U}{\partial X} + \frac{\partial V}{\partial Y} = 0 \tag{1a}$$

$$\frac{\partial UU}{\partial X} + \frac{\partial UV}{\partial Y}$$
$$= -\frac{\partial P}{\partial X} + Pr_0\left[\frac{\partial}{\partial X}\left(f_1\frac{\partial U}{\partial X}\right) + \frac{\partial}{\partial Y}\left(f_1\frac{\partial U}{\partial Y}\right)\right] \tag{1b}$$

$$\frac{\partial UV}{\partial X} + \frac{\partial VV}{\partial Y} = -\frac{\partial P}{\partial Y} + Pr_0\left[\frac{\partial}{\partial X}\left(f_1\frac{\partial V}{\partial X}\right)\right.$$
$$\left. + \frac{\partial}{\partial Y}\left(f_1\frac{\partial V}{\partial Y}\right)\right] + Ra_0^T Pr_0 \Theta \tag{1c}$$

$$\frac{\partial U\Theta}{\partial X} + \frac{\partial V\Theta}{\partial Y} = \left[\frac{\partial}{\partial X}\left(f_2\frac{\partial \Theta}{\partial X}\right) + \frac{\partial}{\partial Y}\left(f_2\frac{\partial \Theta}{\partial Y}\right)\right]. \tag{1d}$$

In the above equations, the primary nondimensional parameters, the Rayleigh number and the Prandtl number, are defined as

$$Ra_0^T = \frac{g\beta\Delta T H^3}{\kappa_0 \nu_0}, \quad Pr_0 = \frac{c_p\rho_0\nu_0}{k_0} = \frac{\nu_0}{\kappa_0}. \tag{2}$$

The equations are nondimensionalized by the dimensions of the square cavity H, the ratio of the thermal diffusivity to the cavity length κ_0/H and the temperature difference between two vertical walls ΔT. The nondimensional property variation functions are defined as

Table 1 Result of grid sensitivity test. Constant properties, $Ra_0 = 10^5$ and $Pr_0 = 1.0$

$(\Delta x)_{avg}$	0.050	0.033	0.025	0.020	→ 0.0
# of elements	400	900	1600	2500	∞
V_{max}	73.245	72.645	72.605	72.435	71.893
Ψ_{max}	11.714	11.165	10.846	10.703	10.014
Nu	4.274	4.417	4.471	4.500	4.616
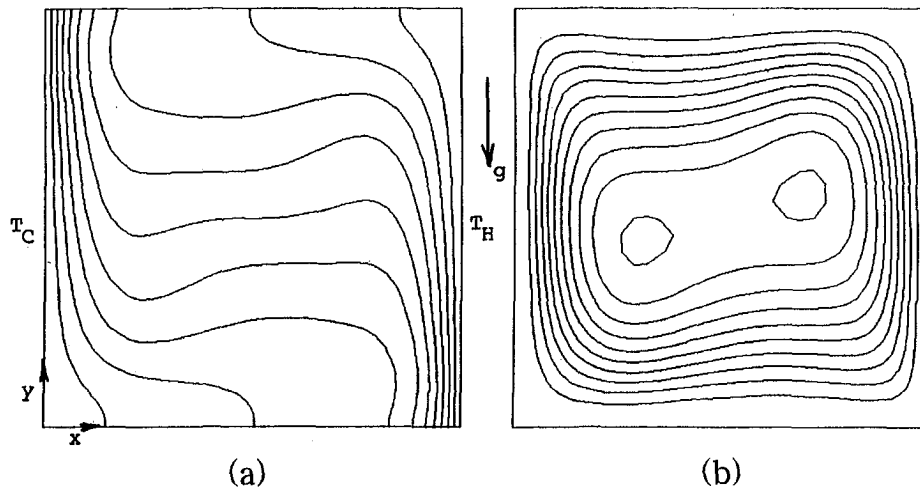
Fig. 1 Plots of (a) temperature and (b) stream function contours for $Ra_0^T = 10^5$ and $Pr_0 = 1.0$. Contour values for temperature are, from left to right, 0.1 to 0.9 by increments of 0.1. Contour values for stream function are, from the boundary to the interior, $0.1\Psi_{c,max}$ to $\Psi_{c,max}$ by increments of $0.1\Psi_{c,max}$ with $\Psi_{max} = 10.85$ and $\Psi_{c,max} = 10.7$.

$$\frac{\mu}{\mu_0} = f_1 = 1 + \alpha_\mu T + \beta_\mu T^2 \qquad (3a)$$

$$\frac{k}{k_0} = f_2 = 1 + \alpha_k T + \beta_k T^2 \qquad (3b)$$

where $f_1 = f_2 = 1$ when fluid properties are constant. For most liquid metals and gases the viscosity and thermal conductivity depart from linearity such that a parabolic fit is a good character-ization. In addition, we chose the same functions for μ and k so that in this way we are able to determine which of these properties dominates the effect on the heat transfer.

The boundary conditions considered in this study are, $U = V = 0$ on all solid boundary walls, $q_y = 0$ on lower and upper walls, $\Theta = 0$ on cold (left) wall, and $\Theta = 1$ on the hot (right) wall for the constant temperature condition or $q_x = $ constant for the constant heat flux condition on the right wall.

In this study, the finite element program FLOTRAN/CFD, a module of the commercial finite element method package ANSYS, was used. The reader is referred to ANSYS (1995) for the details of the numerical model of FLOTRAN/CFD.

3 Results and Discussions

Tests for sensitivity to grid size for this finite element pro-gram were performed for all the values of Ra considered. A graded grid with a cell size which increases away from all of the walls towards the center with a minimum of two computa-tional cells in each boundary layer was used. Representative results of such tests are shown in Table 1. The vertical velocity, which is the essential primitive variable of the flow system, is hardly affected by the grid size, especially for more than 900

elements. The extrapolated results for V_{max} and Ψ_{max} are within five percent and for Nu are within two percent of the benchmark values given by Jones and de Vahl Davis (1983). Based upon the sensitivity study, the computations to determine the effect of variable properties were conducted with a grid of 1600 ele-ments (40 × 40). For this grid, every variable is within ten percent of the values extrapolated to an infinitely fine mesh using Aitken's δ^2 extrapolation (Ralston, 1978).

Constant Properties. First, numerical simulations for con-stant properties ($f_1 = f_2 = 1$) were performed to check the effect of the Prandtl number and to serve as a reference for the variable property tests. Calculations were made for $0.01 \le Pr_0 \le 1$. Higher values of the Prandtl number are not considered since it is well known that Nu becomes nearly constant for large Pr_0 (Incropera and DeWitt, 1996). Figure 1 illustrates the contour plots of the temperature field and stream function for $Ra_0 = 10^5$ and $Pr_0 = 1.0$. The results show the well-developed thermal boundary layer and the adverse temperature gradient near the two vertical boundary walls which produces the typical counterclockwise circulation with two secondary rolls in the core (Mallinson and de Vahl Davis, 1977). As the Prandtl number decreases, the locations of the local maxima of the stream function move toward core region and finally for a very small Prandtl number (0.01) the two secondary rolls disappear and the flow is unicellular. Figure 2 shows the nondimensional temperature and vertical velocity profiles along a horizontal line at the midheight ($Y = 0.5$) as a function of Pr_0. Figure 2(a) shows that thermal boundary layer becomes thicker and the adverse temperature gradient becomes weaker as the Prandtl number decreases. For $Pr_0 = 0.01$, the adverse temperature gradient nearly disappears, causing the secondary rolls to van-

——————— **Nomenclature** ———————

c_p = specific heat
H = dimensions of the enclosure
k = thermal conductivity
Nu = Nusselt Number, $\partial\Theta/\partial X$ aver-
aged over the hot wall
q = heat flux
Ra^Q = Rayleigh number for prescribed
heat flux hot wall
Ra^T = Rayleigh number for isothermal
hot wall

T_0 = mean temperature, $(T_h + T_c)/2$
U, V = nondimensional velocities, $uH/\kappa_0, vH/\kappa_0$
X, Y = nondimensional coordinates, $x/H, y/H$
β = coefficient of volumetric expan-
sion
$\Delta T = T_h - T_c$
κ = thermal diffusivity
μ = viscosity

Θ = nondimensional temperature, $(T - T_c)/\Delta T$, $(T - T_c)/(qH/k)$
ρ = density

Subscripts

c = cold wall
h = hot wall
0 = evaluated at T_0

(a)

(b)

Fig. 2 Plots of (a) temperature and (b) vertical velocity profiles for $Ra_0^T = 10^6$ at $Y = 0.5$
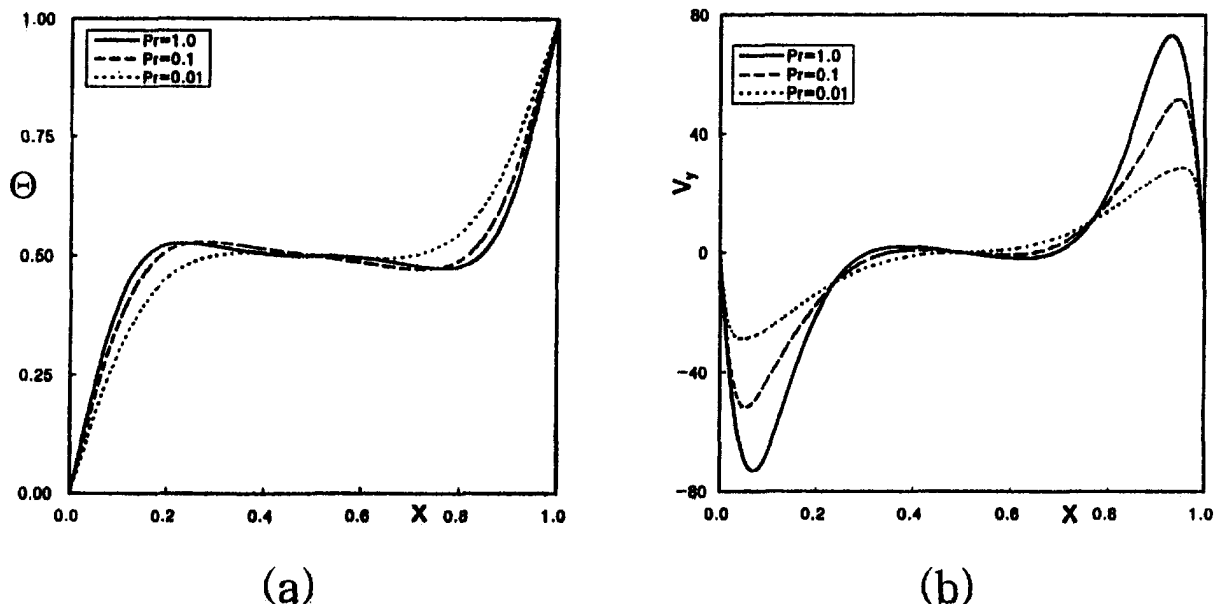
ish. The vertical velocity profile, Fig. 2(b), shows that the points of maximum velocity move toward the boundaries and that the velocity gradient outside boundary layer is quite weak as the Prandtl number decreases. These effects are attributable to the increased thermal diffusivity relative to the momentum diffusivity.

In order to examine quantitatively the effect of the Prandtl number, the calculated values of the Nusselt number, Nu, which represents the total rate of heat transfer across the cavity, are listed in Table 2. (The values of Nu listed in Table 2 agree with those given in Hyun and Lee (1988) and Viskanta et al. (1986) to better than five percent). In general, previous studies considered Nu to be a function of the Rayleigh number only and represented it in the form $Nu_0 = A \, Ra_0^m$, where m is typically between 0.25 to 0.3 (Jacob, 1949; Markatos and Pericleous, 1984) and A is a function of Pr_0. Table 2 lists the values of A and m for this form of correlation.

The overall dependence of Nu as a function of both Ra_0^T and Pr_0 is represented by

$$Nu_0 = 0.185 \, Ra_0^{T^{0.278}} \, Pr_0^{0.089}$$

$$(10^4 \le Ra_0^T \le 10^6, \quad 0.01 \le Pr_0 \le 1.0). \quad (4)$$

According to above correlations, the Prandtl number dependence of Nu is large over the range of Pr_0 considered, even when compared to the dependence on the Rayleigh number.

Temperature-Dependent Conductivity and Viscosity. The effects of a temperature dependent viscosity have been reported in Hyun and Lee (1988), Booker (1976), and Cheno-

weth and Paolucci (1986) using either an exponential law for liquids in which the viscosity decreases with temperature or Sutherland's law for gases for which the viscosity increases with temperature. For constant properties, the flow is asymmetric with equal velocities in the two vertical boundary layers and a zero isotherm at midheight. In general, a viscosity which decreases with temperature causes the upper section of the fluid to increase in temperature and to concentrate the cooler fluid in a smaller lower section. The resulting change in the buoyancy force nearly counteracts the effect of the change in viscosity with the result that the maximum velocities and the overall heat transfer do not change much from the constant property values. Similar results are found for a viscosity which increases with temperature. Since the effects of a viscosity which decreases with temperature have been presented in Hyun and Lee (1988), we restrict this presentation to a viscosity which increases with temperature, i.e., gases for which the conductivity also increases with temperature.

In this case, f_1 and/or f_2, which represent the variation of the property as a function of temperature, are assumed to be a parabolic function, which is reasonable for diatomic gases (Incropera and DeWitt, 1996).

$$f_1 \text{ or } f_2 = 0.5 + 0.5T + T^2 \quad (5)$$

Then, f_1 and f_2 are unity at the average temperature and 0.5 and 2.0 at the cold and hot walls, respectively. Thus the viscosity and conductivity change by the same factor of 2 at both walls. Figure 3 shows the effect of these temperature-dependent properties on temperature and velocity profiles for $Ra_0^T = 10^5$ and $Pr_0 = 1.0$. When viscosity is an increasing function of temperature, the overall temperature in the enclosure is slightly lower than the case of constant properties due to the activated fluid motion near the cold wall where the viscosity is low and the increased viscosity near the hot wall which slows the flow of the hot fluid. Note, however, that the temperatures near both walls are essentially unchanged from the constant property case. Interestingly, changes in the velocity are noticeable in the central region and particularly in the hot boundary layer, but not in the cold boundary layer. The effect of a temperature-dependent conductivity is to alter the temperature gradients near the hot and cold wall proportionately to the change in conductivity. The overall effect, as shown in Fig. 3, is then to increase the temperature in the enclosure and to alter the buoyancy forces accordingly.

Table 2 Nusselt number as a function of Ra_0^T and Pr_0. $Nu = A \, Ra_0^T$

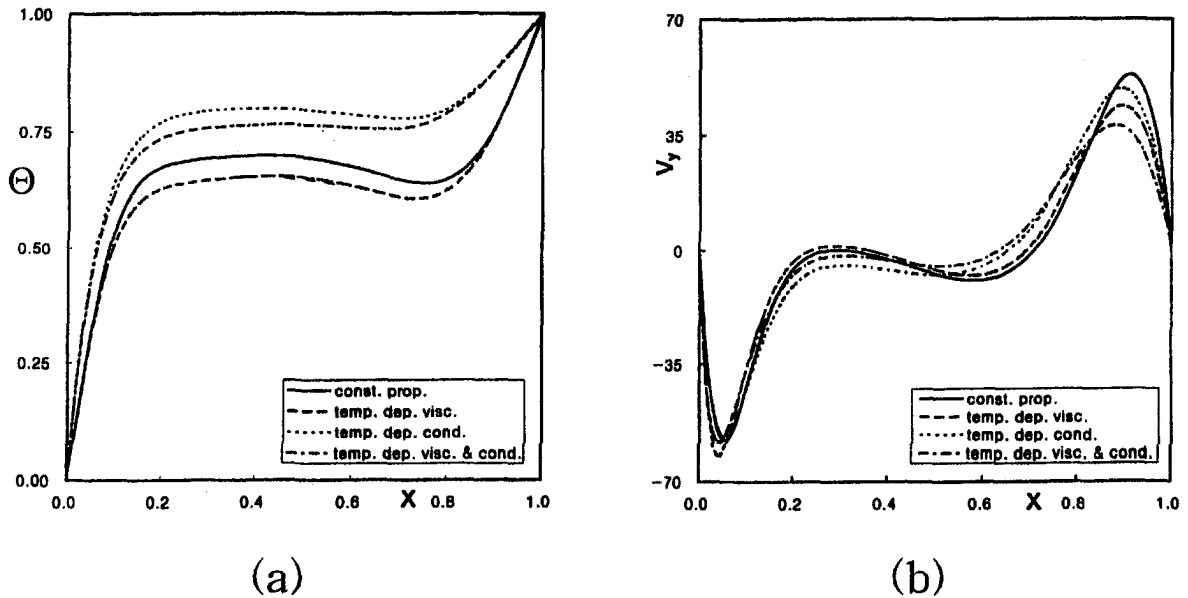| Pr_0	Ra_0^T			A	m
	10^4	10^5	10^6		
0.01	1.540	2.871	5.558	0.118	0.279
0.02	1.701	3.170	6.000	0.135	0.274
0.05	1.894	3.542	6.562	0.158	0.270
0.10	2.011	3.794	7.106	0.166	0.271
0.20	2.102	4.019	7.467	0.167	0.275
0.50	2.186	4.296	8.100	0.160	0.284
1.00	2.226	4.471	8.489	0.155	0.291

Fig. 3 Plots of (a) temperature and (b) vertical velocity profiles for $Ra_0^T = 10^5$ and $Pr_0 = 1.0$ at $Y = 0.743$

As illustrated in Fig. 3, the effect of a simultaneous variation of viscosity and conductivity on the temperature and velocity can be reasonably estimated by combining their separate effects. On the other hand, the overall Nusselt number is essentially unaffected by the variable properties. Values of Nu for variable viscosity only, variable conductivity only, and combined effects differed from the constant property case by no more than -0.5 percent, $+0.2$ percent, and -0.2.

Constant Heat Flux. The final phase of computations was conducted by imposing a constant heat flux condition at the right wall with the left wall maintained at the fixed temperature. In this case, the temperature difference was nondimensionalized with respect to qH/k, i.e., using the temperature difference for one-dimensional conduction from a wall with a prescribed heat flux to a wall of constant temperature, leading to

$$Ra_0^Q = \frac{g\beta(qH/k_0)H^3}{\kappa_0\nu_0} . \qquad (6)$$

Although qH/R_0 is the only available normalizing factor for this situation, it substantially overestimates the temperature differences which exist across the cavity. Table 3 list the maximum (at the top) and minimum (at the bottom) temperatures on the hot wall. Incropera and DeWitt (1996) suggest that for a single vertical plate with a constant heat flux the correlation for an isothermal plate can be used if the Rayleigh and Nusselt numbers are based on the temperature difference measured at the half-height of the plate. Although this isn't particularly useful for predicting the flow patterns and temperature fields for a given q, the idea can be extended to the enclosure. If we require that ΔT be such that the correlation given in Eq. (4) also holds for the constant heat flux case, we find the value labeled $\Delta T_{eff}/$

(qH/R_0) and the location where it occurs, y/H, listed in Table 3. We see that as the Rayleigh number increases, that the value of y/H increases and the value of $\Delta T_{eff}/(qH/R_0)$ diminishes. By multiplying Ra^Q by the entry labeled $\Delta T_{eff}/(qH/R_0)$ we obtain an equivalent Ra^T to use with Eq. (4).

Figure 4 presents the temperature and stream function patterns for constant properties for $Ra_0^Q = 10^6$, which is equivalent to $Ra_0^T = 1.85 \times 10^5$. Near the right wall, the temperature gradient along the vertical direction is similar everywhere due to the constant heat flux and the temperature increases with height due to thermal stratification. Near the left wall, the temperature profile is similar to that of the case for constant temperature walls. That is, a strong temperature gradient at the upper region and a weak one at the lower region. Due to the strong temperature gradient in the left upper region, the downward fluid motion is vigorous and results in a stronger secondary roll in the left region than in the right region.

When the properties varied according to Eq. (3), using the maximum and minimum values of Θ shown in Table 3 the variation was found to be the same as that observed for the isothermal hot wall case, i.e., $f_{Tmin}/f_{Tavg} \approx \frac{1}{2}$ and $f_{Tmax}/f_{Tavg} \approx 2$. This suggests that the behavior should be similar to that depicted in Figure 3. Figure 5 shows the temperature and velocity profiles along a horizontal line in the upper region located at $Y = 0.743$. The temperature profile is similar for all cases except in the upper right region where the temperature is relatively high so that the variations of properties are fairly strong. When both properties are temperature dependent, the adverse temperature gradient is too weak to form a secondary roll near the right wall. In general, the overall effects of temperature-dependent properties are not as strong as those found for isothermal walls. This is presumed to be the equalizing effect of constant temperature at the left wall. The effects illustrated in Fig. 4 were consistent over all Rayleigh numbers examined.

4 Conclusions

An extensive set of numerical results has been obtained to investigate the effect of property variation on natural convective heat transfer over a wide range of Prandtl numbers. For constant properties, when the Prandtl number decreases the thermal boundary layer becomes thicker and the adverse temperature gradient becomes weaker. Consequently, the flow pattern

Table 3 Constant heat flux hot wall

Ra_0^Q	10^4	10^5	10^6	10^7
$\Theta(\text{hotwall})_{max}$	0.699	0.442	0.280	0.171
$\Theta(\text{hotwall})_{min}$	0.433	0.240	0.135	0.076
$\Delta T_{eff}/(qH/R_0)$	0.505	0.307	0.185	0.112
y/H	0.51	0.63	0.76	0.70
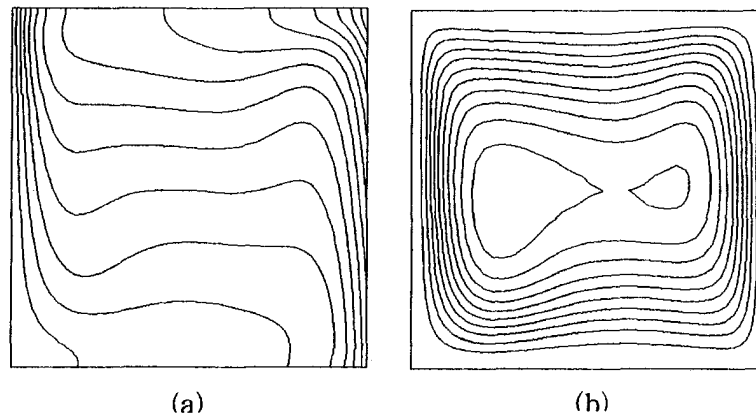
Fig. 4 Plots of (a) temperature and (b) stream function contours for $Ra_0^Q = 10^6$ and $Pr_0 = 1.0$ (equivalent $Ra_0^T = 1.85 \times 10^5$) with constant heat flux at the right wall for constant properties. Contour values of temperature are 0.02 to 0.26, with increments of 0.02. Contour pattern for stream function are the same as Fig. 1 except $\Psi_{max} = 11.37$ and $\Psi_{c,max} = 10.5$.
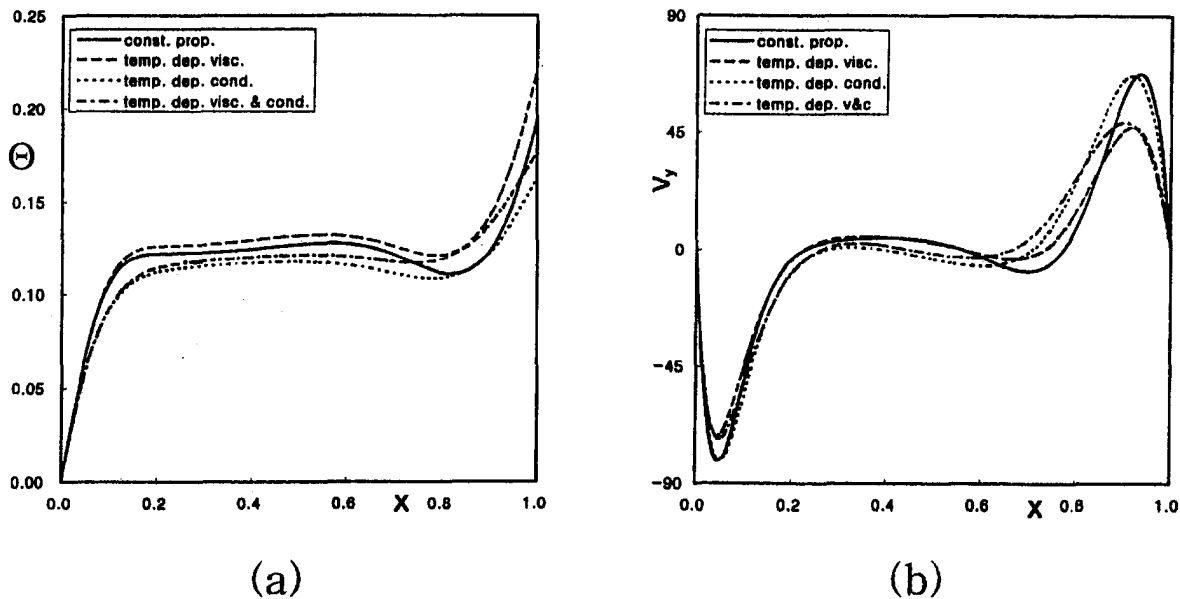
Fig. 5 Plots of (a) temperature and (b) vertical velocity profiles at $Y = 0.743$. Conditions are, $Ra_0^Q = 10^6$ and $Pr_0 = 1.0$ (equivalent $Ra_0^T = 1.85 \times 10^5$) with constant heat flux at the right wall.

changes significantly, even though the Rayleigh number is maintained constant, and the Nusselt number is found to decrease as the Prandtl number decreases. The Nusselt number can be correlated with Ra_0 and Pr_0 according to Eq. (4).

We have also presented results for heating with a constant heat flux which permits one to compute an equivalent Ra^T from Ra^Q to estimate the overall heat transfer using the correlation for an isothermal hot wall, Eq. (4). Although we have not investigated other than the square cavity, we anticipate that the reduction factors will be affected by the aspect ratio since the flow and thermal fields for high narrow cavities are strongly influenced by the aspect ratio as evidenced by terms of the form $(H/L)^n$ appearing in the experimental correlations (Incropera and DeWitt, 1996; Jacob, 1949).

When the conductivity and viscosity are temperature dependent, both the velocities and temperature are affected by the property variation. The flow field showed a fairly weak variation except near boundaries, whereas the temperature field in the central region is strongly affected, especially by the temperature dependent thermal conductivity. For the case of constant heat flux from the right wall, the overall effect of property variation is relatively weak due to the fixed temperature at the cold wall. Although changes were produced in the temperature and velocity fields, there was essentially no change in the overall heat transfer and the constant property correlation, Eq. (4), was accurate to better than one percent.

References

ANSYS User's Manual, 1995, SAS IP.

Booker, J. R., 1976, "Thermal Convection With Strongly Temperature-Dependent Viscosity, *J. Fluid Mechanics*, Vol. 76, pp. 741–754.

Chenoweth, D. R., and Paolucci, S., 1986, "Natural Convection in an Enclosed Vertical Air Layer," *J. Fluid Mechanics*, Vol. 169, pp. 173–210.

Hyun, J. M., and Lee, J. W., 1988, "Transient Natural Convection in a Square Cavity of a Fluid With Temperature-Dependent Viscosity," *Int. J. Heat and Fluid Flow*, Vol. 9, pp. 278–285.

Incropera, F. P., and DeWitt, D. P., 1996, *Introduction to Heat Transfer*, John Wiley and Sons, New York.

Jacob, M., 1949, *Heat Transfer*, Vol. 1, John Wiley and Sons, New York.

Jones, I. P., and de Vahl Davis, G., 1983, "Natural Convection in a Square Cavity: A Comparison Exercise," *Int. J. Num. Methods in Fluids*, Vol. 3, pp. 227–248.

Mallison, G. D., and de Vahl Davis, G., 1977, "Three-Dimensional Natural Convection in a Box: A Numerical Study," *J. Fluid Mechanics*, Vol. 83, pp. 1–31.

Markatos, N. C., and Pericleous, K. A., 1984, "Laminar and Turbulent Natural Convection in an Enclosed Cavity," *Int. J. Heat Mass Transfer*, Vol. 27, No. 5, pp. 755–772.

Ralston, A., A., 1978, *First Course in Numerical Analysis*, McGraw-Hill, New York.

Viskanta, R., Kim, D. M., and Gau, C., 1986, "Three-Dimensional Natural Convection Heat Transfer in a Liquid Metal in a Cavity," *Int. J. Heat and Mass Transfer*, Vol. 29, pp. 475–484.

Yamasaki, T., and Irvine, T. F., 1984, "Laminar Free Convection in a Vertical Tube with Temperature-Dependent Viscosity," *Int. J. Heat and Mass Transfer*, Vol. 27, pp. 1613–1621.

Developing Free Convection in Open-Ended Vertical Eccentric Annuli With Isothermal Boundaries

M. A. I. El-Shaarawi
Professor

E. M. A. Mokheimer [1]
Assistant Professor

Mechanical Engineering Department,
King Fahd University of
Petroleum and Minerals,
Dhahran 31261, Saudi Arabia

A model has been developed to numerically study the developing laminar free convection in vertical open-ended eccentric annuli with isothermal boundary conditions. For a fluid of Prandtl number 0.7 in an annulus of radius ratio 0.5, the developing velocity profiles in addition to the development of the pressure along the annulus are presented. The channel heights required to naturally induce different flow rates have also been obtained for three values of the dimensionless eccentricity, namely, 0.1, 0.5, and 0.7. Variations of the total heat absorbed by the fluid with the channel height are provided for the three values of dimensionless eccentricity.

Introduction

Laminar free convection with simultaneously developing hydrodynamic and thermal boundary layers in vertical eccentric annuli is encountered in many practical applications. Eccentricities might be introduced in nominally concentric annuli as a result of manufacturing tolerances or operating conditions. In atomic reactors, the heat generated by atomic reactions is transferred to the coolant flowing through the annular gap between the fuel element and the coolant channel wall. During the shut-off periods and pump failure accidents the core of the reactor is cooled by natural convection. In vertical electric motors and generators, the heat generated by irreversible electrical and mechanical processes is transferred through the air gap between the rotor and the stator. The transfer of heat by free convection is always a factor in the cooling of such machines and may be the sole means of cooling small types of these devices. Knowledge of the characteristics of the free-convection fluid motion is needed to predict the operating temperatures which must be less than the maximum permitted value.

Fully developed free convection in open-ended vertical annuli is the limiting case for the more general problem of developing free convection in such channels. In the latter case fully developed conditions can be achieved if the annulus is sufficiently high or, more general, if the Rayleigh number has a sufficiently low value. El-Shaarawi and Al-Nimr (1990) presented analytical solutions for the fully developed free convection in open-ended concentric annuli. Four pairs of fundamental boundary conditions, as defined by Reynolds et al. (1963), were investigated. These boundary conditions are obtained by combining each of the two conventional boundary conditions of having one boundary at constant heat flux or at constant temperature with each of the conditions wherein the opposite boundary is kept isothermal at the inlet fluid temperature or adiabatic.

Fully developed forced flow and convection heat transfer in eccentric annuli have been tackled by some investigators. Heyda (1959) determined the Green's function in bipolar coordinates for the potential flow in an eccentric annulus and

then solved the momentum equation for the velocity profile. Snyder (1963) utilized an analytical solution obtained by El-Saden (1959) for conduction heat transfer to solve the differential equation describing the slug flow heat transfer in an eccentric annulus. Using the same technique, Snyder and Goldstein (1965) obtained the fully developed velocity profile for laminar forced flow in eccentric annuli. However, Redberger and Charles (1962) solved the same problem numerically by means of finite difference techniques and bipolar coordinates. Using cylindrical coordinates, Cheng and Hwang (1968) and Trombetta (1972) obtained approximate solutions for the energy equation under different boundary conditions in the case of fully developed laminar forced flow in eccentric annuli. Suzuki et al. (1990) treated numerically the fully developed forced convection in eccentric annuli under two thermal boundary conditions of the second kind.

The developing laminar forced flow and heat transfer in the limiting case of concentric annuli has been investigated by Heaton et al. (1964), Sparrow and Lin (1964), and Coney and El-Shaarawi (1975). On the other hand, the developing laminar free convection in concentric annuli has been studied by El-Shaarawi and Sarhan (1981) and Al-Arabi et al. (1981).

A thorough search of the literature has revealed that no work has been reported for natural convection in vertical open-ended eccentric annuli. Moreover, only three papers by Feldman et al. (1982a, b) and El-Shaarawi et al. (1997) have dealt with developing flow in eccentric annuli. In the two papers by Feldman et al. (1982a, 1982b) the two transverse momentum equations were dropped; the hydrodynamic boundary layer model comprised only two equations, namely, a reduced axial momentum equation and the continuity equation. However, since there are three unknown velocity components in addition to the pressure, this two-equation boundary layer model does not form a complete mathematical model. Consequently, additional assumptions regarding the transverse flows were used to facilitate a solution. These assumptions depend on a relation between the two transverse velocity components in which a constant has to be arbitrarily chosen.

The first objective of the present paper is to present a well-posed mathematical model for the problem under consideration, i.e., a model capable of describing the natural flow and heat transfer in vertical eccentric annuli without need of assumptions dependent on prior knowledge of the mechanism

of transverse flows. The second objective is to develop a numerical algorithm to solve the obtained model. Finally, numerical results are presented for the developing velocity profiles, axial variation of pressure, heights required to suck specified flow rates, and heat transfer parameters under the thermal boundary conditions of having one of the annulus boundaries at an isothermal temperature other than the ambient temperature while the other boundary is maintained at ambient temperature.

Governing Equations

Two-dimensional plan and elevation of the geometry under consideration are shown in Fig. 1(a). This eccentric geometry can easily be described by the bipolar coordinate system (η, ξ and z) shown in Fig. 1(b). The transformation equations from the Cartesian coordinate system (x, y, and z) to this bipolar system are given in the Nomenclature. In this orthogonal coordinate system the two cylindrical boundaries of the annulus coincide with two surfaces having constant values of η (η_i and η_o, which can be expressed in terms of the annulus radius ratio N and the dimensionless eccentricity E as given in the Nomenclature). The other coordinate (ξ) represents a set of eccentric cylinders whose centres lie on the y-axis and which orthogonally intersect the boundaries of the annulus. The transformed geometry in the complex η-ξ plane is, as shown in Fig. 1(c), a slab of length ($\eta_i - \eta_o$) and width equal to the limits of ξ, that is 2π. Figure 1(c) shows also the finite difference grid used for a given value of z.

The vertical eccentric annulus shown in Fig. 1(a) is of finite height, open at both ends and immersed in a stagnant Newtonian fluid of infinite extent maintained at constant temperature T_o. Free convection flow is induced inside this annular channel as a result of heating or cooling one of its vertical

walls at a constant temperature which is different from the ambient temperature while keeping the other wall at ambient temperature. Thus, two cases are under investigation, namely, case (1.I) in which the inner wall is isothermally heated above ambient while the outer wall is kept at the ambient temperature and case (1.O) in which the outer wall is the heated boundary while the inner wall is kept at the ambient temperature. The fluid enters the channel at the ambient temperature T_o and is assumed to have constant physical properties but obeys the Boussinesq approximation according to which its density is allowed to vary with temperature in only the gravitational body force term of the vertical (axial) momentum equation. Thus Boussinesq approximation neglects the compressibility effect everywhere except for the buoyancy force term. Body forces in other than the vertical direction, viscous dissipation, internal heat generation, and radiation heat transfer are absent.

The governing equations in a general orthogonal curvilinear coordinate system are given in two references (Hughes and Gaylord, 1964; Moon and Spencer, 1971). Using the appropriate coordinate transformation scale factors given by Hughes and Gaylord (1964), the governing equations can be obtained in bipolar coordinates under the abovementioned assumptions. However, some assumptions, based on the boundary layer theory (Schlichting, 1987; El-Shaarawi, 1990; El-Shaarawi et al., 1997) will be used to simplify the model. These assumptions include: (1) the pressure is a function of the axial coordinate only ($\partial p/\partial \eta = \partial p/\partial \xi = 0$), (2) the axial diffusions of momentum and energy are neglected ($\partial^2/\partial z^2 = 0$), and (3) the η-velocity component (v) is much smaller than the ξ and z-velocity components (w and u). Introducing the dimensionless parameters given in the Nomenclature, the governing equations (under the foregoing assumptions and taking into consideration that the latter as-

---

─────── **Nomenclature** ───────

a = location of the positive pole of the bipolar coordinate system on the x-axis, equal r_i Sinh η_i or r_o Sinh η_o

A = cross-sectional area of the channel, $\pi(r_o^2 - r_i^2)$

c_p = specific heat of fluid at constant pressure

D_h = equivalent (hydraulic) diameter of annulus, $2(r_o - r_i) = 2a(1 - N)Csch\eta_o$

e = eccentricity (distance between the two centers of the two cylinders forming the eccentric annulus), $a(Coth\eta_o - Coth\eta_i)$

E = dimensionless eccentricity (dimensionless center-to-center distance), $e/(r_o - r_i) = $ Sinh ($\eta_i - \eta_o$)/(Sinh η_i − Sinh η_o)

f = volumetric flow rate, $f = \int_{r_i}^{r_o} 2\pi r u dr = \pi(r_o^2 - r_i^2)\bar{u} = 2 \int_0^\pi \int_{\eta_o}^{\eta_i} uh^2 d\eta d\xi$

F = dimensionless volumetric flow rate, $f/\pi l\gamma$ Gr$^* = 8(1 - N)^2 \int_0^\pi \int_{\eta_o}^{\eta_i} UH^2 d\eta d\xi/\pi$

g = gravitational body force per unit mass (acceleration)

Gr = Grashof number, $\pm g\beta(T_w - T_o)D_h^3/\gamma^2$, the plus and minus signs apply to upward (heating) and downward (cooling) flows, respectively. Thus Gr is always positive

Gr^* = modified Grashof number, $Gr^* = Gr\,D_h/l$

h = coordinate transformation scale factor, $a(Cosh\,\eta - Cos\,\xi)$

H = dimensionless coordinate transformation factor, $h/D_h = 0.5$ Sinh (η_o)/(1 − N)(Cosh (η) − Cos (ξ))

i = index of the numerical grid in the η-direction

j = index of the numerical grid in the ξ-direction

k = thermal conductivity of fluid

l = height of annulus

L = dimensionless height of annulus (value of Z at annulus exit), $1/Gr^*$

m = number of steps of the numerical grid in the ξ-direction

n = number of steps of the numerical grid in the η-direction or infinite-series summation parameter in an analytical solution

N = annulus radius ratio, $r_i/r_o = $ Sinh η_o/Sinh η_i

p = pressure of fluid inside the channel at any cross section

p' = pressure defect at any point, $p - p_s$

p_o = pressure of fluid at annulus entrance, $-\rho u_o^2/2$

p_s = hydrostatic pressure, $\mp\rho_o gz$ where the minus and plus signs are for upward (heating) and downward (cooling) flows, respectively

P = dimensionless pressure defect at any point, $p'D_h^4/\rho_o l^2\gamma^2$ Gr^{*2}

Pr = Prandtl number, $\mu c_p/k$

q = heat gained or lost by fluid from the entrance up to a particular elevation in the annulus, $\rho_o fc_p(T_m - T_o)$

$\bar{q}$ = heat gained or lost by fluid from the entrance up to the annulus exit, i.e., value of q at $z = l$, $\rho_o fc_p(\bar{T}_m - T_o)$

Q = dimensionless heat absorbed from the entrance up to any particular elevation, $q/[\pi\rho_o c_p l\gamma$ Gr* $(T_w - T_o)] = F\theta_m$

$\bar{Q}$ = dimensionless heat absorbed up to the annulus exit, i.e., value of Q at $z = l$, $\bar{q}/[\pi\rho_o c_p l\gamma$ Gr* $(T_w - T_o)] = F\bar{\theta}_m$

---

sumption results in dropping the η-momentum equation) are the following dimensionless equations.

Continuity Equation.

$$\frac{\partial(HW)}{\partial\xi} + \frac{\partial(HV)}{\partial\eta} + 4(1-N)^2\frac{\partial(H^2U)}{\partial Z} = 0 \qquad (1)$$

ξ-Momentum Equation.

$$\frac{W}{H}\frac{\partial W}{\partial\xi} + \frac{V}{H^2}\frac{\partial HW}{\partial\eta} + 4(1-N)^2 U\frac{\partial W}{\partial Z} - \frac{V^2}{H^2}\frac{\partial H}{\partial\xi}$$

$$= \frac{1}{H^3}\left(\frac{\partial^2 HW}{\partial\eta^2} + \frac{\partial^2 HW}{\partial\xi^2}\right) - \frac{2}{H^4}\left(\frac{\partial HW}{\partial\eta} - \frac{\partial HV}{\partial\xi}\right)\frac{\partial H}{\partial\eta}$$

$$+ \frac{8(1-N)^2}{H^2}\frac{\partial H}{\partial\xi}\frac{\partial U}{\partial Z} \qquad (2)$$

z-Momentum Equation.

$$\frac{W}{H}\frac{\partial U}{\partial\xi} + \frac{V}{H}\frac{\partial U}{\partial\eta} + 4(1-N)^2 U\frac{\partial U}{\partial Z}$$

$$= -\frac{1}{4(1-N)^2}\frac{dP}{dZ} + \frac{\theta}{4(1-N)^2}$$

$$+ \frac{1}{H^2}\left[\frac{\partial^2 U}{\partial\xi^2} + \frac{\partial^2 U}{\partial\eta^2}\right] \qquad (3)$$

Energy Equation.

$$\frac{W}{H}\frac{\partial\theta}{\partial\xi} + \frac{V}{H}\frac{\partial\theta}{\partial\eta} + 4(1-N)^2 U\frac{\partial\theta}{\partial Z}$$

$$= \frac{1}{Pr\cdot H^2}\left(\frac{\partial^2\theta}{\partial\xi^2} + \frac{\partial^2\theta}{\partial\eta^2}\right) \qquad (4)$$

The differential continuity Eq. (1) subject to the no-slip conditions on the two boundaries can be written in the following integral form:

$$\bar{U} = \frac{8(1-N)}{\pi(1+N)}\int_0^\pi\int_{\eta_o}^{\eta_i} UH^2 d\eta d\xi. \qquad (5)$$

Equations (1) through (4) are subject to the following boundary conditions

for $Z = 0$ (annulus inlet) and $\eta_o\langle\eta\langle\eta_i$,

$\quad V = W = \theta = 0$ and $U = U_o$, $P = -U_o^2/2$

for $Z \geq 0$ and $\eta = \eta_i$, $U = V = W = 0$,

$\quad \theta = 1$ for case (1.I) or 0 for case (1.O)

for $Z \geq 0$ and $\eta = \eta_o$, $U = V = W = 0$,

$\quad \theta = 0$ for case (1.I) or 1 for case (1.O)

for $Z \geq 0$ and $\xi = 0$ and π (the line of symmetry):

$$\frac{\partial V}{\partial\xi} = \frac{\partial W}{\partial\xi} = \frac{\partial U}{\partial\xi} = \frac{\partial\theta}{\partial\xi} = 0$$

for $Z = L$ (annulus exit) and $\eta_o \leq \eta \leq \eta_i$, $P = 0$

$$\left.\begin{array}{c}\\\\\\\\\\\\\\\\\\\\\end{array}\right\} \qquad (6)$$

The fully developed flow, which occurs if the channel is sufficiently high (i.e., the modified Rayleigh number Ra* has a sufficiently low value) provides a check on the numerical solution to be obtained as it yields the limiting conditions for the developing flow. For fully developed flows, variations in the axial direction vanish ($\partial/\partial Z = 0$), $V = W = 0$ and the

---

Nomenclature (cont.)

r_i = inner radius of annulus

r_o = outer radius of annulus

Ra = Rayleigh number, Gr Pr

Ra* = modified Rayleigh number, Gr* Pr = Ra D_h/l

T = temperature at any point

T_m = mixing-cup (mixed-mean or fluid-bulk) temperature over any cross section at a given z, $\int_A TudA/(A\bar{u})$ $= 2\int_0^\pi\int_{\eta_o}^{\eta_i} Tuh^2 d\eta d\xi/[\pi(r_o^2 - r_i^2)\bar{u}]$

$\bar{T}_m$ = mixing cup temperature at annulus exit, i.e., value of T_m at $z = l$

T_w = temperature of isothermal wall

u = axial (streamwise) velocity component at any point

u_{fd} = fully developed axial velocity profile

u_o = entrance axial velocity, $\bar{u}$

$u_{o,fd}$ = fully developed value of the entrance axial velocity

$\bar{u}$ = average value of u (volume flow rate per unit area), $\int_A udA/A = 2\int_0^\pi\int_{\eta_o}^{\eta_i} uh^2 d\eta d\xi/[\pi(r_o^2 - r_i^2)\bar{u}] = 2\int_0^\pi\int_{\eta_o}^{\eta_i} uh^2 d\eta d\xi/[\pi a^2(1-N^2) Csch^2 \eta_o\bar{u}]$

U = dimensionless axial velocity at any point, $ur_o^2/l\gamma$ Gr*

$\bar{U}$ = dimensionless average axial velocity at any point, $\bar{u}r_o^2/l\gamma$ Gr*

U_{fd} = dimensionless fully developed axial velocity, $u_{fd}r_o^2/l\gamma$ Gr*

$U_{o,fd}$ = fully developed value of the dimensionless axial velocity, $u_{o,fd}r_o^2/l\gamma$ Gr*

U_L = dimensionless axial velocity at the exit

x = the first transverse direction in the cartesian coordinate system

y = the second transverse direction in the cartesian coordinate system

z = axial coordinate in both the Cartesian and bipolar coordinate systems

Z = dimensionless axial coordinate, z/l Gr*

Greek Letters

β = volumetric coefficient of thermal expansion

η = the first transverse bipolar coordinate, related to the cartesian coordinate x by $x = a$ Sinh $(\eta)/$Cosh (η) − Cos (ξ)

η_i = value of η on the inner surface of the annulus, $\log_e [(N(1+E^2) + (1-E^2))/2NE + (((N(1+E^2) + (1-E^2))/2NE)^2 - 1)^{1/2}]$ = Cosh^{-1} $[(N(1+E^2) + (1-E^2))/2NE]$

η_o = value of η on the outer surface of the annulus, $\log_e [(N(1-E^2) + (1+E^2)/2E + (((N(1-E^2) + (1+E^2))/2E)^2 - 1)^{1/2}]$ = Cosh^{-1} $[(N(1-E^2) + (1+E^2))/2E]$

$\Delta\eta$ = numerical grid mesh size in η-direction, $(\eta_i - \eta_o)/n$

θ = dimensionless temperature, $(T - T_o)/(T_w - T_o)$

θ_{fd} = fully developed dimensionless temperature

θ_m = dimensionless mixed-mean temperature, $(T_m - T_o)/(T_w - T_o)$

$\bar{\theta}_m$ = dimensionless mixed-mean temperature at channel exit, $(\bar{T}_m - T_o)/(T_w - T_o)$

μ = dynamic viscosity of fluid

ξ = the second transverse bipolar coordinate, related to the cartesian coordinate y by $y = a$ Sin $(\xi)/$(Cosh (η) − Cos (ξ))

$\Delta\xi$ = numerical grid mesh size in ξ-direction, π/m

ρ_o = fluid density at ambient temperature

---

above governing equations, in the presence of an isothermal boundary, reduce to the following two equations and their boundary conditions:

$$\frac{\partial^2 U_{fd}}{\partial \eta^2} + \frac{\partial^2 U_{fd}}{\partial \xi^2} = \frac{\theta_{fd}}{4(1-N)^2} H^2 \qquad (7)$$

$$\frac{\partial^2 \theta_{fd}}{\partial \eta^2} + \frac{\partial^2 \theta_{fd}}{\partial \xi^2} = 0 \qquad (8)$$

$$\left.\begin{array}{l}
\text{on } \eta = \eta_i, \; U_{fd} = 0, \; \theta_{fd} = \theta_i = 1 \\[4pt]
\quad \text{for case (1.I) or } \theta_{fd} = \theta_i = 0 \text{ for case (1.O)} \\[4pt]
\text{on } \eta = \eta_o, \; U_{fd} = 0, \; \theta_{fd} = \theta_o = 0 \\[4pt]
\quad \text{for case (1.I) or } \theta_{fd} = \theta_o = 1 \text{ for case (1.O)} \\[4pt]
\text{on the symmetry line, i.e., } \xi = 0 \text{ and } \pi, \\[4pt]
\partial \theta_{fd}/\partial \xi = 0 \text{ for both cases}
\end{array}\right\} \quad (9)$$

Equation (8) subject to boundary conditions (9) has the following closed-form solution (El-Saden, 1961).

$$\frac{\theta_{fd} - \theta_o}{\theta_i - \theta_o} = \frac{\eta - \eta_o}{\eta_i - \eta_o} \qquad (10)$$

Equation (7) can be numerically solved, after substituting the above analytical solution (10), to obtain U_{fd}. Then a numerical representation of Eq. (5) can be utilized to obtain the average value of U_{fd}; this is $U_{o,fd}$.

Numerical Analysis and Method of Solution

Equations (1)–(4) can be written in the following finite difference forms, respectively.

$$\frac{H(i, j+1)W(i, j+1) - H(i, j-1)W(i, j-1)}{2\Delta\xi}$$

$$+ \frac{H(i, j)V(i, j) - H(i-1, j)V(i-1, j)}{\Delta\eta}$$

$$+ 4(1-N)^2 H^2(i, j) \frac{U(i, j) - U^*(i, j)}{\Delta Z} = 0 \quad (11)$$

$$\frac{W^*(i, j)}{H(i, j)} \frac{U(i, j+1) - U(i, j-1)}{2\Delta\xi}$$

$$+ \frac{V^*(i, j)}{H(i, j)} \frac{U(i+1, j) - U(i-1, j)}{2\Delta\eta}$$

$$+ 4(1-N)^2 U^*(i, j) \frac{U(i, j) - U^*(i, j)}{\Delta Z}$$

$$= -\frac{1}{4(1-N)^2} \frac{P(i, j) - P^*(i, j)}{\Delta Z}$$

$$+ \frac{\theta}{4(1-N)^2} + \frac{1}{(H(i, j))^2}$$

$$\times \left(\begin{array}{l} \dfrac{U(i-1, j) - 2U(i, j) + U(i+1, j)}{(\Delta\eta)^2} \\[8pt] + \dfrac{U(i, j-1) - 2U(i, j) + U(i, j+1)}{(\Delta\xi)^2} \end{array} \right) \quad (13)$$

$$\frac{W^*(i, j)}{H(i, j)} \frac{\theta(i, j+1) - \theta(i, j-1)}{2\Delta\xi}$$

$$+ \frac{V^*(i, j)}{H(i, j)} \frac{\theta(i+1, j) - \theta(i-1, j)}{2\Delta\eta}$$

$$+ 4(1-N)^2 U^*(i, j) \frac{\theta(i, j) - \theta^*(i, j)}{\Delta Z}$$

$$= \frac{1}{\Pr \cdot (H(i, j))^2} \left\{ \frac{\theta(i-1, j) - 2\theta(i, j) + \theta(i+1, j)}{(\Delta\eta)^2} \right.$$

$$\left. + \frac{\theta(i, j-1) - 2\theta(i, j) + \theta(i, j+1)}{(\Delta\xi)^2} \right\} \quad (14)$$

Using the trapezoidal rule, the integral continuity Eq. (5) can be written as

$$\frac{8(1-N)}{\pi(1+N)} \left(0.5 \sum_{i=2}^{n} U(i, 1)(H(i, 1))^2 \right.$$

$$+ U(i, m+1)(H(i, m+1))^2$$

$$\left. + \sum_{j=2}^{m} \sum_{i=2}^{n} U(i, j)(H(i, j))^2 \right) \Delta\eta\Delta\xi = \bar{U}. \quad (15)$$

$$\frac{W^*(i, j)}{H(i, j)} \frac{W(i, j+1) - W(i, j-1)}{2\Delta\xi} + \frac{V^*(i, j)}{(H(i, j))^2} \frac{H(i+1, j)W(i+1, j) - H(i-1, j)W(i-1, j)}{2\Delta\eta}$$

$$+ 4(1-N)^2 U^*(i, j) \frac{W(i, j) - W^*(i, j)}{\Delta Z} - \frac{(V^*(i, j))^2}{(H(i, j))^2} \frac{H(i, j+1) - H(i, j-1)}{2\Delta\xi}$$

$$= \frac{1}{(H(i, j))^3} \left\{ \frac{H(i-1, j)W(i-1, j) - 2H(i, j)W(i, j) + H(i+1, j)W(i+1, j)}{(\Delta\eta)^2} \right.$$

$$\left. + \frac{H(i, j-1)W(i, j-1) - 2H(i, j)W(i, j) + H(i, j+1)W(i, j+1)}{(\Delta\xi)^2} \right\}$$

$$- \frac{2}{(H(i, j))^4} \left(\frac{H(i+1, j) - H(i-1, j)}{2\Delta\eta} \right) \left(\begin{array}{l} \dfrac{H(i+1, j)W(i+1, j) - H(i-1, j)W(i-1, j)}{2\Delta\eta} \\[8pt] - \dfrac{H(i, j+1)V^*(i, j+1) - H(i, j-1)V^*(i, j-1)}{2\Delta\xi} \end{array} \right)$$

$$+ \frac{8(1-N)^2}{(H(i, j))^2} \frac{H(i, j+1) - H(i, j-1)}{2\Delta\xi} \frac{U(i, j) - U^*(i, j)}{\Delta Z} \quad (12)$$

Due to symmetry, the above equations need to be solved in only half of the slab, i.e., for $0 \leq \xi \leq \pi$. These equations are linearized by assuming that where the product of two unknowns occurs, one of them is given approximately by its value at the previous axial step, the variable superscripted with an asterisk (*). Moreover, in Eq. (12) all the values of V have been deliberately taken at the previous axial step in order to make this equation locally (i.e., within one axial step) uncoupled from the continuity Eq. (11); this makes Eqs. (11)–(15) sufficient to obtain the five unknowns (U, V, W, P, and θ) and enables these equations to be numerically solved in the manner described hereinafter.

In practice, for confined free-convection flows, the dimensions of the channel (l and D) and both the wall and ambient temperatures are normally known (i.e., L is given) while the volumetric flow rate f (and hence F) is unknown. However, since the present governing equations are parabolic in the Z-direction, a marching technique can be used in the Z-direction if the inlet velocity U_o (and hence the volumetric flow rate F) is known. Therefore, the present investigation adopts a method of solution which handles the problem in a reversed manner, i.e., obtaining an unknown dimensionless channel height (L) for a given dimensionless volumetric flow rate (F). Such a reversed manner is dependent on the fact that, for a confined natural (free-convection) flow, the pressure inside the channel (p) will always be less than p_s (the hydrostatic ambient pressure at the same elevation) till the annulus exit is reached. Consequently, the pressure defect p', which equals the difference between the two pressures (inside and outside the annulus, at the same elevation), will always be negative until the annulus top exit is reached. At the exit cross section (i.e., at $Z = L$) the pressure defect p' (and hence the dimensionless pressure P) equals zero. Thus, the unknown channel height (L) for a given volumetric flow rate (F) can be obtained by marching in the Z-direction until the dimensionless pressure P ceases to be negative. The location Z at which $P = 0$ determines the unknown channel height (L). Therefore, the condition $P = 0$ at $Z = L$ is not explicitly imposed on the solution, but continually checked for satisfaction as will be indicated hereunder; recall that Eqs. (2)–(4) are parabolic in Z and need only one condition with respect to Z.

The independent variables are computed, for a given Z, at the intersections of the grid lines of Fig. 1(c) and (i, j) is a typical mesh point. Mesh points are numbered consecutively; i is progressing in the η-direction with $i = 1, 2, 3, \ldots, n + 1$ from the outer wall and j is progressing in the ξ-direction with $j = 1, 2, 3, \ldots, m + 1$ from the wide side of the annulus (at $\xi = 0$). Thus the domain of solution per axial step has been divided into n segments in η-direction and m segments in ξ-direction. Consequently, there are $(n + 1)(m + 1)$ grid points per axial cross section including the boundary points (on the inner and outer cylindrical surfaces and the lines of symmetry, $\xi = 0$ and $\xi = \pi$).

For an annulus of given N and E immersed in a fluid of a given Pr, the numerical solution of the foregoing finite difference equations is obtained by first selecting a value of U_o (i.e., the dimensionless volumetric flow rate F). The values of η_i and η_o corresponding to N and E are calculated by means of the pertinent relations given in the Nomenclature. By selecting the numbers of increments in η and ξ directions (n and m, respectively) the values of $\Delta\eta$ and $\Delta\xi$ can be computed. The finite difference energy Eq. (14) is linearized by taking the values of the coefficients of the convective terms (i.e., U^*, V^*, and W^*) from the preceding axial step. For a given axial location (cross section), this Eq. (14) is applied at each grid point in the cross section next to the entrance cross section (i.e., with $i = 1, 2, 3, \ldots, n, n + 1$, and $j = 1, 2, 3, \ldots, m, m + 1$) taking into consideration the thermal boundary conditions. This results in $[(n - 1)(m + 1)]$ simultaneous linear algebraic equations in the same number of unknowns ($\theta_{i,j}$). Solving this
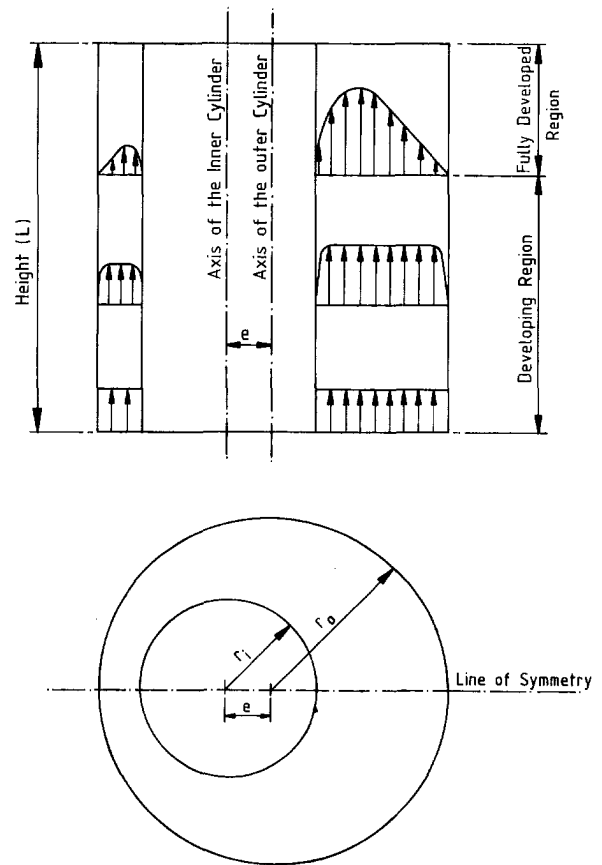

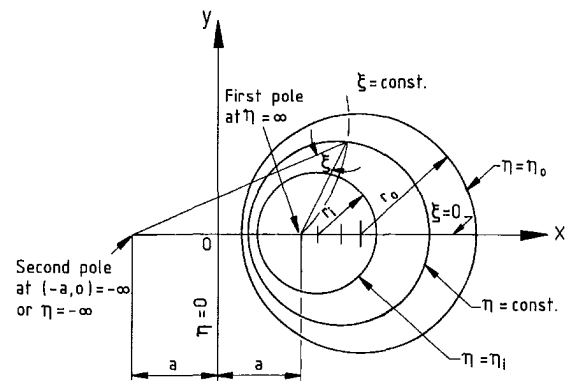Fig. 1(a) Two-dimensional elevation and plan for the geometry under consideration

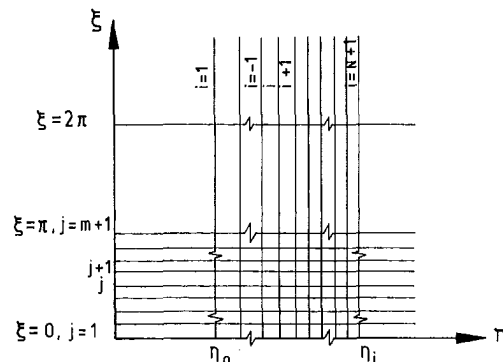Fig. 1(b) Bipolar coordinate system

Fig. 1(c) The transformed geometry in η-ξ plane and the numerical mesh network

set of equations by any matrix technique (Gauss-Seidel iteration scheme, Carnahan et al. (1969), has been used in the present work), one gets the unknown values of θ's at all points of the second cross section. The obtained values of θ's are used in the solution of the linearized finite difference axial momentum Eq. (13). This equation together with the integral continuity Eq. (15) represents two equations in the two unknowns U and P. These two equations can be solved at the first axial step next to the entrance cross section as follows. Applying Eq. (15) throughout the second cross section, Eq. (13) at each interior node of the numerical grid (i.e., with $i = 2, 3, \ldots, n - 1, n$ and $j = 1, 2, 3, \ldots, m, m + 1$) and the boundary conditions (12) (i.e., $U_{1,j} = U_{n+1,j} = 0$, $W_{i,0} = -W_{i,2}$ and $W_{i,m+2} = -W_{i,m}$), one obtains $[(n - 1)(m + 1) + 1]$ simultaneous linear equations in the same number of unknowns ($U_{2,1}, U_{3,1}, \ldots, U_{n,1}$, $U_{2,2}, U_{3,2}, \ldots, U_{n,2}, U_{2,3}, U_{3,3}, \ldots, U_{n,3}, \ldots, U_{2,m+1}, U_{3,m+1}$, $\ldots, U_{n,m+1}$ and P). Solving these equations (i.e., the integral continuity equation simultaneously with the axial momentum equation) by means of a special form of the Gauss-Jordan elimination scheme (El-Shaarawi, 1974), one gets the unknown values of Us and P at all points of the second cross section. Now, Eq. (12) is applied at each interior node to give $(n - 1)(m + 1)$ simultaneous linear equations which when solved give the unknown values of W at this second cross section; Gauss-Seidel iteration scheme (Carnahan et al., 1969) has been used in the present work. Then, Eq. (11) can be used to obtain the unknown values of V at all interior nodes. Repeating this procedure, one can advance axially downstream along the annulus until the dimensionless pressure becomes zero. The axial location at which $P = 0$ defines the channel height, i.e., the exit cross section.

The numerical discretization used in Eqs. (11)–(14) is second-order finite difference approximation of the corresponding boundary layer type Eqs. (1)–(4). Applying the procedures given by Carnahan et al. (1969) shows that the truncation errors resulting from the replacement of the partial differential Eqs. (1)–(4) by their numerical counterparts (11)–(14) tend to zero as the numerical grid sizes tend to zero. Thus, the finite difference Eqs. (11)–(14) are consistent representations of their original differential Eqs. (1)–(4). On the other hand, it is noteworthy that the only reason behind the use of the trapezoidal rule rather than Simpson's rule for the numerical integration of the integral continuity equation is that the pertinent pioneer work of Bodoia and Osterle (1962) did so. Nevertheless, the accuracy of the present numerical work has been validated as will be clarified in this paper.

It is instructive to mention that the linearization of the inertia terms containing the velocity component V (the V's superscripted with an asterisk) in the numerical Eqs. (12)–(13) means taking the values of these V's from the previous axial step. However, it should be recalled that the more accurate values of V's are obtained at any cross section through the application of Eq. (11), as was explained before. Therefore, it is clear that the effect of linearization can be reduced and the accuracy of the obtained values of V can always be increased by using very small axial mesh sizes (particularly near the entrance, where the gradients and the values of V are expected to be large). For this reason, near the entrance cross section, where large gradients exist, very small mesh sizes in the Z-direction were usually chosen. However, as the flow moves away from the entrance the axial step is increased several times. For example, the results to be presented here have been obtained by using very small axial steps near the entrance ($\Delta Z \leq 10^{-10}$ for all the cases considered) then the axial step was increased gradually several times as the flow moves downstream to reach a value no more than $\Delta Z = 10^{-3}$. Such change in the axial grid spacing with distance in the scheme was tested and used before by El-Shaarawi and Sarhan (1981) for the concentric case and by El-Shaarawi et al. (1997) for the developing forced flow in the eccentric case. For example, in the case of a devel-

oping forced flow in eccentric annuli the axial step size was checked for the two different starting values of $\Delta Z = 10^{-7}$ and 10^{-10} at the channel entrance followed by gradual increases to a final value of $\Delta Z = 10^{-3}$ as the flow approaches full development with almost negligible effect on the forced flow results. However, the accuracy pertinent to the smaller axial step size of $\Delta Z = 10^{-10}$ has been preferred in the present free-convection case, at the expense of the computer CPU time, to account for short annuli (of high values of Gr*).

Similarly, suitable mesh sizes in the η and ξ directions were chosen so that the numerical solution of the finite difference equations is practically independent of the increment sizes in all directions. In this respect, preliminary numerical experimentation was first conducted on the relatively simple problem of solving the conduction energy equation in bipolar coordinates. This preliminary numerical experimentation, as reported by El-Shaarawi and Mokheimer (1995), showed that the grid size 20 $\times$ 20 in the η and ξ directions gives a good compromise between the obtained accuracy and computer CPU time. A second stage of grid size experimentation was conducted on an algorithm which utilises a special version of the present computer code to solve the problem of developing laminar forced flow in the entry region of eccentric annuli (El-Shaarawi et al., 1997). In this latter experimentation grid sizes of 10×10, 15×15, 20 $\times$ 20 and 30×22 were tested and the grid of 20×20 has again proved to give good compromise between the accuracy and the computer CPU time. To clarify this point, it might be noteworthy that the grid size 10×10 gave a numerical result for the developing forced flow pressure gradient at the state of full development within 4.5 percent of the corresponding analytical fully developed value while both the grids 20×20 and 30×22 gave the same numerical result with a deviation of only 0.9 percent from the corresponding analytical value. However, the computer execution CPU time per axial step was only 30–35 seconds for the 20×20-grid and 60–80 seconds for the 30×22-grid.

Results and Discussion

All results to be presented in this paper have been obtained using a grid of 20 segments in the η-direction and 20 segments in the ξ-direction. Thus, for each axial step, one has 399 equations in θ, 400 ($19 \times 21 + 1 = 399 + 1$) equations in U and P and 399 equations in W. The solution of these equations required about 35 CPU seconds per one axial step on a main frame computer of WF 77 sys D type.

The validation of the present model, numerical linearization techniques, algorithm, and computer code was first benchmarked for relatively simple known cases then it was checked for the present case. Such a validation has been conducted by four different means as explained hereinafter.

First, numerical solutions of a simplified form of the present energy equation in bipolar coordinates were validated by El-Shaarawi and Mokheimer (1995) for the special case of conduction heat transfer in eccentrically hollow cylinders.

Secondly, a similar algorithm which utilizes a special version of the present computer code was used to solve the problem of developing laminar forced flow in the entry region of eccentric annuli and the obtained results (El-Shaarawi et al., 1997) showed excellent agreement with those of Feldman et al. (1982a) for developing flows and the results of Tiedt (1971), as reported by Shah and London (1978), for fully developed flows.

Thirdly, the free convection results in concentric annuli of El-Shaarawi and Sarhan (1981) provided a means of verification of the present model, algorithm, and the computer code through special runs at a very small eccentricity ($E = 10^{-6}$) under thermal boundary conditions of one wall being isothermal while the opposite is adiabatic. This very low value of $E = 10^{-6}$ was used rather than $E = 0.0$ since the latter can not be used for

computations in bipolar coordinates as it represents a singularity for transformation from the cartesian to bipolar coordinates. Two special computer runs were done for this particular case with $F = 2.5 \times 10^{-3}$ and $F = 4.5 \times 10^{-3}$ and the obtained results for L with $E = 10^{-6}$ were shorter than those of El-Shaarawi and Sarhan (1981) by a maximum difference of only 1.2 percent. This provided a check on the adequacy of the present computer code.

Fourthly, another validation of the present computer code and its numerical results has also been done by checking the trend of the obtained results at large values of Z in annuli of very low values of Gr* (i.e., annuli having large values of L). The results obtained in such cases for the temperature profiles were found to approach the fully developed analytical linear solution given by Eq. (10).

Due to the neglect of the axial diffusion ($\partial^2/\partial Z^2 = 0$) and variations of pressure with the two transverse directions ($\partial P/\partial \eta = \partial P/\partial \xi = 0$), the Grashof number is inherent in the dimensionless formulation of the problem and thus it is not explicitly needed for the solution. However, four other similarity parameters are explicitly required to solve the problem under consideration. These are the annulus radius ratio (N), the dimensionless eccentricity (E), the dimensionless flow rate F (or effectively $U_o = F/(1 - N^2)$) and the Prandtl number (Pr). However, one should recall that the inlet velocity (U_o) and hence the inlet pressure (P_o) and the volumetric flow rate (F) are not predetermined initial conditions independent of the channel height as in the case of forced flows. Rather, each of them is dependent on the channel height and the initial driving temperature ($T_w - T_o$). Moreover, with isothermal boundaries, there is an upper limiting value for U_o which equal to $U_{o,fd}$ (hence, there is an upper limiting value of $F = F_{fd} = U_{o,fd}/(1 - N^2)$); El-Shaarawi and Al-Nimr (1990) dealt with these upper limiting values for concentric annuli.

Computations were carried out for a fluid of Pr = 0.7 in an annulus of $N = 0.5$. The radius ratio 0.5 was chosen since it represents a typical annular geometry with its value of N far enough from unity ($N = 1$) which represents the case of a parallel plate channel. Moreover, the free convection results in concentric annuli of El-Shaarawi and Sarhan (1981) are for this particular radius ratio ($N = 0.5$). These results, as was stated earlier, provided a means of verification of the present model, algorithm, and the computer code through special runs at a very small eccentricity ($E = 10^{-6}$) under thermal boundary conditions of one wall being isothermal while the opposite is adiabatic.

Only a representative sample of the results will be presented. Figure 2(a) shows examples of the developing axial velocity profiles in the widest and narrowest sides of the gap of an annulus of $N = E = 0.5$ under thermal boundary condition 1.O for a uniform inlet velocity $U_o = 18.2 \times 10^{-3}$. This inlet velocity corresponds to a flow rate $F = 0.01365$ which is very near to the fully developed flow rate ($F_{fd} = 0.013806$). It can be seen from Fig. 2(a) that, very near to the entrance (e.g., profiles # 1, 2, and 3), the fluid decelerates near the two walls of the annulus due to formation of the two boundary layers on the walls and accelerates in the core region as a result of the continuity principle. However, further downstream, since the eccentricity increases/decreases the resistance to flow on the narrowest/widest gap side of the annulus, the axial velocity profile develops with increasing/decreasing values on the widest/narrowest gap side of the annulus as the flow moves away from the entrance. Such a development continues until U reaches its invariant fully developed axial-velocity profile (U_{fd}) since the channel is high enough in this presented case. Also, it has been found that the developing temperature profiles (unpresented in the paper) reach the linear fully developed distribution θ_{fd} given by Eq. (10). This provides a check on the adequacy of the present computer code.
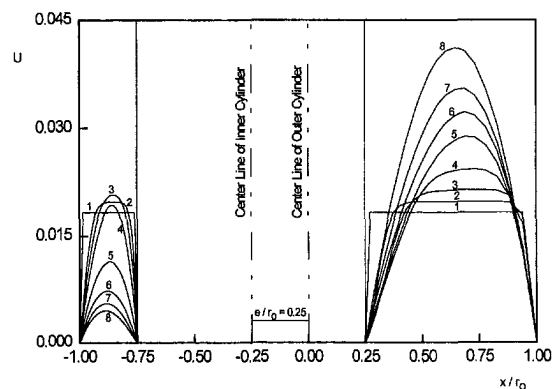
Fig. 2(a) Development of the axial velocity profiles, $N = E = 0.5$, case 1.O, $U_o \times 10^3 = 18.2$. The numbers on the profiles indicate the following values of $Z \times 10^7$: (1) 10^{-3}, (2) 71.8, (3) 212, (4) 712, (5) 3110, (6) 8110, (7) 18100, (8) 128.11 $\times 10^4$ (and above, until full development).
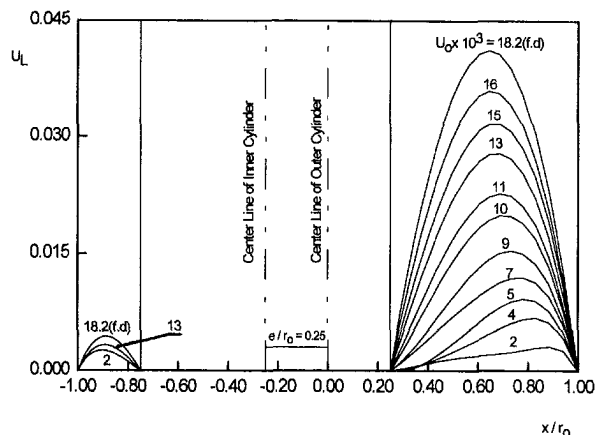
Fig. 2(b) Axial velocity profiles at the channel exit for different flow rates (i.e., different channel heights), $N = E = 0.5$, case 1.O
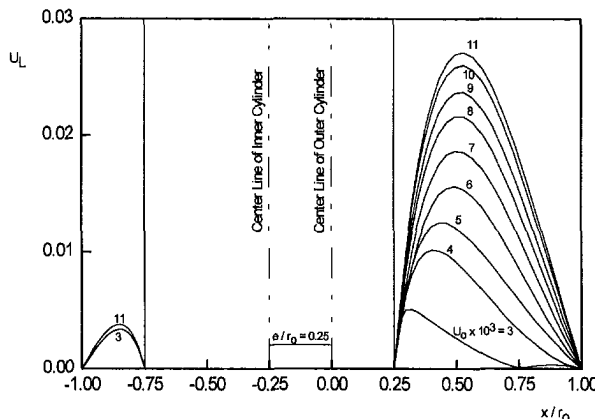
Fig. 2(c) Axial velocity profiles at the channel exit for different flow rates (i.e., different channel heights), $N = E = 0.5$, case 1.I

Figures 2(b) and 2(c) show the axial velocity profiles at the channel exit under boundary conditions 1.O and 1.I, respectively, for some selected values of U_o (i.e., induced flow rates or, implicitly, channel heights). Choosing a value of $F \ll F_{fd}$ (i.e., $U_o \ll U_{o,fd}$) implies a short annulus of a large hydraulic diameter with a large temperature difference ($T_w - T_o$). In other words, it implies a case of a large modified Grashof number (Gr*) and hence the flow leaves the annulus exit before reaching the fully developed flow conditions, as can be seen from these two figures. It can also be seen that, for such short annuli, the uniform velocity at the inlet is transferred at the annulus exit into a profile indicating remarkably high velocities near

the heated boundary since the thermal boundary layer has not penetrated yet far from the heated wall.

For given N and E, the channel height required to naturally induce a specific flow rate is one of the important engineering parameters. For a given F, this height can be determined by monitoring the value of the pressure as the flow moves away from the entrance of the channel till the dimensionless pressure becomes zero. Examples of the axial variation of the dimensionless pressure in an annulus of $N = 0.5$ and $E = 0.7$ are presented in Figs. 3(a) and 3(b), for cases 1.I and 1.O, respectively. These figures show that, for a given U_o (i.e., a given F), the inlet negative pressure ($P_o = -U_o^2/2$) decreases due to friction as the flow moves up in the annulus until a minimum value is attained. It then increases due to buoyancy until the dimensionless pressure becomes zero at the channel exit. Thus, the negative pressure gradient increases until it reaches a zero value at the axial location where the buoyancy force becomes equal to the friction force then it becomes a positive pressure gradient due to the increase in the buoyancy force resulting from the heating effect. The point at which the dimensionless pressure becomes zero determines the channel height and the figures show that the channel height increases as the required induced flow rate increases (i.e., as U_o increases). However, for cases with an isothermal boundary there is an upper limit
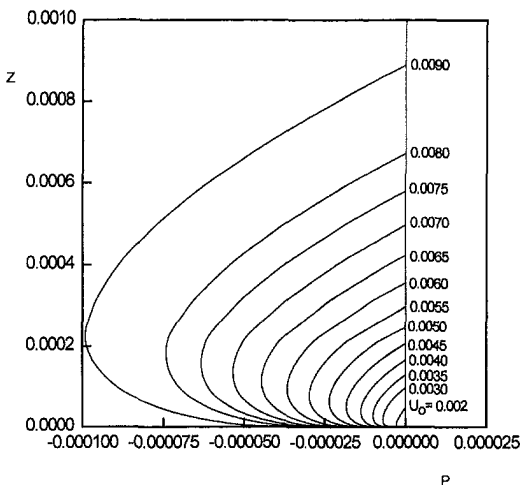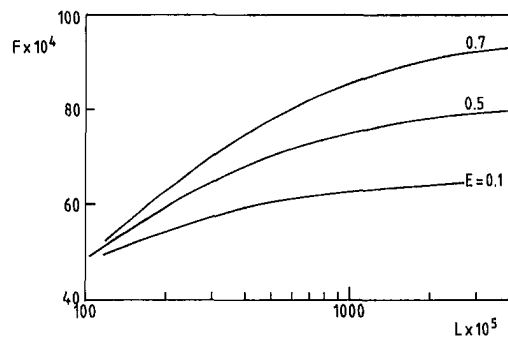
Fig. 4(a) The induced volumetric flow rate versus channel height, for various values of E, $N = 0.5$, case 1.I
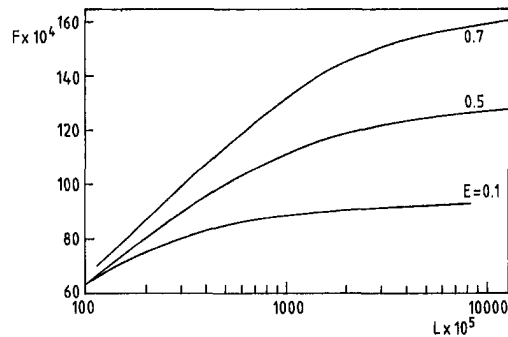
Fig. 4(b) The induced volumetric flow rate versus channel height, for various values of E, $N = 0.5$, case 1.O

for U_o ($=U_{o,fd}$) beyond which there will be no more increase in the induced flow rate regardless of the channel height.

The variation of the induced flow rate with the channel height is shown in Figs. 4(a) and 4(b) for cases 1.I and 1.O, respectively. In these two figures, results are presented for three values of E (0.1, 0.5, and 0.7). It is clear from these figures that, for given N and E, the required channel height to suck up a specific dimensionless flow rate is larger for case I than that for case O. This is attributed to the larger heating surface in case 1.O than in case 1.I. Another observation from Figs. 4(a) and 4(b) is that increasing the eccentricity E causes an increase in F in both cases 1.I and 1.O. This qualitatively agrees with the trend of previously reported forced-flow results in the literature which indicate the increasing E reduces the resistance to flow.

For cases 1.I and 1.O, respectively, Figs. 5(a) and 5(b) give the variation of the heat gained by the fluid from entrance up to the annulus exit ($\bar{Q}$) with the channel height L for three dimensionless eccentricities investigated. These figures show that, for a given annulus (i.e., given N and L), the higher the value of the eccentricity, E, the larger the total heat absorbed by the fluid. This is attributed to the increase in the flow rate with eccentricity as was clarified in Figs. 4(a) and 4(b).

The variation of the dimensionless mixing-cup (mixed-mean) temperature θ_m with Z, for various values of U_o (i.e., various values of F or, implicitly, L) and both boundary conditions considered, is shown in Figs. 6(a) through 6(c) for the three considered values of eccentricity, namely, $E = 0.1$, 0.5, and 0.7, respectively. In each of these figures, curves corresponding to three values of U_o are drawn for each boundary condition. These curves correspond to low, intermediate, and high values of U_o for each boundary condition. Note that for small values of U_o (i.e., F), the curves are shown up to the axial distance at which the pressure defect reached a zero value (i.e., the exit cross section). It is clear from these figures that θ_m for thermal boundary condition 1.O is greater than that for thermal boundary condition 1.I at same Z and F in a given annulus. Again this is due to the larger heating surface in case 1.O than that in case 1.I. On the other hand, with large values of U_o (i.e., near enough
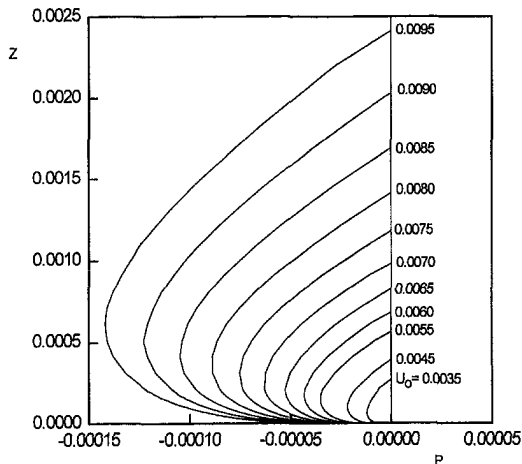

Fig. 3(a) Development of the pressure with Z for different values of the induced volumetric flow rate (i.e., different channel heights), $N = 0.5$, $E = 0.1$, case 1.I

Fig. 3(b) Development of the pressure with Z for different values of the induced volumetric flow rate (i.e., different channel heights), $N = 0.5$, $E = 0.1$, case 1.O

to $U_{o,fd}$) the value of θ_m for either boundary condition attains its fully developed value (which is invariant with Z) before the fluid reaches the annulus top exit. In other words, the flow reaches the state of thermal full development before it becomes hydrodynamically fully developed. This is a feature of natural convection flows in channels with an isothermal boundary, regardless of the value of Pr, as was explained by El-Shaarawi and Al-Nimr (1990). When thermal full development is reached, the θ-profile does not vary with further increase in Z and becomes linear with η as given by Eq. (10). Under these fully developed conditions, the heat passes in the present case from the heated wall to the opposite cooled wall (which maintained at T_o) as if the fluid were stationary, i.e., by pure conduction through laminar layers.

It might be worth mentioning that for free convection flows in vertical eccentric annuli of a given N, under each of the present thermal boundary conditions, there is an upper limiting value for each of F and $\bar{Q}$ (their fully developed values). These upper limiting values (F_{fd} and $\bar{Q}_{fd}$) have been obtained by substituting the analytical solution (10) in Eq. (7) and then solving numerically the resulting equation. In general, the values of F_{fd} and $\bar{Q}_{fd}$ increase with E. In other words, for a given thermal boundary condition, decreasing the eccentricity E requires a shorter annulus to achieve the fully developed flow conditions (which correspond to the pertinent maximum possible volumetric flow rate). For each value of E in the present work, the investigated range of U_o (i.e., F and consequently L) has been chosen to approach the fully developed conditions (which require very high annuli particularly with large values of E). Such fully developed conditions are characterized in Figs. 6(a) through 6(c) by the portions of the presented curves having invariant θ_m with Z. The corresponding results of F_{fd} and $\bar{Q}_{fd}$ pertaining to these invariant θ_m with Z of Figs. 6(a) through 6(c) could have been easily drawn in Figs. 4(a) through 5(b) by changing the scale of the abscissa in these figures. However, the logarithmic scales of the abscissa in Figs. 4(a) through 5(b) were selected so that the effect of the eccen-
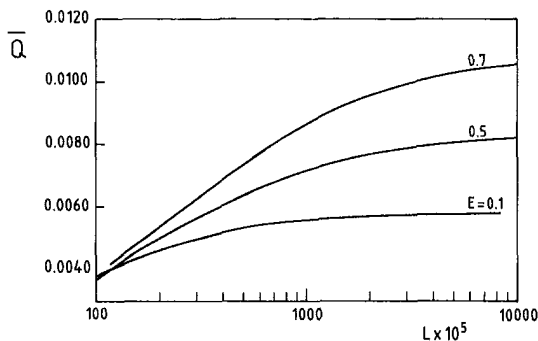
Fig. 6(a) Variation of θ_m with Z for various values of U_o, $N = 0.5$, $E = 0.1$, ------ case 1.I, —— case 1(O)
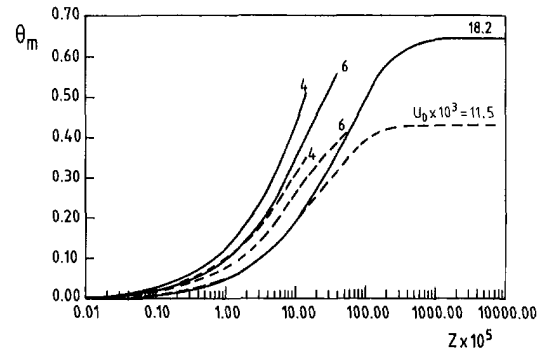
Fig. 6(b) Variation of θ_m with Z for various values of U_o, $N = 0.5$, $E = 0.5$, ------ case 1.I, —— case 1(O)
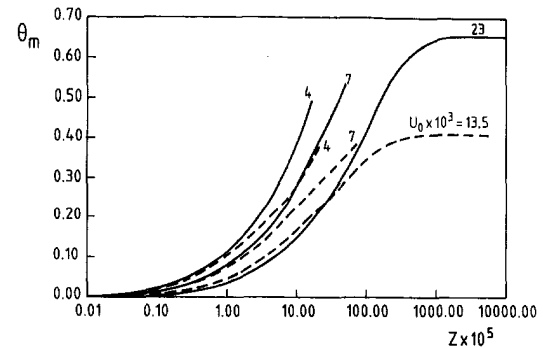
Fig. 6(c) Variation of θ_m with Z for various values of U_o, $N = 0.5$, $E = 0.7$, ------ case 1.I, —— case 1(O)

Fig. 5(a) The total heat absorbed by the fluid against the channel height for various eccentricities, $N = 0.5$, case 1.I

Fig. 5(b) The total heat absorbed by the fluid against the channel height for various eccentricities, $N = 0.5$, case 1.O

tricity on the induced flow rate (F) and the heat absorbed ($\bar{Q}$) can be clearly presented for short annuli (since fully developed conditions can be obtained with low values of E in very much shorter annuli and, moreover, with large values of L the effect of E on both F and $\bar{Q}$ is more pronounced). Nevertheless, for $E = 0.1$, the results presented in Figs. 4(a) through 5(b) are shown until the pertinent fully developed values of F and $\bar{Q}$ have been reached.

Conclusions

A model in bipolar coordinates has been developed to describe the developing laminar free convection in open-ended vertical eccentric annuli. Then, a linearized finite difference algorithm has been developed to numerically solve this model. Numerical results are presented for a fluid of Pr $= 0.7$ in an annulus of radius ratio 0.5. Three values of dimensionless eccentricity and two thermal boundary conditions have been investigated. These thermal boundary conditions are obtained by having one of the annulus walls isothermally heated while the

opposite wall is isothermally cooled and maintained at the inlet-fluid (ambient) temperature.

The results show that both the induced flow rate and the total heat absorbed by the fluid increase with eccentricity. The variations of the induced flow rate and the total heat absorbed by the fluid with the channel height have been presented for use in practical applications. Finally, the obtained results also show that heating the outer boundary of the annulus is more useful for inducing flow (thermosyphons) than heating its inner boundary.

Acknowledgment

References

Al-Arabi, M., El-Shaarawi, M. A. I., and Khamis, M., 1987, "Natural Convection in Uniformly Heated Vertical Annuli," *Int. J. Heat Mass Transfer,* Vol. 30, No. 7, pp. 1381–1389.

Bodoia, J. R., and Osterle, J. F., 1962, "The Development of Free Convection Between Heated Vertical Plates," ASME JOURNAL OF HEAT TRANSFER, Vol. 84, pp. 40–44.

Carnahan, B., Luther, H. A., and Wilkes, J. D., 1969, *Applied Numerical Methods,* John Wiley and Sons, New York, pp. 298–301, 450.

Cheng, K. C., and Hwang, G. J., 1968, "Laminar Forced Convection in Eccentric Annuli," *A. I. Ch. E. Journal,* Vol. 14, No. 3, pp. 510–512.

Coney, J. E. R., and El-Shaarawi, M. A. I., 1975, "Finite Difference Analysis for Laminar Flow Heat Transfer in Concentric Annuli with Simultaneously Developing Hydrodynamic and Thermal Boundary Layers," *Int. J. Numr. Methods Engr.,* Vol. 9, pp. 17–38.

El-Saden, M. R., 1961, "Heat Conduction in an Eccentrically Hollow, Infinitely Long Cylinder with Internal Heat Generation," ASME JOURNAL OF HEAT TRANSFER, Vol. 83, pp. 510–511.

El-Shaarawi, M. A. I., 1974, "Heat Transfer and Hydrodynamics in the Entrance Region of Concentric Annuli with Stationary and Rotating Inner Walls," Ph.D. Dissertation, The University of Leeds, England.

El-Shaarawi, M. A. I., 1990, "Derivation of Boundary Layer Equations for Cases with Curved Boundaries," *Int. J. Engineering Fluid Mechanics,* Vol. 3, No. 2, pp. 113–128.

El-Shaarawi, M. A. I., and El-Nimr, M. A., 1990, "Fully Developed Laminar Natural Convection in Open-ended Vertical Concentric Annuli," *Int. J. Heat Mass Transfer,* Vol. 33, pp. 1873–1884.

El-Shaarawi, M. A. I., and Mokheimer, E., 1995, "Transient Conduction in Eccentrically Hollow Cylinders," *Int. J. Heat Mass Transfer,* Vol. 38, No. 11, pp. 2001–2010.

El-Shaarawi, M. A. I., and Sarhan, A., 1980, "Free Convection Effects on the Developing Laminar Flow in Vertical Concentric Annuli," ASME JOURNAL OF HEAT TRANSFER, Vol. 102, pp. 617–622.

El-Shaarawi, M. A. I., and Sarhan, A., 1981, "Developing Laminar Free Convection in an Open Ended Vertical Annulus with a Rotating Inner Cylinder," ASME JOURNAL OF HEAT TRANSFER, Vol. 103, pp. 552–558.

El-Shaarawi, M. A. I., Abualhamayel, H. I., and Mokheimer, E. M. A., 1997, "Developing Laminar Flow in Eccentric Annuli," ASME *Journal of Fluids Engineering,* Vol. 119, pp. 724–728.

Feldman, E. E., Hornbeck, R. W., and Osterle, J. F., 1982a, "A Numerical Solution of Laminar Developing Flow in Eccentric Annular Ducts," *Int. J. Heat Mass Transfer,* Vol. 25, No. 2, pp. 231–241.

Feldman, E. E., Hornbeck, R. W., and Osterle, J. F., 1982b, "A Numerical Solution of Developing Temperature for Laminar Developing Flow in Eccentric Annular Ducts," *Int. J. Heat Mass Transfer,* Vol. 25, No. 2, pp. 243–253.

Heaton, H. S., Reynolds, W. C., and Kays, W. M., 1964, "Heat Transfer in Annular Passages. Simultaneous Development of Velocity and Temperature Fields in Laminar Flow," *Int. J. Heat Mass Transfer,* Vol. 5, pp. 763–781.

Heyda, J. F., 1959, "A Green's Function Solution for the Case of Laminar Incompressible Flow Between Non-Concentric Cylinders," *J. Franklin Inst.,* Vol. 267, pp. 25–34.

Hughes, W. F., and Gaylord, E. W., 1964, *Basic Equations of Engineering Science* (Schaum's Outline Series), McGraw-Hill, New York, pp. 1–11, 151.

Moon, P., and Spencer, D. E., 1971, *Field Theory Handbook,* 2nd Ed., Springer-Verlag, Berlin, pp. 1–5.

Redberger, P. J., and Charles, M. E., 1962, "Axial Laminar Flow in a Circular Pipe Containing a Fixed Eccentric Core," *The Canadian Journal of Chemical Engineering,* Vol. 40, pp. 148–151.

Reynolds, W. C., Lundberg, R. E., and McCuen, P. A., 1963, "Heat Transfer in Annular Passages. General Formulation of the Problem for Arbitrarily Prescribed Wall Temperatures or Heat Fluxes," *Int. J. Heat Mass Transfer,* Vol. 6, pp. 483–493.

Schlichting, H., 1987, *Boundary Layer Theory,* 7th Ed., McGraw-Hill, New York, pp. 127–149.

Snyder, W. T., 1963, "An Analysis of Slug Flow Heat Transfer in an Eccentric Annulus," *A. I. Ch. E. Journal,* Vol. 9, No. 4, pp. 503–506.

Snyder, W. T., and Goldstein, G. A., 1965, "An Analysis of a Fully Developed Laminar Flow in an Eccentric Annulus," *A. I. Ch. E. Journal,* Vol. 11, No. 3, pp. 462–469.

Sparrow, E. M., and Lin, S. H., 1964, "The Developing Laminar Flow and Pressure Drop in the Entrance Region of Annular Ducts," *J. Basic Engineering,* Vol. 86, pp. 827–834.

Suzuki, K., Szmyd, J. S., and Ohtsuka, H., 1990, "Laminar Forced Convection Heat Transfer in Eccentric Annuli," *Heat Transfer-Japanese Research,* Vol. 20, pp. 169–183.

Trombetta, M. L., 1972, "Laminar Forced Convection in Eccentric Annuli," *Int. J. Heat Mass Transfer,* Vol. 14, pp. 1161–1172.

The Influence of Vapor Bubble Sliding on Forced Convection Boiling Heat Transfer

G. E. Thorncroft[1]

J. F. Klausner

Department of Mechanical Engineering,
University of Florida,
Gainesville, FL 32611

This paper describes experimental efforts aimed at examining the effect of vapor bubble sliding on forced convection boiling heat transfer. Flow boiling experiments using FC-87 were conducted for vertical upflow and downflow configurations. Both slightly subcooled single-phase and saturated annular flow boiling were considered. Significantly higher heat transfer rates were measured for vertical upflow than for downflow with the same wall superheat and slightly subcooled single-phase inlet conditions. This increase in heat transfer is directly attributable to sliding vapor bubbles, which remain attached to the wall during upflow and lift off the wall during downflow. Differences in the measured upflow and downflow heat transfer rates are not as significant for annular flow boiling, which is due in part to the similar vapor bubble dynamics which have been observed for upflow and downflow. Heat transfer experiments in single-phase subcooled upflow with air bubble injection at the heating surface suggest that sliding bubbles enhance the bulk liquid turbulence at the wall, which contributes significantly to the macroscale heat transfer. It is concluded from this work that vapor bubble sliding heat transport can be a significant heat transfer mechanism, and should be considered in the development of mechanistic flow boiling heat transfer models.

1 Introduction

The development of reliable mechanistic boiling heat transfer models requires an understanding of the complex heat transport mechanisms and their mutual interaction. In forced convection boiling, as well as in pool boiling from inclined surfaces, this understanding is further complicated by the fact that vapor bubbles not only remove energy from the heating surface while attached to nucleation sites, but can also potentially remove energy following departure.

Mesler (1988) suggested that the high heat fluxes associated with annular flow boiling are due to secondary nucleation. According to Mesler, secondary nucleation is the process whereby an expanding vapor bubble ruptures the thin annular liquid film, thus causing the film to entrain vapor bubbles as it recedes. These entrained vapor bubbles can then serve as nucleation centers from which bubble growth can proceed within the superheated liquid film. Mesler's hypothesis was not confirmed by Zeng and Klausner (1993), who conducted a photographic investigation of horizontal flow boiling in thin films. Subsequently, Thorncroft and Klausner (1997a) studied high-speed video images of vertical upflow and downflow boiling in the annular flow regime and did not observe any secondary nucleation as postulated by Mesler.

Thorncroft et al. (1998) reported a detailed investigation of the bubble dynamics in slightly subcooled vertical upflow and downflow forced convection boiling using FC-87. Their experiments, which were primarily performed in the isolated bubble regime, reveal a marked difference in the behavior of the bubbles in upflow and downflow. During upflow, vapor bubbles are observed to slide away from the nucleation site in the direction of the flow. The bubbles typically do not lift off the heating surface, except due to occasional local turbulent fluctuations.

In fact, the bubbles continue to grow and remove energy from the heating surface as they slide. At low superheat ($\Delta T_{sat} < 4.0°C$), the majority of vapor bubbles emanate from a few nucleation sites located near the leading edge of the heater. It would appear that the sliding bubbles remove sufficient energy from the heater surface to suppress nucleation downstream. In contrast, during downflow the vapor bubbles regularly lift off the heating surface within close proximity of the nucleation site. Nucleation sites were scattered over the entire surface, and the bubbles would slide only a short time before being lifted off.

The difference in the observed bubble lift-off behavior is attributed to a shear lift force exerted by the liquid near the wall. In upflow, a sliding bubble leads the local flow due to its buoyancy, resulting in a shear lift force which pushes the bubble toward the surface. In downflow, the buoyancy of the bubble will cause it to lag the local flow, which results in a shear lift force which expels the bubble from the surface. It is the change in direction of the buoyancy force (relative to the flow direction) which results in a shear lift force, exerted by the fluid near the wall, which acts toward the wall in upflow and away from the wall in downflow.

Thorncroft et al. (1998) also compared the heat transfer coefficients for slightly subcooled (3–5°C) upflow and downflow boiling with single-phase inlet conditions, which are shown in Fig. 1. It is clear that, for the flow and thermal conditions encompassing the isolated bubble regime, the heat transfer coefficient is significantly greater in upflow than in downflow under otherwise identical conditions. It was postulated that the difference in vapor bubble dynamics was responsible for this heat transfer enhancement; specifically, sliding bubble heat transport appears to be considerably more prevalent in upflow since bubbles do not detach from the heating surface.

The focus of this investigation is to provide experimental evidence to support the hypothesis that sliding bubble heat transport can be significant in flow boiling. The consequences of such a finding are of fundamental importance. It suggests that there exists a secondary heat transfer mechanism in flow boiling that is due to sliding bubbles and not secondary nucle-
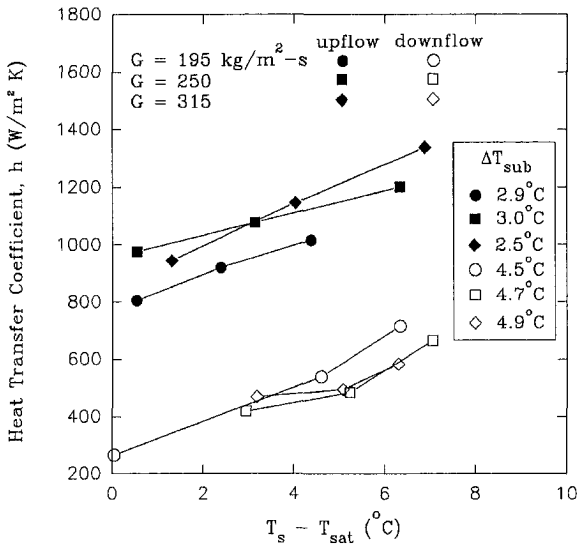
Fig. 1 Comparison of heat transfer coefficient h, versus bulk temperature difference $T_s - T_b$, for upflow and downflow forced convection boiling. Reprinted from Thorncroft et al. (1998).

ation. Moreover, in addition to quantifying the nucleation site density, waiting time, vapor bubble growth rate, and departure diameter for flow boiling, the sliding trajectory and lift-off diameter must also be quantified in order to appropriately model the flow boiling heat transfer.

The vapor bubble sliding process was observed as early as five decades ago by Gunther (1951), but only recently has it received further attention. Cornwell (1990) measured the heat flux from a tube in a bundle of tubes exposed to bubbly flow of saturated water. He observed that, in the presence of bubbly flow, the heat flux was more than double that of single-phase turbulent convection. He proposed that the increase was due to the sliding of vapor bubbles along the surface of the tube. Moreover, he noted that the upstream tubes were entirely responsible for nucleation, and that "liquid convection and the influence of the sliding bubbles account for the total heat transfer" in the downstream tubes. Recently, Houston and Cornwell (1996) performed similar tests using air bubbles injected into the tube bundle to demonstrate that turbulence enhancement caused by the sliding bubbles is as important as microlayer evaporation to the energy removal from the tubes.

Tsung-Chang and Bankoff (1990) presented a theoretical study which demonstrates the importance of microlayer evaporation in highly subcooled nucleate flow boiling heat transfer. They proposed that the sliding of vapor bubbles could increase the microlayer evaporation by a factor of two or more over a stationary bubble.

Yan and Kenning (1996) used liquid crystal thermography to examine the temperature distribution on the surface of an inclined plate in a pool of water subjected to a sliding vapor bubble. They reported that the local heat transfer coefficient in the wake of a sliding vapor bubble was approximately three times that for single-phase natural convection ahead of the bubble. Using air bubbles injected into the flow, they demonstrated that the liquid flow around the bubble creates a localized region of greatly enhanced heat transfer in the wake behind the bubble. Yan et al. (1996) have shown that for small bubbles the majority of heat transfer takes place in the bubble's wake, and the heat transfer contribution due to latent heat transport is significant only for large bubbles.

All of the aforementioned studies have acknowledged the importance of microlayer evaporation energy transport beneath the bubble, but only a few recent studies have sought to quantify the heat transfer contribution due to enhanced bulk turbulence resulting from the sliding bubbles. One notable example is the work of Kenning and Kao (1972), who injected gas bubbles into upward single-phase flow of water in a rectangular test section. They observed that the heat transfer coefficient was increased up to 50 percent over single-phase flow, and suggested that a possible mechanism for this increase is the generation of secondary flow by the motion of the bubbles.

The objectives of this work are twofold: (1) to demonstrate the importance of the sliding bubble energy transport mechanism in forced convection boiling, and (2) to distinguish the importance of bulk turbulent enhancement in the presence of sliding air bubbles.

2 Experiment Description

A vertical flow boiling facility was implemented to achieve upflow or downflow through a transparent boiling test section. The facility uses FC-87 (manufactured by 3M Corporation) as the working fluid, and can achieve boiling during conditions ranging from subcooled single-phase to annular two-phase flow. A detailed description of the experimental facility, along with the methodology utilized in the experiments, are given in Thorncroft et al. (1998); only a brief description is provided here.

A schematic diagram of the facility is shown in Fig. 2. A variable-speed gear pump drives the working fluid through the flow loop. Following the pump, the fluid is filtered to eliminate contaminants. The volumetric flow rate is then measured using either a venturi or vane-type flowmeter, each used to measure a different range of flow rates (venturi, 0.0–1.8 l/min; vane, 3.0–9.0 l/min). The fluid is preheated via four preheaters, then routed by a series of valves (1a&b, 2a&b) to achieve vertical upflow or downflow in a transparent test section. After exiting the test section the flow enters a water-cooled shell-and-tube condenser/receiver which returns the fluid to the subcooled state. A capacitance sensor, described in detail by Thorncroft

--- **Nomenclature** ---

A_s = surface area (m^2 or cm^2)
$d(t)$ = vapor bubble (m)
d_d = vapor bubble departure diameter (m)
G = mass flux (kg/m^2 s)
h = heat transfer coefficient (W/m^2 K)
h_{fg} = heat of vaporization (J/kg K)
n/A = nucleation site density (cm^{-2})
q'' = heat flux (W/m^2)
T = temperature (°C)
t = time (s)

t_d = departure time (s)
t_w = waiting time (s)
x_i = inlet vapor quality

Greek

δ = annular flow liquid film thickness (mm)
ρ = density (kg/m^3)
ΔT_b = bulk temperature difference, $T_s - T_b$ (°C or K)
ΔT_{sub} = subcooling, $T_{sat} - T_b$ (°C or K)

Subscripts

1ϕ = single-phase
I = stationary bubble growth
II = sliding bubble growth and motion
b = bulk flow
s = (heating) surface
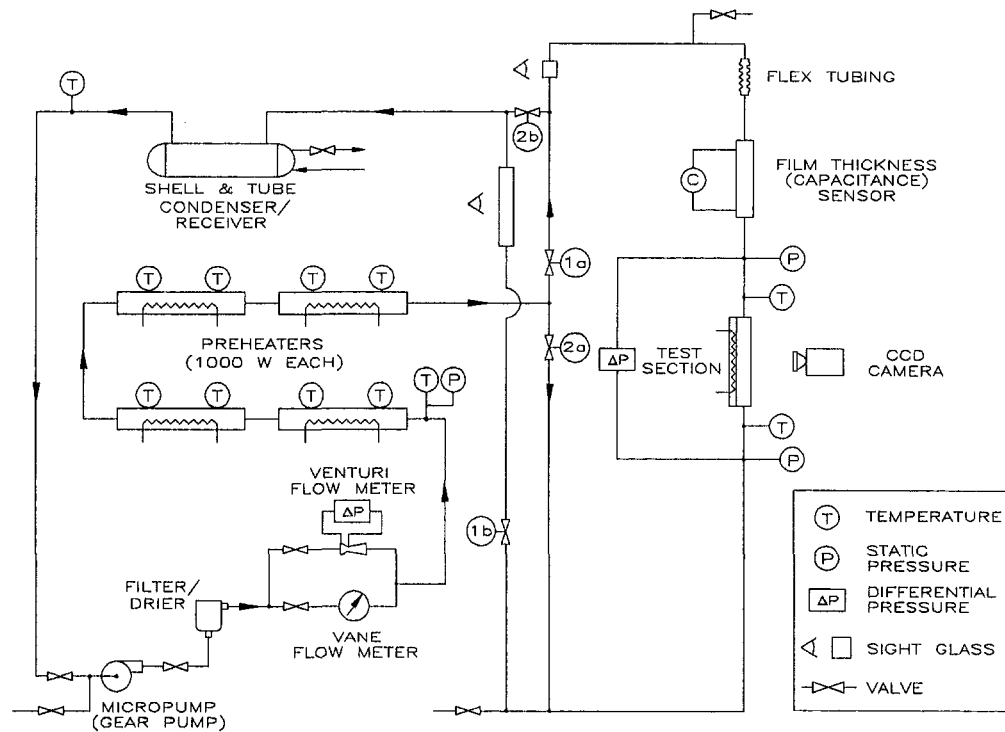sat = saturation
v = vapor
w = wall

Fig. 2 Schematic diagram of vertical flow boiling facility

and Klausner (1997b), is used to measure liquid film thickness in annular two-phase flows. Measurements of pressure, temperature, and flow rate are recorded by a multiplexed 12-bit analog-to-digital converter connected to a personal computer. Visual observations of nucleation and hydrodynamic phenomena in the test section are made using a high-speed motion digital camera, capable of resolving images up to 6000 frames per second; in this work the camera was operated at 2000 frames per second.

The test section flow cross section is square (12.7 × 12.7 mm) and is built of clear cast Lexan. Attached to one inside wall is a DC-powered nichrome heating strip, on which the average wall temperature and heat flux are measured. The system pressure was approximately 1.17 bar, corresponding to a saturation temperature of 40°C. The average wall temperature is measured using six equally spaced thermocouples attached to the underside of the heater. Power to the heater is supplied by a 240 Volt/20 Amp/3-phase AC source, converted to 36 VDC/125A through an autotransformer and rectifier. A rheostat and autotransformer are manually adjusted to control the DC power input to the heater. Two digital voltmeters measure the power into the heater: the voltage across the heater is measured directly, while the current is determined by measuring the voltage across a 1 mΩ shunt connected in series with the heater. The uncertainty in measuring the bulk temperature difference, $T_s - T_b$, is estimated to be within ±0.2°C. The uncertainty in measuring the total heat transfer coefficient, $h = q''/(T_s - T_b)$, is estimated to be within ±1 percent, except for very low values of $T_s - T_b$, in which measurement error is too large to allow for reliable measurements of h; measurements of h were discarded for values of $T_s - T_b$ less than 1°C.

An air injection system was located at the entrance to the test section to allow for the injection of air bubbles at the heater surface (Fig. 3). The nozzle is constructed of 1.6-mm OD brass tubing, crimped at the tip to provide a small (less than 100 μm) opening. The tubing is soldered to the square brass channel containing the working fluid, such that the nozzle tip extends into the boiling test section just below the heater. Compressed air supplied to the nozzle is adjusted by a needle valve in order to obtain flow rates between zero to 50 ml/min. A capillary

tube flow meter was used to measure air flow rate, where the pressure drop across the 0.83 mm ID capillary tube is measured by a Validyne model DP45-16 differential pressure transducer. The flow rate measurement was calibrated using a syringe pump, and the estimated uncertainty of the air flow rate measurement is ±2 ml/min. Prior to entering the test section, the air is first routed through approximately 2 meters of 3.2 mm OD copper tubing, wrapped around the tube carrying heated liquid to the test section in order to equilibrate the air temperature with the bulk liquid temperature prior to the air entering the test section.
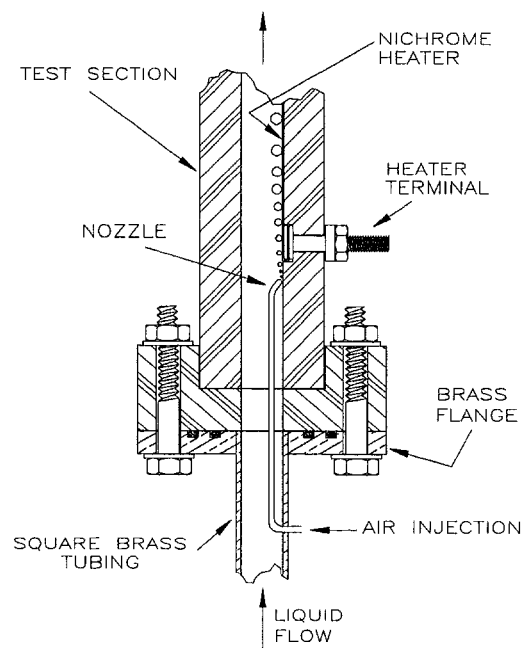

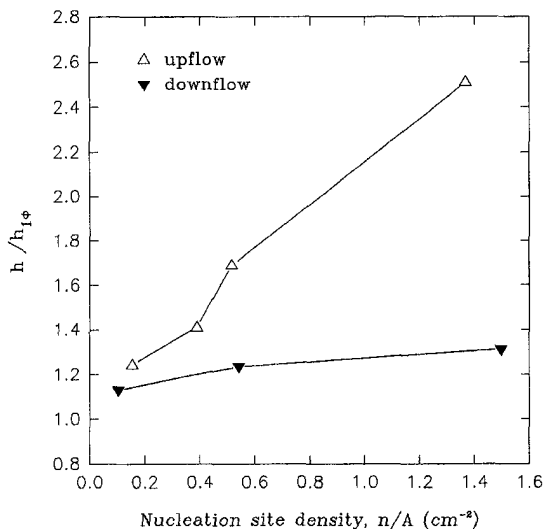Fig. 3 Detail of transparent test section with air injection nozzle

Fig. 4 Heat transfer coefficient ratio, $h/h_{1\phi}$, versus nucleation site density for upflow and downflow boiling in the isolated bubble regime

Measurement of bubble growth and detachment is performed manually by measuring distances on a display screen as played back from video tape; the details of this procedure are described in detail by Thorncroft et al. (1998). The lateral displacement of the vapor bubble is the distance measured from the nucleation site to the bubble centroid. Bubble diameters were estimated as the chord length, measured through the bubble centroid, parallel to the heater surface. Growth curves were obtained by measuring the diameter of an individual bubble from incipience through sliding. The experimental growth rates are approximated by a power-law curve fit of the form $d(t) = Kt^n$. Because of the stochastic nature of the flow and thermal variations, a set of five growth curves were measured for the purpose of estimating the constants K and n.

3 Experimental Results

3.1 Examination of Macroscale Heat Transfer.

3.1.1 Isolated Bubble Boiling Regime. In light of the heat transfer measurements of Thorncroft et al. (1998) shown in Fig. 1, an experiment was performed to further highlight the influences of bubble sliding as it contributes to the macroscale heat transfer in upflow and downflow boiling. The experimental facility was operated to attain single-phase slightly subcooled (approximately 4°C) flow at the entrance of the test section. Sufficient power was applied to the test section to achieve vigorous boiling, and then reduced until only isolated sites were active. This operating procedure eliminates the effect of boiling hysteresis. At each level of heat flow, measurements of thermal and hydrodynamic properties of the flow were recorded, and the number of active nucleation sites estimated. For reference, measurements of single-phase (nonboiling) heat transfer were also made. The measured single-phase heat transfer coefficients were in good agreement with Petukhov's (1970) turbulent heat transfer correlation.

Figure 4 compares the ratio of the measured boiling heat transfer coefficient, h, to the single-phase forced convective heat transfer coefficient, $h_{1\phi}$, for upflow and downflow as a function of the measured nucleation site density. Two trends are apparent: First, $h/h_{1\phi}$ increases as the number of active nucleation sites increases for both upflow and downflow, as expected. However, the heat transfer coefficient increases at a much greater rate in upflow than downflow. This implies that a significantly smaller number of active sites are required to achieve the same heat transfer in upflow as would be achieved

in downflow under the same hydrodynamic conditions. In other words, active nucleation sites in upflow result in greater heat transfer from the surface than those in downflow. It is noted that both $h/h_{1\phi}$ curves appear to converge as $n/A \rightarrow 0$, which is expected, since single-phase flow heat transfer is not dependant upon flow orientation. This result provides strong evidence that there exists a significant heat transfer mechanism related to the sliding of vapor bubbles, since the vapor bubbles have a tendency to remain attached to the heating surface during upflow.

Another important issue to consider is that there does not exist a homogeneous distribution of nucleation sites, especially during upflow. At low values of wall superheat the active nucleation sites are located almost entirely at the leading edge of the heater. At higher wall superheats, nucleation sites can occur throughout the heater surface, but a larger concentration exist at the leading edge of the heater. This is due to the fact that sliding bubbles deplete energy from the heating surface, which reduces the potential for incipience downstream.

3.1.2 Extension to Other Flow Boiling Regimes. The difference in macroscale heat transfer between upflow and downflow forced convection boiling is not limited to the isolated bubble regime. Figure 5 compares the heat transfer coefficients for upflow and downflow measured for one set of single-phase inlet flow conditions. The heat transfer coefficient, h, is plotted against the bulk temperature difference, $T_s - T_b$; the bulk temperature difference is chosen since the inlet flow is single phase, and bulk turbulent convection is the dominant heat transfer mechanism for low values of ΔT_b. The heat transfer coefficient is consistently higher for upflow than downflow over a range of heat flux which extends from the isolated bubble regime to vigorous boiling.

It is noted that a distinct change in slope is apparent in the h versus ΔT_b curve for downflow at $\Delta T_b \approx 17$°C; the increase in slope was observed to correspond with the formation of large (approximately 3–4 mm) plug-shaped bubbles on the heater surface for large values of ΔT_b. In downflow boiling at low values of ΔT_b, bubbles are small, isolated, and carried downstream by the bulk flow. In contrast, at higher values of ΔT_b, the bubbles are larger and resist the drag force imposed by the bulk flow. These bubbles tend to coalesce into larger, plug-shaped bubbles, which remain attached to the heating surface and tend not to be carried downstream; the bubble drag force tends to be balanced by the buoyancy force. These plug-shaped bubbles appear to attach themselves to active nucleation sites
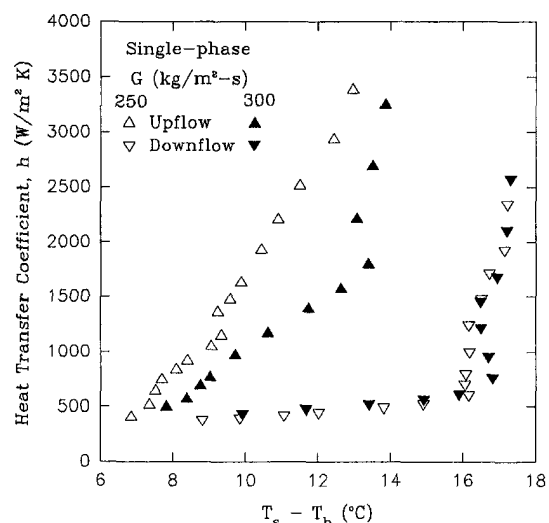

Fig. 5 Comparison of boiling curves for single-phase inlet upflow and downflow. T_b is the bulk fluid temperature entering the test section.
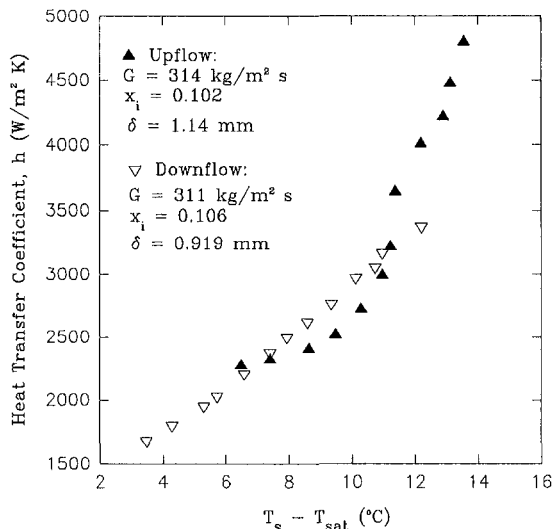
Fig. 6 Comparison of heat transfer coefficient versus wall superheat for annular upflow and downflow boiling

were measured. Meanwhile the nucleation site density, as well as measurements of flow rate, surface temperature, and heat flux were recorded.

The bubble sliding contribution to the total heat transfer was estimated as follows. Following Cornwell (1990), the total heat transfer rate is approximated as

$$q''_{\text{tot}} = q''_{1\phi} + q''_\text{I} + q''_\text{II}, \tag{1}$$

where $q''_{1\phi}$ is the heat flux due to single-phase convection, q''_I is the heat flux due to bubble growth at the nucleation site (i.e., excluding sliding), and q''_II is the heat flux due to bubbles growing and sliding while attached to the heater surface. Experiments show that the rate of heat transfer for single-phase turbulent flow is described well by Petukhov's correlation. It is noted that q''_II represents the combined effect of latent heat transport and enhanced turbulent convection due to bubble agitation of the thermal boundary layer.

The average latent heat transfer rate from a single nucleation site (not including the sliding contribution) can be described as

$$\overline{q_{w,1\text{site}}} = \frac{\rho_v h_{fg}(4/3)\pi(d_d/2)^3}{t_d + t_w}, \tag{2}$$

where ρ_v is the vapor density, h_{fg} is the latent heat of vaporization, d_d is the diameter of the vapor bubble at departure, t_d is the time of departure, and t_w is the waiting time, defined as the time between the departure of the bubble and the incipience of the next bubble at the same site. In essence, Eq. (2) represents the latent heat removal due to the average rate of vapor generation from the nucleation site. The total latent heat transfer rate due to stationary bubble growth (i.e., not including sliding) is then

$$q''_\text{I} = \left(\frac{n}{A}\right)\overline{q_{w,1\text{site}}}, \tag{3}$$

where (n/A) is the nucleation site density.

The following are the flow and thermal conditions and measured bubble data from the flow boiling facility:

Flow and Thermal Conditions:	Measured Bubble Data:
• $G = 242$ kg/m²-s	• $d(t) = (1.78 \times 10^{-3})t^{0.5}$ m
• $\Delta T_\text{sub} = 1.2°$C	• $d_d = 0.124$ mm
• $\Delta T_b = 2.2°$C	• $t_d = 4.9$ ms, $t_w = 17.0$ ms
• $q''_w = 1.41$ kW/m²	• Approx. 10 active sites
• $A_s = 3.9 \times 10^{-3}$ m²	

The time of departure, t_d, was not directly measured; instead it is merely estimated using the mean bubble growth curve (which is a curve-fit based on measurements) and mean (measured) departure diameter. The sliding bubble contribution to the total convective heat transfer can be approximated as

$$\begin{aligned} q''_\text{II} &= q''_\text{tot} - q''_{1\phi} - q''_\text{I} \\ &= 1410 - 680 - 0.16 \text{ (W/m}^2) \\ &= 730 \text{ W/m}^2. \end{aligned}$$

The heat transfer contribution due to sliding bubbles for these conditions is therefore very large, approximately 52 percent of the total heat transfer. Conversely, the contribution to the heat transfer of bubble growth at the nucleation site is negligibly small.

---

on the upstream end of the bubble, while the downstream end tends to break up into smaller bubbles which are carried downstream by the bulk flow. The behavior described above was observed to correspond with the change in slope of the h versus ΔT_b curve for downflow. It is therefore suggested that the formation of plug-shaped bubbles promotes vapor removal from the nucleation sites and from the heater surface, and in this way enhances the energy removal from the heating surface. This behavior was observed only in downflow boiling with single-phase inlet conditions; it was not observed in upflow, since the combined action of drag and buoyancy sweeps the bubbles along the heater surface. This effect further illustrates the strong coupling of vapor bubble dynamics with the bulk flow behavior and its influence on the heat transfer in flow boiling.

Figure 6 displays the heat transfer coefficients for upflow and downflow boiling with annular flow inlet to the test section. In the figure, δ represents the annular film thickness and x_i is the inlet vapor quality. Static bubbles seen in downflow boiling were not observed in either annular upflow or downflow boiling. The higher liquid velocity for annular flow sweeps the bubbles downstream in both upflow and downflow and prevents the formation of larger bubbles. Moreover, the increased liquid velocity and turbulence causes bubbles to slide and lift off similarly in both annular upflow and downflow, and the differences in vapor bubble dynamics between the two conditions were not easily distinguishable. As a result, the h versus ΔT_b curves for annular upflow and downflow are similar. The reason the flow boiling curves are similar is that, beyond a certain bulk liquid velocity, the forces imparted on the vapor bubbles due to the bulk liquid flow far outweigh the buoyancy force of the bubbles. In other words, the effect of buoyancy, and therefore flow orientation is diminished. This hypothesis was confirmed by Thorncroft and Klausner (1998) using an analytical model of vapor bubble dynamics for single-phase inlet flow boiling.

3.2 Estimation of Sliding Heat Transfer. In order to obtain additional evidence and understanding of sliding bubble heat transfer, the following experiment was conducted. Under vertical upflow conditions, vigorous boiling was established on the heating surface of the visual test section; then the heat flux was reduced until only approximately ten nucleation sites were active. Attempts were made to activate only one nucleation site, but this could not be accomplished. Using the high-speed motion video camera, the growth and initial sliding phases of the bubbles from one site were photographed; from this video the growth, departure diameter, and streamwise sliding trajectory
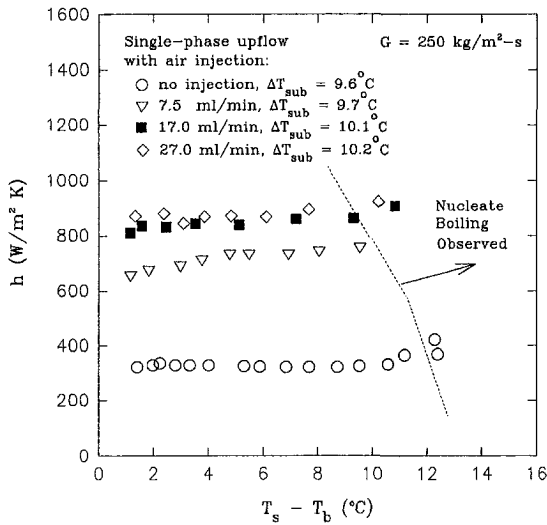
Journal of Heat Transfer

Fig. 7 Measured heat transfer coefficient versus bulk temperature difference for single-phase inlet upflow under various air bubble injection rates

Fig. 8 Measured heat transfer coefficient versus bulk temperature difference for single-phase inlet upflow with air bubble injection under varied liquid subcooling

3.3 Sliding Air Bubble Heat Transfer.

The heat transfer associated with vapor bubble sliding contains contributions from both enhanced turbulent convection and latent heat transport, which could not be discriminated from the preceding experiments. In an attempt to distinguish the contribution of turbulent convection to the heat transfer from that due to latent heat transport, air bubbles were injected along the heating surface as follows. Using the air bubble injection system described in Section 2, subcooled single-phase upflow was established in the test section, and air was injected at the surface of the heater to promote air bubble wall attachment. Air flow rates were chosen such that, at the minimum air injection rate, the conditions resembled nucleation from a single isolated nucleation site, and at the maximum air injection rate, the flow appeared bubbly (7.5–27.0 ml/min). The size of air bubbles exiting the injector were observed to be on the order of 1-mm diameter; it was not possible to identically mimic the vapor generation rate of the nucleate boiling experiments with air injection, since the vapor bubble size was not constant and may have undergone both growth and collapse. At a given air injection rate, power to the test section heater was increased in increments, beginning at zero, and heat transfer coefficients and flow conditions were measured. The heater power was increased in small increments to delay the onset of heterogeneous boiling.

Figure 7 compares the total heat transfer coefficient, h, as a function of bulk temperature difference, $\Delta T_b = T_s - T_b$, for single-phase flow and air bubble injection rates: 7.5 ml/min, 17.0 ml/min, and 27.0 ml/min. As expected, the heat transfer coefficient during single-phase flow without air injection is essentially constant over the range of bulk temperature difference until nucleate boiling is observed. With air bubble injection, h also remains essentially constant with ΔT_b, although the magnitude of h is much greater than that in single-phase flow, and increases with air flow rate. The fact that the heat transfer coefficient does not change with ΔT_b for a given air injection rate suggests that evaporation is not present and thus the bulk turbulent transport must be enhanced by the motion of the air bubbles, resulting in greater heat transport at the wall.

Further evidence of this enhanced bulk turbulent transport can be seen in Fig. 8, which compares heat transfer coefficient profiles for the same air flow rate at different values of liquid subcooling, $\Delta T_{sub} = T_{sat} - T_b$. It is seen that, over the range of liquid subcooling evaluated (3.5° to 10.1°C), the heat transfer coefficient profiles remain approximately constant as ΔT_b is increased, until nucleate boiling is observed. Beyond this point
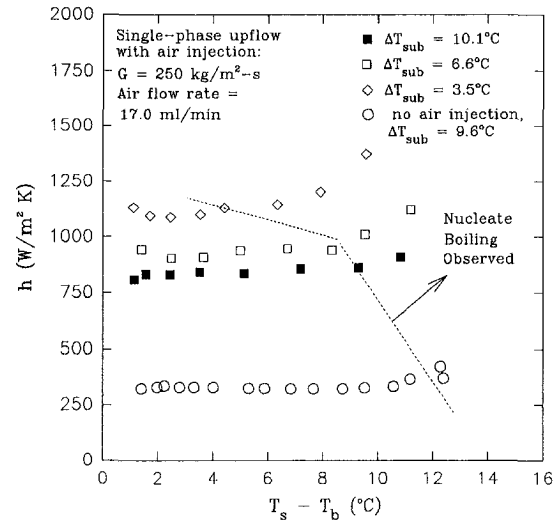
the curves diverge, which is expected, since the onset of heterogeneous boiling occurs at increasingly higher ΔT_b as the liquid subcooling is increased.

A trend observed in Fig. 8 which is difficult to explain is that the heat transfer rates for $\Delta T_{sub} = 3.5°C$ are slightly greater that those for $\Delta T_{sub} = 10.1$ and $6.6°C$. In the absence of evaporation, it is expected that the degree of subcooling should not influence the bulk turbulent heat transport associated with sliding vapor bubbles. Thus the possibility of evaporation at the liquid/air interface of the bubbles cannot be discounted for the $\Delta T_{sub} = 3.5°C$ case. Evaporation may take place due to mass diffusion of vapor into the air bubble itself. Further investigations are warranted to conclusively resolve the understanding of this trend.

The air bubble injection experiments are similar to those performed by Kenning and Kao (1972); it is therefore useful to compare their work with the present study. Figure 9 compares the operating conditions of this work and those of Kenning and Kao. In this work as in theirs, a large improvement in heat transfer is observed with low bubble flows, an effect which diminishes with increased bubble flow. In addition, Fig. 9 illus-
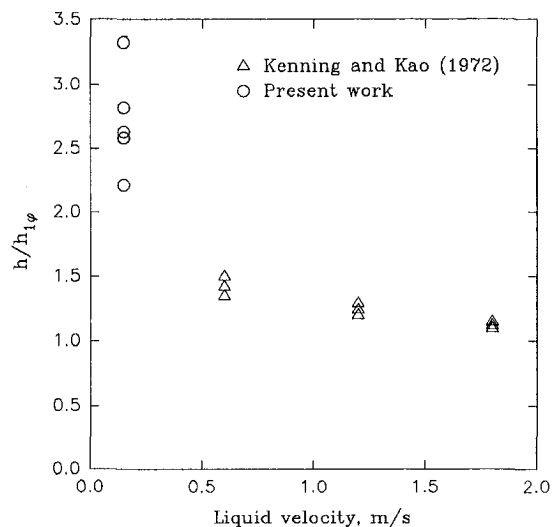
Fig. 9 Ratio of two-phase to single-phase heat coefficient as a function of bulk liquid velocity

trates that the significantly higher heat transfer enhancement in our work occurs at considerably lower bulk fluid velocity. Although the effect of liquid velocity was not examined in this work, the observed behavior is at least reasonable, given the observation of Kenning and Kao that at increased liquid velocity the enhancement diminishes. It should be noted that different fluids were used in this work and that of Kenning and Kao, and a Prandtl number influence may also be responsible for observed differences in $h/h_{1\phi}$.

5 Summary

The experiments presented herein provide conclusive evidence that sliding bubbles enhance heat transfer in forced convection boiling. The distinct differences noted in upflow and downflow boiling heat transfer can be directly attributed to the different bubble sliding trajectories observed in the different flow configurations. In upflow boiling with single-phase flow inlet conditions, it was found that sliding bubble heat transfer enhancement can account for as much as 52 percent of the total energy transfer. In terms of energy transport, the volumetric flow of vapor at the surface is more important under these conditions than the nucleation phenomena itself.

The air bubble injection experiments reported in this work demonstrate that bulk turbulent enhancement is a significant heat transfer mechanism in forced convection boiling. This result is in agreement with the findings of Yan et al. (1996) and Houston and Cornwell (1996). In fact, for the specific experimental conditions considered in this work, it appears that bulk turbulent enhancement accounts for the majority of heat transfer enhancement due to sliding bubbles. It is expected that flow boiling regimes exist for which latent heat transport is as important or more important than bulk turbulent enhancement.

It has been well known that both bulk turbulent convection and nucleate boiling contribute significantly to forced convection boiling heat transfer. The typical modeling practice has been to use a method of superposition to simply add the bulk turbulent heat transfer contribution to that of nucleate boiling. However, in light of the bubble sliding heat transfer enhancement data presented, it may be concluded that the bulk turbulent and nucleate boiling heat transfer mechanisms are in fact interdependent. The bubble dynamics in forced convection boiling are strongly influenced by the bulk flow behavior, and the bulk flow turbulent heat transport appears to be strongly influenced by the bubble dynamics. Since current flow boiling correlations do not attempt to mechanistically account for the sliding bubble heat transfer mechanism, and since they typically rely on a superposition approach, a re-examination of their general validity is warranted.

References

Cornwell, K., 1990, "The Influence of Bubble Flow on Boiling from a Tube in a Bundle," *Int. J. Heat Mass Transfer*, Vol. 33, No. 12, pp. 2579–2584.

Gunther, F. C., 1951, "Photographic Study of Surface-Boiling Heat Transfer to Water with Forced Convection," *Trans. ASME*, Vol. 73, pp. 115–124.

Hewitt, G. F., 1995, "Phenomenological Issues in Forced Convective Boiling," *Convective Flow Boiling*, J. Chen, ed., Taylor and Francis, Washington, DC, pp. 3–14.

Houston, S. D., and Cornwell, K., 1995, "Heat Transfer to Sliding Bubbles on a Tube under Evaporating and Non-evaporating Conditions," *Int. J. Heat Mass Transfer*, Vol. 39, No. 1, pp. 211–214.

Kenning, D. B. R., and Kao, Y. S., 1972, "Convective Heat Transfer to Water Containing Bubbles: Enhancement Not Dependant on Thermocapillarity," *Int. J. Heat Mass Transfer*, Vol. 15, pp. 1709–1717.

Mesler, R., 1988, "Explosive Boiling: A Chain Reaction Involving Secondary Nucleation," ASME HTD-Vol. 96, pp. 487–492.

Mesler, R., 1992, "Improving Nucleate Boiling Using Secondary Nucleation," *Proc. Eng. Found. Conf. Pool External Flow Boiling*, ASME, New York, pp. 43–47.

Mesler, R., and Mailen, G., 1977, "Nucleate Boiling in Thin Liquid Films," *AIChE Journal*, Vol. 23, pp. 954–957.

Petukhov, B. S., Irvine, T. F., and Hartnett, J. P., Eds., 1970, *Advances in Heat Transfer*, Vol. 6, Academic Press, New York.

Thorncroft, G. E., and Klausner, J. F., 1997a, "Suppression of Flow Boiling Nucleation," ASME JOURNAL OF HEAT TRANSFER, Vol. 119, pp. 517–524.

Thorncroft, G. E., and Klausner, J. F., 1997b, "A Capacitance Sensor for Liquid Film Thickness Measurements in a Square Duct," *J. Fluids Eng.*, Vol. 119, pp. 164–169.

Thorncroft, G. E., and Klausner, J. F., 1998, "Gravitational Influence on Vapor Bubble Dynamics in Forced Convection Boiling," *11th Int. Heat Transfer Conference*, Korea.

Thorncroft, G. E., Klausner, J. F., and Mei, R., 1998, "An Experimental Investigation of Bubble Growth and Detachment in Vertical Upflow and Downflow Boiling," *Int. J. Heat Mass Transfer*, Vol. 41, pp. 3857–3871.

Tsung-Chang, G., and Bankoff, S. G., 1990, "On the Mechanism of Forced-Convection Subcooled Nucleate Boiling," ASME JOURNAL OF HEAT TRANSFER, Vol. 112, pp. 213–218.

Wadekar, V. V., and Kenning, D. B. R., 1994, "Flow Boiling: A Role for Wall-Attached Vapour Bubbles?" *Proc. 10th Int. Heat Transfer Conf.*, Brighton, Vol. 7, pp. 563–568.

Yan, Y., and Kenning, D. B. R., 1996, "Flow Boiling in Bubbly Flow," *Convective Flow Boiling*, J. Chen, ed., Taylor and Francis, Washington, DC, pp. 293–298.

Yan, Y., Kenning, D. B. R., and Cornwell, K., 1996, "Sliding and Sticking Vapour Bubbles Under Inclined Plane and Curved Surfaces," *Eurotherm 48: Pool Boiling Conf.*, Paderborn.

Zeng, L. Z., and Klausner, J. F., 1993, "Nucleation Site Density in Forced Convection Boiling," ASME JOURNAL OF HEAT TRANSFER, Vol. 115, pp. 215–221.

Effects of Surface Orientation on the Pool Boiling Heat Transfer in Water/2-Propanol Mixtures

S. Ahmed

V. P. Carey
Mem. ASME

Department of Mechanical Engineering,
University of California,
Berkeley, CA 94720

To explore the role of Marangoni effects in the pool boiling heat transfer of binary mixtures, experiments have been conducted with water/2-propanol mixtures at three different concentrations under normal gravity with different orientations of the heater surface. The system pressure was subatmospheric (~5.5 kPa) and the bulk liquid temperature was near the saturation temperature of the fluids tested. The molar concentrations of 2-propanol tested were 0.015, 0.025, and 0.1. These concentrations of 2-propanol are selected because their strong variation of surface tension with concentration gives rise to high surface tension gradients near the heater surface during nucleate boiling. Boiling curves were obtained both for an upward-facing and a downward-facing heater surface. For each concentration of 2-propanol, the critical heat flux has been reached in both orientations of the heater surface. Models of pool boiling heat transfer and the critical heat flux condition for binary mixtures are tested to correlate the data. Comparison of boiling curves and CHF obtained at different orientations of the heater surface indicates that there is strong gravity independent mechanism of boiling heat transfer in these mixtures.

Introduction

In many technological applications, vaporization of a working fluid is critically important. It facilitates the heat input in Rankine power systems, the cooling effect in vapor compression heat pumps and high heat flux removal in thermal control applications. When the working fluid is a pure substance, as is often the case, the characteristics of the vaporization process can be predicted with reasonable accuracy using the results of extensive research on boiling of pure liquids obtained over the past 60 years. Recent efforts to improve component or system performance have led some developers to consider the use of binary working fluids. In general, researchers have found that some binary mixture working fluids offer the potential for improved thermodynamic efficiency, or superior heat transfer performance. The advantages of using binary mixture working fluids in heat pump systems have been explored by several investigators (see, for instance, Domanski (1986)). This type of investigation invariably points out the fact that the current limited capability to accurately predict the transport processes for boiling of binary mixtures is a major obstacle to the development of heat pump systems using binary working fluids. Another perspective on binary mixture boiling can be obtained by considering two-phase thermal management systems for spacecraft. Systems of this type using pure working fluids have been extensively studied by Degroff et al. (1988) and others.

Presently, there is a considerable amount of published literature on the pool boiling of binary mixtures. Bonilla and Perry (1941) conducted one of the earliest studies on the boiling of mixtures. These investigators experimentally investigated boiling of binary mixtures of aqueous and organic mixtures from a flat horizontal plate. Van Stralen and co-workers (1956–1970) extensively studied pool boiling in binary mixtures. Somewhat later, Thome and Shock (1984) provided an extensive review of the literature on binary mixtures. Bajorek et al. (1990) reported pool boiling heat transfer coefficients for six aqueous ternary mixture systems and compared the experimental data

with the models. Predictive methods for boiling of pure and multicomponent fluids on a low finned tube were investigated by Bajorek et al. (1991). These investigators developed a correlation for nucleate pool boiling of pure fluids on a horizontal low finned tube and used this correlation with plain tube mixture boiling correction factor to predict boiling heat transfer coefficients for binary and ternary mixtures. More recently, Fujita and Tsutsui (1994) measured heat transfer coefficients for nucleate pool boiling of five binary mixtures on a circular copper plate facing upwards. Celata et al. (1994) reported a brief summary of the state of the art of the experiments carried out over the last ten years and also examined available predictive tools for nucleate pool boiling heat transfer in binary mixtures. Celeta et al. (1994) acknowledged the lack of comprehensive tools for the prediction of nucleate pool boiling heat transfer of the mixtures. This inability is tied to the incomplete understanding of the complex transport processes during boiling of the binary mixtures, particularly due to the strong coupling between heat and mass transfer processes. Recently, Thome (1996) reviewed and summarized the up-to-date information on the experimental results and predictive methods of boiling of pure refrigerants and refrigerant mixtures. Most of the studies concluded that the heat transfer coefficient of binary mixtures is generally lower than the molar average of the nucleate pool boiling heat transfer coefficients for the pure components of the mixture. Among the possible reasons for heat transfer deterioration, the most common explanation is that the local boiling point of a binary mixture increases due to the preferential evaporation of the more volatile component at the liquid vapor interface near the heater surface.

Perhaps the most interesting finding of these earlier investigations was that the critical heat flux for some mixtures may significantly exceed the critical heat flux for the pure components. The mechanism responsible for the enhancement has been the subject of debate for a number of years. Reddy and Lienhard (1989) investigated the critical heat flux mechanism for ethanol/water mixture on small horizontal cylinders. Reddy and Lienhard (1989) and other investigators (see, for example, McEligot (1964)) favored the argument that concentration variations in the fluid near the heater surface result in an effective subcooling of the liquid which enhances heat removal from the

Copyright © 1999 by ASME

surface during the boiling process, and consequently, the critical heat flux. While this appears to explain the increase in the critical heat flux in some cases, results of very recent experiments conducted by McGillis and Carey (1996) suggest that in some systems, this mechanism alone cannot be responsible for the increase. Instead, these investigators found that the variation of the critical heat flux correlates more strongly with the surface tension gradient due to concentration gradients near the heated surface.

The concentration difference established as described above will result in a surface tension gradient along the liquid-vapor interface near the heater surface. At low concentrations, the variation of surface tension with concentration exhibits a strong negative slope for a 2-propanol/water mixture, whereas for a methanol and water mixture, the gradient is less steep. In both cases, however, the negative value of the surface tension gradient will produce stronger surface tension near the heated wall and weaker surface tension further away. This imbalance will tend to pull liquid near the interface from the bulk, where surface tension is smaller, to the wall region where surface tension is larger. The higher temperature near the wall will tend to reduce the surface tension compared to the cooler bulk liquid condition. However, in the alcohol/water mixtures considered by McGillis and Carey (1996), changes in the surface tension resulting from the temperature changes are negligible compared to those induced by concentration differences. Beginning with the well-known Zuber correlation for the critical heat flux for an upward-facing flat heated surface, these investigators replaced the restoring effect of buoyancy in the Zuber correlation with the combined effect of buoyancy and surface tension gradients. The final form of McGillis-Carey correlation for the critical heat flux of the binary mixtures can be written as follows:

$$q''_{m,\text{MC}} = q''_{m,sf} \left[1 + c_m \left(\frac{1}{\sigma} \right) \frac{\partial \sigma}{\partial x} (y_b - x_b) \right]^{1/4} \quad (1)$$

where $q''_{m,sf}$ is the CHF correlation for single fluid with specific configuration and geometry of interest. $\sigma^{-1}(\partial\sigma/\partial x)(y_b - x_b)$ is the surface tension gradient parameter that influences the critical heat flux of binary mixtures significantly. The slope of the mixture surface tension curve with respect to the liquid mole fraction of the more volatile component is expressed by $\partial\sigma/\partial x$. In the above expression, x_b is the concentration of the more volatile component in the bulk liquid and y_b is the concentration that would exist in the vapor phase in equilibrium with liquid at a concentration of x_b. McGillis and Carey (1996) found that by adjusting the constant c_m in the correlation, they could match critical heat flux data for both their water/alcohol mixtures as well as the ethanol and water data of Reddy and Lienhard

(1989). Agreement is quite good over the entire range of concentrations tested, and this model correlates these data better than other currently available schemes.

The important point here is that for certain binary fluid mixtures, there is abundant evidence that the surface tension gradients resulting from concentration differences act to enhance the fluid motion towards the heated surface. For some mixtures the effect on the critical heat flux is so great that this effect appears to be substantially stronger than the buoyancy effect at normal gravity. It is difficult, however, to fully assess the magnitude of the Marangoni effect because it is always combined with buoyancy induced by gravity acting towards an upward-facing heated surface. By conducting binary mixture nucleate boiling studies with a downward-facing heater surface, the buoyancy effect would be reversed, and the ability of Marangoni forces to induce liquid motion towards the surface against the buoyancy effect would be directly observable and comparable to results for an upward-facing surface. In addition, the results of this simple study can be utilized effectively in selecting binary mixtures for reduced gravity boiling experiments. There have been few studies on the effect of orientations of the heater surface on the boiling behavior of pure fluids. The effects of surface orientation on nucleate boiling heat transfer were examined by Nishikawa et al. (1983). Jung et al. (1987) studied the effects of enhanced surfaces and surface orientation on nucleate boiling heat transfer in R11. For copper surface, these researchers observed that heat transfer is enhanced for the downward-facing surface relative to the upward-facing surface, especially at low heat flux levels. Similar observations were reported by other investigators.

The present study is intended to investigate the interaction of the gravity vector orientation with Marangoni mechanism during the boiling of binary mixtures. Boiling of 2-propanol/water mixtures at three different concentrations has been investigated for both upward-facing and downward-facing orientations of the heater surface. Four methods of predicting binary mixture heat transfer coefficients were tested in an attempt to correlate the experimental data obtained in this study. These are the correlations of Thome (1983), Stephan and Körner (1969), Schlünder (1982), and Ünal (1986). Thome (1983) developed a correlation for heat transfer coefficients of binary mixture boiling using only phase equilibrium data. Stephan and Körner (1969) used an excess function formulation for determining the wall superheat in the boiling of binary mixture. These investigators, then, evaluated the heat transfer coefficients using the expression for wall superheat. Based on the film theory of mass transfer, Schlünder (1982) proposed a correlation by modeling the growth of a vapor bubble in a binary mixture. In this correlation, only the mass transfer was taken into account

Nomenclature

A_o = empirical constant in Stephan-Körner correlation
A_{12}, A_{21} = activity coefficient constants
B_o = scaling factor in Schlünder correlation
CHF = critical heat flux
c_m = constant in McGillis-Carey correlation
°C = degree centigrade
f = fugacity
g = instantaneous acceleration
g_n = normal gravitational acceleration
h = heat transfer coefficient
h_{fg} = latent heat of evaporation for the mixture

P = pressure
q'' = heat flux
q''_m = critical or maximum heat flux
$q''_{m,\text{MC}}$ = McGillis-Carey CHF
$q''_{m,sf}$ = single-fluid CHF
T = temperature
ΔT_{bp} = temperature difference between the dew point and bubble point
ΔT_{id} = ideal wall superheat for binary mixture
t = time
x = liquid mole fraction
x_p = molar concentration of 2-propanol
x_b = bulk liquid molar concentration

y = vapor mole fraction
y_b = equilibrium vapor mole fraction
β_L = mass transfer coefficient
ρ_l = density of liquid mixture
σ = liquid surface tension
γ_i = activity coefficient
φ_i = fugacity coefficient

Subscripts

b = bulk
c = critical
id = ideal
n = normal or terrestrial
p = 2-propanol
s = saturation
1, 2 = components of the mixture

in computing the local rise in the bubble point temperature. Ünal (1986) suggested a correlation for the heat transfer coefficients of binary mixture boiling based on dimensional analysis. The forms of the correlations are as follows:

Thome (1983):

$$\frac{h}{h_{id}} = \frac{1}{1 + \Delta T_{bp}/\Delta T_{id}} \qquad (2)$$

Stephan and Körner (1969):

$$\frac{h}{h_{id}} = \frac{1}{1 + A_o(0.88 + .12P)|y - x|} \qquad (3)$$

Schlünder (1982):

$$\frac{h}{h_{id}} = \frac{1}{1 + \dfrac{(T_{s2} - T_{s1})|y - x|}{\Delta T_{id}} \left[1 - \exp\left(\dfrac{B_o q''}{\beta_l \rho_l h_{fg}}\right)\right]} \qquad (4)$$

Ünal (1986):

$$\frac{h}{h_{id}} = \frac{1}{[1 + (b_2 + b_3)(1 + b_4)][1 + b_5]} \qquad (5)$$

where

$$b_2 = (1 - x) \ln \frac{1.01 - x}{1.01 - y} + x \ln \frac{x}{y} + |1 - x|^{1.5}$$

$$b_3 = 0 \quad \text{for } x \ge 0.01$$

$$b_3 = (y/x)^{0.1} - 1 \quad \text{for } x \le 0.01$$

$$b_4 = 152(P/P_c)^{3.9}$$

$$b_5 = 0.92|y - x|^{0.001}(P/P_c)^{0.66}$$

and

$$x/y = 1 \quad \text{for } x = y = 0.$$

In Eqs. (2) and (5), the ideal wall superheat, ΔT_{id}, is defined as the molar averaged value of the wall superheats of the pure components at the same heat flux as the mixture. Therefore, ΔT_{id} can be written as

$$\Delta T_{id} = x\Delta T_1 + (1 - x)\Delta T_2. \qquad (6)$$

For the same heat flux for the mixture and the pure components, the ideal heat transfer coefficient, h_{id}, can be evaluated as

$$h_{id} = \frac{q}{\Delta T_{id}} = \frac{1}{x/h_1 + (1 - x)/h_2} \qquad (7)$$

where h_1 and h_2 are the heat transfer coefficients for the pure components of the mixture.

In Eq. (2), ΔT_{bp} is the temperature difference between the dew point and bubble point curves at a fixed molar concentration of the mixture as determined from the phase equilibrium data. The empirical constant A_o in Eq. (3) depends on the particular mixture. Stephan and Körner (1969) determined the value of A_o for 17 mixtures resulting in A_o values ranging from 0.42 to 3.56. They recommended the average value 1.53 for mixtures whose data are not available. The pressure P in Eq. (3) should be expressed in bar. In Eq. (4), T_s is the saturation temperature of the pure components at the same pressure as the mixture, B_o is a scaling factor set equal to 1.0 and the mass transfer coefficient, β_L, was set to a constant value of 0.0002 m/s. In the above correlations, x and y are the liquid and vapor mole fraction of the more volatile component, respectively. Thus, $|y - x|$ can be considered as the mass transfer driving potential in the boiling of binary mixture. While the effects of mass transfer

driving potential was embedded implicitly in the correlation of Thome (1983), the other correlations contain the expression $|y - x|$ explicitly.

In order to evaluate the ideal heat transfer coefficients for binary mixture boiling, correlations for pure component heat transfer coefficients should be selected carefully. This is due to the fact that the accuracy of the predicted heat transfer coefficients for binary mixture boiling is strongly dependent on the satisfactory prediction of pure component heat transfer coefficients. Fujita and Tsutsui (1994) reported that Stephan-Abdelsalam (1980) correlation provided satisfactory prediction of the heat transfer coefficients for five pure single components with considerably different physical properties. Therefore, the Stephan-Abdelsalam correlation (1980) was chosen for single component heat transfer coefficients in the present investigation. Among the correlations presented by Stephan and Abdelsalam, the model for water was used and the model for hydrocarbon was used for 2-propanol. In the present study, Eq. (7) is used for computing ideal heat transfer coefficient. However, in a recent review of the boiling of new refrigerants and refrigerant mixtures, Thome (1996) mentioned that the improved model of Schlünder (1982), developed by Thome (1989), predicts the heat transfer coefficient accurately for mixtures when the ideal heat transfer coefficient is calculated with the Stephan-Abdelsalam (1980) correlation utilizing the mixture physical properties. A computer program was written to evaluate the wall superheat for a given heat flux in order to generate boiling curves of 2-propanol/water mixtures from the correlations. The computation method for the bubble-point temperature and other properties of pure fluids and their mixtures are described in detail by McGillis (1993) and Ahmed (1996). However, the procedure to compute the bubble point temperature of the mixture is briefly discussed here.

For a binary mixture at equilibrium, the pressure, the temperature, and the chemical potential have to be equal for each component. The chemical potential is an abstract concept and therefore, an auxiliary function called fugacity is used to express the abstract in terms of measurable quantities. Phase-equilibrium thermodynamics dictates that the fugacity of the component i in the liquid phase is equal to the fugacity of component i in the vapor.

$$f = f_i^l \qquad (8)$$

The fugacity of component i in the liquid is related to the saturation pressure of pure component i by

$$f_i^l = \gamma_i x_i P_i^s \qquad (9)$$

where γ_i and x_i are the activity coefficient and liquid mole fraction of component i.

The fugacity of component i in the vapor is related to the total pressure by

$$f_i^v = \varphi_i y_i P \qquad (10)$$

where φ_i and y_i are the fugacity coefficient and the vapor mole fraction of component i.

McGillis (1993) assumed that the fugacity coefficient is unity based on low system pressure. From Eqs. (9) and (10), we can write

$$y_i P = \gamma_i x_i P_i^s. \qquad (11)$$

If the activity coefficients of the mixture are known, this equation can be utilized to compute the vapor mole fraction from measurable quantities of liquid mole fraction, total system pressure and the saturation pressure of the pure components. Using two-parameter Margules equation (Prausnitz et al., 1986) and Gibbs-Duhem equation, McGillis (1993) determined the form of the activity coefficients of a binary mixture. The equations are

$$\ln \gamma_1 = [A_{12} + 2(A_{21} - A_{12})x_1]x_2^2$$

and

$$\ln \gamma_2 = [A_{21} + 2(A_{12} - A_{21})x_2]x_1^2 \qquad (12)$$

where A_{12} and A_{21} are the activity coefficient constants.

Using Eq. (11), $y_1 + y_2 = 1$ and $x_1 + x_2 = 1$, the saturation pressure of the mixture can be expressed as

$$P = x_2 \gamma_2 P_2^s + (1 - x_2) \gamma_1 P_1^s. \qquad (13)$$

McGillis (1993) conducted equilibrium experiments to measure the saturation pressures of the pure components and fluid mixtures at different temperatures. Assuming that the parameters in Eq. (12) do not change over the temperature range of interest, McGillis (1993) determined the values of the parameters of the equation for several mixtures. The values of A_{12} and A_{21} for 2-propanol/water mixtures were 0.9768 and 2.4153, respectively. These values were used in the present investigation. The program computes the bubble-point temperature if the pressure of the system and the composition of the binary mixture are known. For given P and x_1 (mole fraction of 2-propanol), the code computes T_{bp} iteratively as described below:

- assume a temperature T
- compute P_1^s and P_2^s from equations for pure component saturation pressure based on T
- compute γ_1 and γ_2 from Eqs. (12)
- evaluate $P_i = \gamma_1 x_1 P_1^s(T) + \gamma_2 x_2 P_2^s(T)$
- check the difference $(P_i - P)$
- assume a new temperature based on this difference
- iterate and get a converged temperature

The wall superheat was computed by subtracting the bubble-point temperature from the wall temperature. The surface tension of liquid mixtures is usually less than a mole-weighted average surface tension of the pure components at the same temperature. For 2-propanol/water mixtures, McGillis and Carey (1996) provided a modified form of the model of Meissner and Michaels (1949) which is valid for the entire range of mole fractions. Excellent agreement was found between this surface tension model and the experimental data. This model, which is used in the present study, is

$$\sigma_m = (\sigma_w - \sigma_p) \exp(-30\sqrt{x_p}) + \sigma_p. \qquad (14)$$

The predicted curves are then compared to the boiling curves obtained from the experiments. It is noteworthy that the heat transfer coefficients of the binary mixture boiling, obtained from the correlations, do not show gravity dependence explicitly although it can be influenced if the pure component heat transfer coefficients depend on gravity. The critical heat flux data obtained in the present investigation are compared with the recent correlation developed by McGillis and Carey (1996) which includes the contribution of Marangoni effects in the CHF condition for pool boiling of binary mixtures. The value of c_m used in the present study was 1.14 as suggested by McGillis and Carey (1996). Zuber's correlation with a correction factor for small heater was used for $q''_{m,sf}$.

Experimental Setup and Procedure

Figure 1(a) shows the layout of the experimental hardware. The test section used in the experiments was a 30.48-cm long square (7.62 cm) channel made of stainless steel. The top plate and the two side plates were 0.64 cm thick and the bottom plate was 1.27 cm thick. The bottom plate had a rectangular cutout to accommodate replaceable heated surface element. The copper heater element and its stainless steel holder is shown in Fig. 1(b). The heater element was made of oxygen-free high-purity copper to ensure that the thermophysical properties of the element were defined to high accuracy. This element was machined
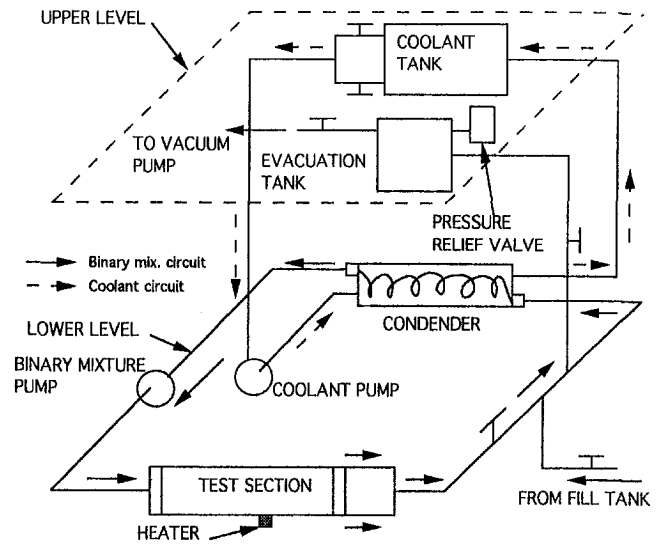

Fig. 1(a) Layout of the experimental system
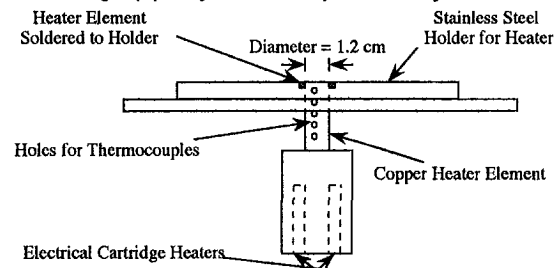
Fig. 1(b) Copper heater element and stainless steel holder

to accommodate two cartridge heaters at the bottom end. The top half of the copper piece was fabricated to provide a long 1.2-cm diameter circular section. In this section, five holes were drilled to the center to hold thermocouple wires. The diameter and the depth of holes were 0.08 cm and 0.6 cm, respectively, and the bead diameter of the K-type thermocouples used in the experiment was about 0.06 cm. Due to uncertainty in the spacing between thermocouples, the change in the heat flux was estimated to be less than one percent. The thermocouples were inserted into the holes and were glued to the circular section of the heater outside the holes. A Metrabyte thermocouple board with integrated cold junction compensation and an IBM DACA board were used to scan the thermocouples and store the temperature in the computer. Along the perimeter of the top section, the copper heating element was silver soldered to the stainless steel holder. The contact area between the stainless steel and the copper was minimized to avoid heat loss. The heat loss was computed from a standard conduction model and it was less than three percent of the heat input. Electric cartridge heaters fitted into the bottom of the copper element provided the heat input which flows along the bar of circular cross section to the flush end exposed to the flow in the test section. The flush end of the copper heater element was a 1.2-cm diameter circular finger. Thermocouples installed along the copper bar allowed measurement of the temperature gradient in the bar, and hence the heat flux to the surface exposed to the flow. Lateral side walls of the test section had rectangular windows made of transparent polycarbonate for flow visualization. The system pump delivered fluid to the inlet header of the test section. A porous plate in the inlet header helped provide even flow distribution in the test section. Flow exiting the test section was piped to the system condenser. A Validyne pressure transducer installed in the test section was used to monitor the pressure in the system. The fluctuation of the measured pressure in the test

section was generally below five percent. However, appropriate correction term was accounted due to the pressure fluctuation in order to represent the data at constant pressure. Experimental uncertainties in the pressure and the differential temperature measurements were ±0.2 kPa (four percent) and $0.2°C$, respectively. Uncertainty in the determination of wall temperature was $1°C$. The heat flux to the exposed heater surface could be determined within ±5 percent. The volume fraction of the mixture was measured by graduated measuring cylinder and the mole fraction of the mixture was computed from a relation (McGillis, 1993). The uncertainty in the value of mole fraction was 0.2 percent. The overall uncertainty in the computation of the bubble point temperature was estimated to be about $1°C$. The uncertainty in the determination of heat transfer coefficient was estimated to be within 15 percent. The boiling curves were repeatable within ±2 percent and the repeatability of the critical heat flux was within ±5 percent.

The experimental setup consisted of two flow circuits; one for the binary mixture and the other for the coolant flow in the condenser. All the components of the setup were arranged in two levels of the rack. The components of the binary mixture circuit were the test section, a pump and the tubes in the condenser and were located at the bottom level. The heater element at the bottom of the test section heated up the binary mixture. The purpose of the pump was to maintain a constant flow in the test section and the condenser. To clarify the use of pump in a pool boiling experiment, it is noteworthy to mention that the test section was designed for normal, reduced, and high-gravity experiments (Ahmed and Carey (1997)) and the pump was necessary for the reduced-gravity experiment. The intention of this design was to provide a weak bulk convective motion that would not affect the nucleate boiling process on the heated surface, but would carry vapor bubbles that leave the surface during the reduced-gravity boiling process to the condenser. The objective was to sustain a steady nucleate boiling process while maintaining constant pressure and bulk concentration in the test section. Test results from the present investigation were compared to the pure pool boiling results of McGillis (1993) for the same mixture and good agreement were observed. Therefore, the effect of the weak convective motion of the mixture on the boiling process was assumed negligible. The coolant circuit consisted of coolant pump, a coolant tank, and the shell of the condenser. The coolant pump and the condenser were located at the bottom level but the coolant tank was mounted on the upper level. To degas the mixture and to control the pressure in the test system, the evacuation tank was mounted on the upper level and was connected to the binary mixture circuit by a short copper tube. Appropriate valves and plumbing were installed in the test system so that the experiment could be conducted for downward-facing heater surface. A support structure for the test system was built using 13/16 in. aluminum Unistrut bar. The test system along with its support structure was mounted in one of the two racks. The computer, data acquisition system, and all the electrical components were mounted on the other rack. The thermocouple and pressure data were monitored using a PC-based data acquisition system.

The binary mixture circuit was evacuated by a vacuum pump. Distilled water and laboratory grade 2-propanol were used to prepare the mixture. The flow of binary mixture from the charging tank filled up the system when the fill port was opened. To degas the mixture, pressure was lowered much below the working pressure of the system which caused the noncondensable gases to leave the mixture. The collected noncondensable gases in the evacuation tank were purged from the experimental system by the vacuum pump. The pressure of the system could be lowered by bleeding vapor from the evacuation tank or could be increased by filling the system with more liquid mixture. When pressure became steady, the pumps were turned on. Electrical power was supplied to the cartridge heater and the heat flux to the binary mixture was controlled by a variac. The heat
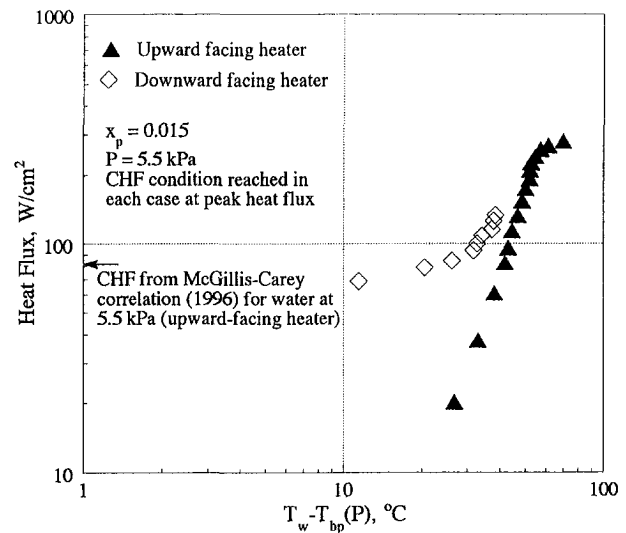

Fig. 2 Boiling curves of water/2-propanol mixture (x_p = 0.015) for upward and downward-facing heater surface

flux was obtained from a least-square fit of the five thermocouples embedded along the heater element and the surface temperature was computed by extrapolation. We assumed that the radial variation of the temperature in the heater rod was negligible since the thermal conductivity of copper is high and the heater was insulated along the circumference. The experiment was continued until the system reached the critical heat flux. The system pressure and temperature were stabilized for the upward facing heater surface and the experiment was conducted for this orientation. At the end of the experiment, there was a cool-down period when the system pressure and the temperature were restabilized. The pumps and the heater were turned off. At that point, the rack was oriented to conduct experiments for the downward-facing configuration. The coolant pump was primed and turned on. Since the components of the binary mixture circuit were at the same level, the binary mixture pump did not need priming for downward-facing orientation. After turning the binary mixture pump on, the heater was turned on and the experiment was continued until the heat flux from the heater reached CHF condition. The test surface of the heater did not change appreciably for four to five complete experimental runs. For most cases, the surface of the heater was cleaned with #320 emery paper and alcohol after each experiment.

Results and Discussions

For a particular experimental run, P was the fluid pressure on the heater element. The pressure fluctuation was within the range of the estimated uncertainty in the measurement. However, the bubble-point temperature of the mixture was computed at the actual pressure for each data point and subtracted from the wall temperature of the heater in order to determine the wall superheat. The procedure to compute the bubble point temperature of binary mixtures are described in detail by Ahmed (1996). Figure 2 shows the boiling curves for a 2-propanol/water binary mixture at two different orientations of the heater surface; upward facing and downward facing. The molar concentration of 2-propanol in the mixture is 0.015. Also shown in the plot is the critical heat flux for water for upward-facing heater surface at the same system pressure computed from McGillis-Carey correlation (1996). It is evident from the plot that the critical heat flux of 2-propanol/water (x_p = 0.015) for an upward-facing heater is greater than that of pure water under the same condition by a factor of three. Comparison between the boiling curves of two orientations reveals the fact that the heat transfer performance of the downward-facing heater is bet-

ter than the upward-facing heater particularly in the low heat flux regime. The heat transfer is enhanced as the heater surface is oriented from horizontal up to horizontal down configuration since buoyancy causes the heated layer of fluid mixture to stay close to the heater surface, and close proximity of growing bubbles to the heater surface increases the microlayer area and/ or decreases its thickness as was observed by Merte (1990). The increase in microlayer area enables more effective area of heat transport from the heater to the evaporating liquid-vapor interface and the decrease in microlayer thickness reduces the heat transfer resistance between the heater surface and the interface. Both of these effects contribute to the enhancement of heat transfer for the downward-facing heater surface. In the case of pure fluids, this improvement in heat transfer is usually offset by lower CHF under such conditions. The lower CHF is usually attributed to blockage of the supply of liquid to the heater surface by bubbles pressed against the surface by buoyancy. This onset of dryout condition can be delayed by using a "positive" binary mixture (such as 2-propanol/water mixture) since there is additional mechanism to bring liquid to the vaporizing interface near the surface. A binary mixture is said to be "positive" when the more volatile component has a lower surface tension than the less volatile component of the mixture. Preferential evaporation of 2-propanol on the heater surface gives rise to surface tension gradients along the liquid-vapor interface near the heated surface which causes liquid to flow towards the heater surface and delays the onset of dryout condition. Unlike an upward-facing heater where the buoyancy effect and the Marangoni effect act together to bring liquid towards the heater surface, the buoyancy effect, in a downward-facing heater surface opposes the flow of liquid due to Marangoni effect. This reduction in the liquid flow towards the heater surface for downward-facing configuration results in lower critical heat flux of 2-propanol/water mixture as compared to the upward-facing configuration. However, the critical heat flux of this 2-propanol/water mixture ($x_p = 0.015$) at downward-facing heater configuration is substantially more than that of pure water at upward-facing configuration. These facts clearly suggest the existence of a gravity-independent mechanism (i.e., Marangoni) to bring liquid towards the heater surface, in addition to gravity-driven flow, in the boiling of 2-propanol/water mixture.

The boiling curves for upward-facing and downward-facing heater surfaces for 0.025 and 0.1 molar concentrations of 2-propanol are shown in Figs. 3 and 4. Although slight heat transfer enhancement is observed for the downward-facing heater over the upward-facing configuration for 0.025 molar concentration, no enhancement is found for 0.1 molar concentration. The critical heat fluxes for both concentrations are higher for upward-facing heater than the downward-facing heater surface.

A comparison of boiling curves for upward-facing heater for all three concentrations is shown in Fig. 5 and the same for downward-facing heater is shown in Fig. 6. It is evident from the plots for each orientation that the critical heat flux is maximum for the lowest concentration of 2-propanol in the 2-propanol/water mixture and decreases with increasing concentration. Figure 5 shows that the heat transfer rate of the binary mixture for upward-facing heater does not change significantly with the concentration for the low mole fraction range tested in the present study. It seems from the plot that the only difference among the three boiling curves is the critical heat flux, the highest CHF attained at the lowest concentration of 2-propanol. However, this similarity in the heat transfer rate for all three concentrations does not hold true for downward-facing heater as is evident in Fig. 6. Heat transfer rate changes significantly with the concentration for downward-facing heater. The lower the concentration of 2-propanol in water, the higher the heat transfer rate and the critical heat flux. The surface tension of pure water is three times higher than that of pure 2-propanol and, therefore, the surface tension of 2-propanol/water mixture decreases with increasing concentration of 2-propanol. However, the surface ten-

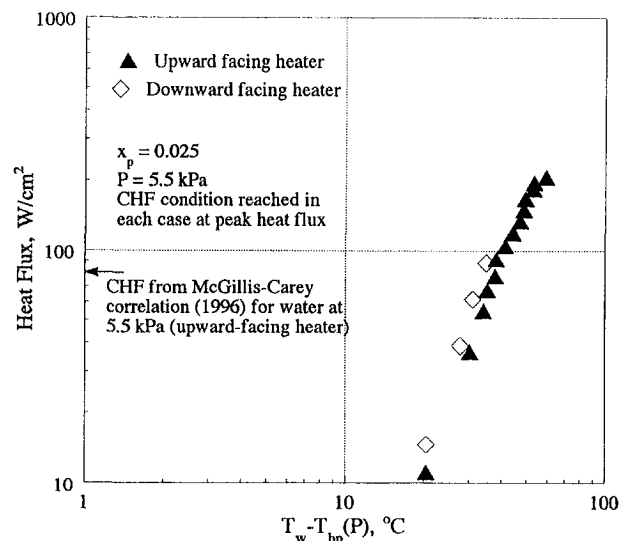**Fig. 3** Boiling curves of water/2-propanol mixture ($x_p = 0.025$) for upward and downward-facing heater surface

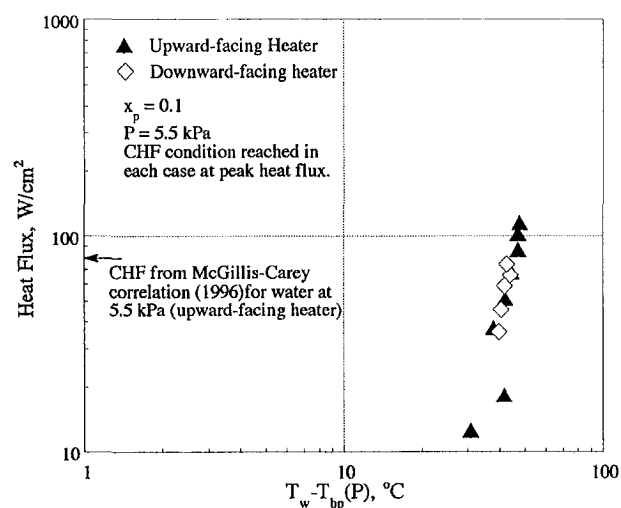**Fig. 4** Boiling curves of water/2-propanol mixture ($x_p = 0.1$) for upward and downward-facing heater surface
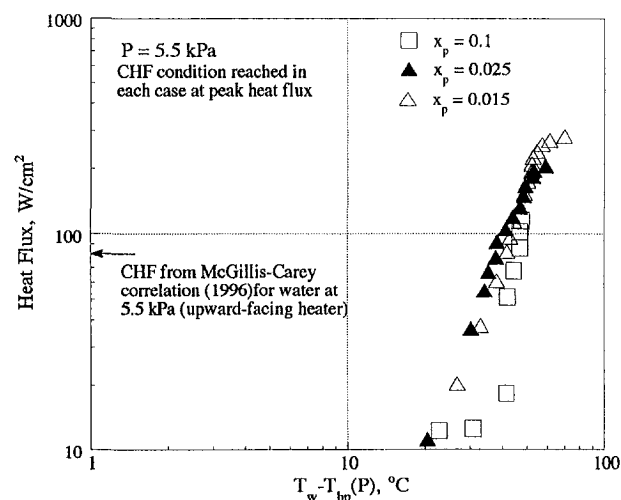

Fig. 5 Comparison of boiling curves at various concentrations of 2-propanol in water/2-propanol mixtures for upward-facing heater surface
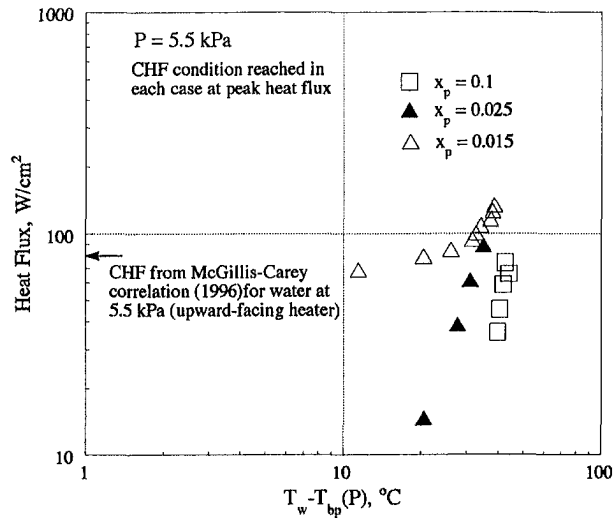
Fig. 6 Comparison of boiling curves at various concentrations of 2-propanol in water/2-propanol mixtures for downward-facing heater surface

Fig. 8 Comparison of the boiling curves for upward-facing heater surface for $x_p = 0.015$ obtained from the experiment and the predictive models of binary mixture boiling with Roshnow's correlation for pure liquid

sion gradient of 2-propanol/water mixture is highest for very low concentration of 2-propanol and approaches zero near 0.2 molar concentration of 2-propanol as shown in Fig. 7. It is evident from Fig. 7 that the surface tension gradient is highly nonlinear and extremely sensitive to the concentration of the mixture in the low concentration range of the water/2-propanol mixture. Small variation in the concentration along the liquid-vapor interface of such mixtures will produce large Marangoni force and will induce liquid motion. Since 2-propanol evaporates preferentially at the heater surface, the surface tension at the liquid-vapor interface near the heater surface is higher than the rest of the liquid-vapor interface of vapor bubbles or vapor columns due to the depletion of the low surface tension component of the mixture. A surface tension gradient is established along the liquid-vapor interface which pulls additional liquid from the bulk towards the heater surface which delays the onset of dryout condition. It is important to note that the pure water boiling experiment was not conducted in the present experimental system since the heat flux for pure water is extremely sensitive to any trace amount of 2-propanol.

Predicted boiling curves obtained from four correlations of binary mixtures are compared with the experimental curves for

$x_p = 0.015$ and are shown in Figs. 8 and 9. However, the heat transfer coefficients for binary mixtures are dependent on the choice of pure component correlation. Fujita and Tsutsui (1994) reported good agreements of Stephan-Abdelsalam model with the pure component heat transfer coefficients for fluids with considerably different properties obtained from their experiment. It is obvious from the figures that Stephan-Abdelsalam correlation is the better choice for pure components heat transfer coefficients investigated in the present study. Among the four models tested, the correlations of Thome (1983) and Schlünder (1982) agrees well with the experimental boiling curve for $x_p = 0.015$ for an upward-facing heater surface. Figure 10 shows similar agreement of the boiling curves for $x_p = 0.025$. The boiling curve for downward-facing heater surface for $x_p = 0.015$ is compared to the predicted boiling curves from the correlation of Thome (1983) and Schlünder (1982) in Fig. 11. For downward-facing heater surface, heat transfer rate increases even for pure fluid due to the increase of microlayer area and/or decrease of microlayer thickness as discussed earlier. In case of a binary mixture with strong Marangoni convection (i.e., $x_p = 0.015$), the heat transfer rate is expected to be even higher due to the
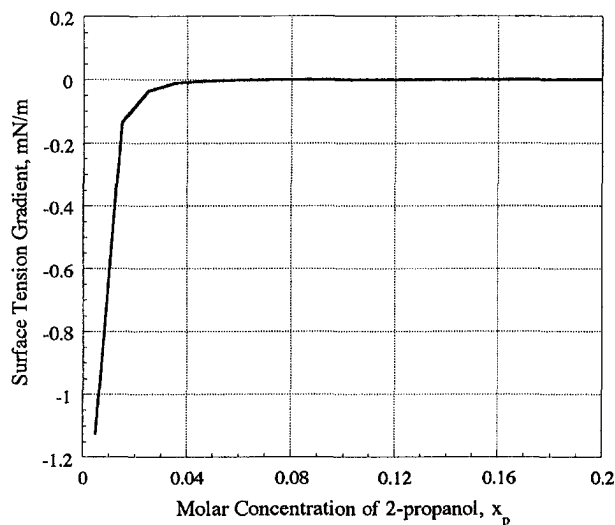

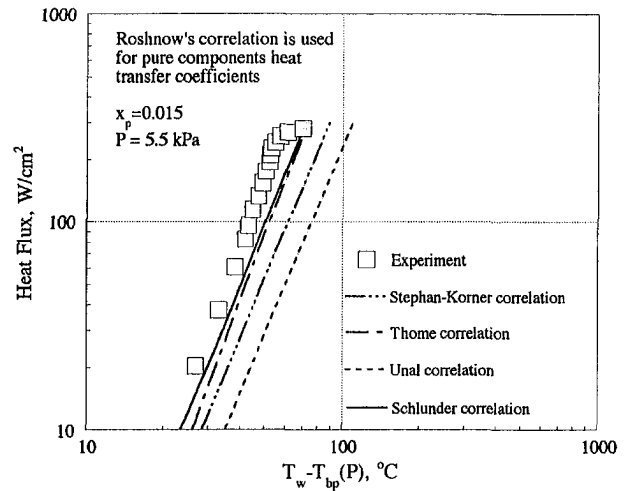Fig. 7 Variation of surface tension gradient with concentration of 2-propanol in a water/2-propanol mixture
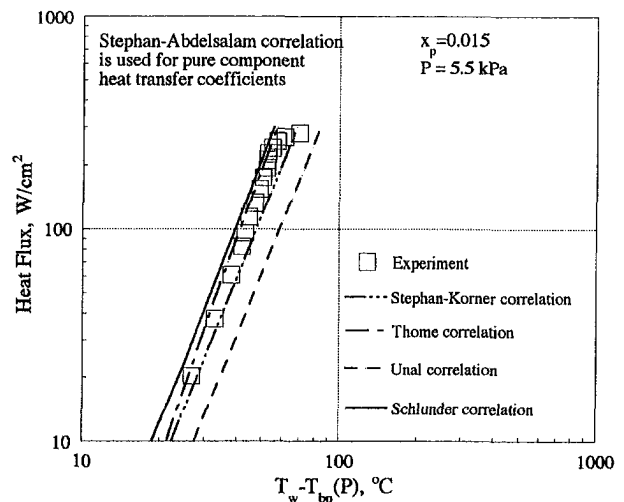

Fig. 9 Comparison of the boiling curves for upward-facing heater surface ($x_p = 0.015$) obtained from the experiment and the predictive models of binary mixture boiling with Stephan-Abdelsalam correlation for pure liquid
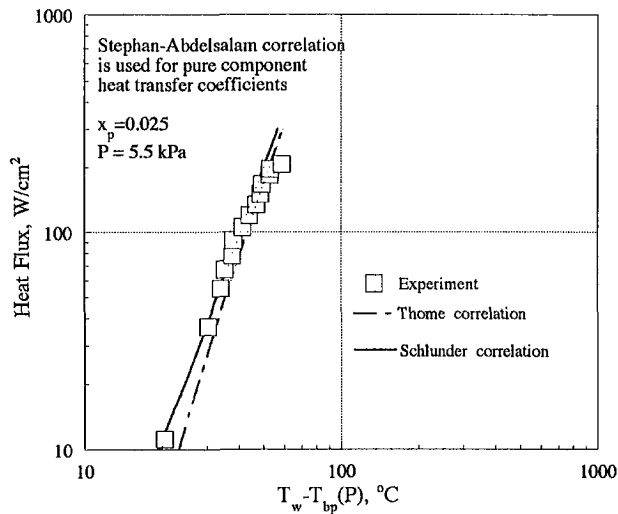
Fig. 10 Comparison of the boiling curves for upward-facing heater surface for x_p = 0.025 obtained from the experiment and Thome's and Schlünder's correlation

Fig. 12 Comparison of the CHF value obtained from the experiment and the McGillis-Carey correlation

flow of liquid from the bulk towards the heater surface. Marangoni effects in the boiling of binary mixture appear to enhance the heat transfer for a downward-facing heater surface in a way that is not accounted for in these correlations. In addition, these correlations have been developed from analytical models, semi-empirical analyses, and experimental results for upward-facing heater surface. The comparison of the experimental results of the CHF condition with the predicted values obtained from McGillis-Carey correlations is depicted in Fig. 12. Agreement is quite good over the heat flux range although the predicted value is lower than the experimental CHF condition. The CHF condition for the boiling of binary mixtures is very sensitive to the surface tension gradient where this gradient is very steep. Therefore, the coefficient c_m in the McGillis-Carey correlation may need to be tuned properly in order to get a better agreement with the present experimental results.

Concluding Remarks

The data obtained in this investigation imply that the Marangoni effect arising from the surface tension gradients due to concentration gradients is an active mechanism in the boiling of binary mixtures such as 2-propanol/water. At a molar con-
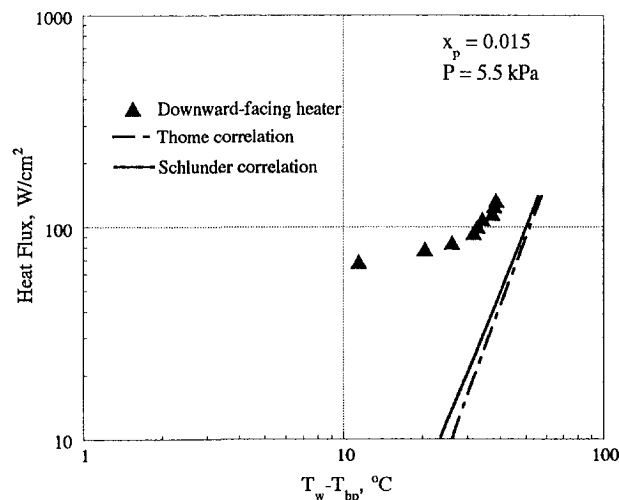
Fig. 11 Comparison of experimental boiling curve for downward-facing heater surface with the correlation of Thome and Schlunder

centration of 0.015 of 2-propanol in water, where the surface tension gradient is highest among the concentration tested, the critical heat flux is a factor of three greater than that of pure water for similar conditions under normal gravity. At low concentration of 2-propanol, the heat transfer performance was enhanced for downward-facing heater compared to the upward-facing case, especially in the low heat flux level. Although heat transfer rate did not change significantly with concentration for upward-facing heater, the rate dramatically changed for downward-facing heater and the heat transfer rate was highest for the lowest concentration. Agreement between the predicted boiling curves for an upward-facing heater surface obtained from the correlations of Thome (1983) and Schlünder (1982) and the present experiment is quite good. However, these correlations cannot predict the boiling curves for downward-facing heater surface. For both orientations, the critical heat flux correlates strongly with the surface tension gradient due to concentration gradient near the surface as proposed by McGillis and Carey (1996).

Acknowledgment

References

Abe, Y., Oka, T., Mori, Y. H., and Nagashima, A., 1994, "Pool Boiling of a Non-azeotropic Binary Mixture under Microgravity," *International Journal of Heat and Mass Transfer*, Vol. 37, No. 16, pp. 2405–2414.

Ahmed, S., 1996, "Marangoni Effects in the Boiling of Binary Fluid Mixtures," Ph.D. thesis, University of California, Berkeley, CA.

Ahmed, S., and Carey, V. P., 1998, "Effects of Gravity on the Boiling of Binary Fluid Mixtures," *International Journal of Heat and Mass Transfer*, Vol. 41, pp. 2469–2483.

Bajorek, S. M., Lioyd, J. R., and Thome, J. R., 1990, "Evaluation of Multicomponent Pool Boiling Heat Transfer Coefficients," *International Heat Transfer Conference*, pp. 39–44.

Bajorek, S. M., Lioyd, J. R., and Thome, J. R., 1991, "Prediction Methods for Boiling of Pure and Multicomponent Fluids on a Low Finned Tube," *Fouling and Enhancement Interactions*, HTD-Vol. 164, pp. 101–108.

Bonilla, C. F., and Perry, C. W., 1941, "Heat Transmission to Boiling Binary Liquid Mixtures," *Chemical Engineering Progresses Symposium Series*, Vol. 37, pp. 685–705.

Celeta, G. P., Cumo, M., and Setaro, T., 1994, "A Review of Pool and Forced Convective Boiling of Binary Mixtures," *Experimental Thermal and Fluid Science*, Vol. 9, pp. 367–381.

Degdroff, W. T., Pietruszewski, C. S., and Downing, R. S., 1988, "Development Status of a Two-Phase Thermal Management System for Large Spacecraft," AIAA Paper 88-2703.

Domanski, P., 1986, "Modeling of a Heat Pump Charged with a Non-Azeotropic Refrigerant Mixture," NBS Technical Note 1218, National Bureau of Standards.

Fujita, Y., and Tsutsui, M., 1994, "Heat Transfer in Nucleate Pool Boiling of Binary Mixtures," *International Journal of Heat and Mass Transfer,* Vol. 37, Suppl. 1, pp. 291–302.

Jung, D. S., Venart, J. E. S., and Sousa, A. C. M., 1987, "Effects of enhanced surfaces and surface orientation on nucleate and film boiling heat transfer in R-11," *International Journal of Heat and Mass Transfer,* Vol. 30, pp. 2627–2639.

McEligot, D. M., 1964, "Generalized Peak Heat Flux for Dilute Binary Mixtures," *AIChE Journal,* Vol. 10, No. 1, pp. 130–131.

McGillis, W. R., 1993, "Boiling from Localized Heat Sources in Pure and Binary Fluid Systems," Ph.D. thesis, University of California, Berkeley, CA.

McGillis, W. R., and Carey, V. P., 1996, "On the Role of Marangoni Effects on the Critical Heat Flux for Pool Boiling of Binary Mixtures," ASME JOURNAL OF HEAT TRANSFER, Vol. 118, No. 1, pp. 103–109.

Merte, H., Jr., 1990, "Nucleate Pool Boiling in Variable Gravity," *Low Gravity Fluid Dynamics and Transport Phenomena (Progress in Astronautics and Aeronautics, Vol. 130)* J. N. Koster and R. L. Sani, eds., AIAA, Washington, DC, pp. 15–69.

Nishikawa, K., Fujita, Y., Uchida, S., and Ohta, H., 1983, "Effect Of Heating Surface Orientation on Nucleate Boiling Heat Transfer," *Proc. ASME-JSME Thermal Eng. Joint Conf.,* Honolulu, Mar. 20–24, ASME, New York, Vol. 1, pp. 129–136.

Prausnitz, J. M., Lichtenthaler, R. N., and Azevedo, E. Gomes de, 1986, *Molecular Thermodynamics of Fluid Phase Equilibria,* 2nd Ed., Prentice-Hall, Englewood Cliffs, NJ.

Reddy, R. P., and Lienhard, J. H., 1989, "The Peak Boiling Heat Flux in Saturated Ethanol-Water Mixtures," ASME JOURNAL OF HEAT TRANSFER, Vol. 111, pp. 480–486.

Schlünder, E. U., 1982, "Über den Wärmeübergang bei der Blasenverdampfung von Gemischen," *Verfahrenstechnik,* Vol. 16, pp. 692–698.

Stephan, K., and Körner, M., 1969, "Calculation of Heat Transfer in Evaporating Binary Liquid Mixtures," *Chem.-Ing. Tech.,* Vol. 41, pp. 409–417.

Stephan, K., and Abdelsalam, M., 1980, "Heat Transfer correlations for Natural Convection Boiling," *International Journal of Heat and Mass Transfer,* Vol. 23, pp. 73–87.

Thome, J. R., 1983, "Prediction of Binary Mixture Boiling Heat Transfer Coefficients Using Only Phase Equilibrium Data," *International Journal of Heat and Mass Transfer,* Vol. 26, pp. 965–974.

Thome, J. R., and Shock, A. W., 1984, "Boiling of Multicomponent Liquid Mixtures," *Advances in Heat Transfer,* Vol. 16, Academic Press, New York, pp. 59–156.

Thome, J. R., 1989, "Prediction of the Mixture Effect on Boiling in Vertical Thermosyphon Reboilers," *Heat Transfer Engineering,* Vol. 10, No. 2, pp. 29–38.

Thome, J. R., 1996, "Boiling of New Refrigerants: a State-of-the-Art Review," *International Journal of Refrigeration,* Vol. 19, No. 7, pp. 435–457.

Ünal, H. C., 1986, "Prediction of Nucleate Pool Boiling Heat Transfer Coefficients for Binary Mixtures," *International Journal of Heat and Mass Transfer,* Vol. 29, pp. 637–640.

Van Stralen, S. J. D., "Heat Transfer to Boiling Binary Liquid Mixtures at Atmospheric and Subatmospheric Pressures," *Chemical Engineering Science,* Vol. 5, pp. 290–296.

Van Stralen, S. J. D., 1966, "The Mechanism of Nucleate Boiling in Pure Liquids and in Binary Mixtures-Part I," *International Journal of Heat and Mass Transfer,* Vol. 9, pp. 995–1020.

Van Stralen, S. J. D., 1966, "The Mechanism of Nucleate Boiling in Pure Liquids and in Binary Mixtures-Part II," *International Journal of Heat and Mass Transfer,* Vol. 9, pp. 1021–1045.

Van Stralen, S. J. D., 1967, "The Mechanism of Nucleate Boiling in Pure Liquids and in Binary Mixtures-Part III," *International Journal of Heat and Mass Transfer,* Vol. 10, pp. 1469–1484.

Van Stralen, S. J. D., 1967, "The Mechanism of Nucleate Boiling in Pure Liquids and in Binary Mixtures-Part IV," *International Journal of Heat and Mass Transfer,* Vol. 10, pp. 1485–1498.

Van Stralen, S. J. D., and Stuyter, W. M., 1969, "Local Temperature Fluctuations in Saturated Pool Boiling of Pure Liquids and Binary Mixtures," *International Journal of Heat and Mass Transfer,* Vol. 12, pp. 187–198.

Van Stralen, S. J. D., and Stuyter, W. M., 1969, "Investigations on the Critical Heat Flux of Pure Liquids and Mixtures Under Various Conditions," *International Journal of Heat and Mass Transfer,* Vol. 12, pp. 1353–1384.

O. Zürcher
Laboratory of Industrial Energetics (LENI)

J. R. Thome
Laboratory of Heat and Mass Transfer
(LTCM)
Mem. ASME

D. Favrat
Laboratory of Industrial Energetics (LENI)

Department of Mechanical Engineering,
Swiss Federal Institute of Technology-
Lausanne,
CH-1015 Lausanane, Switzerland

Evaporation of Ammonia in a Smooth Horizontal Tube: Heat Transfer Measurements and Predictions

Experimental test results for flow boiling of pure ammonia inside horizontal tubes were obtained for a plain stainless steel tube. Tests were run at a nominal saturation temperature of 4°C, nine mass velocities from 20–140 kg/m² s, vapor qualities from 1–99 percent and heat fluxes from 5–58 kW/m². Two-phase flow observations showed that the current test data covered the following regimes: fully stratified, stratified-wavy, intermittent, annular, and annular with partial dryout. The Kattan-Thome-Favrat flow boiling model accurately predicted the local heat transfer coefficients measured in all these flow regimes with only two small modifications to their flow map (to extend its application to G < 100 kg/m² s). Their flow boiling model was also successfully compared to the earlier ammonia flow boiling data of Chaddock and Buzzard (1986). The Gungor-Winterton (1987) correlation instead gave very poor accuracy for ammonia.

1 Introduction

Few experimental test data are available for evaporation of ammonia inside tubes. Previous studies for plain tubes with pure ammonia were presented by Shah (1975) and by Chaddock and Buzzard (1986), both heating their test sections electrically. Shah only reported mean coefficients with different amounts of oil. In the study by Chaddock and Buzzard, pure ammonia was evaporated in a 13.4-mm internal diameter tube at saturation temperatures from $-21°C$ to $-35°C$ and mass velocities of 16.3, 32.6, 65.2, and 130.5 kg/m² s. In the present study with evaporation at 4°C, a double-pipe type of test section with countercurrent flow of hot water was used, which is more appropriate for measuring local flow boiling heat transfer coefficients for stratified types of flow and also at high vapor qualities where part of the annular liquid film has dried out. Because of the large latent heat of ammonia compared to other refrigerants (R-134a, R-22, etc.), the typical mass velocities of practical interest for ammonia direct-expansion evaporators are from about 10–80 kg/m² s while the present tests covered a test range from 20–140 kg/m² s. For a recent comprehensive review of refrigerant flow boiling research, refer to Thome (1996).

The objectives of the present study were to obtain a large number of local flow boiling coefficients for pure ammonia over a wide range of flow conditions, particularly at low mass velocities that had not been investigated in prior tests in this facility, and then compare these boiling data to the new Kattan, Thome, and Favrat (1998a, b, c) flow boiling model.

2 Description of Test Facility and Test Conditions

Figure 1 shows a simplified layout of the refrigerant test loop, depicting only the ammonia flow circuit. The ammonia first passes through a series of horizontal electrically heated preheaters and then through a manifold connected to plain and microfin test sections. The ammonia then enters one of the two test sections (in the present case the plain tube one) after passing

through its inlet sight glass and is heated by countercurrent flow of hot water in the annulus of the double-pipe type of test section. The ammonia leaves through the exit sight glass and then goes through a condenser, a magnetically driven gear type of pump (oil free), a density flowmeter (not used in the present tests), a filter, and finally a calibrated Coriolis mass flowmeter. The circuit also includes gas bottles for the ammonia and a vapor-liquid reservoir for controlling the amount of refrigerant in the circuit and the system's operating pressure (not shown). The hot water flow rate in the annulus is measured with another calibrated Coriolis mass flowmeter and its local temperatures in the test section are measured using four local thermocouples at each of the four locations indicated in Fig. 2. Since ammonia attacks copper and copper alloys, the entire flow loop and its components (test sections, piping, fittings, pump, measurement devices, etc.) were made in stainless steel or other alloy steels.

The sight glasses were 14-mm internal diameter and 100-mm length and were installed just before and just after the test section (see Fig. 2) for viewing the flow and for videotaping flow patterns at the exit. Borosilicate glass was used for the tubular sight glasses.

The test section was made of 439 grade stainless steel welded tubing (thermal conductivity of 28 W/m K). This 0.93-mm thin wall tube had a plain, smooth interior with an internal diameter of 14.00 mm, a test section length of 3.26 m, and a heated length of 3.01 m. The test section was carefully centered inside the outer double-pipe tube with sets of three screws at six intervals along its length, passing the screws with O-ring seals through the outer thick-walled hard plastic tube. The outer tube was formed from two precision machined half-tubes that were fitted with O-rings between the two halfs and compressed with external straps to achieve a highly uniform internal diameter of the outer tube. The outside of the stainless steel test section was uniformly wrapped with a helical wire on a tight pitch to increase the water-side heat transfer coefficient and to enhance circumferential mixing of the hot water in the annulus.

Thermocouples (0.25-mm diameter) were installed in the thin wall of the stainless steel test section at two different axial locations towards the end of the test section, i.e., at T wall 1 and T wall 2 in Fig. 2. Wall thermocouples were located at 0 deg, 60 deg, 120 deg, and 180 deg from the top at each location.
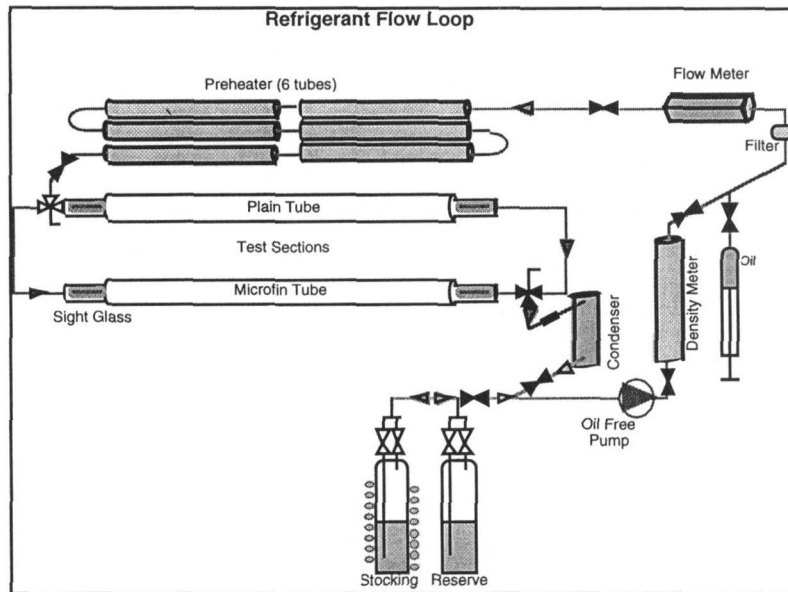
Fig. 1 Simplified diagram of flow loop showing only refrigerant circuit

Shallow grooves were cut in the outside tube wall for installing the thermocouples, with a depth equal to the diameter of the thermocouples, which was 0.25 mm. The wall around each thermocouple was carefully peened over to securely hold it in place. All thermocouples were carefully and accurately calibrated. A computerized data acquisition system was used to record all data. The measurements were made at locations of 2 m and 2.5 m from the refrigerant entrance to avoid any inlet region effects on the refrigerant and water flows.

Flow boiling tests were run at nominal mass velocities of 20, 40, 45, 50, 55, 60, 80, 120, and 140 kg/m² s. All tests were run at a nominal saturation temperature of 4°C at the wall thermocouple location 2 in the test section, which corresponds to a saturation pressure of 4.97 bar (see description in next section). Utilizing the preheater, tests were run over nearly the entire range of vapor qualities. Heat transfer tests were run over a range of relatively low heat fluxes and over a range of relatively high heat fluxes, covering values from 5.2–19.5 kW/m² and from 17.0–71.6 kW/m², respectively. Using hot water the de-

sired heat flux cannot be preset like with electrically heated test sections and hence the measured heat fluxes for individual points in each data set were usually but not always within about ±10 percent of the mean values for the test condition. Vapor qualities covered the entire range from 1–99 percent. For a more complete description of the test facility, but with different test sections, refer to Nidegger, Thome, and Favrat (1997) or Kattan, Thome, and Favrat (1998a).

3 Heat Transfer Measurements

The local heat transfer measurements were obtained from local heat fluxes and wall superheats. The local wall temperatures were determined from the mean of the four wall thermocouples (adjusted to the inner tube wall temperature using Fourier's heat conduction law) installed in the wall at two different axial locations along the test section. The local saturation temperature was obtained from the vapor pressure curve of pure ammonia and the local saturation pressure, which was deter-

---------- **Nomenclature** ----------

A_{Ld} = nondimensional liquid cross-sectional area
A_{vd} = nondimensional vapor cross-sectional area
C = empirical constant
c_{p_L} = liquid specific heat
c_{p_v} = vapor specific heat
D = tube internal diameter
g = gravitational acceleration (= 9.81 m/s²)
G = total mass velocity of liquid plus vapor
G_{strat} = mass velocity of stratified/stratified-wavy flow transition boundary
G_{wavy} = mass velocity of stratified-wavy/annular flow transition boundary
$F_1(q)$ = empirical expression for effect on heat flux on dryout

$F_2(q)$ = empirical expression for effect on heat flux on dryout
Fr = Froude number
h_{cb} = convective boiling heat transfer coefficient of evaporating film
h_{Ld} = dimensionless liquid height in tube
h_{nb} = nucleate boiling heat transfer coefficient
h_{ref} = refrigerant heat transfer coefficient with or without oil
h_{tf} = two-phase heat transfer coefficient
h_v = turbulent vapor-phase heat transfer coefficient on dry perimeter of the tube
h_{wet} = two-phase heat transfer coefficient on wetted perimeter of the tube
k_L = liquid thermal conductivity

k_v = vapor thermal conductivity
m = empirical exponent
M = molecular weight of liquid
P_r = reduced pressure
q = heat flux
R = internal radius of plain tube
x = vapor quality
We = Weber number
α = local void fraction of vapor
δ = thickness of liquid film in annular flow
φ = angle of tube axis with respect to horizontal
μ_L = liquid dynamic viscosity
μ_v = vapor dynamic viscosity
θ_{dry} = dry angle around top of tube in partial wet wall conditions
ρ_L = liquid density
ρ_V = vapor density
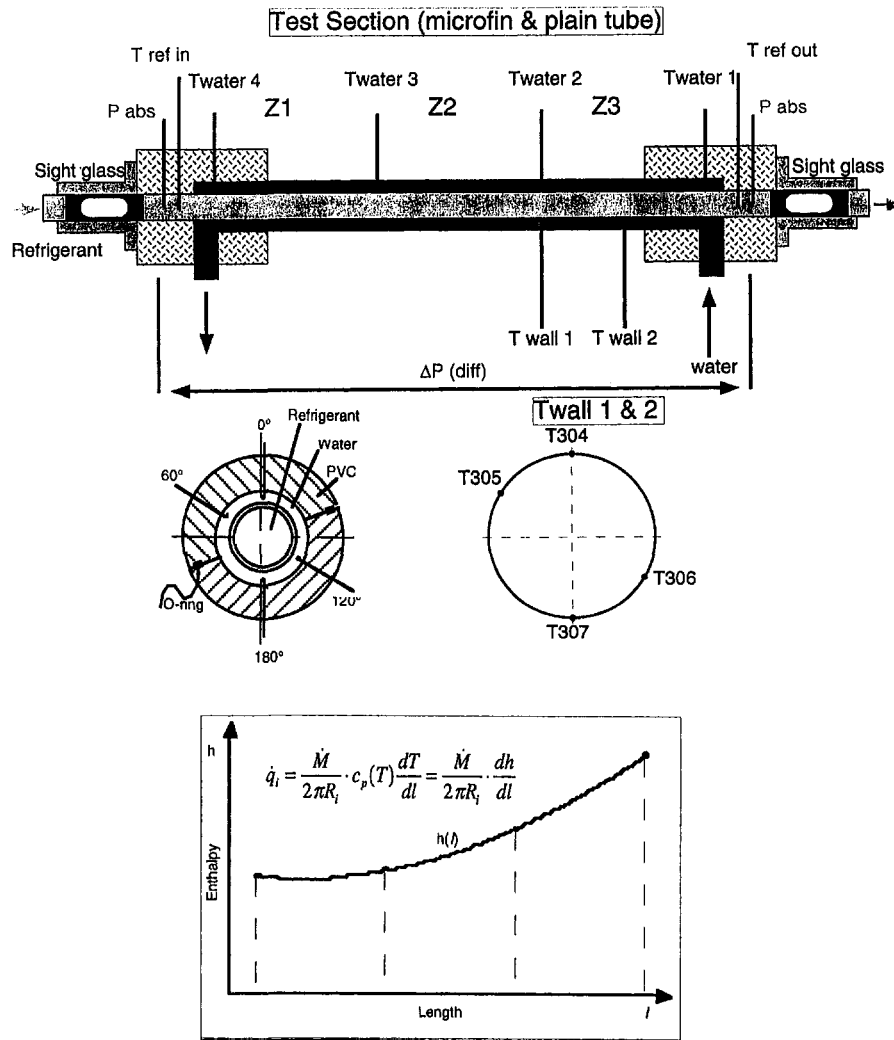σ_L = surface tension of liquid

Fig. 2 Diagrams of the test section, thermocouple locations in the water and tube wall (four each), and the water-side enthalpy variation

mined from a linear interpolation between the measured inlet and outlet pressures. The local heat fluxes were calculated from the slope of splines fit to the enthalpy profiles of the hot water in the annulus based on the water-side temperature measurements (see bottom of Fig. 2) such that true local heat transfer coefficients could be measured similar to electrically heated test sections. Initially, modified-Wilson plot tests were run for measuring some boiling coefficients that verified the integrity of the new enthalpy profile approach and the wall temperature measurements.

The thermocouples were calibrated against a quartz thermometer using a "double precision" method available in the data acquisition system to obtain the highest accuracies possible, that is ±0.03°C. For adiabatic conditions, for example, leaving the rig off all night, all measured temperatures were within a maximum deviation of ±0.05°C and in some isothermal tests the thermocouple readings all agreed to within only ±0.02°C. The refrigerant and hot water mass flow rates were measured using calibrated Coriolis meters with an accuracy of ±0.2 percent, based on the specifications of the manufacturer and our own calibrations. The energy balances in liquid-liquid tests of hot water to refrigerant showed agreement to within ±2 percent or better, with an average of about ±1 percent. The absolute pressures were measured to an accuracy of 0.5 percent according to our calibrations and the measured saturation temperatures agreed with ASHRAE's vapor pressure curve for ammonia

to within 0.2°C. From a statistical propagation of errors analysis the mean uncertainty in the plain tube heat transfer coefficients was about ±5 percent.

4 Experimental Results

In the low heat flux range, nine mass velocities were tested: 20, 40, 45, 50, 55, 60, 80, 120, and 140 kg/m^2 s. Figures 3 to 11 depict these data which were measured at the two axial locations, i.e., wall 1 and wall 2 in Fig. 2, where the mean heat flux of the data shown at each axial location is cited. The data for $G = 55$ kg/m^2 s are not shown since only a few points were taken at high vapor quality. Figures 12–16 show the boiling data for the high heat flux range of tests that included mass velocities of 20, 50, 80, 120, and 140 kg/m^2 s. The mass velocities of individual test points were held to within ±1 kg/m^2 s of the nominal values cited using the speed control on the ammonia pump and a recirculating bypass valve around this pump. The test data were very repeatable . . . an additional second set of the tests were run six months after the first set because of a problem with the pump and little difference was noted in their values with respect to the prior series.

At 20 kg/m^2 s in Figs. 3 and 12, the flow was not able to be held completely stable; fully stratified flow was the dominant regime but stratified-wavy flow (with small amplitude waves) tended to interrupt that regime in a cyclic manner, punctuated

R717 Tsat=4°C 0% oil
Plain Tube, Low Heat Flux
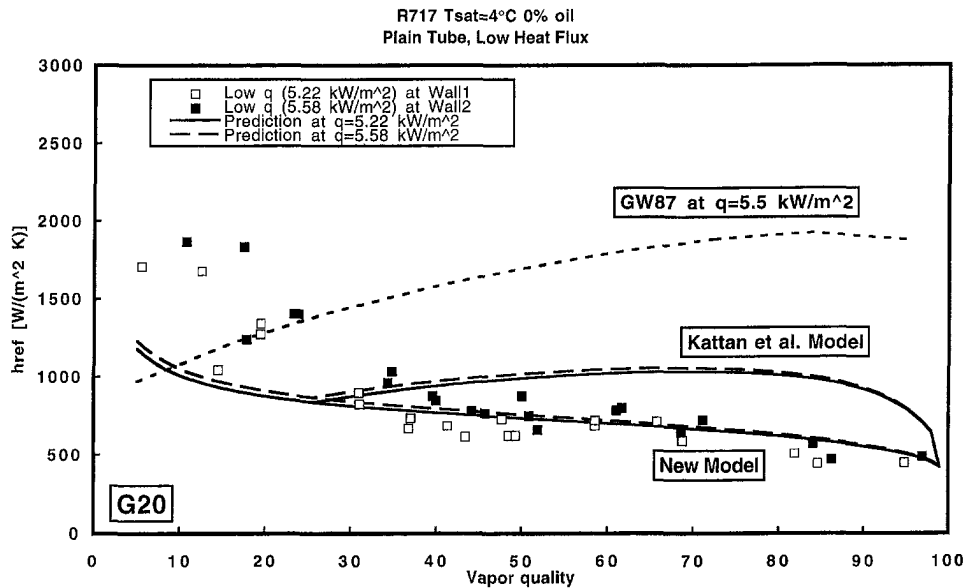
Fig. 3 Flow boiling data at 20 kg/m² s in low heat flux range (Min/Max q in kW/m²: 3.21–8.50 at T Wall 1, 3.04–10.3 at T Wall 2)

R717 Tsat=4°C 0% oil
Plain Tube, Low Heat Flux
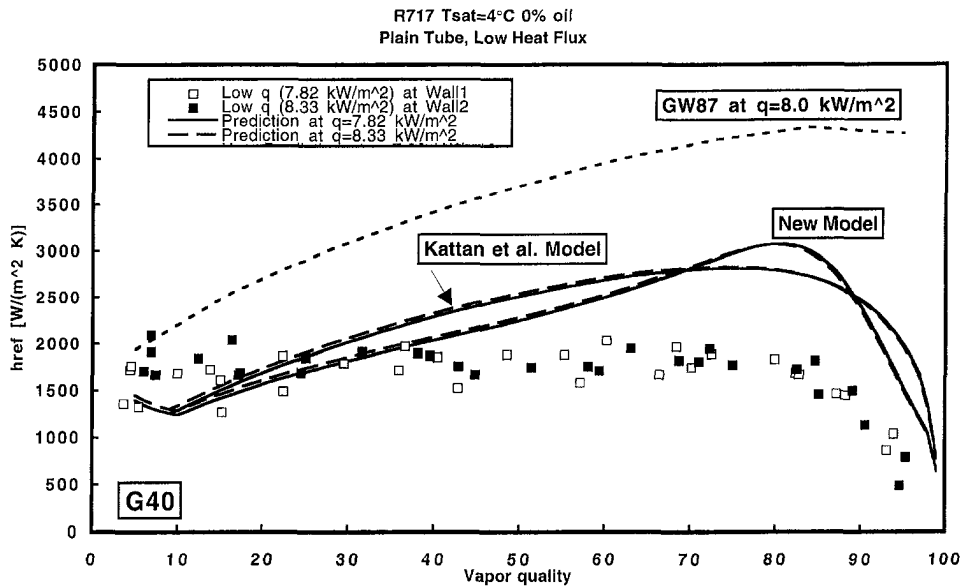
Fig. 4 Flow boiling data at 40 kg/m² s in low heat flux range (Min/Max q in kW/m²: 5.71–9.74 at T Wall 1, 4.01–10.7 at T Wall 2)

by the occasional passage of a large wave. In this regime h_{ref} fell off monotonically as the fraction of the tube wetted by the stratified flow decreased with increasing vapor quality. More vigorous nucleate boiling in the high flux tests apparently was responsible for an increased wetted fraction of the lower perimeter of the tube and hence the much higher coefficients in Fig. 12 than Fig. 3. At 40 kg/m² s, the flow regime was essentially stratified-wavy over the entire vapor quality range of the heat transfer coefficients shown with the wetted portion less than one-half the perimeter. Only an occasional wave had an amplitude large enough to wet the top of the tube and hence the top of the tube was almost always dry. Thus, as can be seen in Fig. 4, h_{ref} is nearly constant in value over a wide range of vapor quality until the waves riding up on the side walls began to dry out at about 80 percent vapor quality and hence h_{ref} fell off as the wetted perimeter of the tube decreased.

For mass velocities from 45–60 kg/m² s, the flow structure became much more complex. As can be seen in Figs. 5, 6, and 7, a peak was reached in h_{ref} versus x in the vicinity of $x = 80$ percent at these three mass velocities (and at 55 kg/m² s that is not shown). Visual observations showed that the flow was in the transition regime between stratified-wavy flow and annular flow. This manifested itself in producing short periods of stratified-wavy flow that wetted a large portion of the sight glass wall and similar periods of annular flow with complete wetting. Thus, compared to stratified-wavy flow where the top of the tube was nearly always dry except for an occasional large amplitude disturbance in the flow, in this transition regime between flow patterns the top wall was dry or wet on a cyclical basis, appearing to be more often wet than dry with increasing vapor quality and increasing mass velocity. This phenomenon results in the peculiar trend in h_{ref} versus x observed in Figs. 5, 6, and

R717 Tsat=4°C 0% oil
Plain Tube, Low Heat Flux
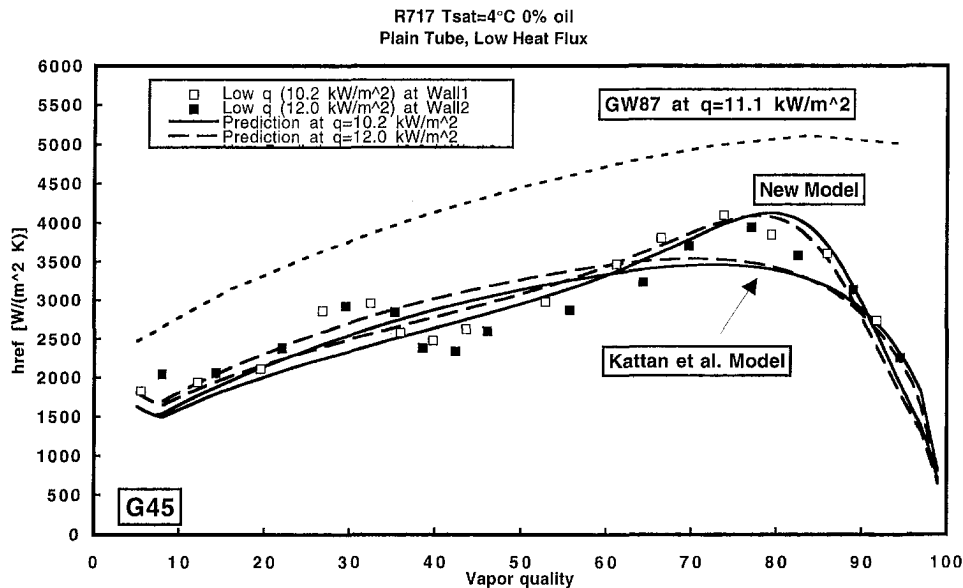
Fig. 5 Flow boiling data at 45 kg/m² s in low heat flux range (Min/Max q in kW/m²: 8.07–11.7 at T Wall 1, 9.17–14.3 at T Wall 2)

R717 Tsat=4°C 0% oil
Plain Tube, Low Heat Flux
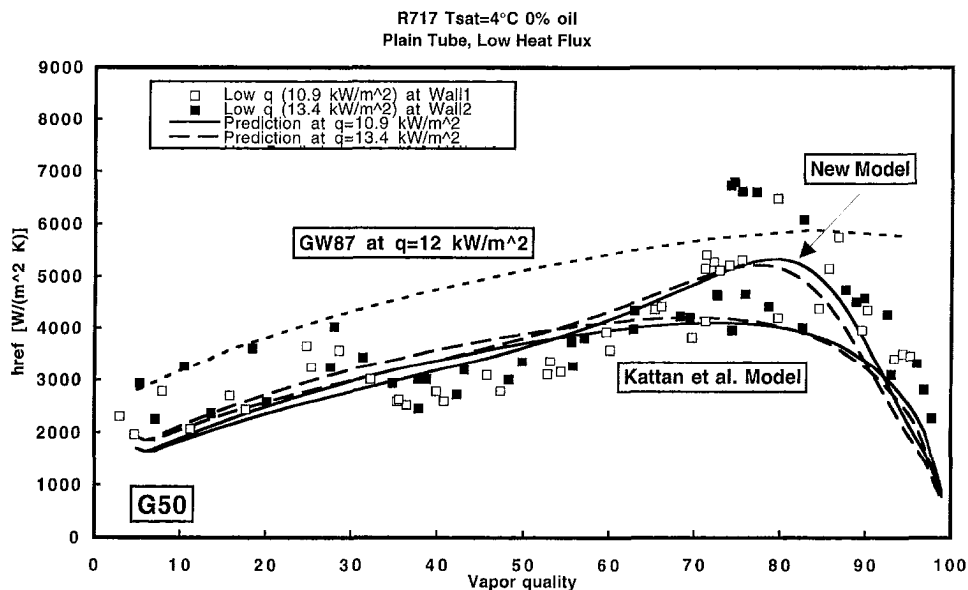
Fig. 6 Flow boiling data at 50 kg/m² s in low heat flux range (Min/Max q in kW/m²: 8.76–12.9 at T Wall 1, 9.92–14.7 at T Wall 2)

7, which was repeatable in the tests run six months after the first ones. The secondary peaks observed at low vapor qualities are apparently caused by flow pattern effects, i.e., it appears in the videos that the structure of the waves in the stratified-wavy regime changes in this range of test conditions.

In comparison, at the mass velocity of 80 kg/m² s for vapor qualities from 1–45 percent in Figs. 8 and 14, the flow was in the stratified-wavy regime with nearly complete wall wetting from the large waves riding up the sides of the tube and then at about $x = 45$ percent converted to annular flow up until its peak in h_{ref} versus x at 90 percent vapor quality. Flow observations after the peak showed that the annular film had partially dried out, first with periodic formation of dry patches on the top perimeter of the tube and then a much more stable dry angle which increased around the tube perimeter with increasing vapor quality. At vapor qualities approaching 100 percent, there was little liquid left in the flowing film and the wetted perimeter

became very narrow such that the flow tended to fluctuate between a wavy film flow and the flow of liquid rivlets along the bottom of the tube.

At the two highest mass velocities, 120 and 140 kg/m² s, the flows were intermittent at low vapor qualities, i.e., large-amplitude waves that continuously washed the top of the tube that kept it always wet with a thin film of liquid, and then converted to annular flow at vapor qualities of about 20–25 percent. The heat transfer coefficients in Figs. 9, 10, and 11 and Figs. 15 and 16 increase steadily as the annular film becomes thinner (and flows faster), eventually reaching its peak at the onset of dryout.

These trends were similar to those identified in Kattan, Thome, and Favrat (1997a, b, c) for refrigerants R-134a, R-123, etc., for tests at mass velocities of 100 kg/m² s in the stratified-wavy flow regime and for mass velocities of 200 kg/m² s and higher that were in the intermittent and annular flow

R717 Tsat=4°C 0% oil
Plain Tube, Low Heat Flux
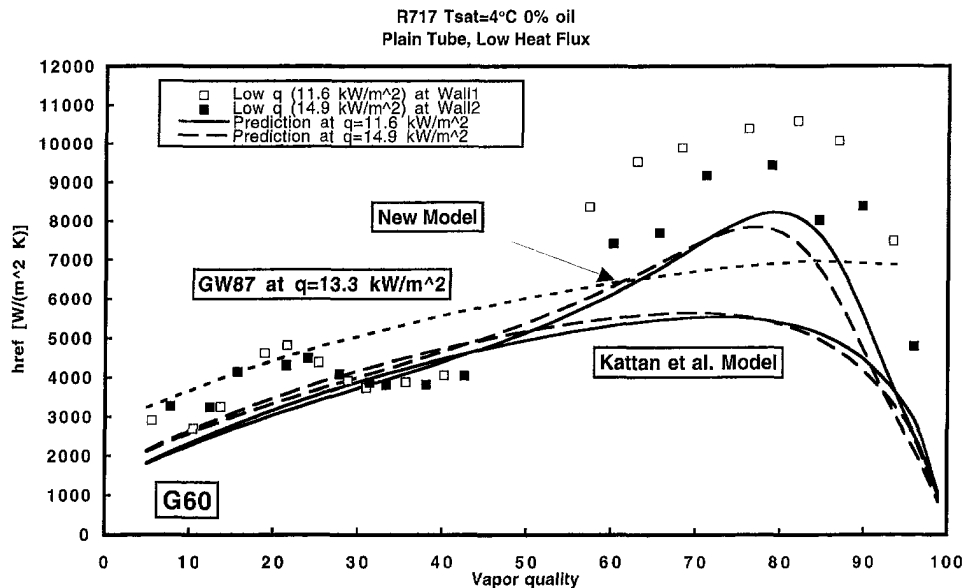
Fig. 7 Flow boiling data at 60 kg/m² s in low heat flux range (Min/Max q in kW/m²: 9.42–12.7 at T Wall 1, 11.9–17.5 at T Wall 2)

R717 Tsat=4°C 0% oil
Plain Tube, Low Heat Flux
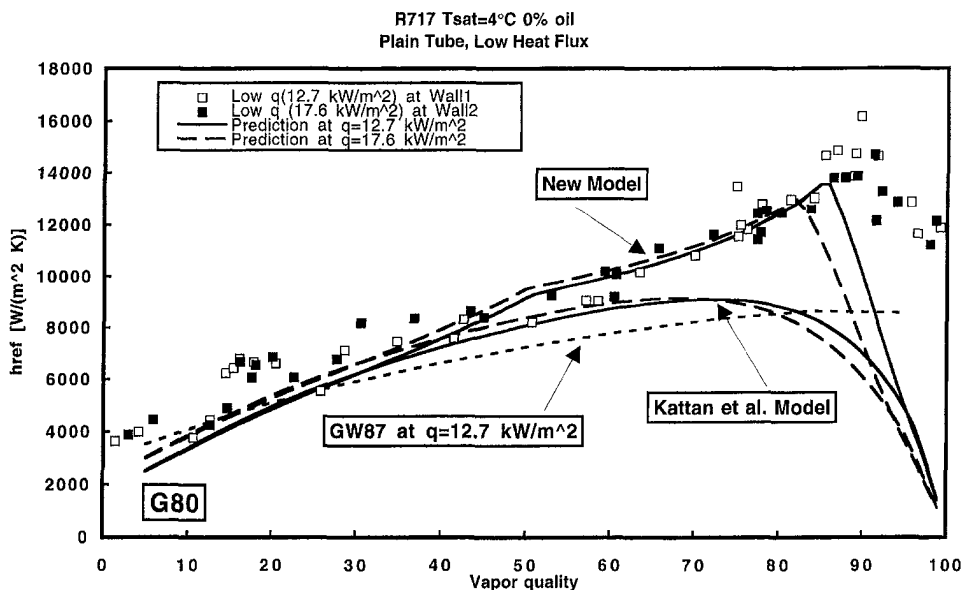
Fig. 8 Flow boiling data at 80 kg/m² s in low heat flux range (Min/Max q in kW/m²: 8.92–13.8 at T Wall 1, 12.7–19.8 at T Wall 2)

regimes, including the falloff in h_{ref} at the onset of dryout in annular flows.

The effect of heat flux is quite evident at G20 where the higher heat flux in Fig. 12 compared to Fig. 3 has increased the local coefficients by nearly a factor of two or more. This can probably be explained by the more vigorous nucleate boiling in the stratified flow at the bottom of the tube, which could easily increase the liquid height and thus wet a larger fraction of the tube's perimeter, making it more effective for wet wall evaporation compared to dry wall, vapor-phase convection. Comparing the data at G50 in Figs. 6 and 13, the effect of higher heat flux on nucleate boiling is evident at low vapor qualities for increasing performance while the heights of the peaks in h_{ref} are nearly identical in both cases, which means that the nucleate boiling contribution is not very significant at high vapor qualities (i.e., the typical conclusion in numerous previous studies). At 80, 120, and 140 kg/m² s the situation is

similar, except that these higher flow rates have higher convective components at low vapor qualities and hence the effect of higher q on the nucleate boiling component is less evident.

5 Comparison of Results to Flow Pattern Based Evaporation Model

Kattan, Thome, and Favrat (1998a, b, c) have recently developed a new flow boiling model for evaporation of pure fluids and mixtures inside of plain horizontal tubes. The method is based on their new two-phase flow pattern map for intube evaporation that includes the effect of heat flux on the onset of dryout in annular flow; the new map is a modified Taitel-Dukler-Steiner map. Their heat transfer model in annular flow is based on turbulent *film* flow where the mean liquid velocity in the film is determined from a void fraction model (i.e., not as turbulent *tubular* flow using the Dittus-Boelter correlation as in
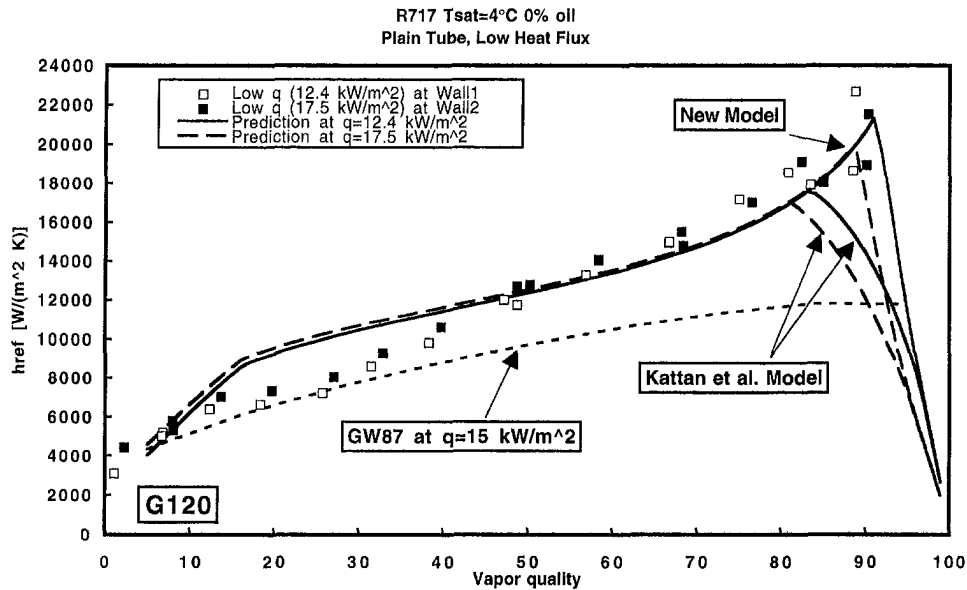
Fig. 9 Flow boiling data at 120 kg/m² s in low heat flux range (Min/Max q in kW/m²: 10.2–14.4 at T Wall 1, 14.2–20.7 at T Wall 2)
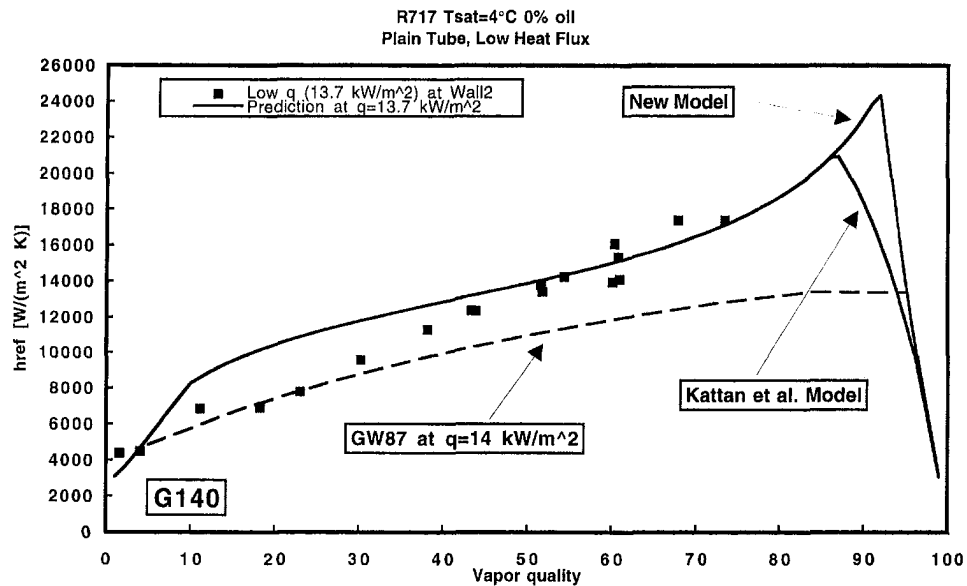
Fig. 10 Flow boiling data at 140 kg/m² s in low heat flux range (Min/Max q in kW/m²: 8.46–9.74 at T Wall 1, 12.1–14.7 at T Wall 2)

other flow boiling prediction methods). The Kattan-Thome-Favrat boiling model predicts local heat transfer coefficients based on the local flow pattern, and presently has methods for predicting heat transfer coefficients in the annular, intermittent, stratified-wavy and stratified flow regimes, where the choice of the method to use is determined locally with the associated flow pattern map. The model also includes equations for predicting the wetted fraction of the tube for (i) stratified types of flow and (ii) for annular flows with partial dryout. The method was developed from an experimental database by Kattan, Thome, and Favrat (1998b) for pure refrigerants R-134a and R-123, the azeotropic refrigerant mixture R-502, and two near-azeotropic mixtures R-402A and R-404A. Zürcher, Thome, and Favrat (1997a) have also shown that the flow pattern map worked very accurately for R-407C as well. In addition, Zürcher, Thome, and Favrat (1997b) have shown that this model without modification (only the local refrigerant-oil mixture viscosity is used

in place of the pure refrigerant value) accurately predicts evaporation of viscous refrigerant-oil mixtures up to local oil concentrations of 50 wt.% oil and local refrigerant-oil viscosities up to 35 cp (170 times that of R-407C) at mass velocities of 200 and 300 kg/m² s and vapor qualities up to about 95 percent.

The Kattan-Thome-Favrat general equation for predicting local flow boiling coefficients in horizontal plain tubes is

$$h_{tp} = \frac{R\theta_{dry}h_v + R(2\pi - \theta_{dry})h_{wet}}{2\pi R} \quad (1)$$

where the heat transfer coefficient on the wetted portion of the tube is comprised of the nucleate boiling and the convective boiling contributions, determined from an asymptotic model as

$$h_{wet} = (h_{nb}^3 + h_{cb}^3)^{1/3} \quad (2)$$

and where h_{nb} is the nucleate pool boiling heat transfer coefficient defined by the *dimensional* Cooper (1984) correlation:

R717 Tsat=4°C 0% oil
Plain Tube, Low Heat Flux (cold water)
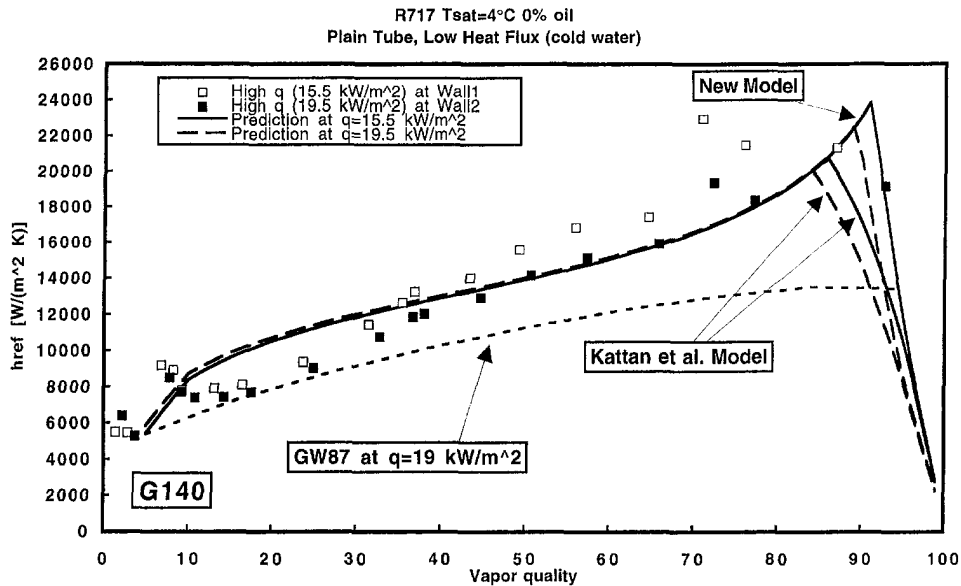
Fig. 11 Additional flow boiling data at 140 kg/m² s in high heat flux range (Min/Max q in kW/m²: 8.46–60.2 at T Wall 1, 11.0–78.0 at T Wall 2)

R717 Tsat=4°C 0% oil
Plain Tube, High Heat Flux
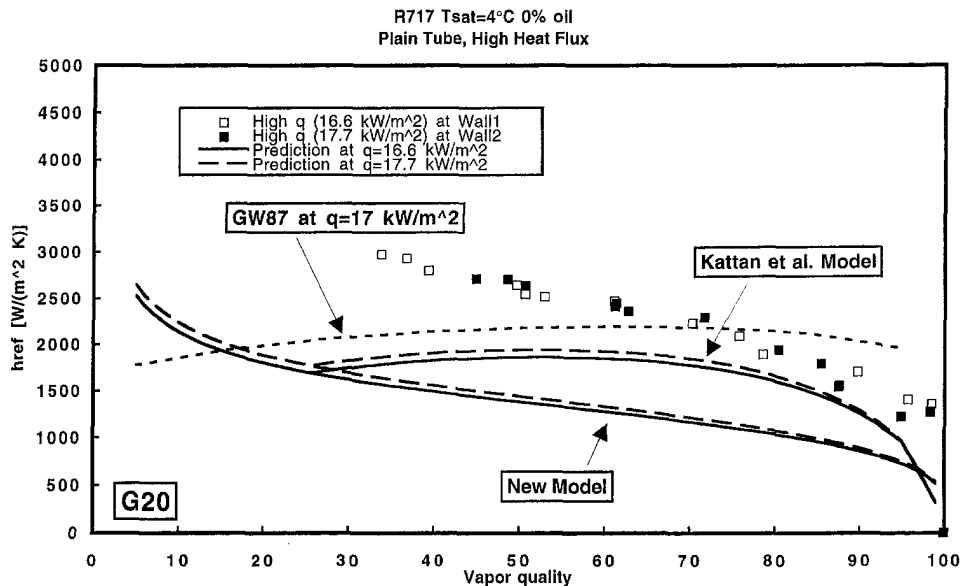
Fig. 12 Flow boiling data at 20 kg/m² s in high heat flux range (Min/Max q in kW/m²: 12.4–21.5 at T Wall 1, 9.69–21.6 at T Wall 2)

$$h_{nb} = 55 \, \text{Pr}^{0.12}(-\log_{10} \text{Pr})^{-0.55} M^{-0.5} q^{0.67}, \qquad (3)$$

where h_{nb} is in W/m² K, P_r is the reduced pressure, M is the fluid molecular weight, and q is the heat flux in W/m². The annular liquid film flow convective boiling heat transfer coefficient h_{cb} and the vapor heat transfer coefficient h_v are formulated as follows, where $C = 0.0133$ and $m = 0.69$ are empirical constants of the turbulent film flow correlation applicable to all fluids and the Dittus-Boelter correlation is used directly for the vapor-phase heat transfer in the tube over the dry perimeter:

$$h_{cb} = C \left(\frac{4G(1-x)\delta}{(1-\alpha)\mu_L} \right)^m \left(\frac{c_{p_L}\mu_L}{k_L} \right)^{0.4} \frac{k_L}{\delta} \qquad (4)$$

$$h_v = 0.023 \left(\frac{G \, x \, D}{\alpha\mu_v} \right)^{0.8} \left(\frac{c_{p_v}\mu_v}{k_v} \right)^{0.4} \frac{k_v}{D}. \qquad (5)$$

The dry angle θ_{dry} represents the perimeter of the tube wall that is dry in stratified flows and for annular flows with partial dryout and is predicted from an expression developed for those conditions; θ_{dry} is zero for annular and intermittent types of flows. The thickness of the annular liquid film δ is determined from the prediction of the local void fraction α using the Rouhani-Axelsson (1970) correlation. For complete details of the heat transfer model and its flow pattern map, refer to Kattan, Thome, and Favrat (1998a, c).

In particular, their five-fluid database showed that existing flow boiling correlations were very inaccurate for predicting fully stratified and stratified-wavy flows that occur at low mass velocities and for annular flow with partial dryout, which occurs at high vapor qualities after the onset of dryout, i.e., after the peak in h_{ref} versus x even though all these older methods predicted the large number of annular flow data to reasonable standard deviations of 12.5–19.5 percent. The new model pre-

R717 Tsat=4°C 0% oil
Plain Tube, High Heat Flux
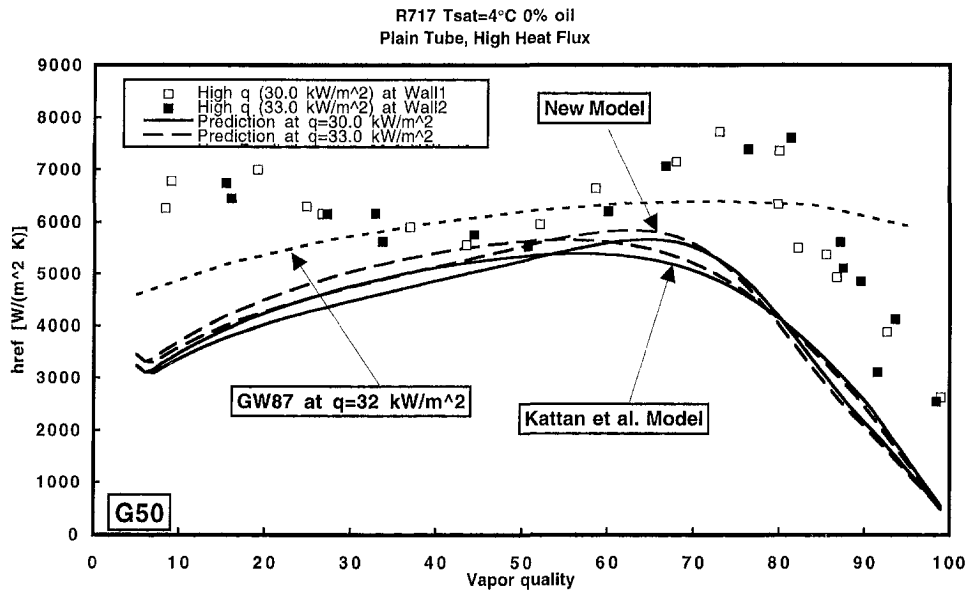
Fig. 13 Flow boiling data at 50 kg/m^2 s in high heat flux range (Min/Max q in kW/m^2: 24.3–32.8 at T Wall 1, 15.0–40.4 at T Wall 2)

R717 Tsat=4°C 0% oil
Plain Tube, High Heat Flux
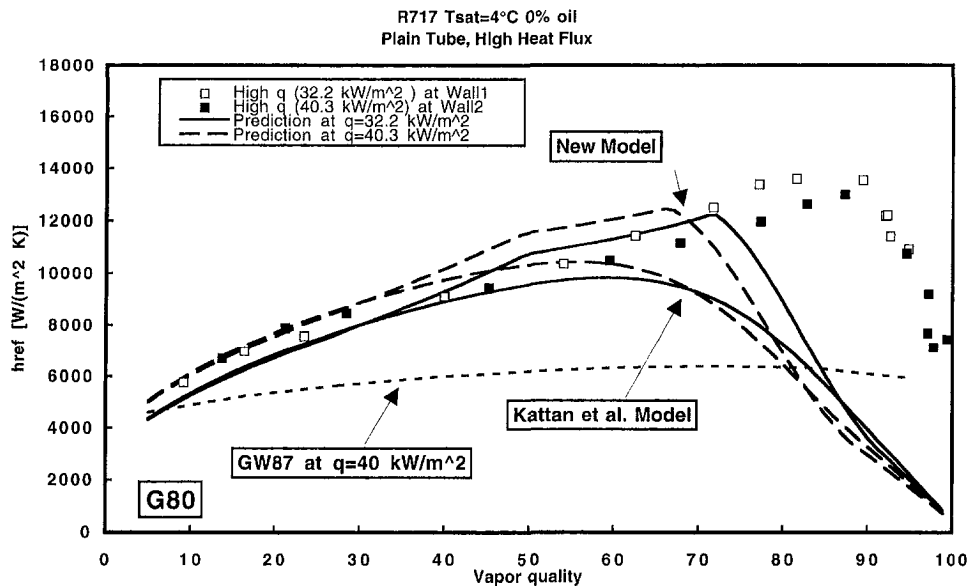
Fig. 14 Flow boiling data at 80 kg/m^2 s in high heat flux range (Min/Max q in kW/m^2: 27.7–35.4 at T Wall 1, 33.8–46.0 at T Wall 2)

dicted stratified-wavy flows as identified by the new flow pattern map to a standard deviation of 19.5 percent compared to 66.8 percent by the Jung (1989) correlation, 36.7 percent by the Shah (1982) correlation, 41.9 percent by the VDI correlation of Steiner (1993), 47.6 percent by the Gungor-Winterton (1986) correlation, and 37.2 percent by the Gungor-Winterton (1987) correlation. For high vapor qualities with $x > 0.85$, the existing methods performed much worse with standard deviations from 84.1–163.1 percent compared to the new model's 26.3 percent, keeping in mind, however, that it is quite difficult to predict these data because the slope in h_{tp} versus x can be very steep after the peak and a one percent error in experimental vapor quality can change h_{ref} by five to ten percent.

The Kattan-Thome-Favrat model had so far only been tested against flow boiling data for $500 \geq G \geq 100$ kg/m^2 s and hence the objective of the present experimental tests was to extend the database to lower mass velocities and thus obtain experimen-

tal heat transfer data in the fully stratified flow regime and more data in the stratified-wavy flow regime to test and further perfect the model. In addition, ammonia is an unusual boiling fluid, having a much higher critical pressure, latent heat, and surface tension and a much smaller liquid density compared to other refrigerants and hydrocarbons, and hence it is desirable to include it in the database.

Figures 3–16 show comparisons of the existing Kattan-Thome-Favrat flow boiling model (labeled as the Kattan et al. model) and the Gungor and Winterton (1987) correlation with its stratified flow correction factor (labeled as GW87 on the graphs) to the current test data. In general the Gungor-Winterton correlation severely overpredicted the low-mass velocity data and underpredicted the high-mass velocity data, while not emulating the trends in the h_{ref} versus x very well. The existing Kattan-Thome-Favrat model worked much better, but still some improvement could be made based on the new flow pattern

R717 Tsat=4°C 0% oil
Plain Tube, High Heat Flux
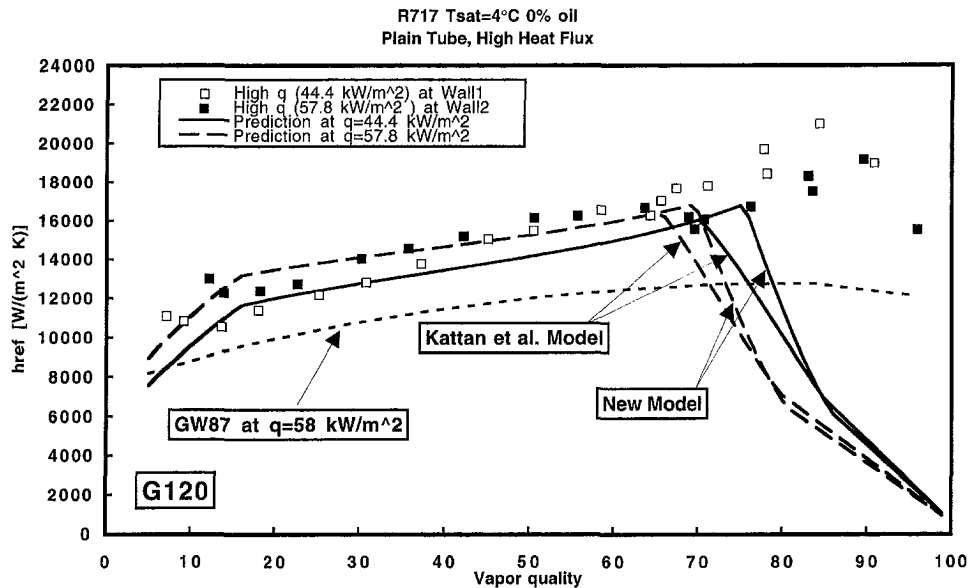
Fig. 15 Flow boiling data at 120 kg/m² s in high heat flux range (Min/Max q in kW/m²: 12.8–49.1 at T Wall 1, 16.8–64.8 at T Wall 2)

R717 Tsat=4°C 0% oil
Plain Tube, High Heat Flux (hot water)
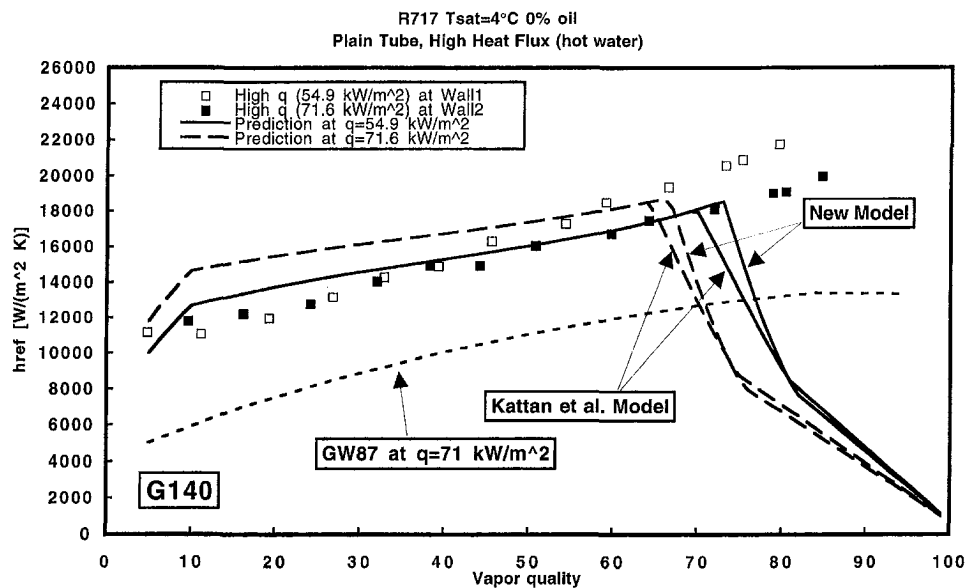
Fig. 16 Flow boiling data at 140 kg/m² s in high heat flux range (Min/Max q in kW/m²: 51.0–59.3 at T Wall 1, 66.1–77.7 at T Wall 2)

observations now available for the first time at $G < 100$ kg/m² s to improve the map.

The existing map is shown in Fig. 17 with the transition boundaries between flow patterns depicted as black lines where I refers to intermittent flow, A refers to annular flow, SW refers to stratified-wavy flow, and S refers to fully stratified flow (the mist flow and bubbly flow regimes occur at mass velocities above 200 kg/m² s and are not shown here). The map is a modified Taitel-Dukler-Steiner flow pattern map that has been inverted to a G versus x format rather than the hard to read (and use) original log-log version, with several other improvements as discussed in Kattan, Thome, and Favrat (1998a), including the prediction of onset of dryout and its effect on the transition boundary from annular to stratified-wavy flow at high vapor qualities (note: annular flow with partial dryout at the top of the tube is classified as stratified-wavy flow on the map). Hence, for the existing map's boundaries, an adiabatic condition

($q = 0$) and a diabatic condition ($q = 13.18$ kW/m²) are shown to illustrate the effect of heat flux of onset of dryout, a boundary which ideally should coincide with the experimental peaks in h_{ref} versus x for annular flow heat transfer data, such as in Fig. 8. All the equations for the transition boundaries are provided in their (1998a) paper. The map is calculated for the particular tube diameter, the particular fluid with its properties at the saturation temperature of interest and the chosen heat flux to produce a map specifically for the conditions being considered (note: PC's are now on every desktop so the flow pattern map is easily generated graphically for convenient use as a research and design tool).

In particular, the transition between between stratified and stratified-wavy flow was found to be too low based on flow pattern observations at $G20$ which were in the fully stratified regime. Hence, the G_{strat} boundary equation was modified empirically by adding the additional term of $20x$ as follows:
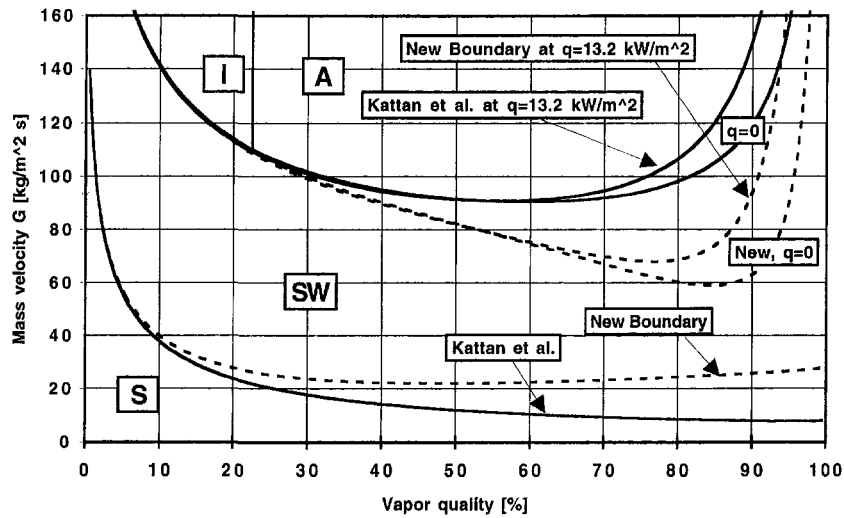
Fig. 17 Predicted flow pattern map for ammonia in a 14.0-mm diameter tube at 4°C

G_{strat}

$$= \left\{ \frac{(226.3)^2 A_{Ld} A_{vd}^2 \rho_v (\rho_L - \rho_v) \mu_L g \cos \varphi}{x^2 (1 - x) \pi^3} \right\}^{1/3} + 20x \quad (6)$$

where G_{strat} is in kg/m^2 s. For a horizontal tube the angle φ is 0 deg such that cos $\varphi = 1.0$. In addition, the transition from stratified-wavy flow to annular flow at high vapor qualities was observed from the new flow pattern data to be too high, which had also been noted earlier in some previous tests with other refrigerants as well. Hence, an additional empirical term has been added to the G_{wavy} equation

$$G_{\text{wavy}} = \left\{ \frac{16 A_{vd}^3 g D \rho_L \rho_v}{x^2 \pi^2 (1 - (2h_{Ld} - 1)^2)^{0.5}} \left[\frac{\pi^2}{25 h_{Ld}^2} \right. \right.$$

$$\left. \left. (1 - x)^{F_1(q)} \left(\frac{\text{We}}{\text{Fr}} \right)_L^{F_2(q)} \right] \right\}^{0.5} + 50 \quad (7)$$

to take this into account with an exponential factor as

$$G_{\text{wavy(new)}} = G_{\text{wavy}} - 75 e^{-[(x^2 - 0.97)^2/x(1-x)]} \quad (8)$$

that has $G_{\text{wavy(new)}}$ in kg/m^2 s and where

$$\left(\frac{\text{We}}{\text{Fr}} \right)_L = \frac{g D^2 \rho_L}{\sigma_L} . \quad (9)$$

The new modifications are shown in Fig. 17 as dashed lines for the new G_{wavy} boundary (at q of 0.0 and 13.18 W/m^2) and the new G_{strat} boundary. Utilizing the new modified flow pattern map, the existing Kattan-Thome-Favrat flow boiling model was again applied to the test conditions, which also are depicted in Figs. 3–16 labeled as the New Model. The movement of these boundaries has an effect on the dry angle calculation θ_{dry} and also tends to move the vapor quality location of the onset of dryout to higher values. It can be seen that the model performs considerably better. Refer to Kattan, Thome, and Favrat (1998a) for complete details of their flow pattern map and flow transition equations.

In Fig. 3 the stratified flow heat transfer data are predicted very accurately for vapor qualities greater than 25 percent, although those at low vapor quality are still not and more work is required to improve the model and the flow pattern map at

low vapor qualities. In Figs. 5, 6, and 7 the peaks in h_{ref} versus x are now well predicted. At $G80$ in Fig. 8, the flow is now correctly modelled as annular from 52 percent vapor quality up to the peak. For $G120$ in Fig. 9 the annular flow data before the peak are now accurately predicted, while for $G140$ in Fig. 11 the location of the peak is now identified and the one data point after the peak is well predicted. For the higher heat flux tests, at $G20$ in Fig. 12 the stronger effect of nucleate boiling still needs to be taken into account in the flow pattern map since it apparently increases the height of the stratified liquid layer and hence wets more of the perimeter, i.e., the adiabatic boundary condition requires a diabatic correction for nucleate boiling. For the other higher flow rates in Figs. 14–16 it can be noted that the annular flow data are accurately modeled but the heat flux effect on the onset of dryout is too strong (the expressions for the parameters $F1(q)$ and $F2(q)$ in Eq. (7)) and moves the location of the predicted peak in h_{ref} versus x too far to the left; the original data used to determine the heat flux correction to this curve in Kattan, Thome, and Favrat (1998c) only had a few values above 20 kW/m^2 and applying it to the present high heat flux conditions represents an extrapolation of the method. For example, based on the large number of new ammonia data at high heat fluxes, this heat flux effect should be relaxed to about one-half its leftward horizontal travel from the $q = 0$ curve in Fig. 17; this would mean that the predicted location of the onset of dryout would move to higher vapor qualities, such that the annular flow heat transfer prediction curves would extend up through these h_{ref} data at high G and high q at high x in Figs. 14–16 and the location of the peaks would be more correctly identified.

6 Comparison of Flow Boiling Model to Independent Data

The Kattan-Thome-Favrat model with its modified flow pattern map has also been compared to the ammonia flow boiling data of Chaddock and Buzzard (1986) in Fig. 18 for a similar size steel tube (13.39-mm internal diameter) obtained at lower pressures, albeit for an electrically heated test section operating at saturation temperatures of $-34.4°$C ($G16.3$), $-26.1°$C ($G32.6$), $-21.8°$C ($G65.2$), and $-21.6°$C ($G130.5$), all for $q = 12.6$ kW/m^2. At 16.3 kg/m^2 s, the model very accurately predicts their whole range of data from 2–92 percent vapor quality, where the flow pattern map identified all these data points as falling in the fully stratified flow regime. The $G32.6$
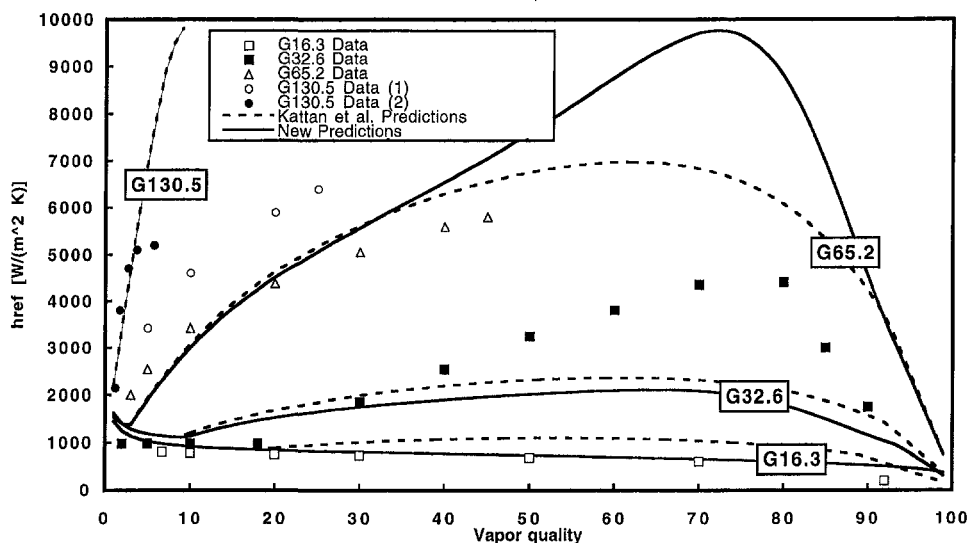
Fig. 18 Comparison of flow boiling predictions to Chaddock and Buzzard (1986) ammonia data

data are accurately predicted at the lower vapor qualities but the large magnitude peak in h_{ref} versus x was not expected for this stratified-wavy flow regime. The $G65.2$ heat transfer data were all identified to be in the stratified-wavy flow regime, almost reaching the annular flow threshold at 47 percent vapor quality, and these data are accurately predicted. At the highest mass velocity of 130.5 kg/m^2 s, their two data sets did not agree with one another, one of which is accurately predicted by the flow boiling model at low vapor quality. Thus, the model has been shown to work quite well for these other independently obtained test data for ammonia. Figures 4 and 13 depict less accurate agreement between the heat transfer model and test data than for the other conditions shown in the other figures, probably from the limitation of the wetting model that assumes a linear variation in the value of θ_{dry} from a value of 0 deg at the annular-to-stratified wavy flow transition boundary to the maximum value of θ_{strat} at the fully stratified flow transition boundary.

Ammonia (like water) as a boiling fluid is a severe test for most boiling models and correlations claiming to be general methods, even those for nucleate pool boiling. Hence, the Kattan-Thome-Favrat model with minor modifications to its flow pattern map has been demonstrated to yield a very reasonable and accurate representation of the ammonia flow boiling data measured here for most of the test conditions covered. In addition, the model originally developed from copper tube data was successfully applied to a new stainless steel tube test section without modification (and the Chaddock and Buzzard steel tube), which proves that a special correction factor to handle stainless steel tubes is not required as proposed by Kandlikar (1990) for his correlation.

7 Summary

- Local flow boiling heat transfer coefficients were measured for ammonia over a wide range of mass velocities, vapor qualities, and heat fluxes in a plain tube at a saturation temperature of 4°C (4.97 bar).
- The Kattan-Thome-Favrat flow pattern map was modified empirically for use with ammonia, based on the new flow pattern observations made during the evaporation tests, while the Kattan-Thome-Favrat heat transfer model was utilized without changes.
- The existing flow boiling model of Kattan-Thome-Favrat using the modified map predicted the present ammonia flow

boiling data for the most part quite accurately as well as the independent ammonia data of Chaddock and Buzzard (1986). Yet more work is required to improve the flow pattern map's predictions for the onset of dryout and the heat transfer model's accuracy at low vapor qualities.

- The Gungor-Winterton (1987) was not very satisfactory for predicting flow boiling coefficients of ammonia, which, however, was not a fluid represented in the database used for its development.

Acknowledgments

References

Chaddock, J., and Buzzard, G., 1986, "Film Coefficients for In-Tube Percentages of Mineral Oil," *ASHRAE Trans.*, Vol. 92, Part 1A, pp. 22–40.

Collier, J. G., and Thome, J. R., 1994, *Convective Boiling and Condensation*, 3rd Ed., Oxford University Press, Oxford, UK.

Cooper, M. K., 1984, "Saturated Nucleate Pool Boiling: A Simple Correlation," *1st U.S. National Heat Transfer Conference*, Vol. 2, pp. 785–793.

Gungor, K. E., and Winterton, R. H. S., 1986, "A General Correlation for Flow Boiling in Tubes and Annuli," *Int. J. Heat Mass Transfer*, Vol. 29, pp. 351–358.

Gungor, K. E., and Winterton, R. H. S., 1987, "Simplified General Correlation for Saturated Flow Boiling and Comparisons of Correlations with Data," *Chem. Eng. Res. Des.*, Vol. 65, pp. 148–156.

Jung, D. S., McLinden, M., Radermacher, R., Didion, D., 1989, "A Study of Flow Boiling Heat Transfer with Refrigerant Mixtures," *Int. J. Heat Mass Transfer*, Vol. 32, No. 9, pp. 1751–1764.

Kandlikar, S. G., 1990, "A General Correlation of Saturated Two-Phase Flow Boiling Heat Transfer Inside Horizontal and Vertical Tubes," ASME JOURNAL OF HEAT TRANSFER, Vol. 112, pp. 219–228.

Kattan, N., Thome, J. R., and Favrat, D., 1998a, "Flow Boiling in Horizontal Tubes, Part 1: Development of a Diabatic Two-Phase Flow Pattern Map," ASME JOURNAL OF HEAT TRANSFER, Vol. 120, pp. 140–147.

Kattan, N., Thome, J. R., and Favrat, D., 1998b, "Flow Boiling in Horizontal Tubes, Part 2: New Heat Transfer Data for Five Refrigerants," ASME JOURNAL OF HEAT TRANSFER, Vol. 120, pp. 148–155.

Kattan, N., Thome, J. R., and Favrat, D., 1998c, "Flow Boiling in Horizontal Tubes, Part 3: Development of a New Heat Transfer Model Based on Flow Patterns," ASME JOURNAL OF HEAT TRANSFER, Vol. 120, pp. 156–165.

Nidegger, E., Thome, J. R., and Favrat, D., 1997, "Flow Boiling and Pressure Drop Measurements for R-134a/Oil Mixtures, Part 1: Evaporation in a Microfin Tube," *HVAC&R Research*, ASHRAE, Vol. 3, No. 1, pp. 38–53.

Rouhani, Z., and Axelsson, E., 1970, "Calculation of Volume Void Fraction in the Subcooled and Quality Region," *Int. J. Heat Mass Transfer*, Vol. 13, pp. 383–393.

Shah, M. M., 1975, "Visual Observations in an Ammonia Evaporator," *ASHRAE Trans.*, Vol. 81, Part 1, pp. 295–306.

Shah, M. M., 1982, "Chart Correlation for Saturated Boiling Heat Transfer: Equations and Further Study," *ASHRAE Trans.,* Vol. 88, Part 1, pp. 185–196.

Steiner, D., 1993, "Heat Transfer to Boiling Saturated Liquids," *VDI-Wärmeatlas (VDI Heat Atlas),* Editor: Verein Deutscher Ingenieure, VDI-Gessellschaft Verfahrenstechnik und Chemie-ingenieurwesen (GCV), Translator: J. W. Fullarton, Düsseldorf.

Thome, J. R., 1996, "Boiling of New Refrigerants: A State-of-the-Art Review," *Int. J. Refrig.,* Vol. 19, No. 7, pp. 435–457.

Zürcher, O., Thome, J. R., and Favrat, D., 1997a, "Prediction of Two-Phase Flow Patterns for Evaporation of Refrigerant R-407C inside Horizontal Tubes," Convective Flow and Pool Boiling Conference, Klöster Irsee, Germany, May 18–23, Paper IX–1.

Zürcher, O., Thome, J. R., and Favrat, D., 1997b, "Intube Flow Boiling of R-407C and R-407C/Oil Mixtures—Part II: Plain Tube Results and Predictions," *J. HVAC&R Research,* ASHRAE, Vol. 4, No. 4, pp. 373–399.

R. Hopkins

A. Faghri
Fellow ASME

D. Khrustalev[1]

Department of Mechanical Engineering,
University of Connecticut,
Storrs, CT 06269-3139

Flat Miniature Heat Pipes With Micro Capillary Grooves

Flat miniature heat pipes (FMHP's) are shown to be very promising in the cooling of electronic component systems. This investigation presents a detailed experimental and theoretical analysis on maximum heat transfer capabilities of two copper-water FMHP's with diagonal trapezoidal micro capillary grooves and one copper-water FMHP with axial rectangular micro capillary grooves. Maximum heat flux on the evaporator wall of the 120-mm long axial grooved heat pipe, with a vapor channel cross-sectional area of approximately 1.5×12 mm^2 and rectangular grooves of dimensions 0.20 mm wide by 0.42 mm deep, exceeded 90 W/cm^2 in the horizontal orientation and 150 W/cm^2 in the vertical orientation. Theoretical prediction of the capillary limitation in the horizontal orientation agreed reasonably well with the experimental data.

1 Introduction

Flat miniature heat pipes are an emerging technology in the cooling of high heat flux electronic devices such as computer chips and thyristors. Jacobs and Hartnett (1991) predicted that chip heat fluxes in mainframe computers will exceed 100 W/cm^2 by the year 2000. Cao et al. (1996) noted that heat fluxes generated by metal oxide semiconductor controlled thyristors are already in the range of 100 W/cm^2 to 300 W/cm^2. North and Avedisian (1993) also investigated heat pipes for cooling high flux/power semiconductors or chips. Many other miniature heat pipe applications exist such as cooling of very thin leading edges of turbine stator vanes and bioengineering reactors used in the separation of biological material. Industrial applications of FMHP's are restricted due to several heat pipe performance limitations (Cao and Faghri, 1993; Faghri, 1995). Most critical of these is the capillary limitation which is the limit of the pumping ability of the capillary structure to provide enough liquid return to the evaporator and is characterized by an increase in the maximum heat flow rate with operating temperature. Boiling limitation can also occur for high-heat-flux applications in which boiling of the working fluid in the wick may form a vapor blanket on the evaporator inner surface and prevent it from being rewetted with returning liquid flow. Boiling limitation usually occurs at elevated operating temperatures and is characterized by a decrease in maximum heat flow rate with an increase in operating temperature (Khrustalev and Faghri, 1995). Consideration of the heat flux restrictions should be made based on FMHP experimental data and corresponding theoretical predictions.

Plesch et al. (1991) performed a limited investigation of copper-water heat pipes with overall dimensions of 7 mm $\times$ 2 mm $\times$ 120 mm with a series of 80 axial rectangular capillary grooves (0.12 mm wide and 0.24 mm deep) machined on the inner surface. Power was uniformly applied to both wide evaporator walls over a surface area of 2 cm^2 and removed at the condenser by a constant temperature (42°C) coolant flow. A maximum heat flux was found of 35 W/cm^2 in the horizontal orientation and 60 W/cm^2 in the vertical orientation where the condenser was above the evaporator.

Cao et al. (1996) tested a 82-mm long copper-water miniature heat pipe with overall dimensions similar to the Plesch et al. (1991) heat pipe. The capillary structure consisted of a series of axial rectangular grooves (0.1 mm wide by 0.25 mm deep) along the entire inner perimeter of the heat pipe and the vapor passage cross-sectional area was approximately 4 mm^2. Maximum heat flux obtained was restricted by the capillary limit and reached 18.3 W/cm^2 with a positive inclination angle of 20°.

Khrustalev and Faghri (1995) developed a one-dimensional model describing the fluid flow and heat and mass transfer in a miniature axial rectangular grooved heat pipe to predict the maximum heat transfer restricted by both capillary limitation and incipience of nucleate boiling. Their model showed reasonably good agreement with limited experimental data of Plesch et al. (1991), however, the existing experimental data were not sufficient for a more profound understanding of FMHP performance limitations. Therefore, it was the objective of this investigation to extensively manufacture, experimentally investigate and theoretically model a variety of flat miniature heat pipes. In particular the experimental investigation will mainly seek out the maximum heat flow rates and heat fluxes that can be applied uniformly to the evaporator wall for a range of operating temperatures, orientations and heating configurations. The predictive model is developed to predict the capillary limitation of all investigated flat miniature heat pipes while a closed-form solution of the predictive model is also included for the limiting case of axial rectangular grooved flat miniature heat pipes.

2 Experimental Investigation

Steady-state performance characteristics of three individual copper-water FMHP's have been experimentally investigated for horizontal and vertical orientations using similar experimental techniques and assumptions discussed in Faghri (1995). The detailed experimental investigation determined the maximum heat flow rates and heat fluxes that can be applied to the evaporator wall for a range of operating temperatures and heating configurations.

Geometrical parameters of the three experimental copper-water FMHP's are given in Fig. 1 for their respective cross sections. Other relevant specifications of all the flat miniature heat pipes such as section lengths and working fluid amounts are given in Table 1. The capillary structures of two of the flat miniature heat pipes (FMHP's #1 and #2) are micro trapezoidal capillary grooves that were at a slight angle to the longitudinal axis of the heat pipe (see Table 1) while FMHP#3 contained rectangular axial grooves.

Copyright © 1999 by ASME

(a) FMHP#1, α = 4°

(b) FMHP#2, α = 18°
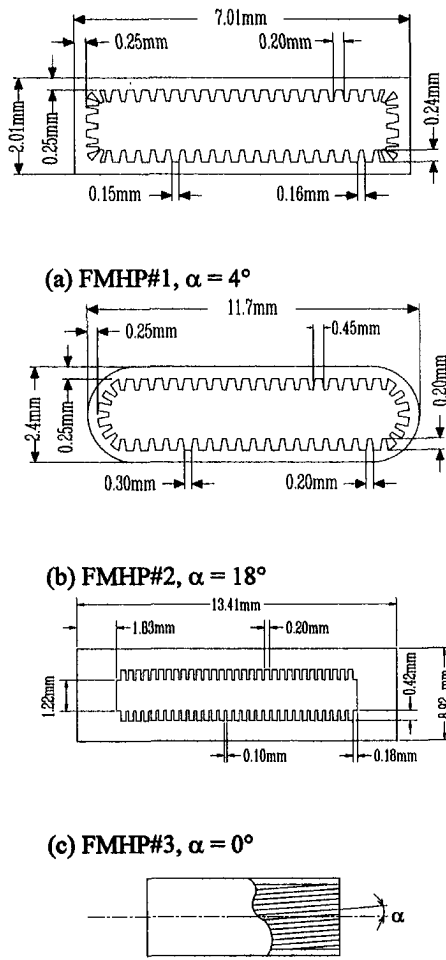
(c) FMHP#3, α = 0°

(d) top view

Fig. 1 Schematic cross sections of experimental flat miniature heat pipes: (a) FMHP#1, (b) FMHP#2, (c) FMHP#3, (d) angle between groove axis and heat pipe centerline

Table 1 Flat miniature heat pipe experimental configurations

	FMHP#1	FMHP#2	FMHP#3
Groove Depth (mm)	0.24	0.20	0.42
Groove Top Width (mm)	0.20	0.45	0.20
Groove Bottom Width (mm)	0.15	0.30	0.20
Fin Top Width (mm)	0.16	0.20	0.10
Total number of grooves	52	50	62
Angle between grooves and heat pipe axis (deg)	4	18	0
Liquid Fill	0.20 ml	20% of volume	0.84 ml
Evaporator Length (mm)	15.6	9.6	15.6
Adiabatic Length (mm)	70.0	56.0	70.0
Condenser Length (mm)	34.4	34.4	34.4
Evaporator Thermocouple Locations (mm)	(3 TC's) 1, 7.8, 14.6	(2 TC's) 2.0, 10.0	(3 TC's) 4.5, 7.3, 10.1
Adiabatic Thermocouple Locations (mm)	(2 TC's) 36.6, 64.6	(2 TC's) 29.0, 48.0	(2 TC's) 37.9, 61.2
Condenser Thermocouple Locations (mm)	(3 TC's) 86.6, 102.8, 119.0	(2 TC's) 67.0, 99.0	(3 TC's) 84.6, 101.8 119.0
Thermocouple mounting method	Clamped to heated side or soldered to thin side	Clamped to heated side	Embedded at corner

Copper-water FMHP's #1 and #2, where the cross-sectional geometry is shown by Figs. 1(a) and 1(b), respectively, were manufactured with trapezoidal micro capillary grooves at a slight angle to the heat pipes longitudinal axis. The capillary groove structure of FMHP's #1 and #2 were manufactured by a rolling method and charged with working fluid by a conventional boiling off method. FMHP#1 and FMHP#2 were, respectively, manufactured by the Furukawa Electric Company and Fujikura, Ltd. with quoted liquid fill amounts of 0.20 ml and 20 percent of interior volume. All other relevant geometric parameters of FMHP#1 and FMHP#2 are provided in Table 1.

Copper-water FMHP#3 was manufactured at The University of Connecticut with an axial and rectangular micro capillary groove structure (0.2 mm wide by 0.42 mm deep). Manufacturing of FMHP#3 began with the capillary grooves being machined by a high-speed dicing saw employing a circular carbon steel blade with high diamond content. The heat pipe body was manufactured in two symmetric halves by this procedure and joined together by a low temperature silver solder. Outer rectangular dimensions of FMHP#3 were relatively large at 8.92 mm × 13.41 mm with a length of 120.65 mm and a wall thickness of 1.83 to 3.43 mm. FMHP#3 was charged with 0.84 ml of water (not including liquid in the filling tubes) which was deter-

─────── **Nomenclature** ───────

D_h = hydraulic diameter (m)
f_l = friction coefficient of the liquid flow
f_{lo} = friction coefficient of the liquid flow with no liquid-vapor interaction
g = gravity constant (m/s^2)
h_{fg} = latent heat of vaporization (J/kg)
L = length (m)
N = number of grooves
p = pressure (N/m^2)
$Q(z)$ = axial heat flow through heat pipe cross section (W)
Q_a = total heat load (W)
q = heat flux (W/m^2)
R = thermal resistance, $(T_e - T_c)/Q$ (K/W)
R_m = meniscus radius of curvature (m)
Re = axial Reynolds number, $\bar{w}D_h^l\rho/\mu$
T = temperature (K)

t_g = equivalent rectangular groove depth (m)
t_t = trapezoidal groove depth (m)
t_v = heat pipe vapor passage thickness (m)
w = axial velocity (m/s)
$\bar{w}$ = mean axial velocity (m/s)
W = equivalent rectangular half-width of trapezoidal groove (m)
W_t = trapezoidal groove half-width (m)
z = axial coordinates (m)

Greek Symbols

α = angle between grooves and longitudinal heat pipe axis (deg)
β_v = 1.33, momentum flux coefficient for the laminar vapor flow
γ = half-angle of a groove (deg)
θ_{men} = meniscus contact angle (deg)
θ_0 = minimum meniscus contact angle (deg)

μ = dynamic viscosity (Pa-s)
ρ = density (kg/m^3)
σ = surface tension (N/m)
φ = inclination angle from horizontal (deg)

Subscripts

a = adiabatic
c = condenser
e = evaporator
l = liquid
men = meniscus
min = minimum
max = maximum
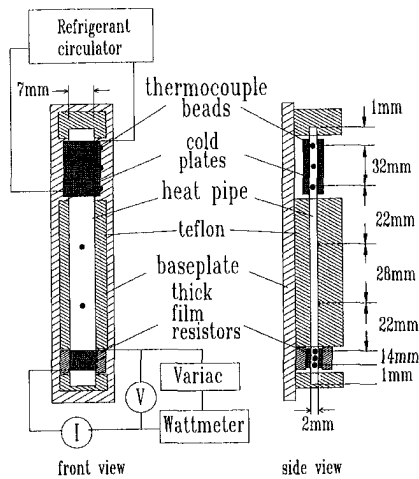v = vapor
ver = vertical
w = wall

Fig. 2 Schematic of flat miniature heat pipe test apparatus (shown here for FMHP#1)

mined by the weighting method after the investigation was completed. It should be noted that the total volume of the axial grooves was approximately 0.63 ml and therefore some surplus liquid existed in the heat pipe. Slight overfill of FMHP#3 was unavoidable since introduction of a determined exact amount is difficult on these small scales. Sufficient fill criteria for FMHP#3 was therefore defined as the fill ratio that produced a sufficiently small temperature drop in the condenser during normal heat pipe operation which signified that the condenser was not blocked with excess liquid.

Experimental Setup. A simple but effective experimental setup was employed for the investigation of flat miniature heat pipes as shown for the case of FMHP#1 in Fig. 2. Slight physical modifications were made for the investigation of the other two heat pipes and are shown in Table 1, which provides a detailed list of the physical attributes of the individual miniature heat pipes. The heat pipe testing apparatus was mounted to a rigid flat stainless steel base plate that contained threaded legs set in each corner which allowed for precise horizontal adjustment of the rigid base plate and flat miniature heat pipes. Nine precisely machined Teflon blocks (±0.05 mm) encased the FMHP's which were configured and designed to provide three functions that included a level base support, insulation for the heat pipe and, in some special cases, a clamping device for the thermocouple-heat pipe contact. A shallow groove was machined along the length of the bottom blocks in order to hold and align the miniature heat pipes in a flat orientation parallel to the rigid baseplate. Six Type "T" copper-constantan (36 gage) thermocouples were soldered to the narrow side surface of FMHP#1 while two thermocouples were also clamped to the wide wall in the adiabatic section as shown in Fig. 2. Heat was applied to the evaporator by two thick film resistors placed on either wide side of the heat pipe. Each resistor had an effective heating area of 0.7 cm^2 and was held in place at the evaporator by a simple Teflon clamp. Contact resistance at the resistor-wall interface was reduced by applying an Omegatherm 101 high thermal conductive paste. The resistors were wired in parallel (when both resistors were powered) and powered by a 0–140 volt variable AC transformer. A pair of Keithley 197A multimeters were used to determine and record the power supplied to the resistors. The first multimeter was used to measure voltage across the resistors and had an accuracy of 0.006 percent of true voltage while the second measured the AC current and had an accuracy of 0.8 percent of true AC current. Actual power input to the heat pipe was adjusted by subtracting experimentally determined heat losses to the environment. The heat losses were found by applying a series of small heat loads to the

evaporator of the heat pipe, with cold plates removed and condenser insulated, and determining the average steady-state adiabatic temperature. Heat losses to the environment of a functioning heat pipe were than closely approximated (less than one percent) versus operating temperature. Heat was removed by copper cold plates clamped by Teflon elements to both wide sides of the heat pipes condenser section as shown in Fig. 2. Contact resistance at the cold plate/heat pipe wall interface was reduced by applying Omegatherm 101 high thermal conductive paste. Coolant was pumped through the cold plates from a Lauda RM-20S constant temperature refrigerator/circulator that was adjusted for every evaporator power setting in order to maintain a constant temperature in the adiabatic section of the heat pipe. Thermocouples were connected to a Fluke 2285B datalogger and were calibrated against the Lauda RM-20S constant temperature liquid bath to an accuracy of 0.3°C. FMHP#2 differed from FMHP#1 in that it was outfitted with six Type "T" thermocouples clamped to the outer wide surface instead of soldered to the thin side walls. This technique was considered valid after repeatability data were taken with FMHP#1 with thermocouples soldered or clamped. The temperatures recorded along FMHP#1 were very similar (±0.2°C) for both methods and therefore confidence was gained that the correct temperatures were obtained using either technique. FMHP#3 was fitted with eight thermocouples: Three thermocouples were placed in the evaporator, two in the adiabatic, and three in the condenser section. These thermocouples were mounted differently to take advantage of the thick walls by embedding the thermocouples in the copper at one corner of the outer rectangular body. Evaporator temperature, for all three FMHP's, was taken to be the temperature monitored by the first thermocouple at the evaporator end as shown in Fig. 2 while the condenser temperature was taken to be the temperature recorded by the last thermocouple located near the end of the condenser section. The flat miniature heat pipe operating temperature was taken to be the average temperature of the thermocouple readings in the adiabatic zone. Additional thermocouples in the evaporator and condenser sections were used to complete the observation of the temperature distribution along the heat pipe axis.

Experimental Procedure. Experimental investigation of the flat miniature heat pipes was accomplished to find the maximum heat load that could be applied to the evaporator section at operating temperatures of 60°, 70°, 80°, 90°, and 95°C. The maximum heat load was found for the cases where the heat load was applied to both wide sides or to a single wide side in both the horizontal (wide or thin) and vertical orientations. In the process the temperature distribution of the heat pipe along the longitudinal axis was observed and recorded. All experimental data were obtained with a systematic and consistent methodology that is as follows. First, the flat miniature heat pipe was positioned in the proper orientation and a small heat load was applied to the evaporator section by use of the thick film resistors. Secondly, the heat pipe operating temperature, defined as the average adiabatic temperature, was obtained and maintained by adjusting the liquid coolant flow temperature to the copper cold plates. Once the operating temperature was obtained, the system was allowed to reach steady-state over 15–20 minutes. After steady-state was reached, temperature readings at all thermocouples were recorded and power to the evaporator was increased by a small increment. This cycle was repeated until dryout of the heat pipe evaporator was observed which was characterized by a sudden and steady rise of the evaporator temperature. To verify that the experimental results were reliable, a significant portion of all experimental points for the heat pipes maximum heat transport capabilities were repeated with negligible difference.

3 Capillary Limitation Analysis

A one-dimensional model describing the fluid flow in a miniature grooved heat pipe has been used to predict the maximum

heat transfer restricted by capillary limitation. The present model of fluid circulation in a flat miniature heat pipe differs from the axial rectangular grooved heat pipe model of Khrustalev and Faghri (1995) by the following main features:

1 The recession of the liquid-vapor meniscus interface to the groove bottom along the liquid flow in a trapezoidal groove is described by the model.

2 The effective groove length for the liquid flow depends on the angle between the groove structure and the heat pipe axis.

3 A closed-form solution has been included for the limiting case of axial rectangular grooves

Accordingly, the following improvements distinguish this model from that of Khrustalev and Faghri (1995). The first improvement over Khrustalev and Faghri (1995) is that the liquid momentum conservation equation is modified to account for the longer return path of angled grooves compared to axial grooves by introducing $\cos \alpha$ as follows:

$$\frac{d}{dz} (p_l + \rho_l g z \sin \varphi) = \frac{f_l}{\cos \alpha} \frac{2\rho_l \bar{w}_l^2}{D_{h,l}} . \tag{1}$$

It is assumed in Eq. (1) that all axial mass transport of the liquid occurs in the grooves and is a quasi one-dimensional viscous flow. The $\cos \alpha$ term was also introduced in the expression for liquid friction factor-Reynolds number product since there was an angle between the directions of the liquid and vapor flows.

$$(f\,\text{Re})_l = (f\,\text{Re})_{lo}\left\{ 1 + \cos \alpha \, \frac{4NW^3}{3\pi D_{h,v}^3} (f\,\text{Re})_v \frac{\nu_v}{\nu_l} \right.$$
$$\left. \times \left[1 - 1.971 \exp\left(-\frac{\pi t_g}{2W} \right) \right] \right\} \tag{2}$$

where t_g and W are the equivalent rectangular groove depth and half-width of the trapezoidal grooves, as shown in Fig. 3, and $(f\,\text{Re})_{lo}$ corresponds to the case of no liquid-vapor interaction (Schneider and DeVos, 1980; Khrustalev and Faghri, 1995). Other governing equations used in this capillary limitation analysis of flat miniature heat pipes are the mass conservation, conservation of vapor momentum, mass and energy balance, and the Laplace-Young equation which describes the interfacial radius of the meniscus curvature related to the liquid-vapor pressure difference. These governing equations are, respectively, listed as Eqs. (3) through (6) and are discussed in detail along with boundary conditions and numerical procedure in Khrustalev and Faghri (1995) and Hopkins (1996).

$$\bar{w}_v \rho_v A_v = N\bar{w}_l \rho_l A_l \equiv N\dot{m}_l \tag{3}$$

$$\frac{d}{dz} (p_v + \rho_v g z \sin \varphi + \rho_v \beta_v \bar{w}_v^2) = -f_v \frac{2\rho_v \bar{w}_v^2}{D_{h,v}} \tag{4}$$

$$\frac{d}{dz} (\rho_l \bar{w}_l A_l) = \frac{1}{h_{fg} N} \frac{dQ(z)}{dz} \tag{5}$$

$$\frac{dp_l}{dz} = \frac{dp_v}{dz} - \frac{d}{dz} \left(\frac{\sigma}{R_m} \right) \tag{6}$$

The solution of Eqs. (1) through (6), along with others presented in Khrustalev and Faghri (1995) and Hopkins (1996), provides the longitudinal distribution of the meniscus radius $R_m(z)$ and hence the meniscus contact angle $\theta_{men}(z)$, which are related for contact angles of $\theta_{men} \geq \theta_0$ (θ_0 is the minimum contact angle for the working fluid-solid wall interface) by

$$\theta_{men}(z) = \arccos \left[\frac{W}{R_m(z)} \right] - \gamma \tag{7}$$

where γ is the half-angle of the groove as shown in Fig. 3. The

(a) evaporator

(b) condenser
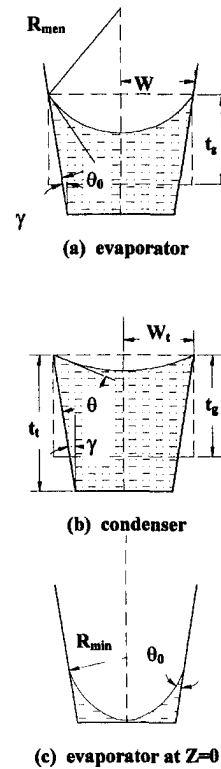
(c) evaporator at Z=0

Fig. 3 Schematic depicting the geometric configuration used in the capillary limitation analysis (a) liquid-vapor meniscus in Region I, (b) liquid-vapor meniscus in Region II, (c) liquid-vapor meniscus at evaporator end cap at Q_{max}

second major improvement over the model of Khrustalev and Faghri (1995) for rectangular grooves, is that there are two intervals of the liquid-vapor meniscus variation along the heat pipe axis with trapezoidal grooves which are shown in Figs. 3(a) and 3(b). Along the first interval, beginning at the evaporator end cap, the meniscus contact angle is constant and at the minimum, $\theta_{men} = \theta_0$, while the meniscus radius varies. In this interval, the meniscus is not attached to the top of the fins and is instead recessed into the groove structure along the z-axis. Along the second interval, usually situated in the condenser zone and the majority of the adiabatic region, the meniscus contact angle, θ_{men}, is larger than θ_0 and varies along the z-axis. Along this interval, the meniscus is attached to the fin top as the condensation process proceeds. For both intervals, the equivalent height of the liquid cross section varies along the liquid flow.

The minimum radius of the liquid-vapor meniscus, shown in Fig. 3(c) as $R_{m,min}$, that can occur along the heat pipe axis (usually at the evaporator end cap) is obtained from the condition that the liquid-vapor interface touches the groove bottom which is geometrically determined as follows:

$$R_{m,min} = \frac{W_t - t_t \tan \gamma}{\cos (\gamma + \theta_0) - \tan \gamma [1 - \sin (\gamma + \theta)]} . \tag{8}$$

$R_{m,min}$, along with other conditions and geometric expressions of the liquid and vapor channels cross-sectional areas and hydraulic diameters, which are fully presented in Hopkins (1996) but not included here, determines the maximum heat transfer through a heat pipe with respect to the capillary limit.

Closed-Form Solution for the Case of Axial ($\alpha = 0$) Rectangular Grooves. For axial rectangular grooves, the system of four ordinary differential equations can be reduced to a single algebraic formula to predict the maximum heat transport capac-

ity, Q_{max}. This reduction can be made based on the following additional simplifying assumptions:

1 There is no first interval in the capillary groove structure. In other words, the meniscus is attached to the top of the fin structure along the full heat pipe axis.

2 The liquid cross-sectional area can be considered constant along the grooves in all expressions.

3 Inertial forces are neglected in the vapor momentum.

4 The length of the fluid circulation path with varying mass flow rate can be substituted by the effective length, L_{eff}, with a constant mass flow rate.

$$L_{eff} = \frac{1}{Q_a} \int_0^{L_t} Q(z)dz \qquad (9)$$

For uniform heat fluxes in the evaporator and condenser sections the effective length is given as the following:

$$L_{eff} = L_e/2 + L_a + L_c/2. \qquad (10)$$

Introducing the liquid and vapor conservation of momentum equations (Eqs. (1) and (4)) and the energy and mass balance equation (Eq. (5)) into the Laplace-Young expression (Eq. (6)) and integrating along the effective length, L_{eff}, the following expression for maximum heat transfer in axial rectangular grooved heat pipes can be found

$$Q_{max} = h_{fg} \left[\frac{\sigma \cos \theta_o}{W L_{eff}} + (\rho_l - \rho_v)g \sin \gamma \right]$$

$$\times \left[(f\,Re)_v \frac{2\mu_v}{D_{h,v}^2 \rho_v A_v} + (f\,Re)_l \frac{2\mu_l}{D_{h,l}^2 \rho_l N A_l} \right]^{-1}. \qquad (11)$$

This closed-form solution is very convenient in the estimation of the maximum heat transport capabilities of axial rectangular grooved flat miniature heat pipes.

4 Results and Discussion

Figure 4 shows the experimentally determined temperatures in the adiabatic section and at the evaporator and condenser end caps of FMHP#3 in horizontal and vertical orientations. The temperature distribution trends of FMHP#1 and FMHP#2 are very similar to FMHP#3 and are not shown here. However, the thermal resistance values discussed below and shown in Fig. 5 allows for easy computation of the approximate temperature drop from evaporator to condenser end cap. It is noted that the temperatures were averaged over 30 readings taken over five minutes to avoid possible errors due to minor temperature fluctuations in the experiment. The temperature distributions shown in Fig. 4 show that the evaporator thermal resistance of FMHP#3 was higher in the vertical orientation while in the horizontal orientation the thermal resistance was higher in the condenser. The higher evaporator thermal resistance in the vertical orientation can be explained by flooding of the evaporator with excess liquid due to gravity. At the heat load of 100 W, FMHP#3 had the total temperature drop from end to end of only 25°C in the horizontal wide orientation.

The effective end cap to end cap thermal resistance of the three FMHP's are shown in Fig. 5 for various orientations where the heat load is applied to both sides. Effective end cap to end cap thermal resistance, R, is defined here as the overall end cap to end cap temperature drop divided by the total applied heat load, Q_a.

$$R = (T_e - T_c)/Q_a \qquad (8)$$

A common characteristic of all thermal resistances presented here is that the thermal resistance of the FMHP's is high at low heat loads as a relatively thick liquid film resides in the evaporator. However, this thermal resistance decreases rapidly
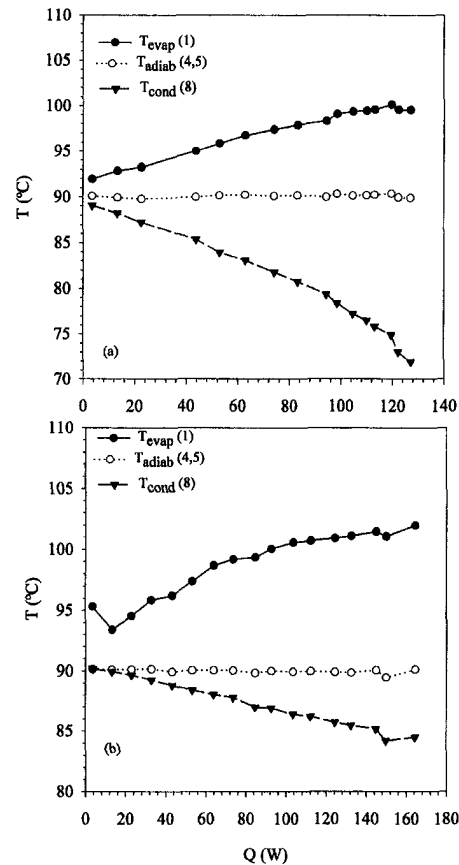
Fig. 4 Temperature distribution along the outer surface of FMHP#3 versus total heat load applied from both sides in (a) horizontal wide at T_V = 90°C; (b) vertical at T_V = 90°C

to its minimum value as the applied uniform heat load is increased. Overall, FMHP#1 was found to have an approximate minimal thermal resistance of 0.5 K/W while FMHP#2 operated with a minimal thermal resistance of 0.3 K/W. FMHP#3 was found to have the minimal thermal resistance of 0.2 K/W for all investigated heat pipes. It should be noted that the thermal resistance is a function of the heated and cooled surface areas in the evaporator and condenser sections, respectively, and was found to be independent of the heat pipe operating temperature.

Figures 6 through 9 present the experimental maximum heat flow rate and maximum heat flux of all flat miniature heat pipes in the range of operating temperature of T_v = 60°C to 95°C. Q_{max} was defined to occur when the evaporator temperature, and hence the end cap to end cap thermal resistance, began to rise unboundedly. All heat flow rates presented have an uncertainty of less than 1 W which included equipment and experimental errors with a 95 percent confidence level. Figures 6 and 7 present the maximum heat flow rate and maximum heat flux of FMHP's #1 and #2. Figure 6(a) presents the results of FMHP#1 when the heat load was applied uniformly to both wide sides of the heat pipe. The dotted lines with symbols indicate the experimental data for the horizontal wide (where the heat pipe was positioned with the heat load applied from the bottom and top of the evaporator), horizontal thin (where the heat pipe was positioned with the heat load applied to wide vertical sides) and vertical orientation where the condenser was above the evaporator. FMHP#1 showed a maximum heat flux of 11.5 W/cm² in the horizontal wide orientation and 18.8 W/cm² in the horizontal thin orientation at T_v = 95°C. A maximum heat flux of 63.0 W/cm² at T_v = 95°C was obtained in the vertical orientation for FMHP#1 with both wide sides subjected to the heat load. The solid and dashed lines without symbols in Fig. 6(a)

Fig. 5 Effective thermal resistance of the flat miniature heat pipes at operating temperature of $T_V = 90°C$ in the (a) horizontal wide orientation and (b) vertical orientation. The heat load is applied to both sides.

show the theoretical prediction results obtained by these efforts for minimum meniscus contact angles of 33 and zero degrees, respectively. While the difference between these two cases is small for trapezoidal grooves, it is sig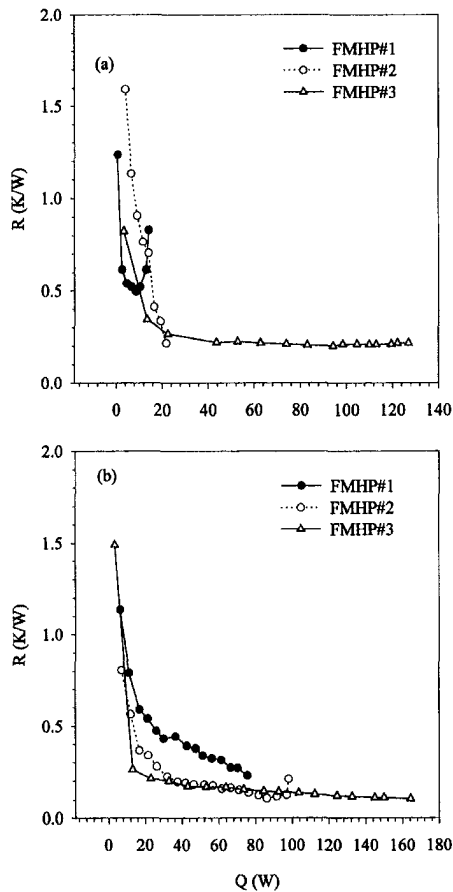nificant for rectangular grooves as will be demonstrated for FMHP#3. Figure 7 presents the maximum heat load and heat flux results for FMHP#1 when the heat load was applied to a single wide side. The maximum heat flux obtained in this orientation was approximately 37.0 W/cm² in the horizontal orientation and 113.2 W/cm² in the vertical orientation. No significant difference was observed in the maximum heat flux between the two horizontal orientations for the single side case unlike for the situation when the heat load was applied to both sides. The 60 percent increase in maximum heat flux for FMHP#1 obtained in the two horizontal orientations when the heat load was applied to both sides may have been caused by a overfill of working fluid. In the horizontal thin orientation, excess liquid may have pooled at the evaporator end cap on the inner thin surface where no heat load was applied providing more liquid for the evaporative heat transfer process through capillary forces through the angled grooves that wrapped around the full inner perimeter of the heat pipe. This would not occur as easily in the horizontal wide orientation since the excess liquid would pool on an inner surface directly subjected to the heat load. For the single heated side case, the excess liquid pooling mechanism cannot be effective because of the higher heat fluxes, which would initiate film boiling in the pool. Figures 6(a) and 7 both show a consistent increase in maximum heat flux with increase in operating temperature. Therefore, for FMHP#1, it was determined that capillary limitation was the controlling heat transfer mechanism in all orientations.

Figure 6(b) presents the experimental maximum heat flow rate and maximum heat flux of FMHP#2 with a heat load applied uniformly to both wide sides where the dashed lines with symbols signify the experimental results. The maximum heat flux found for this heating configuration was 17.3 W/cm² in the horizontal wide orientation and 21.5 W/cm² in the horizontal thin orientation at an operating temperature of $T_v = 95°C$. Once again, a slight increase in the maximum heat flux (20 percent) occurs between the two horizontal orientations possibly due to a slight working fluid overfill of the heat pipe. FMHP#2 in the vertical orientation had a maximum heat flux at $T_v = 95°C$ of 77.2 W/cm² when both wide sides were heated. Performance of FMHP#2 was restricted by the capillary limit in all orientations when heat was applied to both wide sides since the maximum heat flux consistently increased with operating temperature. The predicted values of maximum heat flux in the horizontal orientation found from the capillary limitation analysis are presented as the solid line in Fig. 6(b). Figure 8(a) presents the maximum heat flux obtained for FMHP#2 when heated from a single wide side in the vertical orientation while Fig. 8(b) presents maximum heat load and heat flux results for various horizontal orientations when the heat load was applied to a single wide side. In the vertical orientation the maximum heat flux occurs at an operating temperature of $T_v = 80°C$ and is 120.4 W/cm² while at higher operating temperatures, the maximum heat flux falls to approximately 112.0 W/cm². This signifies for the lower operating temperatures, up to and including $T_v = 80°C$ that the controlling heat transfer mechanism is the capillary limit. However, at higher operating temperatures and respective higher heat fluxes, the boiling limitation becomes the controlling heat transfer mechanism. The maximum heat flux in various horizontal orientations with the
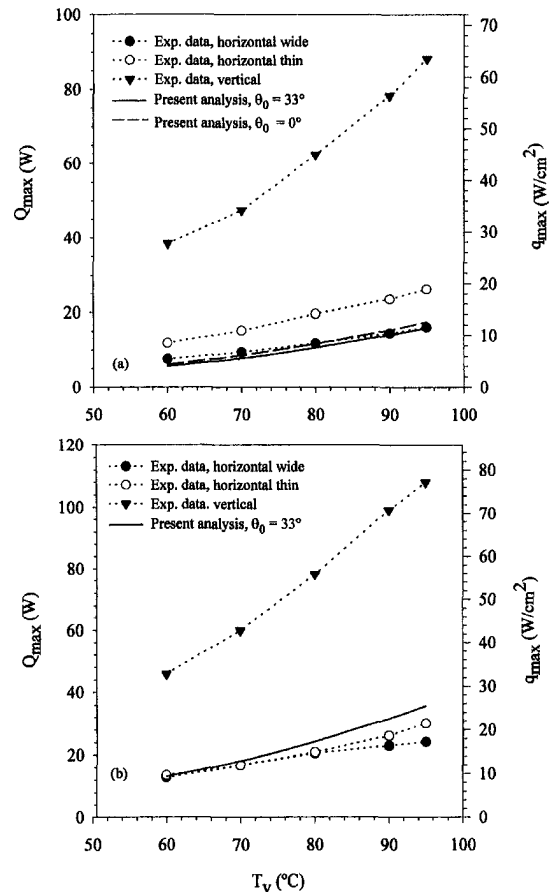

Fig. 6 Maximum heat transfer of (a) FMHP#1 and (b) FMHP#2 heated from both sides in various orientations
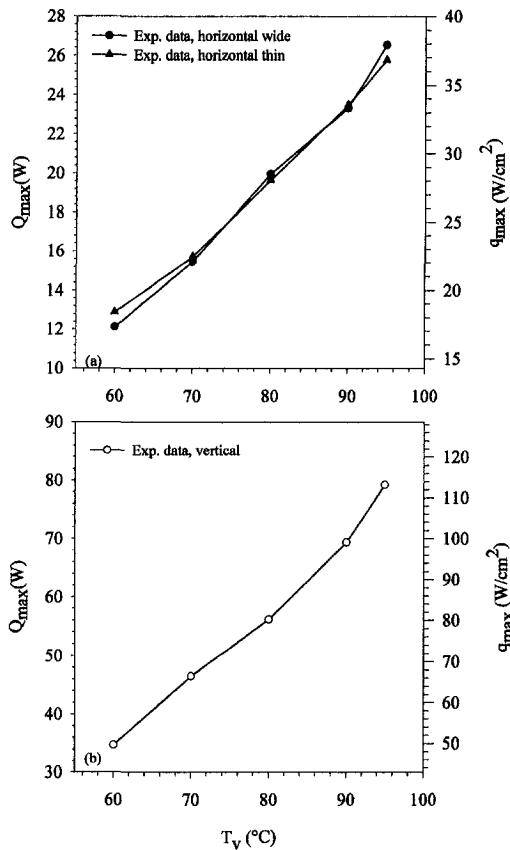
Fig. 7 Maximum heat transfer of FMHP#1 heated from one side in (a) horizontal and (b) vertical orientations

heat load applied to a single side is restricted by the capillary limit and is approximately 40.5 W/cm^2 at an operating temperature of $T_v = 95°C$.

Figure 9(a) presents the experimental maximum heat flow rate and heat flux of FMHP#3 in various orientations over the operating temperature range of $T_v = 60°C$ to $95°C$ when the heat load is applied to both wide sides. Maximum heat flux obtained for FMHP#3 in the horizontal orientation with an uniform heat load applied to both sides was found to be 92.8 W/cm^2. In the vertical orientation, the maximum heat flux occurred at an operating temperature of $T_v = 90°C$ and was 141.8 W/cm^2 and than decreased for an operating temperature of $T_v = 95°C$. Therefore, it was determined that the capillary limitation was the controlling mechanism for FMHP#3 in the horizontal orientation with a heat load applied to both sides and in the vertical orientation up to the operating temperature of $T_v = 90°C$. FMHP#3 was then restricted by the boiling limit in the vertical orientation for operating temperatures above $T_v = 90°C$ when the heat load was applied to both wide sides. Theoretical prediction results for the maximum heat flux in the horizontal orientation are also presented by the dotted and dashed lines based on different minimum meniscus contact angles of zero and 33 degrees. The theoretical values under predicted the experimental results by as much as 35 percent. This is believed to be caused by a significant overfill of working fluid which would increase the experimental results in the gravity field due to liquid pooling effects. The predictive results indicate that a decrease in the minimum contact angle increases the maximum heat flow rate. Contact angles below the minimal values for a given working fluid-wall combination are possible due to surface microroughness. Khrustalev and Faghri (1997) noted that thick liquid films can appear attached to the liquid-vapor meniscus at high heat fluxes. This phenomenon results in the interface curvature equal to that of zero contact angle. For zero contact

angle, the agreement between the dotted theoretical curve and experimental results is better. The question of contact angle effects on maximum heat flux should be further investigated for high-heat-flux miniature heat pipes. The other two theoretical curves in Fig. 9(a) are for the closed-form solutions of zero and 33-degree contact angle which over predict the capillary limitation analysis by approximately ten percent due to the four assumptions discussed above.

Figure 9(b) presents the maximum heat flux obtained with FMHP#3 when the heat load is applied to a single side. In the vertical orientation, a maximum heat flux of approximately 155.0 W/cm^2 was obtained at an operating temperature of $T_v = 70°C$ and $90°C$. Therefore, it is determined that the boiling limit is the critical heat transfer mechanism for all operating temperatures above $T_v = 70°C$ in the vertical orientation. A maximum heat flux of approximately 160 W/cm^2 was obtained for FMHP#3 in the horizontal orientation with the heat load applied to a single wide side for an operating temperature of $T = 90°C$. The maximum heat flux then drops off significantly to approximately 130 W/cm^2 at the operating temperature of $T_v = 95°C$ signifying that the boiling limitation restricts heat pipe performance above $T_v = 90°C$. FMHP#3 in the horizontal wide orientation with the heat load applied to the top of the FMHP provided a maximum heat flux of 154.6 W/cm^2 at the operating temperature of $T_v = 95°C$. It should be noted here that the concept of boiling limit traditionally used in heat pipes can have different meanings for gravity-assisted heat pipes (Fig. 9(a)) and for those operating in zero-gravity environment. For the zero-gravity case, incipience of nucleate boiling can be considered a limitation. A gravity-assisted heat pipe can perform with vapor bubbles forming in the evaporator provided that they can exit the capillary structure. In this case, transition to film boiling is a more likely limitation. This film boiling limitation is as-
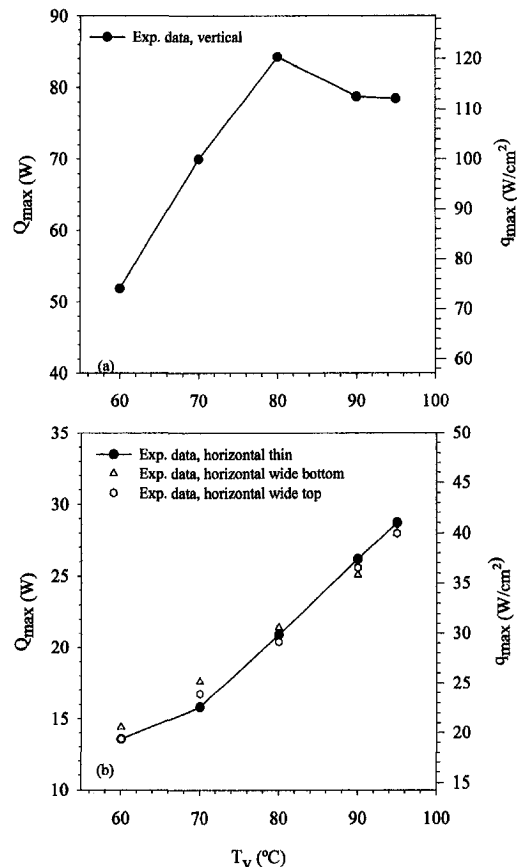

Fig. 8 Maximum heat transfer of FMHP#2 heated from one side in (a) vertical and (b) horizontal orientations
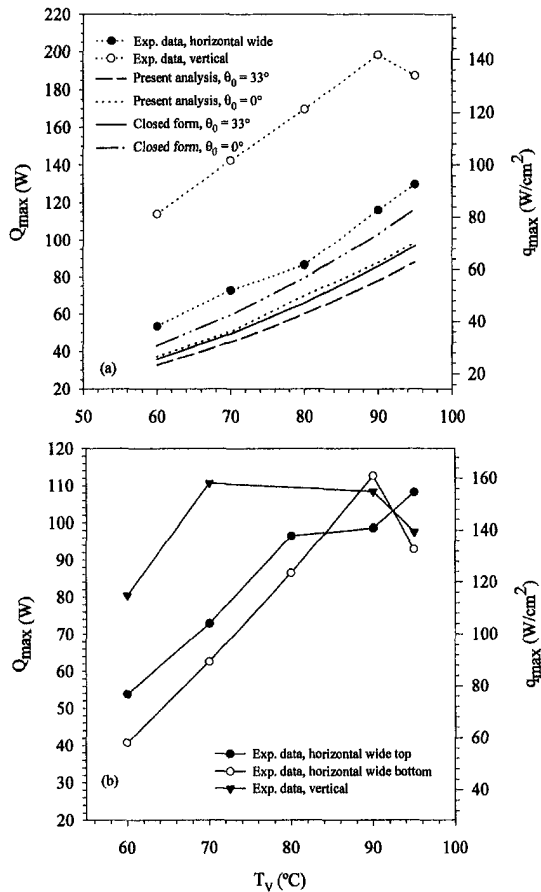
Fig. 9 Maximum heat transfer of FMHP#3 heated in vertical and horizontal orientations from (a) both sides and (b) one side

sumed to be the most important one for the results shown in Fig. 9(b) for higher operating temperatures.

5 Conclusions

Three flat miniature heat pipes were experimentally investigated and theoretically modeled for maximum heat flow rates and heat flux for a range of operating temperatures. The temperature distribution along the heat pipes longitudinal axis and the corresponding thermal resistance were also observed.

FMHP#3 produced the highest obtainable heat flow rate and flux in all orientations in the gravity field. It is concluded from this that flat miniature heat pipes with deep and narrow axial capillary grooves and thicker walls are much more promising

than flat miniature heat pipes with shallower trapezoidal grooves and thin walls. The majority of the experimental data showed that the controlling mechanism of the maximum uniform heat flux at the evaporator was the capillary limitation. However, especially in the vertical orientation, the maximum heat load applied to FMHP#2 and #3 was restricted by the boiling limitation at higher operating temperatures.

A theoretical prediction of the maximum heat transfer was also carried out to compare to the experimental data. Results were good for FMHP#1 and #2 and were reasonable for FMHP#3. However, both experimental results and theoretical predictions undeniably signify that flat miniature heat pipes with a micro capillary groove structure demonstrate excellent performance characteristics and are very promising in the cooling of miniature electronic components with high heat fluxes.

References

Cao, Y., Beam, J. E., and Donovan, B., 1996, "Air-Cooling System for Metal Oxide Semiconductor Controlled Thyristors Employing Miniature Heat Pipes," Journal of Thermophysics and Heat Transfer, Vol. 10, No. 3, pp. 484–489.

Cao, Y., and Faghri, A., 1994, "Micro/Miniature Heat Pipes and Operating Limitations," Journal of Enhanced Heat Transfer, Vol. 1, No. 3, pp. 265–274.

Faghri, A., 1995, Heat Pipe Science and Technology, Taylor & Francis, London.

Hopkins, R., 1996, "Flat Miniature Heat Sinks and Heat Pipes with Micro Capillary Grooves: Manufacturing, Modeling and Experimental Study," Masters thesis, The University of Connecticut, Storrs, CT.

Jacobs, H. R., and Hartnett, J. P., 1991, "Thermal Engineering: Emerging Technologies and Critical Phenomena," Workshop Report, NSF Grant No. CTS-91-04006, pp. 139–176.

Khrustalev, D., and Faghri, A., 1995, "Thermal Characteristics of Conventional and Flat Miniature Axially-Grooved Heat Pipes," ASME JOURNAL OF HEAT TRANSFER, Vol. 117, pp. 1048–1054.

Khrustalev, D., and Faghri, A., 1997, "Thick-Film Phenomenon During High-Heat-Flux Evaporation From Cylindrical Pores," ASME JOURNAL OF HEAT TRANSFER, Vol. 119, pp. 272–278.

North, M. T., and Avedisian, C. T., 1993, "Heat Pipes for Cooling High Flux/High Power Semiconductor Chips," ASME J. Elect. Pack., Vol. 115, pp. 112–117.

Plesch, D., Bier, W., Seidel, D., and Schubert, K., 1991, "Miniature Heat Pipes for Heat Removal From Microelectronic Circuits," Proc. ASME Annual Meeting, Atlanta, GA.

Schneider, G. E., and DeVos, R., 1980, "Nondimensional Analysis for the Heat Transport Capability of Axially-Grooved Heat Pipes Including Liquid/Vapor Interaction," AIAA Paper, No. 80-0214.

Experimental Study of Turbulent Flow Heat Transfer and Pressure Drop in a Plate Heat Exchanger With Chevron Plates

A. Muley[1]
Assoc. Mem. ASME

R. M. Manglik[2]
Mem. ASME

Department of Mechanical, Industrial
and Nuclear Engineering,
University of Cincinnati,
Cincinnati, OH 45221-0072

Experimental heat transfer and isothermal pressure drop data for single-phase water flows in a plate heat exchanger (PHE) with chevron plates are presented. In a single-pass U-type counterflow PHE, three different chevron plate arrangements are considered: two symmetric plate arrangements with $\beta = 30$ deg/30 deg and 60 deg/ 60 deg, and one mixed-plate arrangement with $\beta = 30$ deg/60 deg. For water ($2 < Pr < 6$) flow rates in the $600 < Re < 10^4$ regime, data for Nu and f are presented. The results show significant effects of both the chevron angle β and surface area enlargement factor ϕ. As β increases, and compared to a flat-plate pack, up to two to five times higher Nu are obtained; the concomitant f, however, are 13 to 44 times higher. Increasing ϕ also has a similar, though smaller effect. Based on experimental data for $Re \geq 1000$ and 30 deg $\leq \beta \leq 60$ deg, predictive correlations of the form $Nu = C_1(\beta)D_1(\phi) Re^{p1(\beta)} Pr^{1/3}(\mu/\mu_w)^{0.14}$ and $f = C_2(\beta)D_2(\phi) Re^{p2(\beta)}$ are devised. Finally, at constant pumping power, and depending upon Re, β, and ϕ, the heat transfer is found to be enhanced by up to 2.8 times that in an equivalent flat-plate channel.

Introduction

The plate heat exchanger (PHE) is commonly used for process heating and cooling applications in chemical, food processing, and pharmaceutical industries, among many others. It has found increasing usage in situations where close thermal quality control and mitigation of thermal degradation of end products are primary objectives. The reviews by Shah and Focke (1988), Manglik and Muley (1993), and Manglik (1996) have addressed some aspects of the thermal-hydraulic performance, product development, and design applications of PHEs.

Of the many different types of plate corrugations available (Shah and Focke, 1988), the more commonly used chevron plate pattern is illustrated in Fig. 1. Plates with $\beta = 30$ deg or 60 deg are usually stacked together in either a symmetric or mixed arrangement as shown in Fig. 1(a). The plate surface geometry is characterized by the corrugation inclination angle β, its wavelength λ, amplitude b, and profile (Fig. 1(b)), and the surface enlargement factor ϕ (ratio of effective corrugated surface area to the projected area of the plate). The enhanced heat transfer is directly related to these features, which provide increased effective heat transfer area, disruption and reattachment of boundary layers, swirl or vortex flow generation, and small hydraulic diameter flow channels. Generally both heat transfer coefficients and flow friction losses increase with higher β and ϕ chevron plates (Manglik, 1996).

Several investigators have reported thermal-hydraulic characteristics of chevron plate PHEs (Okada et al., 1972; Marriott, 1977; Focke et al., 1985; Talik et al., 1995a, b; Muley and Manglik, 1995, 1997, 1998; Thonon et al., 1995). The recent survey by Manglik (1996) provides a detailed summary of the available Nu and f correlations for chevron plates. The predictions from most of these equations are observed to disagree considerably with each other and present a rather wide performance envelope (Manglik, 1996). In virtually all studies, separate power-law type curve-fit equations are given for each plate surface with different β that cover a rather limited data set and range of flow conditions. Savostin and Tikhonov (1970), Tovazhnyanski et al. (1980) and Wanniarachchi et al. (1995) have attempted to incorporate β effects into single equations for Nu and f, respectively. However, their equations have different functional forms, with little agreement between their predictions for typical flow conditions and β (Manglik, 1996). The effect of surface enlargement factor ϕ has been largely ignored. This lack of generalized predictive tools inhibits effective usage of chevron plates in many PHE applications.

An experimental investigation of the effects of chevron angle β on the thermal-hydraulic performance of a PHE is reported in this paper. Single-phase turbulent flow[3] of water under cooling conditions is considered. Two symmetric and one mixed chevron plate arrangements, with $\beta = 30$ deg/30 deg, 60 deg/60 deg, and 30 deg/60 deg, respectively, are used. Based on the experimental data and some previously reported results, correlations for Nu and isothermal f are developed that incorporate the influence of β and ϕ along with the Re, Pr, and (μ/μ_w) dependence. Finally, the heat transfer enhancement in these plate arrangements is evaluated.

Experimental Apparatus and Procedure

The experimental apparatus, shown schematically in Fig. 2, consists of two PHEs (a heat source and a heat sink) arranged in series in a closed loop. A variable speed moyno pump circulates the process water stream, which was first heated in one

---

---

[3] In much of the literature, it has been established that chevron corrugations promote early transition to turbulent flow ($400 < Re < 800$), and this issue has been discussed at some length elsewhere (Shah and Focke, 1988; Manglik, 1996; Muley and Manglik, 1997, 1998).
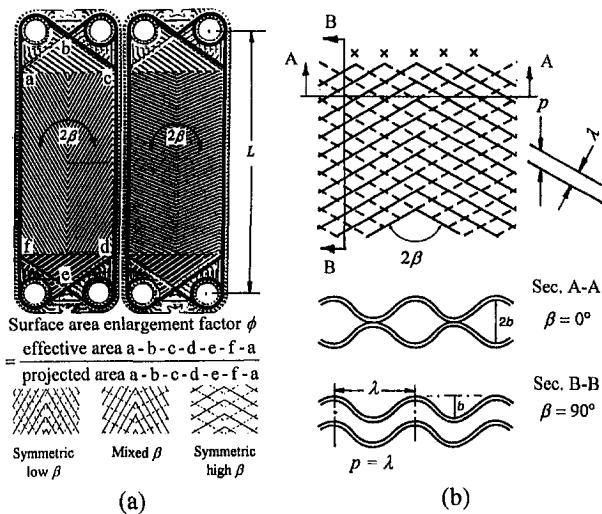
Fig. 1 Chevron plates: (a) different chevron angle plates and their stack arrangements, and (b) geometrical features of plate corrugations

PHE by condensing low-pressure steam and then cooled in the second PHE by means of utility water supply. A micromotion flow meter, differential pressure transducers, and copper-constantan thermocouples, at locations indicated in Fig. 2, provided the primary measurements. The data reported here are for the cooling unit, where a rotameter was used to measure cooling water flow rates. The PHEs and significant portions of the inlet/outlet piping were well insulated to reduce heat losses. Also, static mixers were installed in the outlet ports upstream of the thermocouple probes to ensure accurate "mixed-mean" or bulk temperature measurements. The inlet/outlet thermocouple probes were placed close to the PHE ports in well-insulated pipe sections, and temperature measurements were periodically made by traversing them in the pipe cross section to check and confirm the accuracy of recorded bulk-mean values. All the data were obtained under steady-state conditions (confirmed by unchanging fluid outlet temperatures over a 25 ~ 30 minute period) with close energy balances (less than ± five percent difference between the measured Q for the two fluid streams), and were recorded with a computerized data acquisition system.

The test PHE (cooling unit) was configured in a single-pass U-type (inlet/outlet ports for the two fluid streams on the same end), counterflow arrangement with 12 to 24 chevron plates. Chevron plates made of stainless steel with $\beta = 30$ deg and 60

deg, and $\phi = 1.29$ were used in two symmetric (30 deg/30 deg and 60 deg/60 deg) and one mixed (30 deg/60 deg) arrangements. Measurements for the geometrical details of the plate surface corrugation profiles, which can be represented by a sinusoidal shape, are given in Fig. 3. For all the three plate arrangements, experimental data for Nu and isothermal f were obtained for cooling of hot water ($2 < Pr < 6$) in the turbulent flow regime ($600 < Re < 10^4$). Extended details of the test PHE, plate corrugation measurements, set-up, instrumentation, and operating procedures are given in Muley and Manglik (1998).

Data Reduction. The primary measurements consist of the flow rates of each fluid stream (hot process water and cooling utility water), their inlet and outlet temperatures, and the pressure drop in the process stream between the inlet and outlet of the heat exchanger. The channel flow Reynolds number is based on the equivalent diameter d_e ($=2b$), and all fluid properties were calculated at the bulk mean temperature given by

$$T_{c,b} = (T_{c,i} + T_{c,o})/2; \quad T_{h,b} = (T_{c,b} + \Delta T_{lm}) \quad (1)$$

where, for the two-fluid counterflow arrangement,

$$\Delta T_{lm} = [(T_{h,i} - T_{c,o}) - (T_{h,o} - T_{c,i})]/$$
$$\ln [(T_{h,i} - T_{c,o})/(T_{h,o} - T_{c,i})]. \quad (2)$$

Because the cooling water flow rates were maintained such that $C_c > C_h$ in all the test runs, so as to ensure the process stream provided the dominant thermal resistance, $T_{h,b}$ calculated by Eq. (1) accounts for nonlinear temperature variations of the hot process stream along the length of PHE. The steady-state energy balance on the process and cooling fluids

$$Q = [\dot{m}c_p(T_i - T_o)]_h = [\dot{m}c_p(T_o - T_i)]_c \quad (3)$$

was maintained within ± 5 percent, after accounting for all heat losses, and the average of Q_h and Q_c was taken as the total heat load.

Given the heat load, the overall thermal effectiveness of the heat exchanger is

$$\epsilon = [Q/C_{min}(T_{h,i} - T_{c,i})]. \quad (4)$$

The NTU for the pure counterflow arrangement was calculated as

$$\text{NTU} = [1/(1 - C^*)] \ln [(1 - \epsilon C^*)/(1 - \epsilon)] \quad (5)$$

where $C^* = C_{min}/C_{max}$; for all the test runs in the present experiments $C_h = C_{min}$, and their values range from 1.0 to 7.5

Nomenclature

A_c = channel flow cross section area, m^2
A = actual or effective heat transfer surface area, m^2
b = corrugation depth, mm
C = heat capacity rate, $=\dot{m}c_p$, W/K
c_p = specific heat, J/kg-K
d_e = equivalent diameter, $=2b$, mm
E = frictional pumping power, W/m^2
f = Fanning friction factor, Eq. (11)
h = heat transfer coefficient, W/m^2-K
k = thermal conductivity, W/m-K
L = plate length between ports, m
$\dot{m}$ = mass flow rate, kg/s
N = number of interplate channels
Nu = Nusselt number, $=hd_e/k$
NTU = number of transfer units, Eq. (5)

p_1, p_2 = Reynolds number exponents
Δp = pressure drop, N/m^2
Pr = Prandtl number, $=\mu c_p/k$
Q = heat load, W
Re = Reynolds number, $=\dot{m}d_e/NA_c\mu$
t = plate thickness, mm
ΔT_{lm} = log mean temperature difference, Eq. (2), K
T = temperature, K
U = overall heat transfer coefficient, Eq. (6), W/m^2-K

Greek Symbols

β = corrugation inclination angle relative to flow direction
γ = corrugation profile aspect ratio, $=2b/\lambda$
ϵ = thermal effectiveness, Eq. (4)

λ = wavelength of surface corrugation, Fig. 1(b), mm
μ = dynamic viscosity, kg/m-s
ρ = fluid density, kg/m^3
ϕ = ratio of effective to projected surface area of plate corrugations

Subscripts

b = at bulk fluid temperature
c = cooling water stream
ch = pertaining to chevron plate
h = hot process fluid stream
i = inlet fluid condition
o = outlet fluid condition
pp = pertaining to flat parallel-plate channel
w = at plate wall conditions
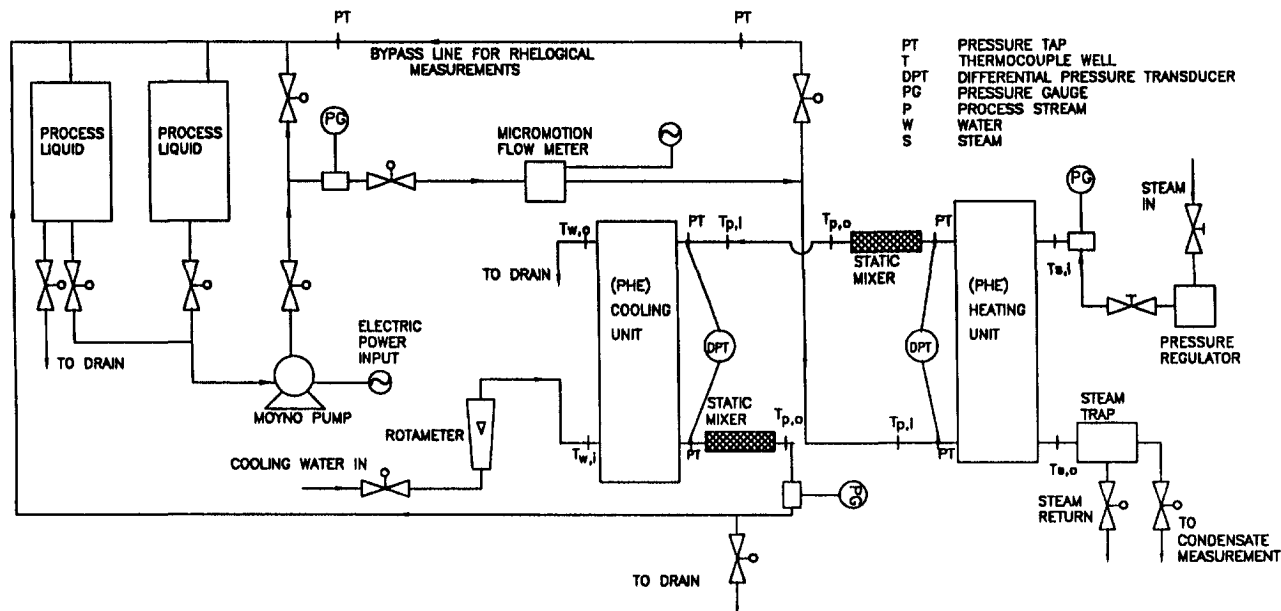
Fig. 2 Schematic of experimental test facility

kW/K. Furthermore, even though only 12 to 24 plates were used in these experiments, the influence of small number of thermal plates on NTU, as suggested by Shah and Focke (1988) was insignificant (less than 0.5 percent). This was so because C^*, $(\epsilon \cdot C^*)$, and $(C^* \cdot \text{NTU})$ values were relatively small in all data sets; the plate effects are significant only when the converse is true (Manglik, 1999). The overall heat transfer coefficient was thus determined from

$$U = (C_{\min}\text{NTU})/A \tag{6}$$

and the heat transfer coefficient for the process fluid stream calculated from the thermal resistance summation

$$(1/Ah_h) = (1/UA) - (t/Ak_{\text{plate}}) - (1/Ah_c). \tag{7}$$

Note that the heat transfer area A is the same on both sides of

Fig. 3 Geometrical characteristics of plate surface corrugations

the plate. However, in order to calculate h_h from Eq. (7), the cooling water side heat transfer coefficient h_c is needed. This was determined from calibration equations that were devised on the basis of extended experiments employing the modified Wilson plot technique, as described in the next subsection. The average wall temperature of the plate was determined iteratively from the heat and resistance balance

$$Q = h_h A(T_b - T_w)_h = (k_w A/t)(T_{w,h} - T_{w,c})$$
$$= h_c A(T_w - T_b)_c. \tag{8}$$

From the measured overall pressure drop across the PHE in the process stream, the core pressure drop can be obtained from

$$\Delta p_{\text{core}} = \Delta p_{\text{measured}} - \Delta p_{\text{port}} - \Delta p_{\text{pipe}}. \tag{9}$$

Here, based on an empirical equation (Shah and Focke, 1988; Kays and London, 1984; Kays, 1950) and the mean port velocity, port losses were estimated by

$$\Delta p_{\text{port}} = 1.5(\rho V_{\text{port}}^2/2). \tag{10}$$

The pressure loss in small pipe sections at the inlet and outlet of the PHE (Δp_{pipe}) was estimated on the basis of smooth tube friction factor and pipe flow velocity. Thus, for the shear loss within the corrugated passages, the Fanning friction factor was calculated as

$$f = \rho d_e \Delta p_{\text{core}}/[2L(\dot{m}/NA_c)^2]. \tag{11}$$

These measurements were made for isothermal conditions, with fluid properties calculated at the mean flow temperature.

Modified Wilson Plot. In order to determine the process fluid heat transfer coefficient from Eq. (7), the cooling water resistance $(1/h_c A)$ needs to be known. For predicting h_c, calibration equations were established for each of the three chevron plate arrangements from data obtained by the modified Wilson plot technique (Shah, 1990; Manglik and Bergles, 1991). This modification of the classical Wilson plot method (Wilson, 1915) essentially incorporates and accounts for variable fluid property effects. Very briefly, on the basis of a power-law type relationship between Nu and Re, Pr, and (μ/μ_w), the resistance balance of Eq. (7) can be expressed as

Fig. 4 Typical modified Wilson plot results for the calibration of cooling water side heat transfer coefficient for β = 30-deg chevron plate

$$
\left[\frac{1}{U} - \left(\frac{t}{k}\right)_w\right]\left[\frac{k}{d_e}\,\mathrm{Re}^a\,\mathrm{Pr}^{1/3}\left(\frac{\mu}{\mu_w}\right)^{0.14}\right]_h = \frac{1}{C'_h}
$$
$$
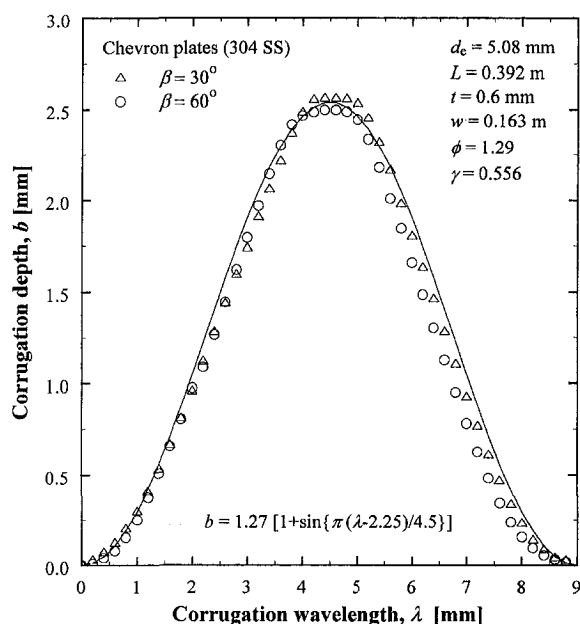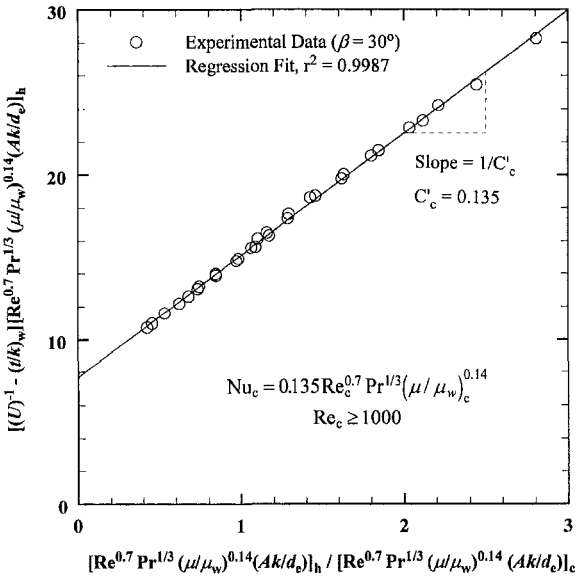+ \frac{1}{C'_c}\left[\frac{k}{d_e}\,\mathrm{Re}^a\,\mathrm{Pr}^{1/3}\left(\frac{\mu}{\mu_w}\right)^{0.14}\right]_h\left[\frac{k}{d_e}\,\mathrm{Re}^a\,\mathrm{Pr}^{1/3}\left(\frac{\mu}{\mu_w}\right)^{0.14}\right]_c^{-1}.
$$

(12)

By acquiring data over an extended range of both cooling water and test fluid flow rates, as per the methodology described in detail by Shah (1990), and Manglik and Bergles (1991), an iterative multiple linear-regression analysis yields the lead coefficients (C'_h, C'_c) and Reynolds exponent (a). Typical results for β = 30 deg/30 deg plates are presented in Fig. 4. Similar results for the other two chevron plate arrangements (β = 60 deg/60 deg and 30 deg/60 deg) can be found in Muley and Manglik (1995, 1998). It may be noted, however, that the cooling water side Nu equation devised in this manner is only a "calibration" equation for the present test facility, valid only over the limited range of Wilson plot data, and should not be considered as a general correlation. In all subsequent experiments, the cooling water side conditions were always maintained within the range of Wilson plot data.

Experimental Uncertainty. For the measurements and derived results presented in this paper, the experimental uncertainties were calculated according to the procedure outlined by Moffat (1988). The maximum errors in the primary measurements of $\dot{m}$, Δp, ΔT_{lm}, and Q were ± 4.1 percent, ± 6.0 percent, ± 4.2 percent, and ± 7.8 percent, respectively, after accounting for errors in both the process and colling water flow streams. Based on this precision and the propagation of error analysis, the maximum uncertainties in Re, f, and Nu were ± 4.2 percent, ± 7.2 percent, and ± 10.4 percent, respectively. Also, as mentioned earlier, for majority of the heat transfer data the energy balance was within ± 5.0 percent. Extended details of the error and uncertainty analyses are given in Muley and Manglik (1998).

Results and Discussion

For cooling of hot water ($2 < \mathrm{Pr} < 6$) flows in the $600 < \mathrm{Re} < 10^4$ range, the experimental Nu data are presented in Fig.

5. They represent two symmetric (β = 30 deg/30 deg and 60 deg/60 deg) and one mixed (β = 30 deg/60 deg) plate arrangements, where the mixed-plate chevron angle can be approximated by $\beta_{\mathrm{avg}} \cong 45$ deg. Also graphed in Fig. 5, are partial predictions for an equivalent flat-plate channel (Kakaç et al., 1987) given by

$$
\mathrm{Nu} = \begin{cases} 1.849(L/d_e)^{-1/3}\,\mathrm{Re}^{1/3}\,\mathrm{Pr}^{1/3}(\mu/\mu_w)^{0.14} \\[4pt] \qquad \mathrm{Re} \leq 2000,\ (L/d_e) = 52.17 \\[4pt] 0.023\,\mathrm{Re}^{0.8}\,\mathrm{Pr}^{1/3}(\mu/\mu_w)^{0.14} \\[4pt] \qquad \mathrm{Re} > 4000. \end{cases}
$$

(13)

The heat transfer enhancement, with two to five times higher Nu than the flat-plate channel, is clearly evident. Higher Nusselt numbers are obtained with increasing β, which reflects the increased intensity of swirl flows generated by the larger β chevron plates. In Fig. 5, the data are also compared with the results of Okada et al. (1972), Focke et al. (1985), and Thonon et al. (1995). The present data are seen to be in good agreement with the results of Okada et al. for all three β arrangements. However, the results of Focke et al., that are based on mass transfer experiments with simulated scaled-up plate surfaces, are more than two times higher for all cases. The Thonon et al. data, on the other hand, are in fair agreement for β = 30 deg, but those for β = 45-deg and 60-deg plates are considerably higher.

These disagreements can perhaps be attributed to, among some other factors, the geometric differences in the chevron plate surface corrugations employed in various studies (Manglik, 1996). These include different shapes of corrugation profiles (Ding and Manglik, 1996), depth b and wavelength λ of the furrows (Okada et al., 1972; Gaiser and Kottke, 1990; Ding and Manglik, 1996), plate surface enlargement factor ϕ (ratio of effective corrugated surface area to its projected area), and flow distribution channel configurations. For example, ϕ = 1.464 in the scaled up surfaces employed by Focke et al. (1985) in their mass transfer studies, as compared with ϕ = 1.29 in the present case. The deeper furrows in the former would tend to induce greater swirl mixing, and hence have higher Nu. Whereas Okada et al. (1972) have employed plates with ϕ = 1.294, and, as such, there is good agreement between their results and present data. The plate surface geometry features have not been reported by Thonon et al. (1995); in fact, few
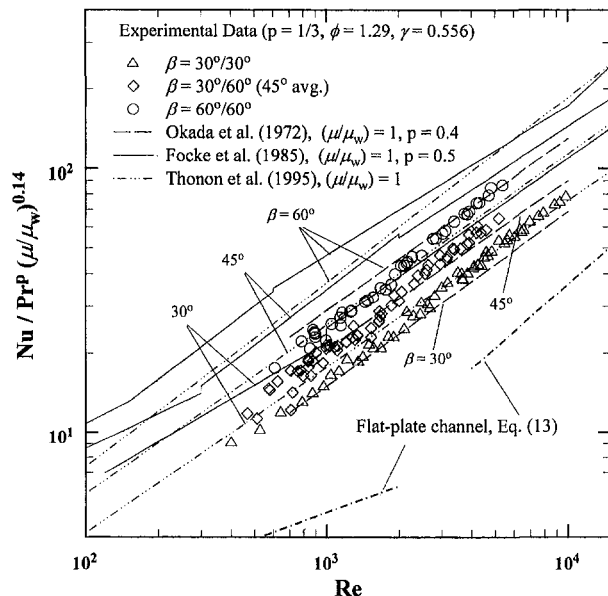

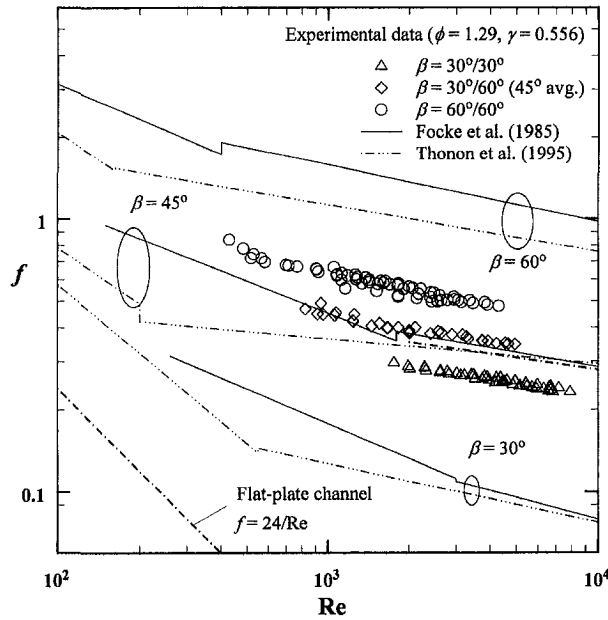**Fig. 5 Variation of Nusselt number with Reynolds number and chevron angle β**

Fig. 6 Variation of isothermal friction factor with Reynolds number and chevron angle β

studies provide these details which makes a meaningful comparison of results rather difficult (Manglik, 1996). Additionally, varying Pr exponent (0.5 and 0.4 in the case of Focke et al. and Okada et al., respectively), and absence of a correction factor for viscosity variations could account for some part of the deviations. In the latter case, as shown by Muley and Manglik (1995, 1997) for typical viscous liquids (Pr ~ 185), a variation of $0.20 < (\mu/\mu_w) < 0.80$ could result in a 3 percent to 20 percent difference in Nu.

The isothermal fanning friction factor data for the three plate arrangements are presented in Fig. 6. Here, the equivalent flat-plate f are predicted from (Kakaç et al., 1987)

$$ f = \begin{cases} 24/\text{Re} & \text{Re} \le 2000 \\ 0.1268 \text{ Re}^{-0.3} & \text{Re} > 2000. \end{cases} \qquad (14) $$

While the chevron plate surface corrugations promote higher heat transfer coefficients (Fig. 5), there is a higher pressure drop penalty as well (Fig. 6). The friction factors are 13 to 44 times higher than those for the flat-plate channel. As would be expected, the swirling fluid motion in the interplate channel results in greater flow friction, which increases with β. The comparison of the experimental f data with results of Thonon et al. (1995) and Focke et al. (1985) in Fig. 6, reveals much larger differences than those observed for the heat transfer. Though there is reasonable agreement between the Thonon et al. and Focke et al. results for $\beta = 45$ deg/45 deg with the experimental data ($\beta = 30$ deg/60 deg, $\beta_{avg} = 45$ deg), their f for $\beta = 30$ deg and 60 deg are significantly different. Typically, the Thonon et al. results for $\beta = 30$ deg are as much as 2.9 times lower, and two times higher for $\beta = 60$ deg; a similar trend is displayed by the Focke et al. results. Given that neither Focke et al. nor Thonon et al. have compared their own results with anything else in the literature, and few details of surface geometry and experimental data reduction are reported, it is difficult to explain these differences.

It is evident from the foregoing that, apart from flow and fluid property parameters, Nu and f are significantly influenced by β. The chevron corrugations also trigger early transition to turbulent flow, and various investigators have documented critical Re values ranging from 400 to 800 (Shah and Focke, 1988;

Manglik and Muley, 1993). In any event, as shown in Muley and Manglik (1997, 1998) Re $\geq$ 1000 essentially characterizes turbulent flow. Regression analyses of the present data with Re $\geq$ 1000 reveal that their trends can be represented by the following functional form:

$$ \text{Nu} = C_1(\beta) \text{ Re}^{p1(\beta)} \text{ Pr}^{1/3}(\mu/\mu_w)^{0.14}, $$

$$ f = C_2(\beta) \text{ Re}^{p2(\beta)}. \qquad (15) $$

In the power-law expression for Nu, the Pr exponent was taken as one-third and the classical Sieder and Tate (1936) viscosity ratio correction factor was used, which is consistent with much of the literature (Manglik 1996; Manglik and Bergles, 1998). Whether the complex interplate channel geometry would dictate different exponents remains to be ascertained; in any event, this would be a second-order refinement. Also, both the lead coefficients [$C_1(\beta)$ and $C_2(\beta)$] and Re exponents [$p1(\beta)$ and $p2(\beta)$] are functions of β. These are found to be described by second-order polynomials and trigonometric functions of β, respectively (Muley and Manglik, 1998). As seen in Fig. 7 from a comparison with some other results cited in the literature (Tovazhnyanski et al., 1980; Focke et al., 1985; Heavner et al., 1993; Thonon et al., 1995), and given the earlier discussion on the differences in the results, these expressions describe the Re exponents in most cases rather well. Here the Re exponents for the two limiting cases of interplate channels ($\beta = 0$ deg and 90 deg) were taken as 0.7 and 0.25 for Nu and f, respectively; such values have been used in the literature for turbulent flows in several other noncircular channels (Kakaç et al., 1987). Thus, the experimental data for Re $\geq$ 1000, 30 deg $\le \beta \le$ 60 deg, and $\phi = 1.29$ can be correlated as

$$ \text{Nu} = [0.2668 - 0.006967\beta + 7.244 \times 10^{-5}\beta^2] $$
$$ \times \text{Re}^{[0.728+0.0543\sin[(\pi\beta/45)+3.7]} \text{ Pr}^{1/3}(\mu/\mu_w)^{0.14} \qquad (16) $$

and

$$ f = [2.917 - 0.1277\beta + 2.016 \times 10^{-3}\beta^2] $$
$$ \times \text{Re}^{-[0.2+0.0577\sin[(\pi\beta/45)+2.1]}. \qquad (17) $$

Comparisons of the predictions from Eqs. (16) and (17) with
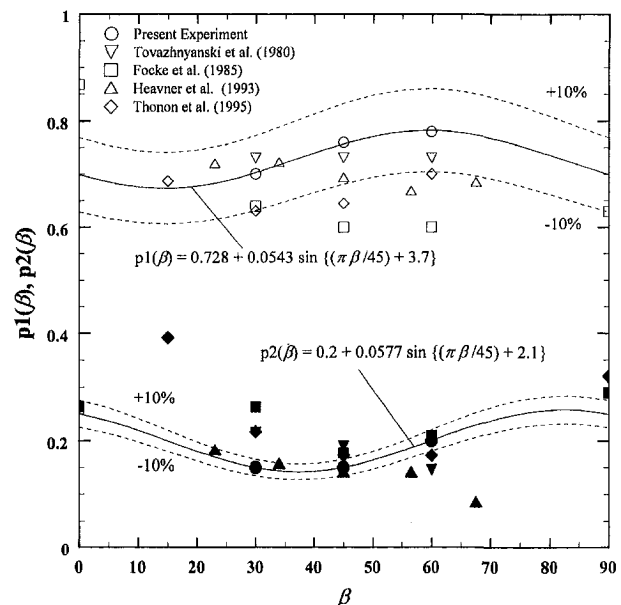
Fig. 7 Correlation of the effect of β on the Re exponent in the power-law representation of Nu and f data
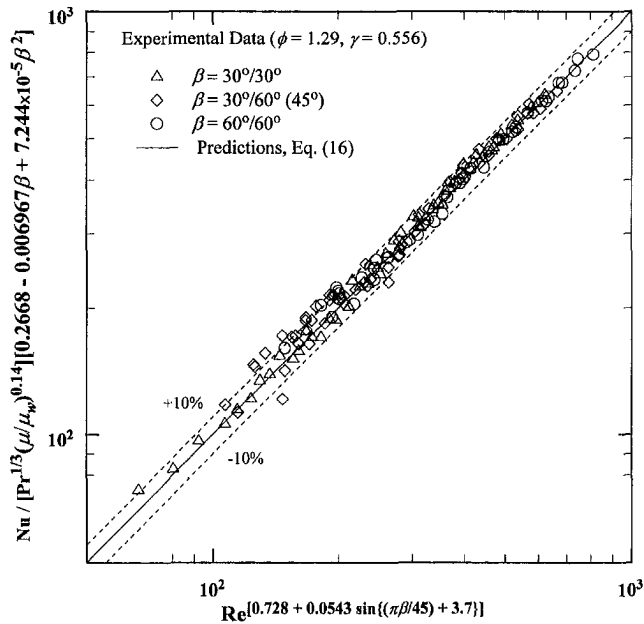
Fig. 8 Comparison of predictions and experimental data for the effect of chevron angle β on Nu in turbulent flows (Re $\geq$ 1000)

the Nu and f data, respectively, are presented in Figs. 8 and 9, and the excellent agreement between the two (within $\pm$10 percent and $\pm$5 percent error bands, respectively) is clearly evident.

Besides the corrugation inclination angle β, the area enlargement factor ϕ also has an influence, and higher heat transfer and pressure drop are obtained with increasing ϕ; deeper corrugations increase the effective surface area as well as promote greater swirl mixing. To extend the applicability of Eqs. (16) and (17), which are limited to $\phi = 1.29$, the present results are correlated with those given in the literature for different ϕ values. This is depicted in Fig. 10, where the normalized Nu and f data for the three chevron plate arrangements are graphed along with the results of Okada et al. (1972), Tovazhnyanski et al. (1980), Focke et al. (1985), and Heavner et al. (1993). As seen from this figure, the effects of ϕ can be represented
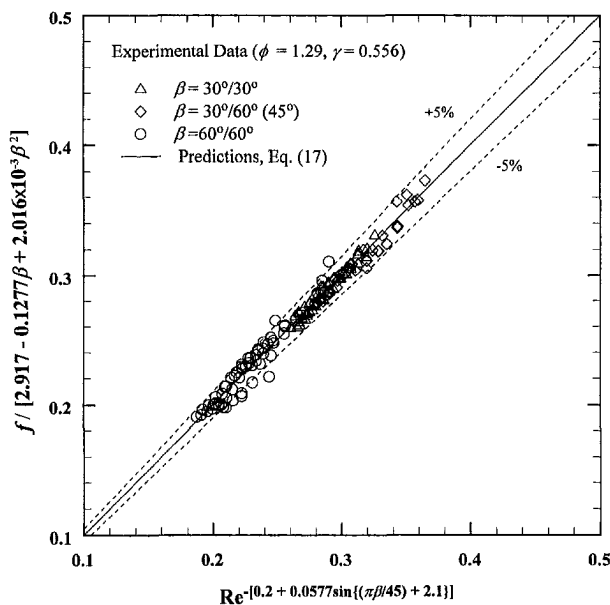
Fig. 9 Comparison of predictions and experimental data for the effect of chevron angle β on isothermal f in turbulent flows (Re $\geq$ 1000)
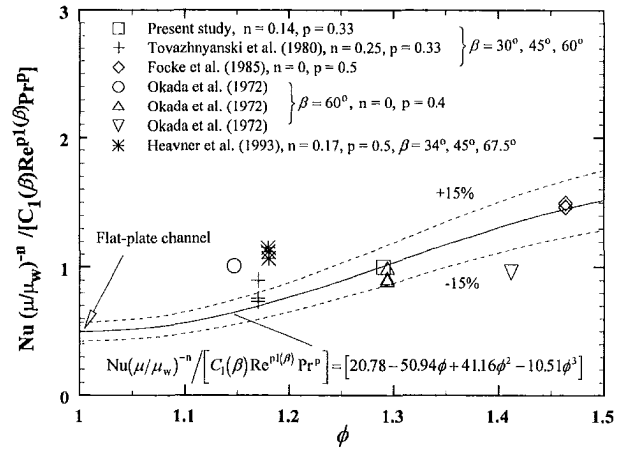
Fig. 10(a)
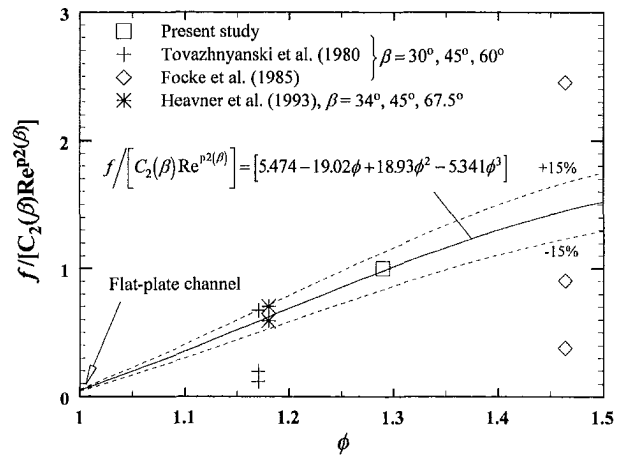
Fig. 10(b)

Fig. 10 Correlation of the effect of surface enlargement factor ϕ in turbulent flows (Re $\geq$ 1000): (a) Nusselt number and (b) isothermal friction factor

by cubic polynomials in the range $1 \leq \phi \leq 1.5$, with $\phi = 1$ for a flat-plate channel. Consequently, Nu and isothermal f can be predicted by the following correlations, which include the effects of β and ϕ:

$$Nu = [0.2668 - 0.006967\beta + 7.244 \times 10^{-5}\beta^2]$$
$$\times [20.78 - 50.94\phi + 41.16\phi^2 - 10.51\phi^3]$$
$$\times Re^{[0.728+0.0543\sin[(\pi\beta/45)+3.7]]} Pr^{1/3}(\mu/\mu_w)^{0.14} \quad (18)$$

and

$$f = [2.917 - 0.1277\beta + 2.016 \times 10^{-3}\beta^2]$$
$$\times [5.474 - 19.02\phi + 18.93\phi^2 - 5.341\phi^3]$$
$$\times Re^{-[0.2+0.0577\sin[(\pi\beta/45)+2.1]]}. \quad (19)$$

Equations (18) and (19) are generally valid for Re $\geq 10^3$, 30 deg $\leq \beta \leq 60$ deg, and $1 \leq \phi \leq 1.5$,[4] with sinusoidal shape chevron corrugations, and the predictions represent much of the available data reasonably well. Additional data, however, would be desirable to further establish their validity.

To quantify the heat transfer enhancement in heat exchangers for different applications, several figures of merit have been proposed in the literature (Webb, 1994; Bergles, 1985; Kays

---

[4] While manufacturing plates with $\phi \approx 1.5$ may be very difficult because of tooling and fixtures limitations, this limit reflects the values of $\phi = 1.412$ and 1.464, respectively, for the Okada et al. (1972) and Focke et al. (1985) data.
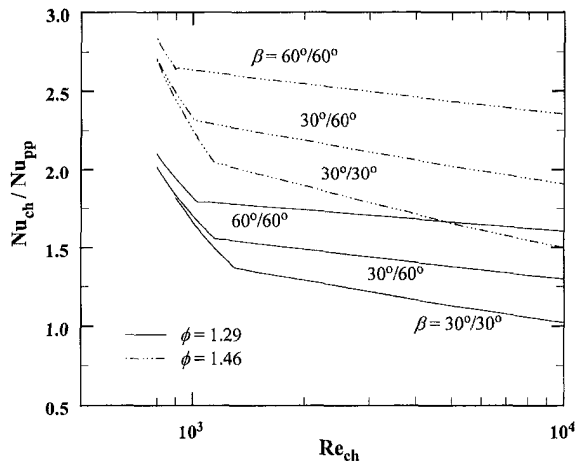
Fig. 11 Effect of chevron angle β and surface enlargement ϕ on heat transfer enhancement in a PHE for fixed surface geometry and constant pumping power constraints

and London, 1984). Relative to an equivalent parallel-plate pack, the enhanced thermal performance of chevron plates, based on the criterion of equal pumping power (E) and fixed surface geometry, can be expressed as

$$[Q_{ch}/Q_{pp}] = [\text{Nu}_{ch}/\text{Nu}_{ch}]_{L,d_e,N,A,E,\Delta T} \qquad (20)$$

where the constraint of equal pumping power

$$(f\,\text{Re}^3)_{ch} = (f\,\text{Re}^3)_{pp} \qquad (21)$$

provides the relationship between the Reynolds numbers for the two channels. Because chevron plates have higher friction factors compared to the parallel-plate channel, Eq. (21) requires that, for a given Re_{ch}, Re_{pp} must be higher. Figure 11 shows the enhancement of heat transfer in chevron plates according to the criterion of Eq. (20). Here, the Nusselt number data for chevron plates have been modified to account for enlargement factor ϕ (reduced to a projected area basis), so that the chevron-plate and parallel-plate channels have the same heat transfer area. It is seen that the heat transfer is enhanced by 1.1 to 2.8 times that in an equivalent parallel-plate channel at equal pumping power. The enhancement is also seen to increase considerably with increasing chevron angle β and surface enlargement ϕ. Typically with $\text{Re}_{ch} = 1500$ and $\phi = 1.29$, the heat transfer rates in chevron plates are 1.2, 1.4, and 1.6 times higher in $\beta = 30$ deg, 45 deg, and 60 deg chevron plates, respectively, than that in parallel-plate channels. However, the heat transfer enhancement diminishes with increasing Re_{ch}. For instance, with $\beta = 30$ deg/30 deg and $\phi = 1.29$, enhanced heat transfer is obtained only when $\text{Re}_{ch} < 10^4$. Also, based on the present results, there appears to be no significant advantage in using a mixed-plate ($\beta = 30$ deg/60 deg) arrangement over a symmetric ($\beta = 45$ deg/45 deg) arrangement in turbulent flows. This observation is reflected in the results previously reported by Heavner et al. (1993) and Muley and Manglik (1997) as well.

Conclusions

Experimental data for Nu and isothermal f in a single-pass PHE with three different chevron plate arrangements (symmetric $\beta = 30$ deg/30 deg and 60 deg/60 deg, and mixed $\beta = 30$ deg/60 deg) are presented. They represent cooling of hot water ($2 < \text{Pr} < 6$) flows in the turbulent regime ($600 < \text{Re} < 10^4$). Compared to flows in an equivalent flat-plate channel, up to five times higher Nu is obtained; however, the concomitant isothermal f is 44 times higher. Along with the fluid flow parameters Re, Pr, and (μ/μ_w), this performance is found to be strongly influenced by the chevron angle β and surface enlarge-

ment ϕ. Based on the parametric trends displayed by the experimental data, and some results reported in the literature, new design correlations for Nu and isothermal f, given by Eqs. (18) and (19), respectively, have been developed. These are valid for $\text{Re} \geq 10^3$, 30 deg $\leq \beta \leq 60$ deg, and $1 \leq \phi \leq 1.5$, and additional data that cover a wider range of these variables would usefully extend their applicability. Furthermore, with the constraint of fixed plate surface geometry and constant pumping power, the heat transfer is enhanced up to 2.8 times that in a flat-plate channel. This enhancement is primarily due to larger effective surface area and swirl flows generated in the troughs of the sinusoidal profile chevron plate corrugations.

Acknowledgments

References

Bergles, A. E., 1985, "Techniques to Augment Heat Transfer," *Handbook of Heat Transfer Applications*, 2nd Ed., W. M. Roshenow et al., eds., McGraw-Hill, New York, Chapter 3.

Ding, J., and Manglik, R. M., 1996, "Analytical Solutions for Laminar Fully Developed Flows in Double-Sine Shaped Ducts," *Heat and Mass Transfer*, Vol. 31, pp. 269–277.

Focke, W. W., Zachariades, J., and Olivier, I., 1985, "The Effect of the Corrugation Inclination Angle on the Thermohydraulic Performance of Plate Heat Exchangers," *International Journal of Heat and Mass Transfer*, Vol. 28, pp. 1469–1479.

Gasier, G., and Kottke, V., 1990, "Effects of Corrugation Parameters on Local and Integral Heat Transfer in Plate Heat Exchangers and Regenerators," *Heat Transfer 1990*, Vol. 5, G. Hetsroni, ed., Hemisphere, New York, pp. 85–90.

Heavner, R. L., Kumar, H., and Wanniarachchi, A. S., 1993, "Performance of an Industrial Plate Heat Exchanger: Effect of Chevron Angle," *AIChE Symposium Series*, Vol. 89, No. 295, pp. 262–267.

Kakaç, S., Shah, R. K., and Aung, W., 1987, *Handbook of Single-Phase Convective Heat Transfer*, John Wiley and Sons, New York.

Kays, W. M., 1950, "Loss Coefficients for Abrupt Changes in Flow Cross Section with Low Reynolds Number Flow in Single and Multiple Tube Systems," *Transactions of ASME*, Vol. 72, pp. 1067–1074.

Kays, W. M., and London, A. L., 1984, *Compact Heat Exchangers*, 3rd Ed., McGraw-Hill, New York.

Manglik, R. M., 1996, "Plate Heat Exchangers for Process Industry Applications: Enhanced Thermal-Hydraulic Characteristics of Chevron Plates," *Process, Enhanced and Multiphase Heat Transfer*, R. M. Manglik and A. D. Kraus, eds., Begell House, New York, pp. 267–276.

Manglik, R. M., 1999, "On the Influence of Number of Thermal Plates on the Performance of Plate Heat Exchangers," *International Communications in Heat and Mass Transfer*, submitted for publication.

Manglik, R. M., and Bergles, A. E., 1991, "Heat Transfer Enhancement of Intube Flows in Process Heat Exchangers by means of Twisted-Tape Inserts," Report No. HTL-18, Heat Transfer Laboratory, Rensselaer Polytechnic Institute, Troy, NY.

Manglik, R. M., and Bergles, A. E., 1998, "Numerical Modeling and Analysis of Laminar Flow Heat Transfer in Non-Circular Compact Channels," *Computer Simulations in Compact Heat Exchangers*, B. Sundén and M. Faghri, eds., Computational Mechanics Publications, Southampton, UK, Chapter 2.

Manglik, R. M., and Muley, A., 1993, "Heat Transfer and Pressure Drop Characteristics of Plate-and-Frame Heat Exchangers: A Literature Review," Report No. TFL-Int-1, Thermal-Fluids Laboratory, University of Cincinnati, Cincinnati, OH, Sept.

Marriott, J., 1977, "Performance of an Alfaflex Plate Heat Exchanger," *Chemical Engineering Progress*, Vol. 73, No. 2, pp. 73–78.

Moffatt, R. J., 1988, "Describing the Uncertainties in Experimental Results," *Experimental Thermal and Fluid Science*, Vol. 1, pp. 3–17.

Muley, A., and Manglik, R. M., 1995, "Experimental Investigation of Heat Transfer Enhancement in a PHE with $\beta = 60°$ Chevron Plates," *Heat and Mass Transfer 95*, Tata McGraw-Hill, New Delhi, pp. 737–744.

Muley, A., and Manglik, R. M., 1997, "Enhanced Heat Transfer Characteristics of Single-Phase Flows in a Plate Heat Exchangers with Mixed Chevron Plates," *Journal of Enhanced Heat Transfer*, Vol. 4, pp. 187–201.

Muley, A., and Manglik, R. M., 1998, "Heat Transfer and Pressure Drop in Plate Heat Exchangers," Thermal-Fluids Laboratory Report No. TFL-2, Department of Mechanical, Industrial and Nuclear Engineering, University of Cincinnati, Cincinnati, OH.

Okada, K., Ono, M., Tomimura, T., Okuma, T., Konno, H., and Ohtani, S., 1972, "Design and Heat Transfer Characteristics of a New Plate Heat Exchanger," *Heat Transfer–Japanese Research*, Vol. 1, No. 1, pp. 90–95.

Savostin, A. F., and Tikhonov, A. M., 1970, "Investigation of the Characteristics of the Plate Heating Surfaces," *Thermal Engineering*, Vol. 17, No. 9, pp. 75–78.

Shah, R. K., 1990, "Assessment of Modified Wilson Plot Techniques for Obtaining Heat Exchanger Design Data," *Heat Transfer 1990*, G. Hetsroni, ed., Hemisphere, New York, pp. 51–56.

Shah, R. K., and Focke, W. W., 1988, "Plate Heat Exchangers and their Design Theory," *Heat Transfer Equipment Design*, R. K. Shah et al., eds., Hemisphere, Washington, DC, pp. 227–254.

Sieder, E. N., and Tate, C. E., 1936, "Heat transfer and pressure Drop of Liquids in Tubes," *Industrial and Engineering Chemistry*, Vol. 28, pp. 1429–1435.

Talik, A. C., Fletcher, L. S., Anand, N. K., and Swanson, L. W., 1995a, "Heat Transfer and Pressure Drop Characteristics of a Plate Heat Exchanger," *Proc. ASME/JSME Thermal Engineering Conference*, Vol. 4, ASME, New York, pp. 321–329.

Talik, A. C., Fletcher, L. S., Anand, N. K., and Swanson, L. W., 1995b, "Heat Transfer and Pressure Drop Characteristics of a Plate Heat Exchanger Using a Propylene-Glycol/Water Mixture as the Working Fluid," *Proc. 1995 National Heat Transfer Conference*, Vol. 12, HTD-Vol. 314, ASME, New York, pp. 83–88.

Thonon, B., Vidil, R., and Marvillet, C., 1995, "Recent Research and Developments in Plate Heat Exchangers," *Journal of Enhanced Heat Transfer*, Vol. 2, Nos. 1–2, pp. 149–155.

Tovazhnyanski, L. L., and Kapustenko, P. A., and Tsibulnik, V., 1980, "Heat Transfer and Hydraulic Resistance in Channel of Plate Heat Exchangers," *Energetika*, Vol. 9, pp. 123–125.

Wanniarachchi, A. S., Ratnam, U., Tilton, B. E., Dutta-Roy, K., 1995, "Approximate Correlations for Chevron-Type Plate Heat Exchangers," *Proc. 1995 National Heat Transfer Conference*, Vol. 12, HTD-Vol. 314, ASME, New York, pp. 145–151.

Webb, R. L., 1994, *Principles of Enhanced Heat Transfer*, John Wiley and Sons, New York.

Wilson, E. E., 1915, "A Basis for Rational Design of Heat Transfer Apparatus," *ASME Transactions*, Vol. 37, pp. 47–82.

Evaporation Heat Transfer and Pressure Drop of Refrigerant R-134a in a Plate Heat Exchanger

Y.-Y. Yan

T.-F. Lin

Department of Mechanical Engineering,
National Chiao Tung University,
Hsinchu, Taiwan, R.O.C.

The evaporation heat transfer coefficient and pressure drop for refrigerant R-134a flowing in a plate heat exchanger were investigated experimentally in this study. Two vertical counterflow channels were formed in the exchanger by three plates of commercial geometry with a corrugated sine shape of a chevron angle of 60 deg. Upflow boiling of refrigerant R-134a in one channel receives heat from the hot downflow of water in the other channel. The effects of the mean vapor quality, mass flux, heat flux, and pressure of R-134a on the evaporation heat transfer and pressure drop were explored. The quality change of R-134a between the inlet and outlet of the refrigerant channel ranges from 0.09 to 0.18. Even at a very low Reynolds number, the present flow visualization of evaporation in a plate heat exchanger with the transparent outer plate showed that the flow in the plate heat exchanger remains turbulent. It is found that the evaporation heat transfer coefficient of R-134a in the plates is much higher than that in circular pipes and shows a very different variation with the vapor quality from that in circular pipes, particularly in the convective evaporation dominated regime at high vapor quality. Relatively intense evaporation on the corrugated surface was seen from the flow visualization. Moreover, the present data showed that both the evaporation heat transfer coefficient and pressure drop increase with the vapor quality. At a higher mass flux the pressure drop is higher for the entire range of the vapor quality but the evaporation heat transfer is clearly better only at the high quality. Raising the imposed wall heat flux was found to slightly improve the heat transfer, while at a higher refrigerant pressure, both the heat transfer and pressure drop are slightly lower. Based on the present data, empirical correlations for the evaporation heat transfer coefficient and friction factor were proposed.

1 Introduction

Plate heat exchangers (PHE) have been widely used in food processing, chemical reaction processes, and other industrial applications for many years. The advantage of using PHE was clearly indicated in the studies from Williams (1996) and Kerner et al. (1987). Particularly, in the last 20 years plate heat exchangers have been introduced to the refrigeration and air conditioning systems as evaporators or condensers for their high efficiency and compactness. Unfortunately, most studies about PHE reported in the open literature focused on the single-phase liquid to liquid heat transfer (Shah and Focke, 1988; Kandlikar and Shah, 1989a, b). There are rather limited data available for the design of plate heat exchangers used as evaporators and condensers.

Due to the serious destruction of the ozone layer in the atmosphere by the CFC refrigerants, various new refrigerants such as R-134a, R-143a, and R-125 were recently developed and introduced into the refrigeration and air conditioning systems. The heat transfer data for these new refrigerants are very scarce. In order to set up the database for using the new refrigerants in the design of the plate pattern for the PHE, evaporation of R-134a flow in a PHE is experimentally investigated in this study.

The study of flow boiling heat transfer characteristics of new refrigerants focused mainly on the flow inside circular tubes. Some enhancement surfaces such as low-fin, high-fin, star-insert, and microfin tubes were experimentally investigated for different refrigerants (D'Yachkov, 1978; Khanpara et al., 1986, 1987; Schlager et al., 1990; Eckels and Pate, 1991; and Reid et al., 1991). Based on a number of experimental data, correlating equations for the boiling heat transfer coefficient were proposed (Gungor and Winterton, 1986; Kandlikar, 1990, 1991). Recently detailed comparison of two-phase heat transfer characteristics for R-134a and R-12 in plain and microfin tubes were conducted by Eckels and Pate (1991) and Wattelet et al. (1992). They showed that the evaporation heat transfer coefficient for R-134a is about 40 percent (Eckels and Pate) and 5–15 percent (Wattelet et al.) higher than R-12, respectively.

In this study, the characteristics of the evaporation heat transfer and pressure drop for refrigerant R-134a flowing in a plate heat exchanger were explored experimentally. Before examining the flow boiling characteristics, a preliminary experiment for measuring water-to-water single-phase convection heat transfer in the plate heat exchanger was performed. The Wilson method (Wilson, 1915) was adopted to calculate the relation between the single-phase convection heat transfer coefficient and flow rate from the measured data. This single-phase heat transfer coefficient can then be used to analyze the data acquired from the two-phase heat transfer experiments.

2 Experimental Apparatus and Procedures

The experimental apparatus established in the present study, schematically shown in Fig. 1, consists of four main loops and
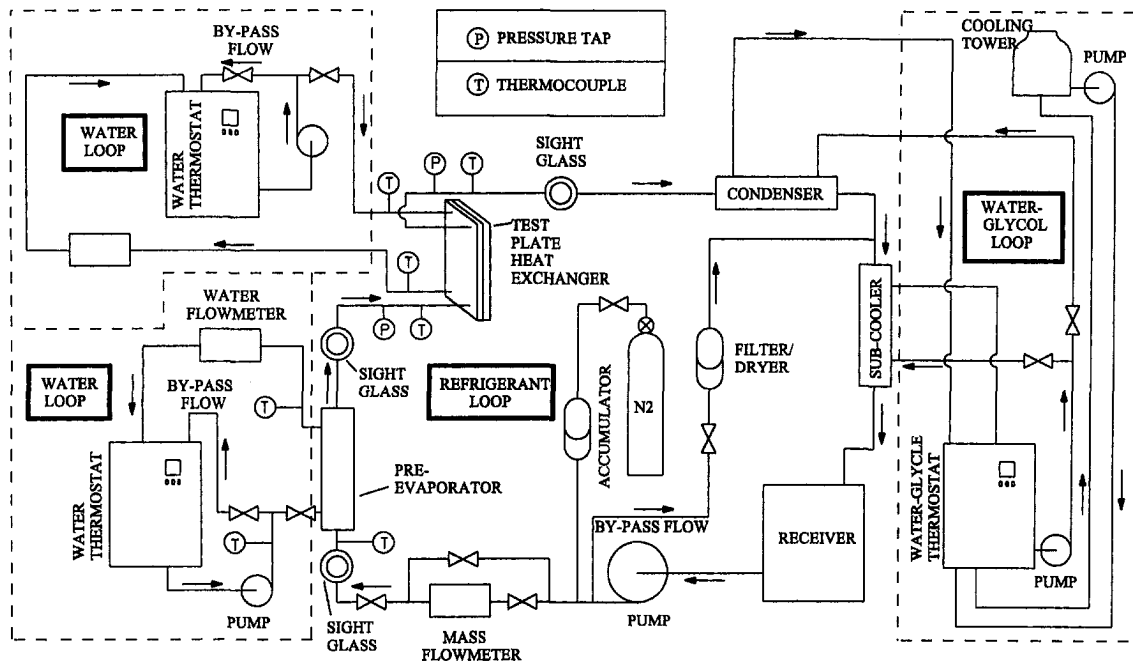
Fig. 1 Schematic diagram of the experimental system

a data acquisition system. It includes a refrigerant loop, two water loops (one for pre-evaporator heating and the other for test section heating), and a cold water-glycol loop. The refrigerant R-134a is circulated in the refrigerant loop. In order to obtain different test conditions of R-134a (including vapor quality, pressure, and heat flux) in the test section, we need to control the temperature and flowrate in the other three loops.

2.1 Refrigerant Loop. The refrigerant loop contains a refrigerant pump, an accumulator, a mass flowmeter, a pre-evaporator, a test section (that is, the plate heat exchanger), a condenser, a subcooler, a receiver, a filter/dryer, and three sight

glasses. The refrigerant pump is driven by a DC motor which is, in turn, controlled by a variable DC output motor controller. The liquid flow rate of R-134a is varied by a rotational DC motor through changing the DC current. The refrigerant flow rate can be further adjusted by opening the bypass valve. In the loop the accumulator is used to dampen the fluctuations of the flow rate and pressure. The refrigerant flow rate was measured by a mass flowmeter with a reading accuracy of ±1 percent. The pre-evaporator is used to evaporate the refrigerant R-134a to a specified vapor quality at the test section inlet by receiving heat from the hot water. Note that the amount of heat transfer from the hot water to the refrigerant in the pre-evaporator is

---

Nomenclature

A = heat transfer area of the plate, m^2

b = channel spacing, m

Bo_{eq} = equivalent all liquid Boiling number, Eqs. (34), (36)

c_p = specific heat, J/kgK

D_h = hydraulic diameter, m

f = friction factor

g = acceleration due to gravity, m/s^2

G = mass flux, kg/m^2s

G_{eq} = equivalent all liquid mass flux, Eqs. (34), (35)

h = heat transfer coefficient, W/m^2K

i_{fg} = enthalpy of vaporization, J/kg

k = conductivity, W/mK

L = length from center of inlet port to center of exit port, m

LMTD = log mean temperature difference, K

Nu = Nusselt number, dimensionless

Nu_r = two phase Nusselt number, $(h_r D_h/k_l)$, Eq. (36)

P = pressure, Pa

Pr = Prandtl number, dimensionless

Q = heat transfer rate, W

q_w'' = imposed wall heat flux, W/m^2

R_{wall} = heat transfer resistance of the wall

Re = Reynolds number, dimensionless

Re_{eq} = equivalent all liquid Reynolds number, Eqs. (33), (34)

T = temperature, °C

U = overall heat transfer coefficient, $W/m^2 K$

u = velocity, m/s

v = specific volume, m^3/kg

w = channel width of the plate, m

W = mass flow rate, kg/s

X = vapor quality

Greek Symbols

ΔP = pressure drop

ΔT = temperature difference, K

ΔX = total quality change in the exchanger

ρ = density, kg/m^3

μ = viscosity, $N \cdot s/m^2$

Subscripts

a = acceleration

ave = average

c, h = at cold side and hot side of the test section

ele = elevation

exp = experiment

f = friction

fg = difference between liquid phase and vapor phase

g = vapor phase

i, o = at inlet and exit of test section

l = liquid phase

lat, sens = latent and sensible heats

m = average value for the two phase mixture or between the inlet and exit

man = the test section inlet and exit manifolds and ports

p = pre-evaporator

r = refrigerant

tp = two phase

w = water

wall = wall/fluid near the wall

Fig. 2 Schematic diagram of plate heat exchanger
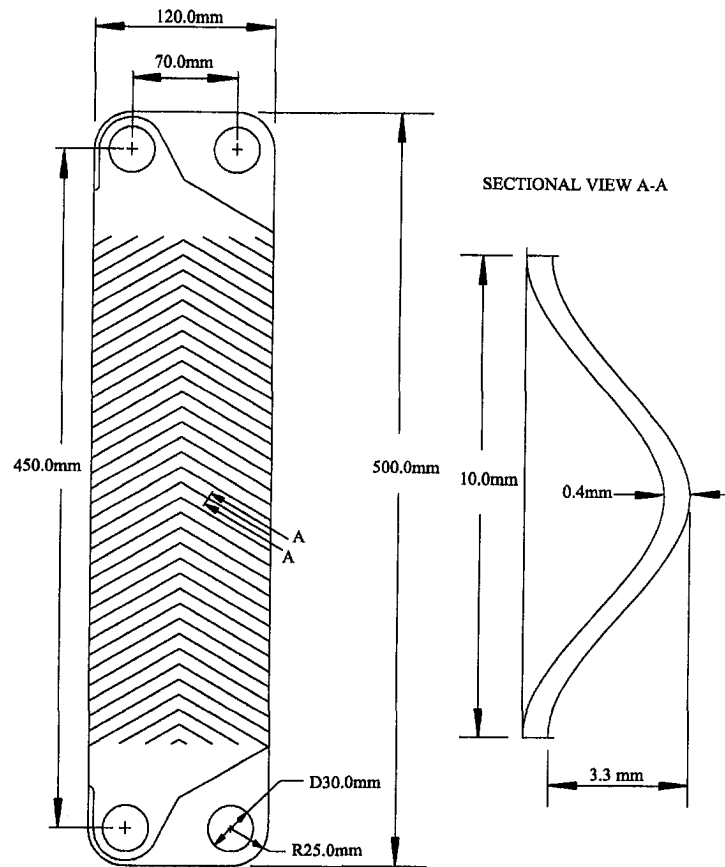
calculated from the energy balance in the water flow. Meanwhile, a condenser and a subcooler are used to condense the refrigerant vapor from the test section by a cold water-glycol loop. The pressure of the refrigerant loop can be controlled by varying the temperature and flow rate of the water-glycol in the condenser. After condensing, the liquid refrigerant flows back to the receiver.

2.2 Plate Heat Exchangers. Two plate heat exchangers were used in the present study, one for the flow visualization and the other for measuring heat transfer and pressure drop data. The plate heat exchanger for collecting data, as schematically shown in Fig. 2, was formed by three commercial SS-316 plates manufactured by the Kaori Heat Treatment Co., Ltd., Taiwan. The plate surfaces were pressed to become grooved with a corrugated sine shape and 60 deg of chevron angle, which is the angle of V-grooves to the plate vertical axis. The thickness of the plates is 0.4 mm and the pitch between the plates is 3.3 mm. The PHE including the inlet and outlet ports is 500.0 mm long. Note that the distance between the inlet port center to outlet port center is 450.0 mm. Each connection port has a diameter of 30.0 mm. The width of the plate is 120.0 mm. Moreover, the pitch of the corrugation on the plate from the side view is 10.0 mm. The corrugated grooves on the right and left outer plates have a V shape but those in the middle plate have a contrary V shape on both sides. This arrangement allows the flow stream to be divided into two different flow directions between the plates. Thus, the flow moves mainly along the grooves in each plate. Due to the contrary V shapes between two neighbor plates the flow streams near the two plates cross each other in each channel. This cross flow results in a significant flow unsteadiness and randomness. In fact, the flow is highly turbulent even when the Reynolds number is low.

For conformity, the plate heat exchanger for visualization was chosen to have the same structure as that described above for the data collection except that the right outer plate was made by transparent acrylic, which was machined and then polished to the same geometry.

In each heat exchanger two vertical counter flow channels are formed by the three plates. Upflow of refrigerant R-134a in one channel is heated by the downflow of hot water in the other channel. The heat transfer rate in the test section is calculated by measuring the water temperature drop between the water channel inlet and outlet and by measuring the water flow rate. The pressure and differential pressure transducers both having reading accuracy of ±0.5 percent are also connected to the inlet and outlet of the plate heat exchanger to measure the associated pressures and differential pressure.

2.3 Water Loop for Test Section. The water loop in the experimental system for circulating the hot water through the test section contains an 80-liter water thermostat with a 4 kW heater and an air-cooled refrigeration system of 3.5 kW cooling capacity, intending to control the water temperature. A 0.5-hp pump with an inverter is used to drive the hot water to the plate heat exchanger with a specified water flow rate. A bypass valve can also be used to adjust the water flow rate. The reading accuracy of measuring the water flow rate is ±0.5 percent.

2.4 Water Loop for Pre-evaporator. Another water loop designed for the pre-evaporator consists of a 125-liter hot-water thermostat with three 2.0-kW heaters and a 0.5-hp water pump to drive the hot water at a specified flow rate to the pre-evaporator. Similarly, a bypass valve is also used to adjust the flow rate. The water flowmeter has a reading accuracy of ±0.5 percent.

2.5 Water-Glycol Loop. The water-glycol loop designed for condensing the R-134a vapor contains a 125-liter thermostat with a water-cooled refrigeration unit. Its cooling capacity is 2 kW for the water-glycol at −20°C. The water-glycol at a specified flow rate is driven by a 0.5-hp pump to the condenser as well as to the subcooler. A bypass valve is also provided to adjust the flow rate.

2.6 Data Acquisition. The data acquisition system includes a recorder, a 24V-3A power supply, and a controller. The recorder records the temperature and voltage data. The water flowmeter and differential pressure transducer need the power supply as a driver to output an electric current of 4 to 20 mA. The IEEE488 interface allows the measured data to transmit from the recorder to the controller, which are then analyzed by the computer immediately.

2.7 Experimental Procedures. In each test the R-134a pressure at the test section inlet was first maintained at a specified level by adjusting the water-glycol temperature and its flow rate. Then, the temperature and flow rate of the hot-water loop for the pre-evaporator were adjusted to keep the vapor quality of R-134a at the test section inlet at the desired value. Finally, the heat transfer rate between the counterflow channels in the test section can be varied by changing the temperature and water flowrate in the water loop for the test section. Additionally, the flow rate of water in the test section should be high enough to have turbulent flow in the water side so that the associated single-phase heat transfer in it is high enough for balancing the evaporation heat transfer in the refrigerant side. In this study, the Reynolds number of the water flow is maintained beyond 200.

3 Data Reduction

An analysis is needed in the present measurement to deduce the heat transfer rate from the water flow to the refrigerant flow in the test section. From the definition of the hydraulic diameter, Shah and Wanniarachchi (1992) suggested the use of two times the mean channel spacing as the hydraulic diameter for the plate heat exchangers when the channel width is much larger than the channel spacing, i.e.,

$$D_h \cong 2b \quad \text{for} \quad w \gg b \qquad (1)$$

Convection heat transfer coefficient and friction factor were calculated from reducing the measured raw data in a computer program. The reduction procedures are given in the following.

3.1 Single-Phase Water-to-Water Heat Transfer. In the initial single-phase water-to-water heat transfer test for the present plate heat exchanger, the fluid properties were calculated according to the average of the inlet and outlet bulk fluid temperatures. The energy balance between the hot and cold water sides was found to be within two percent for all runs. That is

$$\frac{Q_{w,h} - Q_{w,c}}{Q_{\text{ave}}} \le \text{two percent} \qquad (2)$$

$$Q_{w,h} = W_{w,h} c_{p,w} (T_{w,h,i} - T_{w,h,o}) \qquad (3)$$

$$Q_{w,c} = W_{w,c} c_{p,w} (T_{w,c,o} - T_{w,c,i}) \qquad (4)$$

$$Q_{\text{ave}} = \frac{(Q_{w,h} + Q_{w,c})}{2}. \qquad (5)$$

The overall heat transfer coefficient between the two sides can be expressed as

$$U = \frac{Q_{\text{ave}}}{A \cdot \text{LMTD}} \qquad (6)$$

where A is the heat transfer area accounting for the actual corrugated surface of the plate. The log mean temperature difference

(LMTD) is determined from the inlet and exit temperatures of two counterflow channels

$$\text{LMTD} = \frac{\Delta T_1 - \Delta T_2}{\ln (\Delta T_1/\Delta T_2)} \qquad (7)$$

with

$$\Delta T_1 = T_{w,h,i} - T_{w,c,o} \qquad (8)$$

$$\Delta T_2 = T_{w,h,o} - T_{w,c,i}. \qquad (9)$$

In view of the same heat transfer area in the hot and cold water sides, the relation between the overall heat transfer coefficient and the convective heat transfer coefficients on both sides can be expressed as

$$\left(\frac{1}{h_{w,h}}\right) = \left(\frac{1}{U}\right) - \left(\frac{1}{h_{w,c}}\right) - R_{\text{wall}} A \qquad (10)$$

The Wilson method (Wilson, 1915) was applied to calculate $h_{w,h}$ and $h_{w,c}$.

3.2 Two-Phase Evaporation Heat Transfer. First, the total heat transfer rate between the counter flows in the PHE is calculated from the hot-water side,

$$Q_{w,h} = W_{w,h} c_p (T_{w,h,i} - T_{w,h,o}). \qquad (11)$$

Then, the vapor quality entering the test section is evaluated from the energy balance for the pre-evaporator. Based on the measured temperature drop on the water side, the heat transfer in the pre-evaporator is calculated from the relation

$$Q_{w,p} = W_{w,p} c_p (T_{w,p,i} - T_{w,p,o}). \qquad (12)$$

The heat transfer to the refrigerant in the pre-evaporator results in the rise of the refrigerant temperature to the saturated value (sensible heat transfer) and the evaporation of the refrigerant (latent heat transfer). Thus

$$Q_{w,p} = Q_{\text{sens}} + Q_{\text{lat}} \qquad (13)$$

where

$$Q_{\text{sens}} = W_r c_{p,r} (T_{r,p,o} - T_{r,p,i}) \qquad (14)$$

$$Q_{\text{lat}} = W_r \cdot i_{fg} X_{p,o}. \qquad (15)$$

Equations (12)–(15) can be combined to evaluate the refrigerant quality at the exit of the pre-evaporator that is considered to be the same as the vapor quality of the refrigerant entering the test section. Specifically,

$$X_i = X_{p,o} = \frac{1}{i_{fg}} \left[\frac{Q_{w,p}}{W_r} - c_{p,r}(T_{r,p,o} - T_{r,p,i}) \right]. \qquad (16)$$

The change in the refrigerant vapor quality in the test section is then deduced from the heat transfer to the refrigerant in the test section,

$$\Delta X = \frac{Q_{w,h}}{W_r \cdot i_{fg}}. \qquad (17)$$

The determination of the overall heat transfer coefficient for the evaporation of R-134a in the PHE is similar to that for the single-phase heat transfer,

$$U = \frac{Q_{w,h}}{A \cdot \text{LMTD}}. \qquad (18)$$

The log mean temperature difference (LMTD) is determined from the inlet and exit temperatures in the two channels,

Table 1 Parameters and estimated uncertainties

Parameter	Uncertainty
length, width and thickness (m)	± 0.00005 m
area of the plate (m^2)	$\pm 7 \times 10^{-5}$ m^2
Temperature, T (K)	± 0.2 K
ΔT (K)	± 0.3 K, $\pm 4.5\%$
Pressure, P	± 0.002 MPa
Pressure drop, ΔP (Pa)	± 200 Pa
Water flow rate, W_w	$\pm 2\%$
Mass flux of refrigerant, G	$\pm 2\%$
Heat flux of test section, q''_w	$\pm 6.5\%$
Heat transfer rate of pre-evaporator, $Q_{w,p}$	$\pm 6.5\%$
Vapor quality, X	± 0.03
Single-phase water heat transfer coefficient, h_w	$\pm 11\%$
R-134a evaporation heat transfer coefficient, h_r	$\pm 15\%$
Friction factor, f_{tp}	$\pm 5\%$

$$\mathrm{LMTD} = \frac{(\Delta T_1 - \Delta T_2)}{\ln (\Delta T_1 / \Delta T_2)}, \tag{19}$$

where

$$\Delta T_1 = T_{w,h,i} - T_{r,o} \tag{20}$$

$$\Delta T_2 = T_{w,h,o} - T_{r,i} \tag{21}$$

with $T_{r,i}$ and $T_{r,o}$ being the saturated temperatures of R-134a measured directly by the thermocouples in the present study, which were found to be only qualitatively close to the saturated temperatures corresponding, respectively, to the inlet and outlet pressures in the refrigerant flow in the PHE. This inconsistency in the corresponding saturated temperature and pressure is attributed to the highly nonuniform pressure loss in the exchanger, especially in the region near the inlet and exit ports. Thus, the measured $T_{r,i}$ and $T_{r,o}$ are used in the evaluation of LMTD. Finally, the evaporation heat transfer coefficient in the flow of R-134a is evaluated from the equation

$$\frac{1}{h_r} = \frac{1}{U} - \frac{1}{h_{w,h}} - R_{\mathrm{wall}} A \tag{22}$$

where $h_{w,h}$ is determined from the empirical correlation for the single-phase water-to-water heat transfer.

3.3 Friction Factor. To evaluate the friction factor associated with the R-134a evaporation, the frictional pressure drop ΔP_f was calculated by subtracting the acceleration pressure drop ΔP_a, the pressure losses at the test section inlet and exit manifolds and ports $(\Delta P)_{\mathrm{man}}$, and the elevation pressure drop ΔP_{ele} from the measured total pressure drop ΔP_{exp}.

$$\Delta P_f = \Delta P_{\mathrm{exp}} - \Delta P_a - (\Delta P)_{\mathrm{man}} - \Delta P_{\mathrm{ele}} \tag{23}$$

The acceleration and elevation pressure drops were estimated by the homogeneous model for two-phase gas-liquid flow (Collier (1981)),

$$\Delta P_a = G^2 v_{fg} \Delta X \tag{24}$$

$$\Delta P_{\mathrm{ele}} = \frac{g \cdot L}{v_m}, \tag{25}$$

where v_m is the specific volume of the vapor-liquid mixture when the vapor and liquid are homogeneously mixed and is given as

$$v_m = [X_m v_g + (1 - X_m) v_1] = [v_1 + X_m v_{fg}]. \tag{26}$$

The pressure drop in the inlet and outlet manifolds and ports was empirically suggested by Shah and Focke (1988). It is approximately 1.5 times the head due to flow expansion at the inlet

$$(\Delta P)_{\mathrm{man}} \cong 1.5 \left(\frac{u_m^2}{2 v_m} \right)_i \tag{27}$$

where u_m is the mean flow velocity. With the homogeneous model the mean velocity is

$$u_m = G v_m. \tag{28}$$

Based on the above estimation, the acceleration pressure drop, the pressure losses at the test section inlet and exit manifolds and ports, and the elevation pressure drop are rather small. In fact, the frictional pressure drop ranges from 96 percent to 99 percent of the total pressure drop measured. According to the definition

$$f_{tp} \equiv - \frac{\Delta P_f D_h}{2 G^2 v_m L}, \tag{29}$$

the friction factor for the evaporation of R-134a in the plate is obtained.

3.4 Uncertainty Analysis. The uncertainties for the experimental results were determined by a formula proposed by Kline and McClintock (1953). The detailed results from the present uncertainty analysis for the experiments conducted here are summarized in Table 1.

4 Results and Discussion

4.1 Single-Phase Water-to-Water Heat Transfer. Before measuring the R-134a evaporation heat transfer and pressure drop, single-phase water-to-water tests were conducted first. The results from this single-phase experiment were illustrated in Fig. 3 and the measured heat transfer coefficient in the hot side can be correlated by the least-square method as

$$\mathrm{Nu} = 0.2121 \ \mathrm{Re}^{0.78} \ \mathrm{Pr}^{1/3} \left(\frac{\mu_m}{\mu_{\mathrm{wall}}} \right)^{0.14} \tag{30}$$

where the viscosities μ_m and μ_{wall} are, respectively, based on the average bulk fluid and wall temperatures estimated from the measured inlet and outlet temperatures in the hot and cold sides. It was found that even at a very low Reynolds number of 200 the correlation is still appropriate. This is simply because
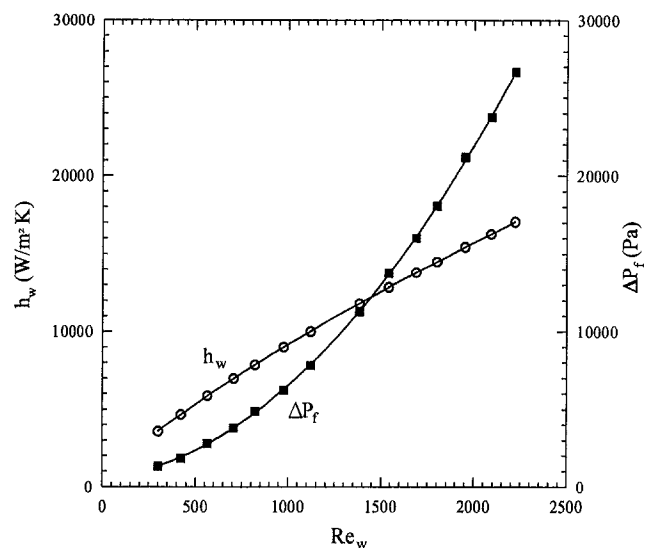

Fig. 3 Heat transfer coefficient and friction pressure drop variations with the Reynolds number for the hot side in single-phase water-to-water test
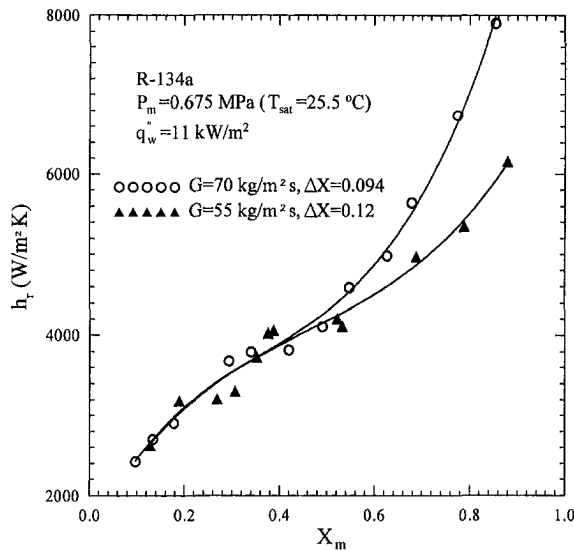
Fig. 4 Variations of evaporation heat transfer coefficient with mean vapor quality for various mass fluxes at $P_m = 0.675$ MPa and $q''_w = 11$ kW/m^2

Fig. 5 Variations of evaporation heat transfer coefficient with mean vapor quality for various mass fluxes at $P_m = 0.8$ MPa and $q''_w = 15$ kW/m^2

the flow in the plate heat exchanger remains turbulent at a very low Reynolds number. Moreover, it is noted that the well-known Sieder-Tate equation (Incropera and Dewitt, 1981) for single-phase turbulent convection heat transfer coefficient in circular pipes is

$$Nu = 0.027 \ Re^{0.8} \ Pr^{1/3} \left(\frac{\mu_m}{\mu_{wall}} \right)^{0.14} \qquad (31)$$

and the corresponding laminar fully developed convection heat transfer coefficient is

$$Nu = 3.66 \sim 4.36. \qquad (32)$$

A comparison of Eq. (30) with Eqs. (31) and (32) shows that the single-phase convection heat transfer coefficient in the water flow through the plate heat exchanger is about eight times of that in a circular pipe at the same Reynolds number.

4.2 Two-Phase Evaporation Heat Transfer.

Effects of the mass flux, heat flux, and system pressure on the evaporation heat transfer of refrigerant R-134a in the plate heat exchanger were examined in the following. Selected measured data are presented in Figs. 4–7 to illustrate the changes of the heat transfer coefficient with the vapor quality for various mass fluxes, heat fluxes, and pressures. In the plots X_m denotes the average vapor quality in the PHE. These results clearly indicate that the evaporation heat transfer coefficient of R-134a in the plate heat exchanger is quite different from that in circular pipe, particularly in the convection dominated regime of high vapor quality. Specifically, at a vapor quality higher than 0.45, the heat transfer coefficient increases almost exponentially with the quality.

Figures 4 and 5 show the effects of the mass flux on the heat transfer coefficient. In Fig. 4, the data for two different mass fluxes of 55 and 70 kg/m^2 s are compared at the same heat flux and system pressure. The total vapor quality changes in the PHE, ΔX, for the two mass fluxes are, respectively, 0.094 and 0.12, as indicated in the plot. Note that at a low-vapor quality ($X_m < 0.45$) the mass flux exhibits an insignificant influence on the heat transfer in the flow. At this low-vapor quality, boiling in the refrigerant appears to be suppressed at this heat flux level for these two mass fluxes. As the vapor quality is above 0.45, the difference in the heat transfer coefficient for

the two mass fluxes begins to grow. The heat transfer coefficient for the higher mass flux rises more quickly than that for the lower mass flux. This is attributed to the fact that at 0.675 MPa the liquid density of R-134a is about 35 times of the corresponding vapor density. Thus, a great increase in the vapor volume during the evaporation process causes the vapor flow to move in a high speed, which in turn breaks the adjacent liquid film into a large number of tiny liquid droplets in the channel. This highly turbulent mist flow results in a substantial rise in the heat transfer coefficient. The high-speed turbulent mist flow continuously wets the heat transfer wall and significantly reduces the resistance of heat transfer from the channel wall to the flow. At a higher mass flux the mist flow is at a higher velocity and the heat transfer is better. A similar trend is noted in Fig. 5 for the higher heat flux of 15,000 W/m^2 and system pressure of 0.8 MPa except that at $G = 70$ kg/m^2 s boiling does not seem completely suppressed at a low-vapor quality. It should be pointed out that there exists a sudden drop in the heat transfer coefficient at $X_m = 0.44$ for $G = 70$ kg/m^2 s. The existence of this drop is conjectured to be due to the sig-

Fig. 6 Variations of evaporation heat transfer coefficient with mean vapor quality for various heat fluxes at $G = 70$ kg/m^2 s and $P_m = 0.8$ MPa
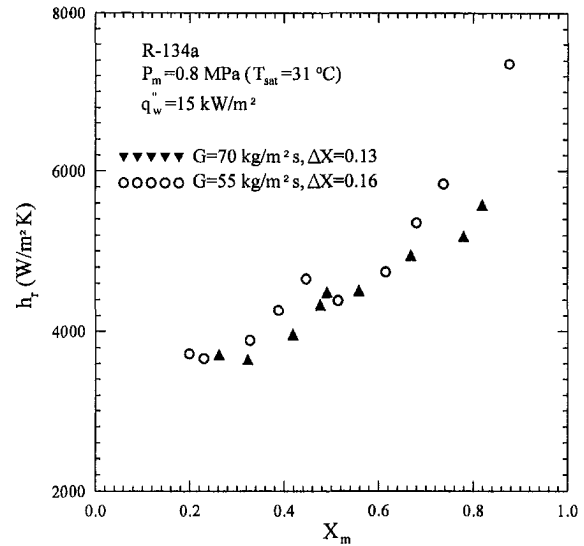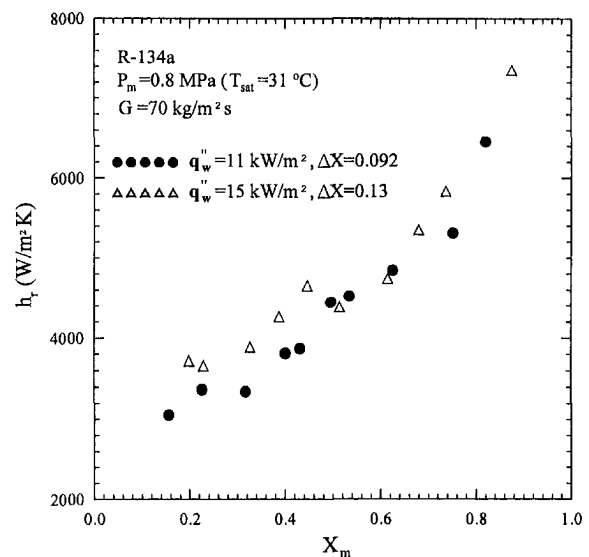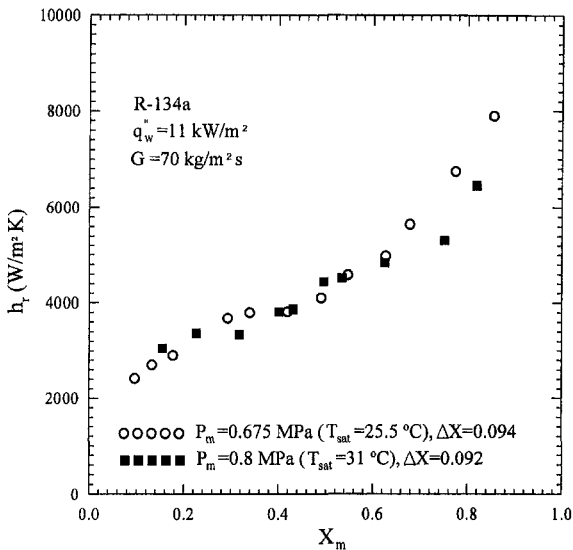
Fig. 7 Variations of evaporation heat transfer coefficient with mean vapor quality for various pressures at $G = 70$ kg/m^2 s and $q''_w = 11$ kW/m^2

Fig. 8 Comparison of the present heat transfer data for the plate heat exchanger with those for circular pipes from Wattelet et al. (1992, 1994) and Eckels and Pate (1991)

nificant suppression of the boiling process when the vapor quality rises to 0.44 with the vapor velocity being high enough to rupture the thin liquid film on the channel wall.

The effects of the heat flux on the heat transfer coefficient are examined in Fig. 6. Two heat fluxes of 11,000 and 15,000 W/m^2 were tested at a given mass flux of 70 kg/m^2 s and pressure of 0.8 MPa. Contrary to the mass flux effect, the heat flux does not show significant effects on the heat transfer in the convection dominated regime. Only at low-vapor quality for the higher flux of 15,000 W/m^2, boiling plays an important role in the heat transfer process. But at the low heat flux of 11,000 W/m^2, the boiling appears to be largely suppressed at a low quality.

Figure 7 illustrates the effects of the system pressure on the evaporation heat transfer. Two cases with the system pressures of 0.675 and 0.80 MPa, which are, respectively, equivalent to the saturated temperatures of 25.5°C and 31°C for R-134a, are examined. In the low-quality regime the pressure effects are small but at the high-quality regime poorer heat transfer is noted at the higher pressure. This is attributed to the lower specific volume of R-134a vapor at a higher system pressure, which, in turn, causes lower vapor flow rate and hence lower shear force to the liquid film on the heat transfer surface. Moreover, the latent heat of vaporization is smaller for a higher R-134a pressure and the channel wall may be partially dried when the vapor quality is high.

It is of interest to compare the evaporation heat transfer coefficients for the plate heat exchanger and for the circular pipes. Data from Wattelet et al. (1992, 1994) and Eckels and Pate (1991) were compared with the present data in Fig. 8. Though the experimental conditions including the tube size, mass flow rate, heat flux level, and pressure for these data are somewhat different, the comparison does clearly show that for $X_m > 0.3$ the heat transfer coefficient for the plate heat exchanger is much higher than that for the circular pipes. Moreover, a large increase in the heat transfer coefficient with the vapor quality is only noted for the plate heat exchanger. This is attributed to fact that the contra V-grooves in the plate heat exchanger cause the flow to become highly turbulent, especially in the form of a highly turbulent mist flow at the high vapor quality.

4.3 Two-Phase Pressure Drop. The variations of the frictional pressure drop in the PHE with the vapor quality are shown in Figs. 9–11 for different mass fluxes, heat fluxes, and pressures. Similar to the evaporation heat transfer coefficient,
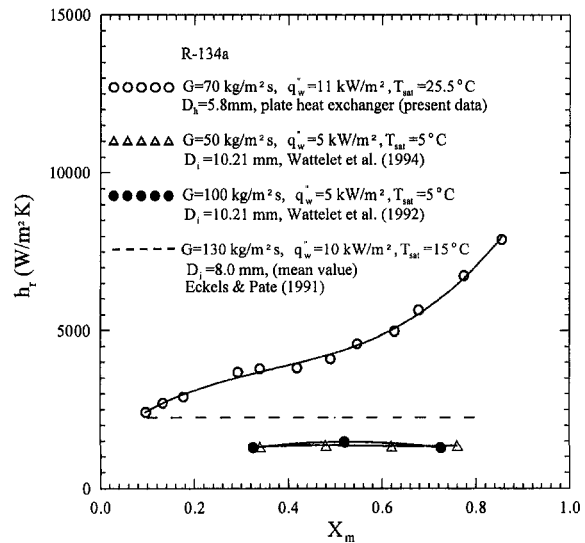
the pressure drop increases with the vapor quality. It is further noted that the higher mass flux results in a higher pressure drop for the entire quality range, as shown in Fig. 9. Moreover, at a higher vapor quality the mass flux effects are stronger. It is of interest to note that the pressure drop is not affected to a noticeable degree by the heat flux, as is evident from Fig. 10. But the pressure drop is reduced with an increase in the system pressure, as is clear from Fig. 11. It is known that for a higher system pressure (that is for a higher saturation temperature), the specific volume of the vapor and the viscosity of the liquid R-134a are lower. Thus, the data in Fig. 11 show that the pressure drop is lower for a lower system pressure. We further note that the rise in the evaporation heat transfer coefficient with the vapor quality is more pronounced than that in the pressure drop.

4.4 Correlation Equations. Correlation equations for the heat transfer coefficient and friction factor associated with the R-134a evaporation in the plate heat exchanger considered here are important in the practical thermal design of the evaporators for various air conditioning and refrigeration systems. Based
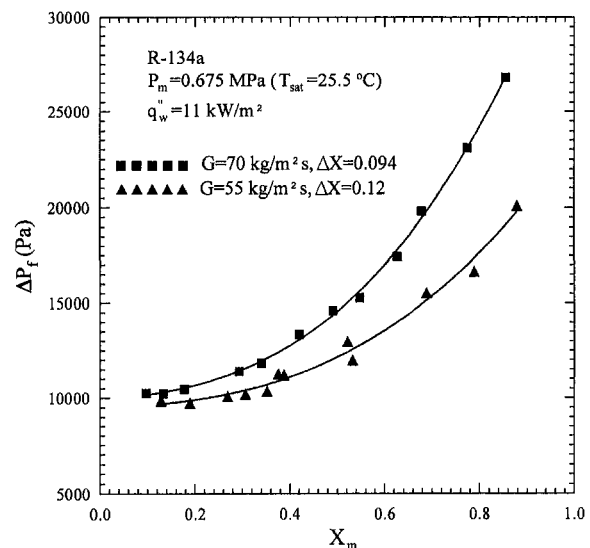
Fig. 9 Variations of frictional pressure drop with mean vapor quality for various mass fluxes at $P_m = 0.675$ MPa and $q''_w = 11$ kW/m^2
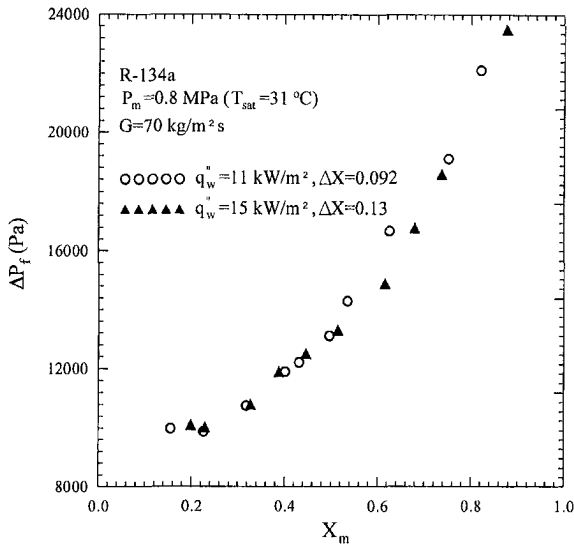
Fig. 10 Variations of frictional pressure drop with mean vapor quality for various heat fluxes at $G = 70$ kg/m^2 s and $P_m = 0.8$ MPa

on the present data the heat transfer coefficient can be correlated as

$$\left(\frac{h_r D_h}{k_l}\right) \mathrm{Pr}_l^{-1/3} \mathrm{Re}^{0.5} \mathrm{Bo}_{eq}^{-0.3} = 1.926 \, \mathrm{Re}_{eq}$$

$$\text{for} \quad 2000 < \mathrm{Re}_{eq} < 10{,}000 \quad (33)$$

where Re_{eq} and Bo_{eq} are, respectively, the equivalent Reynolds and Boiling numbers in which an equivalent mass flux is used in their definitions first proposed by Akers (1958),

$$\mathrm{Re}_{eq} = \frac{G_{eq} D_h}{\mu_l} \quad \text{and} \quad \mathrm{Bo}_{eq} \equiv \frac{q_w''}{G_{eq} \cdot i_{fg}} \quad (34)$$

where

$$G_{eq} = G\left[(1 - X_m) + X_m\left(\frac{\rho_l}{\rho_g}\right)^{0.5}\right]. \quad (35)$$

Figure 12 indicates that this correlation can satisfactorily corre-

Fig. 12 Comparison of the proposed correlation for the evaporation heat transfer coefficient with the present data

late our data with an average deviation of 8.3 percent. For convenience in application, Eq. (33) can be further expressed as

$$\mathrm{Nu}_r = 1.926 \, \mathrm{Pr}_l^{1/3} \, \mathrm{Bo}_{eq}^{0.3} \, \mathrm{Re}^{0.5}\left[(1 - X_m) + X_m\left(\frac{\rho_l}{\rho_g}\right)^{0.5}\right]$$

$$\text{for} \quad 2000 < \mathrm{Re}_{eq} < 10{,}000. \quad (36)$$

Similarly, based on the present data the friction factor can be correlated as

$$\text{for} \quad \mathrm{Re}_{eq} < 6{,}000 \quad f_{tp} \, \mathrm{Re}^{0.5} = 6.947 \times 10^5 \cdot \mathrm{Re}_{eq}^{-1.109} \quad (37)$$

$$\text{for} \quad \mathrm{Re}_{eq} \geq 6{,}000 \quad f_{tp} \, \mathrm{Re}^{0.5} = 31.21 \cdot \mathrm{Re}_{eq}^{0.04557}. \quad (38)$$

This correlation again can well represent our data with a deviation of seven percent (Fig. 13). It should be pointed out that

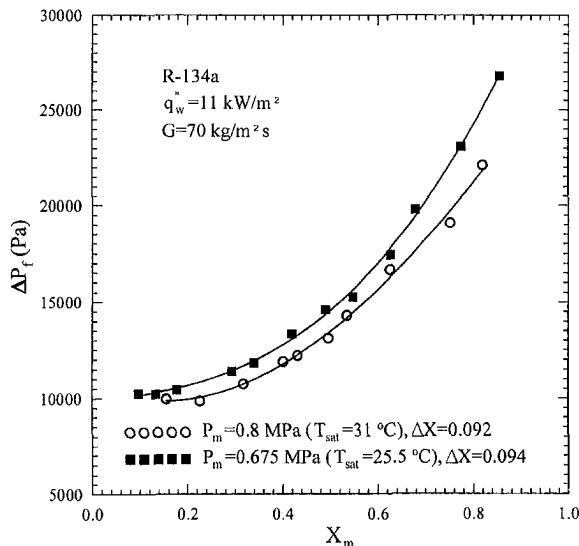**Fig. 11 Variations of frictional pressure drop with mean vapor quality for various pressures at $G = 70$ kg/m^2 s and $q_w'' = 11$ kW/m^2**
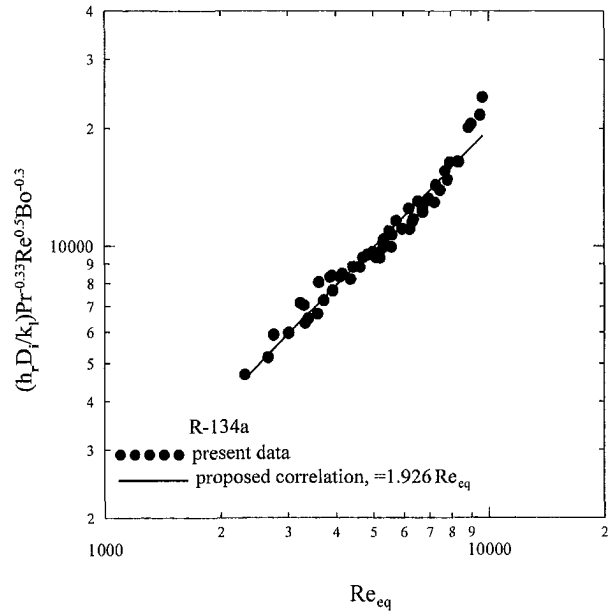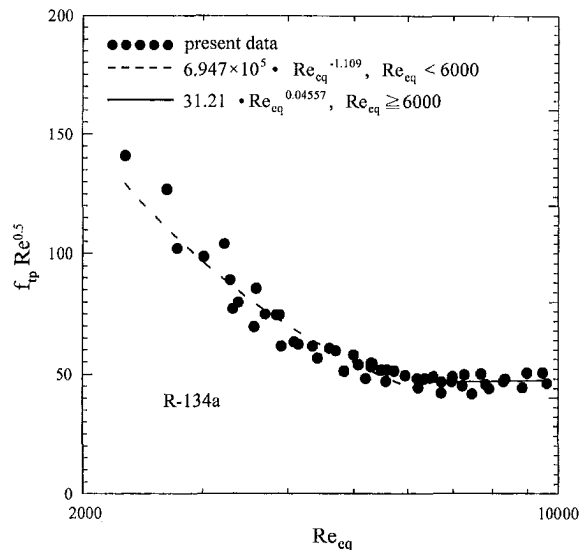

Fig. 13 Comparison of the proposed correlation for the friction factor with the present data
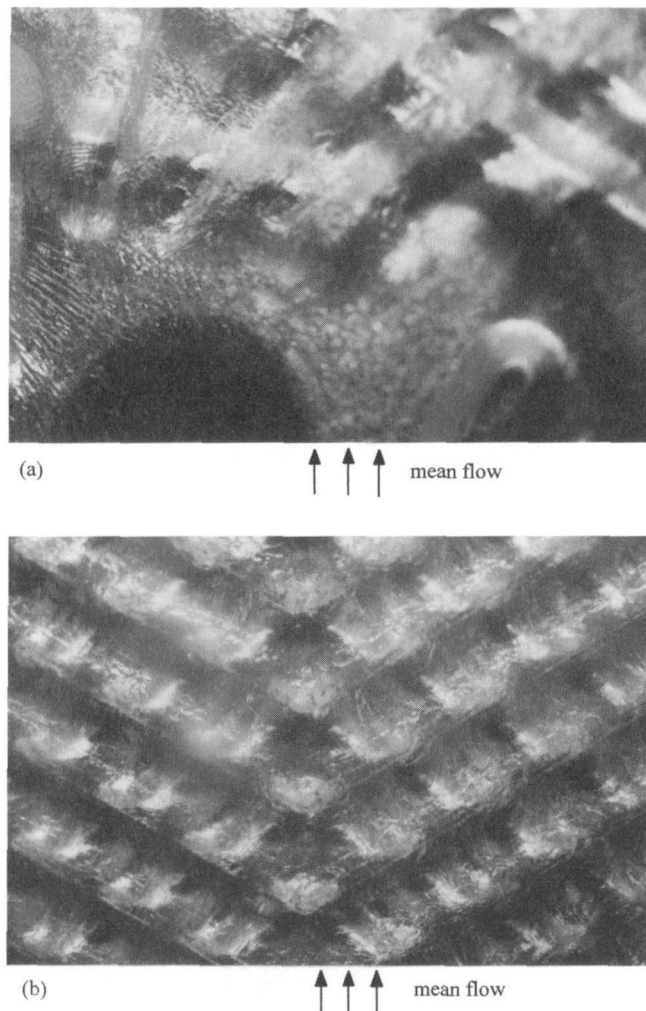
(a) mean flow

(b) mean flow

Fig. 14 Two-phase R-134a flow visualization in the plate heat exchanger at $X_m = 0.15$, $G = 55$ kg/m^2 s, $q_w'' = 11$ kW/m^2, and $P_m = 0.675$ MPa: (a) near the inlet manifolds and ports and (b) downstream near the middle portion of the plate heat exchanger

the above correlating equations can only be applied to the vertical PHE tested here.

4.5 Flow Visualization. To further illustrate the R-134a evaporation in the heat exchanger, the flow photos taken from the transparent test section are shown in Fig. 14 for a typical case with $X_m = 0.15$, $G = 55$ kg/m^2 s, $q_w'' = 11$ kW/m^2, and $P_m = 0.675$ MPa. Based on the homogeneous two-phase gas-liquid model, the estimated mean vapor void fraction and liquid film thickness in the refrigerant channel are, respectively, 0.87 and 0.19 mm. This liquid film is relatively thin and the flow in the refrigerant channel is dominated by the R-134a evaporation at the liquid-vapor interface except near the inlet port where the liquid film is thick. Figure 14(a) clearly indicates that in the region surrounding the inlet port intense nucleate boiling with significant bubble generation occurs. Downstream the high-speed vapor flow due to the intensive interface evaporation exerts substantial shear on the liquid film and some of the film is torn out to produce small liquid droplets moving in the vapor flow. Due to the contra-V grooves on the channel walls in the PHE, the fast vapor and liquid droplet flow ($u_g \approx 0.25$ m/s) over the thin liquid film is in a strong meandering motion on the plates (Fig. 14(b)). The liquid droplets are rather small

and in fact we have turbulent mist flow in the channel. The mist flow is noted to frequently switch from one groove to another between the contra-V structure. Besides, it also shows strong recirculation in each denting cavity on the channel wall. When the vapor quality X_m is higher, the turbulent mist flow is stronger and dominates a larger portion of the channel.

5 Concluding Remarks

The results from the present study indicate that the evaporation heat transfer coefficient for R-134a flow in the PHE is quite higher than that in circular tubes, particularly in the convection dominated regime of high vapor quality. Only at high vapor quality, the mass flux exhibits significant effects on the heat transfer coefficient. Contrary to the mass flux effects, the heat flux does not have significant effects on the heat transfer at high quality, but at a high wall heat flux it shows some influences at low quality. The increase in the system pressure results in a lower heat transfer coefficient in the high vapor quality regime. Both the mass flux and system pressure have some effects on the pressure drop for the entire quality range. A higher mass flux results in a higher pressure drop but a higher system pressure results in a lower pressure drop. Moreover, the rise in the heat transfer coefficient with the vapor quality is larger than that in the pressure drop.

During the course of this investigation it has been recognized that data for the condensation heat transfer are also important in using the plate heat exchangers in various air conditioning and refrigeration systems. This will be conducted in the near future.

Acknowledgments

References

Akers, W. W., Deans, H. A., and Crosser, O. K., 1958, "Condensation heat transfer within horizontal tubes," Chemical Engineering Progress, Vol. 54, pp. 89–90.

Collier, J. G., 1981, Convective boiling and condensation, 2nd Ed. McGraw-Hill, New York, pp. 26–69.

D'Yachkov, F. N., 1978, "Investigation of Heat Transfer and Hydraulics for Boiling of Freon-22 in Internally Finned Tubes," Heat Transfer Sov. Res., Vol. 10, No. 2, pp. 10–19.

Eckels, S. J., and Pate, M. B., 1991, "An Experimental Comparison of Evaporation and Condensation Heat Transfer Coefficients for HFC-134a and CFC-12," Int. J. Refrig., Vol. 14, pp. 70–77.

Gungor, K. E., and Winterton, R. H. S., 1986, "A general correlation for flow boiling in tubes and annuli," Int. J. Heat Mass Transfer, Vol. 29, No. 3, pp. 351–358.

Incropera and Dewitt, 1981, Fundamentals of Heat Transfer, John Wiley and Sons, New York, pp. 399–407.

Kandlikar, S. G., and Shah, R. K., 1989a, "Multipass Plate Heat Exchangers-Effectiveness-NTU Results and Guidelines for Selecting Pass Arrangements," ASME JOURNAL OF HEAT TRANSFER, Vol. 111, pp. 300–313.

Kandlikar, S. G., and Shah, R. K., 1989b, "Asymptotic Effectiveness-NTU Formulas for Multipass Plate Heat Exchangers," ASME JOURNAL OF HEAT TRANSFER, Vol. 111, pp. 314–321.

Kandlikar, S. G., 1990, "A General Correlation for Saturated Two-Phase Flow Boiling Heat Transfer Inside Horizontal and Vertical Tubes," ASME JOURNAL OF HEAT TRANSFER, Vol. 112, pp. 219–228.

Kandlikar, S. G., 1991, "A Model for Correlating Flow Boiling Heat Transfer in Augmented Tubes and Compact Evaporators," ASME JOURNAL OF HEAT TRANSFER, Vol. 113, pp. 966–972.

Kerner, J., Sjogren, S., and Svensson, L., 1987, "Where Plate Exchangers Offer Advantages Over Shell-and-Tube," Power, Vol. 131, pp. 53–58.

Khanpara, J. C., Bergles, A. E., and Pate, M. B., 1986, "Augmentation of R113 In-tube Evaporation with Micro-fin Tubes," ASHRAE Trans., Vol. 92, Part 2B, pp. 506–523.

Khanpara, J. C., Bergles, A. E., and Pate, M. B., 1987, "Local Evaporation Heat Transfer in a Smooth Tube a Micro-Fin Tube Using Refrigerants 22 and 113," ASME HTD-85, pp. 31–39.

Kline, S. J., and McClintock, F. A., 1953, "Describing uncertainties in single-sample experiments," *Mechanical Engineering,* Vol. 75, No. 1, pp. 3–12.

Reid, R. S., Pate, M. B., and Bergles, A. E., 1991, "A Comparison of Augmentation Techniques During in Tube Evaporation of R-113," ASME JOURNAL OF HEAT TRANSFER, Vol. 113, pp. 451–458.

Schlager, L. M., Pate, M. B., and Bergles, A. E., 1990, "Evaporation and Condensation Heat Transfer and Pressure Drop in Horizontal, 12.7-mm Microfin Tubes With Refrigerant 22," ASME JOURNAL OF HEAT TRANSFER, Vol. 112, pp. 1041–1047.

Shah, R. K., and Focke, W. W., 1988, "Plate Heat Exchangers and Their Design Theory," *Heat Transfer Equipment Design,* R. K. Shah, E. C. Subbarao, and R. A. Mashelkar, eds., Hemisphere, Washington, DC, pp. 227–254.

Shah, R. K., and Wanniarachchi, A. S., 1992, "Plate Heat Exchanger Design Theory," *Industrial Heat Exchangers* (Lecture Series No. 1991-04), J.-M. Buchlin, ed., Von Karman Institute for Fluid Dynamics, Belgium.

Wattelet, J., Saiz Jabardo, J. M., Chato, J. C., Panek, J. S., and Souza, A. L., 1992, "Experimental Evaluation of Convective Boiling of Refrigerants HFC-134a and CFC-12," ASME HTD-Vol. 197, pp. 121–127.

Wattelet, J. P., Chato, J. C., Souza, A. L., and Christoffersen, B. R., 1994, "Evaporation characteristics of R-12, R-134a, and a mixture at low fluxes," *ASHRAE Transactions,* Vol. 100, pp. 603–615.

Williams, B., 1996, "Heat transfer savings on a plate," *Heating and Air Conditioning Journal,* Apr., pp. 29–31.

Wilson, E. E., 1915, "A Basis for Traditional Design of Heat Transfer Apparatus," *Trans. ASME,* Vol. 37, pp. 47–70.

Performance Analysis and Optimization of Eccentric Annular Disk Fins

B. Kundu[1]

P. K. Das

Department of Mechanical Engineering,
Indian Institute of Technology,
Kharagpur-721302, India

In the first part of the paper, a semi-analytical method has been described for solving the two-dimensional heat conduction equation in an eccentric annular disk fin circumscribing a circular tube, subjected to convective cooling. Analysis has been done considering both convective and insulated conditions at the fin tip. The effects of surface and tip heat transfer coefficients and eccentricity on the performance of the fin have been studied. Comparative studies have also been made between the performance of concentric and eccentric fins with same radius ratio. Next, the optimum dimensions for eccentric annular fins have been determined using Lagrange multiplier technique. In the scheme, either the fin volume or the heat transfer duty can be taken as the constraint. Finally, it has been shown that when space restriction is imposed on one side of the tube, eccentric annular fins can be designed to have lesser volumes compared to concentric annular fins above a certain heat transfer duty.

1 Introduction

Fins or extended surfaces are often used to enhance the rate of heat transfer from the primary surface. The selection of any particular type of fin depends on the geometry of this surface. Radial or concentric annular fins are one of the most common choices for enhancing the rate of outside heat transfer from circular tubes. It is a well-known fact that the rate of heat transmission from a fin diminishes with its length. This has given rise to a host of research activities for the design of optimum fin shapes. Guceri and Maday (1975) used calculus of variation to find out the profile of the minimum volume circular fin for a given heat transfer duty. They have numerically obtained the optimum profile through a Hamiltonian formulation. The resulting fin geometry needs a large surface area to dissipate the required amount of heat with the minimum volume. The fin profiles become highly wavy in nature which restricts their application. Alternatively, efforts have been spent to find out the dimensions of minimum volume fins where the profile have been selected a priori. Ulmann and Kalman (1989) determined optimised dimensions of annular fins with triangular and parabolic profile as well as with constant heat transfer area. Compared to the above profiles, constant thickness annular fins or disk fins require a larger volume for the same heat transfer duty. Still, they find wide applications in a variety of heat exchanger equipments due to their simple design and for the ease of fabrication. Analysis of concentric annular disk fins is available in a number of references (Kern and Kraus, 1972; Ozisik, 1980). The optimization of such fins, conducted by Brown (1965), indicates an increase both in length and thickness of annular disc fins of optimum design with increased heat transfer duty.

However, where there is a space restriction on one side of the tubes, or there is an angular variation of tube temperature, concentric annular disk fins cannot be used optimally to dissipate maximum amount of heat for a given fin volume. If space restriction is there, the fin volume can be increased by increasing

only the fin thickness when concentric annular disk fins are selected. Obviously this does not guarantee the optimum use of fin material. Instead, a saving in the fin material can be achieved if eccentric annular fins are employed.

Though an exact solution exists (Brown, 1965) for the temperature distribution in concentric annular disk fins, to the best of the knowledge of the authors, the same is not available for eccentric annular fins of constant thickness. The problem of heat conduction in eccentric geometry has been addressed by El-Saden (1961). He has presented an analysis of two-dimensional heat conduction in an eccentrically hollow, infinitely long cylinder with internal heat generation and obtained a closed-form solution for the temperature distribution through the bipolar coordinate transformation. Using the same methodology, fluid dynamic and heat transfer problems in an eccentric annulus have been solved by Snyder (1963) and Snyder and Goldstein (1965). Recently Shigechi et al. (1996) have extended the same analysis for fully developed laminar fluid flow with an axially moving core. From the above works, it is clear that for Poision's equation the physical eccentric domain can be converted into a rectangular one through the bipolar coordinate transformation under different boundary conditions. Thereafter, an analytical solution becomes possible. However, for an eccentric fin, the two-dimensional heat transfer equation cannot be reduced to Poision's form even through the bipolar coordinate transformation as the source term is a function of local fin temperature. Shigechi et al. (1996) adopted a numerical technique to solve the heat transfer problem for fully developed laminar flow in the eccentric annulus with an axially moving core. Kazeminejad et al. (1993) have analyzed the performance of eccentric annular fins for dehumidification of air. They have also used the bipolar coordinate transformation and obtained the temperature profile using a finite difference scheme. The authors have reported that their numerical results compare well with the available exact solution for negligible values of eccentricity.

In the present paper, on the other hand, a semi-analytical method has been adopted to solve the elliptic heat transfer equation in an eccentric annular fin. Fins with constant base temperature, dissipating heat solely by convection (without any dehumidification) have been considered in the analysis. For zero value of eccentricity, the result from the semi-analytical method coincides exactly with the closed-form solution available for concentric annular fins. Next, a methodology has been sug-

Copyright © 1999 by ASME

gested for optimizing the dimensions of eccentric annular fins. The optimization problem has been cast in a generalized form. Depending on the requirement, either fin volume can be minimized for a given rate of heat dissipation or the rate of heat transfer can be maximized for a given fin volume. Finally, it has been demonstrated that when the length of the fin is restricted on one side of the tube, eccentric annular disk fins of optimum design require less volume than concentric annular fins.

2 Physical Model and Mathematical Formulation

Figure 1(a) schematically depicts an eccentric annular fin of thickness $2t$, circumscribing a circular tube of outer radius r_i. The eccentric annular fin can be described by three geometrical parameters namely the inner radius r_i, the outer radius r_o, and the eccentricity e. Alternatively, when the space restriction s ($=r_o - e$), for the fin with respect to the inner tube is specified, the fin can be described by r_i, r_o, and s. As the fin is symmetrical with respect to the diametral plane $X-X$, only one half of the fin may be considered for the analysis of heat transfer. The symmetric half of the fin along with the geometrical details is depicted in Fig. 1(b) and 1(c) for given eccentricity and given space restriction, respectively.

Selecting a cylindrical polar coordinate at O, the center of the tube, the heat transfer equation in the eccentric fin can be written in the nondimensional form as

$$\frac{\partial}{\partial R}\left(R\frac{\partial \theta}{\partial R}\right) + \left(\frac{1}{R}\right)\frac{\partial^2 \theta}{\partial \phi^2} = \left(\frac{\text{Bi}}{\xi}\right)R\theta. \quad (1)$$

Heat loss from the fin has been assumed solely due to convection. The conductivity of the fin material, convective heat transfer coefficient from the fin, and the temperature of the gas stream have been assumed to be constant. Moreover, the temperature variation in the fin, normal to the fin surface, has been neglected based on a thin-fin assumption. The symmetric half of the fin is subjected to the following boundary conditions. The outer surface of the fluid carrying tube or the fin base is at constant temperature. There is no heat transfer in the transverse direction

across the symmetrical diametral plane $X-X$. At the fin tip, either one may assume negligible heat loss or the heat transfer due to conduction in a direction normal to the fin tip can be equated to the convective heat loss from the tip. The boundary conditions is expressed mathematically as follows:

$$\left.\begin{array}{ll}
\theta = 1 & \text{at } R = 1 \quad (0 \le \phi \le \pi) \\[2mm]
\dfrac{1}{R}\dfrac{\partial \theta}{\partial \phi} = 0 & \text{at } \phi = 0 \quad (1 \le R \le \alpha_t) \\[2mm]
\dfrac{1}{R}\dfrac{\partial \theta}{\partial \phi} = 0 & \text{at } \phi = \pi \quad (1 \le R \le \alpha_t) \\[2mm]
r_i\dfrac{\partial \theta}{\partial n} = -\text{Bi}_t\theta & \text{at } R = \alpha_t \quad (0 \le \phi \le \pi)
\end{array}\right\} \quad (2)$$

where $\text{Bi}_t = z_0^2\beta$, $z_0 = \sqrt{\text{Bi}/\xi}$ and $\beta = \text{Bi}_t\xi/\text{Bi}$

$\quad\quad \beta = 0$, no heat loss from the tip

$\quad\quad \beta > 0$, convection from the tip.

Solving Eq. (1) along with first three boundary conditions,

$$\theta - \frac{I_0(Rz_0)}{I_0(z_0)} = [\mathbf{D_0} \quad \mathbf{D_1} \quad \mathbf{D_2} \quad \cdots \quad \mathbf{D_j} \quad \cdots \quad \mathbf{D_n}]\begin{bmatrix} \mathbf{C_0} \\ \mathbf{C_1} \\ \mathbf{C_2} \\ \cdots \\ \mathbf{C_j} \\ \cdots \\ \mathbf{C_n} \end{bmatrix} \quad (3)$$

where

$$D_j = \frac{\cos{(j\phi)}}{I_j(z_0)}\begin{vmatrix} I_j(z_0) & I_j(Rz_0) \\ K_j(z_0) & K_j(Rz_0) \end{vmatrix}. \quad (4)$$

For determining C_j in Eq. (3), the fourth boundary condition of Eq. (2) has to be applied. This has been achieved through a method of collocation as suggested by Sparrow and Lin (1964).

Notation

Bi = Biot number, based on fin surface heat transfer coefficient, hr_i/k

Bi_t = Biot number, based on fin tip heat transfer coefficient, $h_t r_i/k$

C_n = constant used in Eq. (3)

e = eccentricity (m)

h = surface heat transfer coefficient (W/m^2 K)

h_t = tip heat transfer coefficient (W/m^2 K)

$I_n(z)$ = modified Bessel function of first kind of order n and of argument z

j = discrete boundary point (1, 2, 3, ..., $n + 1$)

J = Jacobian

k = thermal conductivity of fin material (W/mK)

$K_n(z)$ = modified Bessel function of second kind of order n and of argument z

n = integer

q = heat transfer rate (W)

q_o = ideal heat transfer rate (W)

Q = nondimensional heat transfer rate, $q/4\pi k r_i(T_w - T_a)$

Q_i = heat transfer rate when the fin tip is insulated

Q_l = heat transfer rate when the fin tip is subjected to convective condition

Q_o = ideal rate of heat transfer from the fin in nondimensional form

r = radial distance from the tube center (m)

r_i = outer radius of the tube (m)

R = r/r_i

r_o = outer radius of eccentric annular fin (m)

r_t = tip distance measured from the tube center (m)

s = space restriction, $r_o - e$ (m)

S = s/r_i

t = half fin thickness (m)

T = local fin temperature (K)

T_a = temperature of the gas medium surrounding the fins (K)

T_w = fin base temperature (K)

V = fin volume (m^3)

U = dimensionless fin volume, $v/2\pi r_i^3$

z_0 = fin parameter, $\sqrt{hr_i^2/kt}$ [$=\sqrt{\text{Bi}/\xi}$]

Greek

α = radius ratio of eccentric annular fin, r_o/r_i

α_t = dimensionless tip distance from the tube center, r_t/r_i

β = tip loss parameter, $h_t t/h r_i$ [$= \text{Bi}_t\xi/\text{Bi}$]

ϵ = dimensionless eccentricity, e/r_i

η = fin efficiency

ϕ = angular position of any point in the fin

ϕ_i = angular position of ith point on the outer circle of the fin measured from the center of the inside circle (tube), see Fig. 1(b) and 1(c) ($\phi_0, \phi_1, \ldots, \phi_n$)

θ = dimensionless temperature, $(T - T_a)/(T_w - T_a)$

$\theta_0 = T_w - T_a$ (K)

ψ_i = angular position of ith point on the outer circle of the fin measured from the center of the outside circle (fin), see Fig. 1(b) and 1(c) ($\psi_0, \psi_1, \ldots, \psi_n$)

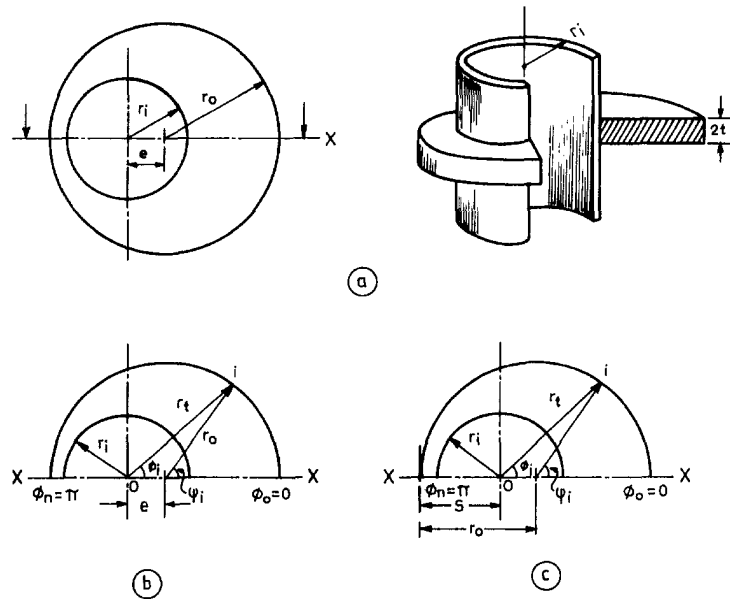ξ = half-thickness of the fin in dimensionless form, t/r_i

Fig. 1 Eccentric annular disk fin; (a) Schematic diagram of an eccentric annular disk fin, (b) Geometrical details of a specified eccentricity, (c) Geometrical details of a specified space restriction

The last boundary condition has been satisfied at a large number of points along the fin tip. The final solution thus obtained, though approximate, yields results of desired accuracy. The following mathematical steps are necessary for obtaining C_j:

$$\text{At} \quad R = \alpha_t; \quad \begin{vmatrix} \sin(\psi_i - \phi_i) & \cos(\psi_i - \phi_i) \\ \dfrac{\partial\theta}{\partial R} & -\dfrac{1}{R}\dfrac{\partial\theta}{\partial\phi} \end{vmatrix} = \text{Bi}_t\theta, \quad (5)$$

where

$$\psi_i = \begin{cases} \sin^{-1}\left(\dfrac{\alpha_t \sin\phi_i}{\alpha}\right) : \phi_i \le \sin^{-1}\left(\dfrac{\alpha}{\alpha_t}\right) \\[3mm] \pi - \sin^{-1}\left(\dfrac{\alpha_t \sin\phi_i}{\alpha}\right) : \phi_i \ge \sin^{-1}\left(\dfrac{\alpha}{\alpha_t}\right). \end{cases} \quad (6)$$

At this point either eccentricity or the space restriction should be specified to determine α_t.

2.1 Performance of Eccentric Fins When Eccentricity is Specified. For a known value of eccentricity, the distance of the fin tip from the center of the tube can be expressed as

$$\alpha_t = \epsilon \cos\phi_i + \sqrt{\alpha^2 - \epsilon^2 \sin^2\phi_i}. \quad (7)$$

The Eq. (5) becomes

$$[A_{ij}][C_jE_j] = [B_i] \quad (8)$$

where

$$A_{ij} = F_1 + F_2$$

$$= \begin{vmatrix} \tan j\phi_i - \cot(\psi_i - \phi_i) & \alpha_t \\ \text{Bi}_t & j\sin(\psi_i - \phi_i) \end{vmatrix}$$

$$\times \begin{vmatrix} I_j(z_0) & K_j(z_0) \\ I_j(z_0\alpha_t) & K_j(z_0\alpha_t) \end{vmatrix} + \begin{vmatrix} \cos(\psi_i - \phi_i) & 0 \\ 0 & z_0\alpha_t \end{vmatrix}$$

$$\times \begin{vmatrix} I_j(z_0) & -K_j(z_0) \\ I_{j+1}(z_0\alpha_t) & K_{j+1}(z_0\alpha_t) \end{vmatrix} \quad (9)$$

$$E_j = \frac{\cos(j\phi_i)}{I_j(z_0)\alpha_t} \quad (10)$$

$$B_i = \left(\frac{1}{I_0(z_0)}\right) \begin{vmatrix} z_0 \cos(\psi_i - \phi_i) & -I_0(z_0\alpha_t) \\ \text{Bi}_t & I_1(z_0\alpha_t) \end{vmatrix}. \quad (11)$$

A family of $(n + 1)$ number of linear equations is described by Eq. (8). They are to be simultaneously solved to get the $(n + 1)$ number of unknowns $(C_0$ to $C_n)$. The temperature field in the fin can now be obtained from Eq. (3) substituting C_j, when inner and outer radii of the fin, its eccentricity and Biot number are specified. Once the solution for temperature distribution in the fin is available, the rate of heat flow through the fin base can be calculated readily:

$$Q = \frac{q}{4\pi K r_i \theta_0} = -\frac{\xi}{\pi} \int_{\phi=0}^{\pi} \frac{\partial\theta}{\partial R}\Big|_{R=1} d\phi. \quad (12)$$

Integrating the above equation,

$$Q = \frac{\xi}{I_0(z_0)}[C_0 - z_0 I_1(z_0)]. \quad (13)$$

Fin efficiency is defined as the ratio of the rate of actual heat transfer from the fin to the rate of ideal heat transfer if the entire fin surface remains at its base temperature. Considering tip heat loss, the nondimensional ideal heat transfer rate Q_o is given by

$$Q_o = \frac{q_o}{4\pi k r_i \theta_0} = \frac{\text{Bi}[(\alpha^2 - 1) + 2\beta\alpha]}{2}. \quad (14)$$

Finally, fin efficiency can be obtained as follows:

$$\eta = \frac{Q}{Q_o} = \frac{2[C_0 - z_0 I_1(z_0)]}{z_0^2 I_0(z_0)[\alpha^2 + 2\beta\alpha - 1]}. \quad (15)$$

2.2 Optimization of Eccentric Fins When Eccentricity is Specified. The dimensionless fin volume is given by

$$U = \frac{V}{2\pi r_i^3} = (\alpha^2 - 1)\xi. \quad (16)$$

For a given Biot number, both the fin volume (U) and rate of heat dissipation (Q) are functions of ξ and α. The optimum dimensions (ξ and α) of the fin can be determined either by maximizing the rate of heat dissipation for a given volume or minimizing the volume for a specified rate of heat transfer. The generalized condition for optimality is obtained from Eqs. (13) and (16) by means of the Lagrange multiplier technique. If the Lagrange multiplier is eliminated, the condition for optimality can be expressed as a Jacobian of Q and U with respect to ξ and α:

$$J\left(\frac{Q, U}{\xi, \alpha}\right) = \frac{\partial(Q, U)}{\partial(\xi, \alpha)} = \begin{vmatrix} \dfrac{\partial Q}{\partial \xi} & \dfrac{\partial U}{\partial \xi} \\[2mm] \dfrac{\partial Q}{\partial \alpha} & \dfrac{\partial U}{\partial \alpha} \end{vmatrix} = 0. \qquad (17)$$

On simplification Eq. (17) becomes

$$2\left(C_0 + \xi\,\frac{\partial C_0}{\partial \xi} - z_0 I_1(z_0)\right) + z_0^2 I_0(z_0)$$

$$+ \frac{C_0 z_0 I_1(z_0)}{I_0(z_0)} - \frac{z_0^2 I_1^2(z_0)}{I_0(z_0)} - \left(\alpha - \frac{1}{\alpha}\right)\frac{\partial C_0}{\partial \alpha} = 0. \quad (18)$$

For determining $\partial C_0/\partial \alpha$ and $\partial C_0/\partial \xi$, Eq. (8) has to be differentiated with respect to α and ξ separately.

$$[A'_{ij}][C_j E_j] + [A_{ij}][C'_j E_j + C_j E'_j] = [B'_i] \qquad (19)$$

where

$$A'_{ij} = F'_1 + F'_2, \qquad (20)$$

and

$$F'_1 = \begin{vmatrix} \psi'_i \cosec^2(\psi_i - \phi_i) & \alpha_t \\ 0 & j\,\sin(\psi_i - \phi_i) \end{vmatrix}$$

$$\times \begin{vmatrix} I_j(z_0) & K_j(z_0) \\ I_j(z_0\alpha_t) & K_j(z_0\alpha_t) \end{vmatrix}$$

$$+ \begin{vmatrix} \tan j\phi_i - \cot(\psi_i - \phi_i) & \alpha'_t \\ Bi_t & j\psi'_i \cos(\psi_i - \phi_i) \end{vmatrix}$$

$$\times \begin{vmatrix} I_j(z_0) & K_j(z_0) \\ I_j(z_0\alpha_t) & K_j(z_0\alpha_t) \end{vmatrix}$$

$$+ \begin{vmatrix} \tan j\phi_i - \cot(\psi_i - \phi_i) & \alpha_t \\ Bi_t & j\,\sin(\psi_i - \phi_i) \end{vmatrix}$$

$$\times \begin{vmatrix} I'_j(z_0) & K_j(z_0) \\ I'_j(z_0\alpha_t) & K_j(z_0\alpha_t) \end{vmatrix}$$

$$+ \begin{vmatrix} \tan j\phi_i - \cot(\psi_i - \phi_i) & \alpha_t \\ Bi_t & j\,\sin(\psi_i - \phi_i) \end{vmatrix}$$

$$\times \begin{vmatrix} I_j(z_0) & K'_j(z_0) \\ I_j(z_0\alpha_t) & K'_j(z_0\alpha_t) \end{vmatrix} \qquad (21)$$

$$F'_2 = \begin{vmatrix} -\psi'_i \sin(\psi_i - \phi_i) & 0 \\ 0 & z_0\alpha_t \end{vmatrix} \begin{vmatrix} I_j(z_0) & -K_j(z_0) \\ I_{j+1}(z_0\alpha_t) & K_{j+1}(z_0\alpha_t) \end{vmatrix}$$

$$+ \begin{vmatrix} \cos(\psi_i - \phi_i) & 0 \\ 0 & z_0\alpha_t)' \end{vmatrix} \begin{vmatrix} I_j(z_0) & -K_j(z_0) \\ I_{j+1}(z_0\alpha_t) & K_{j+1}(z_0\alpha_t) \end{vmatrix}$$

$$+ \begin{vmatrix} \cos(\psi_i - \phi_i) & 0 \\ 0 & z_0\alpha_t \end{vmatrix} \begin{vmatrix} I'_j(z_0) & -K_j(z_0) \\ I'_{j+1}(z_0\alpha_t) & K_{j+1}(z_0\alpha_t) \end{vmatrix}$$

$$+ \begin{vmatrix} \cos(\psi_i - \phi_i) & 0 \\ 0 & z_0\alpha_t \end{vmatrix} \begin{vmatrix} I_j(z_0) & -K'_j(z_0) \\ I_{j+1}(z_0\alpha_t) & K'_{j+1}(z_0\alpha_t) \end{vmatrix} \quad (22)$$

$$E'_j = -\frac{\cos j\phi_i[\alpha'_t I_j(z_0) + \alpha_t I'_j(z_0)]}{[\alpha_t I_j(z_0)]^2} \qquad (23)$$

$$B'_i = \left(\frac{1}{I_0(z_0)}\right)' \begin{vmatrix} z_0 \cos(\psi_i - \phi_i) & -I_0(z_0\alpha_t) \\ Bi_t & I_1(z_0\alpha_t) \end{vmatrix} + \left(\frac{1}{I_0(z_0)}\right)$$

$$\times \begin{vmatrix} z'_0 \cos(\psi_i - \phi_i) - z_0\psi'_i \sin(\psi_i - \phi_i) & -I_0(z_0\alpha_t) \\ 0 & I_1(z_0\alpha_t) \end{vmatrix}$$

$$+ \left(\frac{1}{I_0(z_0)}\right) \begin{vmatrix} z_0 \cos(\psi_i - \phi_i) & -I'_0(z_0\alpha_t) \\ Bi_t & I'_1(z_0\alpha_t) \end{vmatrix} \qquad (24)$$

$$I'_j(z_0\alpha_t) = (z_0\alpha_t)'\left[I_{j+1}(z_0\alpha_t) + \left(\frac{j}{z_0\alpha_t}\right)I_j(z_0\alpha_t)\right] \qquad (25)$$

and

$$K'_j(z_0\alpha_t) = (z_0\alpha_t)'\left[-K_{j+1}(z_0\alpha_t) + \left(\frac{j}{z_0\alpha_t}\right)K_j(z_0\alpha_t)\right], \qquad (26)$$

where the prime means derivative with respect to the ξ or α. At this point according to the requirement of the designer, Eq. (16) and Eq. (18) can be solved simultaneously to find out the maximum rate of heat dissipation for a given fin volume. Alternatively, Eq. (13) can be considered instead of Eq. (16) if minimum fin volume has to be estimated for a given heat transfer duty. The solution of the two nonlinear equations have been obtained numerically through the generalized Newton-Raphson Technique (Stoeker, 1989). The root finding algo-
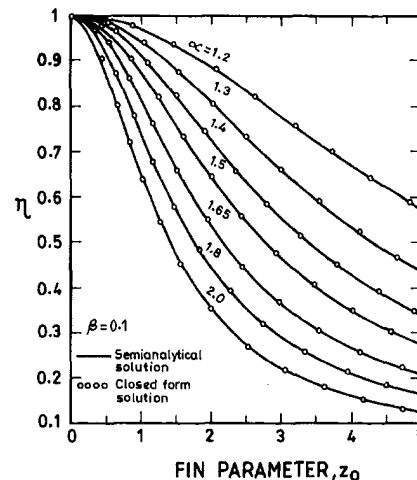

Fig. 2 Efficiency of concentric fins by a semi-analytical and closed-form solution
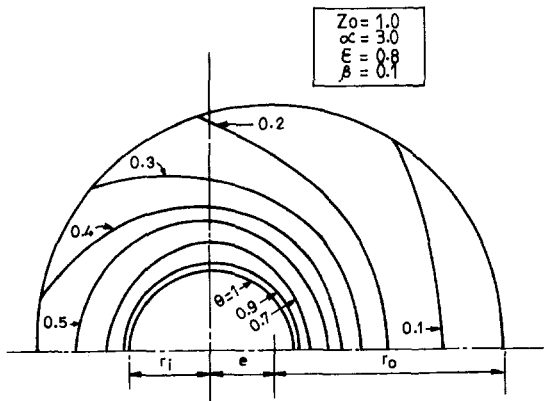
Fig. 3 Isotherms for an eccentric annular fin

Fig. 4 Temperature distribution in an eccentric fin at the plane of symmetry

rithm requires the values of $\partial^2 C_0/\partial\alpha^2$, $\partial^2 C_0/\partial\xi^2$, and $\partial^2 C_0/\partial\alpha\partial\xi$. They have been computed through successive differentiation of Eq. (19). The scheme will yield the optimum values of α and ξ when the eccentricity and the Biot number are specified.

2.3 Optimization of Eccentric Fins With a Given Space Restriction.
When a space restriction is imposed on one side of the eccentric annular fin, the distance of the fin tip from the tube radius becomes fixed at $\phi = \pi$ (Fig. 1(c)). Based on this design criteria, the eccentricity of the fin becomes a function of the space restriction, S. Accordingly the dimensionless distance of the fin tip from the center of the tube is given by

$$\alpha_t = (\alpha - S) \cos \phi_i + \sqrt{\alpha^2 - (\alpha - S)^2 \sin^2 \phi_i}. \quad (27)$$

The scheme of optimization will yield the values of α and ξ when Biot number and S are specified. The method of analysis is identical to that described in the previous section when Eq. (27) is used instead of Eq. (7).

3 Results and Discussion

3.1 Fin Performance.
As no analytical solution for heat transfer in eccentric annular fins is available, a direct assessment of the present semianalytical method is not possible. However, if eccentricity (ϵ) in Eq. (7) is made zero, the fin geometry becomes concentric annular. Considering convective heat loss from the fin tip, the efficiency of concentric annular fin can be obtained following the analysis of Kern and Kraus (1972) as

tip temperatures are encountered at this angular position for all Biot numbers.

Figure 5 shows the effect of eccentricity and the tip loss on the temperature profiles along the plane of symmetry ($\phi = 0$ and $\phi = \pi$), for fins with identical heat transfer coefficients over the fin surface and fin tip. With an increase of eccentricity, the temperature decreases everywhere from the fin base to fin tip along $\phi = 0$ whereas a reverse effect of eccentricity on temperature distribution is observed along $\phi = \pi$. Moreover, the temperature profiles along $\phi = \pi$ is more sensitive to the change of eccentricity. The observed trend can be explained from the fact that with an increase of eccentricity for constant α, the distance of fin tip increases along $\phi = 0$ while it decreases along $\phi = \pi$. Figure 5 also depicts that with an increase of tip loss parameter, the radial temperature gradient decreases and the fin temperature increases at every location for the same boundary conditions. When the convective heat transfer coefficients for both the fin surface and the fin tip are identical, a higher value of tip loss parameter β indicates a thicker fin and a lower value of z_0. Consequently, the temperature gradient decreases with the increase of β. However, a reverse trend will be observed if β is increased keeping z_0 constant.

From Fig. 6, the performance of eccentric fins can be compared vis-a-vis concentric fins with the same radius ratio. For the comparison, identical boundary condition (adiabatic or convective) at the fin tip for two types of fins and a typical eccen-

$$\eta = \left\{ \frac{I_1(z_0\alpha)K_1(z_0) - I_1(z_0)K_1(z_0\alpha) + z_0\beta(I_0(z_0\alpha)K_1(z_0) + I_1(z_0)K_0(z_0\alpha))}{I_0(z_0)K_1(z_0\alpha) + I_1(z_0\alpha)K_0(z_0) - z_0\beta(I_0(z_0)K_0(z_0\alpha) - I_0(z_0\alpha)K_0(z_0))} \right\} \left\{ \frac{2}{z_0(\alpha^2 + 2\alpha\beta - 1)} \right\}. \quad (28)$$

Figure 2 depicts excellent agreement between Eq. (15) and Eq. (28). The temperature distribution in the symmetric half of an eccentric annular fin is shown in Fig. 3 for $\alpha = 3.0$, $z_0 = 1.0$, $\beta = 0.1$, and $\epsilon = 0.8$. Due to eccentricity, diffusion of thermal energy takes place both in the radial and angular directions of the fluid carrying tube. This makes the isothermal contours eccentric with respect to the center of the tube. The effect is more pronounced towards the fin tip.

Figure 4 exhibits the effect of Biot number on the predicted temperature profiles for the case of $\alpha = 2.5$, $\beta = 0.1$, $\epsilon = 1.0$, and $Bi = Bi_t$. To bring out the asymmetric effect, the temperature profiles have been shown at the plane of symmetry, i.e., at $\phi = 0$ and $\phi = \pi$. In general, the fin temperature decreases with an increase of Biot number. However, the temperature profiles are less sensitive to Biot number at $\phi = \pi$. The highest

tricity $\epsilon = 0.5$ has been chosen. Figure 6(a) depicts the fin performance without any tip heat loss while the effect of tip loss can be envisaged from Fig. 6(b). In general, an eccentric fin is less efficient than a concentric fin with the same radius ratio. However, the difference in the fin efficiency diminishes with higher values of α. The fin parameter z_0 influences the performance of an eccentric fin in a unique manner. The difference between the fin efficiency of a concentric fin and a corresponding eccentric one starts increasing with the increase of the fin parameter, reaches a maximum, and then becomes zero asymptotically. The fin efficiency of any type reduces when the tip heat loss is considered while keeping all the other conditions unchanged. As an ideal fin dissipates more heat through the fin tip for the same convective heat transfer coefficient, this is an expected trend. The effect of the tip loss parameter β on the
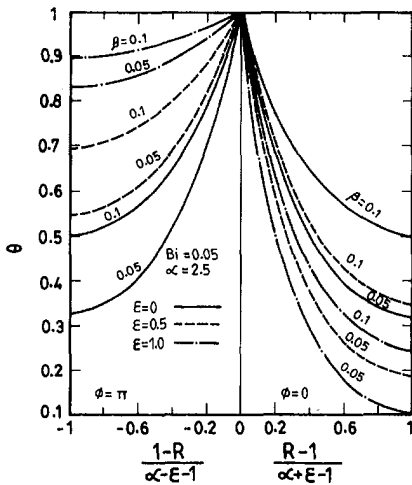
Fig. 5 Effect of tip heat loss on the temperature distribution in the symmetric plane of an eccentric fin

Fig. 7 Effect of tip loss on heat dissipation from eccentric annular fins

performance of eccentric fins can be better understood from Fig. 7. The effect of tip heat loss increases with fin thickness and convective heat transfer coefficient at the fin tip as well as with higher eccentricity for a given radius ratio. The error in the fin efficiency predicted based on insulated tip condition is the minimum for a concentric annular fin. Therefore, caution is to be taken while imposing the insulated tip boundary condition for an eccentric fin.

3.2 Optimum Dimensions of Eccentric Fins. Optimum dimensions of the eccentric fins are obtained numerically by solving Eq. (18) along with a suitable constraint equation. For the design of fins with specified volume constraint, Eq. (16) is taken; while for specified heat transfer duty, Eq. (13) is to be considered. Analyses have been conducted considering identical convective heat transfer coefficients for both the fin surface and fin tip. The salient results are discussed below. For a fixed fin volume U, the heat dissipation rate from the fin surface increases with thickness, reaches a well-defined maximum, and then falls gradually as depicted in Fig. 8(a). Although the heat dissipation is insensitive to fin volume at lower values of fin thickness ξ, there exists a well-defined optimum value of fin thickness which maximizes the heat dissipation for a given fin volume. Curve A in Fig. 8(a), gives the locus for the optimum fin thickness. It is interesting to note that for a given fin volume and constant eccentricity, there is a limiting lowest value of the outer radius (α_{min}) of the eccentric fin. At this value of α, the fin tip coincides with the outer surface of the tube at $\phi = \pi$. For this limiting value of outer radius, the thickness of the eccentric fin becomes maximum:

$$\alpha_{min} = \sqrt{1 + \frac{U}{\xi_{max}}}. \qquad (29)$$

Curve B shows the locus of the maximum thickness for different fin volumes. The optimum dimensions of the eccentric fins of specified fin volume can also be determined from the supplementary Fig. 8(b), where the heat dissipation has been depicted as a function of the outer radius α. Curve C, the locus of optimum design points in Fig. 8(b) corresponds to curve A of Fig. 8(a). The locus of the maximum fin thickness or the minimum α, curve B in Fig. 8(a) coincides with the ordinate of Fig. 8(b).

Next, the fin dimensions have been optimized for specified values of the heat dissipation rate. The results are shown graphically in Figs. 9(a) and 9(b). In these figures, curves D and E, respectively, give the optimum values of thickness and outer radius for given heat dissipation rates.

For a given tube radius, when the heat transfer duty per fin is specified, concentric annular fins of optimum dimensions can
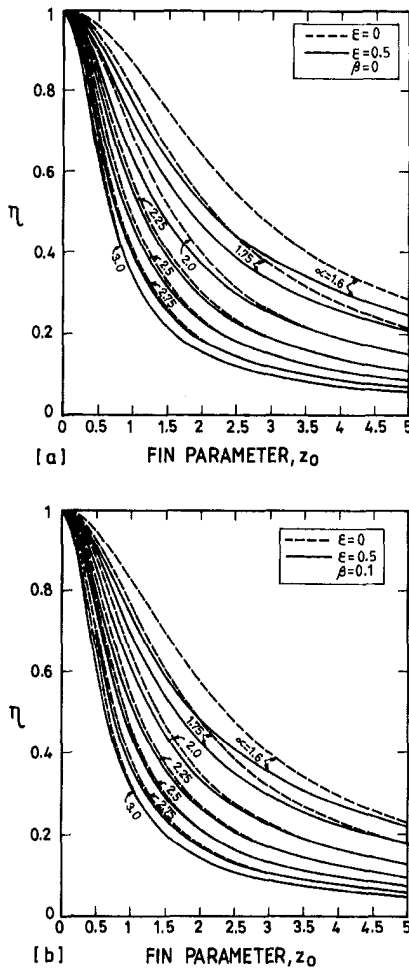

Fig. 6 Comparison between the Efficiency of Concentric and Eccentric Annular Fins for same radius ratio; (a) without tip heat loss ($\beta = 0$) (b) with tip heat loss ($\beta = 0.1$)
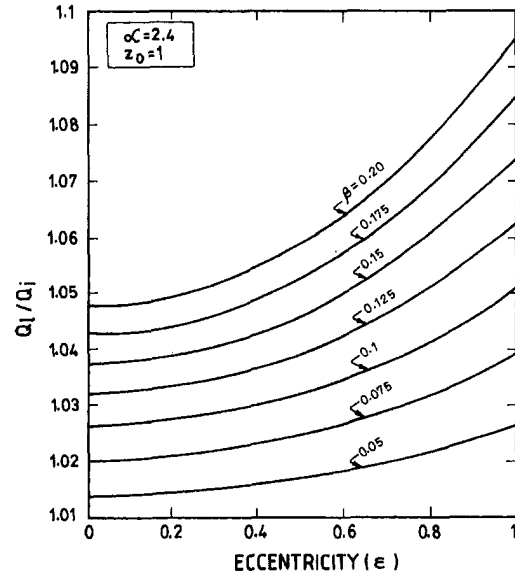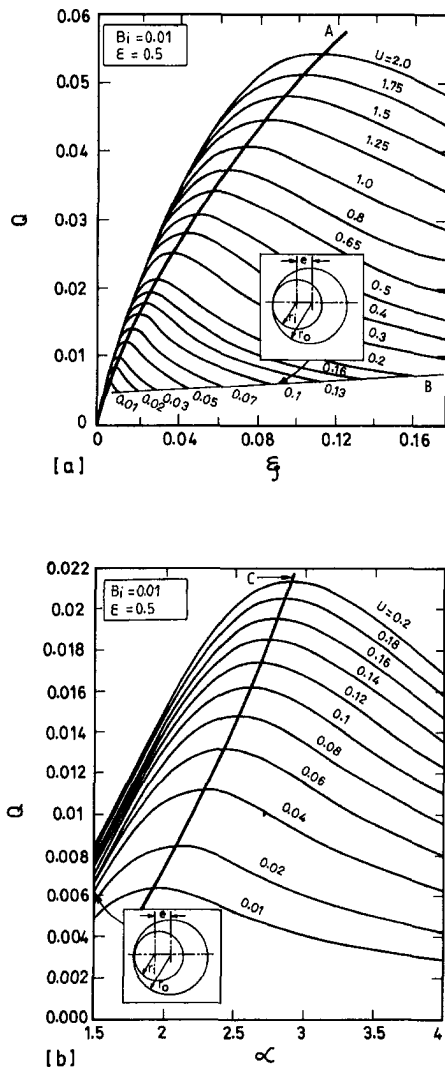
Fig. 8 Heat dissipation from eccentric annular fins for specified fin volumes; (a) heat dissipation as a function of fin thickness (ξ) (b) heat dissipation as a function of outer radius (α)

Fig. 9 Volume of eccentric annular fins for specified heat transfer duties; (a) volume as a function of fin thickness (ξ) (b) volume as a function of outer radius (α)

easily be determined. The optimum design comprises of the value of α and ξ to yield the minimum fin volume. With the increase of heat transfer duty, the minimum fin volume increases signifying an increase in both α and ξ. When a space restriction S is imposed on one side of the fin, the maximum dimension of the outer radius of a concentric fin is fixed ($\alpha_t = \alpha \leq S$). This implies that optimum concentric fins can be provided up to a certain value of heat transfer duty per fin. With an increase of the heat transfer duty, material saving in the fin volume can be done if eccentric annular geometry is selected. In Fig. 10, the fin volumes needed by both concentric and eccentric annular fins have been plotted as a function of the rate of heat dissipation for $S = 1.5$. Curve F depicts the limiting values of the heat transfer duty for which optimum concentric annular fins can be designed for various Biot numbers. As expected, with the increase of Biot number, optimum annular fins can be designed for higher values of Q. For eccentric annular fins, the saving in the fin volume beyond curve F is also obvious from Fig. 10.

4 Conclusion

In the present work, the two-dimensional heat conduction equation for an eccentric annular fin under the convective condition has been solved by a semi-analytical approach. In this approach, the boundary condition at the fin tip has been matched

at a large number of discrete points. The solution agrees with the analytical results when eccentricity is made zero. The analyses included both convective and insulated boundary conditions at the fin tip. Convective heat loss from the fin tip has a pronounced effect on the fin performance with the increase of eccentricity. In general, the fin efficiency of eccentric fins are less than that of concentric fins for the same values of radius
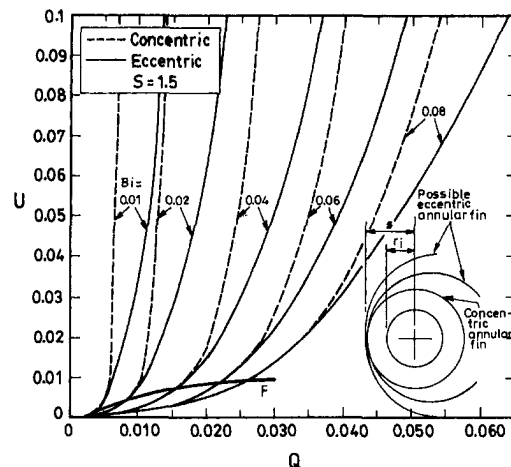
Fig. 10 Comparison of concentric and eccentric fins for a given space restriction

ratio and other parameters. However, this difference diminishes with higher values of radius ratio and fin parameter (z_0). Next, a generalized scheme has been developed to determine the optimized dimensions of eccentric annular fins by the Lagrange multiplier technique. Using the scheme, the designer can choose either the fin volume or the heat transfer duty as the constraint. When the tube radius and eccentricity are specified, there is a minimum heat transfer duty only above which optimum eccentric fins can be provided. This is demonstrated in Fig. 8(a) and 8(b). Finally, it has been shown in Fig. 10 that when space restriction is imposed on one side of the tube, optimum utilization of fin material becomes impossible above a certain heat transfer duty by using circular fins. Under these circumstances eccentric annular fins are better alternatives.

References

Brown, A., 1965, "Optimum Dimensions of Uniform Annular Fins," *Int. J. Heat Mass Transfer,* Vol. 8, pp. 662–665.

El-Saden, M. R., 1961, "Heat Conduction in an Eccentrically Hollow, Infinitely Long Cylinder with Internal Heat Generation," ASME JOURNAL OF HEAT TRANSFER, Vol. 83, pp. 510–512.

Guceri, S., and Maday, C. J., 1975, "A Least Weight Circular Cooling Fins," ASME *Journal of Engineering for Industry,* Vol. 97, pp. 1190–1193.

Kazeminejad, H., Yaghoubi, M. A., and Sepehri, M., 1993, "Effect of Dehumidification of Air on the Performance of Eccentric Circular Fins," *IMechE,* Vol. 207, pp. 141–146.

Kern, Q. D., and Kraus, D. A., 1972, *Extended Surface Heat Transfer,* McGraw-Hill, New York.

Ozisik, M. N., 1980, *Heat Conduction,* John Wiley and Sons, New York.

Shigechi, T., Momoki, S., and Lee, Y., 1996, "Fully developed Laminar Fluid Flow and Heat Transfer in an Eccentric Annulus with an Axially Moving Core," ASME JOURNAL OF HEAT TRANSFER, Vol. 118, pp. 205–209.

Snyder, W. T., and Goldstein, G. A., 1965, "An Analysis of Fully Developed Laminar Flow in an Eccentric Annulus," *AIChE J.,* Vol. 11, pp. 462–466.

Snyder, W. T., 1963, "An Analysis of Slug Flow Heat Transfer in an Eccentric Annulus," *AIChE J.,* Vol. 9, pp. 503–506.

Sparrow, E. M., and Lin, S. H., 1964, "Heat Transfer Characteristics of Polygonal and Plate Fins," *Int. J. Heat Mass Transfer,* Vol. 7, pp. 951–953.

Stoeker, W. F., 1989, *Design of Thermal Systems,* McGraw-Hill, New York.

Ullmann, A., and Kalman, H., 1989, "Efficiency and Optimized Dimensions of Annular Fins of Different Cross-Section Shapes," *Int. J. Heat Mass Transfer,* Vol. 32, pp. 1105–1110.

N. C. DeJong

Assistant Professor,
Baylor University,
Waco, TX 76798

A. M. Jacobi[1]

Associate Professor,
Department of Mechanical and
Industrial Engineering,
University of Illinois,
Urbana, IL 61801
e-mail: a-jacobi@uiuc.edu
Assoc. Mem. ASME

Local Flow and Heat Transfer Behavior in Convex-Louver Fin Arrays

Local and surface-averaged measurements of convection coefficients and core pressure-drop data are provided for an array of convex-louver fins. For a Reynolds number range from 200 to 5400, these data are complemented with a flow visualization study and contrasted with new measurements from a similar offset-strip geometry. The results clarify the effects of boundary layer restarting, shear-layer unsteadiness, spanwise vortices, and separation, reattachment, and recirculation on heat transfer in the convex-louver geometry.

Introduction

Highly interrupted fin surfaces are widely used to enhance the air-side thermal performance of compact heat exchangers. In conventional designs, interrupted fins exploit two enhancement mechanisms to provide a performance improvement over continuous fins: (1) interrupted fins restart the thermal boundary layer and, because the average boundary layer is thinner for several short plates than for one long plate, the average heat transfer coefficient is higher for an interrupted fin; and (2) above some critical Reynolds number, interrupted surfaces can cause vortex shedding, and the mixing and unsteadiness of vortex shedding increase heat transfer.

Conventional interrupted-surface designs essentially consist of arrays of flat plates either aligned with the main flow as in offset-strip fins or at an angle of attack as in louvered-fin designs. For some highly compact heat exchangers, an alternate geometry called the *convex-louver* fin is used. It consists of an array of chevron-shaped louvers as shown in Fig. 1. While considerable research has been focused on offset-strip and louvered fins, much less work has been reported on the convex-louver geometry. The geometrical complexity of this design introduces flow complexity, and it is unclear how the boundary layer restarting and vortex-shedding mechanisms important to conventional interrupted surfaces affect the convex-louver array.

In one of the very few systematic studies of heat transfer for this geometry, Hatada and Senshu (1984) compared the flow, heat transfer, and friction factor characteristics of convex-louver fins to offset-strip fins. They concluded that convex louvers provided better mixing than offset-strip fins, and they attributed the heat transfer enhancement to this increased mixing. They attributed the increase in friction factor to the increase in the maximum core velocity caused by the smaller stream flow area of the convex-louver array. By comparing heat transfer at a fixed pumping power, Hatada and Senshu concluded that convex louvers could be superior to offset-strip fins for the geometrical parameters of their study.

Webb and Gupte (1990) used data and correlations from the literature to compare several interrupted surfaces, including offset strips, convex louvers, conventional louvers, and wavy, slit, and spine fins. Using the data of Hatada and Senshu to evaluate convex louvers, they concluded that convex louvers could be effective in heat exchangers with low air velocities,

where the pumping-power penalty associated with the increased pressure drop would be modest.

Pauley and Hodgson (1994) used flow visualization alone in an attempt to identify which convex-louver designs provide good mixing and hence may be expected to provide high heat transfer. At high Reynolds numbers, Pauley and Hodgson observed the periodic roll-up and downstream advection of spanwise vortices in one array. They also observed two recirculation zones at each convex louver: one recirculation zone was on the concave side of the louver and occupied the enclosed cavity; the other was on the leeward side of the louver. These recirculation zones were described as exhibiting regular, periodic unsteadiness, with fluid entrainment and ejection.

Wang et al. (1996) tested nine convex-louver fin-and-tube heat exchangers as well as a louvered-fin, a wavy-fin, and a plain-fin geometry for comparison purposes. They provided correlations for j and f based on their results for the nine convex-louver geometries. Using a volume goodness factor comparison, they concluded that convex louvers provide significantly better performance than plate or wavy fins but similar performance to louvered fins. In addition, Bemisderfer (1987), Hatada et al. (1989), and Matsushima et al. (1991) have presented very limited computational results for the convex geometry.

Little research has been directed at the convex-louver geometry, its promising thermal performance notwithstanding. Although results for several louver angles over a range of fin pitches and Reynolds numbers have been reported in the literature, only average heat exchanger heat transfer data are available. These prior heat transfer results and limited flow visualization provide little insight into the local flow and heat transfer interactions. That convex louvers promote mixing is clear—it is less clear how mixing is induced. It is unclear how the mechanisms leading to enhanced mixing in this geometry directly affect heat transfer. The purpose of the current study is to develop a deeper understanding of the flow and heat transfer behavior in convex-louver arrays. To this end, new local convective data, core pressure-drop measurements, and flow visualization results will be presented. These spatially resolved data provide a more complete description of the flow and heat transfer in convex-louver arrays. Though a discussion of the results and by contrasting with similar data for a related offset-strip geometry, a clearer description of the important flow features and heat transfer mechanisms will be developed.

Experimental Method

Since mass transfer and heat transfer are analogous, mass transfer experiments were conducted to measure local and spatially averaged surface convective behavior. The naphthalene sublimation technique was used for the mass transfer study;
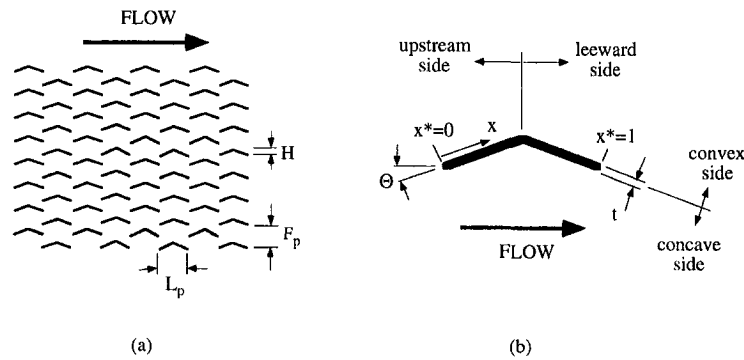

Fig. 1 A top view of the convex-louver fin array; (a) the array configuration and geometric parameters are defined, (b) a single louver element is shown in a scaled-up view

thorough reviews of this method and its application have appeared (Goldstein and Cho, 1995; Souza Mendes, 1991). The apparatus, instrumentation, specimen preparation method, and experimental procedures used in this study have been discussed extensively in a related paper (DeJong and Jacobi, 1997), so only a summary of the methods will be presented.

Apparatus and Instrumentation. The wind tunnel used in these experiments provided an approach velocity that was flat to within two percent, with a turbulence intensity less than two percent (DeJong and Jacobi, 1997). The test section was constructed of clear acrylic and had a flow cross section of 152.4 mm by 152.4 mm. The model array consisted of 64 convex-louver fins in eight rows as shown in Fig. 1. The model fins in the array were hydrodynamically smooth for all the experiments reported. This array was placed in the test section, and platinum RTDs and static pressure taps were located upstream and downstream of the test array. Each convex-louver fin had a louver angle of $\Theta = 20$ deg, a fin thickness of $t = 1.6$ mm, a fin pitch of $F_p = 18.5$ mm, and a fin length of $L_p = 25.4$ mm; thus, $F_p/t = 11.6$, $F_p/L_p = 0.73$, and $F_p/4H = 1$. The fin span (into the page in Fig. 1) was 152.4 mm. Fins in the sixth and seventh rows of the eight-row array were coated with naphthalene. Dummy (uncoated) fins were placed upstream, providing hydrodynamically developed but thermally undeveloped conditions. However, when a proper driving potential is used in data interpretation, the results from this geometry are the same whether dummy or naphthalene-coated fins are used upstream. DeJong et al. (1998) found that for a similar offset-

strip geometry, results were the same in both cases; i.e., thermal wakes had little or no influence on downstream fins. Aoki et al. (1989) reported the same conclusion for a louvered-fin sample. Since convex fins provide more mixing than these arrays (especially the offset-strip array), thermal wakes would have an even smaller effect. The thermal wakes are recovered by the time the flow reaches the downstream fin, causing the presence or absence of naphthalene upstream to have no discernible effect on downstream fins. Naphthalene was only placed to cover the middle third of the specimen span, but the coating extended from the leading to the trailing edge on both sides of each specimen. The edges of the fins (across the $t = 1.6$ mm face) were treated so that no sublimation occurred from these faces. These precautions in specimen design ensured that the wind tunnel wall effects and geometric distortion of the specimen were minimized. Offset-strip fins which were identical except that $\Theta = 0$ deg were also tested.

For the complementary flow visualization experiments, a water tunnel of a construction similar to the wind tunnel was used. Flow visualization was performed by injecting ink into the flow. The same model fin array was used in both the wind tunnel and the water tunnel experiments.

Experimental Procedure. Before mass transfer experiments were conducted, the test specimens were weighed using an analytical balance. For cases where local data were obtained, the naphthalene surface profile was measured using a laser profilometer. This measurement system and its application to naphthalene sublimation have been described previously by Kearney

—————— **Nomenclature** ——————

A = total surface area
A_c = free-flow area of the heat exchanger core
A_f = specimen naphthalene surface area
d_h = hydraulic diameter, $4A_cL_{core}/A$
D_{na} = mass diffusion coefficient of naphthalene in air
f = Fanning friction factor (see Eq. (6))
F_p = fin pitch (see Fig. 1)
h = heat transfer coefficient
h_m = local mass transfer coefficient
H = louver height (see Fig. 1)
j = modified Colburn j factor, $\overline{Sh}/(Re\ Sc^{0.4})$
k = thermal conductivity of air

L_{core} = length of heat exchanger core in the streamwise direction
L_p = louver pitch (see Fig. 1)
m = specimen mass
$\dot{m}$ = mass flow rate
N = number of local sublimation data points
Nu = Nusselt number, hd_h/k
P = pressure
Pr = Prandtl number
Re = Reynolds number, U_cd_h/ν
Sc = Schmidt number
Sh_{Lp} = local Sherwood number, h_mL_p/D_{na}
t = time or fin thickness (see Fig. 1)
U_c = maximum flow velocity through the fin array

x = distance from the leading edge along the fin surface (see Fig. 1)
x^* = dimensionless distance along the length of a fin, $x\cos\Theta/L_p$ (see Fig. 1)

Greek Symbols

δ_{sb} = local naphthalene sublimation depth
μ = dynamic viscosity of air
ν = kinematic viscosity of air
Θ = convex-louver angle (see Fig. 1)
ρ = air density
$\rho_{n,s}$ = density of solid naphthalene
$\rho_{n,v}$ = density of saturated naphthalene vapor

Note: An overbar ($\bar{\ }$) indicates spatial averaging, and Δ indicates a difference.

and Jacobi (1996). A 50-by-36-point scanning grid was used to cover a 5.08 cm by 2.54 cm test area centered on the naphthalene surface. On the basis of repeated scans of a reference surface, these optical methods provided sublimation depths with a 2-σ uncertainty of ± 6 μm. The maximum sublimation depth was typically less than 80 μm, representing a fin thickness change of less than five percent.

After mass and surface-profile data were obtained, the specimens were placed in the test array and exposed to a controlled air flow. Following exposure in the tunnel, the specimens were weighed and scanned again. During each run, upstream and downstream temperatures were sampled every five seconds and averaged over the period of the test. The core pressure drop, pressure drop across an ASME standard orifice plate (to determine flow rate), relative humidity, barometric pressure, and exposure time were also recorded.

Flow visualization was performed by injecting ink at various locations approximately three cm upstream of the first row of fins. Flow velocities were determined from the average transit time required for an ink flow marker to pass through the array.

Data Reduction and Interpretation. The Reynolds number for flow through the test section was defined as

$$\text{Re} = U_c d_h / \nu = 4\dot{m}L_{\text{core}}/A\mu \tag{1}$$

where U_c is the maximum flow velocity through the array. Flow visualization showed a large recirculation zone in the concave portion of the fin at all Reynolds numbers tested, so the minimum free-flow area between a given column of fins used to determine the maximum flow velocity was $(F_p - H - t)*$ fin span. The hydraulic diameter, d_h, is[2]

$$d_h = 4A_c L_{\text{core}}/A = 4(F_p - H - t)L_p/2(L_p + t). \tag{2}$$

The average mass transfer coefficient was determined through

$$\overline{h}_m = \Delta m/A_f \rho_{n,\nu}\Delta t \tag{3}$$

where Δm is the change in mass of the specimen and Δt is the exposure time. The average Sherwood number was calculated using

$$\overline{\text{Sh}} = L_p \overline{h}_m / D_{na}. \tag{4}$$

The Sherwood number is based on louver pitch rather than hydraulic diameter to facilitate comparisons between heat transfer in the convex-louver array and the offset-strip array which have different hydraulic diameters (due to the different minimum cross-sectional areas) but equivalent louver pitches. However, the Reynolds number is based on hydraulic diameter so that equivalent mass flow rates lead to equivalent Reynolds numbers (cf. Eq. (1)). When results are compared to the literature, where use of the Colburn j factor is conventional, all results are scaled with the conventional hydraulic diameter to ensure valid comparisons. Sparrow and Hajiloo suggest a modified Colburn j factor for cases where the Schmidt number is in the intermediate range, as it is here (Sc ≈ 2.35).

$$j = \overline{\text{Sh}}_{d_h}/\text{Re Sc}^{0.4} \tag{5}$$

The core pressure drop, ΔP, was interpreted using the conventional Fanning friction factor,

$$f = \frac{2\Delta P}{\rho U_c^2}\left(\frac{d_h}{4L_{\text{core}}}\right). \tag{6}$$

The local mass transfer coefficients were determined from the sublimation depths using the following relation:

---

[2] For the offset-strip model of these experiments, $d_h = 32.9$ mm, and for the convex-louver geometry, $d_h = 24.7$ mm.
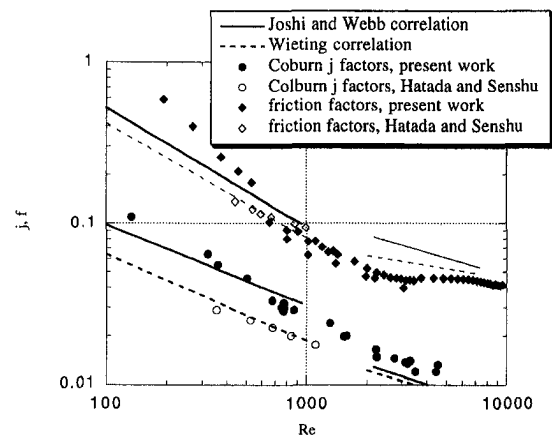
Fig. 2 Fanning friction and Colburn j factors for the offset-strip geometry along with correlations of Joshi and Webb (1987) and Wieting (1975). The data of Hatada and Senshu (1987) are for a somewhat different geometry and are shown for qualitative comparison purposes only.

$$h_m = \rho_{n,s}\delta_{sb}/\rho_{n,\nu}\Delta t. \tag{7}$$

Local Sherwood numbers could then be determined from

$$\text{Sh} = L_p h_m / D_{na}. \tag{8}$$

The local Sherwood numbers were independent of vertical position on the fin. Each local Sherwood number data point is an average of the 50 local Sherwood number data points at a given $x*$ position. As a redundant check, the local Sherwood numbers were integrated and compared to the mass-averaged Sherwood numbers using the following approximation:

$$\overline{\text{Sh}}_{\text{int}} = \frac{1}{A}\int_A \text{Sh}\,dA \approx \frac{1}{N}\sum \text{Sh}. \tag{9}$$

If $\overline{\text{Sh}}_{\text{int}}$ for a particular experiment, as obtained through Eq. (9), were not within ten percent of $\overline{\text{Sh}}$ as determined from the weight measurement (Eq. (4)), the local data for that run were rejected.

Heat transfer data can be inferred from the mass transfer data by employing the heat and mass analogy:

$$\text{Nu} = \text{Sh}(\text{Pr/Sc})^n. \tag{10}$$

Again, a value of n of 0.4 is appropriate for intermediate values of Schmidt number (Sparrow and Hajiloo, 1980).

Uncertainty. Uncertainties in the reduced data were estimated using standard methods (Kline and McClintock, 1953). The uncertainties in Re, $\overline{\text{Sh}}$, and Sh were two percent, five percent, and ten percent, respectively. The uncertainty in ΔP decreased as the Reynolds number increased because the pressure measurement uncertainty was fixed. Therefore, uncertainties in ΔP ranged from approximately 50 percent at very low Reynolds numbers to 0.2 percent at high Reynolds numbers. Above a Reynolds number of 1000, the average uncertainty in ΔP was one percent, leading to an average uncertainty in f of about four percent.

Results and Discussion

Core pressure drop and surface-average mass (heat) transfer results for the offset-strip geometry are shown in Fig. 2 along with the correlations of Joshi and Webb (1987) and Wieting (1975). The correlations have been plotted using the geometrical parameters and the definitions of hydraulic diameter and minimum free-flow area given earlier. The data of Hatada and Senshu (1987) for their closest corresponding geometry are included as well. Their data have also been rescaled using the definition of hydraulic diameter given here. The many length scales involved and the difference in geometries makes a mean-

Fig. 3 Fanning friction and Colburn j factors for the convex-louver array along with friction factors for the offset-strip array. Data of Hatada and Senshu (1987) are for a complete heat exchanger with similar convex-louver dimensions.

ingful comparison difficult. Nonetheless, Fig. 2 serves to validate the current data.

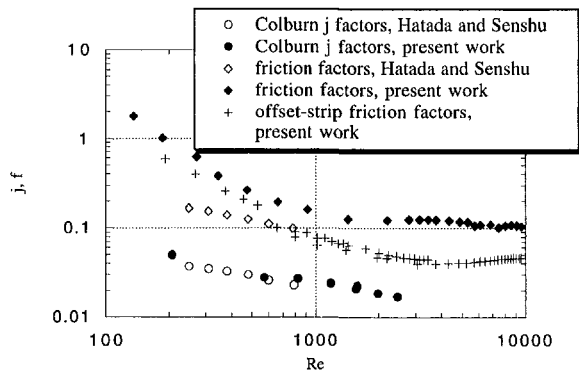Heat transfer and friction data are provided in Fig. 3 for the convex geometry along with friction factors for the offset-strip geometry. The j factors of Hatada and Senshu show good agreement with the current results. The friction factors of the present work are somewhat higher than those of Hatada and Senshu; however, this result is expected because the data of Hatada and Senshu are for a complete heat exchanger—including tubes and flat fin areas—but the data given here are for an array of convex louvers, and the array is more dense than that of Hatada and Senshu. Fin surface condition does not influence this comparison since the fins used by Hatada and Senshu and those of the current study were hydrodynamically smooth. The comparison is included only to corroborate the new data. Figure 3 shows that at low Reynolds numbers—below approximately 600—the f versus Re data for the convex and offset-strip fins are much closer than at higher Reynolds numbers. Likewise, Fig. 4 shows that for Re below about 800, the average Sherwood (Nusselt) numbers for the convex louver are very similar to those of the offset strip. However, at higher Re, the increased form drag causes the friction factor for the convex louver to be dramatically higher than that for the offset-strip fin, and a large heat transfer enhancement is observed. For Re from 1500 to 3000, the convex-louver f is 130 percent higher than for the offset strip, and Sh is 40 percent higher. (Note that pumping power is an inverse function of A_c^3, and the smaller A_c of the convex louvers would result in increased pumping power.) As
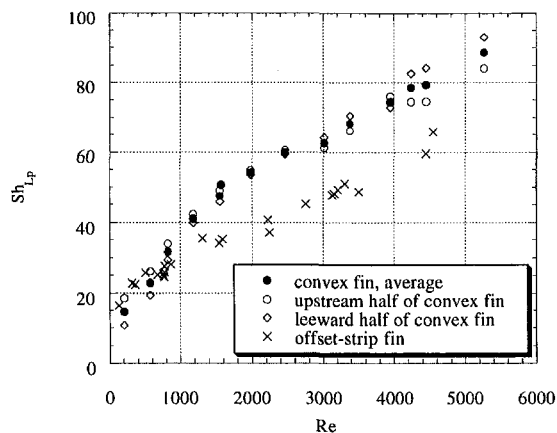

Fig. 4 Sherwood numbers for convex louvers and offset-strip fins. In all the data shown, both the convex and concave sides of the fin are considered.

noted by Webb and Gupte (1990), convex fins in this geometry incur a severe pressure-drop penalty at high Reynolds numbers.

In addition to spatially averaged Sherwood numbers for the entire fin, the Sherwood numbers for the upstream half ($0 < x^* < 0.5$) and leeward half ($0.5 < x^* < 1$) of the convex louver have been shown separately in Fig. 4. The data demonstrate that for low Reynolds numbers (Re < 1800) the upstream half of the convex fin transfers more mass (heat) than the leeward half—up to 70 percent more at the lowest Reynolds number given here. At higher Reynolds numbers (>2800) the leeward half transfer more mass—up to ten percent at the highest Reynolds number shown. At low Reynolds numbers the flow is characterized by boundary layer restarting and steady recirculation in confined regions. At higher Reynolds numbers, the flow becomes unsteady with discrete spanwise vortices. In order to gain a better understanding of the flow behavior and its relation to heat transfer, the flow visualization results must be considered and contrasted with detailed, spatially resolved Sh data.

The important flow structures in this geometry are evident in the photographs shown in Fig. 5. At a Reynolds number of 481, the flow shown in Fig. 5(a) is steady. A geometric separation occurs at the leading edge of the fin, and a shear layer extends from the leading to the trailing edge, trapping a steady recirculation zone in the cavity formed on the concave side of the fin. Although very difficult to see in Fig. 5(a), careful observation showed that for Re = 481 a geometric separation also occurs on the convex side of the fin at $x^* = 0.5$; the flow appears to reattach near the trailing edge of the convex side of the fin, trapping a very small steady recirculation zone on the convex side of the leeward portion of the louver. These two recirculation zones became more evident when the dye stream was suddenly halted. Dye remained "trapped" in the two recirculation zones long after the rest of the dye exited the array. In Fig. 5(a), flow in the concave separation zone circulates in a clockwise direction, and flow in the convex separation zone circulates slowly in a counterclockwise direction. At a Reynolds number of 238 (not shown in the figure), a separated region on the convex side of the fin was not observed. The convex-side recirculation zone may be more clearly seen in Fig. 5(b); at this Reynolds number of 882 the flow remains steady, and the recirculation zones are larger.

At higher Reynolds numbers, as shown in Fig. 5(c), a third recirculation zone appears to have formed near the trailing edge of the fin. This flow structure may form at the trailing edge due to interaction between the convex-side recirculation zone and the flow passing along the concave side of the fin. Because the convex-side separated region circulates counterclockwise, a region of very high shear results near the trailing edge of the fin, where flow that passed along the concave side of the louver interacts with this separation bubble. At a sufficiently high Reynolds number, this shear stress is resolved by the formation of a tertiary recirculation zone with a clockwise rotation. It may be reasonable to view this recirculation pattern as the division of the convex-side recirculation zone into two counterrotating cells. The Reynolds number at which this flow pattern is established remains somewhat unclear; it was observed at Re = 1563 but not at Re = 882. Its formation may be linked to the size of the convex-side recirculation zone, which at a Reynolds number of 1563 is more than two fin thickness wide, as demonstrated in the steady-flow results shown in Fig. 5(c).

The flow was observed to become unsteady near the array exit for Reynolds numbers around 1900. In a fashion similar to that manifest in the offset-strip geometry (see DeJong and Jacobi, 1997), unsteadiness was observed nearer the entrance to the array as the Reynolds number increased; i.e., flow unsteadiness begins at downstream locations and moves upstream as the Reynolds number increases. Flow unsteadiness first appears in the free shear layer on the concave side of the fin. This shear layer becomes wavy, and eventually roller vortices form. These vortices are carried downstream to impinge on the concave fin surface
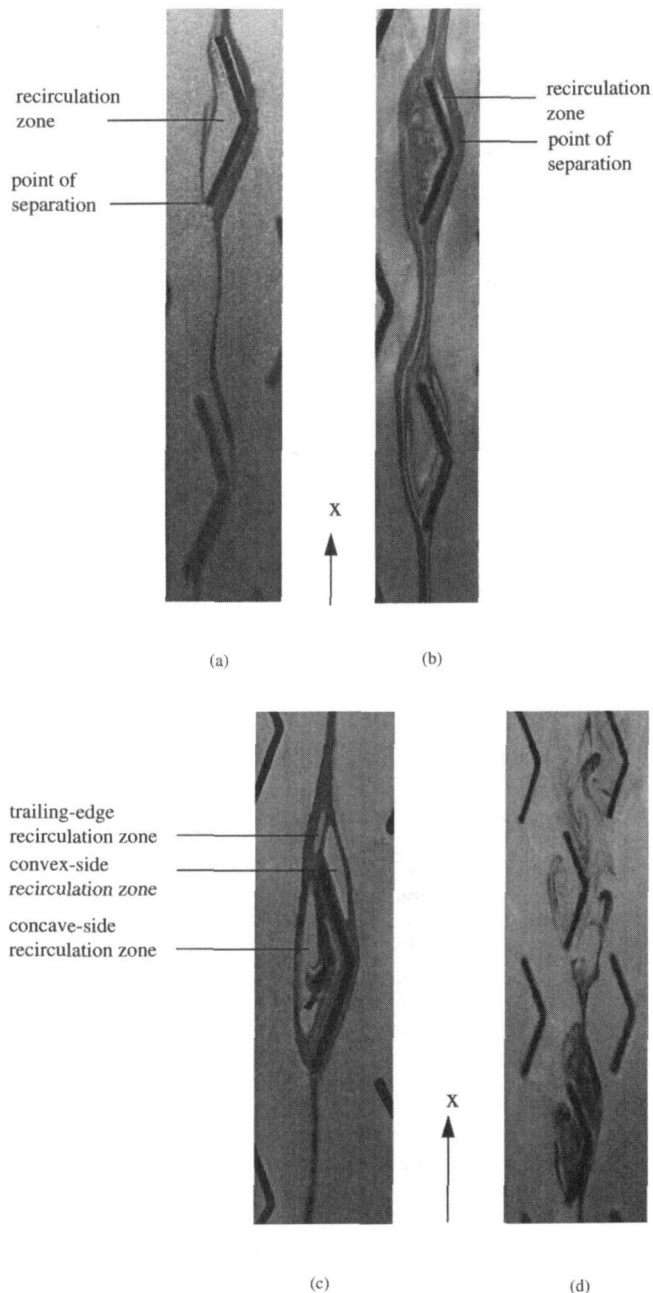
Fig. 5 Dye-in-water results for flow through the convex-louver array. The array is viewed from above, corresponding to the arrangement shown schematically in Fig. 1. The flow direction is from the bottom to the top of the page. (a) Re = 481, (b) Re = 882, (c) Re = 1563, (d) Re = 2967.

near the trailing edge of the fin. At a sufficiently high Reynolds number, such as for the Re = 2967 case shown in Fig. 5(d), shear layer instability on the concave side of the fin results in periodic entrainment and ejection of fluid from the recirculation zone (as described by Pauley and Hodgson, 1994). The trailing-edge recirculation zone is much larger at these high Reynolds numbers, and it also exhibits unsteadiness in location and size.

The flow features described above have a profound effect on convective mass (heat) transfer in the convex-louver geometry. Local convective data are shown for two Reynolds numbers in Fig. 6, where Sh is plotted as a function of location on the fin, x^*, for the concave and convex sides of the fin. As shown in Fig. 6(a), for a Reynolds number of 488, the convection coefficient is high near the leading edge of the convex side of the fin and is smaller for downstream locations on the upstream

half of the fin. This behavior, from $x^* = 0$ to 0.5 on the convex side of the fin, is consistent with boundary layer growth. On the leeward half on the convex side, the convection coefficient is highest near the trailing edge ($x^* = 1$) and decreases as the flow passes backward up the surface due to the counterclockwise circulation associated with the convex-side separation zone. Mass transfer is low on the leeward half due to the low fluid velocity in the small separation zone. On the convex side of the fin, mass transfer is lowest near $x = 0.5$, where the geometric flow separation occurs. Likewise on the concave side, mass transfer is lowest near the separation point at $x^* = 0$ on the concave side of the fin. Mass transfer is higher near the trailing edge of the concave side, where the surface-normal velocities associated with the clockwise recirculation zone thin the boundary layer. Surface-normal flow is also responsible for Sh at $x^* = 0.45$ being larger than Sh at $x^* = 0.55$ on the concave side of the fin, as demonstrated in Fig. 6(a).

At higher Reynolds numbers, as shown in Fig. 6(b), the leeward portion of the concave side exhibits very high heat transfer. This behavior is due to unsteadiness in the free shear layer originating at the leading-edge separation point. Eventually, roller vortices form in this shear layer and are advected downstream. These vortices impinge near the trailing edge of the fin, profoundly increasing heat transfer. Such behavior is not observed on an offset-strip fin at the same Reynolds number, as may be seen in the example data provided in Fig. 6(b). Although the offset-strip fin data shown in Fig. 6(b) show a simple decrease in local convection coefficient due to boundary layer growth as the flow passed along the straight surface of the fin, it should be noted that even offset-strip fins can exhibit complex local heat transfer behavior (see DeJong and Jacobi, 1997). Mass transfer is higher along the upstream half of the convex side of the convex louver than along the upstream half of the offset-strip fin because of the higher flow velocity (due to the smaller cross-sectional area) and because flow acceleration thins the boundary layer. For the convex louver, a significant increase in convection coefficient is also observed at the trailing edge, on the convex side of the fin. This enhancement is due to the large surface-normal velocities and advected unsteadiness associated with the trailing-edge recirculation zone. Flow unsteadiness, advected to the leeward portion of the concave and convex sides of the fin, substantially increases heat transfer on the leeward half of the fin. The net result is that as the flow becomes unsteady, heat transfer on the leeward half of the fin is larger than on the upstream half. Recall that flow unsteadiness is first evident in the array at Reynolds numbers around 1900. This Reynolds number is approximately where the leeward half of the fin begins to transfer more heat than does the upstream half of the fin, as shown in Fig. 4. The local data and flow visualization results clearly explain the surface-averaged data.

Conclusions

Although convex-louver fins may hold promise for some heat exchanger applications, little prior research on the flow and heat transfer in this geometry has appeared in the open literature; furthermore, no prior work has presented local heat transfer results for this geometry. In the current paper, local heat transfer, spatially-averaged heat transfer, core pressure-drop, and flow visualization results were presented to gain a clearer understanding of the flow and heat transfer interactions. Only one geometry was studied in the current work, and the exact Reynolds numbers at which each heat transfer mechanism begins to contribute will depend on the array dimensions; nevertheless, the heat transfer mechanisms and increasing flow complexity important to this convex-louver geometry are likely to be important in all convex-louver designs. The key to heat transfer enhancement in this geometry is flow unsteadiness. Future research should examine methods for precipitating flow unsteadiness at lower Reynolds numbers, either through the promotion of self-sustained flow oscillations within the array—as occurs
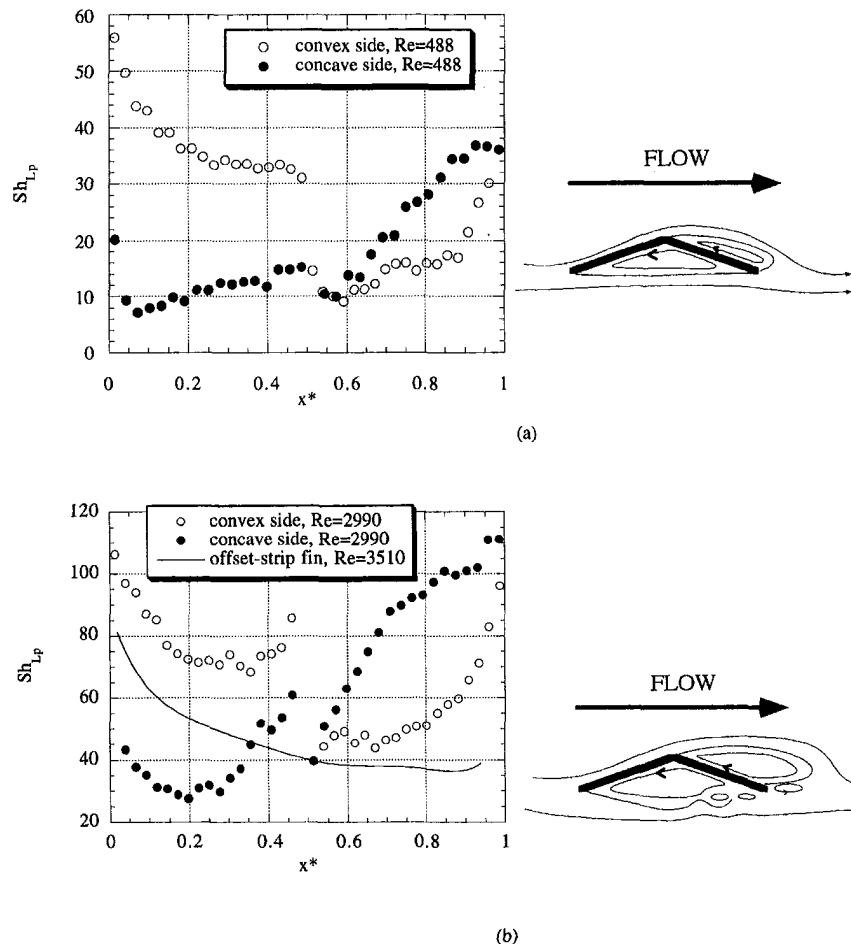
Fig. 6 Local mass transfer measurements over the entire surface of the convex louver. (a) Re ≈ 488, (b) Re = 2990, shown with offset-strip fin results. The cartoon to the right of each plot shows the main features of the flow for that Reynolds number.

in current designs—or though manipulation of the approaching flow. If the heat transfer enhancement associated with unsteadiness could be achieved at low Reynolds numbers, where the convex-louver form drag is lower, the overall thermal performance would be improved.

Acknowledgments

References

Aoki, H., Shinagawa, T., and Suga, K., 1989, "An Experimental Study of the Local Heat Transfer Characteristics in Automotive Louvered Fins," *Experimental Thermal and Fluid Science*, Vol. 2, pp. 293–300.

Bemisderfer, C. H., 1987, "Heat Transfer: A Contemporary Analytical Tool for Developing Improved Heat Transfer Surfaces," *ASHRAE Transactions*, Vol. 93, Part 1, pp. 1157–1167.

DeJong, N. C., and Jacobi, A. M., 1997, "An Experimental Study of Flow and Heat Transfer in Parallel-Plate Arrays: Local, Row-by-Row and Surface Average Behavior," *International Journal of Heat and Mass Transfer*, Vol. 40, pp. 1365–1378.

DeJong, N. C., Zhang, L. W., Jacobi, A. M., Balachandar, S., and Tafti, D. K., 1998, "A Complementary Experimental and Numerical Study of the Flow and Heat Transfer in Offset Strip-Fin Heat Exchangers," ASME JOURNAL OF HEAT TRANSFER, Vol. 120, pp. 690–698.

Goldstein, R. J., and Cho, H. H., 1995, "A Review of Mass Transfer Measurements Using the Naphthalene Sublimation Technique," *Experimental Thermal and Fluid Science*, Vol. 10, pp. 416–434.

Hatada, T., and Senshu, T., 1984, "Experimental Study on Heat Transfer Characteristics of Convex Louver Fins for Air Conditioning Heat Exchangers," ASME Paper 84-HT-74, ASME, New York.

Hatada, T., Ueda, H., Oouchi, T., and Shimizu, T., "Improved Heat Transfer Performance of Air Coolers by Strip Fins Controlling Air Flow Distribution," *ASHRAE Transactions*, Vol. 95, Part 1, pp. 166–170.

Joshi, H. M., and Webb, R. L., 1987, "Heat Transfer and Friction in the Offset Strip-Fin Heat Exchanger," *Int. J. Heat Mass Transfer*, Vol. 30, pp. 69–83.

Kays, W. M., and London, A. L., 1984, *Compact Heat Exchangers*, 3rd Ed., McGraw-Hill, New York.

Kearney, S. P., and Jacobi, A. M., 1996, "Local Convective Behavior and Fin Efficiency in Shallow Banks of In-Line and Staggered, Annularly Finned Tubes," ASME JOURNAL OF HEAT TRANSFER, Vol. 118, pp. 317–326.

Kline, S. J., and McClintock, F. A., 1953, "Describing Uncertainties in Single Sample Experiments," *Mechanical Engineering*, Vol. 75, pp. 3–8.

Matsushima, H., Hatada, T., Endo, T., and Senshu, T., 1991, "Three-dimensional Simulation of Forced Convection and Heat Transfer in Heat Exchangers with Convex Strip Fins by the Finite Element Method," ASME Paper 91-HT-18, ASME, New York.

Pauley, L. L., and Hodgson, J. E., 1994, "Flow Visualization of Convex Louver Fin Arrays to Determine Maximum Heat Transfer Conditions," *Experimental Thermal and Fluid Science*, Vol. 9, pp. 53–60.

Souza Mendes, P. R., 1991, "A Review of Mass Transfer Measurements Using the Naphthalene Sublimation Technique," *Experimental Thermal and Fluid Science*, Vol. 4, pp. 510–523.

Sparrow, E. M., and Hajiloo, A., 1980, "Measurements of Heat Transfer and Pressure Drop for an Array of Staggered Plates Aligned Parallel to an Air Flow," ASME JOURNAL OF HEAT TRANSFER, Vol. 102, pp. 426–432.

Wang, C. C., Chen, P. Y., and Jang, J. Y., 1996, "Heat Transfer and Friction Characteristics of Convex-Louver Fin-and-Tube Heat Exchangers," *Experimental Heat Transfer*, Vol. 9, pp. 61–78.

Webb, R. L., and Gupte, H., 1990, "Design of Light Weight Heat Exchangers for Air-to-Two Phase Service," *Compact Heat Exchangers: A Festschrift for A. L. London*, R. K. Shah, A. D. Kraus, and D. Metzger, eds., Hemisphere, New York, pp. 311–334.

Wieting, A. R., 1975, "Empirical Correlations for Heat Transfer and Flow Friction Characteristics of Rectangular Offset-Fin Plate-Fin Heat Exchangers," ASME JOURNAL OF HEAT TRANSFER, Vol. 97, pp. 488–490.

Heat Transfer Through an Extended Surface Containing He II

S. W. Van Sciver

Mechanical Engineering Department,
FAMU-FSU College of Engineering,
National High Magnetic Field Laboratory,
1800 E. Paul Dirac Drive,
Tallahassee, FL 32310
e-mail: vnsciver@magnet.fsu.edu
Mem. ASME

A semi-analytic solution for the heat transfer process between a He II pressurized bath and a saturated tube-type heat exchanger is presented. The problem is modeled with an extended surface heat transfer formulation analogous to that in conventional conduction. The process is governed by Kapitza conductance and counterflow within the bulk fluid in the tube. The resulting nonlinear differential equation may be integrated for the special case of constant properties, yielding a simple solution applicable to design and analysis of practical heat exchangers.

Introduction

Liquid helium is a common coolant for many large cryogenic systems. For most superconducting magnet systems, liquid helium is required primarily because the superconductor must be maintained in this temperature regime to achieve the desired performance. In some special cases, He II (or superfluid helium) below 2.2 K is the coolant of choise, mostly because of its uniquely high heat conductivity. For example, at a heat flux of 10 kW/m^2, the effective thermal conductivity of He II is about three orders of magnitude greater than that of copper; making the bath that surrounds a magnet essentially isothermal. Thus, unlike other common fluids, heat transport in He II is usually dominated by this conduction-like mechanism in the bulk fluid.

Most cryogenic systems that use He II consist of a pressurized He II bath cooled by a saturated bath type heat exchanger (Fig. 1). Typical operating temperatures are around 1.8 K. Commonly, the heat exchanger consists of a simple closed-end vessel or tube immersed in the pressurized bath (Bon Mardion et al., 1977; Pfotenhauer et al., 1992; Welton, et al., 1996). The pressurized He II reservoir is in thermal contact with the saturated bath through the surface of the heat exchanger. The rate of heat transfer is controlled by the heat transfer coefficient at the surface of the exchanger. For a He II heat exchanger, this heat transfer coefficient is primarily determined by the Kapitza conductance mechanism, where the thermal interface heat exchange is dependent on the the surface material and its preparation. Usually, these heat exchangers are made from copper, or similar high-conductivity metal, to minimize the thermal resistance due to conduction in the bulk metal.

The present paper addresses the problem of a saturated bath He II heat exchanger, with an emphasis on the solution to the nonlinear conduction equation appropriate to the problem. To familiarize the reader with the background of this problem, a brief review of the unique properties of He II is given. That section is followed by a general discussion of the heat exchanger problem of present interest including a formulation of the extended surface differential equation. Finally, an analytic solution to this differential equation is presented for different boundary conditions, with a discussion of its application to practical system design.

Review of He II Properties

Liquid helium is a unique fluid for a number of reasons. It has the lowest critical properties of any common fluid, with a

$T_c = 5.2$ K and $p_c = 0.23$ MPa. However, of greater interest is the fact that below 2.2 K, liquid helium displays a number of properties that can only be described by invoking quantum mechanical physical descriptions. For example, below 2.2 K liquid helium transitions into a second liquid phase, superfluid helium or He II. He II is the equilibrium phase at absolute zero, in contradiction to classical arguments that would expect helium to solidify at the lowest temperatures. Solid helium can only be obtained under an external pressure greater than 2.5 MPa.

The properties of He II are dominated by the quantum mechanical nature of the fluid. The state and transport properties are best understood in terms of models which treat the liquid as a mixture of two interpenetrating fluid components. This two-fluid nature allows the He II to carry large amounts of heat with extremely small temperature gradients and to flow through narrow constrictions without significant viscous loss. The transport properties of He II are what make the fluid of interest to technical applications.

The heat transport properties of He II have been extensively investigated and reported (see, for example, Bon Mardion et al., 1979; Linnet et al., 1975; Van Sciver, 1978). Experimental investigations on heat transport in channels of moderate diameter ($d > 1$ mm) have generally been described in terms of the Gorter-Mellink nonlinear heat transport relationship,

$$q = -\left(f^{-1}(T, p) \frac{dT}{dx} \right)^{1/3}, \tag{1}$$

where $f^{-1}(T, p)$ is the He II heat conductivity function for turbulent flow (Van Sciver, 1986). For heat transfer problems, such as the present involving a heat exchanger, Eq. (1) can be applied in a similar manner to Fourier's Law for ordinary conduction heat transfer. Further, based on the two-fluid model for He II, $f^{-1}(T, p)$ can be fit to the expression

$$f^{-1}(T, p) = f^{-1}(T_\lambda, p)[t^{5.6}(1 - t^{5.6})]^3 . \tag{2}$$

At saturated vapor pressure, $f^{-1}(T, p)$ has a maximum at 1.923 K and a peak value of about 13,000 kW^3/m^5 K. The temperature and pressure dependence of this function is given in Fig. 2. In general, these data are accurate to about ±10 percent at saturated vapor pressure and compare favorably to experiments up to about 0.7 MPa.

Thermal boundary conductance occurring at the interface between a solid and liquid He II is also of importance to the present heat transfer problem. For low to moderate heat fluxes, this process is dominated by the Kapitza conductance of the solid (Kapitza, 1941). The Kapitza conductance occurs as a result of the impedance mismatch that restricts the flow of thermal excitations, called phonons, between the two media (Pol-
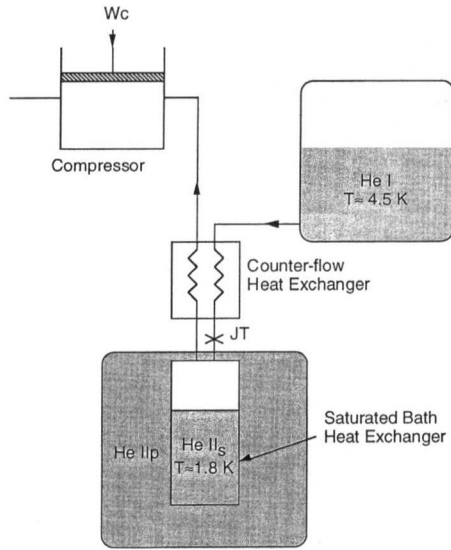
Copyright © 1999 by ASME

Fig. 1 Schematic of an He II refrigeration system. The saturated bath heat exchanger is the vertically oriented closed-end tube in the lower reservoir.

Fig. 2 He II turbulent heat conductivity function, $f^{-1}(T, p)$

lack, 1969). In most cases, the Kapitza conductance is defined in terms Newton's Law of cooling,

$$q = h_K \Delta T_s |_{\Delta T_s \to 0}, \qquad (3)$$

where ΔT_s is $(T_s - T_b)$. In the limit of small ΔT, h_K is often described by a fairly simple semi-empirical relationship,

$$h_K = aT^n, \qquad (4)$$

where n is between 2 and 4 and a is an experimentally determined quantity dependent on the solid material and surface condition. Measurements have shown that the magnitude of h_K at a given temperature varies by as much as an order of magnitude among samples (Snyder, 1970). Part of this variation can be attributed to surface condition: oxidation, impurities or condensates, which results in a lower value of h_{K0}. For copper, the Kapitza conductance coefficients are generally in the range 400 $< a <$ 900 W/m^{2}K^4 with $n \approx 3$ yielding a typical value at 1.8 K of about 4 kW/m^{2}K.

Problem Statement

We consider a saturated He II heat exchanger consisting of a high-conductivity metal tube immersed in a constant tempera-

ture pressurized bath of He II (see the lower portion of Fig. 1). The tube is shown vertically oriented although the heat transfer analysis is independent of heat exchanger orientation. Heat transport within the He II contained in the heat exchanger is governed by the counterflow process and therefore is described by Eq. (1). Heat transfer between the contained He II and the surrounding bulk liquid is entirely due to the Kapitza conductance of the tube material and conduction within the heat exchanger material. Thus for the heat exchanger, the overall heat transfer coefficient, U, may be given by

$$U = \left(\frac{1}{h_{Ki}} + \frac{w}{k_s} + \frac{1}{h_{Ko}} \right)^{-1} \qquad (5)$$

where k_s is the thermal conductivity of the heat exchanger material and w is the wall thickness. Kapitza conductance subscripts refer to the inside (i) and outside (o) surface. The goal of the present work is to develop a relationship that will treat this problem.

In simple terms, the heat exchanger must have sufficient surface area to meet the temperature difference requirement at the maximum heat flux. This somewhat obvious requirement sets a lower limit for the wetted surface area,

---

Nomenclature

a = Kapitza coefficient (W/m$^2 \cdot$K^4)
A = cross-sectional area (m^2)
C = specific heat (J/kg$\cdot$K)
d = diameter (m)
$f(T)^{-1}$ = turbulent He II heat conductivity function (W^3/m$^5 \cdot$K)
g = acceleration of gravity (m/s)
h_{fg} = latent heat (J/kg)
h = heat transfer coefficient (W/m$^2 \cdot$K)
k = thermal conductivity (W/m$\cdot$K)
L = length (m)
m = fin parameter (m)
M = fin total heat transfer (W)
p = pressure (Pa)
P = cooled perimeter (m)

q = heat flux density (W/m^2)
Q = heat rate (W)
R = gas constant
S = entropy (J/kg$\cdot$K)
t = reduced temperature (T/T_λ)
T = temperature (K)
U = overall heat transfer coefficient (W/m$^2 \cdot$K)
V = volume (m^3)
v = specific volume (m^3/kg)
w = thickness (m)
x = position variable (m)

Greek

α = angle
β = boundary condition coefficient
ϵ = effectiveness
γ = boundary condition coefficient

η = efficiency
ρ = density (kg/m^3)
Θ = reduced temperature

Subscripts

b = bath
c = critical
f = fin
i = inside
l = liquid
K = Kapitza
o = outside
s = solid
svp = saturated vapor pressure
λ = at lambda temperature
0 = at $x = 0$

Fig. 3 Pressure-temperature phase diagram helium. Curves displayed are typical temperature profiles along the length of a saturated bath heat exchanger. T_0 occur at the free surface, $x = 0$. $T(x)$ is below the free surface and it thus at higher pressure corresponding to the hydrostatic head.

Fig. 4 Maximum heat flux at the free surface of a saturated bath of He II for different orientations relative to horizontal

$$A_s = \frac{Q}{U\Delta T}\bigg|_{max} , \qquad (6)$$

where the overall heat transfer coefficient is given by Eq. (5).
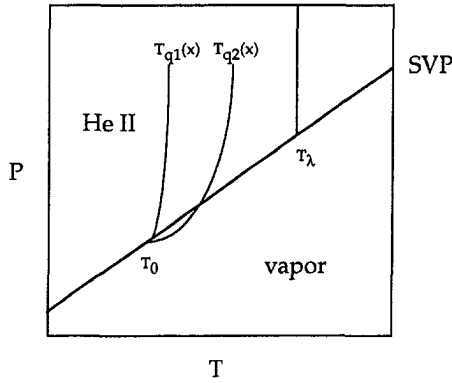
A second general requirement for He II heat exchangers is that boiling should occur only at the free surface. In saturated He II, boiling will initiate whenever the bulk fluid temperature exceeds the saturation temperature at the local pressure. Bulk boiling should be avoided since it will reduce the surface heat transfer rate and thereby degrade the performance of the heat exchanger. This limitation has been previously mentioned in the context of a large He II system for the NHMFL hybrid magnet (Van Sciver et al., 1996) and subsequently demonstrated experimentally (Welton et al., 1998).

The bulk boiling requirement can be qualitatively understood by referring to the P-T phase diagram for helium, Fig. 3. We assume that the temperature at the liquid surface is fixed at the saturation temperature corresponding to the pressure, p_0. However, due to the heat load within the saturated bath, the local temperature of the fluid within the heat exchanger will increase. If this temperature increases to a sufficient level to exceed the local saturation condition anywhere within the heat exchanger, then boiling will occur. The critical condition for boiling is defined by the temperature profile crossing the saturated vapor pressure curve (Curve $T_{q2}(x)$ in Fig. 3) or more specifically when the temperature gradient at the liquid-vapor interface becomes greater than the slope of the saturated vapor pressure curve,

$$\frac{dT}{dx}\bigg]_{x=0} \geq \rho_l g \sin \alpha \frac{dT}{dp}\bigg]_{SVP} , \qquad (7)$$

where ρ_l is the liquid density and g is the acceleration of gravity. α is the angle of the heat exchanger tube relative to horizontal and is introduced to take care of the cases where the tube is not vertical. Equation (7), combined with the Clausius-Clapeyron equation, with the assumption that the vapor may be approximated by an ideal gas,

$$\frac{dp}{dT} = \frac{h_{fg}}{T\Delta v} \approx \frac{h_{fg}p}{RT^2} , \qquad (8)$$

which leads to a relationship for the maximum heat removal rate of a heat exchanger,

$$Q_{max} = A\left(\frac{\rho g \sin \alpha R T^2 f^{-1}}{h_{fg}p_0}\right)^{1/3} , \qquad (9)$$

where R is the gas constant. These are reasonable approxima-

tions for saturated He II heat exchangers as described in the present context. Figure 4 is a plot of the maximum heat flux at the free surface of a heat exchanger as a function of the free-surface temperature for the vertical orientation. At the peak temperature 1.87 K, this expression yields a maximum heat flux at the bulk liquid interface, Q/A, of 14 kW/m^2.
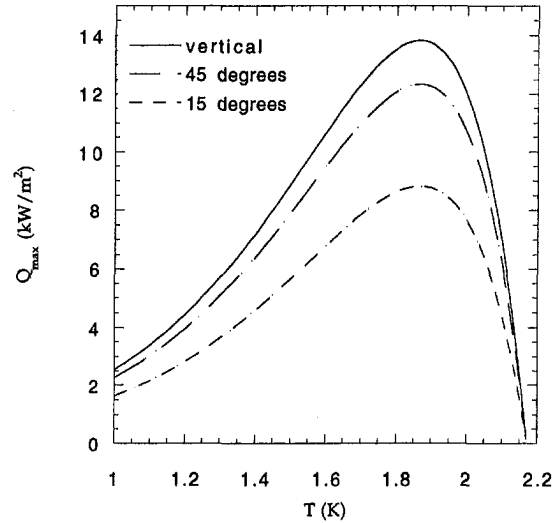
As a third requirement we consider that saturated He II heat exchangers, which consist of closed-end channels, may be limited in their effectiveness due to temperature gradients within the bulk fluid in a similar fashion to the way conventional fin effectiveness is controlled by aspect ratio and material thermal conductivity. If the tube diameter is too small for a given length, a situation can occur where the He II within the heat exchanger will develop a sizable temperature gradient. This effect will cause the temperature at the lower end of the heat exchanger to approach T_b, thus reducing the heat transfer rate at the lower end. This condition, which should be avoided, can be analyzed in terms of the heat transport in the bulk He II which is the subject of the next section.

Analysis

For the present problem, we assume that the heat transport in a saturated He II heat exchanger can be analyzed in term of the nonlinear turbulent counterflow equation with a surface heat transfer condition dependent on Kapitza conductance (Shajii et al., 1990). The differential equation that describes this process is

$$\frac{d}{dx}\left(f^{-1}\frac{dT}{dx}\right)^{1/3} + \frac{PU}{A}(T_b - T) = 0 \qquad (10)$$

where P is the cooled perimeter and A is the cross-sectional area of the He II. U is the overall heat transfer coefficient, which in this case is equal to the series thermal resistances on the inner and outer surfaces of the heat exchanger, Eq. (5). Note the similarity between Eq. (10) and the conduction fin equation, with the only exception being the nonlinear form of the first term. Also note that in Eq. (10), we have chosen the convention with the x-coordinate measured from the top free surface into the bulk liquid and since the heat exchanger operates at lower temperature (and pressure) relative to the surrounding bath, dT/dx and $(T_b - T)$ are both positive.

Complete solution to Eq. (10) requires numerical techniques since the thermal transfer functions, f^{-1} and U are both temperature dependent. Such a solution has been previously reported

Fig. 5 Schematic of He II fin heat exchanger with boundary conditions and dimensionless temperature profile

(Warren, 1984; and Huang et al., 1996; Welton, 1998). However, normally He II heat exchangers are designed to operate at low ΔT in the fluid allowing a reasonable approximation to be obtained by assuming constant properties. The advantage of the constant property assumption is that it allows for an analytic solution.

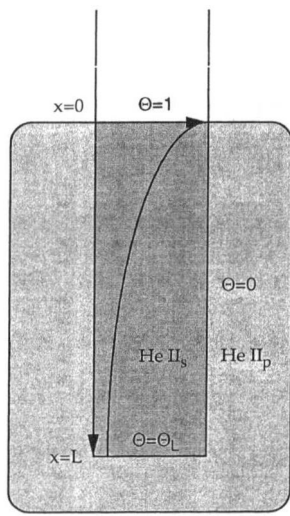Due to the nonlinear nature of the counterflow heat transport equation, the analytic solution has a different form than that of ordinary conduction. However, the similarity to the conduction fin equation suggests that we adopt a formulation like that available in conduction heat transfer texts (Incropera and DeWitt, 1990). Therefore, we approach the solution to Eq. (10) by writing it in nondimensional form,

$$\frac{d}{dx}\left(\frac{d\Theta}{dx}\right)^{1/3} - m^{4/3}\Theta = 0, \tag{11}$$

where the following variables are defined:

$$\Theta = (T_b - T)/(T_b - T_0) \quad \text{and}$$

$$m^{4/3} = PU(T_b - T_0)^{2/3}/f^{-1/3}A,$$

with T_0 being the temperature of the fluid at the free surface. Equation (11) is a second-order nonlinear ordinary differential equation requiring two boundary conditions. Figure 5 displays an idealized heat exchanger with boundary conditions and a schematic temperature profile. At $x = 0$, $\Theta_0 = 1$ by definition. At $x = L$, the boundary condition depends on the design of the heat exchanger. In this context, there are usually four cases considered:

1 Convection heat transfer: $(f^{-1}d\Theta/dx)^{1/3}]_L = U\Theta_L(T_b - T_0)^{2/3}$
2 Adiabatic: $d\Theta/dx^{1/3}]_L = 0$
3 Prescribed temperature: $\Theta(L) = \Theta_L$
4 Infinite length $(L \to \infty)$: $\Theta(L) = 0$

Note that the parameter $(mL)^{4/3}$ scales the heat transfer to the bath to that carried by counterflow through the bulk fluid much the same way $(mL)^2$ scales the process in conventional fin problems. In general, $(mL)^{4/3}$ is of order unity, but it can be either greater or less than 1. As in the case of conventional fin design, if $(mL)^{4/3} \gg 1$, which approaches boundary condition no. 4, then the solution becomes essentially independent of the boundary condition at $x = L$.

Table 1 Coefficients of Eq. (12) for different boundary conditions: $\beta = AU^3(T_b - T_0)^2/2Pf^{-1}$

Boundary condition	γ	Θ_L^2
Convection heat transfer	$\Theta_L^2 - \beta\Theta_L^4$	$\dfrac{1}{2\beta} - \left[\dfrac{1}{4\beta^2} - \dfrac{(1 - (Q/M)^4)}{\beta}\right]^{1/2}$
Adiabatic	Θ_L^2	$1 - (Q/M)^4$
Prescribed temperature	†	†
Infinite length	0	0

† value is determined by implicit solution.

Total Heat Transfer. By making the substitution $y = -(d\Theta/dx)^{1/3}$ and using the chain rule, $dy/dx = (dy/d\Theta)\cdot(d\Theta/dx)$, Eq. (11) can be integrated one time to yield an expression for the total heat removal rate, $Q = -A(f^{-1}d\Theta/dx)^{1/3}]_{x=0}$, of the heat exchanger. The resulting expression may be written

$$Q = M(1 - \gamma)^{1/4}, \tag{12}$$

where $M = 1.19A(mf^{-1}(T_b - T_0))^{1/3}$ is analogous to the coefficient of total heat transfer for a conventional fin. The numerical coefficient, $1.19 = 2^{1/4}$, is obtained through the intergration procedure. The dimensionless coefficient γ is a function of the particular boundary condition imposed at $x = L$. These are given in Table 1. Obviously, for the adiabatic or convection boundary conditions, Eq. (12) can be inverted to obtain a value for Θ_L as a function of Q. Also, for practical situations with $\gamma \ll 1$, the infinite channel solution represents a good approximation, $Q = M$.

Temperature Profile. Equation (11) can be integrated a second time to determine the temperature profile $\Theta(x)$ in the He II within the heat exchanger for a given set of boundary conditions. This solution depends on the temperature at the lower end, $\Theta(L)$, which can be obtained either by use of the appropriate boundary condition for a given Θ_L or by determining $\Theta(L)$ for a given Q from Eq. (11) or Table 1 and then utilizing the prescribed temperature end condition. The resulting general solution for the temperature profile within the heat exchanger is obtained by solution of the integral

$$\int_\theta^1 \frac{d\Theta}{(\Theta^2 - \gamma)^{3/4}} = 1.68mx, \tag{13}$$

where again γ depends on choise of boundary conditions (see Table 1). The numerical proportionality coefficient, $1.68 = 2^{3/4}$, again comes from the integration procedure. All cases except the infinite length, Eq. (13), may only be solved by approximate or numerical methods. For the infinite channel case, where $\Theta_L = 0$ and $\gamma = 0$, Eq. (13) may be simply integrated to yield the expression

$$\Theta(x) = \left[\frac{1}{0.84mx + 1}\right]^2. \tag{14}$$

Figure 6 displays this curve on a semi-log plot. Note that for ordinary conduction, the infinite-length solution should yield a pure exponential as shown by the straight line in Fig. 6.

For nonzero values of γ, Eq. (13) represents an implicit solution for the temperature profile. Therefore, one must perform a numerical integration for a given set of boundary conditions. First consider the adiabatic boundary condition. In this case $\gamma = \Theta_L^2$, the numerical integration of Eq. (13) is straightforward, in the present context being carried out using a simple spreadsheet routine. This result is shown in Fig. 7 for different assumed values of Θ_L. Clearly, for values of $\Theta_L < 0.1$, the solution may be approximated by the infinite channel case. Also, note that the end point of each curve, corresponding to the lower
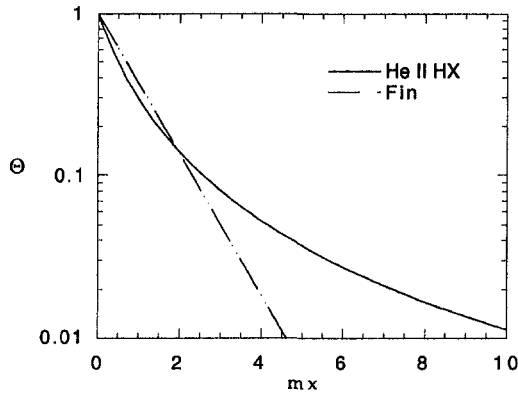
Fig. 6 Dimensionless temperature versus length for an infinitely long heat exchanger. The dashed line is the exponential solution appropriate for ordinary conduction.

limit $\Theta = \Theta_L$, establishes the dimensionless length, mL, of that heat exchanger operating condition. For example, a heat exchanger operating at $\Theta_L^2 = 0.5$ will need to have a dimensionless length of $mL \approx 1.2$.

The solution for the convection boundary condition is similar to the above except now $\gamma = \Theta_L^2 - (AU^3(T_b - T_0)^2 / 2Pf^{-1})\Theta_L^4$. One should note, however, that since He II has such a high conductivity, under almost all practical situations, the second term is negligible making the difference between adiabatic and convection end conditions very small. Thus, the curves in Fig. 7 may frequently be used for either case.

The solution for the prescribed boundary condition at $x = L$ is approached in a slightly different way. Since the value of γ is not known, it must be determined by solution of the definite integral, Eq. (13), for the lower limit Θ_L at $x = L$. Iteration of the integration process will yield the appropriate value of γ for the set of conditions. The numerical integrations in Fig. 7 give this solution where, in this case, the values of L correspond to any length less than the adiabatic length.

One can also obtain a reasonable approximate solution for $\Theta_L \approx 1$. For these conditions, we can expand the denominator of the integrand using $(\Theta^2 - \Theta_L^2) = (\Theta - \Theta_L)(\Theta + \Theta_L) \approx 2(\Theta - \Theta_L)$. The integral then can be simply analyzed to give

$$(1 - \Theta_L)^{1/4} - (\Theta - \Theta_L)^{1/4} = 0.707mx. \qquad (15)$$

This expression is plotted in Fig. 8 for several values of Θ_L
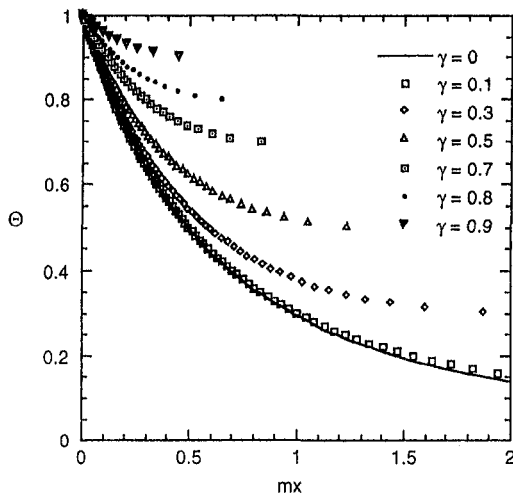
Fig. 7 Dimensionless temperature versus length for finite length heat exchangers with adiabatic end boundary conditions. Also shown by the solid line is the infinite channel length solution, $\gamma = 0$.
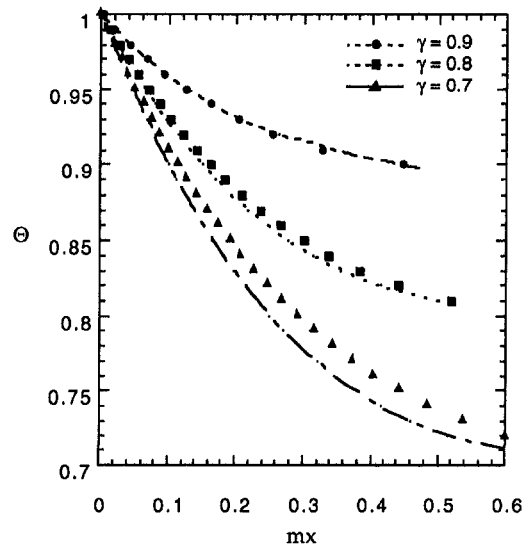
Fig. 8 Dimensionless temperature versus length for the approximate solution with $\Theta_L \approx 1$, shown by the continuous curves. The numerical results from Fig. 7 are given by the data points: ● ($\Theta = 0.9$); ■ ($\Theta = 0.8$); △ ($\Theta = 0.7$).

near unity. The smooth curves are the approximate solution (Eq. (15)) while the data points are the numerical integrals from Fig. 7. Clearly, the approximation appears to be reasonable for values of $\Theta_L > 0.7$.

Performance. Extended surfaces containing He II also have performance terms analogous to that of conduction fins. Using the usual definition of heat exchanger effectiveness and the appropriate form of Eq. (12), the following expression is obtained:

$$\epsilon_f = \frac{Q_{\text{actual}}}{UA(T_b - T_0)} = \left[\frac{2Pf^{-1}(1 - \gamma)}{U^3A(T_b - T_0)^2}\right]^{1/4}. \qquad (16)$$

Note that for typical values, $f^{-1} = 10,000$ kW ^{3}/m^{5}K; $U = 2$ kW/m^2 K, and $\Delta T = 50$ mK, $\epsilon_f \approx 30(P/A)^{1/4}$ are in SI units. Thus, for reasonable geometries, $\epsilon_f \gg 1$. For short heat exchangers, where $\Theta_L \approx 1$, this expression simply reduces to a ratio of the actual to base areas. For $\Theta_L \ll 1$, we still find the effectiveness to $\epsilon_f \gg 1$ because the effective area is still much greater than that of the base. This result is primarily due to the very large heat conductivity of the He II as compared to the Kapitza conductance. Therefore, He II heat exchangers of this type will always be very effective.

In a similar fashion, the heat exchanger efficiency is given by

$$\eta_f = \frac{Q}{UA_{\text{fin}}(T_b - T_0)} = \epsilon_f\left(\frac{A}{A_{\text{fin}}}\right). \qquad (17)$$

This value is very nearly unity for all but the longest heat exchangers, where $\Theta_L \ll 1$. For typical values, one finds that $\eta_f \approx 1$ unless $mL > 1$.

Summary

An analytic solution to the constant property He II heat transfer equation for extended surfaces is presented. The solution is different, although analogous to the conduction heat transfer fin equation. All the conventional fin equation terms are defined using this solution. The results may be easily applied to design of He II heat exchangers for low-temperature applications.

Acknowledgments

References

Bon Mardion, G., Claudet, G., Seyfert, P., and Verdier, J., 1977, "He II in Low Temperature and Superconductive Magnet Engineering," *Advances in Cryogenic Engineering,* Vol. 23, pp. 358–362.

Bon Mardion, G., Claudet, G., and Seyfert, P., 1979, "Practical Data on Steady State Heat Transport in Superfluid Helium at Atmospheric Pressure," *Cryogenics,* Vol. 19, p. 45.

Linnet, C., and Frederking, T. H. K., 1975, "Thermal Conditions at the Gorter Mellink Counterflow Limit between 0.01 and 3 Bar," *Journal Low Temp. Phys.,* Vol. 21, pp. 449–462.

Huang, Y., and Van Sciver, S. W., 1996, "Forced Flow He II Heat Exchangers," *Cryogenics,* Vol. 36, pp. 535–46.

Incropera, F. P., and Dewitt, D. P., 1990, *Fundamentals of Heat and Mass Transfer,* John Wiley and Sons, New York, Chapter 3.

Kapitza, P. L., 1941, "The Study of Heat Transfer on Helium II," *Journal of Physics (USSR),* Vol. 4, p. 181.

Pfotenhauer, J. M., 1992, "Design Issues for a Superfluid Helium Subcooler," *Heat Transfer and Superconducting Magnetic Energy Storage,* ASME HTD-Vol. 211, pp. 33–38.

Pollack, G. L., 1969, "Kapitza Resistance," *Reviews of Modern Physics,* Vol. 41, p. 48.

Shajii, A., Huang, Y., Daugherty, M., Witt, R., and Van Sciver, S. W., 1990, "Design and Performance of Forced Flow He II Heat Exchangers," *Advances in Cryogenic Engineering,* Vol. 35, pp. 1165–1172.

Snyder, N. S., 1970, "Heat Transport through Helium II-Kapitza Conductance," *Cryogenics,* Vol. 10, p. 89.

Van Sciver, S. W., 1978, "Kapitza Conductance of Aluminum and Heat Transport Through Subcooled He II," *Cryogenics,* Vol. 18, pp. 521–527.

Van Sciver, S. W., 1986, *Helium Cryogenics,* Plenum Press, New York.

Van Sciver, S. W., and Welton, S. J., 1996, "Analysis and Characterization of Saturated Bath Heat Exchangers," *1996 Proceedings ICEC16/ICMC,* Kitakushu, Japan, Elsevier, New York, pp. 527–530.

Warren, R. P., 1984, "Heat Flow in a He II Filled Fin," *Advances in Cryogenic Engineering,* Vol. 29, pp. 335–342.

Welton, S. J., et al., 1996, "Design, Development and Testing of the JT Refrigerators for the 45-T Hybrid Magnet," *Advances in Cryogenic Engineering,* Vol. 41, pp. 1283–1290.

Welton, S. J., Bartholomew, K., Homans, M., and Van Sciver, S. W., 1998, "Heat Transport in Saturated He II with Surface Heat Transfer in the Turbulent Counterflow Regime," *Advances in Cryogenic Engineering,* Vol. 43, to be published.

Mechanisms of Thermo-Solutal Transport and Segregation in High-Pressure Liquid-Encapsulated Czochralski Crystal Growth

Y. F. Zou[1]

G.-X. Wang[2]
Assistant Professor,
Assoc. Mem. ASME

H. Zhang
Assistant Professor,

V. Prasad
Professor,
e-mail: prasad@pml.eng.sunysb.edu,
Fellow ASME

Consortium for Crystal Growth Research,
State University of New York
at Stony Brook,
Stony Brook, NY 11794-2300

The mechanism of dopant transport and segregation in high-pressure liquid-encapsulated Czochralski (HPLEC) grown III-V compound crystals (e.g., GaAs, InP) has been numerically studied using an integrated model, MASTRAPP. The model approximates the melt flow in the crucible as a quasi-steady-state, laminar, and axisymmetric flow, but the gas flow is considered as turbulent. Based on the physics of the growth process, a two-time-level scheme has been implemented where the dopant transport and growth are simulated at a smaller time scale while flow and temperature solutions are obtained from quasi-static calculations. Detailed numerical analyses are performed for the conditions of pure crystal rotation, pure thermally driven natural convection, and pure crucible rotation as well as for mixed flow with all of these forces present simultaneously. The dopant transport and segregation in these cases are well correlated to the corresponding melt flow pattern. Very weak radial segregation is predicted for pure crystal rotation because the resulting melt flow leads to a fairly flat solute boundary layer. The natural convection, on the other hand, produces a nonuniform boundary layer along the melt/crystal interface. This leads to a strong radial segregation with a high concentration along the central axis of the crystal. The crucible rotation has a similar effect. The combined effect of all of these flow mechanisms produces a strong radial segregation, whose extent depends on the relative strength of the driving forces. In all of these cases, strong melt flows lead to thin boundary layers that result in decreased longitudinal segregation. The predictions agree well with the experimental observations reported in the literature.

1 Introduction

Inhomogeneity is one of the most important quality concerns in the case of melt-grown single crystals, which results from the macroscopic and microscopic segregation of dopants and impurities during the growth. Macrosegregation is related to large-scale dopant transport in the melt. Microsegregation which is generally referred to as the striation, on the other hand, is introduced by the variation of the growth conditions at a small length and/or time scale, e.g., the fluctuations of the growth rate, melt flow velocity, and/or melt temperature, etc. This study focuses on macrosegregation, particularly, the effect of melt flow on dopant transport that produces the dopant segregation in as-grown crystals.

Dopant concentration and macrosegregation in the melt affect the crystal quality in two ways. As the crystal is pulled and the solute is rejected at the crystal/melt interface because of the partitioning effects, the concentration of dopant continually increases in the melt. This results in a higher dopant incorporation in the crystal with its height (axial or longitudinal segregation) even if the partition coefficient remains constant from beginning to the end of the growth process. Dopant concentration can also vary radially along the crystal/melt interface because of the recirculatory convective motions in the melt.

Czochralski (Cz) growth is a commonly used industrial process to produce bulk single crystals for semiconductors. The effect of melt flow on segregation in Cz grown crystals has long been recognized, and various measures have been taken to prevent it. For example, the crystal rotation was introduced to yield symmetric growth conditions and suppress the dopant segregation (Hurle and Cockayne, 1994). Benson (1965) experimentally determined the radial segregation in Cz grown silicon crystals, and found that the segregation strongly depends on the rates of crystal and crucible rotation, crystal pulling velocity, crystal diameter, etc. The first attempt to explain the dependency of radial segregation upon the growth conditions in terms of the melt flow patterns was made by Carruthers (1967) through a series of experiments. Baralis and Persino (1968) also found strong dopant segregation in pulled germanium crystals, which could be correlated with the flow patterns under their experimental conditions. Later, it was shown that an applied magnetic field can suppress the transient flows and temperature fluctuations in the system (Hurle and Series, 1985). Induced eddy currents by the magnetic field can significantly modify the convective flow field in the melt, which has a strong influence on the radial dopant segregation (Hurle and Series, 1985; Kim and Langlois, 1989).

Various approximate analytical models have been developed to understand and quantify the dopant segregation in a Cz grown crystal. For example, Burton et al. (1953) simplified the Cz process as a semi-infinite disk rotating on a semi-infinite melt surface. Solute transport in the melt can therefore be analyzed

Copyright © 1999 by ASME

by using the similarity solution of a rotating disk. Burton's analysis, which is referred to as the BPS model, provides useful understanding and prediction on the development of the axial dopant segregation. This analysis has been further refined and extended by several investigators. For example, instead of using the asymptotic approximation, Wilson (1978) has numerically solved the self-similar velocity field due to crystal rotation. Favier (1981) extended the BPS model to include the initial transient effect. Recently, the effect of an applied magnetic field on solute transport has been analyzed by employing the boundary layer theory (Hurle and Series, 1985; Wheeler, 1989) together with the magnetic effect on the melt flow. These analyses have been further extended to study the solute striation phenomena (Hurle et al., 1968; Wilson, 1980; Garandet, 1993). A recent review of these models can be found in Garandet et al. (1994).

Most of the above analyses assume a uniform distribution of solute in the boundary layer along the crystal/melt interface, i.e., no radial segregation is taken into account. This may be true for an infinitely large disk rotating over an infinitely large melt surface. In a real system, a much more complex flow is expected in the melt because of the co-existence of thermal buoyancy and surface tension forces and rotations of the crystal and crucible. All these factors contribute to the radial solute segregation, which can not be treated by a simplified analysis. Attempts have therefore been made recently to improve the BPS-type models by including the effect of melt flow in the boundary layer (Yen and Tiller, 1992; Ostrogorsky and Muller, 1992; Zuo and Guo 1996).

However, when severe radial solute segregation exists, a full-scale numerical analysis of solute transport in the melt is necessary. Due to limitations on computation power and intrinsic difficulties with the numerical technique, only limited studies have been conducted to examine the combined axial and radial dopant transport in Cz systems. Kim and Langlois (1986, 1989) were probably the first to perform numerical simulations of dopant segregation in Cz growth of silicon with and without an applied magnetic field, by solving full Navier-Stokes equations in the melt. A reasonable agreement was reported between the predicted radial distributions and the experimental measurements. However, no detailed information on process conditions and solute transport in the melt were provided in the paper.

To grow III-V compound single crystals, e.g., GaAs, InP, by Cz technique, a high-pressure system (as opposed to very low pressure for the growth of elemental semiconductors, e.g., Si, Ge, etc.) is needed because of the high equilibrium vapor pressures required by the volatile components of these compounds under molten conditions. It also requires encapsulation of the compound melt by a highly viscous liquid, such as B_2O_3, to prohibit escape of the volatile component from the melt since the vapor pressure of this component in the furnace gas is always low. A full-scale numerical simulation of such systems therefore becomes very challenging. Recently, an integrated numerical model, MASTRAPP[3], has been developed (Zhang and Prasad, 1995; Zhang et al., 1996b) to simulate the high-pressure liquid-encapsulated Czochralski (HPLEC) growth of semiconductor compounds. The model simulates the melt flow in the crucible, the gas flow in the furnace, and radiative heat transfer among the growing crystal, meniscus, and chamber wall. The model can capture accurately the curved crystal/melt interface by using a multizone adaptive grid generation (MAGG) technique (Zhang and Moallemi, 1995; Zhang et al., 1996a). A thermal elastic stress model is also incorporated into the model to calculate stresses in the growing crystal (Zou et al., 1996; Zou, 1997).

Semi-insulating III-V compound substrates are the key pre-requisites for high-speed devices and optoelectronic integrated circuits (OEIC's). Doping with iron is widely used in InP growth to produce semi-insulating InP crystals. Iron is a midgap acceptor that can compensate the residual shallow donors of InP to produce semi-insulating material with resistivity at least 10^7 ohm−cm. Iron, however, has a very small solubility in InP crystal and the equilibrium partition coefficient is estimated to be about 0.001. Such small partition coefficient of iron leads to its severe segregation in an InP crystal. Recently, we have extended the MASTRAPP scheme to model the macrosegregation of dopant (Zou et al., 1997; Zou, 1997) in HPLEC growth of InP. Because of the nature of the solute transport, transient mass transport equations are solved to simulate the dynamic process. To minimize the computation load, a two time-scale scheme has been developed that solves thermal transport (flow and

---

[3] Multizone Adaptive Scheme for Transport and Phase-Change Processes.

Nomenclature

b = radius of the crucible (m)
C = nondimensional solute concentration, C^*/C_0
C_0 = initial solute concentration (wt%)
C_p = specific heat (Jkg^{-1} K^{-1})
D_m = solute diffusivity in the melt (m^2 s^{-1})
Gr = Grashof number, $g\beta b^3(T_c - T_f)/\nu^2$
g = acceleration due to gravity (ms^{-2})
H = crystal height (m)
k = thermal conductivity (Wm^{-1} K^{-1})
k_0 = equilibrium solute partition coefficient
$\mathbf{k}$ = unit vector in z direction
L = latent heat (Jkg^{-1})
$\mathbf{n}$ = unit vector normal to the crystal/melt interface
P = nondimensional pressure, $p^*b^2/\rho\nu^2$
Pr = Prandtl number, ν/α
R = radial coordinate (m)
ΔR = width of control element

Re = rotation Reynolds number, $\omega b^2/\nu$
S = source term in dopant transport equation, defined in Eq. (8)
Sc = Schmidt number, ν/D
Ste = Stefan number, $C_p(T_c - T_f)/L$
t = nondimensional time, $t^*\nu_m/b^2$
Δt^* = time step (s)
T = temperature (K)
T_c = crucible wall temperature (K)
T_f = melting temperature of the melt (K)
$\mathbf{u}$ = nondimensional flow velocity vector, $\mathbf{u}^*b/\nu_m$
$\mathbf{V}_{\text{pull}}$ = nondimensional pulling velocity of crystal, $V^*_{\text{pull}}b/\nu_m\mathbf{k}$
z = nondimensional axial coordinate
Δz = height of the control element

Greek Symbols

α = thermal diffusivity (m^2 s^{-1})
β = thermal expansion coefficient (K^{-1})

θ = nondimensional temperature, $(T - T_f)/(T_c - T_f)$
ρ = density (kg m^{-3})
μ = kinetic viscosity (N sm^{-2})
ν = kinematic viscosity (m^2 s^{-1})
ω = rotation rate of crystal or crucible (s^{-1})

Subscripts and Superscripts

* = dimensional variables
av = average
bo = boric oxide
c = crucible
f = freezing point
g = gas
i = melt, encapsulant, inert gas, or crystal
j = index of control elements in R direction
m = melt
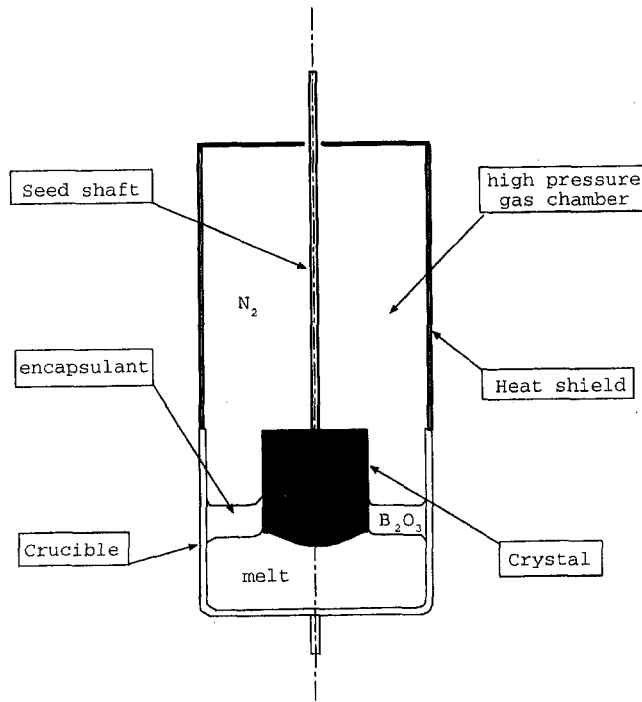n = nth time step
s = seed or crystal

Fig. 1 A schematic of the computational domain, the growth partion of the HPLEC furnace

temperature) and solute transport at different time levels. This is consistent with the physics of the process since the flow and temperature fields change much more slowly than the dopant redistribution. More specifically, a quasi-steady-state scheme is used to calculate the flow and temperature fields, but a small time step is used to solve the solute transport problem. A strong radial dopant segregation has been predicted for the HPLEC growth of InP crystals. Previously, we have reported some preliminary results on this problem with a much large dopant partition coefficient, $k_0 = 0.1$. The focus of that work was on the generic features of the model and thermal stress development in an InP crystal. Here, we present a more detailed analysis of the melt flow pattern and its effect on solute transport under varying conditions. This allows a better understanding of the melt transport mechanisms that can produce the crystal inhomogeneity. A rather detailed description of the numerical scheme employed for the calculation of the solute transport is also presented here.

2 Model Development and Numerical Scheme

A detailed description of the physical model and numerical scheme, MASTRAPP, for HPLEC growth can be found elsewhere (Zhang and Prasad, 1995; Zhang et al., 1996b; Zou et al., 1996, 1997; Zou, 1997). Here, we present only a brief outline of the scheme for completeness.

Figure 1 shows a schematic of the computational domain which includes the melt in the crucible, the encapsulant layer over the melt, the crystal growing from the melt, and the pressurized gas between the quartz heat shield and the encapsulant, all of which are enclosed in a stainless steel chamber (Prasad et al., 1994). A quartz heat shield sits on top of the quartz crucible and rotates with the crucible at the same speed. The crucible wall is hot and is maintained at a uniform temperature. The temperature of the shield is high at the bottom and decreases continuously along the height. Indeed, the conditions of the heat shield depend on the flow and temperature fields on the outside. The crystal, while it is slowly growing up, is rotated to eliminate asymmetry and the height of the melt drops accordingly. The

physical properties of the materials are assumed to be temperature independent but vary with the phase. The encapsulant/inert gas interface is assumed to be flat in most of the region except near the crystal where an iterative method is used to determine the shape of the free surface based on the force balance of gravity and surface tension. A 45-deg wetting angle is assumed between the crystal and the melt. The Marangoni effect (both melt and encapsulant) is neglected since the encapsulant (B_2O_3) is a highly viscous liquid. The crystal/melt interface is curved depending on the energy balance conditions. It is also assumed that the melt is a dilute solution, that is, the buoyancy effect due to the presence of dopant particles is negligible.

With these assumptions, the growth process can be described mathematically by the following nondimensional governing equations for a multiphase, multi-component medium, in an axisymmetric system:

$$\frac{\partial \overline{\rho}_i}{\partial t} + \nabla \cdot \overline{\rho}_i \mathbf{u}_i = 0, \tag{1}$$

$$\frac{\partial \overline{\rho}_i \mathbf{u}_i}{\partial t} + \nabla \cdot (\overline{\rho}_i \mathbf{u}_i \mathbf{u}_i)$$

$$= \nabla \cdot (\overline{\mu}_{i,\text{eff}} \nabla \mathbf{u}_i) - \frac{\partial P}{\partial z} + \overline{\rho}_i \, \text{Gr}_i \, \theta \mathbf{k}, \tag{2}$$

$$\frac{\partial \overline{\rho}_i \overline{C}_{pi} \theta}{\partial t} + \nabla \cdot (\overline{\rho}_i \overline{C}_{pi} \mathbf{u}_i \theta) = \frac{1}{\text{Pr}_m} \nabla \cdot (\overline{k}_{i,\text{eff}} \nabla \theta), \tag{3}$$

$$\frac{\partial C}{\partial t} + \nabla \cdot (\mathbf{u}_i C) = \frac{1}{\text{Sc}_m} \nabla \cdot (\overline{D}_{\text{eff}} \nabla C) + S, \tag{4}$$

where overbar means averaging, the subscript "i" represents the melt, encapsulant, inert gas, and crystal (including seed), respectively. The subscript "eff" stands for the effective diffusivities of momentum, heat and dopant for turbulent flow condition. For laminar flow, all effective diffusivities are set to one. The definitions of symbols used in these equations can be found in the Nomenclature. The characteristic scales used to nondimensionalize the equations are, length: radius of the crystal b, velocity: ν_m/b, pressure: $\rho_m \nu_m^2/b^2$, time b^2/ν_m, with subscript "m" referring to the properties of the melt. The physical properties with overbar in Eqs. (1) to (4) are nondimensionalized with the corresponding property in the melt. The nondimensional temperature $\theta = (T - T_f)/(T_c - T_f)$ and nondimensional dopant concentration $C = C^*/C_0$ are based on T_f, the equilibrium freezing temperature of the crystal; T_c, the crucible wall temperature; and C_0, the initial dopant concentration in the melt. The nondimensional controlling parameters in Eqs. (1)–(4) are: Grashof number, $\text{Gr}_i = g\beta_i b^3 (T_c - T_f)/\nu_i^2$, Prandtl number, $\text{Pr}_i = \nu_i/\alpha_i$, and Schmidt number, $\text{Sc}_m = \nu_m/D_m$. It should be noted that different material properties need to be used to calculate the corresponding Gr_i and Pr_i in gas (g) and melt (m).

No-slip boundary conditions are used along all of the solid surfaces. The crucible wall is assumed to be at uniform temperature, T_c. The temperature on the heat shield decreases linearly along the height until it reaches a low temperature at the top surface (Zou, 1997). A comprehensive radiation model is used to calculate the radiation heat transfer between various surfaces in the chamber. The details of the radiation model can be found in Nunes et al. (1996). The movement of the crystal/melt interface is determined by the energy balance along the interface:

$$\frac{\text{Pr}_m}{\text{Ste}_m} \mathbf{V}_{\text{pull}} \cdot \mathbf{n} = \overline{k}_s \nabla \theta_s \cdot \mathbf{n} - \nabla \theta_m \cdot \mathbf{n} \tag{5}$$

where Stefan number, $\text{Ste}_m = C_{pm}(T_c - T_f)/L$, $\mathbf{V}_{\text{pull}}$ is the nondimensional pulling velocity with respect to the melt-free surface, and $\mathbf{n}$ is the unit vector normal to the crystal/melt

interface. The solute segregation along the crystal/melt interface is governed by the solute balance condition at the interface:

$$C(1 - k_0)\mathbf{V_{pull}} \cdot \mathbf{n} = -\frac{1}{Sc_m} \nabla C \cdot \mathbf{n} \qquad (6)$$

where k_0 is the equilibrium partition coefficient which is defined as the ratio of the concentration of dopant in the solid to that in the liquid at the interface. The partition coefficient k_0 is generally a function of temperature and dopant concentration. For dilute solution such as the case here, k_0 can be considered as constant. For iron (Fe) as dopant in InP, k_0 is estimated to be about 0.001.

The above equations and boundary conditions are solved by using the MASTRAPP Scheme (Zhang and Prasad 1995; Zhang et al., 1996b). The scheme employs curvilinear finite volume method for the discretization of the governing equations with multizone adaptive grid generation technique (MAGG) for grid refinement and clustering as the solution evolves. An adaptive optimization of grids is used to guarantee the grid smoothness and orthogonality in the vicinity of the internal interfaces. See Appendix for the discussion on accuracy of the numerical scheme.

Because a slow pulling rate is used in most of the InP growth, the variation in thermal conditions of the system is fairly small over a rather long time period and therefore, a quasi-steady-state assumption has been widely used in the simulation of the growth process (Derby and Brown, 1988; Zhang and Prasad, 1995). On the other hand, solute partitioning at the melt/crystal interface is a transient phenomenon, and solute concentration at the interface keeps changing continuously with time. To reduce the computation load, a two-level time scheme is incorporated into the MASTRAPP model. This two-level time scale solves quasi-steady-state temperature and velocity fields at different crystal heights. In between, however, a transient solute transport equation is solved using a much smaller time step while the crystal is being grown. Meanwhile, the velocity and temperature fields are kept the same as that at the previous crystal height.

While solving the concentration equation, a source term is included in the first control volume on the melt side of the interface to account for the dopant rejection from the crystal due to solute partitioning. At each time step Δt, the following amount of dopant is rejected from the melt/crystal interface (for $k_0 < 1$) into the control element next to the interface:

$$C^*(1 - k_0)V^*_{pull}\Delta t^* \Delta R \qquad (7)$$

where ΔR is the width of the control grid. Following Kim and Langlois (1989), this dopant can be taken as a source and is distributed in the control element next to the interface, providing the source term S in Eq. (4) as

$$S_j = C(1 - k_0)V_{pull}/\Delta z_j \qquad (8)$$

for the jth control element in the melt next to the melt/crystal interface, with Δz as the height of the element. For all other elements, the source term S is taken zero.

As the crystal grows, the melt level drops and the computational domain for dopant transport is changed. This change is simulated by moving the melt grid line down and generating a new grid system. Such movement of the grid system, however, does not maintain exactly the areas of each control element and thus adds additional mass because of the nonorthogonal coordinate system used here. Even though this extra mass is very small between the two time steps, it can accumulate and lead to large errors after a period of time. A concentration correction method is therefore developed to conserve the mass during the growth. The extra mass generated at each time step is calculated and then subtracted from the entire volume of the dopant by proportionally correcting the dopant concentration at each node. In this way, the largest correction is implemented in the boundary layer near the crystal/melt interface where the dopant concentration is highest. With the concentration correction, the balance of the dopant in the melt can be controlled within 0.1 percent.

It should be pointed out that the above formulation is written in a generic form that is valid for both laminar and turbulent flows in the gas and melt. In HPLEC systems, gas turbulence is strong, which is simulated using the standard $k-\epsilon$ model (Zhang et al., 1996b). The melt is considered to be laminar since InP crystal diameter is small (50 to 75 mm) and melt height is low. It should, however, be noted that even for such small-diameter crystal growth, melt flow may develop into a transient, fluctuating flow regime (Muller, 1989). In addition, three-dimensional effect may also be important in certain cases. Detailed description of flow instability and transition in a CZ system can be found in several papers, for example, by Muller (1989) and by Ristorcelli and Lumley (1992), and will not be discussed here for brevity.

3 Results and Discussions

Several transport mechanisms are involved in generating melt flows in an encapsulated high-pressure Cz system, for example, crystal and crucible rotations, buoyancy due to temperature difference between the crucible wall and crystal, heat loss from the melt surface, and surface tension along the free surface due to temperature variation, etc. An analysis of the effect of the resulting flow patterns on solute transport in the melt and macro-segregation in the growing crystal, and the physical mechanisms involved constitutes the major part of the present work.

The HPLEC furnace operating at the USAF Research Laboratory at Hanscom, MA, for InP growth has been considered for the present study. However, only a portion of the furnace is included in the computational domain and a generalized study is performed to examine the transport mechanisms that dominate the high pressure growth of III-V compounds. The system grows a 40-mm diameter crystal from the melt in a 100-mm diameter crucible. The initial melt height is taken as 23 mm, and the thickness of the B_2O_3 encapsulant is 5 mm (see Prasad et al. (1994) for details of the furnace). A constant temperature condition is used for the crucible wall surface with linearly decreasing temperature along the heat shield wall, which is estimated from the global simulation and special experiments (Prasad et al., 1994; Zhang et al., 1997). Unless specified, the equilibrium partition coefficient is assumed to be $k_0 = 0.001$ (for Fe in InP). The other physical properties of InP and nitrogen gas used for the present calculation are given in Table 1.

First, calculations are performed for three basic cases: pure crystal rotation, pure crucible rotation, and pure thermal buoyancy-driven flow. The solute transport mechanisms associated with the corresponding melt flows are investigated under these special conditions. Next, calculations are performed for the real case including all of these physical phenomena with a real partition coefficient of iron in InP, $k_0 = 0.001$. The induced flow pattern and its effect on solute transport in the melt are then discussed, which demonstrate the relative effect of each physical mechanism and its interaction. Finally, simulations are also performed to examine the effect of the pulling rate and the partition coefficient.

3.1 Effect of Crystal Rotation. Pure rotation of a growing crystal without any thermal effect is a classic case addressed by the various stagnant film or boundary layer analyses, i.e., BPS-type models (Burton et al., 1953; Wilson 1978, Wheeler, 1989). In the present case, full Navier-Stokes equations are solved instead of assuming similarity for semi-infinite geometry. However, to simplify the numerical treatment, a flat crystal/melt interface is assumed with crystal being pulled at a constant speed.

Table 1 Physical properties of InP (Jordan, 1985a, b), boric oxide (Hurle and Cockayne, 1994), and nitrogen gas

InP Melt

T_f	K	1335
h_{sl}	Jkg^{-1}	7.26×10^5
ρ_m	kgm^{-3}	5050
D_m(Fe)	m^2s^{-1}	10^{-8}
C_{p_m}	$Jkg^{-1} K^{-1}$	424
k_m	$Wm^{-1}K^{-1}$	22.8
β_m	K^{-1}	4.44×10^{-4}
ν_m	$m^2 s^{-1}$	1.62×10^{-7}
ϵ_m		0.04
ϕ_{sl}	°	45

InP Solid

ρ_s	kgm^{-3}	4710
C_{p_s}	$Jkg^{-1}K^{-1}$	378
k_s	$Wm^{-1}K^{-1}$	8.86
ϵ_s		0.2

Boric Oxide

ρ_{bo}	kgm^{-3}	1520
$C_{p_{bo}}$	$Jkg^{-1}K^{-1}$	1830
k_{bo}	$Wm^{-1}K^{-1}$	1.85

Gas (40 bar, 700 K)

ρ_g	kgm^{-3}	18.9
C_{p_g}	$Jkg^{-1}K^{-1}$	1107
k_g	$Wm^{-1}K^{-1}$	5.04×10^{-3}
ν_g	m^2s^{-1}	1.568×10^{-6}
τ_s	K^{-1}	8.76×10^{-6}

Fig. 3 Radial dopant distribution along the melt/crystal interface for the case of pure crystal rotation, $Re_s = 10^3$, 2×10^3, and 5×10^3

Figure 2 shows the melt flow field (left) and concentration distribution (right) for the case of pure crystal rotation with a rotation rate with $Re_s = \omega_s b^2/\nu_m = 10^3$. In Fig. 2, the melt flows upward to the crystal along the central axis due to the pumping effect of the crystal rotation. The resulting jet flow impinges on the crystal, makes a turn, and then flows radially outward along the crystal/melt interface. Because of a finite size of both the crucible and the crystal, the melt moves downward when it reaches the crucible wall, and thus forms a large recirculating cell in the melt.

During the growth, the dopant is rejected from the interface because of very limited solubility of the dopant in the crystal due to low partition coefficient. The rejected dopant piles up in the area near the crystal/melt interface, and then diffuses away from the interface into the bulk melt, as shown by the dense isoconcentration curves near the crystal/melt interface in Fig. 2. The melt flow influences the solute transport in two ways. First, as the melt flows along the crystal/melt interface, it carries the dopant with it. 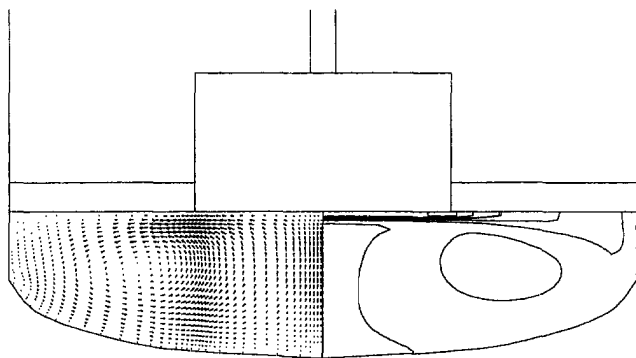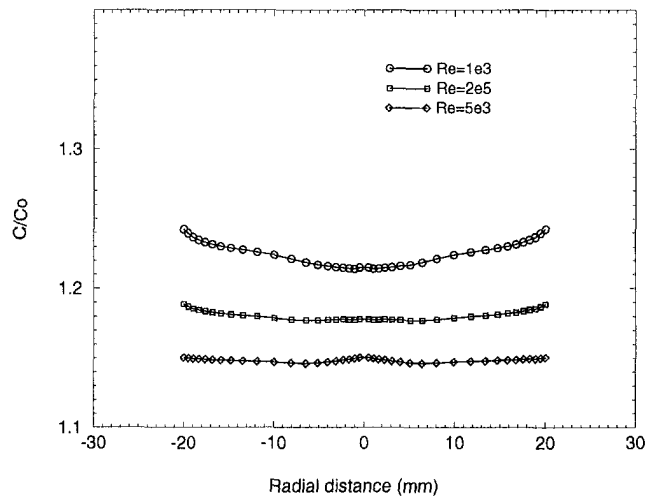As a consequence, the dopant is washed away from underneath the crystal and accumulates in the upper corner of the melt near the crucible. This effect of the melt flow on dopant distribution is evident by long stretch of the isoconcentration lines along the crystal/melt and melt/encapsulant interfaces (Fig. 2). Secondly, the existence of a velocity boundary layer near the crystal makes the solute boundary layer much thinner compared to the case of pure diffusion, thereby reducing the axial solute segregation. In other words, more solute or dopant can be transported away from the crystal/melt interface due to melt convection, which results in lesser accumulation of the solute at the interface, and therefore, reduced longitudinal segregation. In the bulk melt, far way from the crystal/melt interface, a somewhat uniform dopant distribution is predicted.

Figure 3 shows the radial distribution of dopant concentration at the melt/crystal interface for three rotation rates, $Re_s = 10^3$, 2×10^3, and 5×10^3, at the same crystal height. The calculations are performed with all other conditions remaining the same except the crystal rotation rate. In general, fairly uniform distribution of dopant is obtained in all cases studied here. Only about two percent radial dopant segregation is predicted for the low rotation rate ($Re_s = 10^3$), and less than one percent for high rotation rate $Re_s = 5 \times 10^3$.

The effect of the melt flow on longitudinal segregation can also be examined in Fig. 3 by comparing the nondimensional concentrations at the crystal/melt interface for the same crystal height. It shows a strong effect of the crystal rotation rate on longitudinal segregation. For example, for the same crystal height grown (27 mm), the average interface solute concentra-
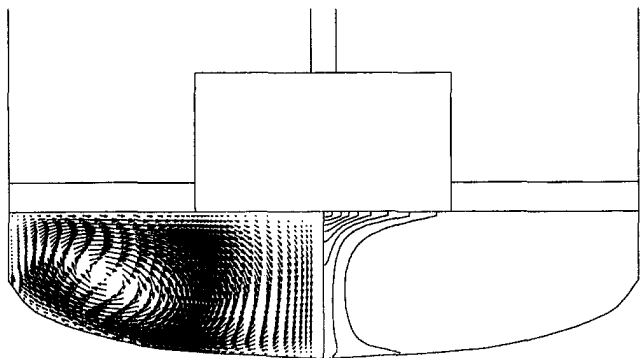

Fig. 2 Flow field and isoconcentration lines for the case of pure crystal rotation, $Re_s = 10^3$

Fig. 4 Flow field and isoconcentration lines for the case of pure nature convection, $Gr_m = 10^6$
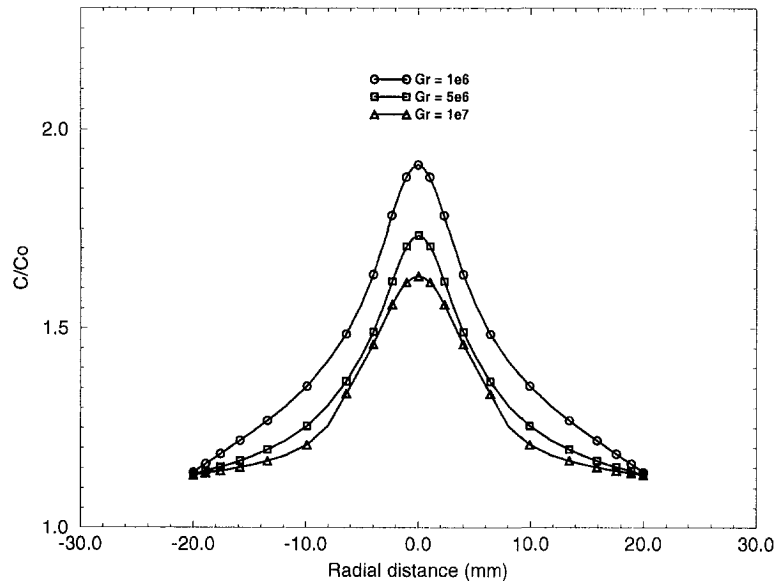
Fig. 5 Radial dopant distribution along the melt/crystal interface for the case of pure natural convection for three Grashof numbers: $Gr_m = 10^6$, 5×10^6, and 10^7

tion increases by about 23 percent for a lower rotation rate ($Re_s = 10^3$) compared to about 15 percent for a higher rotation rate ($Re_s = 5 \times 10^3$). This variation in longitudinal segregation can be explained by the decrease in the solute boundary layer thickness as the crystal rotation rate is increased.

It is interesting to note that a rather small radial dopant segregation is predicted even when the full Navier-Stokes equation is solved for finite sizes of the crystal and crucible. This indicates that, as far as the radial segregation is concerned, the classic BPS-type models (Burton et al., 1953; Wilson, 1978) represent a good approximation of the system for pure crystal rotation case. In a real system, however, the buoyancy-driven convection can dramatically change the melt flow pattern and therefore the solute transport. In the next section, the solute transport with pure thermal convection and without crystal rotation is investigated in detail.

3.2 Effect of Thermally Driven Convection. For a crystal to grow, a temperature gradient from the melt to the crystal must be established. The crucible wall is therefore kept at a temperature higher than the freezing temperature to maintain a superheated melt in the crucible. This asymmetry in temperature conditions produces buoyancy-driven flows in the melt. The effect of natural convection on solute transport in the melt is investigated here by performing calculations for the same system considered earlier, with a temperature difference between the crucible and the growing crystal but without rotation. Figure 4 shows the calculated velocity fields and isoconcentration lines in the melt for the case $Gr_m = g\beta b^3(T_c - T_f)/\nu_m^2 = 10^6$. As we can see, a single recirculatory cell is produced in the crucible with melt flowing up along the hot crucible and then making a turn towards the crystal center. The melt flows downward under the crystal.

When the melt flows over the crystal/melt interface from the outer region towards central axis radially, it pushes dopant inwards. As a result, the dopant accumulates in the central region underneath the crystal, and a solute-rich region is formed there, as shown by dense isoconcentration curves in Fig. 4. A large radial segregation is then predicted because of the nonuniformity in the thickness of the solute boundary layer along the crystal/melt interface, as shown in Fig. 5 which presents the dopant concentration along the crystal/melt interface for $Gr_m = 10^6$, 5×10^6, and 10^7, for a given crystal height. For the case of $Gr_m = 10^6$, about 70 percent increase in dopant concentration

is calculated from the edge of the crystal to the center. Although the flow structure remains the same, increasing the thermal driving force, Gr_m, strengthens the melt flow and thereby decreases the solute boundary layer thickness as well as the radial segregation. For example, the radial segregation decreases from about 70 percent to 40 percent with an increase in Gr_m from 10^6 to 10^7. Increasing Grashof number also decreases the axial segregation by reducing the dopant concentration at all radial locations. At the same crystal height, the maximum nondimensional dopant concentration at the crystal/melt interface decreases from 1.92 to 1.63, or about 18 percent when Gr_m is increased from 10^6 to 10^7 (Fig. 5). The nondimensional dopant concentration on the edge of the crystal remains almost the same as Gr_m varies.

3.3 Effect of Crucible Rotation. The third important driving force for the melt flow is the rotation of the crucible although only a small rotation rate is considered here. A typical flow pattern due to crucible rotation is given in Fig. 6 for a rotation rate with $Re_c = \omega_c b^2/\nu_m = 5 \times 10^2$. The melt near the crucible bottom surface is driven towards the crucible side wall but the melt near the encapsulant layer and crystal flows towards the center. In the center region, melt flow is very weak and multiple cells may develop, which is especially true for the case with a higher rotation rate (not shown here). Further increase in crucible rotation rate may lead to flow oscillations. This kind
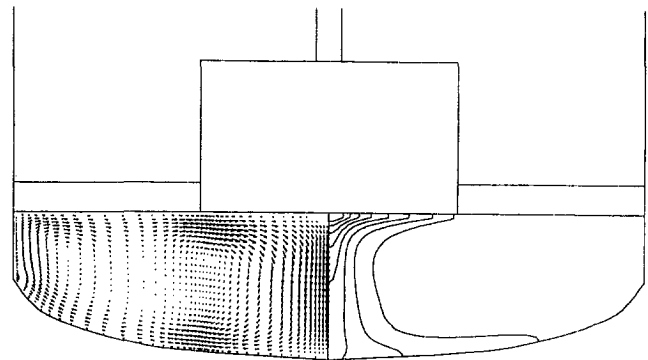

Fig. 6 Flow field and isoconcentration lines for the case of pure crucible rotation, $Re_c = 5 \times 10^2$
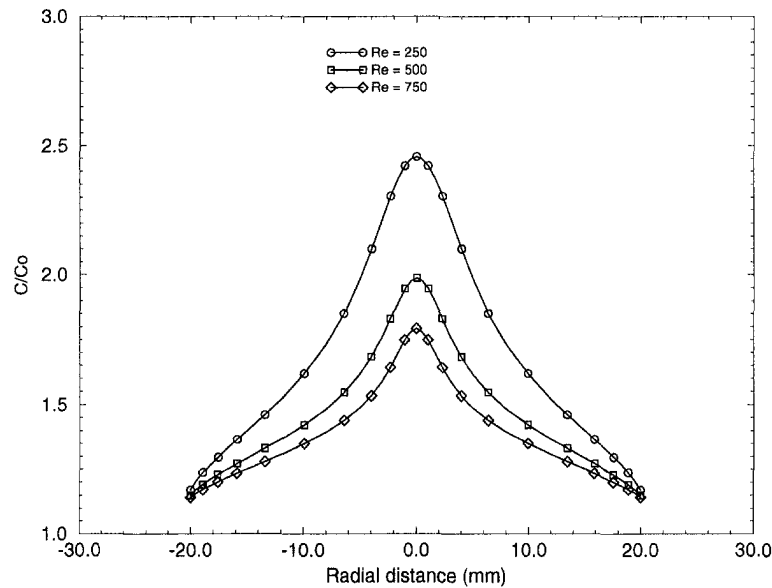
Journal of Heat Transfer

Fig. 7 Radial dopant distribution along the melt/crystal interface for the case of pure crucible rotation for three Reynolds numbers: $Re_c = 2.5 \times 10^2$, 5×10^2, and 7.5×10^2

of melt flow is similar to that induced by thermal buoyancy as shown in Fig. 4, except for the variation of the flow inside the cell. Figures 6 also present the corresponding isoconcentration curves which show a similar pattern as that seen in Fig. 4 for the case of pure natural convection. As the melt flows towards the crystal center, it pushes the solute into that region. As a result, the solute piles up underneath the crystal and a strong radial segregation in dopant is produced. This can be observed more clearly in Fig. 7 which presents the dopant distribution along the melt/crystal interface for three rotation rates, $Re_c = 250, 500$, and 750. As expected, there exist highest concentrations at the center which decrease continuously towards the edge of the crystal. Increasing the crucible rotation rate improves the radial segregation, due to the increased melt flow velocity and decreased solute boundary layer, as illustrated earlier.

3.4 Combined Effect in HPLEC Growth.

In a real HPLEC growth system, both crystal and crucible rotations as well as the buoyancy-driven convection affect the solute transport in the melt. In addition, in real growth, the crystal/melt interface is curved because of the complex thermohydrodynamic phenomena, radiation heat transfer and phase change. The curvature of the crystal/melt interface can also contribute to radial segregation. The effect of a curved crystal/melt interface on segregation has been investigated by many researchers but generally for the Bridgman growth (Coriell and Sekerka, 1979; Kaddeche et al., 1996). The emphasis here is on the effects of convection on radial segregation in the presence of a curved crystal/melt interface that is calculated by the model using energy balance conditions.

As shown in the previous paragraphs, crystal rotation and buoyancy force lead to counterrotating cells in the melt, and crucible rotation has the same effect on melt flow as that of the thermal buoyancy. In a system where all of these three forces exist simultaneously, a complex flow pattern is expected. Figure 8 shows the calculated results for a case with crystal rotation ($Re_s = 10^3$), countercrucible rotation ($Re_c = -5 \times 10^2$), and natural convection ($Gr_m = 10^6$). The calculations also include the turbulent gas flow ($Gr_g = 10^7$ based on crucible radius and the temperature difference, $T_C - T_f$),[4] radiation heat transfer between the crystal

and the chamber wall, a curved melt/crystal interface, and thermal-elastic stress in the growing crystal although the present discussion will not be extended to the stress field.

Figure 8 shows the flow, temperature, and stress fields in the entire system at a given crystal height, $H = 15$ mm. The left side of the figure presents the streamlines in both the gas and the melt and the von Mises thermal elastic stress in the crystal, while the right side shows the isotherms in the gas, encapsulant layer and crystal as well as the isoconcentration curves in the melt. A three-cell flow structure is developed in the melt. In the center of the crucible underneath the crystal, the melt is pumped up along the center line. It is then thrown out along the crystal/melt interface, similar to the case of pure crystal
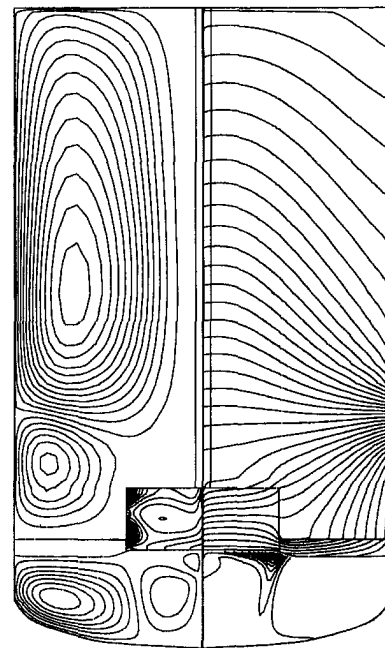
Fig. 8 Streamlines, isotherms, iso-stress lines, and isoconcentration lines for HPLEC growth with both crystal and crucible rotations and natural convection at crystal heights: $H = 15$ mm. ($Gr_m = 10^6$, $Re_s = 10^3$, $Re_c = -5 \times 10^2$, $Gr_g = 10^7$, $k_0 = 0.001$, $V^*_{pull} = 10$ mm/hr, and $Sc = 16.2$).

---

[4] The Grashof number will exceed 10^9 if it is based on the height of the gas region and a temperature difference between the encapsulant surface and the furnace walls that are cooled.
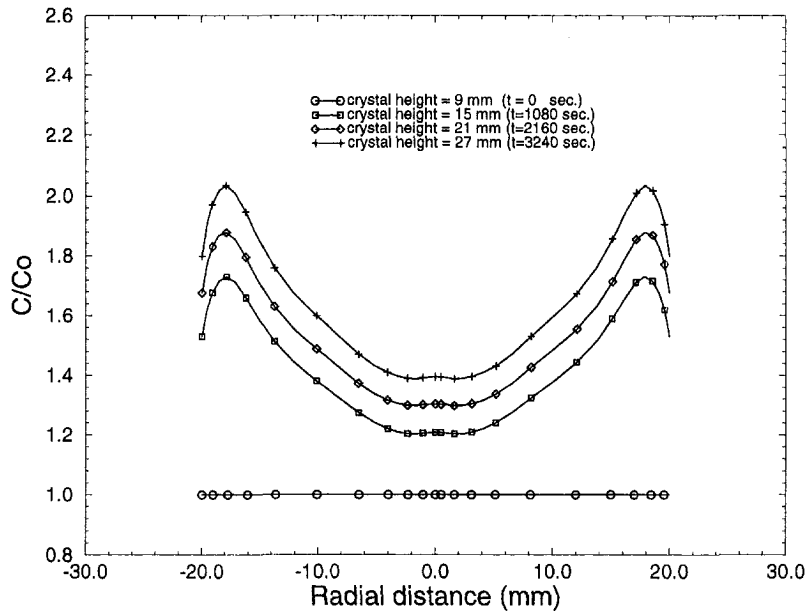
Fig. 9 Radial dopant distribution along the melt/crystal interface in a HPLEC system with both crystal and crucible rotations and natural convection at four growing crystal heights: H = 9, 15, 21, 27 mm. (Gr_m = 10^6, Re_s = 10^3, Re_c = -5×10^2, Gr_g = 10^7, k_0 = 0.001, V_{pull}^* = 10 mm/hr, and Sc = 16.2).

rotation. On the other hand, the melt flows up along the hot crucible wall as in the case of pure natural convection, and then flows inwards along the encapsulant/melt interface to the crystal. This inward flow cannot penetrate into the region underneath the crystal because of the outward flow introduced by the crystal rotation. Consequently, the two opposing melt flows meet at the location near the edge of the crystal and both turn downwards to the bottom of the crucible, leading to the formation of two separate recirculating cells. The third small cell in the center underneath the crystal results from the jet-like flow due to the pumping effect of the crystal rotation. The computations have also shown that the flow pattern does not change much as the crystal height increases under the conditions studied here (not shown here, see Zou et al. (1997)).

Figure 8 demonstrates that the flow structure dictates the solute transport in the melt. The melt flow introduced by the crystal rotation tries to wash away the dopant rejected from the crystal into the melt underneath the encapsulant. Because of an equally strong flow from the crucible wall, the momentum of the outward flow vanishes quickly and most of the dopant remains in the melt underneath the crystal. The outward melt flow due to crystal rotation also resists inward flow resulting from the thermal buoyancy, and thus prevents the accumulation of the dopant in the central region. As a result of these two opposing effects, a dopant-rich zone is formed, in this case, close to the edge of the crystal with a part of it directly underneath the crystal. Because of a nonuniform solute boundary layer along the crystal/melt interface, a strong radial dopant segregation is then expected, as shown in Fig. 9.

Figure 9 presents the radial solute redistributions along the crystal/melt interface for four crystal heights corresponding to the growth conditions in Fig. 8. (At a crystal height of 9 mm, it is assumed that the dopant is uniformly distributed in the melt.) In all cases, H > 9 mm, the location for maximum dopant concentration is located close to the edge of the crystal. In this case, there is about 40 percent difference between the maximum and minimum dopant concentration across the crystal. During the growth, the radial segregation pattern remains the same due to an almost identical melt flow structure. However, the dopant concentrations at the interface keeps increasing as the crystal height is increased.

The calculated radial dopant segregation shown in Fig. 9 agrees qualitatively well with the experimental observations for some elemental semiconductors grown by the Cz method. For example, Baralis and Perosino (1968) have grown germanium crystals doped with radioactive antimony using the Cz method with and without the crystal rotation. In the case without crystal rotation, they found a high impurity concentration in the center of the crystal, which was also confirmed by the resistivity measurement. For crystals grown with crystal rotation, their optical density measurement indicated a low dopant concentration in the central region of the crystal and a much higher concentration in the region close to the edge of the crystal. This is qualitatively in a good agreement with Fig. 9 which includes both crystal rotation and thermally driven flow. Similar radial segregation pattern as that in Fig. 5 for pure buoyancy-driven convection has also been observed by Hoshikawa et al. (1984) in silicon crystal growth with an applied vertical magnetic field when the magnetic field is not strong enough to dampen the natural convection effects. The melt flow patterns predicted in Figs. 4 and 8 have also been confirmed by Carruthers (1967) and Mukherjee et al. (1996) using model liquid experiments.

Our model results in Fig. 9 are also in good agreement with the resistivity measurements of iron-doped InP wafers obtained by Bliss (1998) at the U.S. Air Force Research Laboratory at Hanscom. They have measured the resistivity of several commercial iron-doped wafers with different diameters. For a small-diameter wafer, they found a small resistivity in the wafer center, indicating a small iron concentration there. Along the radial direction, the resistivity increases to a maximum followed by a quick decrease. Such variation of the resistivity along the radial direction agrees qualitatively with our model prediction since a high iron concentration stands for a high resistivity. In the case of wafers of larger diameter, very different dopant distribution patterns were observed, indicating complex flow conditions that are not considered here. In addition, some three-dimensional effects are also observed in the resistivity data.

3.5 Mechanisms of Thermo-Solutal Phenomena in a HPLEC System. The model calculations presented above demonstrate that the solute transport and segregation are strong functions of the flow pattern in the melt, which is dictated by
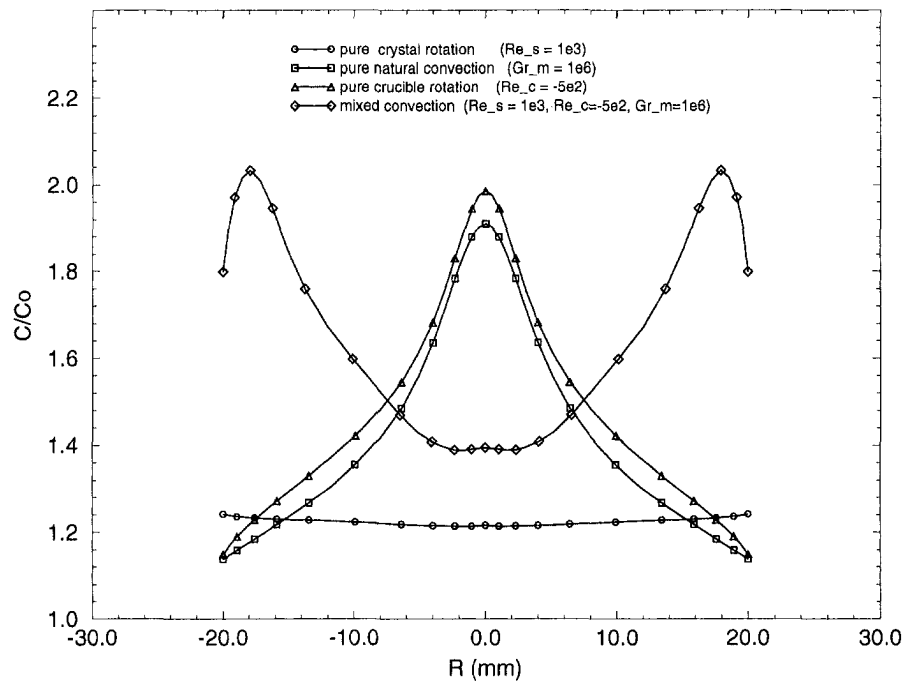
Fig. 10 Comparison of the radial dopant distribution for four cases: pure crystal rotation ($Re_s = 10^3$), pure natural convection ($Gr_m = 10^6$), pure crucible rotation ($Re_c = 5 \times 10^2$), and a HPLEC growth with both crystal and crucible rotations and natural convection ($Gr_m = 10^6$, $Re_s = 10^3$, and $Re_c = -5 \times 10^2$) at the same crystal heights $H = 27$ mm

physical mechanisms of the driving forces. This can be further illustrated by plotting results for the various cases together, as in Fig. 10. It is evident from this figure that a strong radial segregation is introduced by natural convection, 70 percent compared to 2 percent in the case of pure crystal rotation. Adding crystal rotation has two effects on radial segregation. The first is to decrease the extent of radial segregation. In Fig. 10 with $Re_s = 10^3$ and $Gr_m = 10^6$, adding crystal rotation decreases the radial segregation from about 70 percent to 40 percent. The second effect is to change the dopant profile and move the location for the peak along the crystal/melt interface. In Fig. 10, the maximum dopant concentration at the crystal/melt interface shifts from the center in the case of pure natural convection to the location close to the edge of the crystal. Both of these effects help in improving the crystal quality.

For given diameters of the crystal and crucible, the parameter that can represent the relative strength of the crystal rotation and buoyancy force is $Re_s/Gr_m^{1/2}$. When $Re_s/Gr_m^{1/2}$ is very large, melt flow in the crucible is dominated by the flow induced by the crystal rotation. A uniform solute boundary layer will eventually develop along the crystal/melt interface, and radial solute segregation will diminish. On the other hand, when $Re_s/Gr_m^{1/2}$ is very small, the thermal buoyancy-driven convection is dominant, and a nonuniform solute boundary layer will develop along the crystal/melt interface with a larger thickness at the center of the crystal and a severe radial dopant segregation. In the case of Figs. 9 and 10, $Re_s/Gr_m^{1/2} = 1$, a 40 percent dopant segregation along the crystal/melt interface is calculated. It is expected that by further increasing $Re_s/Gr_m^{1/2}$ larger than 1, the location with maximum dopant concentration can be pushed out of the crystal range, and a more uniform radial dopant distribution can be achieved in the crystal. This conclusion agrees qualitatively with the experimental observations (Benson, 1965; Carruthers, 1967). However, it may not be practical to rotate crystal at high speeds because of engineering limitations, e.g., eccentricity, shaft support, and control. A compromise is generally made in industrial growth primarily based on trial and error and experience. The results presented here

show that the use of a process model can help in developing such optimal conditions.

We should point out again that our present model only considers the simplest flow condition in a HPLEC system, that the melt flow in the crucible is stable, axisymmetrical, and laminar. In a real system, the laminar flow can be easily destabilized and the flow can become unsteady and three-dimensional, especially when the crucible rotation is added. Nevertheless, the present model provides a first full-scale numerical simulation of macrosegregation in a HPLEC system for InP growth. The present model not only provides the information on dopant segregation in a small InP crystal growth system, but also establishes a reference for future research on dopant segregation in a Czochralski system with more complicated physical phenomena such as three-dimensional effect, and oscillatory and/or turbulent melt flows. Efforts are being made now to incorporate more and more of these complexities into the model, particularly in the case of large-diameter silicon single crystal growth (Zhang et al., 1998).

3.6 Effects of Pulling Rate and Segregation Coefficient. The longitudinal and radial segregation are also affected by the crystal pulling rate and the partition coefficient k_0. Decreasing the crystal pulling rate has little effect on the gas and melt flow, but a significant effect on the dopant concentration at the melt/crystal interface due to the variation in the amount of dopant rejected from the crystal. The effect of the pulling rate can be illustrated by comparing Fig. 11 with Fig. 9, where Fig. 11 shows the solute concentration for a reduced pulling rate (5 mm/h versus 10 mm/h in Fig. 9). As is expected, the faster the pulling rate, the more solute is rejected from the interface. By decreasing the pulling rate by 50 percent, the nondimensional solute concentration at the crystal height of 27 mm has been decreased from 2.04 to 1.44, and the radial segregation has diminished from 40 percent to 16 percent.

The solute partition coefficient k_0 also has a significant effect on dopant segregation in the case of pure diffusion, in particular when k_0 is very small (Garandet et al., 1994). The sensitivity
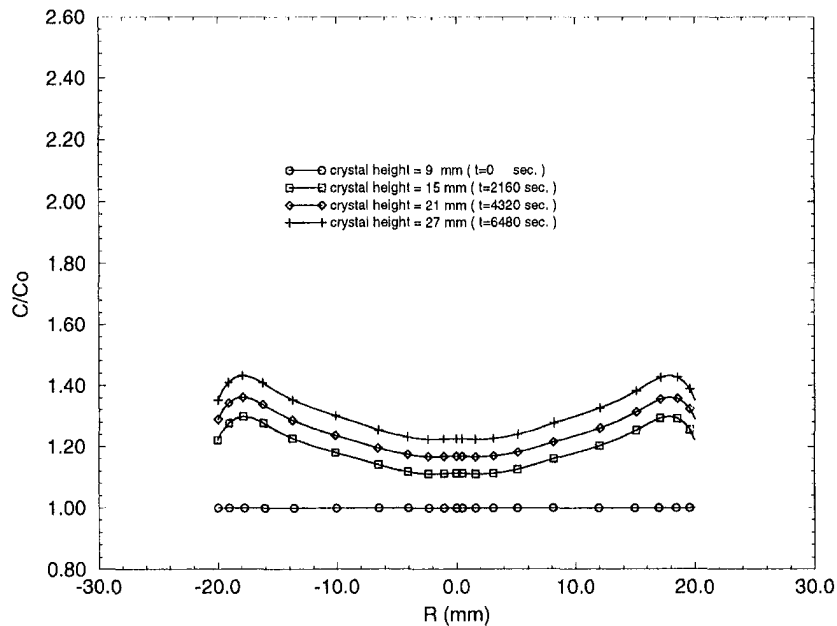
Fig. 11 Dopant distribution along the interface for pulling velocity V^*_{pull} = 5 mm/hr. (k_0 = 0.001). All other parameters remain the same as in Fig. 9.

of the solute segregation on partition coefficient k_0 is greatly decreased as the solute transport in Cz system is strongly enhanced by the melt flow. This can be seen by comparing the dopant concentration in Fig. 9 (k_0 = 0.001) with that in Fig. 12 for k_0 = 0.01. Increasing k_0 by one order of magnitude made little change in the value of dopant concentration. The segregation pattern shown in both Figs. 9 and 12 look the same as that shown in our earlier result with k_0 = 0.1 (Zou et al., 1997). Clearly, smaller segregation coefficient means more solute rejection during the growth. The effect, however, is very small in the present case. For example, the maximum nondimensional concentration of dopant at the crystal height of 27 mm are 2.04, 2.0, and 1.84, corresponding to the partition coefficient

of 0.001, 0.01, and 0.1, respectively, and the radial segregation is almost the same as about 40 percent.

4 Conclusions

A numerical analysis has been carried out to investigate the effect of the flow pattern on solute transport in a high pressure Czochralski crystal growth system. The present study focuses on the melt flow introduced by the crystal and crucible rotations and the buoyancy force, which are believed to be the main driving forces for melt convection in a HPLEC system. The previously developed MASTRAPP model with special modification for two time-level calculations, has been used to perform the simulation, and some important conclusions are as follows:
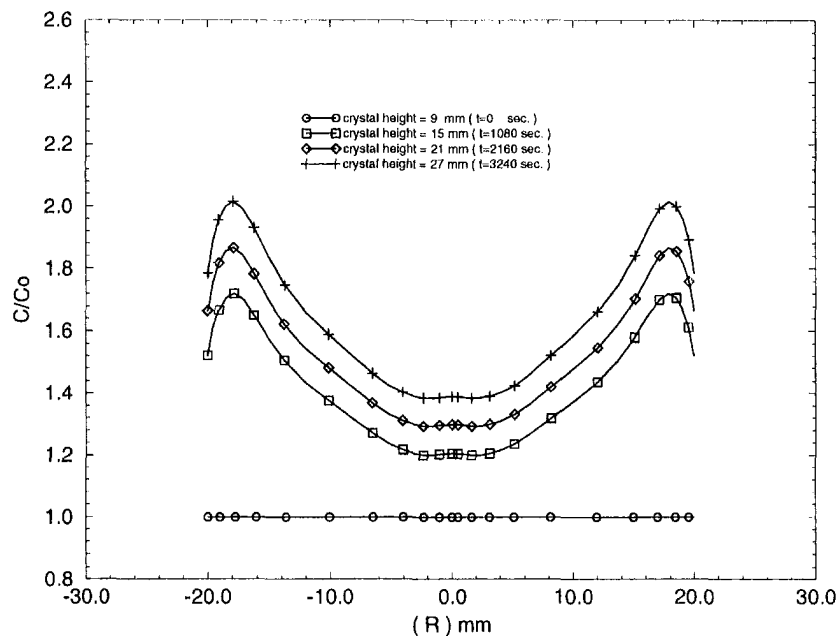

Fig. 12 Dopant distribution along the interface for segregation coefficient k_0 = 0.01 (V^*_{pull} = 10 mm/hr). All other parameters remain the same as in Fig. 9.

- Solute transport in the Cz growth is primarily controlled by the melt convection in the crucible. Both axial and radial segregation are functions of the flow pattern and flow strength. Overall, increasing the flow strength decreases the solute boundary layer thickness and leads to the reduction in both axial and radial solute segregation.
- A fairly uniform solute distribution along the crystal/melt interface is obtained for the cases of pure crystal rotation, which is consistent with the classic BPS assumption. A very small radial solute segregation exists even when the rotation Reynolds number is low and the system is finite.
- For the case of pure buoyancy-driven convection, most of the solute is accumulated in the center of the crystal, leading to a severe radial dopant segregation. An increase in natural convection effects, i.e., increasing Gr_m, reduces the radial segregation by decreasing the solute boundary layer thickness.
- The patterns of melt flow and dopant segregation generated for the case of pure crucible rotation are similar to that due to pure natural convection, and a severe radial segregation develops.
- A 40 percent dopant segregation has been calculated for HPLEC growth of InP crystals for $Gr_m = 10^6$, $Re_s = 10^3$, and $Re_c = -5 \times 10^2$ (compared to 70 percent for pure natural convection and two percent for pure crystal rotation). The maximum solute concentration exists at a location close to the edge of the crystal, which agrees qualitatively with the experimental observations reported in the literature.
- The BPS-type models are not suitable for analysis of segregation under real growth conditions.
- A high ratio of $Re_s/Gr_m^{1/2}$ is needed to eliminate the radial segregation of dopant in the Cz growth.
- The crystal pulling rate also has a significant effect on both the longitudinal and radial segregation.
- On the other hand, the solute partition coefficient has weak effect on longitudinal and radial segregation for the cases considered here.

Acknowledgments

References

Anselmo, A., Prasad, V., Koziol, J. and Gupta, K. P., 1993, "Oscillatory Convection in Low Aspect Ratio Czochralski Melts," *J. Crystal Growth*, Vol. 134, pp. 116–140.

Baralis, G., and Perosino, M. C., 1968, "Convection-Induced Impurity Distribution During Germanium Crystal Pulling," *J. Crystal Growth*, Vol. 3, pp. 651–655.

Benson, K. E., 1965, "Radial Solute Distribution in Czochralski-Grown Silicon Crystals," *Electrochem. Technol.*, Vol. 3, pp. 332–335.

Bliss, D., 1998, private communication.

Burton, J. A., Prim, R. C., and Slichter, W. P., 1953, "The Distribution of Solute in Crystals Grown from the Melt. Part I. Theoretical," *J. Chem. Phys.*, Vol. 21, pp. 1987–1991.

Coriell, S. R., and Sekerka, R. F., 1979, "Lateral Solute Segregation during Unidirectional Solidification of a Binary Alloy with a Curved Solid-Liquid Interface," *J. Crystal Growth*, Vol. 46, pp. 479–482.

Derby, J. J. and Brown, R. A., 1988, "On the Quasi-Steady-State Assumption in Modeling Czochralski Crystal Growth," *J. Crystal Growth*, Vol. 87, pp. 251–160.

Favier, J. J., 1981, "Macrosegregation—I Unified Analysis during Non-Steady State Solidification," *Acta Metall.*, Vol. 29, pp. 197–204.

Carruthers, J. R., 1967, "Radial Solute Segregation in Czochralski Growth," *J. Electrochem. Soc.: Solid State Sci.*, Vol. 114, pp. 959–962.

Garandet, J. P., 1993, "Microsegregation in Crystal Growth From the Melt: An Analytical Approach," *J. Crystal Growth*, Vol. 131, pp. 431–438.

Garandet, J. P., Favier, J. J., and Camel, D., 1994, "Segregation Phenomena in Crystal Growth from the Melt," *Handbook of Crystal Growth*, Vol. 2, Chapter 12, pp. 659–705.

Hoshikawa, K., Kohda, H., and Hirata, H., 1984, "Homogeneous Dopant Distribution of Silicon Crystal Grown by Vertical Magnetic Field-Applied Czochralski Method," *Japan. J. Appl. Phys.*, Vol. 23, pp. L37–L39.

Hurle, D. T. J. and Cockayne, B., 1994, "Czochralski Growth," *Handbook of Crystal Growth*, Vol. 2, Chapter 3, pp. 99–211.

Hurle, D. T. J. and Series, R. W., 1985, "Effective Distribution Coefficient in Magnetic Czochralski Growth," *J. Crystal Growth*, Vol. 73, pp. 1–9.

Hurle, D. T. J., Jakeman, E., and Pike, E. R., 1968, "Striated Solute Distributions Produced by Temperature Oscillations during Crystal Growth from the Melt," *J. Crystal Growth*, Vol. 3/4, pp. 633–640.

Jordan, S., 1985a, "Estimated Thermal Diffusivity, Prandtl Number and Grashof Number of Molten GaAs, InP, and GaSn," *J. Crystal Growth*, Vol. 71, pp. 551–558.

Jordan, S., 1985b, "Some Thermal and Mechanical Properties of InP Essential to Crystal Growth Modeling," *J. Crystal Growth*, Vol. 71, pp. 559–565.

Kaddeche, S., Garandet, J. P., Barat, C., Ben Hadid, H., and Henry, D., 1996, "Interface Curvature and Convection Related Macrosegregation in the Vertical Bridgman Configuration," *J. Crystal Growth*, Vol. 168, pp. 144–152.

Kim, K. M., and Langlois, W. E., 1986, "Computer Simulation of Boron Transport in Magnetic Czochralski Growth of Silicon," *J. Electrochem. Soc. Solid-State Sci. Tech.*, Vol. 133, pp. 2586–2590.

Kim, K. M., and Langlois, W. E., 1989, "Dopant Segregation in CZ and MCZ silicon crystal growth: A Comparison between experiment and numerical simulation," *J. Electrochem. Soc. Solid-State Sci. Tech.*, Vol. 136, pp. 1137–1142.

Muller, G., 1988, *Crystal growth from the melt*, Springer-Verlag, Berlin.

Mukherjee D. K., Prasad, V., Dutta, P., and Yuan, T., 1996, "Liquid Crystal Visualization of the Effects of Crucible and Crystal Rotation on Cz Melt Flows," *J. Crystal Growth*, Vol. 169, pp. 136–149.

Nunes, E. M., Naraghi, M. H. N., Zhang, H., and Prasad, V., 1996, "Combined Radiation-Convection Modeling for Material Processes: Application to Crystal Growth," *Transport Phenomena in Materials and Manufacturing Processes*, ASME HTD-Vol. 323, pp. 27–37.

Ostrogorsky, A. G., and Muller, G., 1992, "A Model of Effective Segregation Coefficient, Accounting for Convection in the Solute Layer at the growth Interface," *J. Crystal Growth*, Vol. 121, pp. 587–598.

Prasad, V., Bliss, D. F., and Adamski, J. A., 1994, "Thermal Characterization of the High Pressure Crystal Growth System for In-Situ Synthesis and Growth of InP Crystal," *J. Crystal Growth*, Vol. 142, pp. 21–30.

Ristorcelli, J. R., and Lumley, J. L., 1992, "Instability, Transition and Turbulence in the Czochralski Crystal Melt," *J. Crystal Growth*, Vol. 116, pp. 447–460.

Wheeler, A. A., 1989, "Boundary Layer Models in Czochralski Crystal Growth," *J. Crystal Growth*, Vol. 97, pp. 64–75.

Wilson, A. O., 1978, "A New Look at the Burton, Prim, and Slichter Model of Segregation during Crystal Growth from the Melt," *J. Crystal Growth*, Vol. 44, pp. 371–376.

Wilson, A. O., 1980, "The Effect of Fluctuating Growth Rates on Segregation in Crystals Grown from the Melt I. No Back Melting," *J. Crystal Growth*, Vol. 48, pp. 435–450.

Wolff, F., and Viskanta, R., 1988, "Solidification of a Pure Metal at a Vertical Wall in the Presence of Liquid Superheat," *Int. J. Heat Mass Transfer*, Vol. 31, pp. 1735–1744.

Yen, C. T., and Tiller, W. A., 1992, "Incorporating Convection into One-dimensional Solute Redistribution during Crystal Growth from the Melt I. The Steady State Solution," *J. Crystal Growth*, Vol. 118, pp. 259–167.

Zhang, H., and Prasad, V., 1995, "A Multizone Adaptive Process Model for Crystal Growth at Low and High Pressures," *J. Crystal Growth*, Vol. 155, pp. 47–65.

Zhang, H., and Moallemi, M. K., 1995, "A Multizone Adaptive Grid Generation Technique for Simulation of Moving and Free Boundary Problems," *Numerical Heat Transfer, Part B*, Vol. 27, pp. 255–276.

Zhang, H., Moallemi, M. K., and Prasad, V., 1996a, "A Numerical Algorithm Using Multizone Grid Generation for Multiphase Transport Processes with Moving and free Boundaries," *Numerical Heat Transfer, Part B*, Vol. 29, pp. 399–421.

Zhang, H., Prasad, V., and Bliss, D. F., 1996b, "Transport Phenomena in High Pressure Crystal Growth Systems for III-V Compounds," *J. Crystal Growth*, Vol. 169, pp. 250–260.

Zhang, H., Zheng, L. L., Prasad, V., and Larson, D. F., Jr., 1997, "Local and Global Simulations of Bridgman and Czochralski Crystal Growth," ASME JOURNAL OF HEAT TRANSFER, in press.

Zhang, T., Wang, G.-X., Ladeinde, F., and Prasad, V., 1998, "Turbulent Transport of Oxygen in Czochralski Growth of Large Silicon Crystals," *The Proceedings of the 12th Int. Conf. Crystal Growth*, Israel, accepted for publication.

Zou, Y. F., 1997, "Coupled Convection, Segregation, and Thermal Stress Modeling of Low and High Pressure Czochralski Crystal Growth," Doctoral thesis, State University of New York, Stony Brook, NY.

Zou, Y. F., Zhang, H., and Prasad, V., 1996, "Dynamics of Melt-Crystal Interface and Thermal Stresses in Czochralski Crystal Growth Processes," *J. Crystal Growth*, Vol. 166, pp. 476–482.

Zou, Y. F., Wang, G. X., Zhang, H., Prasad, V., and Bliss, D. F., 1997, "Macrosegregation, Dynamics of Interface and Stresses in High Pressure LEC Growth Crystals," *J. Crystal Growth* Vol. 180, pp. 524–533.

Zuo, R., and Guo, Z., 1996, "Two-Dimensional Analysis on Solute Segregation in Crystal Growth From Melt: I. Solution at Crystal/Melt Interface," *J. Crystal Growth*, Vol. 158, pp. 377–384.

APPENDIX

Accuracy of Numerical Scheme

The MASTRAPP-based numerical scheme has been extensively validated against experimental results for solidification and numerical simulation of crystal growth reported in the literature. The predictions by MASTRAPP is within five percent of that reported by Anselmo et al. (1993) on Cz Si growth. The predictions also agree well with the experimental data of Wolff and Viskanta (1988) on solidification in a closed cavity (Zhang et al., 1996a). Indeed, this agreement is better than that obtained by other numerical predictions.

For each case presented in this paper, the simulation starts with a crystal height of about 9 mm with a uniform solute concentration everywhere in the melt. Between the two quasi-static states, the crystal grows by 0.2 mm which corresponds to 72.0 s for pulling rate of 10 mm/h. The time step used to solve the solute transport equation is then selected to be 2.88 s (i.e., 25 time steps between the two quasi-static states). The melt height is dropped as the crystal grows between the two time steps, while the flow and temperature fields remain unchanged. Upon every new quasi-static simulation, the flow field and interface shape are updated. All of the calculations reported here were performed using 82×42 nodes. For a case when crystal grows from 9.0 mm to 27.0 mm, 90 quasi-static steps are needed, which takes about 72 hours on IBM SP2 (parallel scaleble) machine using a single node.

It should be noted that a mesh of 82×42 used for the present calculations comes from a compromise between the computation load and numerical accuracy. Because of the complexity of the system we deal with, even a small increase in the number of grids leads to a dramatic increase in the computation time. Although we have employed an advanced adaptive grid generation technique which can adjust the grid distribution and cluster them in the region of high gradients, such as near the boundaries and the interface, grid-independent results can only be obtained for flow and temperature fields. It is still too coarse to give grid-independent results for solute field because of the thin solute boundary layer ahead of the melt/crystal interface $(Sc > 1)$. Note that somewhat smooth solute concentration gradients have been predicted in most of the cases considered here because of a relatively high diffusivity of Fe in InP melt, $D_m = 10^{-8}$ m^2/s which gives $Sc = 16.2$. Since we are primarily interested in the analysis and understanding of thermal-solutal transport mechanisms in the HPLEC system and not in the quantitative predictions at this stage, small errors of this kind can be tolerated. In particular, the trend established here should not change with the grid refinement.

Numerical Determination of Thermal Dispersion Coefficients Using a Periodic Porous Structure

F. Kuwahara[1] and A. Nakayama[1]

Nomenclature

A = surface area vector
A_{int} = total interface between the fluid and solid
Cp = Specific heat at constant pressure
D = size of square rod
H = size of structural unit
i, j = unit vectors in the x and y directions
u, v = microscopic velocity components in the x and y directions
T = microscopic temperature
p = microscopic pressure
k = thermal conductivity
ΔT = macroscopic temperature difference across a structural unit
Re = Reynolds number based on H and the macroscopically uniform velocity
Pe = Peclet number based on H and the macroscopically uniform velocity
V = control volume
x, y = Cartesian coordinates
X, Y = coordinates set along the macroscopic flow direction and its normal
θ = macroscopic flow angle
ϵ = porosity
ν = kinematic viscosity
ρ = density

Subscripts and Superscripts

dis = dispersion
f = fluid
s = solid
tor = tortuosity

---

[1] Department of Mechanical Engineering, Shizuoka University, 3-5-1 Johoku, Hamamatsu 432, Japan.

Special Symbols

$\langle\ \rangle$ = volume average
$\langle\ \rangle^f$ = intrinsic volume average

Introduction

Detailed flow and temperature fields inside a microscopic structure may be investigated numerically using a periodic structure rather than treating complex porous media in reality. Recently, Kuwahara et al. (1996) conducted a numerical experiment using a periodic structure, to determine the transverse thermal dispersion coefficient, purely from a theoretical basis. A macroscopically uniform flow is assumed to pass through a lattice of square rods placed regularly in an infinite space, where a macroscopically linear temperature gradient is imposed perpendicularly to the flow direction, following Arquis et al. (1991, 1993). Full Navier-Stokes and energy equations were solved numerically to describe the microscopic velocity and temperature fields at a pore scale. Then, these microscopic results were integrated over a unit structure to evaluate the transverse thermal dispersion coefficient. Two distinct expressions for the transverse thermal coefficient, as a function of the porosity and Peclet number, have been established for the low and high Peclet number ranges. It has been found that the resulting expressions agree fairly well with the experimental data. However, Kuwahara et al. (1996) had to give up carrying out exhaustive numerical experiments for determining the longitudinal (streamwise) thermal dispersion coefficients.

It is interesting to note that it took a few years for even Yagi et al. (1960), the initiative researchers who were the first to measure the effective longitudinal thermal conductivities of packed bed, to convince themselves that there were nothing wrong with their experimental data for the longitudinal dispersion coefficient (Wakao and Kaguei, 1982). Naturally those who are not very much familiar with transport in porous media are surprised to find the experimental data, which consistently indicate that the longitudinal dispersion coefficient is much larger than the transverse one. In this study we shall carry out a numerical experiment to investigate the longitudinal dispersion coefficient, following a numerical approach similar to the one suggested by Kuwahara et al. (1996) for the transverse dispersion coefficient. This time a macroscopically linear temperature gradient shall be imposed in parallel to the macroscopic flow direction to determine the longitudinal thermal dispersion coefficient. Both the microscopic and macroscopic results for the longitudinal dispersion coefficient are compared against those for the transverse one, so as to elucidate the difference between the transverse and longitudinal dispersion mechanisms.
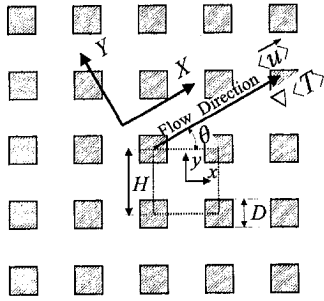
Fig. 1 Physical model and its coordinate system

Numerical Model and Boundary Conditions

We shall consider a macroscopically uniform flow with an angle θ meandering through an infinite number of square rods placed in a regular fashion, as illustrated in Fig. 1. Thus, the macroscopic velocity field follows

$$\langle \mathbf{u} \rangle = |\langle \mathbf{u} \rangle|(\cos \theta \mathbf{i} + \sin \theta \mathbf{j}) \tag{1}$$

where $\langle \ \rangle$ denotes volume average, namely,

$$\langle \phi \rangle = \frac{1}{V} \int_{V_f} \phi dV \tag{2}$$

where V_f is the volume occupied by the fluid such that $\epsilon = V_f/V$ is the porosity. The control volume V is much smaller than a macroscopic characteristic length and can be taken as H^2 for this periodic structure.

Two distinct macroscopic temperature fields are considered to obtain the transverse and longitudinal dispersions. We impose a macroscopically linear temperature gradient perpendicularly to the macroscopic flow direction, namely,

$$\nabla \langle T \rangle = \frac{\Delta T}{H}(-\sin \theta \mathbf{i} + \cos \theta \mathbf{j}) \quad \text{:transverse dispersion} \tag{3}$$

to determine the transverse thermal dispersion, and a macroscopically linear temperature gradient in parallel to the macroscopic flow direction, namely,

$$\nabla \langle T \rangle = \frac{\Delta T}{H}(\cos \theta \mathbf{i} + \sin \theta \mathbf{j}) \quad \text{:longitudinal dispersion} \tag{4}$$

to determine the longitudinal thermal dispersion.

Due to the periodicity of the model, only one structural unit as indicated by dashed lines may be taken as a calculation domain for the steady case. The governing equations for the whole domain (i.e., fluid and solid phases) are given as follows:

$$\nabla \cdot \mathbf{u} = 0 \tag{5}$$

$$(\nabla \cdot \mathbf{u})\mathbf{u} = -\frac{1}{\rho_f} \nabla p + \nu \nabla^2 \mathbf{u} \tag{6}$$

$$\rho_f C_{p_f} \nabla \cdot (\mathbf{u}T) = k_f \nabla^2 T \quad \text{:fluid} \tag{7}$$

$$k_s \nabla^2 T = 0 \quad \text{:solid} \tag{8}$$

where the subscripts f and s denote fluid and solid phases, respectively. The corresponding boundary, compatibility, and periodic constraints are given as follows:
On the solid walls:

$$\mathbf{u} = 0 \tag{9}$$

$$T|_s = T|_f \tag{10a}$$

$$k_s \frac{\partial T}{\partial n}\bigg|_s = k_f \frac{\partial T}{\partial n}\bigg|_f. \tag{10b}$$

On the periodic boundaries:

$$\mathbf{u}|_{x=-H/2} = \mathbf{u}|_{x=H/2} \tag{11a}$$

$$\mathbf{u}|_{y=-H/2} = \mathbf{u}|_{y=H/2} \tag{11b}$$

$$\int_{-H/2}^{H/2} udy\bigg|_{x=-H/2} = \int_{-H/2}^{H/2} udy\bigg|_{x=H/2} = H|\langle \mathbf{u} \rangle| \cos \theta \tag{12a}$$

$$\int_{-H/2}^{H/2} vdx\bigg|_{y=-H/2} = \int_{-H/2}^{-H/2} vdx\bigg|_{y=H/2} = H|\langle \mathbf{u} \rangle| \sin \theta. \tag{12b}$$

For the temperature boundary conditions we impose

$$T|_{x=-H/2} = T|_{x=H/2} + \Delta T \sin \theta \tag{13a}$$

$$T|_{y=-H/2} = T|_{y=H/2} - \Delta T \cos \theta \tag{13b}$$

as we determine the transverse thermal dispersion, and

$$T|_{x=-H/2} = T|_{x=H/2} - \Delta T \cos \theta \tag{13c}$$

$$T|_{y=-H/2} = T|_{y=H/2} - \Delta T \sin \theta \tag{13d}$$

as we determine the longitudinal thermal dispersion.

For numerical computations, SIMPLE algorithm for the pressure-velocity coupling, as proposed by Patankar and Spalding (1972), is adopted to correct the pressure and velocity fields. Further details on this numerical procedure can be found in Patankar (1980) and Nakayama (1995).

The Reynolds number, based on the Darcian velocity $|\langle \mathbf{u} \rangle|$ and length of structural unit H as Re $= |\langle \mathbf{u} \rangle|H/\nu$, was varied from 10^{-2} to 10^3; the ratio of the solid phase thermal conductivity to the fluid phase k_s/k_f from 2 to 100; and the porosity ϵ, from 0.1 to 0.96, whereas the Prandtl number was set to 0.71 and 10. The macroscopic flow angle θ was varied every 5 deg to investigate geometric effects on the dispersion coefficients. All computations were performed using the computer system CONVEX 220 at Shizuoka University Computer Center.

Results and Discussion

Following Cheng (1978), Vafai and Tien (1981), and Nakayama (1995), the microscopic energy Eqs. (7) and (8) are integrated over an elementary control volume. These two macroscopic energy equations may be combined to form a macroscopic energy equation for the saturated porous medium, introducing the thermal dispersion tensor under the thermal equilibrium condition.

When the macroscopically linear temperature gradient is imposed along the Y direction normal to the X-direction of the macroscopic flow, the YY-components of the thermal dispersion tensor $\bar{\bar{k}}_{dis}$ can readily be determined from

$$(k_{dis})_{XX} = \frac{-\dfrac{\rho_f C_{p_f}}{H^2}}{(\Delta T/H)} \int_{-H/2}^{H/2} \int_{-H/2}^{H/2} (T - \langle T \rangle)(\mathbf{u} - \langle \mathbf{u} \rangle^f)dxdy$$
$$\cdot (-\sin \theta \mathbf{i} + \cos \theta \mathbf{j}) \tag{14}$$

where $\langle \mathbf{u} \rangle^f$ is the intrinsic average velocity vector. Similarly, when the macroscopically linear temperature gradient is imposed along the X-direction of the macroscopic flow, the XX-component of $\bar{\bar{k}}_{dis}$ can readily be determined from

$$(k_{dis})_{XX} = \frac{-\dfrac{\rho_f C_{p_f}}{H^2}}{(\Delta T/H)} \int_{-H/2}^{H/2} \int_{-H/2}^{H/2} (T - \langle T \rangle)(\mathbf{u} - \langle \mathbf{u} \rangle^f)dxdy$$
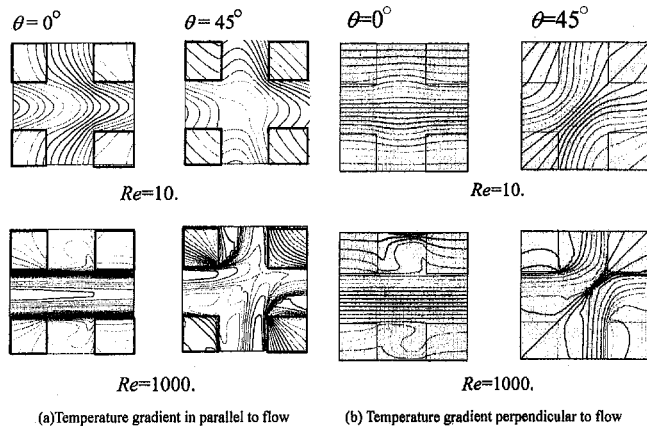$$\cdot (\cos \theta \mathbf{i} + \sin \theta \mathbf{j}). \tag{15}$$

Fig. 2 Microscopic temperature fields

Fig. 3 Apparent thermal conductivity due to longitudinal dispersion

Since the results for the case of the temperature gradient imposed perpendicularly to the flow direction can be found in the previous paper (Kuwahara et al. 1996), we shall focus on the results for the case when the temperature gradient is imposed in parallel to the macroscopic flow, so as to elucidate the difference in the two cases.

Typical microscopic temperature fields obtained at $\theta = 0$ deg and 45 deg for two different Reynolds numbers, namely Re = 10 and 10^3, are presented in Figs. 2. The temperature fields (Fig. 2(a)) for the case when the macroscopic temperature gradient aligns with the macroscopic flow, are compared against those for the previous case of the perpendicularly imposed temperature gradient (Fig. 2(b)). It can be seen that the isotherms for the case of the macroscopic temperature gradient aligning with the macroscopic flow are distorted considerably along the macroscopic flow direction, even when the Reynolds number is as low as 10 (See the upper figure in Fig. 2(a)). On the other hand, the distortions in the isotherms for the case of the macroscopic temperature gradient perpendicular to the macroscopic flow are not significant even for the case of high Reynolds number (see the lower figure in Fig. 2(b)) in which flow reversals take place.

This marked difference in the distortions, observed for the isotherms in the two distinct cases, is closely associated with the fact that the macroscopic net flow does not exist in the direction perpendicular to the macroscopic flow. Along this direction, only weak mixing actions due to microscopic wake and flow reversals are solely responsible for the transverse mechanical dispersion. (The microscopic velocity fields may be found in Kuwahara et al. (1996).) Naturally, we expect that the longitudinal effective thermal conductivity (dispersion coefficient) is much more significant than the transverse one. This unique feature associated with convective heat transfer in porous media often puzzles those who are accustomed to applying the boundary layer theory to clear fluid flow problems. Thus, one should bear in mind that the boundary layer approximations, based on the assumption of negligible longitudinal diffusion, may fail even for the case of macroscopically unidirectional flow through a porous medium.

The microscopic temperature results obtained for various flow angles are processed using (15), and the resulting effective thermal conductivity $(k_{\mathrm{dis}})_{XX}$ due to the longitudinal thermal dispersion is plotted for the case of $\epsilon = 0.64$ in Fig. 3. The figure suggests that the lower and higher Peclet number data follow two distinct limiting lines. The lower Peclet number data vary in proportion to Pe^2, as suggested by Taylor (1953) in the classical study of solute in a fluid flowing in a tube, whereas the high Peclet number data vary in proportion to Pe. (Note that the previous numerical study by Kuwahara et al. (1996) suggests that the thermal conductivity $(k_{\mathrm{dis}})_{YY}$ due to the transverse thermal dispersion varies in proportion to $Pe^{1.7}$ and Pe in the low and high Peclet number ranges, respectively.)
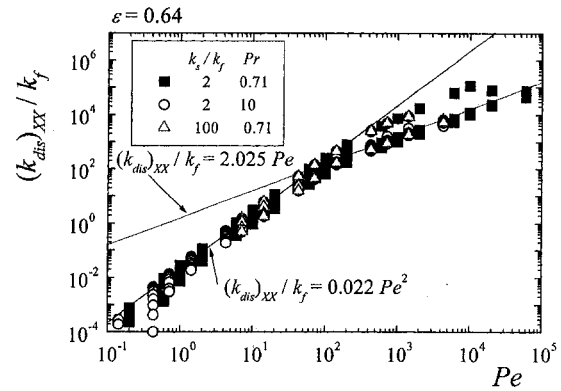
Exhaustive computations were conducted to extract functional relationships for the longitudinal thermal dispersion conductivities at low and high Peclet number ranges. The thermal dispersion conductivities obtained for different ϵ were plotted against ϵ to investigate the porosity dependency, as illustrated in the previous study on the transverse dispersion. The resulting expressions for the longitudinal thermal dispersion coefficients in the low and high Peclet number ranges are given below along with those for the transverse ones reported earlier:

For the longitudinal dispersion:

$$\frac{(k_{\mathrm{dis}})_{XX}}{k_f} = 0.022 \frac{\mathrm{Pe}_D^2}{(1 - \epsilon)} \quad \text{for} \quad (\mathrm{Pe}_D < 10) \quad (16a)$$

$$\frac{(k_{\mathrm{dis}})_{XX}}{k_f} = 2.7 \frac{\mathrm{Pe}_D}{\epsilon^{1/2}} \quad \text{for} \quad (\mathrm{Pe}_D > 10). \quad (16b)$$

For the transverse dispersion (Kuwahara et al., 1996):

$$\frac{(k_{\mathrm{dis}})_{YY}}{k_f} = 0.022 \frac{\mathrm{Pe}_D^{1.7}}{(1 - \epsilon)^{1/4}} \quad \text{for} \quad (\mathrm{Pe}_D < 10) \quad (17a)$$

$$\frac{(k_{\mathrm{dis}})_{YY}}{k_f} = 0.052(1 - \epsilon)^{1/2} \mathrm{Pe}_D \quad \text{for} \quad (\mathrm{Pe}_D > 10) \quad (17b)$$

where the relationship $\mathrm{Pe}_D = \mathrm{Pe}(1 - \epsilon)^{1/2}$ is used.

In Fig. 4, the foregoing correlations (16b) and (17b) for the high Peclet number range are compared for the case of $\epsilon = 0.5$, against the analysis of Koch and Brady (1985) based on the Stokes flow as well as the experimental data obtained by Fried and Combarnous (1971) for the longitudinal and transverse dispersion coefficients in packed bed. The figure shows that the present correlation (16b) obtained from the numerical experiment agrees very well with the experimental data for the axial thermal dispersion coefficient, whereas the correlation (17b) for the transverse thermal dispersion stays somewhat under the
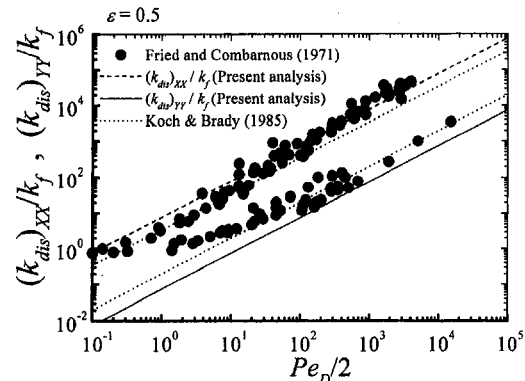

Fig. 4 Comparison of the prediction and experiment

corresponding experimental data. Both the predicted correlations and experimental data clearly show that the level of the longitudinal dispersion is much higher than the transverse dispersion. Overall agreement between the present correlations and the experimental data can be seen to be good, in light of the simplicity of the present periodic model.

Concluding Remarks

A successful attempt was made to numerically investigate the longitudinal thermal dispersion coefficient, considering a macroscopically uniform flow through a periodic model of square rods. The present numerical experiment confirms that the longitudinal dispersion is substantially higher than the transverse dispersion. The predicted apparent conductivities agree well with the experimental data.

References

Arquis, E., Caltagirone, J. P., and Le Breton, P., 1991, "Détermination des propriétés de dispersion d'un milieu périodique à partir de l'analyse locale des transferts," *C.R. Acad. Sci. Paris, II,* Vol. 3, No. 13, pp. 1087–1092.

Arquis, E., Caltagirone, J. P., and Delmas, A., 1993, "Derivation in thermal conductivity of porous media due to high interstitial flow velocity," *Proc. 22nd Int. Thermal Conductivity Conf.,* Temp, AZ, Nov.

Cheng, P., 1978, "Heat transfer in geothermal systems," *Advances in Heat Transfer,* Vol. 14, pp. 1–105.

Fried, J. J., and Combarnous, M. A., 1971, "Dispersion in porous media," *Advances in Hydro. Science,* Vol. 7, pp. 169–282.

Kuwahara, F., Nakayama, A., and Koyama, H., 1996, "A Numerical Study of Thermal Dispersion in Porous Media," ASME JOURNAL OF HEAT TRANSFER, Vol. 118, pp. 756–761.

Koch, D. L., and Brady, J. F., 1985, "Dispersion in fixed beds," *J. Fluid Mech.,* Vol. 154, pp. 399–427.

Nakayama, A., 1995, *PC-aided numerical heat transfer and convective flow,* CRC Press, Boca Raton, FL.

Patankar, S. V., 1980, *Numerical heat transfer and fluid flow,* Hemisphere, Washington, DC.

Patankar, S. V., and Spalding, D. B., 1972, "A calculation procedure for heat, mass and momentum transfer in three-dimensional parabolic flows," *Int. J. Heat Mass Transfer,* Vol. 15, pp. 1787–1806.

Taylor, G. I., 1953, "Dispersion of solute matter in solvent flowing slowly through a tube," *Proc. Roy. Soc. London,* Vol. A219, pp. 186–203.

Vafai, K., and Tien, C. L., 1981, "Boundary and inertia effects on flow and heat transfer in porous media," *Int. J. Heat Mass Transfer* Vol. 24, pp. 195–203.

Wakao, N., and Kaguei, S., 1996, *Heat and mass transfer in packed beds,* Gordon and Breach, New York, p. 203.

Yagi, S., Kunii, D., and Wakao, N., 1960, "Studies on axial effective thermal conductivities in packed beds," *AIChE J.,* Vol. 6, pp. 543–546.

Evaluation of Thermal Conductivities of Disordered Composite Media Using a Fractal Model

R. Pitchumani[1]

Nomenclature

d = fractal dimension
k = thermal conductivity ($W/m \cdot K$)
v = fiber volume fraction in the composite

[1] Department of Mechanical Engineering, University of Connecticut, Storrs, CT 06269. Assoc. Mem. ASME.

Subscripts

e = effective thermal conductivity
f = fiber
m = matrix
x, y = coordinate directions (Fig. 1(a))

Introduction

The effective properties of composite materials play an important role in the design of structures for several applications. In particular, since many of the composite fabrication techniques involve thermal processing (for example, curing of thermoset composites, fusion bonding of thermoplastic composites, etc.), the effective thermal properties of composites constitute an important process design parameter. Determination of the thermal properties of composites is therefore vital for a successful design and manufacture of composite materials. Toward this end, this paper focuses on the evaluation of the transverse thermal conductivities of composite materials.

Physically, the transverse conductivity of a composite is a function of (i) the reinforcement and matrix conductivities, (ii) the reinforcement volume fraction in the composite, v, and (iii) the relative arrangement of the reinforcements in the composite. A critical—and challenging—step in the estimation of the composite properties is the description of the disordered reinforcement arrangements in practical microstructures. The approaches in the literature have resorted to one of two paths—either idealizing the arrangements as being ordered arrays and describing the relative reinforcement arrangements by means of an appropriate interreinforcement spacings in a repeating unit cell (see for example, Behrens, 1968; Han and Cosner, 1981; Murlidhar, 1990), or simulating disordered arrangements by statistical means and utilizing multipoint correlation functions (Smith and Torquato, 1989; Kim and Torquato, 1990). In the composites found in practice, the reinforcements hardly assume an ordered arrangement, and the former approach yields conductivity estimates that could differ considerably from the actual values. The latter approach, on the other hand, yields upper and lower *bounds* on the composite properties (Milton, 1982; Hashin, 1983; Smith and Torquato, 1989; Kim and Torquato, 1990).

A viable alternative approach was proposed by the author (Pitchumani and Yao, 1991) wherein principles of fractal geometry (Feder, 1988) were invoked to characterize the relative reinforcement arrangements in unidirectional fiber-reinforced composites, by means of two *fractal dimensions*. A generalized unit cell was constructed in terms of the fractal dimensions and the fiber volume fraction, for analysis of heat conduction. An analytical thermal conductivity model was developed in terms of the fractal dimensions and the fiber volume fraction. The model predictions were shown to compare well with the published data in the literature, for the case of ordered fiber arrangements, over a wide range of fiber-matrix conductivity ratios and fiber volume fractions.

This paper explores the application of the technique to realistic disordered composite microstructures comprising cross sections of unidirectional fiber reinforcements, including fiber clusters. Several disordered fiber arrangements were generated through computer simulations, and their conductivities evaluated using three methods: (I) Fractal characterization combined with a *simplified* analysis of the resulting generalized unit cell, as presented in Pitchumani and Yao (1991), (II) Fractal characterization combined with a *numerical* analysis of the resulting generalized unit cell, and (III) Complete numerical solution of heat transfer through the disordered arrangement, which yields the exact conductivity of the microstructures. Comparisons of the results from Methods (I) and (II) with the exact conductivities from Method (III) are presented to illustrate the power of the fractal technique in characterizing realistic disordered microstructures, even in the presence of fiber clusters.

corresponding experimental data. Both the predicted correlations and experimental data clearly show that the level of the longitudinal dispersion is much higher than the transverse dispersion. Overall agreement between the present correlations and the experimental data can be seen to be good, in light of the simplicity of the present periodic model.

Concluding Remarks

A successful attempt was made to numerically investigate the longitudinal thermal dispersion coefficient, considering a macroscopically uniform flow through a periodic model of square rods. The present numerical experiment confirms that the longitudinal dispersion is substantially higher than the transverse dispersion. The predicted apparent conductivities agree well with the experimental data.

References

Arquis, E., Caltagirone, J. P., and Le Breton, P., 1991, "Détermination des propriétés de dispersion d'un milieu périodique à partir de l'analyse locale des transferts," *C.R. Acad. Sci. Paris, II,* Vol. 3, No. 13, pp. 1087–1092.

Arquis, E., Caltagirone, J. P., and Delmas, A., 1993, "Derivation in thermal conductivity of porous media due to high interstitial flow velocity," *Proc. 22nd Int. Thermal Conductivity Conf.,* Temp, AZ, Nov.

Cheng, P., 1978, "Heat transfer in geothermal systems," *Advances in Heat Transfer,* Vol. 14, pp. 1–105.

Fried, J. J., and Combarnous, M. A., 1971, "Dispersion in porous media," *Advances in Hydro. Science,* Vol. 7, pp. 169–282.

Kuwahara, F., Nakayama, A., and Koyama, H., 1996, "A Numerical Study of Thermal Dispersion in Porous Media," ASME JOURNAL OF HEAT TRANSFER, Vol. 118, pp. 756–761.

Koch, D. L., and Brady, J. F., 1985, "Dispersion in fixed beds," *J. Fluid Mech.,* Vol. 154, pp. 399–427.

Nakayama, A., 1995, *PC-aided numerical heat transfer and convective flow,* CRC Press, Boca Raton, FL.

Patankar, S. V., 1980, *Numerical heat transfer and fluid flow,* Hemisphere, Washington, DC.

Patankar, S. V., and Spalding, D. B., 1972, "A calculation procedure for heat, mass and momentum transfer in three-dimensional parabolic flows," *Int. J. Heat Mass Transfer,* Vol. 15, pp. 1787–1806.

Taylor, G. I., 1953, "Dispersion of solute matter in solvent flowing slowly through a tube," *Proc. Roy. Soc. London,* Vol. A219, pp. 186–203.

Vafai, K., and Tien, C. L., 1981, "Boundary and inertia effects on flow and heat transfer in porous media," *Int. J. Heat Mass Transfer* Vol. 24, pp. 195–203.

Wakao, N., and Kaguei, S., 1996, *Heat and mass transfer in packed beds,* Gordon and Breach, New York, p. 203.

Yagi, S., Kunii, D., and Wakao, N., 1960, "Studies on axial effective thermal conductivities in packed beds," *AIChE J.,* Vol. 6, pp. 543–546.

Evaluation of Thermal Conductivities of Disordered Composite Media Using a Fractal Model

R. Pitchumani[1]

Nomenclature

d = fractal dimension
k = thermal conductivity (W/m·K)
v = fiber volume fraction in the composite

[1] Department of Mechanical Engineering, University of Connecticut, Storrs, CT 06269. Assoc. Mem. ASME.

Introduction

The effective properties of composite materials play an important role in the design of structures for several applications. In particular, since many of the composite fabrication techniques involve thermal processing (for example, curing of thermoset composites, fusion bonding of thermoplastic composites, etc.), the effective thermal properties of composites constitute an important process design parameter. Determination of the thermal properties of composites is therefore vital for a successful design and manufacture of composite materials. Toward this end, this paper focuses on the evaluation of the transverse thermal conductivities of composite materials.

Physically, the transverse conductivity of a composite is a function of (i) the reinforcement and matrix conductivities, (ii) the reinforcement volume fraction in the composite, v, and (iii) the relative arrangement of the reinforcements in the composite. A critical—and challenging—step in the estimation of the composite properties is the description of the disordered reinforcement arrangements in practical microstructures. The approaches in the literature have resorted to one of two paths—either idealizing the arrangements as being ordered arrays and describing the relative reinforcement arrangements by means of an appropriate interreinforcement spacings in a repeating unit cell (see for example, Behrens, 1968; Han and Cosner, 1981; Murlidhar, 1990), or simulating disordered arrangements by statistical means and utilizing multipoint correlation functions (Smith and Torquato, 1989; Kim and Torquato, 1990). In the composites found in practice, the reinforcements hardly assume an ordered arrangement, and the former approach yields conductivity estimates that could differ considerably from the actual values. The latter approach, on the other hand, yields upper and lower *bounds* on the composite properties (Milton, 1982; Hashin, 1983; Smith and Torquato, 1989; Kim and Torquato, 1990).

A viable alternative approach was proposed by the author (Pitchumani and Yao, 1991) wherein principles of fractal geometry (Feder, 1988) were invoked to characterize the relative reinforcement arrangements in unidirectional fiber-reinforced composites, by means of two *fractal dimensions.* A generalized unit cell was constructed in terms of the fractal dimensions and the fiber volume fraction, for analysis of heat conduction. An analytical thermal conductivity model was developed in terms of the fractal dimensions and the fiber volume fraction. The model predictions were shown to compare well with the published data in the literature, for the case of ordered fiber arrangements, over a wide range of fiber-matrix conductivity ratios and fiber volume fractions.

This paper explores the application of the technique to realistic disordered composite microstructures comprising cross sections of unidirectional fiber reinforcements, including fiber clusters. Several disordered fiber arrangements were generated through computer simulations, and their conductivities evaluated using three methods: (I) Fractal characterization combined with a *simplified* analysis of the resulting generalized unit cell, as presented in Pitchumani and Yao (1991), (II) Fractal characterization combined with a *numerical* analysis of the resulting generalized unit cell, and (III) Complete numerical solution of heat transfer through the disordered arrangement, which yields the exact conductivity of the microstructures. Comparisons of the results from Methods (I) and (II) with the exact conductivities from Method (III) are presented to illustrate the power of the fractal technique in characterizing realistic disordered microstructures, even in the presence of fiber clusters.
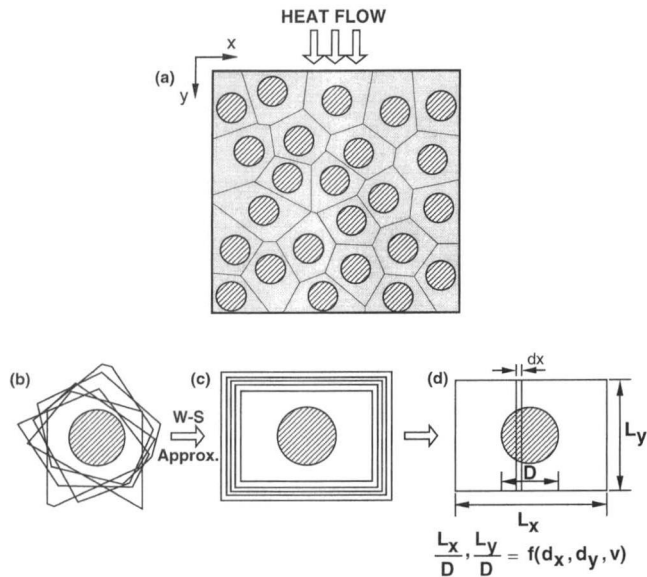
Fig. 1 Schematic illustration of a disordered microstructure, and the construction of the equivalent rectangular unit cell

The fractal description of composite microstructures, discussed in detail in Pitchumani and Yao (1991), is briefly reviewed first, followed by a discussion of the three methods of evaluating the composite conductivities, and the presentation of the results of the study.

Fractal Description of Composite Microstructures

A composite cross section such as that illustrated in Fig. 1(*a*) exhibits statistical self-similarity over a small range of length scales spanning a few fiber diameters around a fiber (Pitchumani and Yao, 1991). Since heat conduction is a directional phenomenon, the scaling phenomenon may be described in terms of two fractal dimensions, d_x and d_y, based on linear measures along two orthogonal (*x-y*) axes defining the plane of the microstructure. The fractal dimensions d_x and d_y provide a measure of the extent of contiguity of the fibers in the *x* and *y*-directions, respectively. A closely packed array corresponds to a high degree of contiguity of fibers, and therefore, has a fractal dimension value close to unity. Conversely, a sparse arrangement results in smaller values of the fractal dimensions (close to 0). The procedure for the evaluation of d_x and d_y may be found in Pitchumani and Yao (1991).

For a given disordered fiber arrangement in a microstructure, generalized polygonal unit cells—called the Wigner-Seitz cells (Kittel, 1986)—may be identified surrounding each fiber, as shown in Fig. 1(*a*). The Wigner-Seitz cells of various shapes and sizes may be transformed by virtue of a Wigner-Seitz (W-S) approximation (Kittel, 1986) to equivalent rectangular cells that preserve the fiber volume fraction of the original cell. The schematics Fig. 1(*b*) to (*c*) represent this transformation, which results in an array of rectangular cells surrounding a fiber. Note that since the size of a rectangular cell represents the interfiber spacings along two orthogonal directions on the microstructure, the various rectangular cells therefore signify the different scales of interfiber spacings within the microstructure. In fact, it is these various interfiber spacings along two orthogonal directions in the composite that are characterized by the fractal dimensions, d_x and d_y. This suggests that an equivalent rectangular unit cell incorporating the scaling information (Fig. 1(*d*)), can be derived in terms of the two fractal dimensions, d_x and d_y, and the fiber volume fraction, *v*, as detailed in Pitchumani and Yao (1991).

Thermal Conductivity Evaluation

Three heat conduction models are examined in this study to relate the transverse composite conductivities to the geometric parameters—d_x, d_y, and *v*—and the fiber-matrix conductivity ratio, k_f/k_m. Two of the methods are based on analyses of the equivalent rectangular unit cell (Fig. 1(*d*)). A third method utilizes numerical solution of the governing heat conduction equation in the disordered microstructure in its entirety to obtain the exact conductivity of the composite.

Method I: Simplified Analysis of the Generalized Unit Cell. The first method is based on a simplified analysis of heat conduction through the rectangular unit cell shown in Fig. 1(*d*), which is subject to a constant temperature difference across its height, and insulated conditions on its sides. The principal assumption in this method is that internal heat flow within the unit cell is strictly along the global heat flow direction. The effective thermal resistance, and in turn the transverse thermal conductivity, of the unit cell are then evaluated as a parallel combination of the resistances of infinitesimally small strips (such as the one shown in Fig. 1(*d*)) spanning the entire cell. Note that the thermal resistance of a strip that covers the fiber and the matrix regions is obtained as the sum (i.e., a series combination) of the restances of the fiber and the matrix segments within the strip. Omitting the intermediate mathematical steps, the final expression for the transverse conductivity ratio k_{ey}/k_m in the *y*-direction may be written as

$$\frac{k_{ey}}{k_m} = \left[1 - \left(1 + \frac{\pi}{2c} \right) \bar{v} \right]$$

$$+ \frac{2\bar{v}}{c\sqrt{1-c^2}} \tan^{-1} \sqrt{\frac{1+c}{1-c}} \quad c \geq -1$$

$$= \left[1 - \left(1 + \frac{\pi}{2c} \right) \bar{v} \right]$$

$$+ \frac{\bar{v}}{c\sqrt{c^2-1}} \ln \left(-c + \sqrt{c^2-1} \right) \quad c \leq -1$$

where

$$c = \left(\frac{k_f/k_m - 1}{k_f/k_m} \right) \left(\frac{4v}{\pi} \right)^{(1-\delta)/2}, \bar{v} = \left(\frac{4v}{\pi} \right)^{(1+\delta)/2},$$

$$\text{and } \delta = \frac{d_y - d_x}{d_y - 2d_yd_x + d_x}. \tag{1}$$

The transverse conductivity in the *x*-direction (k_{ex}/k_m) may be obtained by interchanging d_x and d_y in the above equations.

Method II: Numerical Analysis of the Generalized Unit Cell. The simplifying assumption underlying Method I solution may be relaxed and the equations governing steady-state heat conduction through the two-phase (fiber-matrix) unit cell (Fig. 1(*d*)) may be solved numerically to obtain more accurate estimates of the composite thermal conductivities. The fiber-matrix interface is subject to continuity of temperature and heat flux. The governing equations were solved using an alternating direction implicit (ADI) finite difference scheme, with control volume formulation for heterogeneous media (Patankar, 1980). Based on considerations of convergence of the numerical results and a fine resolution of the fibrous regions in the composite, a 41×41 grid with a time step of 0.005 sec. was found to be adequate for all the computations.

Method III: Numerical Analysis of Conduction in Disordered Microstructures. Experimental validation of the results of Methods I and II above requires knowledge of the

actual composite microstructures used in the experiments, for determination of the fractal dimensions. Although conductivity data are reported in the literature, the microstructural details are often not readily available. In lieu of the experimental data, therefore, the thermal conductivities of the simulated disordered microstructures were evaluated by means of a numerical modeling of heat conduction through the composite medium. The numerical solution scheme is similar to that outlined in Method II above, with the exception that the domain under consideration is the entire composite cross section instead of the rectangular unit cell. A 111×111 square grid and a time step of 0.0005 sec. was employed in the computational procedure. The thermal conductivities so obtained are referred to as the exact conductivities in this paper, and serves as a benchmark for comparison with the results of Methods I and II above.

Results and Discussion

The fractal technique was employed to describe several disordered fiber arrangements constructed by means of computer simulations. The simulation procedure consisted of obtaining the x and y-coordinates of the fiber locations within a macrocell of a fixed size, using a pseudo-random number generator. In all the simulations, the number of fibers was kept constant at 50, while the fiber diameter was varied according to the specified volume fraction. Further, the fiber cross sections were assumed to be rigid, impenetrable disks. Therefore, random fiber placement trials during the simulation that resulted in overlapping of the cross sections were discarded and a new placement was attempted until a nonoverlapping position was found.

For each of the microstructures generated, the two fractal dimensions, d_y and d_x, were computed, and the thermal conductivities were obtained by the three methods described in the previous section. The computations, carried out on a Silicon Graphics RISC 4000 workstation, required about $1-2$ CPU minutes, which included the time for the microstructural generation, calculation of fractal dimensions, and the evaluation of the conductivities. By way of comparison, it may be noted that the simulations for obtaining the improved upper and lower bounds typically call for several CPU hours of computational time (Smith and Torquato, 1989; Kim and Torquato, 1990).

The present study was conducted with a focus on demonstrating the effectiveness of the fractal technique in describing the complex geometry of realistic fiber arrangements in composite media. To this end, several microstructural variations were analyzed, for fiber volume fractions in the range 30–50 percent, and a fixed fiber-matrix conductivity ratio, k_f/k_m, of 10. The applicability of the model for other conductivity ratios was addressed in an earlier publication (Pitchumani and Yao, 1991), and are not repeated here. The volume fractions of 30–50 percent were chosen for this study based on the fact that they constitute an appropriate range wherein discernable differences in microstructural arrangements are possible for a given overall fiber volume fraction. At higher volume fractions, the fiber arrangements tend to assume ordered configurations, as considered in Pitchumani and Yao (1991), whereas the dilute volume fraction range of 0–30 percent is less frequently encountered in practical applications of continuous fibrous composites. However, the validity of the model in the dilute volume fraction range of 0–30 percent may be readily verified by considering the limiting case of $v = 0$, for which the model (Eq. (1)) correctly yields the effective thermal conductivity to be that of the matrix conductivity.

The simulation results are presented in Fig. 2 for five of the microstructures studied. Also tabulated are the measured fractal dimensions, and the computed transverse conductivity ratios along the x and y-coordinate directions. It may be seen that in general, the fractal dimensions increase with increasing fiber volume fraction, reflecting the increased degree of fiber contiguity. Since the fiber is more conducting than the matrix, a larger
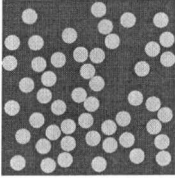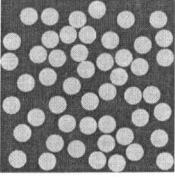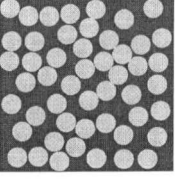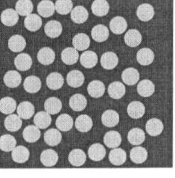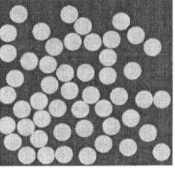
Microstructure		Thermal Conductivities	
(a)	$d_x = 0.506$ $d_y = 0.571$ $v = 30\%$		k_{ex}/k_m k_{ey}/k_m
		Method I	1.50 1.56
		Method II	1.62 1.69
		Method III	1.65 1.69
(b)	$d_x = 0.629$ $d_y = 0.627$ $v = 40\%$		k_{ex}/k_m k_{ey}/k_m
		Method I	1.83 1.83
		Method II	1.99 1.98
		Method III	2.00 2.00
(c)	$d_x = 0.727$ $d_y = 0.690$ $v = 50\%$		k_{ex}/k_m k_{ey}/k_m
		Method I	2.29 2.20
		Method II	2.48 2.36
		Method III	2.54 2.42
(d)	$d_x = 0.673$ $d_y = 0.617$ $v = 40\%$		k_{ex}/k_m k_{ey}/k_m
		Method I	1.88 1.79
		Method II	2.04 1.94
		Method III	2.03 2.00
(e)	$d_x = 0.692$ $d_y = 0.673$ $v = 40\%$		k_{ex}/k_m k_{ey}/k_m
		Method I	1.85 1.81
		Method II	2.00 1.96
		Method III	2.07 2.00

Fig. 2 Fractal characterization of the disordered microstructures studied, and comparison of the thermal conductivities of the microstructures, evaluated using the three methods

value of the fractal dimension in a particular direction corresponds to a higher transverse conductivity in that direction. This is evident not only in the increasing conductivities with volume fraction but also in the relative magnitudes of the two transverse conductivities for any given volume fraction.

A comparison of the conductivities obtained from the three methods shows that the simplified model (Method I) yields conductivities that are accurate to within about ten percent with respect to the exact conductivities (Method III). Note that the predictions of the simplified model are consistently lower than the exact values. This is attributed to the simplifying assumption of strictly unidirectional heat flow within the unit cell, which leads to an overprediction of the thermal resistance and an underprediction of the thermal conductivities. On the other hand, Method II, which is based on a numerical analysis of the generalized unit cell, yields closer estimates of the conductivities, to within about two to three percent of the exact values, in all the cases. This indicates that the fractal dimensions provide a very good description of the composite microstructures, and

that the relative inaccuracy of Method I, is almost entirely due to the approximations inherent in the simplified model.

Fiber Clusters. The application of the technique to characterizing microstructures consisting of fiber clusters was also studied. Clustered arrangements were obtained in the simulations by squaring the random numbers generated, so as to introduce a bias in the fiber arrangement. Two types of clustered arrangements were examined—one set with a preferential bias along one of the coordinate directions (i.e., the random numbers were squared only in the direction of bias), and a second set with clustering in both the x and the y-directions. Sample results of the simulations are presented in Figs. 2(d) and 2(e).

Figure 2(d) shows the microstructure with a preferential bias of the fiber clusters along the x-direction. As expected for this arrangement, the fractal dimension in the bias direction is seen to be larger (i.e., $d_x > d_y$) owing to the close packing of the fibers in that direction. An arrangement with fibers clustered towards the bottom-left corner of the macrocell (in both the x and y-directions), is shown in Fig. 2(e). In both Figs. 2(d) and 2(e), as before, Method II is seen to yield accurate estimates of the conductivity, while Method I predicts the conductivity to within about ten percent. The results in Figs. 2(d) and 2(e) further demonstrate that the fractal dimensions provide an effective means of quantitatively differentiating between reinforcement arrangements that have the same overall fiber volume fraction. This constitutes an important distinguishing feature of the present technique relative to the traditional approaches which don't provide for such a quantitative distinction.

The foregoing results suggest that the fractal dimensions provide an effective way of constructing geometrically equivalent ordered arrangements of a given disordered microstructure. The conductivity of the equivalent unit cell may be evaluated by resorting to the published results on ordered arrangements (for example, Han and Cosner, 1981), without the need for a separate numerical calculation. From a fundamental viewpoint, therefore, the fractal dimensions provide a bridge for the ordered array analyses in the literature to be applicable to practical microstructures. Furthermore, the description of realistic microstructures in terms of the fractal dimensions provides for estimation of other composite properties, such as permeabilities, elastic moduli, etc.

References

Behrens, E., 1968, "Thermal conductivities of composite materials," *Journal of Composite Materials*, Vol. 2, No. 1, pp. 2–17.

Feder, J., 1988, *Fractals*, Plenum, New York.

Han, L. S., and Cosner, A. A., 1981, "Effective Thermal Conductivities of Fibrous Composites," ASME JOURNAL OF HEAT TRANSFER, Vol. 103, pp. 387–392.

Hashin, Z., 1983, "Analysis of Composite Materials—A Survey," ASME JOURNAL OF APPLIED MECHANICS, Vol. 50, pp. 481–505.

Kim, I. C., and Torquato, S., 1990, "Determination of the effective conductivity of heterogeneous media by Brownian motion simulation," *Journal of Applied Physics*, Vol. 68, No. 8, pp. 3892–3903.

Kittel, C., 1986, *Introduction to Solid State Physics*, John Wiley and Sons, New York.

Milton, G. W., 1982, "Bounds on the elastic and transport properties of two-component composites," *Journal of the Mechanics and Physics of Solids*, Vol. 30, pp. 177–191.

Muralidhar, K., 1990, "Equivalent conductivity of heterogeneous medium," *International Journal of Heat and Mass Transfer*, Vol. 33, No. 8, pp. 1759–1765.

Patankar, S. V., 1980, *Numerical Heat Transfer and Fluid Flow*, Hemisphere, Washington DC.

Pitchumani, R., and Yao, S. C., 1991, "Correlation of Thermal Conductivities of Unidirectional Fibrous Composites Using Local Fractal Techniques," ASME JOURNAL OF HEAT TRANSFER, Vol. 113, pp. 788–796.

Pitchumani, R., and Ramakrishnan, B., 1999, "A Fractal Geometry Model for Evaluating Permeabilities of Porous Preforms Used in Liquid Composite Molding," *International Journal of Heat and Mass Transfer*, Vol. 42, No. 12, pp. 2219–2232.

Smith, P. A., and Torquato, S., 1989, "Computer simulation results for bounds on the effective conductivity of composite media," *Journal of Applied Physics*, Vol. 65, No. 3, pp. 893–900.

A Thermal Potential Formulation of Hyperbolic Heat Conduction

A. Barletta[1,2] and E. Zanchini[1]

Nomenclature

c = specific heat, (J kg^{-1} K^{-1})
i = $\sqrt{-1}$, imaginary unit
k = thermal conductivity, (W m^{-1} K^{-1})
n = non-negative integer number
$\mathbf{n}$ = unit outward normal to the boundary surface $\partial\Gamma$
L = thickness of the slab, (m)
p = Laplace transformed variable
q = x-component of the heat flux density, (W m^{-2})
q_s = power generated per unit volume, (W m^{-3})
$\mathbf{q}$ = heat flux density, (W m^{-2})
$\mathbf{q}_I^{(d)}$ = solenoidal part of $\mathbf{q}_I$
t = time, (s)
T = temperature, (K)
x = spatial coordinate, (m)
$\mathbf{x}$ = position vector, (m)
α = $=k/(\rho c)$, thermal diffusivity, (m^2 s^{-1})
η = dimensionless time defined in Eq. (15)
θ = dimensionless temperature defined in Eq. (15)
λ_n = nth dimensionless coefficient defined in Eq. (20)
μ_n = nth dimensionless coefficient defined in Eq. (20)
ξ = dimensionless coordinate defined in Eq. (15)
Ξ = dimensionless parameter defined in Eq. (15)
ρ = mass density, (kg m^{-3})
τ = thermal relaxation time, (s)
φ = thermal potential, (K)
ϕ = dimensionless thermal potential defined in Eq. (15)
χ = dimensionless heat flux density defined in Eq. (15)
ψ = arbitrary time-independent solution of the Laplace equation
Ω = dimensionless parameter defined in Eq. (15)
ω_n = nth dimensionless coefficient defined in Eq. (20)

Superscripts and Subscripts

$-$ = gauge transformed values of φ_I and $\mathbf{q}_I^{(d)}$
I = value of a quantity when $t = 0$
0 = value of a quantity at the boundary
$'$ = dummy integration variable

Introduction

In the last few decades, the theory of hyperbolic heat conduction has been shown to be a satisfactory extension of Fourier's theory of heat conduction in the case of highly nonstationary heat transfer phenomena. The review papers on this subject by Joseph and Preziosi (1989, 1990) and by Özisik and Tzou (1994) describe both the theoretical and the experimental developments in this field.

The mathematical model proposed by this theory is based on a generalization of Fourier's law which is called Cattaneo-Vernotte's equation and is given by

that the relative inaccuracy of Method I, is almost entirely due to the approximations inherent in the simplified model.

Fiber Clusters. The application of the technique to characterizing microstructures consisting of fiber clusters was also studied. Clustered arrangements were obtained in the simulations by squaring the random numbers generated, so as to introduce a bias in the fiber arrangement. Two types of clustered arrangements were examined—one set with a preferential bias along one of the coordinate directions (i.e., the random numbers were squared only in the direction of bias), and a second set with clustering in both the x and the y-directions. Sample results of the simulations are presented in Figs. 2(d) and 2(e).

Figure 2(d) shows the microstructure with a preferential bias of the fiber clusters along the x-direction. As expected for this arrangement, the fractal dimension in the bias direction is seen to be larger (i.e., $d_x > d_y$) owing to the close packing of the fibers in that direction. An arrangement with fibers clustered towards the bottom-left corner of the macrocell (in both the x and y-directions), is shown in Fig. 2(e). In both Figs. 2(d) and 2(e), as before, Method II is seen to yield accurate estimates of the conductivity, while Method I predicts the conductivity to within about ten percent. The results in Figs. 2(d) and 2(e) further demonstrate that the fractal dimensions provide an effective means of quantitatively differentiating between reinforcement arrangements that have the same overall fiber volume fraction. This constitutes an important distinguishing feature of the present technique relative to the traditional approaches which don't provide for such a quantitative distinction.

The foregoing results suggest that the fractal dimensions provide an effective way of constructing geometrically equivalent ordered arrangements of a given disordered microstructure. The conductivity of the equivalent unit cell may be evaluated by resorting to the published results on ordered arrangements (for example, Han and Cosner, 1981), without the need for a separate numerical calculation. From a fundamental viewpoint, therefore, the fractal dimensions provide a bridge for the ordered array analyses in the literature to be applicable to practical microstructures. Furthermore, the description of realistic microstructures in terms of the fractal dimensions provides for estimation of other composite properties, such as permeabilities (Pitchumani and Ramakrishnan, 1998), elastic moduli, etc.

References

Behrens, E., 1968, "Thermal conductivities of composite materials," *Journal of Composite Materials,* Vol. 2, No. 1, pp. 2–17.

Feder, J., 1988, *Fractals,* Plenum, New York.

Han, L. S., and Cosner, A. A., 1981, "Effective Thermal Conductivities of Fibrous Composites," ASME JOURNAL OF HEAT TRANSFER, Vol. 103, pp. 387–392.

Hashin, Z., 1983, "Analysis of Composite Materials—A Survey," ASME JOURNAL OF APPLIED MECHANICS, Vol. 50, pp. 481–505.

Kim, I. C., and Torquato, S., 1990, "Determination of the effective conductivity of heterogeneous media by Brownian motion simulation," *Journal of Applied Physics,* Vol. 68, No. 8, pp. 3892–3903.

Kittel, C., 1986, *Introduction to Solid State Physics,* John Wiley and Sons, New York.

Milton, G. W., 1982, "Bounds on the elastic and transport properties of two-component composites," *Journal of the Mechanics and Physics of Solids,* Vol. 30, pp. 177–191.

Muralidhar, K., 1990, "Equivalent conductivity of heterogeneous medium," *International Journal of Heat and Mass Transfer,* Vol. 33, No. 8, pp. 1759–1765.

Patankar, S. V., 1980, *Numerical Heat Transfer and Fluid Flow,* Hemisphere, Washington DC.

Pitchumani, R., and Yao, S. C., 1991, "Correlation of Thermal Conductivities of Unidirectional Fibrous Composites Using Local Fractal Techniques," ASME JOURNAL OF HEAT TRANSFER, Vol. 113, pp. 788–796.

Pitchumani, R., and Ramakrishnan, B., 1999, "A Fractal Geometry Model for Evaluating Permeabilities of Porous Preforms Used in Liquid Composite Molding," *International Journal of Heat and Mass Transfer,* Vol. 42, No. 12, pp. 2219–2232.

Smith, P. A., and Torquato, S., 1989, "Computer simulation results for bounds on the effective conductivity of composite media," *Journal of Applied Physics,* Vol. 65, No. 3, pp. 893–900.

A Thermal Potential Formulation of Hyperbolic Heat Conduction

A. Barletta[1,2] and E. Zanchini[1]

Nomenclature

c = specific heat, (J kg^{-1} K^{-1})
i = $\sqrt{-1}$, imaginary unit
k = thermal conductivity, (W m^{-1} K^{-1})
n = non-negative integer number
$\mathbf{n}$ = unit outward normal to the boundary surface $\partial\Gamma$
L = thickness of the slab, (m)
p = Laplace transformed variable
q = x-component of the heat flux density, (W m^{-2})
q_g = power generated per unit volume, (W m^{-3})
$\mathbf{q}$ = heat flux density, (W m^{-2})
$\mathbf{q}_I^{(d)}$ = solenoidal part of $\mathbf{q}_I$
t = time, (s)
T = temperature, (K)
x = spatial coordinate, (m)
$\mathbf{x}$ = position vector, (m)
α = $=k/(\rho c)$, thermal diffusivity, (m^2 s^{-1})
η = dimensionless time defined in Eq. (15)
θ = dimensionless temperature defined in Eq. (15)
λ_n = nth dimensionless coefficient defined in Eq. (20)
μ_n = nth dimensionless coefficient defined in Eq. (20)
ξ = dimensionless coordinate defined in Eq. (15)
Ξ = dimensionless parameter defined in Eq. (15)
ρ = mass density, (kg m^{-3})
τ = thermal relaxation time, (s)
φ = thermal potential, (K)
ϕ = dimensionless thermal potential defined in Eq. (15)
χ = dimensionless heat flux density defined in Eq. (15)
ψ = arbitrary time-independent solution of the Laplace equation
Ω = dimensionless parameter defined in Eq. (15)
ω_n = nth dimensionless coefficient defined in Eq. (20)

Superscripts and Subscripts

$-$ = gauge transformed values of φ_I and $\mathbf{q}_I^{(d)}$
I = value of a quantity when $t = 0$
0 = value of a quantity at the boundary
$'$ = dummy integration variable

Introduction

In the last few decades, the theory of hyperbolic heat conduction has been shown to be a satisfactory extension of Fourier's theory of heat conduction in the case of highly nonstationary heat transfer phenomena. The review papers on this subject by Joseph and Preziosi (1989, 1990) and by Özisik and Tzou (1994) describe both the theoretical and the experimental developments in this field.

The mathematical model proposed by this theory is based on a generalization of Fourier's law which is called Cattaneo-Vernotte's equation and is given by

Copyright © 1999 by ASME

$$\mathbf{q} + \tau \frac{\partial \mathbf{q}}{\partial t} = -k\nabla T. \qquad (1)$$

Obviously, Eq. (1) reduces to Fourier's law both for stationary phenomena and for materials with a vanishing thermal relaxation time τ. The distributions of temperature and of heat flux density within the material are determined by Eq. (1) together with the local energy balance equation. For a solid body with constant values of the mass density ρ and of the specific heat c, the local energy balance equation can be expressed as

$$-\nabla \cdot \mathbf{q} + q_g(\mathbf{x}, t) = \rho c \frac{\partial T}{\partial t}, \qquad (2)$$

where $q_g(\mathbf{x}, t)$ is the prescribed power generated per unit volume within the solid body. Under the assumption that τ and k are constants, Eqs. (1) and (2) are usually employed to obtain either a partial differential equation for the temperature or a partial differential equation for the heat flux density. Both the differential equations are hyperbolic and predict a finite propagation speed $\sqrt{\alpha/\tau}$ for a thermal disturbance. Therefore, two formulations of the theory are presented in the literature: one is based on the partial differential equation fulfilled by the temperature, the other is based on the partial differential equation fulfilled by the heat flux density. In the framework of hyperbolic heat conduction, every analytical or numerical evaluation available in the literature is based either on the temperature formulation or on the heat flux formulation. In particular, the advantages of the heat flux formulation in the case of specified heat fluxes at the boundaries are pointed out in Frankel et al. (1985).

Both formulations predict the onset of sharp wavefronts if either the boundary temperature or the boundary heat flux undergoes discontinuous time evolutions. Indeed, the presence of sharp wavefronts may lead to mathematical difficulties when numerical methods are applied to hyperbolic heat conduction. For instance, Glass et al. (1985, 1987) have shown that numerical oscillations occur in finite difference solutions of problems with step changes of either the boundary temperature or the boundary heat flux.

In the following, a new formulation of hyperbolic heat conduction is proposed. This formulation is based on the definition of a scalar field called thermal potential. By employing this scalar field, one can easily determine both the temperature field and the heat flux density field. In Tzou (1996), a scalar field, called heat flux potential, has been defined. The heat flux potential is such that its gradient coincides with the heat flux density $\mathbf{q}$ and fulfils a partial differential equation which, except for the sign in front of the source term and an arbitrary time function, coincides with the equation fulfilled by the temperature field. The thermal potential defined here differs from the heat flux potential defined by Tzou (1996). In particular, it will be shown that the thermal potential is not affected by discontinuities, even if step changes of the boundary temperature or of the boundary heat flux occur.

The Thermal Potential

Let us consider a solid body such that its mass density ρ, its specific heat c, its thermal conductivity k, and its thermal relaxation time τ can be considered as constants. The region of space occupied by the solid body is denoted by Γ and its boundary by $\partial\Gamma$.

As it is easily verified, Fourier's law implies that the heat flux density $\mathbf{q}$ is an irrotational vector field and that the temperature field is a scalar potential for $\mathbf{q}$. On the other hand, Eq. (1) implies that the temperature field does not represent a scalar potential for the heat flux density vector. In other words, unlike Fourier's law, Cattaneo-Vernotte's constitutive equation allows the existence of cases in which the heat flux density is not orthogonal to an isothermal surface. In fact, if at some instant

of time t a surface is isothermal, a vector field orthogonal to this surface is given by ∇T. Then, in order to check if $\mathbf{q}$ is orthogonal to the isothermal surface, one can inspect if the relation $\mathbf{q} \times \nabla T = 0$ holds. Equation (1) implies $\mathbf{q} \times \nabla T = 0$ either if $\tau = 0$ or if $\partial\mathbf{q}/\partial t$ is parallel to $\mathbf{q}$. The first condition corresponds to the limit of validity of Fourier's law, while the second necessarily occurs in one-dimensional problems but can be violated in two-dimensional or three-dimensional problems.

As is well known, the vector field $\mathbf{q}$ admits a scalar potential if $\nabla \times \mathbf{q} = 0$. Although this condition is always fulfilled when Fourier's law holds, Cattaneo-Vernotte's constitutive equation does not imply its validity. In fact, the heat flux density distribution $\mathbf{q}_I(\mathbf{x})$ at time $t = 0$ can be chosen arbitrarily and, in general, $\nabla \times \mathbf{q}_I \neq 0$. Moreover, it is easily verified that Eq. (1) can be rewritten as

$$-\tau \frac{\partial}{\partial t}(e^{t/\tau}\mathbf{q}) = k\nabla(e^{t/\tau}T). \qquad (3)$$

As a consequence of Eq. (3), the time derivative of $\exp(t/\tau)\nabla \times \mathbf{q}$ is zero, so that $\nabla \times \mathbf{q}$ is equal to $\exp(-t/\tau)\nabla \times \mathbf{q}_I$. Therefore, the condition $\nabla \times \mathbf{q} = 0$ holds at every instant of time if it holds at time $t = 0$, and in any case $\nabla \times \mathbf{q} = 0$ in the limit $t \to +\infty$. The distribution of heat flux density $\mathbf{q}_I(\mathbf{x})$ at time $t = 0$ needs neither be irrotational nor solenoidal. However, on account of Helmholtz's decomposition theorem (see, for instance, Korn and Korn, 1961), an arbitrary vector field can be expressed as the sum of an irrotational vector field and a solenoidal vector field. Therefore, there exist a time-independent scalar field $\varphi_I(\mathbf{x})$ and a time-independent vector field $\mathbf{q}_I^{(d)}(\mathbf{x})$ such that $\nabla \cdot \mathbf{q}_I^{(d)} = 0$ and $\mathbf{q}_I = -k\nabla\varphi_I + \mathbf{q}_I^{(d)}$.

Obviously, the choice of the fields $\varphi_I(\mathbf{x})$ and $\mathbf{q}_I^{(d)}(\mathbf{x})$ is not unique. In fact, also the gauge transformed fields $\overline{\varphi}_I(\mathbf{x}) = \varphi_I(\mathbf{x}) + \psi(\mathbf{x})$ and $\overline{\mathbf{q}}_I^{(d)}(\mathbf{x}) = \mathbf{q}_I^{(d)}(\mathbf{x}) + k\nabla\psi(\mathbf{x})$ fulfill both the condition $\nabla \cdot \overline{\mathbf{q}}_I^{(d)} = 0$ and the condition $\mathbf{q}_I = -k\nabla\overline{\varphi}_I + \overline{\mathbf{q}}_I^{(d)}$, provided that the gauge function $\psi(\mathbf{x})$ is any solution of the Laplace equation $\nabla^2\psi(\mathbf{x}) = 0$. However, if $\mathbf{q}_I^{(d)}(\mathbf{x})$ is fixed, the scalar field $\varphi_I(\mathbf{x})$ is determined up to an arbitrary additive constant. As a consequence, if one fixes $\mathbf{q}_I^{(d)}(\mathbf{x})$, then Eq. (3) implies the existence of a scalar field φ called *thermal potential* such that

$$T = \tau e^{-t/\tau} \frac{\partial\varphi}{\partial t}, \qquad (4)$$

$$\mathbf{q} = e^{-t/\tau}(\mathbf{q}_I^{(d)} - k\nabla\varphi). \qquad (5)$$

Equations (4) and (5) define the thermal potential only up to an arbitrary additive constant. If one substitutes Eqs. (4) and (5) in Eq. (3), one obtains an identity, provided that φ has regular first and second-order derivatives. Equations (4) and (5) ensure that φ has the physical dimensions of a temperature. Moreover, if $\mathbf{q}_I$ is irrotational and if $\mathbf{q}_I^{(d)}(\mathbf{x})$ is chosen as equal to zero, the heat flux density field $\mathbf{q}$ is orthogonal to the surfaces $\varphi = $ constant. It must be pointed out that the quantity called thermal potential and defined through Eqs. (4) and (5) has no finite limit when $\tau \to 0$. In fact, only if both $\partial\varphi/\partial t$ and $\nabla\varphi$ tend to infinity, the right-hand sides of Eqs. (4) and (5) do not vanish in the limit $\tau \to 0$. Therefore, the thermal potential is defined only within the theory of hyperbolic heat conduction, while it becomes singular in the limit of validity of Fourier's theory. By employing Eqs. (4), (5) and the energy balance expressed by Eq. (2), one obtains the hyperbolic differential equation fulfilled by φ, namely

$$\alpha\nabla^2\varphi + \frac{e^{t/\tau}}{\rho c} q_g = \tau \frac{\partial^2\varphi}{\partial t^2} - \frac{\partial\varphi}{\partial t}. \qquad (6)$$

In the thermal potential formulation, the first and second kind boundary conditions are easily expressed as constraints on φ by employing Eqs. (4) and (5), as follows:

$$\left.\frac{\partial \varphi}{\partial t}\right|_{\partial \Gamma, t \geq 0} = \frac{e^{t/\tau}}{\tau} T_0(\mathbf{x}, t), \qquad (7)$$

$$(\nabla \varphi \cdot \mathbf{n})|_{\partial \Gamma, t \geq 0} = \frac{1}{k} [(\mathbf{q}_I^{(d)} \cdot \mathbf{n})|_{\partial \Gamma, t \geq 0} - e^{t/\tau} q_0(\mathbf{x}, t)], \quad (8)$$

where $T_0(\mathbf{x}, t)$ and $q_0(\mathbf{x}, t)$ are the boundary distributions of temperature and heat flux. Moreover, if the distributions of heat flux density and temperature at time $t = 0$, $\mathbf{q}_I(\mathbf{x})$ and $T_I(\mathbf{x})$, are prescribed, the initial conditions on φ are given by

$$\left.\frac{\partial \varphi}{\partial t}\right|_{\Gamma \backslash \partial \Gamma, t=0} = \frac{1}{\tau} T_I(\mathbf{x}), \qquad (9)$$

$$\nabla \varphi|_{\Gamma \backslash \partial \Gamma, t=0} = \nabla \varphi_I(\mathbf{x}), \qquad (10)$$

where $\Gamma \backslash \partial \Gamma$ is the set of points of Γ which do not belong to $\partial \Gamma$. Since both φ and φ_I are defined up to an additive constant, Eq. (10) can be rewritten as

$$\varphi|_{\Gamma \backslash \partial \Gamma, t=0} = \varphi_I(\mathbf{x}). \qquad (11)$$

A Plane Slab Problem: The Thermal Potential Formulation

Let us consider an infinitely wide plane slab with thickness L and such that its mass density ρ, its specific heat c, its thermal conductivity k, and its thermal relaxation time τ can be considered as constants. Let the x-axis be orthogonal to the slab and such that one surface is at $x = 0$ and the other at $x = L$. When $t = 0$, the temperature T and the heat flux density $\mathbf{q}$ are zero at every position $0 < x < L$, so that also $\varphi_I(\mathbf{x})$ can be considered as zero within the slab. When $t \geq 0$, the temperature T is equal to the constant value T_0 at $x = 0$, while, at $x = L$, the x-component of the heat flux density is equal to the constant value $-q_0$. Moreover, no heat generation occurs within the slab. The symmetry of the problem ensures that the heat flux density is everywhere parallel to the x-axis and that both T and q depend only on x and t. On account of Eqs. (4) and (5), also the thermal potential φ depends only on x and t.

In the thermal potential formulation, on account of Eqs. (6) – (9) and (11), the governing equations are

$$\alpha \frac{\partial^2 \varphi}{\partial x^2} = \tau \frac{\partial^2 \varphi}{\partial t^2} - \frac{\partial \varphi}{\partial t}, \qquad (12)$$

$$\left.\frac{\partial \varphi}{\partial t}\right|_{x=0, t \geq 0} = \frac{e^{t/\tau}}{\tau} T_0, \quad \left.\frac{\partial \varphi}{\partial x}\right|_{x=L, t \geq 0} = \frac{e^{t/\tau}}{k} q_0, \qquad (13)$$

$$\varphi|_{0 < x < L, t=0} = 0, \quad \left.\frac{\partial \varphi}{\partial t}\right|_{0 < x < L, t=0} = 0. \qquad (14)$$

By introducing the dimensionless quantities

$$\theta = \frac{T}{T_0}, \quad \chi = \frac{q}{q_0}, \quad \phi = \frac{\varphi}{T_0},$$

$$\xi = \frac{x}{\sqrt{\alpha \tau}}, \quad \eta = \frac{t}{\tau}, \quad \Omega = \frac{q_0 \sqrt{\alpha \tau}}{T_0 k}, \quad \Xi = \frac{L}{\sqrt{\alpha \tau}}, \quad (15)$$

Eqs. (12) – (14) can be rewritten as

$$\frac{\partial^2 \phi}{\partial \xi^2} = \frac{\partial^2 \phi}{\partial \eta^2} - \frac{\partial \phi}{\partial \eta}, \qquad (16)$$

$$\left.\frac{\partial \phi}{\partial \eta}\right|_{\xi=0, \eta \geq 0} = e^{\eta}, \quad \left.\frac{\partial \phi}{\partial \xi}\right|_{\xi=\Xi, \eta \geq 0} = \Omega e^{\eta}, \qquad (17)$$

$$\phi|_{0 < \xi < \Xi, \eta=0} = 0, \quad \left.\frac{\partial \phi}{\partial \eta}\right|_{0 < \xi < \Xi, \eta=0} = 0. \qquad (18)$$

Equations (16) – (18) can be easily solved by employing the Laplace transform method (see Debnath, 1995). Thus, $\phi(\xi, \eta)$ can be expressed as

$$\phi(\xi, \eta) = -1 + (1 + \Omega \xi) e^{\eta}$$

$$- \frac{2}{\Xi} \sum_{n=0}^{\infty} \frac{\sin (\omega_n \xi)}{\omega_n^2 \sqrt{1 - 4\omega_n^2}} \{ [\omega_n + \Omega(-1)^n \lambda_n] e^{\lambda_n \eta}$$

$$- [\omega_n + \Omega(-1)^n \mu_n] e^{\mu_n \eta} \} \quad (19)$$

where, for every $n \geq 0$,

$$\lambda_n = \tfrac{1}{2} [1 + \sqrt{1 - 4\omega_n^2}], \quad \mu_n = \tfrac{1}{2} [1 - \sqrt{1 - 4\omega_n^2}],$$

$$\omega_n = \left(n + \frac{1}{2}\right) \frac{\pi}{\Xi}. \qquad (20)$$

As a consequence of Eqs. (4), (5), and (15), the dimensionless temperature θ and the dimensionless heat flux χ can be expressed as

$$\theta = e^{-\eta} \frac{\partial \phi}{\partial \eta}, \qquad (21)$$

$$\chi = -\frac{1}{\Omega} e^{-\eta} \frac{\partial \phi}{\partial \xi}. \qquad (22)$$

Equations (19) – (22) yield

$$\theta(\xi, \eta) = 1 + \Omega \xi$$

$$+ \frac{2}{\Xi} \sum_{n=0}^{\infty} \frac{\sin (\omega_n \xi)}{\omega_n^2 \sqrt{1 - 4\omega_n^2}} \{ \mu_n [\omega_n + \Omega(-1)^n \mu_n] e^{-\lambda_n \eta}$$

$$- \lambda_n [\omega_n + \Omega(-1)^n \lambda_n] e^{-\mu_n \eta} \}, \quad (23)$$

$$\chi(\xi, \eta) = -1 - \frac{2}{\Omega \Xi} \sum_{n=0}^{\infty} \frac{\cos (\omega_n \xi)}{\omega_n \sqrt{1 - 4\omega_n^2}} \{ [\omega_n + \Omega(-1)^n \mu_n] e^{-\lambda_n \eta}$$

$$- [\omega_n + \Omega(-1)^n \lambda_n] e^{-\mu_n \eta} \}. \quad (24)$$

The limit $\tau \to 0$ of the right-hand side of Eq. (23), i.e., the limit in which Fourier's law holds, can be easily evaluated by employing Eqs. (15) and (20) and is given by

$$\frac{T(x, t)}{T_0} = 1 + \frac{q_0 x}{kT_0} - \frac{4}{\pi^2} \sum_{n=0}^{\infty} \frac{\sin ((n + 1/2)\pi x/L)}{(2n + 1)^2}$$

$$\times \left[(2n + 1)\pi + \frac{2q_0 L}{kT_0} (-1)^n \right] e^{-(n+1/2)^2 \pi^2 \alpha t/L^2}. \quad (25)$$

Equation (25) coincides with the solution of Fourier's equation for zero initial temperature, temperature T_0 at $x = 0$ and zero heat flux at $x = L$ plus the solution of Fourier's equation for zero initial temperature, zero temperature at $x = 0$, and heat flux q_0 supplied at $x = L$. These solutions of Fourier's equation are available in Carslaw and Jaeger (1948). Moreover, the limit $\tau \to 0$ of the right-hand side of Eq. (24) can be expressed as

$$\frac{q(x, t)}{q_0} = -1 + \frac{2}{\pi} \sum_{n=0}^{\infty} \frac{\cos ((n + 1/2)\pi x/L)}{2n + 1}$$

$$\times \left[\frac{\pi kT_0}{q_0 L} (2n + 1) + 2(-1)^n \right] e^{-(n+1/2)^2 \pi^2 \alpha t/L^2}. \quad (26)$$

Indeed, it can be easily checked that Eqs. (25) and (26) are in agreement with Fourier's law, $q = -k \partial T/\partial x$. Moreover, it is easily verified that the limit of validity of Fourier's law can be
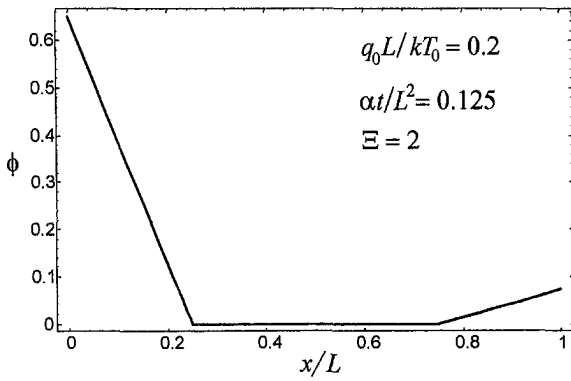
Fig. 1 Plot of ϕ versus x/L for $q_0L/(kT_0)$ = 0.2, $\alpha t/L^2$ = 0.125 and Ξ = 2

Fig. 2 Plots of θ versus x/L for $q_0L/(kT_0)$ = 0.2 and $\alpha t/L^2$ = 0.125. The solid line refers to Ξ = 2 and the dashed line to $\Xi \to +\infty$.
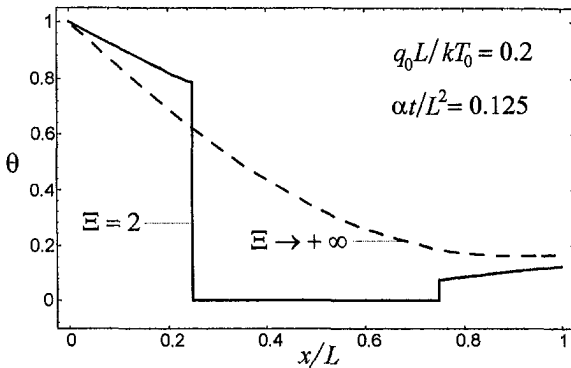

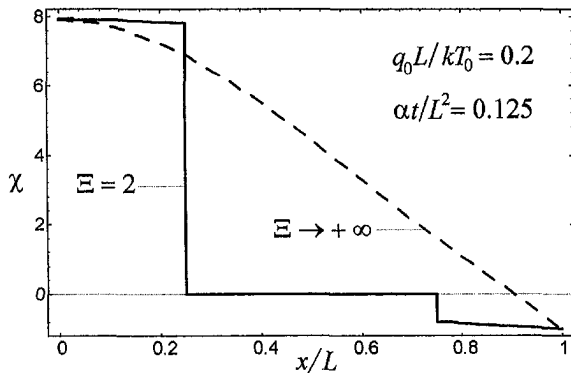**Fig. 3** Plots of χ versus x/L for $q_0L/(kT_0)$ = 0.2 and $\alpha t/L^2$ = 0.125. The solid line refers to Ξ = 2 and the dashed line to $\Xi \to +\infty$.

also obtained by considering fixed values of the quantities $\Omega\Xi$ = $q_0L/(kT_0)$, $\eta/\Xi^2 = \alpha t/L^2$, $\xi/\Xi = x/L$ and by taking the limit $\Xi \to +\infty$.

In Fig. 1, a plot of the dimensionless thermal potential ϕ, evaluated through Eq. (19), is represented as a function of x/L for $\Xi = 2$ and $\Omega = 0.1$ at the dimensionless time $\eta = 0.5$, so that $q_0L/(kT_0) = 0.2$ and $\alpha t/L^2 = 0.125$. In Figs. 2 and 3, plots of the dimensionless temperature θ and of the dimensionless heat flux χ, respectively, are represented for the same values of $q_0L/(kT_0)$ and $\alpha t/L^2$ considered in Fig. 1, both in the case $\Xi = 2$ and in the limiting case $\Xi \to +\infty$. Figures 1–3 reveal that, if $\Xi = 2$, no thermal signal travelling with speed $\sqrt{\alpha/\tau}$ has yet reached the region $0.25 < x/L < 0.75$. Moreover, these figures show that, in the case $\Xi = 2$, both θ and χ have

a sharp wavefront, so that they are discontinuous functions of x/L. On the contrary, in Fig. 1, the dimensionless thermal potential ϕ presents no discontinuity.

Conclusions

A new formulation of hyperbolic heat conduction based on a scalar field called thermal potential has been proposed. The definition of thermal potential ensures that Cattaneo-Vernotte's constitutive equation becomes an identity. Moreover, the energy balance equation yields a hyperbolic differential equation fulfilled by the thermal potential. The thermal potential formulation has been employed to obtain the temperature distribution and the heat flux density distribution for a plane slab with a prescribed temperature on one boundary and a prescribed heat flux density on the other boundary. It has been shown that the thermal potential is not affected by discontinuities, even if step changes in the time evolution of either the boundary temperature or the boundary heat flux occur. Therefore, the thermal potential formulation seems to be specially useful when these step changes are present and numerical methods are employed.

References

Carslaw, H. S., and Jaeger, J. C., 1948, *Conduction of Heat in Solids,* Clarendon Press, Oxford, pp. 100, 113.

Debnath, L., 1995, *Integral Transforms and their Applications,* CRC Press, New York, Chapter 3.

Frankel, J. I., Vick, B., and Özisik, M. N., 1985, "Flux formulation of hyperbolic heat conduction," *Journal of Applied Physics,* Vol. 58, pp. 3340–3345.

Glass, D. E., Özisik, M. N., McRae, D. S., and Vick, B., 1985, "On the numerical solution of hyperbolic heat conduction," *Numerical Heat Transfer,* Vol. 8, pp. 497–504.

Glass, D. E., Özisik, M. N., and Vick, B., 1987, "Non-Fourier effects on transient temperature resulting from periodic on-off heat flux," *International Journal of Heat and Mass Transfer,* Vol. 30, pp. 1623–1631.

Joseph, D. D., and Preziosi, L., 1989, "Heat waves," *Review of Modern Physics,* Vol. 61, pp. 41–73.

Joseph, D. D., and Preziosi, L., 1990, "Addendum to the paper 'Heat waves'," *Review of Modern Physics,* Vol. 62, pp. 375–391.

Korn, G. A., and Korn, T. M., 1961, *Mathematical Handbook for Scientists and Engineers,* McGraw-Hill, New York, p. 162.

Özisik, M. N., and Tzou, D. Y., 1994, "On the Wave Theory in Heat Conduction," ASME JOURNAL OF HEAT TRANSFER, Vol. 116, pp. 526–535.

Tzou, D. Y., 1996, *Macro- to Microscale Heat Transfer: The Lagging Behaviour,* Taylor and Francis, Washington, DC, p. 34.

A Conservative Iterative-Based Zonal Decomposition Scheme for Conduction Heat Transfer Problems

O. E. Ruiz[1] and W. Z. Black[1,2]

A new conservative iterative-based zonal decomposition technique for the solution of complex heat conduction problems is proposed. This numerical technique is based on dividing the domain into subdomains and ensuring that the heat flux and temperature are continuous at the boundary between subdomains. An example problem is used to illustrate the zonal de-

[1] George W. Woodruff School of Mechanical Engineering, Georgia Institute of Technology, Atlanta, GA 30332.
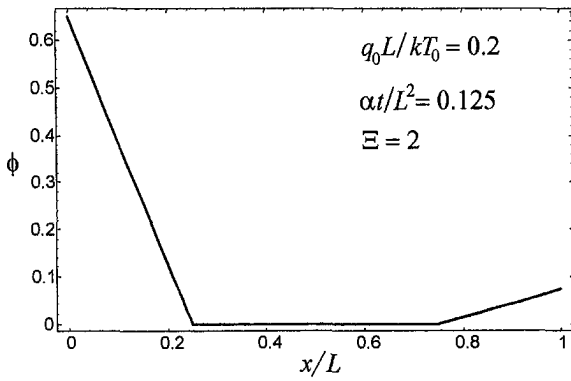
[2] Fellow ASME.

Fig. 1 Plot of ϕ versus x/L for $q_0L/(kT_0) = 0.2$, $\alpha t/L^2 = 0.125$ and $\Xi = 2$

Fig. 2 Plots of θ versus x/L for $q_0L/(kT_0) = 0.2$ and $\alpha t/L^2 = 0.125$. The solid line refers to $\Xi = 2$ and the dashed line to $\Xi \to +\infty$.

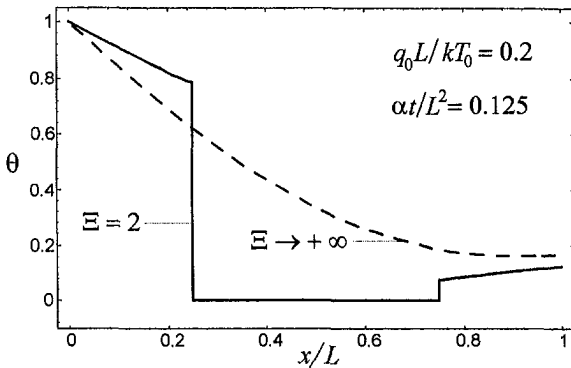**Fig. 3** Plots of χ versus x/L for $q_0L/(kT_0) = 0.2$ and $\alpha t/L^2 = 0.125$. The solid line refers to $\Xi = 2$ and the dashed line to $\Xi \to +\infty$.
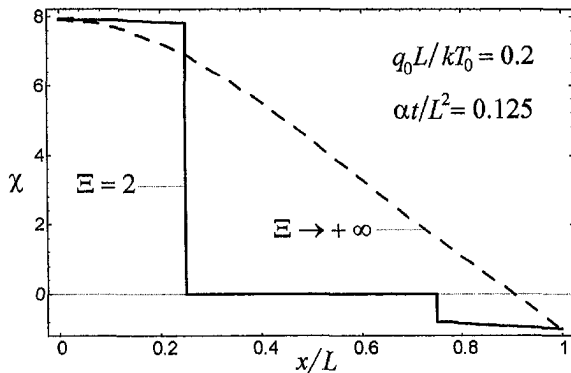
a sharp wavefront, so that they are discontinuous functions of x/L. On the contrary, in Fig. 1, the dimensionless thermal potential ϕ presents no discontinuity.

Conclusions

A new formulation of hyperbolic heat conduction based on a scalar field called thermal potential has been proposed. The definition of thermal potential ensures that Cattaneo-Vernotte's constitutive equation becomes an identity. Moreover, the energy balance equation yields a hyperbolic differential equation fulfilled by the thermal potential. The thermal potential formulation has been employed to obtain the temperature distribution and the heat flux density distribution for a plane slab with a prescribed temperature on one boundary and a prescribed heat flux density on the other boundary. It has been shown that the thermal potential is not affected by discontinuities, even if step changes in the time evolution of either the boundary temperature or the boundary heat flux occur. Therefore, the thermal potential formulation seems to be specially useful when these step changes are present and numerical methods are employed.

References

Carslaw, H. S., and Jaeger, J. C., 1948, *Conduction of Heat in Solids,* Clarendon Press, Oxford, pp. 100, 113.

Debnath, L., 1995, *Integral Transforms and their Applications,* CRC Press, New York, Chapter 3.

Frankel, J. I., Vick, B., and Özisik, M. N., 1985, "Flux formulation of hyperbolic heat conduction," *Journal of Applied Physics,* Vol. 58, pp. 3340–3345.

Glass, D. E., Özisik, M. N., McRae, D. S., and Vick, B., 1985, "On the numerical solution of hyperbolic heat conduction," *Numerical Heat Transfer,* Vol. 8, pp. 497–504.

Glass, D. E., Özisik, M. N., and Vick, B., 1987, "Non-Fourier effects on transient temperature resulting from periodic on-off heat flux," *International Journal of Heat and Mass Transfer,* Vol. 30, pp. 1623–1631.

Joseph, D. D., and Preziosi, L., 1989, "Heat waves," *Review of Modern Physics,* Vol. 61, pp. 41–73.

Joseph, D. D., and Preziosi, L., 1990, "Addendum to the paper 'Heat waves'," *Review of Modern Physics,* Vol. 62, pp. 375–391.

Korn, G. A., and Korn, T. M., 1961, *Mathematical Handbook for Scientists and Engineers,* McGraw-Hill, New York, p. 162.

Özisik, M. N., and Tzou, D. Y., 1994, "On the Wave Theory in Heat Conduction," ASME JOURNAL OF HEAT TRANSFER, Vol. 116, pp. 526–535.

Tzou, D. Y., 1996, *Macro- to Microscale Heat Transfer: The Lagging Behaviour,* Taylor and Francis, Washington, DC, p. 34.

A Conservative Iterative-Based Zonal Decomposition Scheme for Conduction Heat Transfer Problems

O. E. Ruiz[1] and W. Z. Black[1,2]

A new conservative iterative-based zonal decomposition technique for the solution of complex heat conduction problems is proposed. This numerical technique is based on dividing the domain into subdomains and ensuring that the heat flux and temperature are continuous at the boundary between subdomains. An example problem is used to illustrate the zonal de-

also obtained by considering fixed values of the quantities $\Omega\Xi = q_0L/(kT_0)$, $\eta/\Xi^2 = \alpha t/L^2$, $\xi/\Xi = x/L$ and by taking the limit $\Xi \to +\infty$.

In Fig. 1, a plot of the dimensionless thermal potential ϕ, evaluated through Eq. (19), is represented as a function of x/L for $\Xi = 2$ and $\Omega = 0.1$ at the dimensionless time $\eta = 0.5$, so that $q_0L/(kT_0) = 0.2$ and $\alpha t/L^2 = 0.125$. In Figs. 2 and 3, plots of the dimensionless temperature θ and of the dimensionless heat flux χ, respectively, are represented for the same values of $q_0L/(kT_0)$ and $\alpha t/L^2$ considered in Fig. 1, both in the case $\Xi = 2$ and in the limiting case $\Xi \to +\infty$. Figures 1–3 reveal that, if $\Xi = 2$, no thermal signal travelling with speed $\sqrt{\alpha/\tau}$ has yet reached the region $0.25 < x/L < 0.75$. Moreover, these figures show that, in the case $\Xi = 2$, both θ and χ have

composition technique for both steady and transient problems. This numerical technique results in accuracy which equals or exceeds traditional finite difference solutions and solution times which are significantly less than traditional finite difference solutions. A numerical relaxation parameter is introduced and its value is optimized to provide the most rapid convergence to an accurate solution.

Introduction

Recently, the complexity and extent of heat transfer numerical solutions have grown in parallel with the technological advances in computational resources. This note introduces a new numerical technique based on an iterative zonal decomposition scheme which can provide increased numerical accuracy while at the same time requiring less computational expense. The zonal decomposition method is particularly well suited for problems that involve moving boundaries in which a mismatch of grids is possible across boundaries in the solution domain. This method is also a logical approach to problems that involve phase change, domains that have distinct variations in thermal properties, and those problems that can be divided into regions with large and small temperature gradients. Zonal decomposition consists of subdividing the computational domain into various subdomains with independent grids that are selectively refined. This allows for better planning of the computational grid and an overall smaller number of grid points required to accurately represent the numerical solution. Information is communicated at the zonal boundaries by requiring a continuity of temperature and heat flux at the zonal boundary.

While zonal decomposition methods have seen limited application in solving fluid mechanics problems (Rai, 1984, 1985; Hessenius and Rai, 1986; Walters et al., 1986), they have not been exploited to solve complicated heat transfer problems. In the area of computational fluid dynamics, zonal decomposition schemes have been used to model complex geometries in supersonic and subsonic flow fields. Rai (1984) presented a finite difference grid-patching scheme to solve the transient Euler equations in geometrically complex problems. An implicit version of the scheme was presented in Rai (1985). Walters et al. (1986), following the grid patching scheme presented by Rai (1985), discussed the impact of the scheme on the convergence of the solution. Tan and Pecht (1990) wrote one of the few zonal decomposition papers applied to the steady-state heat conduction equation. Several other papers have discussed domain decomposition techniques which are zonal decomposition schemes implemented on parallel platforms. For example, Dawson et al. (1991) used a domain decomposition algorithm to solve for the temperature distribution in a solid with discontinuous grids. Douglas and Yang (1996) presented an iterative domain decomposition scheme with nonoverlapping continuous grids to solve a general class of partial differential equations. Yang (1996) presented another iterative domain decomposition scheme to solve elliptic problems.

Analysis

To solve heat conduction boundary value problems by numerical techniques, the heat conduction equation must be discretized in the domain of interest. To lower the computational expense without compromising the numerical accuracy, independently generated nonoverlapping grids that are fine in areas of high-temperature gradient and coarse in low-gradient areas will be used. Inherent in this approach is the fact that discontinuous computational grids will be generated. Other numerical schemes that have been developed to address the problem of discontinuous grids are grid embedding (Benek et al., 1983) and interpolation (Ciment and Sweet, 1973).

The zonal decomposition scheme is developed on the simplified grid shown in Fig. 1. The computational domain is arbi-
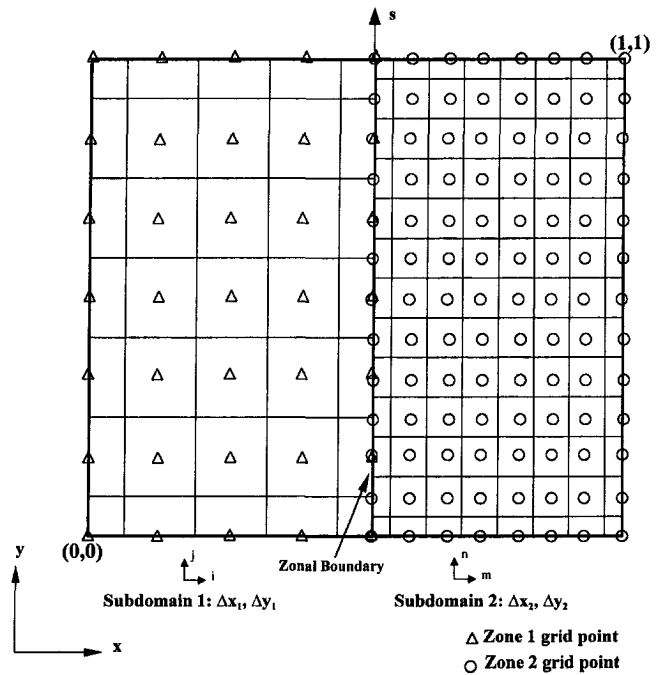

Fig. 1   Example of a discontinuous Cartesian grid

trarily divided into subdomains with independently sized grids and the boundaries between the subdomains are called zonal boundaries. At the zonal boundary, both the temperature distribution and the heat transfer flux must be continuous,

$$\tilde{T}_1(s) = \tilde{T}_2(s), \tag{1}$$

$$\mathbf{q}_1''(s) = \mathbf{q}_2''(s), \tag{2}$$

where s is the location along the zonal boundary. Equation (2) imposes the required condition of conservation of energy across the zonal boundary,

$$\int_{\Gamma_1} \mathbf{q}_1''(s) \cdot d\Gamma_1 = \int_{\Gamma_2} \mathbf{q}_2''(s) \cdot d\Gamma_2. \tag{3}$$

The heat fluxes at the zonal boundaries can be determined by using a second-order backward difference approximation in subdomain 1 and a second-order forward difference approximation in subdomain 2. This technique is called a conservative method because Eqs. (1)–(3) require that the solution satisfy continuity of temperature and heat flux at all zonal boundaries and it conserves energy.

Based on previous work (Tan and Pecht, 1990; Douglas and Yang, 1996; Yang, 1996), a new iterative conservative zonal decomposition scheme is proposed. The scheme uses two-step iterations to pass data between the subdomains. Initial temperature and flux distributions are assumed at the zonal boundaries of subdomains 1 and 2. An estimate of the temperature distribution at iteration step $r + \frac{1}{2}$ for the zonal boundary of subdomain 1 can be calculated as follows:

$$\tilde{T}_1^{r+1/2} = \theta \tilde{T}_1^r + (1 - \theta)\tilde{T}_1^{r-1/2}. \tag{4}$$

This estimate uses information from the previous iteration and from the previous half-iteration and balances them using a relaxation parameter θ which must have a value between 0 and 1. The temperature distribution estimate given by Eq. (4) is used as a Dirichlet boundary condition at the zonal boundary between subdomains 1 and 2. The temperature distribution T_1 in subdomain 1 at iteration step $r + \frac{1}{2}$ can therefore be determined using traditional finite difference techniques.
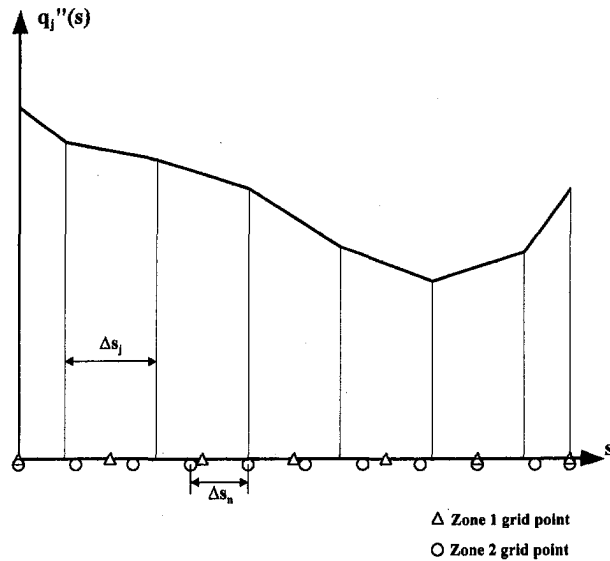
Fig. 2 Zonal boundary 1 heat flux distribution

Using the resulting temperature distribution $(T_1^{r+1/2})$, the heat flux distribution $(q_1''^{r+1/2})$ along the zonal boundary of subdomain 1 can be calculated. A piecewise linear distribution of the heat flux along this zonal boundary can be assumed as shown in Fig. 2. The flux distribution along zonal boundary 1 must be integrated to enforce energy conservation on a cell-by-cell basis of zonal boundary 2,

$$q_2''^{r+1/2}(s_n) = \frac{1}{\Delta s_n} \int_{s_n - \Delta s_n/2}^{s_n + \Delta s_n/2} q_1''^{r+1/2}(s_j) ds. \qquad (5)$$

The j and n indexes correspond to vertical location in subdomains 1 and 2, respectively.

An estimate for the flux distribution across zonal boundary 2 at iteration step $r + 1$ can be calculated based on the previous results according to the equation

$$q_2''^{r+1} = \theta q_2''^{r+1/2} + (1 - \theta) q_2''^r. \qquad (6)$$

This equation uses flux information from the previous iteration steps to determine an estimate of the heat flux across zonal boundary 2 at iteration step $r + 1$. A Neumann boundary condition can be imposed at the zonal boundary of subdomain 2 using the flux distribution estimate $(q_2''^{r+1})$. The temperature distribution in subdomain 2 (T_2^{r+1}) can be calculated using traditional finite difference techniques. The zonal boundary temperature distribution in subdomain 2 at iteration step $r + 1$ $(\check{T}_2^{r+1})$ is obtained from these results (T_2^{r+1}). Finally, the zonal boundary temperature distribution in subdomain 2 is then interpolated to the grid points at the zonal boundary of subdomain 1. This process completes a full iteration of the zonal decomposition scheme. If the relaxation parameter is equal to 1, the zonal decomposition scheme reduces to the one used by Tan and Pecht (1990).

Iterations must continue until the solution satisfies specified convergence criteria. In this study, three convergence parameters are employed. The first parameter, L_∞, quantifies the variation in the temperature distribution in both subdomains at each iteration step,

$$L_\infty = \max \left[\left| \frac{T_1^{r+1} - T_1^r}{T_1^r} \right|, \left| \frac{T_2^{r+1} - T_2^r}{T_2^r} \right| \right]. \qquad (7)$$

The second convergence parameter, D, quantifies the relative error or the degree of discontinuity between the zonal boundary temperature distributions in the two subdomains,

$$D = \max \left[\left| \frac{\check{T}_2^{r+1} - \check{T}_1^{r+1/2}}{\check{T}_1^{r+1/2}} \right| \right]. \qquad (8)$$

Finally, an interface energy balance convergence parameter, IEB, is used to assess the magnitude of the residual fluxes at the zonal boundary between the subdomains,

$$\text{IEB} = \left| \sum_n q_2''^{r+1}(s_n) \Delta s_n - \sum_j q_1''^{r+1/2}(s_j) \Delta s_j \right|. \qquad (9)$$

This numerical scheme can be used to solve steady-state as well as transient heat conduction problems as will be illustrated in the following example problem.

Problem Statement. To demonstrate the utility and accuracy of the zonal decomposition scheme, the results predicted by the zonal decomposition technique will be compared to the results from the known analytical solution for both a steady and transient problem. The problem involves a solid in rectangular coordinates in which the domain has constant properties and no internal heat sources. The governing energy equation is

$$\frac{\partial T}{\partial t} = \alpha \left(\frac{\partial^2 T}{\partial x^2} + \frac{\partial^2 T}{\partial y^2} \right), \quad 0 \le x \le 1 \text{ m}, \quad 0 \le y \le 1 \text{ m} \qquad (10)$$

and the following initial and boundary conditions were imposed:

$$T(x, y, 0) = T_0, \qquad (11)$$

$$\left. \frac{\partial T}{\partial x} \right|_{(0,y,t)} = 0, \qquad (12)$$

$$T(x, 0, t) = T_0, \qquad (13)$$

$$\left. \frac{\partial T}{\partial y} \right|_{(x,1,t)} = 0, \qquad (14)$$

$$-k \left. \frac{\partial T}{\partial x} \right|_{(1,y,t)} = h[T(1, y, t) - T_{amb}]. \qquad (15)$$

This relatively simple problem will permit the introduction of the new numerical technique without undue complexity.

The zonal decomposition scheme will be illustrated with the grid distribution shown in Fig. 1 in which a zonal boundary is placed at $x = \frac{1}{2}$ m to divide the domain in two subdomains. Based on the boundary conditions, subdomain 2 will contain areas with sharp gradients and therefore a finer grid in this subdomain will logically lead to improved accuracy. A relatively coarser grid can be used in subdomain 1 to reduce the total number of grid points in the domain without jeopardizing the accuracy of the solution.

Analytical Solution. This problem can be solved analytically by separation of variables. The steady-state analytical solution is

$$T_{ss}(x, y) = T_0 + \sum_{n=1}^{\infty} C_n \sin (\lambda_n y) \cos (\lambda_n x), \qquad (16)$$

$$C_n = \frac{2(T_{amb} - T_0)}{\lambda_n \left(\cosh (\lambda_n) + \frac{k}{h} \lambda_n \sinh (\lambda_n) \right)}, \qquad (17)$$

$$\lambda_n = (2n - 1) \frac{\pi}{2}. \qquad (18)$$

The transient solution can also be obtained by separation of variables,

Table 1 Example problem steady-state solution comparison

	Location (x,y)						
	(0, 1.0)	**(0.5, 1.0)**	**(1.0, 1.0)**	**(0, 0.5)**	**(0.5, 0.5)**	**(1.0, 0.5)**	**(1.0, 0.1)**
Analytical	76.70 °C	69.97 °C	50.14 °C	83.20 °C	77.17 °C	53.86 °C	73.24 °C
Finite Difference $\Delta x = 0.1, \Delta y = 0.1$	76.70 °C (0.0 %)	70.00 °C (0.04 %)	50.14 °C (0.0 %)	83.18 °C (0.02 %)	77.18 °C (0.01 %)	53.90 °C (0.07 %)	74.97 °C (2.36 %)
Zonal Decomposition $\Delta x_1 = 0.1, \Delta y_1 = 0.1$ $\Delta x_2 = 0.1, \Delta y_2 = 0.1$	76.60 °C (0.13 %)	69.90 °C (0.10 %)	50.11 °C (0.06 %)	83.09 °C (0.13 %)	77.04 °C (0.17 %)	53.87 °C (0.02 %)	74.96 °C (2.35 %)
Zonal Decomposition $\Delta x_1 = 0.1, \Delta y_1 = 0.1$ $\Delta x_2 = 0.05, \Delta y_2 = 0.05$	76.58 °C (0.16 %)	69.87 °C (0.14 %)	50.11 °C (0.06 %)	83.08 °C (0.14 %)	77.03 °C (0.18 %)	53.84 °C (0.04 %)	73.66 °C (0.57 %)

$$T(x, y, t) = T_{ss}(x, y)$$

$$+ \sum_{m=1}^{\infty} \sum_{n=1}^{\infty} D_{mn} e^{-\alpha \cdot (\beta_m^2 + \lambda_n^2)t} \cos(\beta_m x) \sin(\lambda_n y), \quad (19)$$

$$D_{mn} = \frac{-2C_n(\lambda_n \sinh \lambda_n \cos \beta_m + \beta_m \cosh \lambda_n \sin \beta_m)}{\left(1 + \dfrac{\sin(2\beta_m)}{2\beta_m}\right)(\beta_m^2 + \lambda_n^2)}, \quad (20)$$

$$\beta_m \tan \beta_m = \frac{h}{k}. \quad (21)$$

Discussion of Results. A steady-state solution was obtained by using a finite difference scheme with a uniform grid ($\Delta x = \Delta y = 0.1$ m) and also with the zonal decomposition scheme. The material properties used were those of aluminum ($k = 204$ W/m-K, $\alpha = 8.418 \times 10^{-5}$ m^2/s). The constant temperature boundary condition T_o was assigned a value of 100°C. The heat transfer coefficient (h) and ambient temperature (T_{amb}) values selected were 1000 W/m^2-K and 40°C, respectively. The relaxation parameter θ was set to 0.80 for these calculations. The zonal decomposition convergence parameters L_∞, D, and IEB were set to values of 10^{-6}, 10^{-6}, and 10^{-9} W/m, respectively. These convergence parameters are very conservative and allow proper modeling of the physical process. These values produced a total of 20 zonal decomposition iterations before convergence.

The temperatures determined by the analytical solution are compared to the values predicted by the uniform grid finite difference solution and by the zonal decomposition solution for two different grid spacings. The first case considers a uniform grid discretization in both subdomains which is identical to the grid used in the finite difference solution. The second case considers grid spacings $\Delta x_1 = \Delta y_1 = 0.1$ m in subdomain 1 and finer grid spacings $\Delta x_2 = \Delta y_2 = 0.05$ m in subdomain 2. This case was used to assess the accuracy of the solution when the grids are discontinuous across the zonal boundary. Percent differences between the steady-state analytical solution temperatures and the values determined by numerical solutions are shown in Table 1. By comparing the values in Table 1 it can be seen that the zonal decomposition solutions are as accurate as the finite difference solution when the grid is uniform. The results for the second zonal decomposition case with a finer grid in zone 2 indicates improved accuracy at the corner location (1 m, 0.1 m) where the temperature gradients are high due to the assumed boundary conditions.

Values for temperature distribution for the transient form of the example problem were calculated for the same material properties, same geometric parameters, and identical convergence criteria used in the steady-state problem. A Crank-Nicholson scheme was used to discretize the governing equations in time. The relaxation parameter θ in Eq. (4) and Eq. (6) was

set equal to 0.80. A time step of 1.0 sec was used for the time interval. Table 2 illustrates a comparison between the analytical solution, the finite difference solution with a uniform grid, and the zonal decomposition solution for two different grid sizes at times of 1000 and 2000 sec. These results show that the zonal decomposition solutions are as accurate as the uniform grid finite difference results. The predicted temperature at the grid point location (1.0, 0.1) has the lowest accuracy when compared to the other grid points considered. The zonal decomposition solution that used a finer grid in zone 2 shows an overall improvement in the accuracy of the solution.

Zonal Decomposition Relaxation Parameter

A very important issue that must be considered with the zonal decomposition method is convergence of the solutions in each of the subdomains. A range of relaxation parameters θ, defined in Eq. (4) and Eq. (6), was used with the intention of selecting a value which would accelerate the convergence of the zonal decomposition solution. Figure 3 illustrates the number of iterations that were required for convergence to the solution of the example problem as a function of the relaxation parameter θ, when using a discontinuous grid. The curve is relatively flat for a relaxation parameter in the range of 0.5 to 0.8. As the convergence parameter approaches zero, the scheme does not converge. These results show that the optimum value for the relaxation parameter which corresponds to a minimum in the number of iterations required for convergence of the example problem was approximately 0.82.

Conclusions

The zonal decomposition technique discussed in this note is particularly well suited for complex heat conduction problems in which the solution domain can be divided into several subregions. This technique can easily accommodate problems which have discontinuous grid spacings at the boundaries that separate the subdomains. Subdividing the problem domain can improve accuracy, because finer grid spacing can be used in regions of expected high gradients. Furthermore, coarse grids in areas of small temperature gradients will reduce the number of nodal equations that must be solved without jeopardizing the overall solution accuracy. A simple example problem was selected to illustrate the method without undue complexity. For this problem the zonal decomposition and traditional finite difference solutions show similar accuracy and require equivalent computational time. However, when more complex problems are considered, the increased accuracy of the zonal decomposition scheme becomes more evident and computational times required to achieve an accurate solution are significantly reduced. Even though savings in the computation time are problem dependent, the zonal decomposition scheme converges to a solution in about one-half the time when compared to traditional

Table 2 Example problem transient solution comparison

| Transient Solution At 1000 seconds	Location (x,y)						
	(0, 1.0)	(0.5, 1.0)	(1.0, 1.0)	(0, 0.5)	(0.5, 0.5)	(1.0, 0.5)	(1.0, 0.1)
Analytical	99.29 °C	93.20 °C	60.15 °C	99.41 °C	94.01 °C	61.19 °C	74.92 °C
Finite Difference $\Delta x = 0.1, \Delta y = 0.1$	99.27 °C (0.02 %)	93.29 °C (0.10 %)	60.17 °C (0.03 %)	99.39 °C (0.02 %)	94.09 °C (0.09 %)	61.26 °C (0.11 %)	76.65 °C (2.31 %)
Zonal Decomposition $\Delta x_1 = 0.1, \Delta y_1 = 0.1$ $\Delta x_2 = 0.1, \Delta y_2 = 0.1$	99.18 °C (0.11 %)	92.95 °C (0.27 %)	60.08 °C (0.12 %)	99.31 °C (0.10 %)	93.76 °C (0.27 %)	61.17 °C (0.03 %)	76.63 °C (2.28 %)
Zonal Decomposition $\Delta x_1 = 0.1, \Delta y_1 = 0.1$ $\Delta x_2 = 0.05, \Delta y_2 = 0.05$	99.20 °C (0.09 %)	92.99 °C (0.23 %)	60.11 °C (0.07 %)	99.33 °C (0.08 %)	93.80 °C (0.22 %)	61.16 °C (0.05 %)	75.34 °C (0.56 %)
Transient Solution At 2000 seconds							
Analytical	94.90 °C	85.59 °C	55.71 °C	96.12 °C	88.27 °C	57.82 °C	74.12 °C
Finite Difference $\Delta x = 0.1, \Delta y = 0.1$	94.96 °C (0.06 %)	85.72 °C (0.15 %)	55.74 °C (0.05 %)	96.15 °C (0.03 %)	88.36 °C (0.10 %)	57.88 °C (0.10 %)	75.85 °C (2.33 %)
Zonal Decomposition $\Delta x_1 = 0.1, \Delta y_1 = 0.1$ $\Delta x_2 = 0.1, \Delta y_2 = 0.1$	94.71 °C (0.20 %)	85.42 °C (0.20 %)	55.64 °C (0.13 %)	95.95 °C (0.18 %)	88.06 °C (0.24 %)	57.80 °C (0.03 %)	75.83 °C (2.31 %)
Zonal Decomposition $\Delta x_1 = 0.1, \Delta y_1 = 0.1$ $\Delta x_2 = 0.05, \Delta y_2 = 0.05$	94.74 °C (0.17 %)	85.43 °C (0.19 %)	55.66 °C (0.09 %)	95.97 °C (0.16 %)	88.07 °C (0.23 %)	57.78 °C (0.07 %)	74.54 °C (0.57 %)
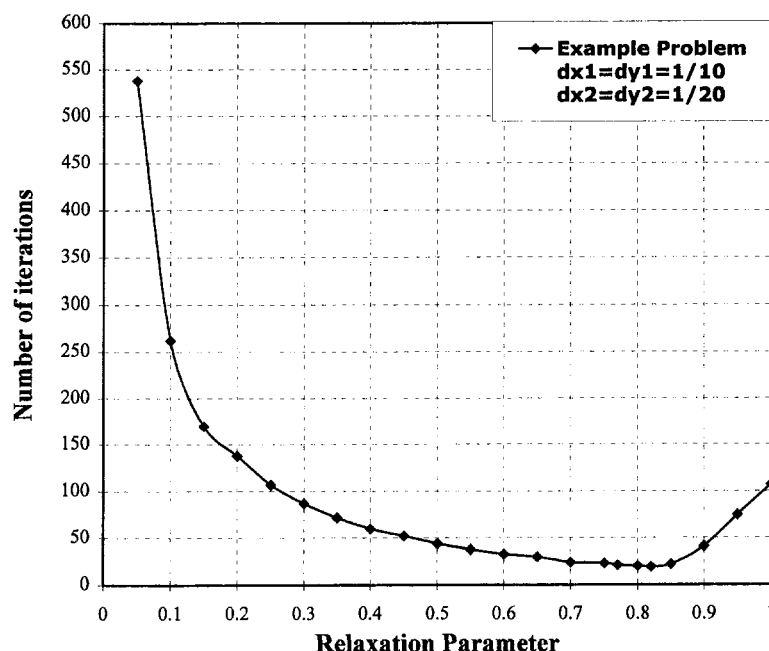
Fig. 3 Convergence dependence on relaxation parameter

finite difference techniques, even when very efficient sparse matrix solving algorithms are used. This conclusion was based on a number of test cases that are not discussed here.

A numerical relaxation parameter θ that was used to iteratively calculate both the heat flux and temperature distributions along the zonal boundary between subdomains is proposed in the paper. The variation in the number of iterations to convergence with the relaxation parameter is determined for the example problem. When values for θ in the range of 0.75–0.82 are used, the solution time is minimized for the example problem considered in this study. In general, θ values between 0.5–0.8 show a range of robust convergence.

References

Benek, J. A., Steger, J. L., and Dougherty, F. C., 1983, "A Flexible Grid Embedding Technique With Application to the Euler Equations," AIAA paper 83-1944.

Ciment, M., and Sweet, R. A., 1973, "Mesh Refinements for Parabolic Equations," Journal of Computational Physics, Vol. 12, pp. 513–525.

Dawson, C. N., Du, Q., and Dupont, T. F., 1991, "A Finite Difference Domain Decomposition Algorithm for Numerical Solution of the Heat Equation," Mathematics of Computation, Vol. 57, No. 195, pp. 63–71.

Douglas, J., Jr., and Yang, D., 1996, "Numerical Experiments of a Nonoverlapping Domain Decomposition Method for Partial Differential Equations," Numerical Analysis: A. R. Mitchell 75th Birthday Volume, D. Griffiths and G. A. Watson, eds., World Scientific Publishing, River Edge, NJ, pp. 85–97.

Hessenius, K. A., and Rai, M. M., 1986, "Applications of a Conservative Zonal Scheme to Transient and Geometrically Complex Problems," Computer and Fluids, Vol. 14, No. 1, pp. 43–58.

Rai, M. M., 1984, "A Conservative Treatment of Zonal Boundaries for Euler Equation Calculations," AIAA paper 84-0164, Reno, NV.

Rai, M. M., 1985, "An Implicit, Conservative, Zonal-Boundary Scheme for Euler Equation Calculations," AIAA paper 85-0488, Reno, NV.

Tan, C. H., and Pecht, M., 1990, "A Zonal Decomposition Methodology for Detailed Temperature Field Evaluation," ASME Journal of Electronic Packaging, Vol. 112, pp. 260–266.

Walters, R. W., Thomas, J. L., and Switzer, G. F., 1986, "Aspects and Applications of Patched Grid Calculations," AIAA paper 86-1063, Atlanta, GA.

Yang, D., 1996, "A Parallel Iterative Nonoverlapping Domain Decomposition Procedure for Elliptic Problems," IMA Journal of Numerical Analysis, Vol. 16, pp. 75–91.

Thermal Conductivity of a Material Containing a Layer of Thin Strips or a Staggered Array of Thin Strips

C. Y. Wang[1]

The effective conductivity of a composite containing layers of thin strips is found by conformal mapping and the method of eigenfunction expansions and matching.

1 Introduction

The theoretical prediction of the effective thermal conductivity of composite materials has always been difficult. There exist approximate micromechanical methods such as mixture theory, homogenization, and self-consistent schemes with limited ranges of applicability (Christensen, 1979; Aboudi, 1991). These methods, however, fail for a class of composites where the volume fraction of one phase is negligible, such as a material containing thin strips of different property. Although the volume fraction is zero, the effect on conductivity is nontrivial.

The purpose of the present paper is twofold. First we deduce, through complex transforms, some closed-form solutions of the thermal effect of a composite that contains a single thin fiber or a single row of thin fiber strips.

Secondly we shall present some numerical results for a composite that contains an infinite staggered array of thin strips. This geometry is related to the rectangular array of thin fibers first studied by Wang (1994), but the staggered array may be more advantageous even though the amount of materials used is the same.

Although this paper is written in terms of heat transfer, the results may be applied to electric and magnetic statics, potential flow, mass diffusion, and the flow through porous media. The latter has been studied by Martinez et al. (1992), who considered a regular array of insulated strips.

The strips will be assumed to be either insulated or perfectly conducting. The partially conducting case requires a different modeling process, and will not be addressed in this paper.

2 Effect of a Single Strip and a Single Row of Strips

Consider first a single thin strip in an infinite medium. Since the domain is infinite, the single strip does not alter the global effective property of the medium. There are, however, local effects. Let the cross section of the strip be at $x = 0$, $|y| \le b$. Let the strip be insulated and a flux or temperature gradient of -1 is applied at $x \to \pm\infty$. Since the temperature satisfies Laplace's equation, the solution is

$$T(x, y) = -\text{sign } (x) \text{ Re}[\sqrt{z^2 + b^2}] \quad (1)$$

where $z = x + iy$. There are no local effects for an insulated strip with a vertical flux in the y direction. Equation (1) shows there is a temperature jump across the strip and the maximum local temperature increase from that without the strip is b at the midpoint $(0, 0)$.

Now consider a vertical perfectly conducting strip. There is no effect if the flux is horizontal. If the flux is vertical ($T_y|_{y\to\pm\infty} = -1$) the solution is

$$T(x, y) = -\text{sign } (y) \text{ Im}[\sqrt{z^2 + b^2}]. \quad (2)$$

This temperature is continuous everywhere.

If we set $z = ib + re^{i\theta}$, $r \ll b$ we find in both cases the flux or temperature gradient has a weak singularity ($\sim r^{-1/2}$) at the edges of the strips.

Now consider an infinite array of vertical strips each of width $2b$ arranged along the y-axis with period of 2. The strips are all in the same ($x = 0$) plane, and resemble a thin two-dimensional screen. Again there is no effect if the strips are perfectly conducting under a horizontal flux. If the strips are insulated one can use the Swarz-Christoffel transform (Milne-Thomson, 1960) to derive the solution

$$T(x, y) = -\text{sign } (x) \frac{2}{\pi} \text{Re}\left\{ \sinh^{-1}\left[i\lambda \cosh\left(\frac{\pi z}{2}\right)\right]\right\} \quad (3)$$

where $\lambda = 1/\cos(\pi b/2) > 1$. A similar solution for this case was also derived by Martinez et al. (1992). On the axis $y = 0$ as $x \to \infty$. Equation (3) gives

$$T \sim -x - \frac{2}{\pi} \ln (\lambda) + 0(e^{-\pi x}). \quad (4)$$

Thus as a whole the strips give a collective additional temperature drop (resistance) of

$$\Delta T = \frac{4}{\pi} \ln\left[\frac{1}{\cos\left(\dfrac{\pi b}{2}\right)}\right] > 0. \quad (5)$$

This resistance would effect the property of the composite.

Consider perfectly conducting strips each one vertical and arranged one unit apart along the x-axis like a grate or open venetian blind. If the heat flux is vertical the solution is

$$T(x, y) = -\text{sign } (y) \frac{2}{\pi} \text{Re}\left\{ \sinh^{-1}\left[i\lambda \cos\left(\frac{\pi z}{2}\right)\right]\right\} \quad (6)$$

where $\lambda = 1/\cosh (\pi c/2) < 1$ and c is the half-width of a strip. Equation (6) is not the conjugate of Eq. (3). Similarly along $x = 0$ as $y \to \infty$, Eq. (6) becomes

$$T \sim -y - \frac{2}{\pi} \ln \lambda + 0(e^{-\pi y}) \quad (7)$$

which gives the additional temperature recovery due to the conducting grate

$$\Delta T = \frac{4}{\pi} \ln\left[\frac{1}{\cosh\left(\dfrac{\pi c}{2}\right)}\right] < 0. \quad (8)$$

3 Effect of an Array of Strips

Complex transform does not apply when there is a doubly periodic array of strips in the medium. Martinez et al. (1992) used finite differences and Wang (1994) used eigenfunction expansions and point match to solve the regular rectangular array of thin strips. In this paper we study the more difficult case of the staggered array of strips. Figure 1(*a*) shows the cross section. Due to symmetry properties we need to consider only the rectangular subregion enclosed by the dashed lines. Let the dimensional temperature be T_1 and T_0 at the corners shown. Normalize all lengths by L and define the nondimensional temperature

[1] Departments of Mathematics and Mechanical Engineering, Michigan State University, East Lansing, MI 48824. Mem. ASME.
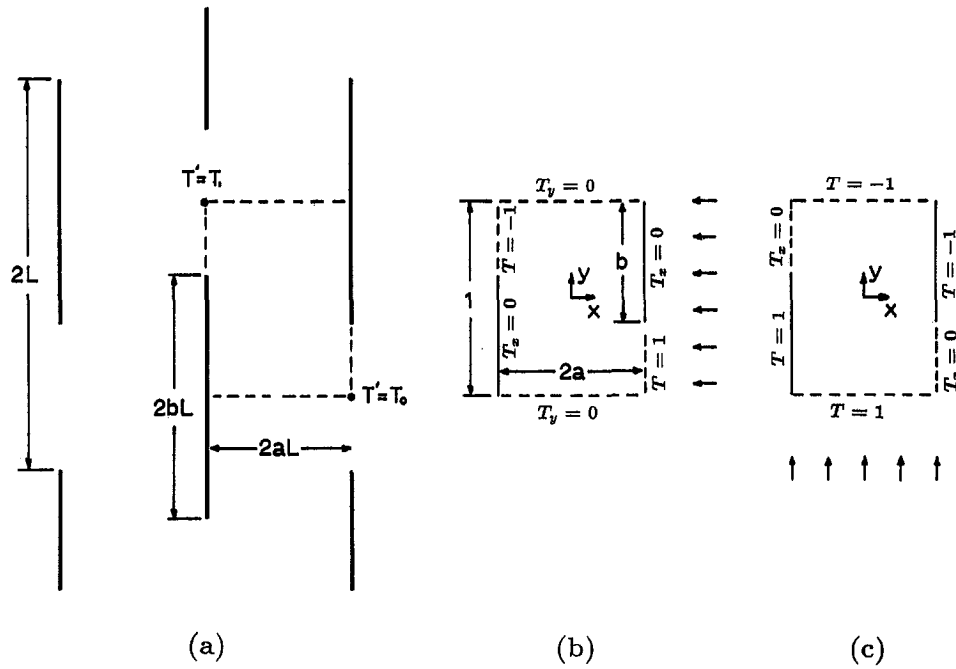
Copyright © 1999 by ASME

Fig. 1 (a) Cross section of a staggered array of strips, (b) a subregion for insulated strips under perpendicular flux, (c) a subregion for perfectly conducting strips under parallel flux

$$T = \frac{2T' - T_0 - T_1}{T_0 - T_1}. \qquad (9)$$

Now if the strips are adiabatic only the conductivity in the direction normal to the strips is affected. The boundary conditions on the subregion are shown in Fig. 1(b), where a set of cartesian axes is placed at the center. The general solution to

$$T_{xx} + T_{yy} = 0 \qquad (10)$$

and satisfying top and bottom boundary conditions $T_y(x, \pm\frac{1}{2}) = 0$ is

$$T(x, y) = A_0 x + B_0 + \sum_1^\infty [A_n e^{\alpha_n(x-a)}$$
$$+ B_n e^{-\alpha_n(x+a)}] \cos [\alpha_n(y + \tfrac{1}{2})] \qquad (11)$$

where $\alpha_n = n\pi$. The side boundary conditions also imply polar antisymmetry property

$$T(x, y) = -T(-x, -y). \qquad (12)$$

Using Eqs. (11), (12) and compare like harmonics one obtains $B_0 = 0, B_n = -(-1)^n A_n$ $(n \neq 0)$. Thus the number of unknown constants is cut in half,

$$T(x, y) = A_0 x + \sum_1^\infty A_n[e^{\alpha_n(x-a)}$$
$$- (-1)^n e^{-\alpha_n(x+a)}] \cos [\alpha_n(y + \tfrac{1}{2})]. \qquad (13)$$

The remaining boundary conditions are on $x = a$:

$$\frac{\partial T}{\partial x}(a, y) = 0, \quad \frac{1}{2} - b < y \le \frac{1}{2} \qquad (14)$$

$$T(a, y) = 1, \quad -\frac{1}{2} \le y < \frac{1}{2} - b. \qquad (15)$$

Since these conditions are mixed, one cannot use Fourier inversion but point match is possible. We truncate A_n to N terms and

satisfy Eqs. (14), (15) at $N + 1$ equally spaced points along $x = a$.

$$y_i = \frac{(i - 0.5)}{N + 1} - 0.5 \quad i = 1 \text{ to } N + 1 \qquad (16)$$

$$A_0 + \sum_1^N A_n \alpha_n[1 + (-1)^n e^{-2\alpha_n a}] \cos [\alpha_n(y_i - 0.5)] = 0,$$
$$y_i > 0.5 - b \qquad (17)$$

$$A_0 a + \sum_1^N A_n[1 - (-1)^n e^{-2\alpha_n a}] \cos [\alpha_n(y_i - 0.5)] = 1,$$
$$y_i < 0.5 - b \qquad (18)$$

Including A_0, there are $N + 1$ unknowns and linear equations. The accuracy can be improved by increasing N. We find for $N = 30$ the maximum error is less than two percent near the tip of the strip at $(a, 0)$, where a week singularity in the derivative of T exists. If N is increased to 60 the error is about one percent.

Now consider the other extreme when the strips are perfectly conducting. In this case the strips only affect the heat transfer in the direction parallel to the strips. Due to symmetry considerations, the boundary conditions on the subregion is shown in Fig. 1(c). Again using polar antisymmetry property and $T(x, \pm1/2) = \mp1$ the general solution is found to be

$$T(x, y) = -2y + \sum_1^\infty C_n[e^{\alpha_n(x-a)}$$
$$+ (-1)^n e^{-\alpha_n(x+a)}] \sin [\alpha_n(y + \tfrac{1}{2})]. \qquad (19)$$

The boundary conditions to be satisfied are

$$T(a, y) = -1, \quad \tfrac{1}{2} - b < y \le \tfrac{1}{2} \qquad (20)$$

$$\frac{\partial T}{\partial x}(a, y) = 0, \quad -\frac{1}{2} \le y < \frac{1}{2} - b. \qquad (21)$$

Truncate C_n to N terms and choose N points along the boundary. Equations (20), (21) become
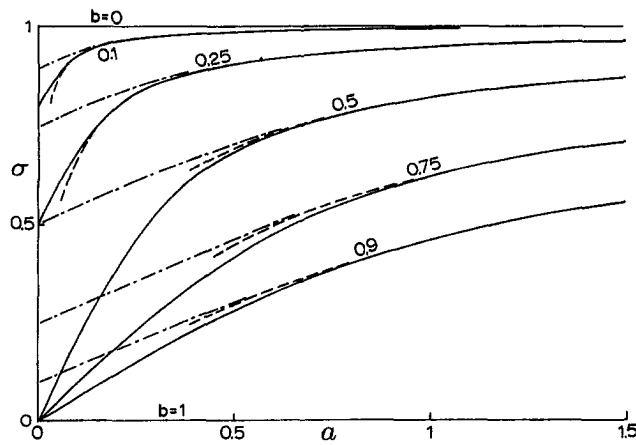
Fig. 2 Effective perpendicular conductivity for staggered insulated strips. —— results using method of Section 3, - - - Eq. (25), – · – · – results for the rectangular array, adapted from Wang (1994).

$$\sum_{1}^{N} C_n[1 + (-1)^n e^{-2\alpha_n a}] \sin [\alpha_n(y_i + 0.5)] = 2y_i - 1,$$

$$y_i > 0.5 - b \quad (22)$$

$$\sum_{1}^{N} C_n \alpha_n[1 - (-1)^n e^{-2\alpha_n a}] \sin [\alpha_n(y_i + 0.5)] = 0,$$

$$y_i < 0.5 - b \quad (23)$$

where $y_i = (i - 0.5)/N - 0.5$. The magnitude of the error is similar to the insulated case.

4 Effective Conductivity

The effective normal conductivity of a composite containing a staggered array of insulated strips can be computed by considering the heat flux across the $x = 0$ line in Fig. 1(b). Let σ be the ratio of effective conductivity to the conductivity of the imbedding medium. One obtains

$$\sigma = a \int_{-1/2}^{1/2} \frac{\partial T}{\partial x}\bigg|_{x=0} dy = aA_0. \quad (24)$$

The coefficient A_0 obtained in the previous section is a function of both a and b. If $a \gg 1$ one can envision widely separated thin screens. Using the additional temperature drop (Eq. (5)) every $2a$ distance, an approximate formula can be derived

$$\sigma = \cfrac{1}{1 + \cfrac{1}{2a}\Delta T} = \cfrac{1}{1 + \cfrac{2}{\pi a}\ln\left[\cfrac{1}{\cos\left(\cfrac{\pi b}{2}\right)}\right]},$$

$$a \gg 1. \quad (25)$$

On the other hand if $a \ll 1$ the strips become stacked together. The heat flux would be completely blocked if $b \geq 1/2$ and channels of width $(1 - 2b)$ exist if $b < 1/2$. Thus

$$\sigma = \begin{cases} 0 & b \geq \frac{1}{2} \\ 1 - 2b & b < \frac{1}{2} \end{cases}, \quad a \to 0. \quad (26)$$

The numerical solution using Eq. (24) is compared with the approximate formulas in Fig. 2. We see Eq. (25) is fairly accurate when $a > 1$. Due to its limited range of validity Eq. (25) is not extended to small values of a.

The effective tangential conductivity of a composite containing a staggered array of perfectly conducting strips is slightly more involved. The vertical heat flux should be integrated along a path which avoids the conducting strips. We take the path $(-a, 0.5), (0, 0.5), (0, -0.5), (a, -0.5)$ in Fig. 1(c),

$$\sigma = \frac{1}{4a}\left[\int_{-a}^{0} -\frac{\partial T}{\partial y}\bigg|_{y=0.5} dx + \int_{-0.5}^{0.5}\right.$$

$$\left. -\frac{\partial T}{\partial x}\bigg|_{x=0} dy + \int_{0}^{a} -\frac{\partial T}{\partial y}\bigg|_{y=-0.5} dx\right]$$

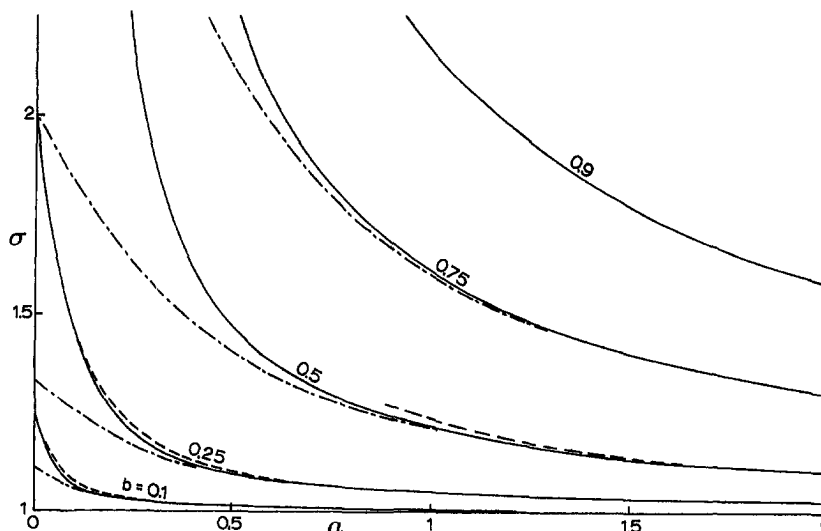$$= 1 - \frac{1}{2a}\sum B_n[1 - (-1)^n e^{-2\alpha_n a}]. \quad (27)$$

Fig. 3 Effective tangential conductivity for staggered perfectly conducting strips. —— results using method of Section 3, - - - Eq. (28), – · – · – results for the rectangular array, from Wang (1994).

For b small we can make use of the single conducting grate solution. Adjusting for appropriate length scales we find from Eq. (8) the approximate formula

$$\sigma = \frac{1}{1 + 2a\Delta T} = \frac{1}{1 + \dfrac{8a}{\pi} \ln \left[\dfrac{1}{\cosh\left(\dfrac{\pi b}{4a}\right)} \right]} . \quad (28)$$

Equation (28) gives the correct limit for $b < 0.5$ and $a \to 0$,

$$\sigma = \frac{1}{1 - 2b} . \quad (29)$$

Figure 3 shows the effective conductivity computed from eigenfunction expansions. We see Eq. (28) is accurate for $b < 0.25$. Note that for $b \geq 0.5$ conductivity approaches infinity as $a \to 0$, since the strips would become continuous conductors.

5 Discussions

We have determined the thermal properties of a composite containing staggered periodic thin strips. Usually these fiber inclusions have vastly different conductivities than their imbedding medium. Thus the ideal cases of perfectly conducting or insulated strips are reasonable models. These strips may represent flat fiber bundles such as those used in fiber-reinforced composites.

In contrast to a composite with circular cylindrical fibers the conductivity of a composite with aligned flat strips show a high degree of anisotropy. In fact the conductivity in one direction may be unaffected while that in the other direction can be greatly altered. Such property may be utilized to optimize composite materials since usually transport property or strength of a composite is not essential in every direction.

We now compare the differences in the effective conductivities between the present staggered array and a rectangular array studied by Wang (1994). The results of the rectangular array are adapted to the current geometrical definitions and included in our plots. Figure 2 shows the conductivity for a staggered array of insulated strips is smaller than that of the rectangular array. The difference is small for large spacing a since each plane or panel of strips becomes independent. However, for small a the stagger causes large drops in conductivity, perhaps due to the shielding effect between successive panels. On the other hand, Fig. 3 shows the stagger of conducting strips increases conductivity. Again, for small a, the difference may be substantial, especially if $b \geq 0.5$ where $\sigma \to 1/(1 - b)$ for the rectangular array and $\sigma \to \infty$ for the staggered array.

In conclusion, stagger may be utilized to increase or decrease conducting (thermal, electrical, mass diffusion) without changing the amount of materials in the composite. Our Figs. (2), (3) should be useful in the design of composite materials. Note that since the volume fraction is zero, all homogenization theories would result in σ identically equal to 1, which is quite misleading.

References

Aboudi, J., 1991, *Mechanics of Composite Materials,* Elsevier, Amsterdam.

Christensen, R. M., 1979, *Mechanics of Composite Materials,* John Wiley and Sons, New York.

Martinez, M. J., Dykhuizen, R. C., and Eaton, R. R., 1992, "The Apparent Conductivity for Steady Unsaturated Flow in Periodically Fractured Porous Media," *Water Resources Res.,* Vol. 28, No. 11, pp. 2879–2887.

Milne-Thomson, L. M., 1960, *Theoretical Hydrodynamics,* McMillan, New York.

Wang, C. Y., 1994, "Conductivity of materials containing fibers of rectangular cross section," *Mech. Mat.,* Vol. 17, pp. 71–77.

Thermal Contact Conductance of Sintered Copper Coatings on Ferro-Alloy

E. Marotta,[1] L. S. Fletcher,[2] T. Aikawa,[3] K. Maki,[3] and Y. Aoki[3]

Nomenclature

C = contriction parameter
D = asperity slope
E' = effective modulus of elasticity ($1/E' = (1 - \nu_1^2)/E_1 + (1 - \nu_2^2)/E_2$)
F = flatness
H = thermal contact conductance
h' = thermal contact conductance of coated surface
k = thermal conductivity
m = combined average absolute slope of profile (rad) ($= \sqrt{m_1^2 + m_2^2}$)
P = pressure
R = combined roughness (RMS) ($= \sqrt{\sigma_1^2 + \sigma_2^2}$)
T_m = mean interface temperature
t = coating thickness
H = microhardness
H_e = effective microhardness
W = waviness
γ = index of deformation
$\tan \theta$ = absolute slope of profile

Subscripts

a = average
app = apparent
q = root mean square (RMS)
s = substrate
c = coating, coating
$1, 2$ = one side substrate and other side of substrate

Introduction

Some internal combustion engines are composed of aluminum blocks with steel cylinder sleeves and ferrous alloy valve seats. A heat transfer analysis of the engine requires an understanding of the thermal resistances associated with the various engine components. The combustion of the fuel mixture in an internal combustion engine generates exhaust gases, which are at extremely high temperatures and pressures. The exhaust gas surrounds the exhaust valve as it leaves the combustion chamber, and the resulting high temperatures cause the exhaust valve and valve seat to reach comparable temperatures. In order to avoid damage, heat is transferred from the exhaust valve to the valve seat as they come into contact with each other during the opening and closing cycle. The heat removed from the exhaust valve to the valve seat is subsequently transferred to the engine block and then to the coolant that circulates near the valve seat and throughout the engine block.

For b small we can make use of the single conducting grate solution. Adjusting for appropriate length scales we find from Eq. (8) the approximate formula

$$\sigma = \frac{1}{1 + 2a\Delta T} = \frac{1}{1 + \dfrac{8a}{\pi} \ln \left[\dfrac{1}{\cosh\left(\dfrac{\pi b}{4a}\right)} \right]} \,. \quad (28)$$

Equation (28) gives the correct limit for $b < 0.5$ and $a \to 0$,

$$\sigma = \frac{1}{1 - 2b} \,. \quad (29)$$

Figure 3 shows the effective conductivity computed from eigenfunction expansions. We see Eq. (28) is accurate for $b < 0.25$. Note that for $b \geq 0.5$ conductivity approaches infinity as $a \to 0$, since the strips would become continuous conductors.

5 Discussions

We have determined the thermal properties of a composite containing staggered periodic thin strips. Usually these fiber inclusions have vastly different conductivities than their imbedding medium. Thus the ideal cases of perfectly conducting or insulated strips are reasonable models. These strips may represent flat fiber bundles such as those used in fiber-reinforced composites.

In contrast to a composite with circular cylindrical fibers the conductivity of a composite with aligned flat strips show a high degree of anisotropy. In fact the conductivity in one direction may be unaffected while that in the other direction can be greatly altered. Such property may be utilized to optimize composite materials since usually transport property or strength of a composite is not essential in every direction.

We now compare the differences in the effective conductivities between the present staggered array and a rectangular array studied by Wang (1994). The results of the rectangular array are adapted to the current geometrical definitions and included in our plots. Figure 2 shows the conductivity for a staggered array of insulated strips is smaller than that of the rectangular array. The difference is small for large spacing a since each plane or panel of strips becomes independent. However, for small a the stagger causes large drops in conductivity, perhaps due to the shielding effect between successive panels. On the other hand, Fig. 3 shows the stagger of conducting strips increases conductivity. Again, for small a, the difference may be substantial, especially if $b \geq 0.5$ where $\sigma \to 1/(1 - b)$ for the rectangular array and $\sigma \to \infty$ for the staggered array.

In conclusion, stagger may be utilized to increase or decrease conducting (thermal, electrical, mass diffusion) without changing the amount of materials in the composite. Our Figs. (2), (3) should be useful in the design of composite materials. Note that since the volume fraction is zero, all homogenization theories would result in σ identically equal to 1, which is quite misleading.

References

Aboudi, J., 1991, *Mechanics of Composite Materials,* Elsevier, Amsterdam.
Christensen, R. M., 1979, *Mechanics of Composite Materials,* John Wiley and Sons, New York.
Martinez, M. J., Dykhuizen, R. C., and Eaton, R. R., 1992, ''The Apparent Conductivity for Steady Unsaturated Flow in Periodically Fractured Porous Media,'' *Water Resources Res.,* Vol. 28, No. 11, pp. 2879–2887.
Milne-Thomson, L. M., 1960, *Theoretical Hydrodynamics,* McMillan, New York.
Wang, C. Y., 1994, ''Conductivity of materials containing fibers of rectangular cross section,'' *Mech. Mat.,* Vol. 17, pp. 71–77.

Thermal Contact Conductance of Sintered Copper Coatings on Ferro-Alloy

E. Marotta,[1] L. S. Fletcher,[2] T. Aikawa,[3] K. Maki,[3] and Y. Aoki[3]

Nomenclature

- C = contriction parameter
- D = asperity slope
- E' = effective modulus of elasticity ($1/E' = (1 - \nu_1^2)/E_1 + (1 - \nu_2^2)/E_2$)
- F = flatness
- H = thermal contact conductance
- h' = thermal contact conductance of coated surface
- k = thermal conductivity
- m = combined average absolute slope of profile (rad) ($= \sqrt{m_1^2 + m_2^2}$)
- P = pressure
- R = combined roughness (RMS) ($=\sqrt{\sigma_1^2 + \sigma_2^2}$)
- T_m = mean interface temperature
- t = coating thickness
- H = microhardness
- H_e = effective microhardness
- W = waviness
- γ = index of deformation
- $\tan\theta$ = absolute slope of profile

Subscripts

- a = average
- app = apparent
- q = root mean square (RMS)
- s = substrate
- c = coating, coating
- $1, 2$ = one side substrate and other side of substrate

Introduction

Some internal combustion engines are composed of aluminum blocks with steel cylinder sleeves and ferrous alloy valve seats. A heat transfer analysis of the engine requires an understanding of the thermal resistances associated with the various engine components. The combustion of the fuel mixture in an internal combustion engine generates exhaust gases, which are at extremely high temperatures and pressures. The exhaust gas surrounds the exhaust valve as it leaves the combustion chamber, and the resulting high temperatures cause the exhaust valve and valve seat to reach comparable temperatures. In order to avoid damage, heat is transferred from the exhaust valve to the valve seat as they come into contact with each other during the opening and closing cycle. The heat removed from the exhaust valve to the valve seat is subsequently transferred to the engine block and then to the coolant that circulates near the valve seat and throughout the engine block.
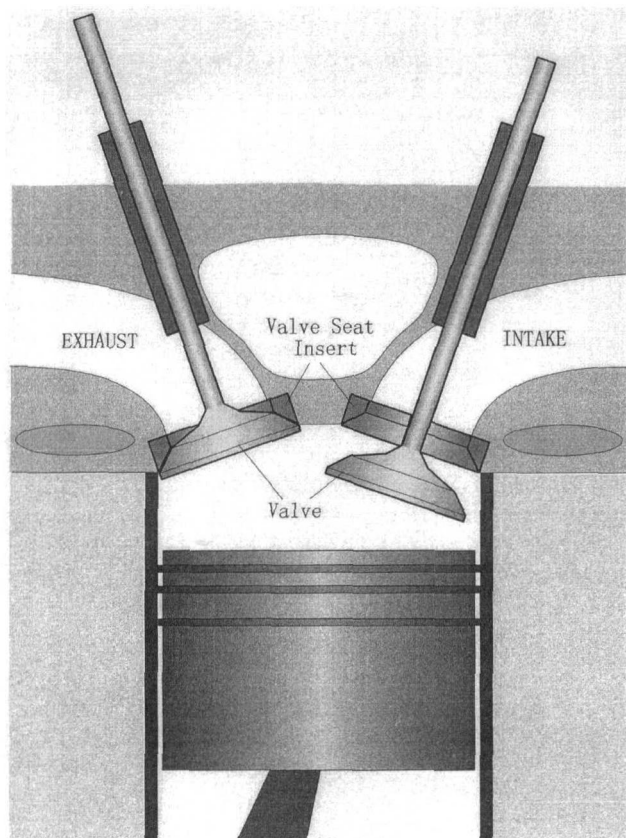
Fig. 1 Configuration of valve seat and engine block contact

The contact between a valve seat and the block of an internal combustion engine, utilized extensively in aluminum engines (Fig. 1), presents a significant barrier to heat dissipation. Heat transfer across pressed junctions (e.g., the valve seat/engine block junction) is restricted because the real contact area is only a small percentage of the apparent contact area due to surface irregularities such as surface roughness, which limits contact to a relatively few small spots. As a result, heat is constrained to pass primarily through narrow bridges of contact between the two surfaces. In order to improve the heat transfer between the valve seat and the engine block, sintered ferrous valve seats with sintered copper coatings have been proposed with the expectation that the copper/aluminum junction will result in improved heat dissipation. It is clear that the heat transfer rate across these junctions greatly effects the overall temperature of the exhaust valve and, ultimately, the engine's performance and fuel efficiency.

A review of the literature for coated surfaces (Cooper et al., 1969; Mal'kov and Dobashin, 1969; Mikic and Carnasciali, 1969; Antonetti and Yovanovich, 1985; and Kang et al., 1989) reveals that most studies of thermal contact conductance for uncoated or metallic coated surfaces have not dealt with sintered materials. Hence, a study of sintered metals that also contains sintered metallic coatings hot-pressed onto their surfaces would be beneficial for automotive applications. Further, there appears to be no in-depth experimental study that evaluates the thermal contact resistance or conductance for valve seat/engine block junctions. In addition, experimental data for the use of sintered coatings to enhance the thermal contact conductance and thus decrease the effects due to poor surface imperfections found at valve seat/engine block junctions are severely lacking.

This experimental study evaluates the thermal contact conductance for several commercially important sintered alloys over a range of pressures and temperatures which approximate conditions at a valve seat/engine block interface for an internal combustion engine. In addition, sintered copper coatings hot-pressed onto a sintered ferrous substrate are investigated for possible enhancement of the thermal contact conductance.

This experimental study also examines the appropriateness of the use of an existing model developed for coated metallic surfaces for use over the range of parameters employed in an engine block. A thermal contact conductance model developed for plastic asperity deformation of uncoated surfaces was also compared to the experimental data. This analysis adds greatly to the knowledge of whether this existing model can be utilized to predict thermal contact conductance values at higher pressures and temperatures than previously studied.

Experimental Program

This experimental investigation involved the evaluation of the thermal conductance for several sintered copper coatings hot-pressed onto a ferro-alloy, as well as several metallic alloys, that were processed in a similar manner. The details of the experimental test facility used in this investigation, along with its construction and operation, has been previously reported by Marotta and Fletcher (1996). A series of thermal contact conductance tests were conducted for ferrous alloys that were coated with sintered powder copper hot-pressed onto the sintered powder ferro-alloy substrate.

Since the surface profile of the contacting surfaces has a profound effect on the measured thermal contact conductance values, all surfaces were characterized to provide root mean square (RMS) and centerline average (CLA) roughness, RMS and average waviness, overall flatness deviation, and RMS asperity slope information. The surface microhardness also influences the thermal contact conductance values. Consequently, the Vickers microhardness of the bare (including the cast aluminum alloy fluxmeter) and copper coated ferro-alloy specimens were measured for an indentor load range of 25 to 1000 grams force. The surface characteristics and hardness information are provided in Table 1.

The experimental investigation was conducted at pressures from 2.5 to 25 MPa (363 to 3625 psi) with sintered copper coating thicknesses ranging from 0.02 to 0.2 cm (7.87 to 78.7 mils). In order to make an appropriate comparison, tests were conducted at mean interface temperatures of 100°C, 125°C, 175°C, and 200°C (212°F, 257°F, 347°F, and 392°F). The experimental results include the thermal contact conductance for each copper coating thickness and bare surface over the range of pressures investigated.

The average overall uncertainty in thermal contact conductance values for each specimen is approximately 12 percent with a maximum of 16.0 percent. The uncertainty due to the temperature difference at the ferro-alloy/cast aluminum alloy interface had a maximum magnitude of 13.5 percent, using the technique described by Kline and McClintock (1953).

Results and Discussions

The thermal contact conductance results were obtained for several copper coating thicknesses and base materials at test conditions which approximate some of the conditions (such as interface pressure) that exist at a valve seat/engine block interface of an internal combustion engine. These thermal contact conductance data are presented as a function of mean interface pressure and temperature.

The thermal contact conductance data for the uncoated ferro-alloy sample in contact with uncoated cast aluminum alloy are presented in Fig. 2 as functions of both increasing and decreasing apparent contact pressure and mean interface temperature. The thermal contact conductance values ranged from 3,600 to 10,300 W/m²-K (626 to 1,791 Btu/ft²-hr °F) over the range of temperatures and pressures. The relatively low magnitude of the thermal contact conductance can be attributed to the low

Table 1 Thermal conductivity, Vicker's microhardness, and surface metrological data for test specimens

| Base Material-Fluxmeter Material	Coating Material	Ks/Kc (W/m K)	Hs/Hc (kg/mm²)	t mm	Ra um	Rq um	Wa um	Wq um	F um	Asperity Slope rad
Ferro-alloy Aluminum 319 alloy FAL-1	Uncoated Uncoated	24-26/ NA 150-158	390/ NA 112	0.0	1.12 1.23	1.34 1.56	2.37 1.11	2.77 1.33	19.6 18.3	0.197 0.225
Copper-alloy Aluminum 319 alloy FAL-2	Uncoated Uncoated	356-388/ NA 150-158	67.5/ NA 112	0.0	1.36 1.83	1.55 2.26	2.34 1.65	2.75 2.04	19.5 23.1	0.242 0.246
Ferro-alloy Aluminum 319 alloy FAL-3	Cu Coated Ferro-allo Uncoated	24-26/356-388 150-158	390/97 112	0.2	1.66 1.52	2.23 1.88	1.55 1.36	1.91 1.65	21.3 16.7	0.270 0.237
Ferro-alloy Aluminum 319 alloy FAL-5	Cu Coated Ferro-allo Uncoated	24-26/356-388 150-158	390/106 112	0.5	1.14 1.60	1.42 2.01	1.54 1.64	1.81 2.26	16.4 22.3	0.270 0.225
Ferro-alloy Aluminum 319 alloy FAL-6	Cu Coated Ferro-allo Uncoated	24-26/356-388 150-158	390/90 112	1.0	1.21 1.54	1.5 1.92	1.86 1.61	2.17 1.91	20 19.35	0.229 0.231
Ferro-alloy Aluminum alloy FAL-7	Cu Coated Ferro-allo Uncoated	24-26/356-388 150-158	390/60 112	2.0	1.22 1.44	1.49 1.82	2.19 1.56	2.62 1.99	19.1 21.1	0.317 0.235
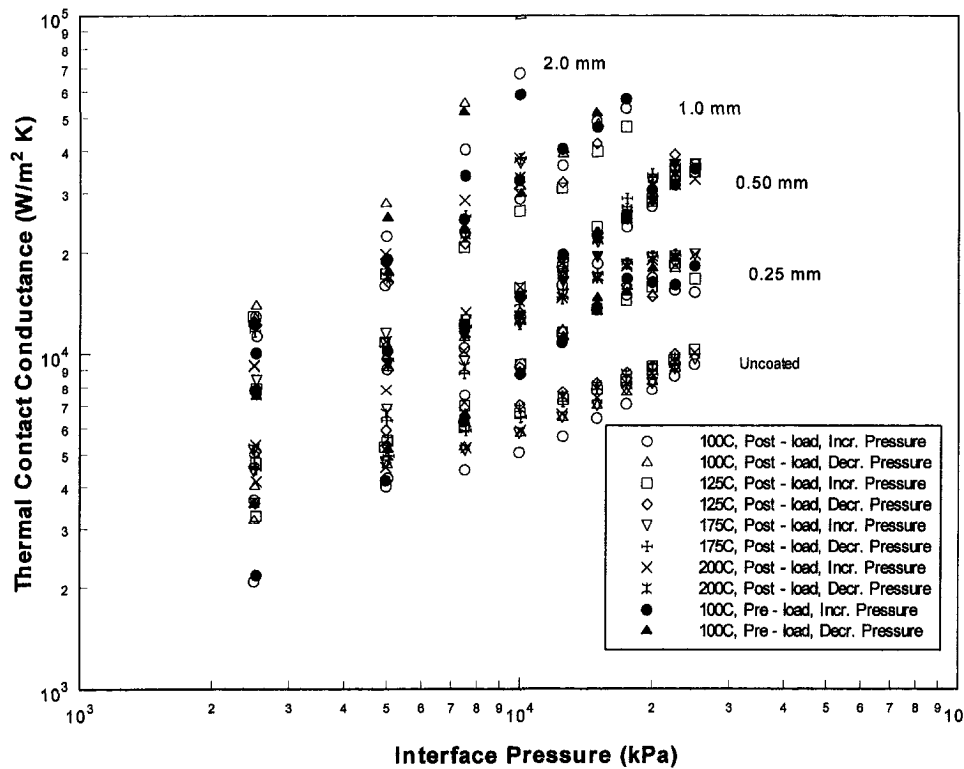
Fig. 2 Thermal contact conductance as a function of apparent interface pressure for uncoated and coated ferro-alloys in junction with uncoated aluminum 319

thermal conductivity of the ferro-alloy and its relatively high hardness (as shown in Table 1), which results in a very small actual contact area. The thermal contact conductance data also indicates a hystersis effect, which suggests plastic deformation of the asperities. The thermal contact conductance data obtained from this experimental test will be used as a baseline for comparison to copper coated ferro-alloy specimens.

The thermal contact conductance data for the 0.2 and 0.5 mm sintered copper coating thicknesses, hot-pressed onto the ferro-alloy specimen, in contact with uncoated cast aluminum alloy are also shown in Fig. 2 as functions of both increasing and decreasing apparent contact pressure and mean interface temperature. The magnitude of the thermal contact conductance values was enhanced by factors of two and four, respectively, toward the higher interface pressures, while the hystersis effect observed for the uncoated ferro-alloy specimen was nonexistent. In addition, a maximum value for the thermal contact conductance can be observed as evident in the data at the higher apparent interface pressures.

The thermal contact conductance data for the 1.0 and 2.0 mm sintered copper coating thicknesses applied to a ferro-alloy specimen in contact with an uncoated cast aluminum alloy are again shown in Fig. 2 as functions of apparent interface pressure and interface temperature. The thermal contact conductance
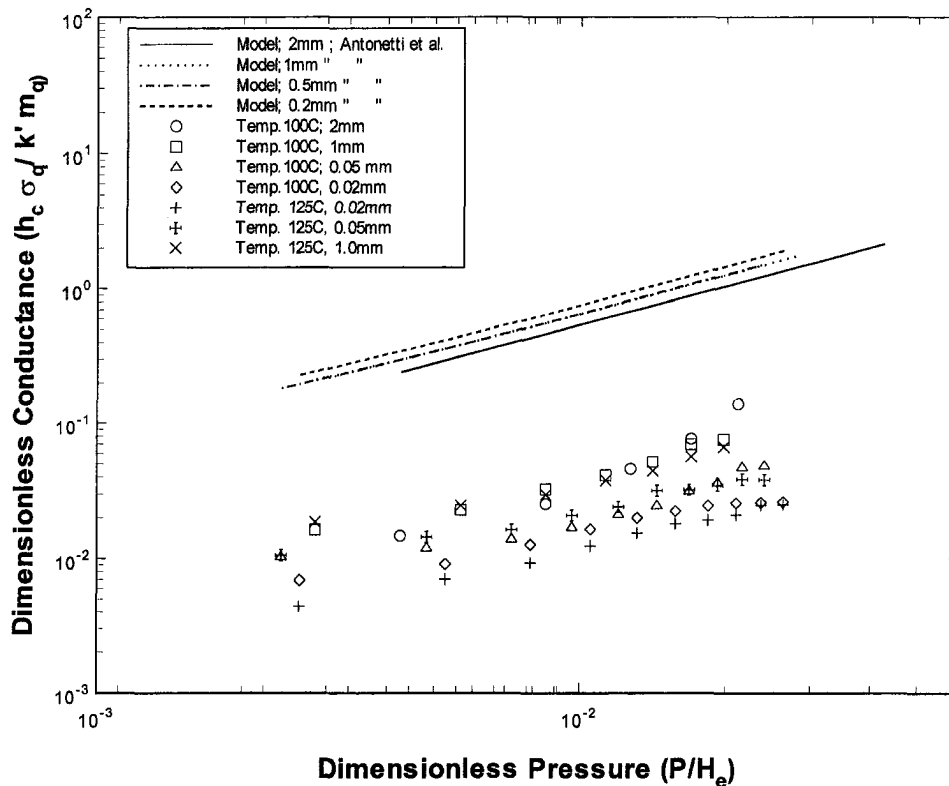
Fig. 3 A comparison of the dimensionless thermal contact conductance values with the Antonetti and Yovanovich coated plastic model correlation

data for the 2.0 mm coating thickness show a hysteresis effect with increasing and decreasing pressure while the 1.0 mm coating thickness does not. This suggests that the coating thickness is sufficiently large to cause plastic deformation of the aspersities while the 1.0 mm coating thickness still exhibits elastic deformation.

A priori assumption of the mode of deformation can lead to wrong conclusions; one such example is the prediction of thermal contact conductance for two surfaces in contact. To determine the mode of deformation, an index developed by Mikic (1974) helps predict whether elastic or plastic deformation dominates or whether a combination of either two modes of deformation is present. The mode of deformation can be determined from the value of the parameter

$$\gamma = \frac{H}{E' \tan \theta} \qquad (1)$$

where elastic deformation dominates for values greater than or equal to 3 and plastic deformation dominates for values less than or equal to 0.33. Thus, Mikic (1974) concluded that the mode of deformation depends on material properties and the shape of the asperity slope. Based on Mikic's equation, the value for γ equals 0.052 for the base materials employed. Thus, we conclude that plastic deformation will dominate at the asperity contacts. From this conclusion, the plastic model correlations by Antonetti and Yovanovich (1985) for coated surfaces and Cooper, Mikic, and Yovanovich (1969) for uncoated surfaces were employed for comparison.

A comparison of the dimensionless thermal contact conductance values with an existing plastic model developed by Antonetti and Yovanovich (1985) for soft coatings on hard substrates is shown by Fig. 3. The model assumes plastic deformation a priori of the surface asperities to reduce the experimental data into the corresponding dimensionless parameters. Therefore, in comparing the experimental data to the model, plastic deforma-

tion of the sintered copper coatings was assumed. This assumption then allows the experimental data measured for the sintered copper coatings to be compared to the model. The equation for the plastic model correlation developed by Antonetti and Yovanovich (1985) for coated surfaces is

$$h_c' = h_c \left(\frac{H}{H'} \right)^{0.93} \left(\frac{k_1 + k_2}{C_2 k_1 + k_2} \right) . \qquad (2)$$

h_c is the uncoated contact conductance, H' is the effective hardness of the layer-substrate combination, C_2 is the constriction parameter correction factor, and k_1 and k_2 are the thermal conductivity of the base materials (sintered ferro-alloy and cast aluminum alloy). Therefore, the coated contact conductance is the product of the uncoated contact conductance, a mechanical modification factor (the ratio of the hardnesses), and the thermal modification factor due to the coating.

The slopes of the sintered copper coatings plotted as a function of dimensionless thermal conductance versus dimensionless pressure, as shown in Fig. 3, approximate that of the correlation; however, the correlation predicts values that are one order of magnitude higher than the experimental data. The dimensionless thermal conductance data also show considerable spread between the 2.0-mm sintered copper coating and the 0.2-mm sintered copper coating. The data does show higher thermal contact conductance with increasing sintered copper coating thickness; however, an optimum thickness appears to exist at 1.0 mm, as shown by the indistinguishable differences in thermal conductance data between the 1.0 mm and 2.0 mm sintered copper coatings.

A comparison of the dimensionless thermal contact conductance values with the existing plastic model correlation for uncoated surfaces developed by Cooper, Mikic, and Yovanovich (1969) is shown by Fig. 4. The equation for the Cooper, Mikic, Yovanovich correlation is
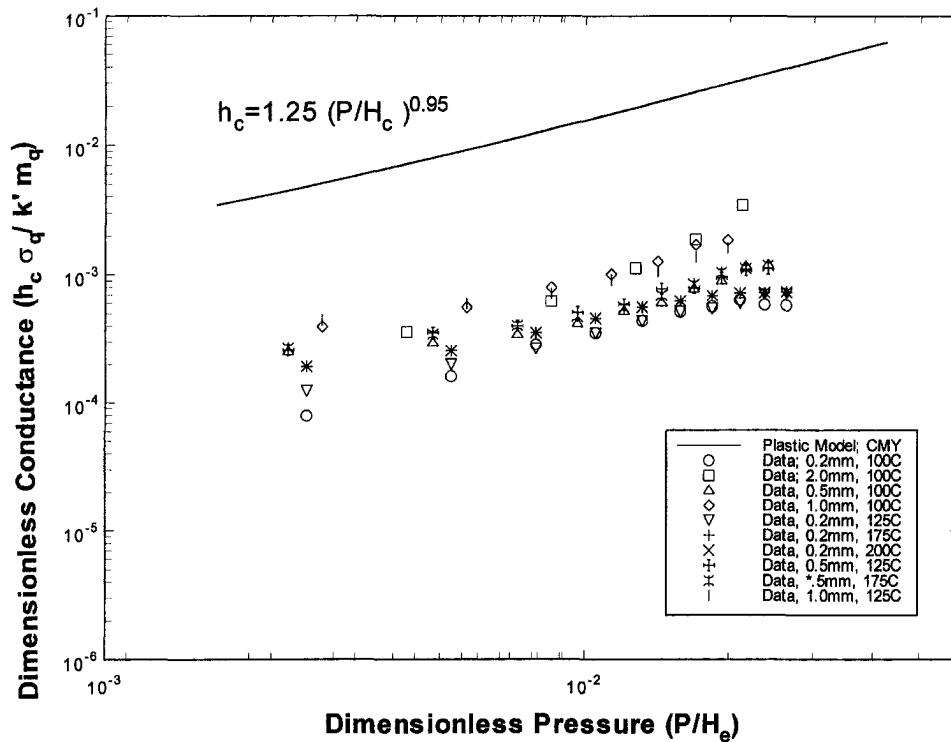
$$h_c = 1.25 (P/H_c)^{0.95}$$

Fig. 4 A comparison of the dimensionless thermal contact conductance values with Cooper, Mikic, and Yovanovich plastic model correlation

$$h_c = 1.45 \left(\frac{m}{\sigma}\right)\left(\frac{2k_1k_2}{k_1 + k_2}\right)\left(\frac{P}{H}\right)^{0.985}. \quad (3)$$

This model also assumes plastic deformation a priori of the surface asperities to predict the thermal contact conductance at the contacting surfaces. This comparison between the experimental thermal contact conductance values and the values predicted by the correlation was considered because of the extremely high coating thicknesses that were sintered onto the ferro-alloy specimens. The assumption is that the coating thicknesses are so large that both the mechanical and thermal modification factors (due to the ferro-alloy substrate) have no influence on the thermal contact conductance. Therefore, the only influencing factors are both the mechanical and thermal parameters of the individual abutting surfaces (sintered copper and cast aluminum alloy).

The correlation developed by Cooper, Mikic, and Yovanovich (CMY) predicts the thermal contact conductance, which is one order of magnitude higher that the measured values, with considerably less scatter between individual coating thicknesses than the correlation developed by Antonetti and Yovanovich for coated surfaces. The slopes of the experimental data also better approximate the CMY correlation equation. Since these substrate and coating materials were initially powders that were hot-pressed and sintered, mechanical behavior similar to bulk materials cannot be expected (different levels of porosity may exist). In addition, the models developed by Cooper, Mikic, and Yovanovich and Antonetti and Yovanovich were for isotropic surfaces with assumptions of circular contact points and a Gaussian distribution of surface heights or peaks.

Conclusions

The thermal contact conductance for this exhaust valve/valve seat configuration was measured for interface temperatures between 100 and 200°C (212 and 392°F) for a range of interface pressures between 2.5 and 25 MPa (363 and 3625 psi).

The thermal contact conductance data for the 1.0 and 2.0 mm sintered copper coating thicknesses applied to a ferro-alloy specimen in contact with an uncoated cast aluminum alloy ranged from 3,600 to 56,900 W/m^2-K (626 to 9896 Btu/ft^2-hr °F), while the thermal contact conductance values for the 2.0 mm coating thickness ranged from 17,200 to 160,000 W/m^2-K (2,991 to 27,826 Btu/ft^2-hr °F) for the range of interface pressures and temperatures that produced acceptable uncertainties.

The magnitude of the thermal contact conductance values was enhanced by factors of 2 and 4, respectively, for the 0.2 and 0.5 mm coating thicknesses, while the magnitude increased by factors 5.5 and 15.5, respectively, for the 1.0 and 2.0 mm coating thicknesses at the higher interface pressure when compared to the uncoated junction. In addition, the hystersis effect observed for the uncoated ferro-alloy/aluminum junction does not exist for the three lower sintered copper coating thicknesses.

The correlation developed by Cooper, Mikic, and Yovanovich for uncoated surfaces predicts the thermal contact conductance with less scatter between individual coating thicknesses than the correlation developed by Antonetti and Yovanovich for coated surfaces. Such factors as material composition, interface porosity, and anisotropic surface roughness will cause the measured thermal contact conductance values to deviate from the values predicted by the two models.

References

Antonetti, V. W., and Yovanovich, M. M., 1985, "Enhancement of Thermal Contact Conductance by Metallic Coatings: Theory and Experiments," ASME JOURNAL OF HEAT TRANSFER, Vol. 107, pp. 513–519.

Cooper, M., Mikic, B. B., and Yovanovich, M. M., 1969, "Thermal Contact Conductance," International Journal of Heat and Mass Transfer, Vol. 12, No. 2, pp. 279–300.

Kang, T. K., Peterson, G. P., and Fletcher, L. S., 1989, "Enhancing the Thermal Contact Conductance Through the Use of Thin Metallic Coatings," ASME JOURNAL OF HEAT TRANSFER, Vol. 112, pp. 864–871.

Kline, S. J., and McClintock, F. A., 1953, "Describing Uncertainties in Single-Sample Experiments," Mechanical Engineering, Vol. 75, No. 1, pp. 1–8.

Mal'kov, V. A., and Dobashin, P. A., 1969, "The Effect of Soft-Metal Coatings and Linings on Contact Thermal Resistance," *Inzhenerno-Fizicheschii Zhurnal*, Vol. 17, No. 5, pp. 871–879.

Marotta, E. E., and Fletcher, L. S., 1996, "Thermal Contact Conductance of Refractory Ceramic Coatings," *Journal of Thermophysics and Heat Transfer*, Vol. 10, No. 1, pp. 10–18.

Mikic, B. B., 1974, "Thermal Contact Conductance; Theoretical Considerations," *International Journal of Heat and Mass Transfer*, Vol. 17, No. 2, pp. 205–214.

Mikic, B. B., and Carnasciali, G., 1969, "The Effect of Thermal Conductivity of Plating Material on Thermal Contact Resistance," ASME Paper No. 69-WA/HT-9, ASME Winter Annual Meeting, Los Angeles, CA, Nov. 16–20.

O'Callaghan, P. W., Smith, B., Probert, S. D., and Al-Astrabadi, F. R., 1981, "Prediction of Optimal Interfacial Filler Thickness for Minimum Thermal Contact Resistance," AIAA Paper No. 81-1166, AIAA 16th Thermophysics Conference, Palo Alto, CA, June 23–25.

Thermal Analysis of Solids at High Peclet Numbers Subjected to Moving Heat Sources

O. Manca,[1] B. Morrone,[1] and S. Nardini[2]

A three-dimensional heat transfer model has been developed to obtain the conductive thermal field inside a brick-type solid under a moving heat source with different beam profiles. The problem in quasi-steady state has been approximated by neglecting the axial diffusion component; thus, for Peclet numbers greater than 5, the elliptic differential equation becomes a parabolic one along the motion direction. The dependence of the solution on the radiative and convective heat losses has been highlighted. Thermal fields are strongly dependent on different spot shapes and on the impinging jet; this situation allows control of the parameters involved in the technological process.

Nomenclature

Bi = Biot number, Eq. (3)
c = specific heat, J kg^{-1} K^{-1}
h = convective heat transfer coefficient, W m^{-2} K^{-1}
k = thermal conductivity, W m^{-1} K^{-1}
l = length, m
L = dimensionless length, Eq. (3)
N = conduction-to-radiation number, Eq. (3)
Pe = Peclet number, Eq. (3)
q = heat flux, W m^{-2}
r = radius of the spot, m
Re$_{jet}$ = Reynolds jet number
T = temperature, K
T^+ = normalized nondimensional temperature
u = velocity of the workpiece, m s^{-1}
$x, y, z; X, Y, Z$ = Cartesian coordinates, m; dimensionless Cartesian coordinates, Eq. (3)

Greek Symbols

α = thermal diffusivity, m^2 s^{-1}
ϵ = emissivity
ρ = density, kg m^{-3}
σ = Stefan-Boltzmann constant, W m^{-2} K^{-4}

Subscripts

a = ambient
b = bottom surface
D = donut
g = gas
G = Gaussian
in = initial for $x \to -\infty$
l = lateral surface
r = reference
u = upper surface
0 = at the origin of the coordinates system
$x, y, z; X, Y, Z$ = coordinates; dimensionless coordinates

Superscripts

$*$ = dimensionless

Introduction

In the last two decades, there has been a considerable increase in studies concerning the conductive thermal fields induced in solids by localized moving heat sources. As far as these sources are concerned, they are related both to the laser and electron beam applications and to the sliding contacts.

Numerical methods are the most powerful tools to solve the thermal models describing the processed solid, especially when dealing with complex geometries, nonlinear boundary conditions and temperature-dependent thermal properties. Some examples of three-dimensional fields have been given by Mazumder and Steen (1980), De Almeida and Hinds (1983), and Roy and Modest (1993) for a moving circular Gaussian heat source, and by Kou et al. (1983), who expanded the work on moving heat sources carried out by Carslaw and Jaeger (1959).

The typical parameters involved in the process for any particular application should be evaluated in such a way as to optimize the material processing, in order to forecast the behavior of the solid and to simplify the physical model. The Peclet number, which compares the thermal diffusion term (thermal diffusivity of the solid) in the direction of the motion to the convective component (velocity and characteristic length), is the main nondimensional parameter governing the heat transfer mechanism in the system. For very high speeds, hence large Peclet numbers, thermal diffusion along the moving direction of the heat source is negligible compared to the convective term. This has been pointed out by Yuen (1988), Modest and Abakians (1986), and Jaluria and Singh (1983). These authors agreed on the fact that simplified models work well for Pe > 10.

In the following a simplified three-dimensional quasi-steady state thermal conductive model in a solid with finite depth and width but with infinite length under a moving heat source has been numerically solved. The proposed model allows for both convective and radiative surface heat losses, and variable properties. The convective heat transfer is due to an impinging jet. Numerical results in terms of temperature profiles will be presented for Peclet numbers equal or greater than five with Gaussian and donut-shaped thermal sources.

Mathematical Description and Numerical Procedure

A heat source (e.g., a laser spot), having a defined power distribution, strikes the upper surface of a brick-type workpiece of infinite extent in the scanning direction and of finite width

Mal'kov, V. A., and Dobashin, P. A., 1969, "The Effect of Soft-Metal Coatings and Linings on Contact Thermal Resistance," *Inzhenerno-Fizicheschii Zhurnal,* Vol. 17, No. 5, pp. 871–879.

Marotta, E. E., and Fletcher, L. S., 1996, "Thermal Contact Conductance of Refractory Ceramic Coatings," *Journal of Thermophysics and Heat Transfer,* Vol. 10, No. 1, pp. 10–18.

Mikic, B. B., 1974, "Thermal Contact Conductance; Theoretical Considerations," *International Journal of Heat and Mass Transfer,* Vol. 17, No. 2, pp. 205–214.

Mikic, B. B., and Carnasciali, G., 1969, "The Effect of Thermal Conductivity of Plating Material on Thermal Contact Resistance," ASME Paper No. 69-WA/HT-9, ASME Winter Annual Meeting, Los Angeles, CA, Nov. 16–20.

O'Callaghan, P. W., Smith, B., Probert, S. D., and Al-Astrabadi, F. R., 1981, "Prediction of Optimal Interfacial Filler Thickness for Minimum Thermal Contact Resistance," AIAA Paper No. 81-1166, AIAA 16th Thermophysics Conference, Palo Alto, CA, June 23–25.

Thermal Analysis of Solids at High Peclet Numbers Subjected to Moving Heat Sources

O. Manca,[1] B. Morrone,[1] and S. Nardini[2]

A three-dimensional heat transfer model has been developed to obtain the conductive thermal field inside a brick-type solid under a moving heat source with different beam profiles. The problem in quasi-steady state has been approximated by neglecting the axial diffusion component; thus, for Peclet numbers greater than 5, the elliptic differential equation becomes a parabolic one along the motion direction. The dependence of the solution on the radiative and convective heat losses has been highlighted. Thermal fields are strongly dependent on different spot shapes and on the impinging jet; this situation allows control of the parameters involved in the technological process.

Nomenclature

Bi = Biot number, Eq. (3)
c = specific heat, J kg^{-1} K^{-1}
h = convective heat transfer coefficient, W m^{-2} K^{-1}
k = thermal conductivity, W m^{-1} K^{-1}
l = length, m
L = dimensionless length, Eq. (3)
N = conduction-to-radiation number, Eq. (3)
Pe = Peclet number, Eq. (3)
q = heat flux, W m^{-2}
r = radius of the spot, m
Re_{jet} = Reynolds jet number
T = temperature, K
T^{+} = normalized nondimensional temperature
u = velocity of the workpiece, m s^{-1}
$x, y, z; X, Y, Z$ = Cartesian coordinates, m; dimensionless Cartesian coordinates, Eq. (3)

Greek Symbols

α = thermal diffusivity, m^2 s^{-1}
ϵ = emissivity
ρ = density, kg m^{-3}
σ = Stefan-Boltzmann constant, W m^{-2} K^{-4}

Subscripts

a = ambient
b = bottom surface
D = donut
g = gas
G = Gaussian
in = initial for $x \rightarrow -\infty$
l = lateral surface
r = reference
u = upper surface
0 = at the origin of the coordinates system
$x, y, z; X, Y, Z$ = coordinates; dimensionless coordinates

Superscripts

$*$ = dimensionless

Introduction

In the last two decades, there has been a considerable increase in studies concerning the conductive thermal fields induced in solids by localized moving heat sources. As far as these sources are concerned, they are related both to the laser and electron beam applications and to the sliding contacts.

Numerical methods are the most powerful tools to solve the thermal models describing the processed solid, especially when dealing with complex geometries, nonlinear boundary conditions and temperature-dependent thermal properties. Some examples of three-dimensional fields have been given by Mazumder and Steen (1980), De Almeida and Hinds (1983), and Roy and Modest (1993) for a moving circular Gaussian heat source, and by Kou et al. (1983), who expanded the work on moving heat sources carried out by Carslaw and Jaeger (1959).

The typical parameters involved in the process for any particular application should be evaluated in such a way as to optimize the material processing, in order to forecast the behavior of the solid and to simplify the physical model. The Peclet number, which compares the thermal diffusion term (thermal diffusivity of the solid) in the direction of the motion to the convective component (velocity and characteristic length), is the main nondimensional parameter governing the heat transfer mechanism in the system. For very high speeds, hence large Peclet numbers, thermal diffusion along the moving direction of the heat source is negligible compared to the convective term. This has been pointed out by Yuen (1988), Modest and Abakians (1986), and Jaluria and Singh (1983). These authors agreed on the fact that simplified models work well for Pe > 10.

In the following a simplified three-dimensional quasi-steady state thermal conductive model in a solid with finite depth and width but with infinite length under a moving heat source has been numerically solved. The proposed model allows for both convective and radiative surface heat losses, and variable properties. The convective heat transfer is due to an impinging jet. Numerical results in terms of temperature profiles will be presented for Peclet numbers equal or greater than five with Gaussian and donut-shaped thermal sources.

Mathematical Description and Numerical Procedure

A heat source (e.g., a laser spot), having a defined power distribution, strikes the upper surface of a brick-type workpiece of infinite extent in the scanning direction and of finite width
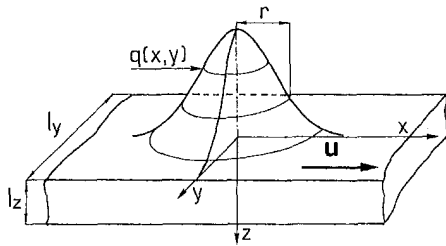
Fig. 1 Sketch of the workpiece

and thickness, which moves with a uniform velocity (Fig. 1). A fraction of the incident radiation is reflected. Furthermore, there is a heat transfer by radiation and convection from the outer surfaces. The convective heat transfer is due to an impinging gas jet on the upper surface.

The following hypotheses have been made: (1) the solid moves with constant velocity u; (2) the solid is isotropic; (3) the thermal properties of the workpiece are temperature dependent, except for the density; (4) the material is an opaque body and the reflectivity is assumed constant; (5) the heat source distribution is either a Gaussian or a donut-shaped beam; (6) there is no melting in the medium and on its surface.

According to the theory of moving heat sources (Rosenthal, 1946), the conductive problem in the solid for a quasi-steady state and by neglecting the thermal diffusion along the motion direction is

$$\frac{\partial}{\partial y}\left(k(T)\frac{\partial T}{\partial y}\right) + \frac{\partial}{\partial z}\left(k(T)\frac{\partial T}{\partial z}\right) = -\rho c u \frac{\partial T}{\partial x}$$

$$\text{for} \quad 0 \leq |x| < +\infty, 0 \leq y \leq l_y/2, \quad 0 \leq z \leq l_z \quad (1)$$

$$T \rightarrow T_{in} \quad \text{for} \quad x \rightarrow +\infty, 0 < y < l_y/2, \quad 0 < z < l_z \quad (2a)$$

$$-k\frac{\partial T}{\partial y} = h_l(T - T_g) - \epsilon_l(T^4 - T_a^4)$$

$$\text{for} \quad y = l_y/2, |x| < +\infty, \quad 0 < z < l_z \quad (2b)$$

$$\frac{\partial T}{\partial y} = 0 \quad \text{for} \quad y = 0, |x| < +\infty, \quad 0 < z < l_z \quad (2c)$$

$$-k\frac{\partial T}{\partial z} = q(x, y) - h_u(T - T_g) - \epsilon_u(T^4 - T_a^4)$$

$$\text{for} \quad z = 0, |x| < +\infty, \quad 0 < y < l_y/2 \quad (2d)$$

$$-k\frac{\partial T}{\partial z} = h_b(T - T_g) - \epsilon_b(T^4 - T_a^4)$$

$$\text{for} \quad z = l_z, |x| < +\infty, \quad 0 < y < l_y/2 \quad (2e)$$

where the heat flux $q(x, y)$ is: for the Gaussian spot $q_0 \cdot \exp[-(x^2 + y^2)/r_G^2]$ and for the donut one $q_0 \cdot [(x^2 + y^2)/r_D^2] \cdot \exp[-(x^2 + y^2)/r_D^2]$.

One of the main aims of this study is the validation of this simplified three-dimensional thermal model. The analysis has been carried out in terms of Peclet number and the following dimensionless variables and parameters are introduced:

$$X = \frac{x}{l_r}; \quad Y = \frac{y}{l_r}; \quad Z = \frac{z}{l_r}; \quad L_Y = \frac{l_y}{l_r}; \quad L_Z = \frac{l_z}{l_r};$$

$$\rho^* = \frac{\rho}{\rho_r} \approx 1; \quad c^* = \frac{c}{c_r}; \quad k^* = \frac{k}{k_r}$$

$$T^* = \frac{T}{T_r}; \quad \text{Pe} = \frac{ul_r}{2\alpha_r}; \quad \text{Bi} = \frac{hl_r}{k_r}; \quad N = \frac{k_r T_r/l_r}{\sigma_r T_r^4} \quad (3)$$

where T_r is the reference temperature, equal to $q_0 l_r/k_r$. The

reference length l_r is the radius of the spot, i.e., either r_G for Gaussian spot or r_D for donut one.

The values h_u, h_l, and h_b are the local convective coefficients for upper, lateral, and bottom surfaces of the workpiece, respectively. The evaluation of the outer surface convective coefficients has been made in the following way: h_u by means of the correlation for the impinging cooling jet (Martin, 1977; Goldstein et al., 1986; and Huang and El-Genk, 1994); h_l by employing the correlations for forced convection over plates; h_b through the correlations for rear surface proposed by Sogin (1964) and Mitchell (1971). The Reynolds number in the previous correlations was evaluated as in Martin (1977, pp. 3–5). For further details refer to Manca et al. (1995a).

The results will be presented in terms of normalized temperature $T^+ = 2(T^* - T_{in}^*)$ Pe $L_z L_y/\pi$.

The governing nonlinear Eq. (1) with nonlinear boundary conditions (2) has been solved using a step-by-step finite difference technique. The solution has been obtained by starting the numerical integration from the geometrical coordinate that mimics the temperature value at $X \rightarrow -\infty$ with a given temperature. The convective derivative has been discretized with a backward difference formula, as suggested by De Almeida and Hinds (1983). The energy balance equation for each element of volume surrounding a node can be written following the suggestions by Patankar (1980, p. 101).

Due to the nonlinearities induced by the variable thermophysical properties and by the thermal radiation, the solution has been obtained nesting two iterations one inside the other. The first one deals with the dependence of properties on the temperature, while the second one, nested inside the first, deals with surface radiation. The solution to the linear algebraic system has been obtained by the Gauss-Siedel method. The number of nodes used to calculate the solution has been determined iteratively starting from a coarse mesh. Once a rough solution is obtained, the spatial steps along all the coordinate axes are halved. This procedure is repeated until a percent difference of less than 0.1 is attained between two successive trials. The length of the workpiece has been divided into 193 nodes along the X-axis. The spatial steps along the Y and Z-axes depend on the dimensions of L_Y and L_Z (e.g., for $L_Y = L_Z = 1.0$, $n_Y = n_Z = 15$).

Results and Discussion

The dimensionless data employed in the present study can be obtained from the following dimensional data: $l_y = 0.0125$ and 0.125 m, $l_z = 0.0125$ and 0.125 m, diameter of the impinging jet equal to 0.022 m, and the reference length equal to 0.0125 m. The values of the emissivity have been set equal to 0.8 and the absorbed laser power equal to 1000 W. When the dependence of thermophysical properties on the temperature has been considered, reference was made to data given in Metal Handbook (1981) for a 10-18 steel material. The reference thermophysical properties have been evaluated at 293 K. The temperature of the impinging jet, supposed to be helium, has been set equal to 290 K and the plate-to-nozzle spacing equal to 7.0. The workpiece velocities ranged from $5 \cdot 10^{-3}$ m/s to $5 \cdot 10^{-2}$ m/s. The dimensionless temperature profiles have been obtained at Peclet numbers equal to 5 and 10 for the Gaussian spot, and for the donut spot at Pe = 10, with the radiative number, N, being equal to 30. Since the Biot number is a function of the Reynolds number of the impinging jet, then Re_{jet} has been taken as the independent variable. Results are reported at the following Re_{jet} values: 0, $2.0 \cdot 10^3$ and $1.0 \cdot 10^4$. The values of dimensionless thickness, L_Z, and width, L_Y, were equal to 1.0 or 10 for the Gaussian spot and 1.0 for the donut one.

The numerical procedure has been validated by comparing its results to an analytical three-dimensional solution to the thermal field in a solid with constant thermophysical properties, adiabatic surfaces and a circular Gaussian heat source (Manca
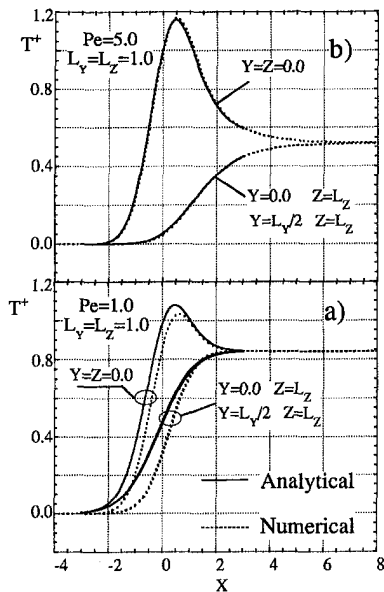
Fig. 2 Analytical and numerical temperature profiles for Gaussian spot versus axial coordinate for $L_Y = L_Z = 1.0$, at different locations for (a) Pe = 1.0, (b) Pe = 5.0

et al., 1995b). This solution took into account the axial diffusion (along the X-axis).

Dimensionless thermal profiles as a function of the different Peclet numbers are shown in Fig. 2, where the numerical results are compared to the analytical ones. There is an excellent agreement between the profiles for Pe = 5.0 with a maximum deviation of 0.1 percent. Figure 2 shows that the upstream diffusion along X decreases with increasing Peclet numbers. In fact, at Pe = 1 (Fig. 2(a)), there is a significant deviation between the two models, due to the fact that the actual diffusive contribution to the heat removal preheats the upstream region of the solid, not yet exposed to the heat source. Instead, for Peclet numbers equal to or greater than 5.0 the proposed parabolic model can approximate in a very satisfactory manner the elliptic model all over the workpiece. This comparison has also been for greater thickness and width of the workpieces showing no differences with respect to the case presented in Fig. 2. Anyway, this behavior should have been expected since the numerical model takes into account the diffusion along the Y and Z-axes.

In the following, some results for the Gaussian and donut spots at Pe equal to or greater than 5.0 are shown. The temperature profiles along the X coordinate for the Gaussian spot at Pe = 5.0 and 10, for the following boundary conditions: linear adiabatic (without heat losses) and nonlinear with radiative and convective heat losses, are shown in Figs. 3 and 4, respectively. For the sake of brevity, in the following discussion the two aforementioned models will be simply indicated as linear and nonlinear, respectively. In Fig. 3(a) it can be pointed out that, for $Re_{jet} = 2.0 \cdot 10^3$, the influence of the impinging jet on the temperature profiles is almost negligible at $Y = Z = 0$, where the maximum temperature values are attained. The deviation between the two configurations ($Re_{jet} = 0$ and $Re_{jet} = 2.0 \cdot 10^3$) increases when X is greater than 4.0, because the linear case tends to an asymptotic value equal to erf($L_Y/2$) (Manca et al., 1995b), while the nonlinear one, with heat losses, tends to zero for $X \rightarrow +\infty$. A similar behavior can be observed at $Y = L_Y/2$, $Z = 0$ (Fig. 3(b)). Greater deviations can be found at $Y = L_Y/2$ and $Z = L_Z$ (Fig. 3(c)). This is mainly due to the upper surface convective heat transfer rather than to the existence of heat losses induced by the impinging jet, related to the presence of the wake and the lateral surface convective heat transfer. At higher Peclet number (equal to 10), the percent deviations

between the two cases ($Re_{jet} = 0$ and $Re_{jet} = 2.0 \cdot 10^3$) are almost the same at $Y = Z = 0$ (Fig. 4(a)), whereas at $Y = L_Y/2$ and $Z = 0$ the discrepancies decrease (Fig. 4(b)). At $Y = L_Y/2$ and $Z = L_Z$ (Fig. 4(c)), the differences are quite negligible. One can notice a completely different behavior with $Re_{jet} = 1.0 \cdot 10^4$, which presents temperature values much lower than the other two cases. It is worth noting that the maximum temperature locations tend to $X = 0$ as Re_{jet} increases for both the Peclet numbers. The difference between the maximum temperature with $Re_{jet} = 0$ and that with $Re_{jet} = 1.0 \cdot 10^4$ decreases as Pe increases as shown in Figs. 3 and 4. This is due to the fact that the convective energy transfer, caused by the workpiece motion, becomes more important compared to the jet convective heat transfer for higher Pe number.

The dimensionless spatial temperature distributions along X for a donut heat source, at different locations, for a Peclet number equal to 10 are reported in Fig. 5. The comparison between the linear and nonlinear cases, for $Re_{jet} = 2.0 \cdot 10^3$, shows smaller differences between the profiles than those for the case with a Gaussian spot, at $Y = 0.0$ (Fig. 5(a)) and $Y = L_Y/2$ (Fig. 5(b)). The locations at which the maximum temperatures are attained are shifted downstream along X relative to the maximum values of the heat flux ($X = \pm1$). For this configuration the most affected region turns out to be that at $Y = L_Y/2$ on the upper surface, due to the particular shape of the heat flux. The $Re_{jet} = 1.0 \cdot 10^4$ value strongly modifies the temperature distribution, as already observed for the Gaussian spot. The temperature profiles are now almost symmetric with respect to $X = 0.0$. For this Re_{jet} number the temperatures at the bottom surface, $Z = L_Z$, are higher than the corresponding ones on the upper surface, $Z = 0$, at X greater than 2.0.
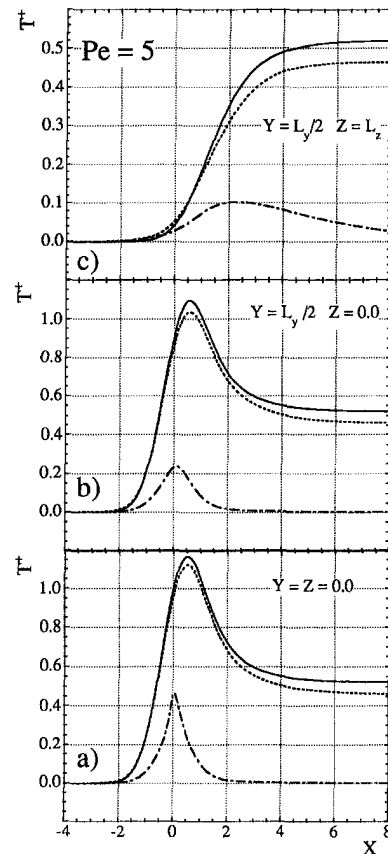

Fig. 3 Temperature profiles for Gaussian spot with Pe = 5 versus axial coordinate for $L_Y = L_Z = 1.0$, at (a) $Y = Z = 0.0$; (b) $Y = L_Y/2$, $Z = 0.0$; (c) $Y = L_Y/2$, $Z = L_Z$; $Re_{jet} = 0$ ———; $Re_{jet} = 2.0 \cdot 10^3$ – – – – – – –; $Re_{jet} = 1.0 \cdot 10^4$ – · – · – · – · –
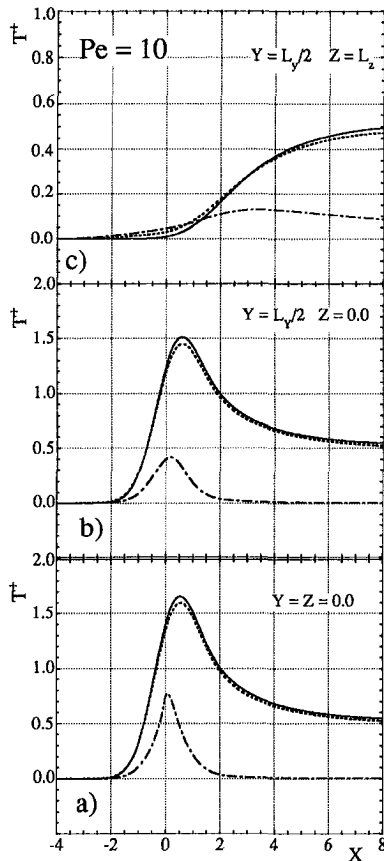
Fig. 4 Temperature profiles for Gaussian spot with Pe = 10 versus axial coordinate for $L_Y = L_Z = 1.0$, at (a) $Y = Z = 0.0$; (b) $Y = L_Y/2$, $Z = 0.0$; (c) $Y = L_Y/2$, $Z = L_Z$; $Re_{jet} = 0$ ———; $Re_{jet} = 2.0 \cdot 10^3$ – – – – – – –; $Re_{jet} = 1.0 \cdot 10^4$ – · – · – · – · –

Figure 6 shows thermal profiles as functions of X at Pe = 10 for $L_Y = 1.0$ and $L_Z = 10$, Fig. 6(a), and for $L_Y = 10$ and $L_Z = 1.0$, Fig. 6(b). The temperature distribution for $Re_{jet} = 2.0 \cdot 10^3$ was not shown in figure since it is very close to the linear case.
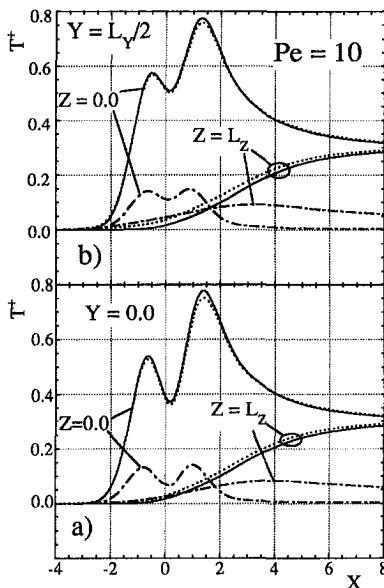

Fig. 5 Temperature profiles for donut spot versus axial coordinate for $L_Y = L_Z = 1.0$ with Pe = 10, and at different locations: (a) $Y = 0.0$, (b) $Y = L_Y/2$. $Re_{jet} = 0$ ———; $Re_{jet} = 2.0 \cdot 10^3$ – – – – – – –; $Re_{jet} = 1.0 \cdot 10^4$ – · – · – · – · –.
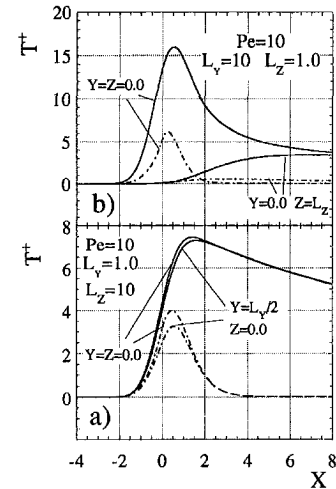

Fig. 6 Temperature profiles for Gaussian spot with Pe = 10 versus axial coordinate: (a) $L_Y = 1.0$ and $L_Z = 10$, at $Y = Z = 0.0$ and $Y = L_Y/2$, $Z = 0.0$; (b) $L_Y = 10$ and $L_Z = 1.0$, at $Y = Z = 0.0$ and $Y = 0$, $Z = L_Z$. $Re_{jet} = 0$ ———; $Re_{jet} = 1.0 \cdot 10^4$ – · – · – · – · –.

In Fig. 6(a) the upper surface ($Z = 0$) temperature profiles at $Y = 0$ and $Y = L_Y/2$ are very close because for $L_Y = 1.0$ the Gaussian heat flux distribution is nearly uniform between 0 and $L_Y/2$. The bottom surface ($Z = L_Z = 10$) not shown is unaffected by the thermal source and the solid behaves as a semi-infinite one, for the considered length of the workpiece. In Fig. 6(b), when L_Z is equal to 1.0 and $L_Y = 10$, the thermal disturbance reaches the bottom surface ($Z = L_Z$) and the upper one ($Z = 0$) is affected by the finite thickness. In this case the most part of the Gaussian heat flux distribution strikes the surface and this implies higher temperature values than the previous case (Fig. 6(a)). The temperature profiles at $Y = L_Y/2$ are not shown here since their values are uniformly equal to zero. At the highest presented Re_{jet} value (10^4), the temperature profiles are quite different from those at $Re_{jet} = 0.0$. In fact, in Figs. 6(a) and 6(b) The temperature profiles show lower maxima located at about $X = 0.0$. These figures confirm that the temperature profiles on the surface present similar behavior when Re_{jet} is equal to 10^4, for any L_Y and L_Z. Then, by comparing the profiles shown in Figs. 4 and 6 one can notice that the ratio $T^+/L_Y L_Z$ presents the same order of magnitude. This is because the $L_Y L_Z$ product is included in the definition of T^+. For $Re_{jet} = 0$ the maximum temperatures of the thicker body ($L_Z = 10$) are lower than those for the solids with $L_Z = 1.0$, whereas the asymptotic value is attained at higher X values and it is very close to the one for $L_Y = L_Z = 1.0$. For $L_Y = 10$ and $L_Z = 1.0$ the maximum temperature is similar to the one for $L_Y = L_Z = 1.0$ and its asymptotic value is lower. This is due to the energy diffusion occurring toward the inner part of the body. The variation of the thickness of the body, L_Z, shows a more significant modification in the upper surface temperature, compared to the variation of the width L_Y, for the same absorbed energy.

As far as the donut spot is concerned, no pictures similar to Fig. 6 are reported for larger L_Y and L_Z, since they show an analogous trend to that presented in Fig. 6.

Conclusions

It has been determined that at Peclet number not lower than 5, the axial diffusive heat transfer along the motion direction can be neglected, in accordance with Modest and Abakians (1986), even for solids with finite thickness. This approximation makes the three-dimensional elliptic partial differential equation a parabolic one along the motion direction. A maximum deviation between the proposed numerical solution and the analytical one of about 0.1 percent was observed. The simplified

model has been extended to a donut spot. Small differences between the adiabatic linear and the nonlinear cases, for Re_{jet} up to $2.0 \cdot 10^3$, have been noticed. At higher Re_{jet} numbers $(1.0 \cdot 10^4)$ the thermal profiles are almost symmetric with respect to the origin $X = 0$. This trend has been observed for different thickness and width of the workpiece.

Acknowledgments

References

Carslaw, H. S., and Jaeger, J. C., 1959, *Conduction of Heat in Solids*, 2nd Ed., Clarendon Press, Oxford, UK.

De Almeida, S. M., and Hinds, B. K., 1983, "Finite-Difference Solution to the Problem of Temperature Distribution under a Moving Heat Source, Using the Concept of a Quasi-Steady State," *Numerical Heat Transfer*, Vol. 6, pp. 17–27.

Goldstein, R. J., Behbahani, A. I., and Heppelmann, K. K., 1986, "Streamwise Distribution of the Recovery Factor and the Local Heat Transfer Coefficient to an Impinging Circular Air Jet Flow," *International Journal of Heat and Mass Transfer*, Vol. 29, No. 7, pp. 1227–1235.

Huang, L., and El-Genk, M. S., 1994, "Heat transfer of an Impinging Jet on a Flat Surface," *International Journal of Heat and Mass Transfer*, Vol. 27, No. 13, pp. 1915–1923.

Jaluria, Y., and Singh, A. P., 1983, "Temperature Distribution in a Moving Material Subjected to Surface Energy Transfer," *Computational Methods in Applied Mechanics and Engineering*, Vol. 41, pp. 145–157.

Kou, S., Sun, D. K., and Le, Y. P., 1983, "A Fundamental Study of Laser Transformation Hardening," *Metallurgical Transactions*, Part A, Vol. 14A, pp. 643–653.

Manca, O., Morrone, B., Nardini, S., 1995a, "Thermal Models in Moving Heat Sources with High Peclet Numbers," ASME Paper 95-WA/HT-24, pp. 1–11.

Manca, O., Morrone, B., and Naso, V., 1995b, "Quasi-Steady-State Three-Dimensional Temperature Distribution Induced by a Moving Circular Gaussian Heat Source in a Finite Depth Solid," *International Journal of Heat and Mass Transfer*, Vol. 38, No. 7, pp. 1305–1315.

Martin, H., 1977, "Heat and Mass Transfer between Impinging Gas Jet and Solid Surfaces," *Advances in Heat Transfer*, Vol. 13, pp. 1–60.

Mazumder, J., and Steen, W. M., 1980, "Heat Transfer Model for CW Laser Material Processing," *Journal of Applied Physics*, Vol. 51, pp. 941–947.

Metals Handbook, 1981, 9th Ed. ASM, Metal Park, OH.

Mitchell, J. W., 1971, "Base Heat Transfer in Two-Dimensional Subsonic Fully Separated Flow," ASME JOURNAL OF HEAT TRANSFER, Vol. 93, pp. 342–348.

Modest, M. F., and Abakians, H., 1986, "Heat Conduction in a Moving Semi-Infinite Solid Subjected to Pulsed Laser Irradiation," ASME JOURNAL OF HEAT TRANSFER, Vol. 108, pp. 597–601.

Patankar, S. V., 1980, *Numerical Heat Transfer and Fluid Flow*, Hemisphere, Washington, DC.

Rosenthal, D., 1946, "The Theory of Moving Sources of Heat and its Applications to Metal Treatments," *Transactions of the ASME*, Vol. 68, pp. 849–866.

Roy, S., and Modest, M. F., 1993, "CW Laser Machining of Hard Ceramics—I. Effects of Three-Dimensional Conduction, Variable Properties and Various Laser Parameters," *International Journal of Heat and Mass Transfer*, Vol. 36, No. 14, pp. 3515–3528.

Sogin, H. H., 1964, "A Summary of Experiments on Local Heat Transfer from the Rear of Bluff Obstacles to a Low Speed Airstream," ASME JOURNAL OF HEAT TRANSFER, Vol. 86, pp. 200–202.

Yuen, W. Y. D., 1988, "Heat Conduction in Sliding Solids," *International Journal of Heat and Mass Transfer*, Vol. 31, No. 3, pp. 637–646.

Prediction of Heat Transfer in Turbulent, Transpired Boundary Layers

J. Sucec[1]

Considered here is turbulent boundary layer flow with injection or suction and pressure gradient along the surface. The velocity and thermal inner laws for transpired turbulent boundary layers are represented by simple power law forms which are then used to solve the integral form of the thermal energy equation. Solving this equation leads to the variation of Stanton number with position, x, along the surface. Predicted Stanton numbers are compared with experimental data for a number of different cases. These include both blowing and suction with constant blowing fractions, F, in zero and non-zero pressure gradients and more complicated situations in which the blowing fraction, F, varies with position or where F or the surface temperature have step changes in value.

[1] Department of Mechanical Engineering, University of Maine, Orono, ME 04469-5711. Mem. ASME.

Nomenclature

$C_f = 2\tau_w / \rho u_s^2$ skin friction coefficient
h_x = local surface coefficient of heat transfer
K = von Karman's constant
Pr, Pr_t = molecular and turbulent Prandtl number
q_w = wall heat flux
$Re_x = u_s x / \nu$ Reynolds number
T, T_w, T_s = local, wall and freestream temperatures
y = space coordinate perpendicular to surface
ν = kinematic viscosity
ρ = mass density
τ_w = local wall shear stress

Introduction

A fundamental heat transfer problem is that of predicting the local convective heat flux along a surface with transpiration effects and pressure gradient. Applications include blades and vanes of gas turbine power plants, rocket nozzles, and combustor liners.

One of the most commonly employed parameters used to characterize the transpiration process is the blowing fraction for incompressible flow, F, $F = \nu_w / u_s$, where ν_w is the local y component of velocity at the surface and u_s is the local freestream velocity. F, in general, can vary with position, x, along the surface and can be positive (blowing) or negative (suction).

Considering transpired turbulent boundary layers, including cases of $F = 0$, the largest and most complete detailed collection of experimental heat transfer and fluid flow data was generated by W. M. Kays and co-workers at Stanford University (Moffat and Kays, 1984). Experimental Stanton number data for zero pressure gradient and constant values of F is given in Moffat and Kays (1968) while data for F variable with position and variable wall temperature is presented in Whitten et al. (1967). For accelerating turbulent boundary layers with transpiration, experimental heat transfer data is available in Thielbahr et al. (1972) and Kearney et al. (1973). Orlando et al. (1974) and Blackwell (1972) present Stanton number data for adverse pressure gradients.

Among the many heat transfer prediction techniques for $F = 0$ is the simple integral method of Ambrok (1957), integral methods using the inner law only, Thomas and Al-Shariff (1981), Hrycak (1992), finite difference methods such as that of Harasgama et al. (1993), and the more recent integral method of Sucec and Lu (1990).

Methods for predicting heat transfer rates across turbulent transpired boundary layer flows consist almost entirely of numerical finite difference solutions of the governing partial differential equations of mass, momentum, and energy. These include the algebraic mixing length model of Kays (1972) and of Moffat and Kays (1984). Other algebraic mixing lengths models were used by Powell and Strong (1970) and by Cebeci and Mosinskis (1971). Jones and Launder (1973), using the $k-\epsilon$ model of turbulence, presented a limited number of heat transfer solutions with transpiration. Torii, Nishiwaki, and Hirata (1966) present an integral method for zero pressure gradient,

model has been extended to a donut spot. Small differences between the adiabatic linear and the nonlinear cases, for Re_{jet} up to $2.0 \cdot 10^3$, have been noticed. At higher Re_{jet} numbers ($1.0 \cdot 10^4$) the thermal profiles are almost symmetric with respect to the origin $X = 0$. This trend has been observed for different thickness and width of the workpiece.

Acknowledgments

This work has been supported by a 60 percent 1995 MURST grant. The authors would like to thank the reviewers and the editors for their useful suggestions and comments.

References

Carslaw, H. S., and Jaeger, J. C., 1959, *Conduction of Heat in Solids,* 2nd Ed., Clarendon Press, Oxford, UK.

De Almeida, S. M., and Hinds, B. K., 1983, "Finite-Difference Solution to the Problem of Temperature Distribution under a Moving Heat Source, Using the Concept of a Quasi-Steady State," *Numerical Heat Transfer,* Vol. 6, pp. 17–27.

Goldstein, R. J., Behbahani, A. I., and Heppelmann, K. K., 1986, "Streamwise Distribution of the Recovery Factor and the Local Heat Transfer Coefficient to an Impinging Circular Air Jet Flow," *International Journal of Heat and Mass Transfer,* Vol. 29, No. 7, pp. 1227–1235.

Huang, L., and El-Genk, M. S., 1994, "Heat transfer of an Impinging Jet on a Flat Surface," *International Journal of Heat and Mass Transfer,* Vol. 27, No. 13, pp. 1915–1923.

Jaluria, Y., and Singh, A. P., 1983, "Temperature Distribution in a Moving Material Subjected to Surface Energy Transfer," *Computational Methods in Applied Mechanics and Engineering,* Vol. 41, pp. 145–157.

Kou, S., Sun, D. K., and Le, Y. P., 1983, "A Fundamental Study of Laser Transformation Hardening," *Metallurgical Transactions,* Part A, Vol. 14A, pp. 643–653.

Manca, O., Morrone, B., Nardini, S., 1995a, "Thermal Models in Moving Heat Sources with High Peclet Numbers," ASME Paper 95-WA/HT-24, pp. 1–11.

Manca, O., Morrone, B., and Naso, V., 1995b, "Quasi-Steady-State Three-Dimensional Temperature Distribution Induced by a Moving Circular Gaussian Heat Source in a Finite Depth Solid," *International Journal of Heat and Mass Transfer,* Vol. 38, No. 7, pp. 1305–1315.

Martin, H., 1977, "Heat and Mass Transfer between Impinging Gas Jet and Solid Surfaces," *Advances in Heat Transfer,* Vol. 13, pp. 1–60.

Mazumder, J., and Steen, W. M., 1980, "Heat Transfer Model for CW Laser Material Processing," *Journal of Applied Physics,* Vol. 51, pp. 941–947.

Metals Handbook, 1981, 9th Ed. ASM, Metal Park, OH.

Mitchell, J. W., 1971, "Base Heat Transfer in Two-Dimensional Subsonic Fully Separated Flow," ASME JOURNAL OF HEAT TRANSFER, Vol. 93, pp. 342–348.

Modest, M. F., and Abakians, H., 1986, "Heat Conduction in a Moving Semi-Infinite Solid Subjected to Pulsed Laser Irradiation," ASME JOURNAL OF HEAT TRANSFER, Vol. 108, pp. 597–601.

Patankar, S. V., 1980, *Numerical Heat Transfer and Fluid Flow,* Hemisphere, Washington, DC.

Rosenthal, D., 1946, "The Theory of Moving Sources of Heat and its Applications to Metal Treatments," *Transactions of the ASME,* Vol. 68, pp. 849–866.

Roy, S., and Modest, M. F., 1993, "CW Laser Machining of Hard Ceramics—I. Effects of Three-Dimensional Conduction, Variable Properties and Various Laser Parameters," *International Journal of Heat and Mass Transfer,* Vol. 36, No. 14, pp. 3515–3528.

Sogin, H. H., 1964, "A Summary of Experiments on Local Heat Transfer from the Rear of Bluff Obstacles to a Low Speed Airstream," ASME JOURNAL OF HEAT TRANSFER, Vol. 86, pp. 200–202.

Yuen, W. Y. D., 1988, "Heat Conduction in Sliding Solids," *International Journal of Heat and Mass Transfer,* Vol. 31, No. 3, pp. 637–646.

Prediction of Heat Transfer in Turbulent, Transpired Boundary Layers

J. Sucec[1]

Considered here is turbulent boundary layer flow with injection or suction and pressure gradient along the surface. The velocity and thermal inner laws for transpired turbulent boundary layers are represented by simple power law forms which are then used to solve the integral form of the thermal energy equation. Solving this equation leads to the variation of Stanton number with position, x, along the surface. Predicted Stanton numbers are compared with experimental data for a number of different cases. These include both blowing and suction with constant blowing fractions, F, in zero and non-zero pressure gradients and more complicated situations in which the blowing fraction, F, varies with position or where F or the surface temperature have step changes in value.

Nomenclature

$C_f = 2\tau_w / \rho u_s^2$ skin friction coefficient
h_x = local surface coefficient of heat transfer
K = von Karman's constant
Pr, Pr_t = molecular and turbulent Prandtl number
q_w = wall heat flux
$Re_x = u_s x / \nu$ Reynolds number
T, T_w, T_s = local, wall and freestream temperatures
y = space coordinate perpendicular to surface
ν = kinematic viscosity
ρ = mass density
τ_w = local wall shear stress

Introduction

A fundamental heat transfer problem is that of predicting the local convective heat flux along a surface with transpiration effects and pressure gradient. Applications include blades and vanes of gas turbine power plants, rocket nozzles, and combustor liners.

One of the most commonly employed parameters used to characterize the transpiration process is the blowing fraction for incompressible flow, F, $F = \nu_w / u_s$, where ν_w is the local y component of velocity at the surface and u_s is the local freestream velocity. F, in general, can vary with position, x, along the surface and can be positive (blowing) or negative (suction).

Considering transpired turbulent boundary layers, including cases of $F = 0$, the largest and most complete detailed collection of experimental heat transfer and fluid flow data was generated by W. M. Kays and co-workers at Stanford University (Moffat and Kays, 1984). Experimental Stanton number data for zero pressure gradient and constant values of F is given in Moffat and Kays (1968) while data for F variable with position and variable wall temperature is presented in Whitten et al. (1967). For accelerating turbulent boundary layers with transpiration, experimental heat transfer data is available in Thielbahr et al. (1972) and Kearney et al. (1973). Orlando et al. (1974) and Blackwell (1972) present Stanton number data for adverse pressure gradients.

Among the many heat transfer prediction techniques for $F = 0$ is the simple integral method of Ambrok (1957), integral methods using the inner law only, Thomas and Al-Shariff (1981), Hrycak (1992), finite difference methods such as that of Harasgama et al. (1993), and the more recent integral method of Sucec and Lu (1990).

Methods for predicting heat transfer rates across turbulent transpired boundary layer flows consist almost entirely of numerical finite difference solutions of the governing partial differential equations of mass, momentum, and energy. These include the algebraic mixing length model of Kays (1972) and of Moffat and Kays (1984). Other algebraic mixing lengths models were used by Powell and Strong (1970) and by Cebeci and Mosinskis (1971). Jones and Launder (1973), using the $k-\epsilon$ model of turbulence, presented a limited number of heat transfer solutions with transpiration. Torii, Nishiwaki, and Hirata (1966) present an integral method for zero pressure gradient,

[1] Department of Mechanical Engineering, University of Maine, Orono, ME 04469-5711. Mem. ASME.

Copyright © 1999 by ASME

constant positive blowing fraction, F, flows. Their method is complicated by the need to generate the approximate profiles for the velocity by successive approximations solution of the integrated x momentum equation. In addition, they assume equal thicknesses of the velocity and thermal boundary layers in their analysis.

In the present work, power-law profiles are employed for both the velocity inner law profile and the thermal inner law profile. With these, all integrations required in the integral form of the x momentum equation and in the thermal energy equation, can be performed analytically. This gives two nonlinear ordinary differential equations that are solved by a Runge-Kutta method to yield the thermal and the hydrodynamic boundary layer thicknesses, δ_t^+ and δ^+, as a function of position x. With these, the heat transfer law implied by the thermal inner law is solved for the Stanton number as a function of x.

Analysis

Considered in this analysis will be steady on the average, constant property, turbulent, two-dimensional boundary layer flow over a plane porous surface when there is negligible viscous dissipation. Upon changing to inner variables, $u^+ = u/u^*$, $y^+ = u^* y/\nu$ where $u^* = \sqrt{\tau_w/\rho}$, the integral form of the x momentum equation for transpired flow can be shown to be as follows.

$$u_s \frac{d}{dx} \int_0^{\delta^+} u^+ dy^+ - \frac{d}{dx} \int_0^{\delta^+} u^* u^{+2} dy^+ + \frac{u_s}{u^*} \frac{du_s}{dx} \delta^+$$
$$= \frac{u^{*2} + u_s^2 F}{\nu} \quad (1)$$

In Eq. (1), the velocity profile needed, $u^+ = u^+(x, y^+)$, is taken to be the inner law, or law of the wall, for a transpired turbulent flow. This is given by both experiment and derivation in Stevenson (1963) as follows next.

$$\frac{2}{\nu_w^+} [(1 + \nu_w^+ u^+)^{1/2} - 1] = \frac{1}{K} \ln y^+ + C \quad (2)$$

In this work, a one-seventh power-law form is used to approximate the right side of Eq. (2), namely that

$$\frac{1}{K} \ln y^+ + C \approx 8.75 (y^+)^{1/7}. \quad (3)$$

Using Eq. (3), Eq. (2) can be solved for u^+ in a transpired flow and yields the following result.

$$u^+ = 8.75 y^{1/7} + \frac{\nu_w^+}{4} (8.75 y^{+1/7})^2 \quad (4)$$

Using Eq. (4) as the approximate velocity profile in Eq. (1) gives the following ordinary differential equation for δ^+.

$$A_0 \frac{d\delta^+}{dx} + B_0 \delta^+ \frac{dF}{dx} + C_0 \delta^+ \left(\frac{1}{u_s} \frac{du_s}{dx} \right) = \frac{u_s \delta^+}{\nu} [1 + F u_s^{+2}] \quad (5)$$

A_0, B_0, and C_0 are known, complicated functions of δ^+, F and u_s^+, where u_s^+ is given by evaluating Eq. (4) at $y^+ = \delta^+$. Setting $y^+ = \delta^+$ in Eq. (4), noting that $\nu_w^+ = F u_s^+$ and defining $\Delta = 8.75 \delta^{+1/7}$ gives the result for u_s^+ shown next.

$$u_s^+ = \Delta/(1 - 0.25 F \Delta^2) \quad (6)$$

Next Eq. (5) is solved for $\delta^+(x)$ which leads to $u_s^+(x)$, both of which are needed to solve the thermal problem.

Now, the integral form of the thermal energy equation can be written as follows after changing to inner variables, u^+, y^+, and T^+ where $T^+ = \rho c_p u^* (T_w - T)/q_w$, $\delta_t^+ = \delta_t u^*/\nu$, $T_s^+ = \rho c_p u^* (T_w - T_s)/q_w$.

$$\frac{d}{dx} \left[\frac{q_w}{u^*} \int_0^{\delta_t^+} u^+ (T_s^+ - T^+) dy^+ \right] = \frac{q_w}{\nu} (1 + \nu_w^+ T_s^+) \quad (7)$$

The distribution of T^+, needed for the integration required in Eq. (7), is taken to be the thermal inner law. Experimental and theoretical evidence for the existence of a thermal inner law is given in Isaacson and Al Saji (1969) and by Faraco-Medeiros and Silva-Freire (1992) for transpired turbulent flows. Kader (1991) offers more theoretical support for the thermal inner law in flow with pressure gradients. The thermal inner law form follows next for transpired turbulent flows.

$$\frac{2}{\nu_w^+} [(1 + \nu_w^+ T^+)^{1/2} - 1] = \frac{Pr_t}{K} \ln y^+ + C_t(Pr) \quad (8)$$

As was done earlier, Eqs. (2) and (3), in connection with the velocity field, the right-hand side of Eq. (8) is replaced by a power-law approximation of it. After examining, the power law fits to the thermal inner law used in Johnk and Hanratty (1962), a good average value of the coefficient of y^+ is 6.0 and of the power is $1/5.85 = 0.1709$. Comparing this power-law form to the actual logarithmic form of the right side of Eq. (8), for $Pr_t = .85$, indicated agreement within seven percent for $y^+ < 1000$. With these and a fit to the $C_t(Pr)$, Eq. (8) is solved for T^+ and yields the following for a transpired flow, where $b = 13.2 \, Pr - 9.37$.

$$T^+ = (6y^{+0.1709} + b) + \frac{\nu_w^+}{4} (6y^{+0.1709} + b)^2 \quad (9)$$

In general, of course, the velocity profile has a wake contribution added to the inner law of Eq. (4) (Coles, 1971), and the inner law for temperature, Eq. (9), also has a wake contribution added to its right-hand side (Isaacson and Al Saji, 1969; Faraco-Medeiros and Silva-Freire, 1992). Part of the approximation in the present procedure is the neglect of these velocity and thermal wakes. For Prandtl numbers greater than about 0.6, most of the resistance to heat transfer in a turbulent flow is concentrated fairly near the wall in the inner layers and, therefore, the wakes may not be that important in the determination of the local Stanton number. With transpiration, there are situations in which this isn't true. It is known (Whitten et al., 1967), that the effect of blowing, $F > 0$, is to accentuate the effect of the wakes and, thus, they may be more important at the higher positive values of F.

Using Eqs. (4) and (9) in the thermal energy equation, Eq. (7), yields an ordinary differential equation with δ_t^+ as its dependent variable. This equation is shown next for the case of specified surface temperature with $\Delta T = T_w(x) - T_s$.

$$\frac{d\delta_t^+}{dx} + A_1 \frac{dF}{dx} + A_2 \frac{du_s^+}{dx} + \frac{A_3}{\Delta T} \frac{d}{dx} (\Delta T) = A_4 \quad (10)$$

The coefficients A_1 through A_4 are algebraically complicated, known functions of δ_t^+, δ^+, u_s^+, and F. The blowing factor F is a given function of x as is also the case for the surface temperature variation, $T_w(x)$. du_s^+/dx is found from the differentiation of Eq. (6) with respect to x. Once δ_t^+ is found as a function of x from the numerical solution of Eq. (10), the local Stanton number, St_x, is found by rearrangement of the expression for T_s^+ giving the following result.

$$St_x = \frac{h_x}{\rho c_p u_s} = \frac{1}{u_s^+ T_s^+} \quad (11)$$

T_s^+ is found by evaluating Eq. (9) at $y^+ = \delta_t^+$. Doing this and making use of $\nu_w^+ = F u_s^+$ yields the following result. b is given previously as $b = 13.2 \, Pr - 9.37$ and $\Delta_t^+ = 6\delta_t^{+0.1709} + b$
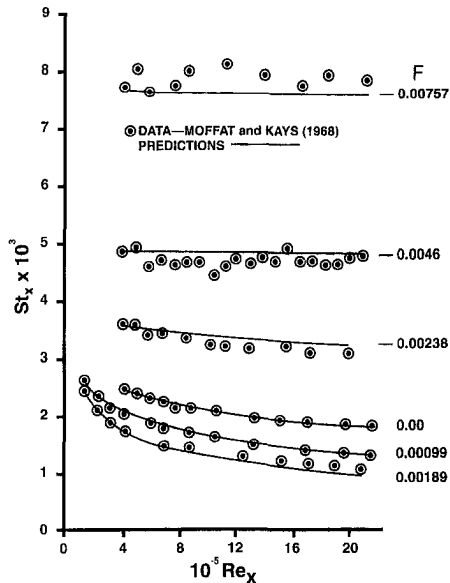
Fig. 1 Predictions and data, constant u_s

$$T_s^+ = \Delta_t^+ + \frac{Fu_s^+}{4}\Delta_t^{+2} \qquad (12)$$

Solution Procedure for the Equations

Equations (5) and (10) were solved for $\delta^+(x)$ and $\delta_t^+(x)$ by finite differences using a fourth-order Runge-Kutta procedure. The initial conditions needed by these first-order ordinary differential equations are the starting values, at $x = x_0$, $\delta^+(x_0)$ and $\delta_t^+(x_0)$. From the measured values of $C_f/2$ and of St_x at the first data point, one forms $u_s^+ = \sqrt{2/C_f}$ and uses this in Eq. (6) to solve for δ^+ at x_0. Similarly, the starting value of St_x is used in Eq. (11) which, when combined with Eq. (12) gives δ_t^+ at $x = x_0$.

The step size, Δx, used in solving was continually cut in half until two successive solutions gave results which are sensibly independent of the step size used. A typical example of this step size refinement is a case of Blackwell (1972) where $F = +0.001$ and $u_s \sim x^{-0.15}$. Here Δx was reduced until the change in St_x was about 0.02 percent and led to a nondimensional step size $\Delta x/L$ equal to 0.0032.

Results and Discussion

Predicted local Stanton numbers, St_x, as a function of position, x, are compared to experimental data in the various figures.

The integral solution for St_x was tested first for the limiting case of no transpiration, $F = 0$, and for zero pressure gradient. One of the comparisons of predictions with data for this case is shown as the third curve from the bottom in Fig. 1 where the experimental data is from Moffat and Kays (1968). As can be seen, agreement between predictions and data is very good for this simplest of test cases with the maximum error in the predicted St_x being less that three percent. Data shown on the figures are for specified wall temperature with most data sets being for constant T_w except for Fig. 7 where there are step changes in T_w.

The experimental data in Fig. 1 are all for u_s = constant for constant values of F which range from strong suction, $F = -0.00757$ to moderately strong blowing, $F = +0.00189$, and are from Moffat and Kays (1968). The solid curves are the predicted Stanton numbers, St_x, using the integral method of the present work. There is good agreement between predictions and data. The agreement between the top curve, $F = -0.00757$,
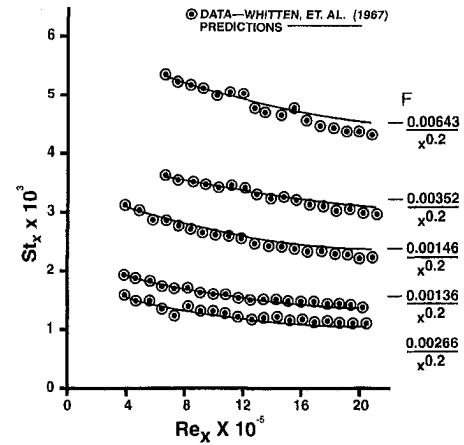
and data may not appear to look all that good, but, in fact, the maximum difference is about five percent. For strong blowing, $F = +0.00385$, predictions had degraded to unacceptable levels.

In Fig. 2, the experimental data is from Whitten et al. (1967) and is for u_s = constant, but with F variable, specifically F inversely proportional to $x^{0.2}$, $F \sim x^{-0.2}$. The agreement of predictions with data is comparable to that for the simpler case in Fig. 1.

Figure 3 contains experimental data due to Blackwell (1972). All the data shown in this figure are for different constant values of F and for flows which are experiencing a mild adverse pressure gradient where freestream velocity, $u_s(x)$, is inversely proportioned to distance x to the 0.15 power, $u_s(x) \sim x^{-0.15}$. The largest difference between the predicted Stanton number and data at $F = -0.002$ is about eight percent. It is seen that, overall, the agreement between the predictions, the solid curves, and data is quite good. This was somewhat surprising for $F > 0$, particularly for $F = 0.002$ and $F = 0.004$, since the fairly large velocity wake strength associated with a $u_s(x) \sim x^{-0.15}$ is being made effectively larger by the larger positive blowing rates of $F = 0.002$ and 0.004. However, this same adverse pressure gradient, which increases the strength of the wake in the velocity field, has the opposite effect on the temperature field. That is, it decreases the wake strength for the temperature field. Evidence for this is given in Kader (1991) and So (1994).

Shown in Fig. 4 is data from Blackwell (1972) and predictions by the present integral method for what are probably the most complex cases. The data is for moderate decceleration, $u_s(x) \sim x^{-0.15}$, and for blowing fraction, F, varying with position x, to the negative 0.17 power, $F(x) \sim x^{-0.17}$. Once again,
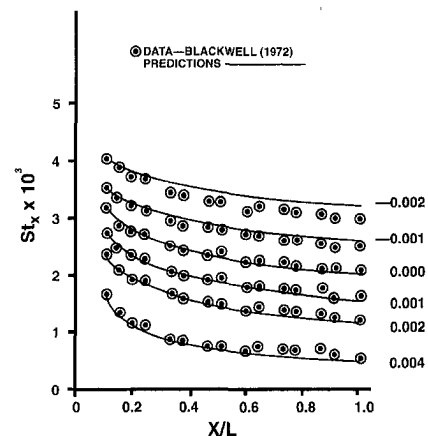

Fig. 2 Predictions and data, constant u_s, $F \sim x^{-0.20}$

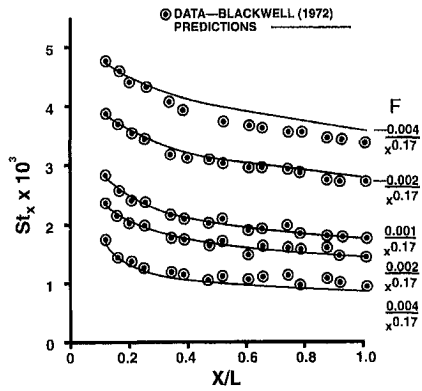Fig. 3 Predictions and data, $u_s \sim x^{-0.15}$

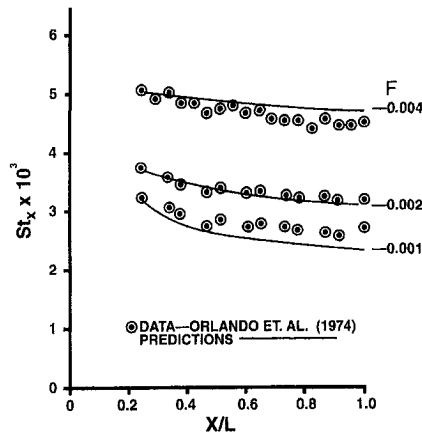**Fig. 4** Predictions and data, $u_s \sim x^{-0.15}$, $F \sim x^{-0.17}$, $L = 2.286$ m

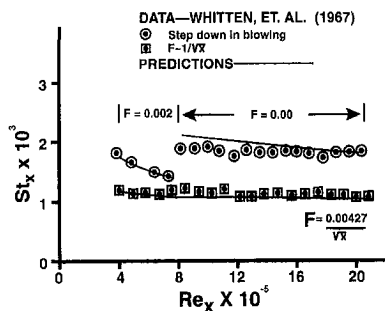**Fig. 5** Predictions and data, $u_s \sim x^{-0.275}$, $L = 2.286$ m (7.5 feet)

Fig. 6 Predictions and data, u_s = constant. Bottom curve, $F \sim x^{-0.5}$; upper curve, step change in blowing, $F = 0.002$ for $Re_x < 8 \times 10^5$, $F = 0.00$ for $Re_x > 8 \times 10^5$.

Fig. 7 Predictions and experimental data. Upper figure, constant u_s, $\Delta T = 12.5°C$ for $Re_x < 8 \times 10^5$, $\Delta T = 24.7°C$ for $8 \times 10^5 < Re_x < 16 \times 10^5$, $\Delta T = 32.5°C$ for $Re_x > 16 \times 10^5$. Lower figure, $F = 0.001$, $u_s \sim x^{-0.15}$, $L = 2.44$ m, step change in surface temperature at $x/L = 0.45$: $F = -0.002$, $u_s \sim x^{-0.275}$, $L = 2.44$ m, step change in surface temperature at $x/L = 0.43$.

as was the case in an earlier figure, the agreement of predicted St_x with data for the top curve is better that it may appear to be. The maximum difference between predictions and data is about 6.5 percent for $F \sim -0.004/x^{0.17}$. In general, the agreement between predictions and data is good in Fig. 4 except for the highest blowing rate.

Figure 5 shows the data of Orlando et al. (1974) and predictions for the case of a strong adverse pressure gradient where $u_s(x) \sim x^{-0.275}$. This leads to a large value of velocity wake strength which is effectively reduced by suction. It can be seen that predictions have definitely degraded for the lowest suction value of F shown, namely, $F = -0.001$.

Data of Whitten et al. (1967) is shown in Fig. 6 along with Stanton number predictions of the present integral method. The data is for zero pressure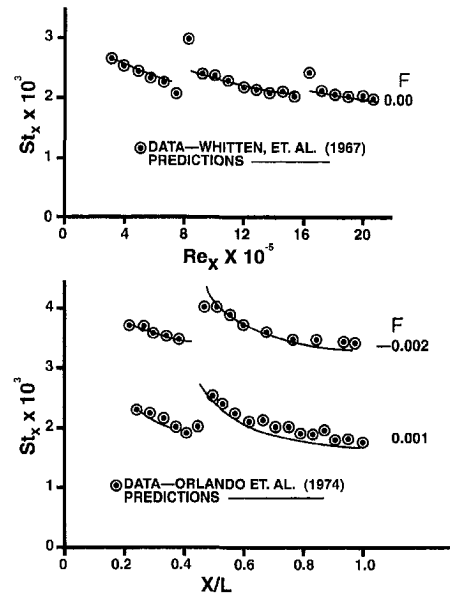 gradient. In the lowest data set, F varies inversely as the square root of position x and predictions seem to be very good. The upper data set and predictive curve is for a step change in blowing, that is, $F = +0.002$ for $Re_x < 8 \times 10^5$ and $F = 0.00$ for $Re_x > 8 \times 10^5$. This was modeled in the integral solution by a steep ramp in F which caused F to change from 0.002 to 0.00 in a very short distance just before $Re_x = 8 \times 10^5$. Agreement between predictions and data is good except just downstream of the step.

In Fig. 7, data and predictions are shown for situations where step changes in temperature occur on the surface. The data on the upper portion of the figure is for u_s a constant and $F = 0$ and is from Whitten et al. (1967). For $Re_x < 8 \times 10^5$, the surface temperature, T_w, is constant. There are step changes in surface temperature at both $Re_x = 8 \times 10^5$ and 16×10^5. It is evident from the figure that the predictions do well except in the immediate vicinity of the two step changes in surface temperature. Figure 7 also shows two cases of Orlando et al. (1974). For $F = -0.002$, $u_s(x) \sim x^{-0.275}$ the one step in wall temperature occurs at $x/L = 0.43$, and for $F = +0.001$, $u_s(x) \sim x^{-0.15}$ the step is at $x/L = 0.45$. Predictions are reasonably good.

Some comparisons will now be made to finite difference solutions in the literature. In four of the cases predicted by Cebeci and Mosinskis (1971), with F values from -0.0075 to 0.00189, their average error was 4.2 percent while the present integral method's average error is 3.2 percent. For four cases considered by Powell and Strong (1970), one of which was a variable surface temperature and another which had a step decrease in F from 0.002 to 0.0, their finite difference predictions' error was 3.6 percent versus the 3.1 percent error of the integral method of this work. Both of the finite difference procedures above used algebraic mixing length turbulence models. Finally, comparison was made to the k-ϵ turbulence model prediction by Jones and Launder (1973) for a case where F changes from 0.0 to 0.0039 at a point on the surface which also experiences a strong acceleration of the flow over a part of the surface. Their average predictive error, for this difficult case, is 15.2 percent while the present integral method gives 17 percent. Thus, it is seen that the predictions of the simple integral method

are comparable in accuracy to the three finite difference methods discussed above.

Concluding Remarks

An integral method has been developed to predict the Stanton number distribution in turbulent flow with pressure gradients along a transpired surface with either a prescribed surface temperature or a prescribed heat flux. The present method makes use of only the inner laws, for the velocity distribution and the temperature distribution, employing an easy to use power-law representation of them.

In spite of the absence of velocity and thermal wakes, predictions compare well with data and are as accurate as finite difference predictions, however, the present integral method is far simpler and requires less computational time.

Future work should include the wake portion of the velocity and temperature profiles in order to make reasonably good predictions in cases of strong blowing, where $F > 0.003$ and cases of strong adverse pressure gradients.

References

Ambrok, G. S., 1957, "Approximate Equation for the Thermal Boundary Layer With Variations in Boundary Layer Structure," *Soviet Physics, Technical Physics*, Vol. 2, No. 9, pp. 1979–1986.

Blackwell, B. F., 1972, "The Turbulent Boundary Layer on a Porous Plate: An Experimental Study of the Heat Transfer Behavior with Adverse Pressure Gradients," Ph.D. thesis, 141 pages, Stanford University, Stanford, CA.

Cebeci, T., and Mosinskis, G., 1971, "Calculation of Incompressible Turbulent Boundary Layers With Mass Transfer, Including Highly Accelerating Flows," ASME JOURNAL OF HEAT TRANSFER, Vol. 93, pp. 271–280.

Coles, D., 1971, "A Survey of Data for Turbulent Boundary Layers with Mass Transfer," Rand Corporation Report, No. P-4697, pp. 25-1–25-15.

Faraco-Medeiros, M. A., and Silva-Freire, A. P., 1992, "The Transfer of Heat in Turbulent Boundary Layers with Injection or Suction: Universal Laws and Stanton Number Equations," *Int. J. of Heat Mass Transfer*, Vol. 35, pp. 991–995.

Harasgama, S. P., Tarada, F. H., Baumann, R., Crawford, M. E., and Neelankantan, S., 1993, "Calculation of Heat Transfer to Turbine Blading Using Two Dimensional Boundary Layer Methods," ASME Paper No. 93-GT-79.

Hrycak, P., 1992, "High Reynolds Number Heat Transfer for Turbulent Flow with Zero Pressure Gradient," ASME HTD-Vol. 210, *Fundamentals of Forced Convection Heat Transfer*, M. A. Ebadian and P. H. Oosthuizen, eds., pp. 59–65.

Isaacson, L. K., and Al Saji, S. J., 1969, "Temperature Laws for a Turbulent Boundary Layer with Injection and Heat Transfer," *AIAA Journal*, Vol. 7, pp. 157–159.

Johnk, R. E., and Hanratty, T. J., 1962, "Temperature Profiles for Turbulent Flow of Air in a Pipe—I The Fully Developed Region," *Chemical Engineering Science*, Vol. 17, pp. 867–879.

Jones, W. P., and Launder, B. E., 1973, "The Calculation of Low Reynolds Number Phenomena with a Two Equation Model of Turbulence," *Int. J. Heat Mass Transfer*, Vol. 16, pp. 1119–1130.

Kader, B. A., 1991, "Heat and Mass Transfer in Pressure Gradient Boundary Layer," *Int. J. Heat Mass Transfer*, Vol. 34, No. 11, pp. 2837–2857.

Kays, W. M., 1972, "Heat Transfer to the Transpired Turbulent Boundary Layer," *Int. J. Heat Mass Transfer*, Vol. 15, pp. 1023–1044.

Kearney, D. W., Kays, W. M., and Moffat, R. J., 1973, "Heat Transfer to a Strongly Accelerated Turbulent Boundary Layer: Some Experimental Results, Including Transpiration," *Int. J. Heat Mass Transfer*, Vol. 16, pp. 1289–1305.

Moffat, R. J., and Kays, W. M., 1968, "The Turbulent Boundary Layer on a Porous Plate: Experimental Heat Transfer with Uniform Blowing and Suction," *Int. J. Heat Mass Transfer*, Vol. 11, pp. 1547–1566.

Moffat, R. J., and Kays, W. M., 1984, "A Review of Turbulent Boundary Layer Heat Transfer Research at Stanford, 1958–1983," *Advances in Heat Transfer*, Vol. 16, Academic Press, New York, pp. 241–365.

Orlando, A. F., Moffat, R. J., and Kays, W. M., 1974, "Turbulent Transport of Heat and Momentum in a Boundary Layer Subject to Deceleration, Suction and Variable Wall Temperature," Report No. HMT-17, Department of Mechanical Engineering, Stanford University, Stanford, CA.

Powell, T. E., and Strong, A. B., 1970, "Calculation of Two Dimensional Turbulent Boundary Layer with Mass Addition and Heat Transfer," *Proc. 1970 Heat Transfer and Fluid Mechanics Institute*, Stanford University Press, Stanford, CA, pp. 153–165.

So, R. M. C., 1994, "Pressure Gradient Effects on Reynolds Analogy for Constant Property Equilibrium Turbulent boundary Layers," *Int. J. Heat Mass Transfer*, Vol. 37, No. 1, pp. 27–41.

Stevenson, T. N., 1963, "A Law of the Wall for Turbulent Boundary Layers with Suction or Injection," Report Aero No. 166, College of Aeronautics, Cranfield, 18 pp., also available from NTIS as N64-19323.

Succc, J., and Lu, Y., 1990, "Heat Transfer Across Turbulent Boundary Layers With Pressure Gradient," ASME JOURNAL OF HEAT TRANSFER, Vol. 112, pp. 906–912.

Thielbahr, W. H., Kays, W. M., and Moffat, R. J., 1972, "The Turbulent Boundary Layer on a Porous Plate: Experimental Heat Transfer With Uniform Blowing and Suction, With Moderately Strong Acceleration," ASME JOURNAL OF HEAT TRANSFER, Vol. 94, pp. 111–118.

Thomas, L., and Al-Shariff, M. M., 1981, "An Integral Analysis for Heat Transfer in Turbulent, Incompressible Boundary Layer Flow," ASME JOURNAL OF HEAT TRANSFER, Vol. 103, pp. 772–777.

Torii, K., Nishiwaki, N., and Hirata, M., 1966, "Heat Transfer and Skin Friction in Turbulent Boundary Layer with Mass Injection," *Proceedings of the Third International Heat Transfer Conference*, Vol. 3, Chicago, pp. 34–48.

Whitten, D. G., Kays, W. M., and Moffat, R. J., 1967, "The Turbulent Boundary Layer on a Porous Plate: Experimental Heat Transfer with Variable Suction, Blowing and Surface Temperature," Report No. HMT-3, Department of Mechanical Engineering, Stanford University, Stanford, CA.

Heat Flux Measurements in Homogeneous Curved Shear Flow

A. G. L. Holloway[1] and S. A. Ebrahimi-Sabet[2]

Turbulent heat fluxes were measured far downstream of a fine heating wire stretched spanwise across a curved, uniform shear flow. The turbulence was approximately homogeneous and the overheat small enough to be passive. Strong destabilizing and stabilizing curvature effects were produced by directing the shear toward the center of curvature and away from the center of curvature, respectively. The dimensionless turbulent shear stress was strongly affected by the flow curvature, but the dimensionless components of the turbulent heat flux were found to be relatively insensitive.

1 Introduction

The effect of prolonged flow curvature on uniformly sheared, isothermal homogenous turbulence has been studied experimentally by Holloway and Tavoularis (1992). In this experiment, turbulence with a self-preserving sheared structure (where ratios of Reynolds' stresses were constant) was developed in a straight wind tunnel and was then passed into a curved wind tunnel with a constant centerline radius. Depending on the relative orientation of the shear and curvature, the dimensionless shear stress $\rho_{uv} = \overline{uv}/u'v'$ increased or decreased; and, consequently, the turbulence was destabilized or stabilized. (u and v are the streamwise and transverse components of fluctuating velocity, primes denote RMS values.) The effects of the curvature on ρ_{uv} were found to correlate with the curvature parameter $S = (U/R)/(dU/dn)$, where U is the mean centerline speed, R is the centerline radius of curvature, and dU/dn is the mean shear transverse to the flow. When the mean velocity increased towards the center of curvature ($S < 0$) the turbulence was destabilized. When the mean velocity increased away from the center of curvature ($S > 0$) the turbulence was stabilized.

The effect of curvature on the dimensionless components of the turbulent heat flux $\rho_{u\theta} = \overline{u\theta}/u'\theta'$ and $\rho_{v\theta} = \overline{v\theta}/v'\theta'$ (θ is

[1] Associate Professor, Department of Mechanical Engineering, University of New Brunswick, Fredericton, NB E3B 5A3, Canada.

[2] Graduate Student, Department of Chemical Engineering and Applied Chemistry, University of Toronto, Toronto, Ont., M5S 3E5, Canada.

are comparable in accuracy to the three finite difference methods discussed above.

Concluding Remarks

An integral method has been developed to predict the Stanton number distribution in turbulent flow with pressure gradients along a transpired surface with either a prescribed surface temperature or a prescribed heat flux. The present method makes use of only the inner laws, for the velocity distribution and the temperature distribution, employing an easy to use power-law representation of them.

In spite of the absence of velocity and thermal wakes, predictions compare well with data and are as accurate as finite difference predictions, however, the present integral method is far simpler and requires less computational time.

Future work should include the wake portion of the velocity and temperature profiles in order to make reasonably good predictions in cases of strong blowing, where $F > 0.003$ and cases of strong adverse pressure gradients.

References

Ambrok, G. S., 1957, "Approximate Equation for the Thermal Boundary Layer With Variations in Boundary Layer Structure," *Soviet Physics, Technical Physics,* Vol. 2, No. 9, pp. 1979–1986.

Blackwell, B. F., 1972, "The Turbulent Boundary Layer on a Porous Plate: An Experimental Study of the Heat Transfer Behavior with Adverse Pressure Gradients," Ph.D. thesis, 141 pages, Stanford University, Stanford, CA.

Cebeci, T., and Mosinskis, G., 1971, "Calculation of Incompressible Turbulent Boundary Layers With Mass Transfer, Including Highly Accelerating Flows," ASME JOURNAL OF HEAT TRANSFER, Vol. 93, pp. 271–280.

Coles, D., 1971, "A Survey of Data for Turbulent Boundary Layers with Mass Transfer," Rand Corporation Report, No. P-4697, pp. 25-1–25-15.

Faraco-Medeiros, M. A., and Silva-Freire, A. P., 1992, "The Transfer of Heat in Turbulent Boundary Layers with Injection or Suction: Universal Laws and Stanton Number Equations," *Int. J. of Heat Mass Transfer,* Vol. 35, pp. 991–995.

Harasgama, S. P., Tarada, F. H., Baumann, R., Crawford, M. E., and Neelankantan, S., 1993, "Calculation of Heat Transfer to Turbine Blading Using Two Dimensional Boundary Layer Methods," ASME Paper No. 93-GT-79.

Hrycak, P., 1992, "High Reynolds Number Heat Transfer for Turbulent Flow with Zero Pressure Gradient," ASME HTD-Vol. 210, *Fundamentals of Forced Convection Heat Transfer,* M. A. Ebadian and P. H. Oosthuizen, eds., pp. 59–65.

Isaacson, L. K., and Al Saji, S. J., 1969, "Temperature Laws for a Turbulent Boundary Layer with Injection and Heat Transfer," *AIAA Journal,* Vol. 7, pp. 157–159.

Johnk, R. E., and Hanratty, T. J., 1962, "Temperature Profiles for Turbulent Flow of Air in a Pipe—I The Fully Developed Region," *Chemical Engineering Science,* Vol. 17, pp. 867–879.

Jones, W. P., and Launder, B. E., 1973, "The Calculation of Low Reynolds Number Phenomena with a Two Equation Model of Turbulence," *Int. J. Heat Mass Transfer,* Vol. 16, pp. 1119–1130.

Kader, B. A., 1991, "Heat and Mass Transfer in Pressure Gradient Boundary Layer," *Int. J. Heat Mass Transfer,* Vol. 34, No. 11, pp. 2837–2857.

Kays, W. M., 1972, "Heat Transfer to the Transpired Turbulent Boundary Layer," *Int. J. Heat Mass Transfer,* Vol. 15, pp. 1023–1044.

Kearney, D. W., Kays, W. M., and Moffat, R. J., 1973, "Heat Transfer to a Strongly Accelerated Turbulent Boundary Layer: Some Experimental Results, Including Transpiration," *Int. J. Heat Mass Transfer,* Vol. 16, pp. 1289–1305.

Moffat, R. J., and Kays, W. M., 1968, "The Turbulent Boundary Layer on a Porous Plate: Experimental Heat Transfer with Uniform Blowing and Suction," *Int. J. Heat Mass Transfer,* Vol. 11, pp. 1547–1566.

Moffat, R. J., and Kays, W. M., 1984, "A Review of Turbulent Boundary Layer Heat Transfer Research at Stanford, 1958–1983," *Advances in Heat Transfer,* Vol. 16, Academic Press, New York, pp. 241–365.

Orlando, A. F., Moffat, R. J., and Kays, W. M., 1974, "Turbulent Transport of Heat and Momentum in a Boundary Layer Subject to Deceleration, Suction and Variable Wall Temperature," Report No. HMT-17, Department of Mechanical Engineering, Stanford University, Stanford, CA.

Powell, T. E., and Strong, A. B., 1970, "Calculation of Two Dimensional Turbulent Boundary Layer with Mass Addition and Heat Transfer," *Proc. 1970 Heat Transfer and Fluid Mechanics Institute,* Stanford University Press, Stanford, CA, pp. 153–165.

So, R. M. C., 1994, "Pressure Gradient Effects on Reynolds Analogy for Constant Property Equilibrium Turbulent boundary Layers," *Int. J. Heat Mass Transfer,* Vol. 37, No. 1, pp. 27–41.

Stevenson, T. N., 1963, "A Law of the Wall for Turbulent Boundary Layers with Suction or Injection," Report Aero No. 166, College of Aeronautics, Cranfield, 18 pp., also available from NTIS as N64-19323.

Sucec, J., and Lu, Y., 1990, "Heat Transfer Across Turbulent Boundary Layers With Pressure Gradient," ASME JOURNAL OF HEAT TRANSFER, Vol. 112, pp. 906–912.

Thielbahr, W. H., Kays, W. M., and Moffat, R. J., 1972, "The Turbulent Boundary Layer on a Porous Plate: Experimental Heat Transfer With Uniform Blowing and Suction, With Moderately Strong Acceleration," ASME JOURNAL OF HEAT TRANSFER, Vol. 94, pp. 111–118.

Thomas, L., and Al-Shariff, M. M., 1981, "An Integral Analysis for Heat Transfer in Turbulent, Incompressible Boundary Layer Flow," ASME JOURNAL OF HEAT TRANSFER, Vol. 103, pp. 772–777.

Torii, K., Nishiwaki, N., and Hirata, M., 1966, "Heat Transfer and Skin Friction in Turbulent Boundary Layer with Mass Injection," *Proceedings of the Third International Heat Transfer Conference,* Vol. 3, Chicago, pp. 34–48.

Whitten, D. G., Kays, W. M., and Moffat, R. J., 1967, "The Turbulent Boundary Layer on a Porous Plate: Experimental Heat Transfer with Variable Suction, Blowing and Surface Temperature," Report No. HMT-3, Department of Mechanical Engineering, Stanford University, Stanford, CA.

Heat Flux Measurements in Homogeneous Curved Shear Flow

A. G. L. Holloway[1] and S. A. Ebrahimi-Sabet[2]

Turbulent heat fluxes were measured far downstream of a fine heating wire stretched spanwise across a curved, uniform shear flow. The turbulence was approximately homogeneous and the overheat small enough to be passive. Strong destabilizing and stabilizing curvature effects were produced by directing the shear toward the center of curvature and away from the center of curvature, respectively. The dimensionless turbulent shear stress was strongly affected by the flow curvature, but the dimensionless components of the turbulent heat flux were found to be relatively insensitive.

1 Introduction

The effect of prolonged flow curvature on uniformly sheared, isothermal homogenous turbulence has been studied experimentally by Holloway and Tavoularis (1992). In this experiment, turbulence with a self-preserving sheared structure (where ratios of Reynolds' stresses were constant) was developed in a straight wind tunnel and was then passed into a curved wind tunnel with a constant centerline radius. Depending on the relative orientation of the shear and curvature, the dimensionless shear stress $\rho_{uv} = \overline{uv}/u'v'$ increased or decreased; and, consequently, the turbulence was destabilized or stabilized. (u and v are the streamwise and transverse components of fluctuating velocity, primes denote RMS values.) The effects of the curvature on ρ_{uv} were found to correlate with the curvature parameter $S = (U/R)/(dU/dn)$, where U is the mean centerline speed, R is the centerline radius of curvature, and dU/dn is the mean shear transverse to the flow. When the mean velocity increased towards the center of curvature ($S < 0$) the turbulence was destabilized. When the mean velocity increased away from the center of curvature ($S > 0$) the turbulence was stabilized.

The effect of curvature on the dimensionless components of the turbulent heat flux $\rho_{u\theta} = \overline{u\theta}/u'\theta'$ and $\rho_{v\theta} = \overline{v\theta}/v'\theta'$ (θ is

Copyright © 1999 by ASME

the fluctuating temperature) in uniformly sheared flow has not been previously studied and is the subject of the present investigation. The experiment was to stretch a very-small-diameter heating wire across the entrance to the curved tunnel and measure the heat flux in its thermal wake. The wire produced very little drag but added sufficient heat to be sensible. Far downwind of the wire, the mean shear was uniform and the turbulence nearly homogeneous across the thermal wake; which had an approximately Gaussian shaped mean temperature profile and associated heat flux.

The development of the wake of a thermal line source in uniformly sheared turbulence has been studied extensively by Karnik and Tavoularis (1989). They measured many features of the temperature and velocity fields, in particular, they found $\rho_{uv} = 0.45$ throughout the flow while $\rho_{u\theta}$ and $\rho_{v\theta}$ were antisymmetric about the position of peak mean temperature with peak absolute values of 0.45 and 0.35, respectively, coincident with the positions of maximum mean temperature gradient.

The effects of surface curvature on $\rho_{u\theta}$ and $\rho_{v\theta}$ in heated boundary layers has been studied, but only by few investigators. Gibson and Verriopulos (1984) studied a convex boundary layer with $\delta/R_w = 0.01$ (δ is the boundary layer thickness and R_w is the wall curvature) and found that both the streamwise and transverse heat fluxes, $\overline{u\theta}$ and $\overline{v\theta}$, decreased relative to a flat boundary layer. This reduction was mainly due to the reduction in turbulence activity produced by curvature. Surprisingly, the temperature fluctuations, θ^2, were not significantly different from those in a flat boundary layer; and therefore, $\rho_{u\theta}$ and $\rho_{v\theta}$ were also reduced. Prior to the start of curvature, $\rho_{u\theta} = 0.60$ and $\rho_{v\theta} = 0.57$; while, after prolonged curvature, $\rho_{u\theta} = 0.55$ and $\rho_{v\theta} = 0.45$. You, Simon, and Kim (1986) and Kim and Simon (1988) studied a convex boundary layer with $\delta/R_w = 0.03$, and, consistent with Gibson and Verriopoulos (1984), they found that $\overline{u\theta}$ and $\overline{v\theta}$ were reduced; but contrary to Gibson and Verriopolous (1984), they found that θ^2 was also reduced. Unfortunately they do not provide enough information to evaluate the resulting effect on $\rho_{u\theta}$ and $\rho_{v\theta}$.

A concave turbulent boundary layer with $\delta/R_w = 0.008$ was studied by Gibson and Servat-Djoo (1981). They found that both $\overline{u\theta}$ and $\overline{v\theta}$ increased with the increase in turbulence activity resulting from curvature; but, that $\rho_{u\theta}$ and $\rho_{v\theta}$ maintained their flat-plate values of 0.61 and 0.56 throughout the curved boundary layer. Hollingsworth et al. (1992) reported turbulent Prandtl number estimates for the outer part of a concave boundary layer that were significantly larger than those measured in uncurved boundary layers. They concluded that concave curvature has a greater effect on momentum transport than heat transport.

One might expect the effects of curvature on ρ_{uv} and $\rho_{v\theta}$ to be similar, and certainly this is true where a perfect analogy exists between the momentum deficit, $-u$, and the overheat, θ; because, there $\rho_{u\theta} = -1$, and necessarily $\rho_{uv} = -\rho_{v\theta}$. However, in the present flow the wake turbulence is almost entirely produced by the uniform shear, so that $\rho_{u\theta}$ is much weaker, and ρ_{uv} and $\rho_{v\theta}$ are potentially more independent. A less complete analogy is that of Reynolds, which assumes a turbulent Prandtl number of unity and gives the relationship $\rho_{uv}/\rho_{v\theta} = l_\theta/l_u$ in terms of the momentum and temperature mixing lengths. In both the convex and concave heated boundary layer studies cited above, $\rho_{uv}/\rho_{v\theta} \sim 0.9$, while in the present study it ranges from 0.6 to 1.0.

Two strongly curved flow experiments are reported in the following; one had $S = -0.13$ (destabilized) and the other had $S = +0.08$ (stabilized). In both experiments the turbulence structure was strongly affected, but $\rho_{u\theta}$ and $\rho_{v\theta}$ were little different from those measured by Karnik and Tavoularis (1989) for uncurved flow.

2 Experimental Apparatus

The experiment with $S = -0.13$ was performed in the wind tunnel at the University of New Brunswick. This tunnel has a compound test section comprised of a 3.0-m long straight section, at the start of which is a shear generator, and a curved section having a 3.0-m centerline radius and 1.57-m length (see Fig. 1). The shear generator is composed of 23 parallel channels, each with a different flow resistance tuned to produce a linear mean velocity profile in its wake (for a detailed description see Karnik and Tavoularis 1987). The cross section of the initial straight section is 0.57-m square; the curved tunnel was made smaller (0.5 m) to remove the developed boundary layers. The tunnel was designed to allow the measurement of streamwise development along the wind tunnel centerline and transverse profiles at selected locations. The experiment with $S = +0.08$ (stabilizing curvature) was performed in a wind tunnel at the University of Ottawa which is similar, but smaller, than the one at the University of New Brunswick (for a description see Holloway and Tavoularis (1992)).

The heating system consisted of a fine nichrome wire stretched spanwise across the entrance to the curved test section (see Fig. 1). Wire tension was adjusted to avoid flow-induced vibration. The nichrome heating wire had a 0.113-mm diameter and a nominal resistivity of 106 Ω/m. A power of 30 W/m was required to produce a wire operating temperature of approximately 170°C. Assuming the boundary layer air surrounding the wire to be at this temperature, and the mean wind speed in the vicinity of the wire to be approximately 7 m/s, the estimated Reynolds number, Re = Ud/ν = 30. Under these conditions the Richardson number, Ri = $g\alpha\theta d/U^2 = 2 \times 10^{-6}$, and buoyancy effects could therefore be neglected.

3 Instrumentation

The cold wire and cross wires used for temperature and velocity measurement were held in very close proximity using a specially built probe holder. The cross-wire probe axis was tangent to the s-direction, while the cold-wire probe axis was at an angle of 60 deg. The sensing elements of the cross wire and the cold wire were all parallel to the (s, n) plane and separated by a spanwise distance of 1.5 mm or approximately five percent of the half-width of the thermal wake.

The cross wires were powered by constant temperature bridges (Dantec CTA Bridge Type 56C17), and the bridge voltage, E, was related to the cooling velocity, U_{eff}, according to the modified "King's law"

$$\frac{E^2}{T_w - T_f} = A + BU_{\text{eff}}^n \qquad (1)$$

where T_w is the wire operating temperature, T_f is the fluid temperature, and A, B, and n are calibration constants evaluated by least-squares fitting. The cross wires (Dantec Type 55P61) were made of tungsten and were 1.25 mm long, 5 μm in diameter, and were separated by 1 mm. The wire operating temperature was 220°C, and T_f was determined using the simultaneous temperature measurements.

The air temperature-rise above ambient was measured by placing one cold wire far upwind of the heating wire and another in the thermal wake. Both wires were supplied with a constant current from a passive bridge. By adjusting the currents (around 0.33 mA), the sensitivities of the two wires were matched such that the difference in wire temperatures, ΔT, was proportional to the difference in voltages, E_w, across each wire

$$\Delta T = G(E_{w_2} - E_{w_1}), \qquad (2)$$

where G is the measured sensitivity. Both the mean temperature rise, ΔT, and the temperature fluctuations, θ, were derived from Eq. (2). The ambient temperature was also recorded and combined with ΔT to estimate T_f for use in Eq. (1). Both platinum cold wires (Dantec type 55P31) were 0.4 mm long and 1 μm in diameter. The experiment performed at the University of Ottawa used a cold wire to measure θ but the mean temperature
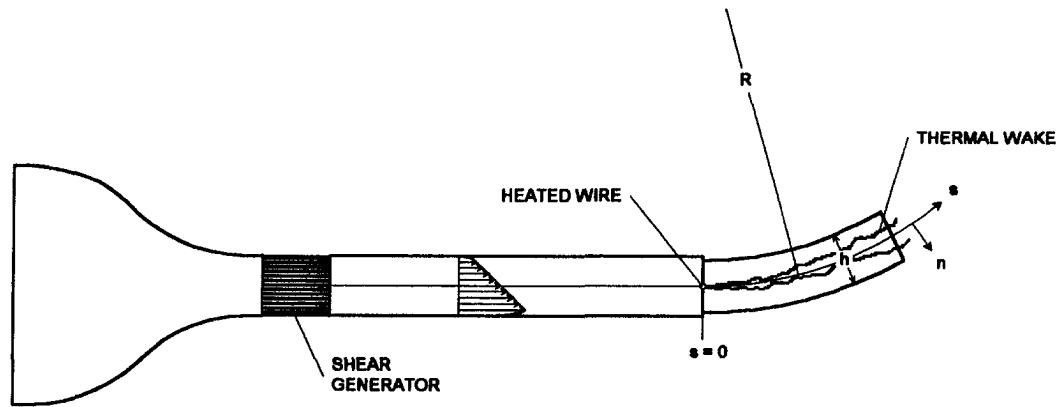
Fig. 1 Schematic of wind tunnel and heated wake showing the definition of the curvilinear coordinates. For the direction of shear shown the curvature has a stabilizing effect ($S > 0$). When the direction of the shear is reversed the curvature has a destabilizing effect ($S < 0$).

was measured separately using a pair of glass-coated thermistor beads.

The electrical signals from the velocity and temperature bridges were low-pass filtered, amplified, and then digitized simultaneously using a four-channel 12-bit ADC with a range of 2.5 volts. Twenty time series of 4096 points for both temperature and velocity were gathered at a rate of 500 Hz and used for calculating the heat fluxes. Streamwise integral length scales of the velocity were determined by integrating the autocorrelation to its first zero and applying Taylor's "frozen flow" hypothesis. The autocorrelations were computed using time records digitized at 2 kHz.

Uncertainty estimates for the measurements reported in this paper are summarized in Table 1. These values arise mostly from bias errors since each reported data point is the average of 81,920 statistically independent samples. The types of errors considered for the velocity statistics included (1) calibration, (2) temperature sensitivity, (3) digitization error, and (4) probe and flow misalignment. The errors considered for the temperature statistics included (1) velocity sensitivity, (2) electronic noise, (3) instrument drift, and (4) digitization error. Note that all the temperature statistics have been presented in a normalized form such that the sensitivity, G, shown in Eq. (2) is not important. Electronic and flow noise on the cold-wire channel was measured in an isothermal air stream and subtracted from the signals under the assumption that these were uncorrelated with temperature fluctuations.

The greatest single error in the present measurements of dimensionless heat flux results from the physical separation of the velocity and temperature probes. It was determined from the two-point velocity-temperature covariance measurements reported by Tavoularis and Corrsin (1981) for heated shear flow that the peak magnitudes of $\rho_{u\theta}$ and $\rho_{v\theta}$ will be *underestimated* by 0.035. Further uncertainty in the heat flux measurements arises from the mutual velocity sensitivity of the velocity and temperature probes as well as all of the sources listed above for both velocity and temperature. In the present work, the false velocity-temperature correlation due to the velocity sensitivity of the cold wires was found to be significant only at the outer edge of the thermal wake, $|n_\theta/b| > 3$, where the temperature

fluctuations were weak. To minimize the effect of instrument drift on the dimensionless heat fluxes, values were calculated for each of the 20 data records and subsequently averaged.

4 Results and Discussion

Velocity and temperature profiles were measured transverse to the flow at three streamwise positions: $s/d = 1300, 6600$, and 12,000; where d is the diameter of the heating wire and s is measured along the tunnel centerline starting from the wire. The velocity measurements at $s/d = 1300$ showed significant wake effects and therefore were not included in the present paper. However, by $s/d = 6600$, the velocity statistics were more homogeneous and very similar to those measured without the heating wire in place. The temperature and velocity statistics from $s/d = 6600$ and $s/d = 12,000$ showed a strong similarity and form the basis of the present study of curvature effects on the turbulent heat flux.

4.1 Velocity. The mean and RMS velocity for both flows ($S = +0.08$ and $S = -0.13$) are shown in Figs. 2 and 3. Near the tunnel centerline, the mean shear and rms velocities are nearly uniform, and the turbulence intensities, relative to the mean centerline speed, are less than ten percent. In the stabilized case ($S = +0.08$), the turbulent kinetic energy decayed along the tunnel, while in the destabilized case ($S = -0.13$) the turbulent kinetic energy grew. Integral length scales from both flows are summarized in Table 2.

Profiles of $\rho_{uv} = \overline{uv}/u'v'$ are shown in Fig. 4. Note that for $S = +0.08$, ρ_{uv} has been made positive to accommodate the experimental convenience of creating this flow by reversing the shear direction rather than the tunnel curvature. In each flow ρ_{uv} was nearly uniform in the transverse direction and had similar values at both streamwise positions. This implies that the wake turbulence has decayed by this point and a nearly uniform turbulence structure exists throughout the portion of the thermal wake under study.

The values of ρ_{uv} differ substantially (by nearly a factor of 2) between the stabilized and destabilized flows, and are in agreement with the measurements reported by Holloway and

Table 1 Experimental uncertainties

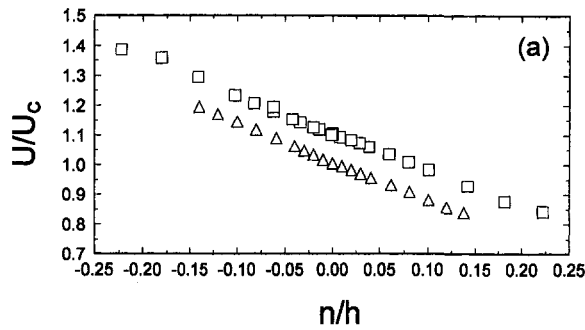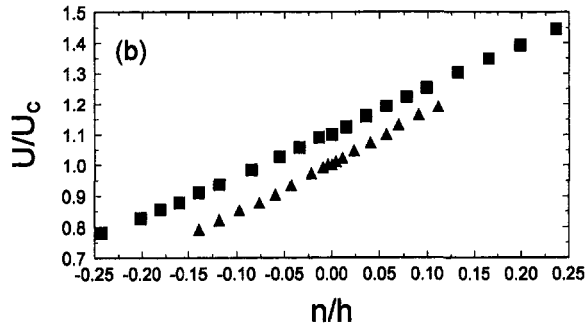|	U/U_c	u'/U_c	ρ_{uv}	$\Delta T/\Delta T_c$	$\overline{\theta^2}/\overline{\theta_t^2}$	$\rho_{u\theta}$	$\rho_{v\theta}$	n/h	n_θ/b
Uncertainty 20:1 odds	0.03	0.007	0.02	0.17	0.05	0.04	0.04	0.004	0.21

Fig. 2(a)

Fig. 2(b)

Fig. 2 (a) Mean velocity profiles in the destabilized shear flow (S = −0.13); △ s/d = 6600, □ s/d = 12,000. The profile at s/d = 12,000 has been shifted up by 0.1 units. (b) Mean velocity profiles in the stabilized shear flow (S = 0.08); ▲ s/d = 6600, ■ = 12,000. The profile at s/d = 12,000 has been shifted up by 0.1 units.
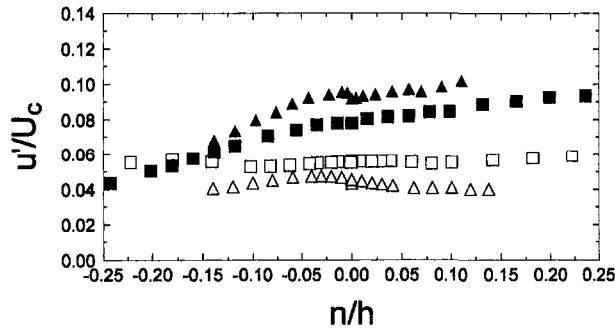

Fig. 3 Transverse profiles of the rms streamwise velocity component for destabilized and stabilized shear flow; symbols are defined in Fig. 2

Table 2 A summary of wake half-widths and velocity length scales

s/d	$S = +0.08$		$S = -0.13$	
	b (mm)	Luu (mm)	b (mm)	Luu (mm)
6600	23	46	23	55
12,000	35	42	33	75

Tavoularis (1992) for the isothermal curved shear flow. The value of ρ_{uv} measured by Karnik and Tavoularis (1989) in a heated straight shear flow is intermediate between those measured in the two present flows.

4.2 Temperature. The transverse profiles of mean temperature shown in Fig. 5 were used to determine a local center, n_p, and half-width, b, of the thermal wake at each streamwise position. These were then used to align the transverse profiles of the other temperature statistics, using the new variable $n_\theta =$
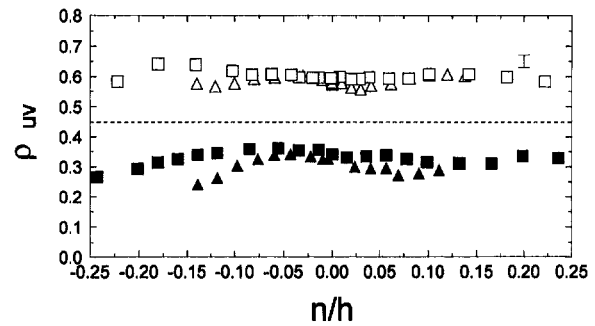

Fig. 4 Transverse profiles of $\rho_{uv} = \overline{uv}/u'v'$ for destabilized and stabilized shear flow; symbols are defined in Fig. 2. Note that the sign of ρ_{uv} for the stabilized case (solid symbols) has been reversed to account for the change in the shear direction. The dashed line represents the measurements of Karnik and Tavoularis (1989) for uncurved shear flow.
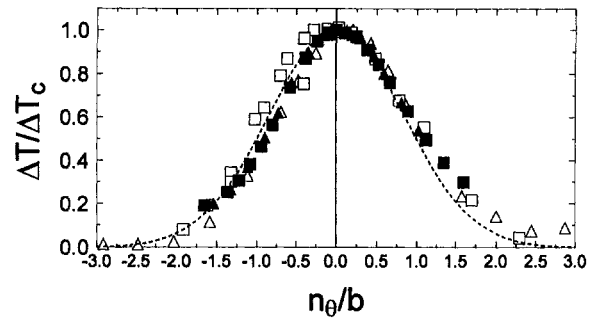

Fig. 5 Transverse mean temperature profiles for destabilized and stabilized shear flow; symbols are defined in Fig. 2. The dashed line represents the Gaussian distribution.
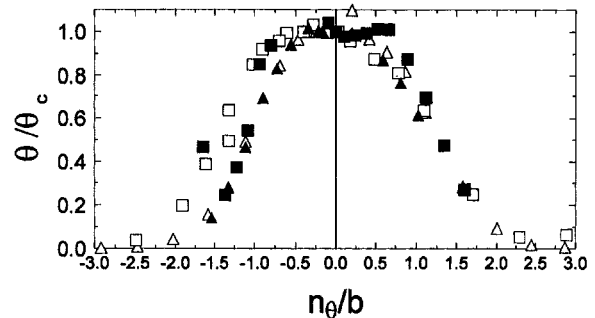

Fig. 6 Transverse profiles of the temperature variance in destabilized and stabilized shear flow; symbols are defined in Fig. 2

$n - n_p$, and to normalize the transverse dimension, respectively. The peak mean temperature decayed along the wind tunnel centerline according to a power law with an exponent of 0.9. Values of b are summarized in Table 2.

Normalized transverse profiles of the temperature variance, $\overline{\theta^2}$, are shown in Fig. 6. They differ substantially in shape with some being single peaked and some, possibly like those measured by Karnik and Tavoularis (1989), being double peaked. The temperature variance was found to decay along the wind tunnel centerline according to a power law with an exponent of 1.9.

Transverse profiles of the heat flux correlation coefficient, $\rho_{u\theta} = \overline{u\theta}/u'\theta'$, are presented in Fig. 7 (the sign of $\rho_{u\theta}$ in the stabilized flow has been altered similar to that of ρ_{uv}). Profiles from both flows are nearly zero at $n_\theta = 0$, tend to zero at the edge of the thermal wake, and have maxima and minima near the points of maximum mean temperature gradient. It is surpris-
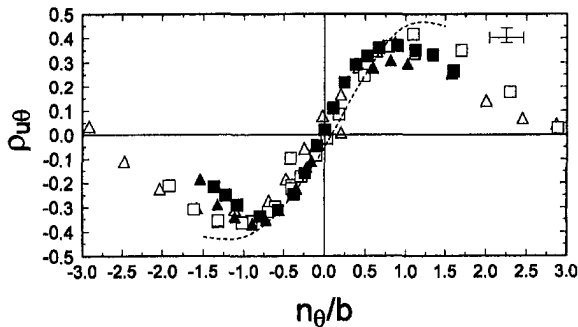
Fig. 7 Transverse profiles of $\rho_{u\theta} = \overline{u\theta}/u'\theta'$ for destabilized and stabilized shear flow; symbols are defined in Fig. 2. Note that the sign of $\rho_{u\theta}$ for the stabilized case (solid symbols) has been reversed to account for the change in the shear direction. The dashed line represents the measurements of Karnik and Tavoularis for uncurved shear flow at a similar distance from the heating wire.
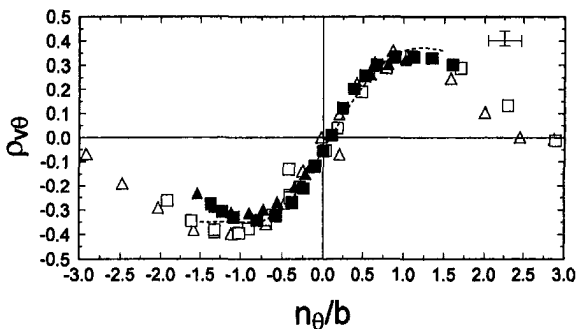

Fig. 8 Transverse profiles of $\rho_{v\theta} = \overline{v\theta}/v'\theta'$ for destabilized and stabilized shear flow; symbols are defined in Fig. 2. The dashed line represents the measurements of Karnik and Tavoularis (1989) for uncurved shear at a similar distance from the heating wire.

ing that the profiles of $\rho_{u\theta}$ from the stabilized and destabilized flows are so close; given the dramatic difference in turbulence structure shown in Fig. 4. The peak values of $\rho_{u\theta}$ are lower than those measured by Karnik and Tavoularis (1989); a result which is in part due to the greater separation of the velocity and temperature probes used in this study. Based on these results one might conclude, at least in this homogeneous flow, that $\rho_{u\theta}$ is less sensitive to flow curvature than ρ_{uv}.

Transverse profiles of the heat flux correlation coefficient, $\rho_{v\theta} = \overline{v\theta}/v'\theta'$, are presented in Fig. 8. Profiles from both flows overlap with a high degree of similarity. The only significant difference between the stabilized and destabilized flows is on the inside of the wake where heat is transported towards the center of curvature. Nevertheless, these results show that $\rho_{v\theta}$ is substantially less sensitive to flow curvature than ρ_{uv}.

That $\rho_{u\theta}$ and $\rho_{v\theta}$ are less sensitive to flow curvature than is ρ_{uv} in this uniformly sheared flow is consistent with most of the boundary layer studies cited in the Introduction; an exception being the convex boundary layer measurements of Gibson and Verriopolous (1984). However, it is surprising that $\rho_{u\theta}$ and $\rho_{v\theta}$ have been found to be so insensitive to flow curvature which strongly affected ρ_{uv}. A firm explanation of this finding is lacking and until one is provided the present results should be treated with some skepticism. It is plausible, however, that the heat transport in this particular flow results from smaller scale motions than those which are most affected by curvature; whereas, in the boundary layer studies cited earlier, the velocity and temperature length scales would necessarily be of comparable size.

5 Summary

Heat fluxes were measured downwind of a thermal line source in both stabilized and destabilized curved, homogeneous

shear flows. In the stabilized flow, the shear correlation coefficient, $\rho_{uv} = \overline{uv}/u'v'$, was 25 percent smaller than that of uncurved shear flow while in destabilized flow ρ_{uv} was 25 percent greater. In contrast, the dimensionless components of the heat flux, $\rho_{u\theta}$ and $\rho_{v\theta}$, measured in both flows, were practically equal to each other and to those measured in uncurved homogeneous shear flow. The heat fluxes, $\overline{u\theta}$ and $\overline{v\theta}$, were affected by curvature through its effect on the turbulence kinetic energy of the flow. These results are in agreement with most previous studies in curved boundary layers which found momentum transport more strongly affected by flow curvature than heat transport.

References

Gibson, M. M., and Servat-Djoo, K., 1981, "Measurements in the heated turbulent boundary layer on a mildly curved concave surface," *5th Symposium on Turbulent Shear Flows*, Ithaca, NY, pp. 14.7–14.12.

Gibson, M. M., and Verriopoulos, C. A., 1984, "Turbulent boundary layer on a mildly curved convex surface: Part 2, Temperature field measurements," *Expt. in Fluids*, Vol. 2, pp. 73–80.

Hollingsworth, D. K., Moffat, R. J., and Kays, W. M., 1992, "The Effect of Concave Surface Curvature on the Turbulent Prandtl Number and the Thermal Law of the Wall," *Exp. Thermal Fluid Sci.*, Vol. 5, pp. 299–306.

Holloway, A. G. L., and Tavoularis, S., 1992, "The effect of curvature on sheared turbulence," *J. Fluid Mech.*, Vol. 237, pp. 569–603.

Karnik, U., and Tavoularis, S., 1987, "Generation and manipulation of uniform shear with the use of screens," *Experiments in Fluids*, Vol. 5, pp. 247–254.

Karnik, U., and Tavoularis, S., 1989, "Measurements of heat diffusion from a continuous line source in a uniformly sheared turbulent flow," *J. Fluid Mech.*, Vol. 202, pp. 233–261.

Kim, J., and Simon, T. W., 1988, "Measurements of the Turbulent Transport of Heat and Momentum in Convexly Curved Boundary Layers: Effects of Curvature, Recovery and Free-Stream Turbulence," ASME *Journal of Turbomachinery*, Vol. 110, pp. 80–87.

Tavoularis, S., and Corrsin, S., 1981, "Experiments in Nearly Homogeneous Turbulent Shear Flow With a Uniform Mean Temperature Gradient: Part 1," *J. Fluid Mech.*, Vol. 104, pp. 311–347.

You, S. M., Simon, T. W., and Kim, J., 1986, "Boundary Layer Heat Transfer and Fluid Mechanics Measurements on a Mildly-Curved Convex Wall," *Proc. 8th Int. Heat Transfer Conf.*, Vol. 3, pp. 1089–1091.

Radiation Effects on Laminar Mixed Convection in an Inclined Square Duct

W.-M. Yan[1] and H.-Y. Li[1]

Nomenclature

a = width or height of a square duct, respectively, m

f = friction factor, $2\overline{\tau}_w/(\rho\overline{w}^2)$

[1] Department of Mechanical Engineering, Huafan University, Shih Ting, Taipei 22305, Taiwan, R.O.C.

Fig. 7 Transverse profiles of $\rho_{u\theta} = \overline{u\theta}/u'\theta'$ for destabilized and stabilized shear flow; symbols are defined in Fig. 2. Note that the sign of $\rho_{u\theta}$ for the stabilized case (solid symbols) has been reversed to account for the change in the shear direction. The dashed line represents the measurements of Karnik and Tavoularis for uncurved shear flow at a similar distance from the heating wire.
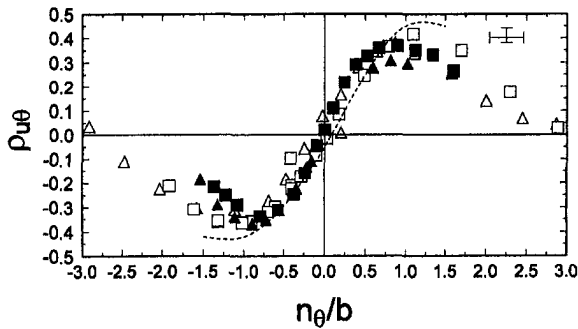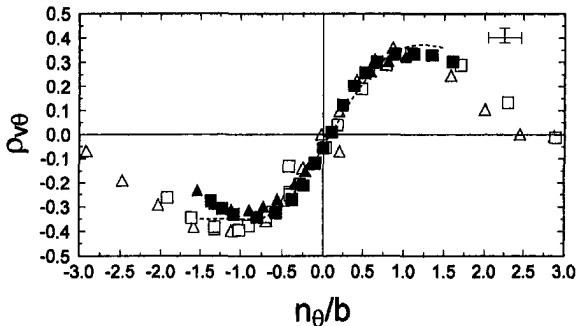

Fig. 8 Transverse profiles of $\rho_{v\theta} = \overline{v\theta}/v'\theta'$ for destabilized and stabilized shear flow; symbols are defined in Fig. 2. The dashed line represents the measurements of Karnik and Tavoularis (1989) for uncurved shear at a similar distance from the heating wire.

ing that the profiles of $\rho_{u\theta}$ from the stabilized and destabilized flows are so close; given the dramatic difference in turbulence structure shown in Fig. 4. The peak values of $\rho_{u\theta}$ are lower than those measured by Karnik and Tavoularis (1989); a result which is in part due to the greater separation of the velocity and temperature probes used in this study. Based on these results one might conclude, at least in this homogeneous flow, that $\rho_{u\theta}$ is less sensitive to flow curvature than ρ_{uv}.

Transverse profiles of the heat flux correlation coefficient, $\rho_{v\theta} = \overline{v\theta}/v'\theta'$, are presented in Fig. 8. Profiles from both flows overlap with a high degree of similarity. The only significant difference between the stabilized and destabilized flows is on the inside of the wake where heat is transported towards the center of curvature. Nevertheless, these results show that $\rho_{v\theta}$ is substantially less sensitive to flow curvature than ρ_{uv}.

That $\rho_{u\theta}$ and $\rho_{v\theta}$ are less sensitive to flow curvature than is ρ_{uv} in this uniformly sheared flow is consistent with most of the boundary layer studies cited in the Introduction; an exception being the convex boundary layer measurements of Gibson and Verriopolous (1984). However, it is surprising that $\rho_{u\theta}$ and $\rho_{v\theta}$ have been found to be so insensitive to flow curvature which strongly affected ρ_{uv}. A firm explanation of this finding is lacking and until one is provided the present results should be treated with some skepticism. It is plausible, however, that the heat transport in this particular flow results from smaller scale motions than those which are most affected by curvature; whereas, in the boundary layer studies cited earlier, the velocity and temperature length scales would necessarily be of comparable size.

5 Summary

Heat fluxes were measured downwind of a thermal line source in both stabilized and destabilized curved, homogeneous
shear flows. In the stabilized flow, the shear correlation coefficient, $\rho_{uv} = \overline{uv}/u'v'$, was 25 percent smaller than that of uncurved shear flow while in destabilized flow ρ_{uv} was 25 percent greater. In contrast, the dimensionless components of the heat flux, $\rho_{u\theta}$ and $\rho_{v\theta}$, measured in both flows, were practically equal to each other and to those measured in uncurved homogeneous shear flow. The heat fluxes, $\overline{u\theta}$ and $\overline{v\theta}$, were affected by curvature through its effect on the turbulence kinetic energy of the flow. These results are in agreement with most previous studies in curved boundary layers which found momentum transport more strongly affected by flow curvature than heat transport.

Acknowledgments

References

Gibson, M. M., and Servat-Djoo, K., 1981, "Measurements in the heated turbulent boundary layer on a mildly curved concave surface," *5th Symposium on Turbulent Shear Flows*, Ithaca, NY, pp. 14.7–14.12.

Gibson, M. M., and Verriopoulos, C. A., 1984, "Turbulent boundary layer on a mildly curved convex surface: Part 2, Temperature field measurements," *Expt. in Fluids*, Vol. 2, pp. 73–80.

Hollingsworth, D. K., Moffat, R. J., and Kays, W. M., 1992, "The Effect of Concave Surface Curvature on the Turbulent Prandtl Number and the Thermal Law of the Wall," *Exp. Thermal Fluid Sci.*, Vol. 5, pp. 299–306.

Holloway, A. G. L., and Tavoularis, S., 1992, "The effect of curvature on sheared turbulence," *J. Fluid Mech.*, Vol. 237, pp. 569–603.

Karnik, U., and Tavoularis, S., 1987, "Generation and manipulation of uniform shear with the use of screens," *Experiments in Fluids*, Vol. 5, pp. 247–254.

Karnik, U., and Tavoularis, S., 1989, "Measurements of heat diffusion from a continuous line source in a uniformly sheared turbulent flow," *J. Fluid Mech.*, Vol. 202, pp. 233–261.

Kim, J., and Simon, T. W., 1988, "Measurements of the Turbulent Transport of Heat and Momentum in Convexly Curved Boundary Layers: Effects of Curvature, Recovery and Free-Stream Turbulence," ASME *Journal of Turbomachinery*, Vol. 110, pp. 80–87.

Tavoularis, S., and Corrsin, S., 1981, "Experiments in Nearly Homogeneous Turbulent Shear Flow With a Uniform Mean Temperature Gradient: Part 1," *J. Fluid Mech.*, Vol. 104, pp. 311–347.

You, S. M., Simon, T. W., and Kim, J., 1986, "Boundary Layer Heat Transfer and Fluid Mechanics Measurements on a Mildly-Curved Convex Wall," *Proc. 8th Int. Heat Transfer Conf.*, Vol. 3, pp. 1089–1091.

Radiation Effects on Laminar Mixed Convection in an Inclined Square Duct

W.-M. Yan[1] and H.-Y. Li[1]

Nomenclature

a = width or height of a square duct, respectively, m
f = friction factor, $2\overline{\tau}_w/(\rho\overline{w}^2)$

---

[1] Department of Mechanical Engineering, Huafan University, Shih Ting, Taipei 22305, Taiwan, R.O.C.

Copyright © 1999 by ASME

G, G^* = dimensional and dimensionless incident radiation, $G^* = G/(4\bar{n}^2\sigma T_w^4)$

Gr = Grashof number, $g\beta(T_w - T_o)a^3/\nu^2$

$\bar{h}$ = circumferentially averaged heat transfer coefficient, W/m^2.°C

m, m' = direction of the discrete ordinates

n = dimensionless direction coordinate normal to the duct wall

$\bar{n}$ = refractive index

N = order of the discrete ordinates method

N^* = order of the phase function

N_c = conduction-to-radiation parameter, $k\bar{\beta}/(4\bar{n}^2\sigma T_w^3)$

Nu = peripherally averaged Nusselt number, $\bar{h}a/k$

$\bar{P}$ = dimensionless cross-sectional mean pressure

Pr = Prandtl number, ν/α

q = heat flux

Ra = Rayleigh number, Pr Gr

Ra* = modified Rayleigh number, Ra cos δ

Re = Reynolds number, $\bar{w}a/\nu$

T = temperature, °C

U, V, W = dimensionless velocity components in X, Y, and Z directions, respectively

$\bar{w}$ = inlet mean velocity, m/s

X, Y, Z = dimensionless rectangular coordinate, $X = x/a$, $Y = y/a$, $Z = z/(\text{Re}a)$

Z^* = Z/Pr

Greek Symbols

α = thermal diffusivity, m^2/s

β = coefficient of thermal expansion

$\bar{\beta}$ = extinction coefficient

δ = duct inclination angle

Δ = mixed convection parameter, (Ra/Re) sin δ

ϵ_w = wall emissivity

θ = dimensionless temperature, T/T_w

θ_o = dimensionless temperature ratio, T_o/T_w

μ, η, ζ = direction cosines

ξ = dimensionless vorticity in axial direction

ρ = density, kg/m^3

σ = Stefan-Boltzman constant

$\bar{\sigma}$ = scattering coefficient

τ = dimensionless optical thickness

τ_w = wall shear stress, kPa

ψ = dimensionless radiation intensity, $\pi I/(\bar{n}^2\sigma T_w^4)$

ϕ = scattering phase function

ω = single scattering albedo

Ω, Ω' = outward and inward direction of radiation

Subscripts

b = bulk fluid quantity

c = convective

o = condition at inlet

r = radiative

w = value at wall

Introduction

Simultaneous convection and radiation in participating media is important in many areas, including the cooling of electronic equipment, design of channel-type solar energy collectors, and analysis of combustion chambers. The problem of mixed convection heat transfer has received much attention. But the effects of thermal radiation on mixed convection heat transfer in inclined ducts have not been widely studied although they are always encountered in many practical situations.

Laminar mixed convection heat transfer has been examined in horizontal ducts (Hishida et al., 1982; Abou-Ellail and Morcos, 1983; Chou and Hwang, 1987; Mahaney et al., 1987; Incropera et al., 1988) and in a vertical rectangular duct (Cheng et al.,

1995). In many practical situations, the duct is not horizontal and the problems of mixed convection in inclined ducts become important. A numerical solution for the problem of mixed convection heat transfer in the entrance region of inclined rectangular ducts was studied by Morcos and Abou-Ellail (1983). Cheng and Yuen (1985) presented a series of photographs of developing secondary flow patterns in the thermal entrance region of inclined tubes for laminar mixed convection flow. Morcos et al. (1986) performed an experiment study on laminar mixed convection heat transfer in the entrance region of inclined rectangular ducts. A numerical study of combined forced and free convection for laminar flow in the entrance region of isothermal inclined tubes was carried out by Choudhury and Patankar (1988). The results showed that the buoyancy effects have a considerable influence on the fluid flow and heat transfer characteristics of the development flow. Recently mixed convection heat and mass transfer in inclined rectangular ducts was examined by Yan (1994, 1995). The results disclosed that the buoyancy induced by the thermal and mass diffusion has a significant impact on flow structure and heat transfer performance. All of the work in the foregoing literature survey neglects the radiation effect. However, there are many engineering applications where the simultaneous influence of thermal buoyancy and radiation must be considered.

Forced convection in a channel with radiation effect only (i.e., without buoyancy effect) has been studied by several investigators (Chen, 1966; Wasset and Edwards, 1976; Azad and Modest, 1981) during the past 30 years for ducts subjected to prescribed heat flux or wall temperature at the wall surfaces. In these studies, various approximate methods were used to formulate thermal radiation problems in participating media. Recently, Huang et al. (1990) examined the effects of radiation on mixed convection heat transfer in a horizontal duct. They found that the radiation effect tends to reduce the buoyancy effects. It is noted from the above reviews that there are no numerical studies for combined radiation and mixed convection in the entrance region of inclined ducts. This motivates the present investigation which is to examine the effects of radiation on mixed convection in an inclined square duct.

Analysis

Consideration is given to a steady laminar upward flow in the entrance region of a square duct inclined at angle δ to the horizontal, as shown in Fig. 1. The fluid, which is assumed to be gray, absorbing, emitting, and scattering, enters the channel with a uniform velocity $\bar{w}$ and a constant inlet temperature T_o. The surface of the walls are maintained at a constant temperature T_w.

As a first step, dimensionless variables are introduced as follows:

$$X = x/a \quad Y = y/a$$

$$Z = z/(a \cdot \text{Re}) \quad U = ua/\nu$$

$$V = va/\nu \quad W = w/\bar{w}$$

$$\bar{P} = \bar{p}/(\rho_o\bar{w}^2) \quad P' = p'/(\rho\nu^2/a^2)$$

$$\theta = T/T_w \quad \text{Re} = \bar{w}a/\nu$$

$$\text{Pr} = \nu/\alpha \quad \text{Gr} = g\beta(T_w - T_o)a^3/\nu^2$$

$$\text{Ra} = \text{Pr Gr} \quad Z^* = Z/\text{Pr}$$

$$\text{Ra}^* = \text{Ra} \cdot \cos \delta \quad \Delta = (\text{Ra}/\text{Re}) \sin \delta$$

$$N_c = k\bar{\beta}/(4\bar{n}^2\sigma T_w^3) \quad \tau = \bar{\beta}a$$

$$\omega = \bar{\sigma}/\bar{\beta} \quad G^* = G/(4\bar{n}^2\sigma T_w^4)$$
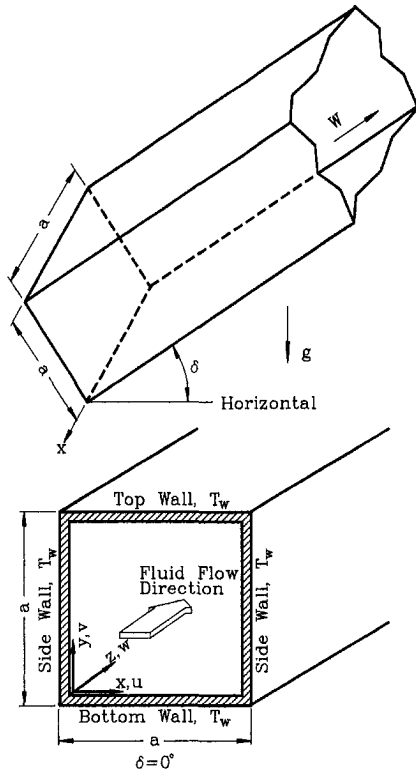
$$\theta_o = T_o/T_w \quad (1)$$

Fig. 1 Schematic diagram of the physical system

With these variables, the governing equations in vorticity-velocity formulation are (Yan, 1994, 1995)

$$\partial^2 U/\partial X^2 + \partial^2 U/\partial Y^2 = \partial\xi/\partial Y - \partial^2 W/\partial X\partial Z \quad (2)$$

$$\partial^2 V/\partial X^2 + \partial^2 V/\partial Y^2 = -\partial\xi/\partial X - \partial^2 W/\partial Y\partial Z \quad (3)$$

$$U\partial\xi/\partial X + V\partial\xi/\partial Y + W\partial\xi/\partial Z + \xi(\partial U/\partial X + \partial V/\partial Y)$$
$$+ (\partial W/\partial Y \cdot \partial U/\partial Z - \partial W/\partial X \cdot \partial V/\partial Z) = \partial^2\xi/\partial X^2$$
$$+ \partial^2\xi/\partial Y^2 - (\mathrm{Ra}\cdot\cos\delta/\mathrm{Pr})\cdot[(\partial\theta/\partial X)/(1 - \theta_o)] \quad (4)$$

$$W/\partial X + V\partial W/\partial Y + W\partial W/\partial Z = -d\bar{P}/dZ + \partial^2 W/\partial X^2$$
$$+ \partial^2 W/\partial Y^2 + \Delta/\mathrm{Pr}\cdot(\theta - \theta_o)/(1 - \theta_o) \quad (5)$$

$$U\partial\theta/\partial X + V\partial\theta/\partial Y + W\partial\theta/\partial Z = [\partial^2\theta/\partial X^2 + \partial^2\theta/\partial Y^2$$
$$+ (1 - \omega)\tau^2/N_c\cdot(G^* - \theta^4)]/\mathrm{Pr} \quad (6)$$

where $\xi = \partial U/\partial Y - \partial V/\partial X$ is the axial vorticity.

The dimensionless incident radiation G^* in the energy equation is determined from the solution of the radiative transfer equation. For an absorbing, emitting, and scattering medium, the nondimensional radiative transfer equation is given by

$$\mu\partial\psi/\partial X + \eta\partial\psi/\partial Y + \tau\psi$$
$$= (1 - \omega)\tau\theta^4 + \frac{\omega\tau}{4\pi}\int_{\Omega'=4\pi}\phi(\Omega', \Omega)\psi d\Omega' \quad (7)$$

where $\psi = \pi I/(\bar{n}^2\sigma T_w^4)$ is the dimensionless intensity of radiation at a point (X, Y) in the direction Ω defined by the direction cosines μ, η, and ζ, ω is the single scattering albedo, and $\phi(\Omega', \Omega)$ is the scattering phase function, which is expressed in terms of Legendre polynomials

$$\phi(\Omega', \Omega) = \sum_{n=o}^{N^*} a_n P_n(\mu'\mu + \eta'\eta + \zeta'\zeta). \quad (8)$$

For a gray, opaque, diffusely emitting and reflecting surface, the boundary condition is

$$\psi_W(\Omega) = \epsilon_W + \frac{(1 - \epsilon_W)}{\pi}\int_{\mathbf{n}\cdot\Omega'<o}|\mathbf{n}\cdot\Omega'|\psi_W(\Omega')d\Omega'$$
$$\mathbf{n}\cdot\Omega > o \quad (9)$$

where ϵ_W is the wall emissivity and $\mathbf{n}$ is the unit normal vector pointing away from the duct wall into the medium.

Once the dimensionless radiation intensity ψ is known, the dimensionless radiation flux vector and incident radiation are determined from their definitions as

$$\mathbf{Q}_r = \mathbf{q}_r/(4\bar{n}^2\sigma T_W^4) = 1/(4\pi)\cdot\int_{\Omega=4\pi}\Omega\psi d\Omega \quad (10a)$$

$$G^* = G/(4\bar{n}^2\sigma T_W^4) = 1/(4\pi)\cdot\int_{\Omega=4\pi}\psi d\Omega. \quad (10b)$$

The boundary conditions for the convective governing equations are given by

$$U = V = W = 0, \theta = 1 \quad \text{at the duct walls} \quad (11a)$$

$$W = 1, U = V = \xi = 0, \theta = \theta_o \quad \text{at the entrance } Z = 0. \quad (11b)$$

After the developing velocity and temperature fields are obtained, the circumferentially averaged friction factor and Nusselt number are computed to represent the hydrodynamic and thermal characteristics of the duct flow. The conventional definition for the product of the peripheral average friction factor and Reynolds number is based on the axial velocity gradient on the duct wall, i.e.,

$$f\,\mathrm{Re} = -2(\overline{\partial W/\partial n})_W. \quad (12)$$

Energy transport from the duct wall to the gas flow is by conduction and radiation, i.e.,

$$q_t = q_c + q_r = k\partial T/\partial n + q_r. \quad (13)$$

The total Nusselt number is defined as

$$\mathrm{Nu}_t = \bar{h}a/k = q_t a/[k(T_W - T_b)]. \quad (14)$$

It is conveniently written as

$$\mathrm{Nu}_t = \mathrm{Nu}_c + \mathrm{Nu}_r$$
$$= (\overline{\partial\theta_W/\partial n})/(1 - \theta_b) + (\tau\overline{Q_r}/N_c)/(1 - \theta_b). \quad (15)$$

In this work, there are eight independent parameters: Δ, Ra^*, Pr, N_c, τ, ω, ϵ_w, and θ_o. Δ is a mixed convection parameter defined by Eq. (1) that contains the ratio of the Rayleigh number Ra to the Reynolds number Re, modified by an inclination angle factor $\sin\delta$. Ra^* is a modified Rayleigh number given by Eq. (1). The conduction-to-radiation parameter N_c characterizes the relative importance of conduction with respect to radiation. The effect of radiation is getting strong as the N_c decreases. To conveniently discuss the effects of thermal radiation on mixed convection in an inclined square duct, the Prandtl number Pr, temperature ratio θ_o, single scattering albedo ω, and wall emissivity ϵ_w are fixed to be 0.7, 0.3, 0 and 0.5, respectively. While the other parameters, Δ, Ra^*, N_c, and τ, are selected systematically to investigate their influences.

Solution Method

The mass, momentum, and energy equation, along with their boundary conditions, are solved by the vorticity-velocity method for three-dimensional parabolic flow (Yan, 1994, 1995). A marching technique based on the Du Fort-Frankel scheme (Roache, 1971) is developed for the solution of Eqs. (2)–(6), in which the unknowns U, V, W, ξ, θ, and $d\bar{P}/dZ$ are coupled.

The S_N or the discrete ordinates method (Fiveland, 1988; Kim and Baek, 1991; Modest, 1993) is applied for the solution of the radiative transfer equation. In this approximation, a set

of discrete directions is chosen to discretize the solid angle 4π. The integro-differential radiative transfer equation, Eq. (7), is evaluated at each of the discrete directions and the integral term is replaced by a numerical quadrature. The resulting discrete ordinates form of the radiative transfer equation is

$$\mu_m \partial \psi_m / \partial X + \eta_m \partial \psi_m / \partial Y + \tau \psi_m$$

$$= (1 - \omega)\tau\theta^4 + \frac{\omega\tau}{4\pi} \sum_{m'} w_{m'}^* \phi_{m'm} \psi_{m'}. \quad (16)$$

The discrete form of the phase function $\phi_{m'm}$ is given by

$$\phi_{m'm} = \sum_{n=0}^{N^*} a_n P_n (\mu_{m'}\mu_m + \eta_{m'}\eta_m + \zeta_{m'}\zeta_m). \quad (17)$$

The accuracy of the S_N method depends on the choice of the quadrature scheme. To avoid directionally biasing the solution, a complete symmetrical scheme is preferred. In this work, the momentum-matching technique suggested by Carson and Lathrop (1968) is applied to calculate the discrete directions and quadrature weights. The total number of the discrete directions is 24 when the S_6 scheme is used for a two-dimensional geometry. The control volume approach (Modest, 1993) is applied to solve for the solution of the dimensionless radiative intensity, radiation flux, and incident radiation. In this work, the temperature and incident radiation are computed iteratively at each axial location until the following criterion is satisfied,

$$\epsilon = \text{Max } |\phi_{i,j}^{m+1} - \phi_{i,j}^m| / \text{Max } |\phi_{i,j}^{m+1}| < 10^{-5},$$

$$\phi = \theta \quad \text{or} \quad G^*. \quad (18)$$

Results and Discussion

Although the presentation of the local friction factor and Nusselt number is a major goal in this work, developments of axial velocity and temperature profiles are of engineering interest and useful in clarifying the heat transfer mechanism. The developing profiles of the axial velocity W and temperature θ along the symmetric plane $X = 0.5$ are shown in Fig. 2. For comparison purposes, the results without radiation effect are included in these subplots by the dashed curves. It is well known that the axial velocity profiles for purely forced convection without buoyancy effects are symmetric with respect to the $Y = 0.5$ line. Overall inspection on Figs. 2(a)–2(d) reveals that near the entrance, the velocity profile (curve A) is fairly uniform over the cross plane. As the flow moves downstream, the curves are distorted due to the buoyancy effects, and the nature of the distortion depends on the magnitude of Δ and Ra*. At the farthest downstream location (curve F, $Z^* = 2.0$), the effects of buoyancy forces disappear and a fully developed profile is attained. Figure 2(a) shows the W profiles for $\Delta = 5$ and Ra* $= 10^5$. It is clear from the definition of Δ and Ra* that this combination of a small Δ and a large Ra* yields the case of mixed convection heat transfer in a horizontal duct. In Fig. 2(a), near the inlet, the velocity (curve A) is uniform and symmetric. But as the flow goes downstream, this symmetry is lost and the locations of the maximum axial velocity move toward the bottom wall due to the buoyancy-driven secondary flow. This is typical of mixed convection in a horizontal duct (Chou and Hwang, 1987). Figure 2(b) presents the developing W profiles for $\Delta = 200$ and Ra* $= 10^5$. In contrast to Fig. 2(a), the maximum velocity is now displaced toward the top wall for curve C. This is because increasing the value of Δ while keeping Ra* fixed introduces the aiding buoyancy forces in the main flow direction. Therefore, the W profiles are affected by the cross-stream buoyancy as well as by the aiding buoyancy forces in the axial direction. The W profiles for $\Delta = 200$ and Ra* $= 100$ are shown in Fig. 2(c), which corresponds to the case of mixed convection heat transfer in a vertical duct. Thus, the developing W profiles in Fig. 2(c) show no influence of
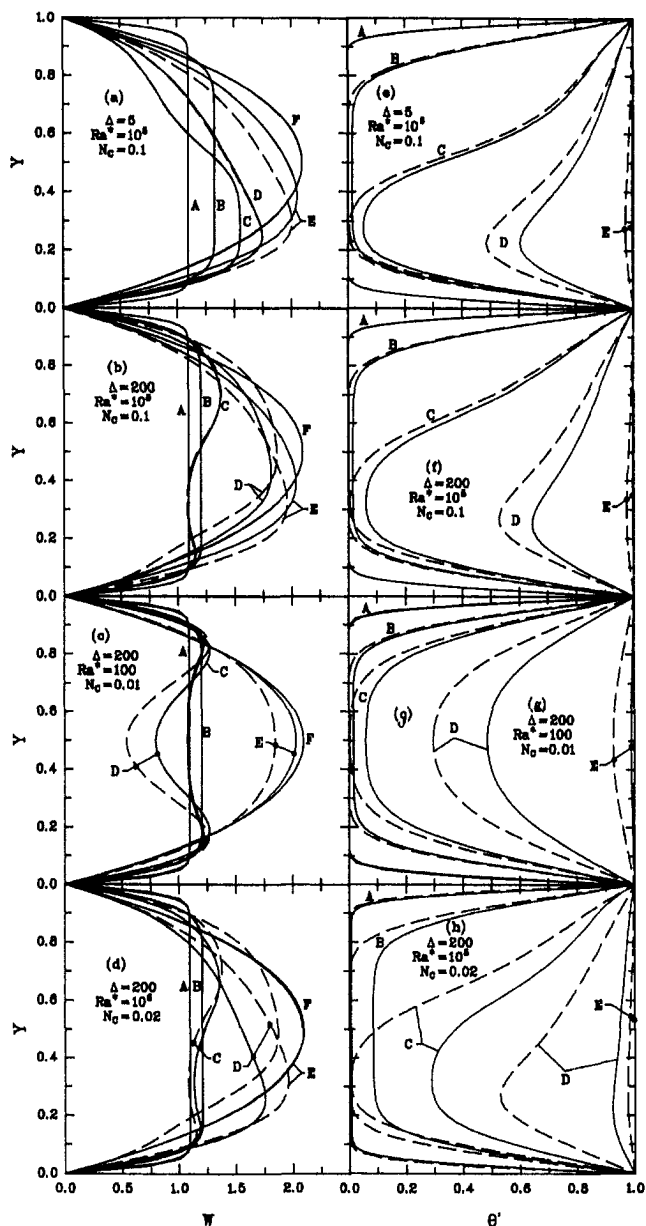

Fig. 2 Developments of axial velocity and temperature profiles for Ra* $= 1 \times 10^5$, $\Delta = 200$, $N_c = 0.1$, $\tau = 1$, $\omega = 0$, $\epsilon_w = 0.5$. (A: $Z^* = 0.00034$, B: $Z^* = 0.0041$, C: $Z^* = 0.0124$, D: $Z^* = 0.0418$, E: $Z^* = 0.191$, F: $Z^* = 1.0$)

cross-stream buoyancy force and the curves are symmetric about the $Y = 0.5$ line. The W profiles (curves C and D) are distorted and a maximum velocity appears somewhere between the heated walls and the centerline. This is due to the fact that the buoyancy force near the ducts walls acts in the main flow direction. Therefore, the effects of buoyancy is to raise the W velocity at the center to maintain the overall mass balance. The effects of radiation on the distribution of velocity W can be illustrated in Figs. 2(b) and 2(d). Comparing the solid curves with the dashed curves, we note that both results with and without radiation effects in Figs. 2(b) and 2(d) are similar in the region near entrance. As the flow goes downstream, the effect of radiation becomes more significant which tends to reduce W near the bottom wall ($Y = 0$). This implies that the friction factor would be attenuated at a downstream region when radiation is accounted for. The conduction-to-radiation parameter N_c gives the relative importance of heat transfer by conduction with respect to radiation. Therefore, the effect of radiation
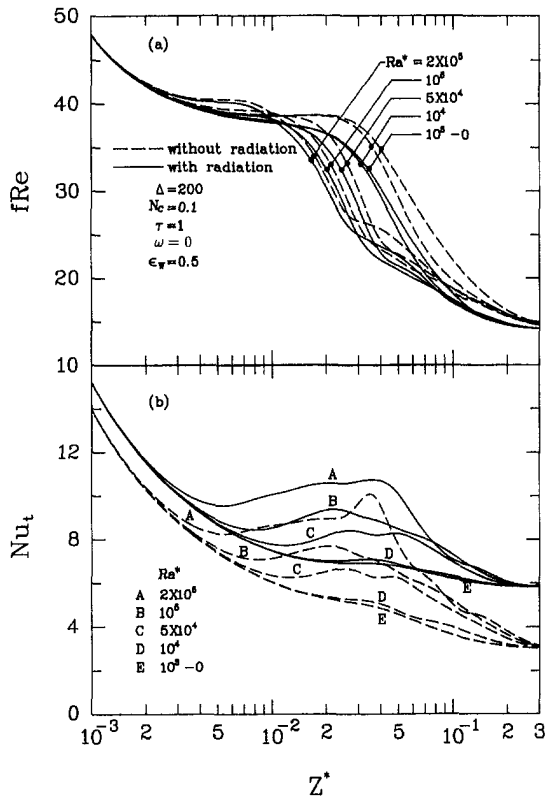
Journal of Heat Transfer

Fig. 3 Effects of Ra* on the variations of friction factor and Nusselt number for $\Delta = 200$, $N_c = 0.1$, $\tau = 1$, $\omega = 0$, $\epsilon_w = 0.5$

increases as N_c decreases, which is noted in Figs. 2(b) and 2(d).

The developments of the temperature profiles at different axial locations are shown in Figs. 2(e)–2(h). The temperature in the central portion of the duct increases gradually as the flow moves downstream due to the heating of the wall. A comparison of the temperature profiles with and without radiation reveals that near the inlet the effect of radiation on the thermal development is insignificant (curve A). But at the downstream location, radiation effect tends to equalize the temperature in the flow. Close inspection on Figs. 2(f) and 2(h) shows that as the conduction-to-radiation parameter N_c decreases, the development of temperature profile is faster for a system with a stronger radiation effect ($N_c = 0.02$). This can be understood by recognizing that the radiative heat flux is an additional mode of energy transport and as the magnitude of N_c decreases, the importance of the radiation term in Eq. (7) increases, relative to the terms of conduction and convection. This causes an increase of the energy transport which leads to flatter temperature profiles. An overall inspection on Figs. 2(e)–2(h) discloses that the normal temperature gradients at the bottom wall are greater than those at the top wall and the minimum value for θ at each curve is located near the bottom wall. The locations of minimum θ are shifted toward the top wall as the value of Δ is increased from 5 to 200 or Ra* is decreased from 10^5 to 100. This is clearly seen in Fig. 2(g). In Fig. 2(g), due to the case of $\Delta = 200$ and Ra* = 100 being the limiting case of mixed convection heat transfer in a vertical duct, the θ profiles are symmetric with respect to the $Y = 0.5$ line.

Figure 3 shows the axial variations of f Re and Nu_t for different modified Rayleigh number Ra*. The effect of increasing Ra* at a fixed Δ is to increase the combined buoyancy effects. In Fig. 3, near the entrance, the buoyancy effects are insignificant and all the curves do indeed fall along one curve. As the flow proceeds downstream, the buoyancy effects become important and each curve of the f Re and Nu branches out from

the curve E. The effect of Ra* is practically negligible when Ra* $\leq 1 \times 10^3$. A monotonic decrease in Nu or f Re near the inlet is caused by the entrance effect. The onset of buoyancy effect occurs at some axial location from the inlet depending mainly upon the value of Ra*. A minimum local Nu will not appear unless the entrance effect is balanced out by the buoyancy effects. After reaching the local minimum point, the variation of local Nu generally shows an increase to a maximum local Nu. At downstream region, the local Nu gradually approaches the asymptotic value given by the Graetz solution when the temperature profile becomes fully developed. Also noted in Fig. 3 are that in all cases the Nu_t with radiation is larger than that without radiation. This is due to two effects. The first is that radiation is additional mechanism for heat transfer through the fluid resulting in an increased heat flux. Secondly, the radiation source term augments the rate of thermal development so that the bulk temperature approaches the wall temperature at a more rapid rate. Both effects act to increase the local total Nusselt number Nu_t. Near the entrance, the Nu_t is raised only by the additional radiative heat flux, while further downstream, the more rapid thermal development contributes when the bulk temperature approaches the wall temperature. But this is not the case for f Re. A small f Re is noted for the system with consideration of radiation effect because the radiation effect tends to reduce the buoyancy effect, which in turn, cause a small f Re, relatively to that without radiation.

The effects of mixed convection parameter Δ on the axial variations of f Re and Nu for Ra* $= 1 \times 10^5$, $N_c = 0.1$, $\tau = 1$, $\omega = 0$ and $\epsilon_w = 0.5$. are presented in Fig. 4. For clear illustration, the results near the inlet are specifically plotted in the inset in Fig. 4. Near the entrance, the buoyancy effects are insignificant and all the curves do indeed fall along one curve, which corresponds to the case of forced convection. As the flow moves downstream, the buoyancy effects become important and each curve of the friction factor branches out from the curve
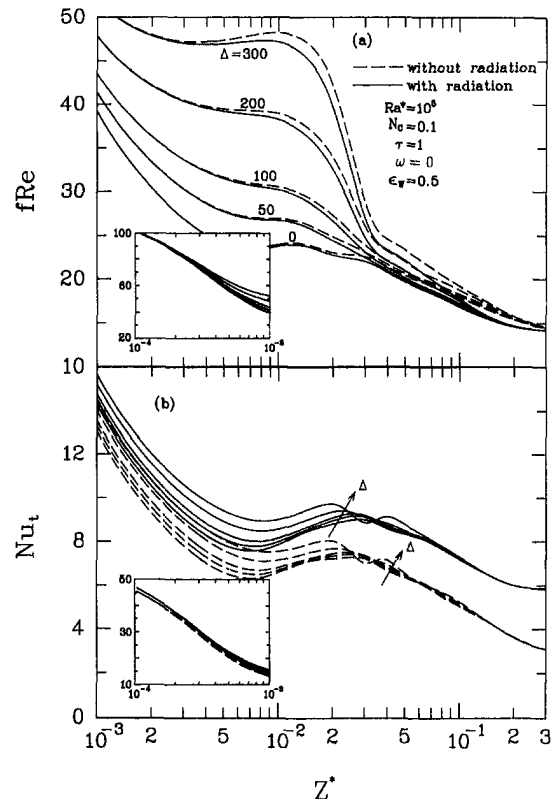

Fig. 4 Effects of Δ on the variations of friction factor and Nusselt number for Ra* $= 1 \times 10^5$, $N_c = 0.1$, $\tau = 1$, $\omega = 0$, $\epsilon_w = 0.5$

of $\Delta = 0$. The buoyancy effects are the most pronounced at the highest value of Δ since this parameter represents a ratio of natural convection to forced convection effects. At $\Delta = 300$, the local maximum value of f Re occurs at approximately $Z^* = 1.0 \times 10^{-2}$. Finally, the curves decrease asymptotically to the value of 14.7 when the velocity profile becomes fully developed.

The axial variations of friction factor f Re and Nusselt number Nu_t are presented in Fig. 5 for different values of N_c. From Fig. 5, we note that the f Re and Nu distributions for $N_c = 1$ are essentially the same as those without radiation. For lower values of N_c, i.e., $N_c = 0.02$, radiation becomes more important, and the deviation between the results with and without radiation are more pronounced. The Nu_t increases with the decrease in the N_c due to the strong radiation effect. On the contrary, the f Re decreases as N_c decreases. This is due to the fact that in the presence of radiation, temperature field becomes relatively flatter as shown in Fig. 2. The buoyancy effect is thus reduced, which in turn causes a reduction in f Re at downstream region.

The effects of optical thickness τ on local f Re and Nu_t are shown in Fig. 6. It is easy to see that Nu_t increases and f Re decreases as the optical thickness increases. This is expected, because the interaction between mixed convection and radiation is more significant for a larger optical thickness τ.

Conclusion

Combined mixed convection and radiation of an absorbing, emitting, and scattering fluid in an inclined square duct has been studied in this work. The vorticity-velocity method is employed for the solution of the three-dimensional parabolic governing equation. The radiative transfer equation is solved by the discrete ordinates method. The effects of the modified Rayleigh number Ra*, mixed convection parameter Δ, conduction-to-radiation parameter N_c, and optical thickness τ on the character-

Fig. 6 Effects of τ on the variations of friction factor and Nusselt number for Ra* $= 1 \times 10^5$, $\Delta = 200$, $N_c = 0.1$, $\omega = 0$, $\epsilon_w = 0.5$

istics of fluid flow and heat transfer are examined in detail. The following conclusions are obtained:

1 The buoyancy forces distort the axial velocity and temperature distributions and the nature of the distortion depends on the relative magnitudes of Δ and Ra*.

2 The axial distributions of f Re and Nu are characterized by a drop near the inlet due to the entrance effect, but the decay is attenuated by the onset of secondary flow.

3 Within the range of parameters under investigation, the buoyancy effects are practically negligible only when Ra* $\leq 1 \times 10^3$.

4 In the presence of radiation, the thermal development develops at a more rapid rate relative to that without radiation.

5 The Nusselt number Nu_t is enhanced by the presence of radiation, in comparison with that without consideration of radiation. The extent of enhancement in Nu_t increases with a decrease (increase) in $N_c(\tau)$, i.e., when the effect of radiation gets stronger.

References

Abou-Ellail, M. M. M., and Morcos, S. M., 1983, "Buoyancy Effects in the Entrance Region of Horizontal Rectangular Channels," ASME JOURNAL OF HEAT TRANSFER, Vol. 105, pp. 924–928.

Azad, F. H., and Modest, M. F., 1981, "Combined Radiation and Convection in Absorbing, Emitting and Anisotropically Scattering Gas-Particulate Tube Flow," Int. J. Heat Mass Transfer, Vol. 24, pp. 1681–1697.

Carlson, B. G., and Lathrop, K. D., 1968, "Transport Theory—the Method of Discrete Ordinates," Computing Method in Reactor Physics, Edited by H. Greenspan, C. N. Kelber, and D. Okrent, eds., Gordon & Breach Press, New York, pp. 165–266.
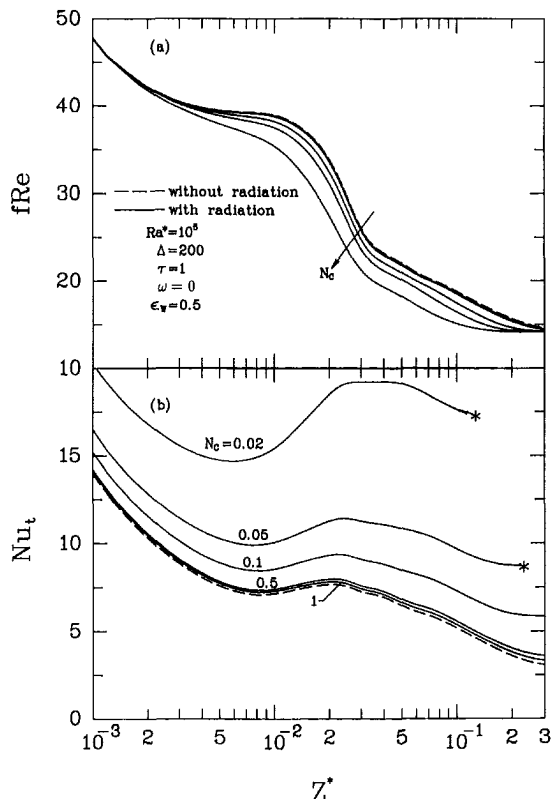
Fig. 5 Effects of N_c on the variations of friction factor and Nusselt number for Ra* $= 1 \times 10^5$, $\Delta = 200$, $\tau = 1$, $\omega = 0$, $\epsilon_w = 0.5$
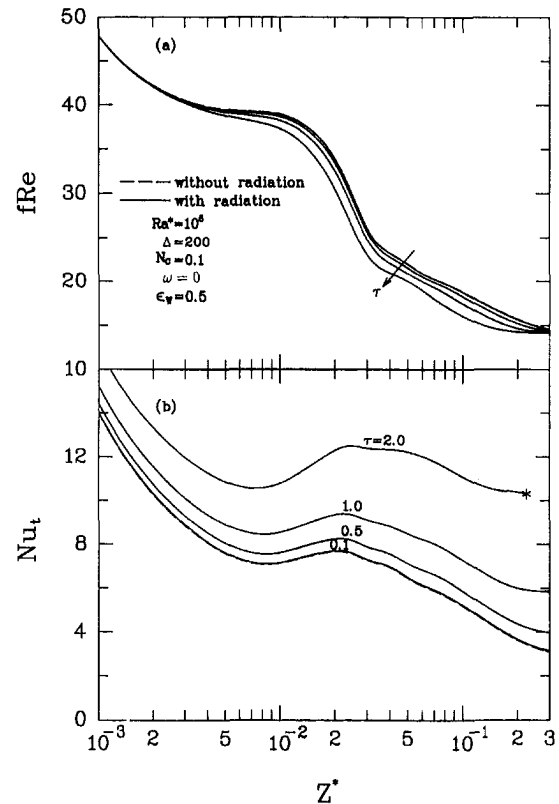
Chen, J. C., 1966, "Laminar Heat Transfer in a Tube with Nonlinear Radial Heat-Flux Boundary Conditions," *Int. J. Heat Mass Transfer,* Vol. 9, pp. 433–440.

Cheng, C. H., Weng, C. J., and Aung, W., 1995, "Buoyancy Effect on the Flow Reversal of Three-Dimensional Developing Flow in a Vertical Rectangular Duct—A Parabolic Model Solution," ASME JOURNAL OF HEAT TRANSFER, Vol. 117, pp. 238–241.

Cheng, K. C., and Yuen, F. P., 1985, "Flow Visualization Studies on Secondary Flow Pattern for Mixed Convection in the Entrance Region of Isothermally Heated Inclined Pipes," *Fundamentals of Forced and Mixed Convection,* ASME HTD-Vol. 42, pp. 121–130.

Chou, F. C., and Hwang, G. J., 1987, "Vorticity-Velocity Method for Graetz Problem with the Effect of Natural Convection in a Horizontal Rectangular Channel with Uniform Wall Heat Flux," ASME JOURNAL OF HEAT TRANSFER, Vol. 109, pp. 704–710.

Choudhury, D., and Patankar, S. V., 1988, "Combined Forced and Free Laminar Convection in the Entrance Region of an Inclined Isothermal Tube," ASME JOURNAL OF HEAT TRANSFER, Vol. 110, pp. 901–909.

Fiveland, W. A., 1988, "Three-Dimensional Radiative Heat Transfer Solutions by the Discrete-Ordinates Method," *AIAA J. Thermophysics and Heat Transfer,* Vol. 2, pp. 309–316.

Hishida, M., Nagano, Y., and Montesclaros, M. S., 1982, "Combined Forced and Free Convection in the Entrance Region of an Isothermally Heated Horizontal Pipe," ASME JOURNAL OF HEAT TRANSFER, Vol. 104, pp. 153–159.

Huang, J. M., Lin, J. D., and Chou, F. C., 1990, "Combined Radiation and Laminar Mixed Convection in the Thermal Entrance Region of Horizontal Isothermal Rectangular Channels," *Numer. Heat Transfer,* Part A, Vol. 18, pp. 113–125.

Incropera, F. P., Knox, A. L., and Maughan, J. R., 1988, "Effect of Wall Heat Flux Distribution on Laminar Mixed Convection in the Entry Region of a Horizontal Rectangular Duct," *Numer. Heat Transfer,* Vol. 13, pp. 427–450.

Kim, T. A., and Baek, S. W., 1991, "Analysis of Combined Conductive and Radiative Heat Transfer in a Two-Dimensional Rectangular Enclosure Using the Discrete Ordinates Method," *Int. J. Heat Mass Transfer,* Vol. 34, pp. 2265–2273.

Mahaney, H. V., Incropera, F. P., and Ramadhyani, S., 1987, "Development of Laminar Mixed Convection Flow in a Horizontal Rectangular Duct with Uniform Bottom Heating," *Numer. Heat Transfer,* Vol. 12, pp. 137–155.

Modest, M. F., 1993, *Radiative Heat Transfer,* McGraw-Hill, New York, pp. 541–571.

Morcos, E. M., and Abou-Ellail, M. M. M., 1983, "Buoyancy Effects in the Entrance Region of an Inclined Multirectangular Channel Solar Collector," ASME *Journal of Solar Energy Engineering,* Vol. 105, pp. 157–162.

Morcos, S. M., Hilal, M. M., Kamel, M. M., and Soliman, M. S., 1986, "Experimental Investigation of Mixed Laminar Convection in the Entrance Region of Inclined Rectangular Channels," ASME JOURNAL OF HEAT TRANSFER, Vol. 108, pp. 574–579.

Roache, P. J., 1971, *Computational Fluid Dynamics,* Reinhold, New York, pp. 61–64.

Wassel, A. T., and Edwards, D. K., 1976, "Molecular Radiation in a Laminar or Turbulent Pipe Flow," ASME JOURNAL OF HEAT TRANSFER, Vol. 98, pp. 101–107.

Yan, W. M., 1994, "Mixed Convection Heat and Mass Transfer in Inclined Rectangular Ducts," *Int. J. Heat Mass Transfer,* Vol. 37, pp. 1857–1866.

Yan, W. M., 1995, "Transport Phenomena of Developing Laminar Mixed Convection Heat and Mass Transfer in Inclined Rectangular Ducts," *Int. J. Heat Mass Transfer,* Vol. 38, pp. 2905–2914.

Numerical Solutions of Three-Dimensional Non-Grey Gas Radiative Transfer Using the Statistical Narrow-Band Model

F. Liu[1]

Three-dimensional non-grey gas radiation analyses were conducted using the statistical narrow-band model along with up-dated band parameters. The exact narrow-band averaged radiative transfer equation was solved using a ray-tracing method. Accurate numerical results were presented for non-grey real gas radiative transfer in a three-dimensional rectangular enclosure containing (i) an isothermal pure water vapor at 1000 K and 1 atm, (ii) an isothermal and inhomogeneous H_2O/N_2 mixture at 1000 K and 1 atm, and (iii) a nonisothermal and homogeneous mixture of $CO_2/H_2O/N_2$ at 1 atm.

[1] Associate Research Officer, Combustion Technology, Institute for Chemical Process and Environmental Technology, National Research Council, Ottawa, ON K1A 0R6, Canada. e-mail: fengshan.liu@ncr.ca.

1 Introduction

Development of computationally efficient and accurate gas radiative property models for non-grey gas radiation analysis has been an active research subject in recent years. Most of the research attention has been paid to develop absorption coefficient-based models due to its compatibility with the radiative transfer equation (RTE) in standard form. These include the weighted-sum-of-grey-gases models (Hottel and Sarofim, 1967; Denison and Webb, 1993) and the K-distribution method (Goody and Yung, 1989) as well as its variants (Lee et al., 1996; Parthasarathy et al., 1996).

Band models appear to be attractive in terms of efficiency and accuracy based on their principles. However, their applications to multidimensional problems are seriously restricted by the following two factors. First, band models provide band transmissivity rather than the fundamental property, i.e., gas absorption coefficient. As a consequence, most of the solution methods cannot be readily used. Secondly, band averaging of the RTE gives rise to additional source terms which are very difficult to deal with and require much more computing time (Kim et al., 1991; Liu et al., 1997). Despite the difficulties of applying band models to multidimensional problems, results of narrow-band models are often treated as accurate and used as benchmark solution in the evaluation of other approximate models when exact line-by-line (LBL) results are not available (Soufiani and Djavdan, 1994; Parthasarathy et al., 1996; Bedir et al., 1997).

Non-grey gas radiation results reported in the literature are either for *real gases,* i.e., H_2O and CO_2, in one-dimensional parallel-plates geometry; e.g., Kim et al. (1991), Denison and Webb (1993), or for "synthetic gas" with specified gas absorption coefficient in three dimensions, such as those based on Edwards' exponential wide-band model and the Elsasser model for line structure (Tang and Brewster, 1994). Accurate results of three-dimensional non-grey radiation analysis of real gases are typically lacking, primarily due to the unacceptable computing time required by performing LBL calculations in multidimensions. With this situation in mind, the present work aims at reporting accurate numerical results of three-dimensional non-grey gas radiation using the statistical narrow-band (SNB) model in inhomogeneous and nonisothermal media. These results are useful in evaluating the accuracy of other approximate gas radiation models.

2 Numerical Method and the Statistical Narrow-Band Model

The exact narrow-band averaged RTE presented by Kim et al. (1991) was solved using a ray-tracing method in three-dimensional Cartesian coordinates. Interested readers should refer to the papers by Kim et al. (1991) and Liu et al. (1997) for details. The ray-tracing method used in this work is essentially a modified version of the discrete transfer method developed by Lockwood and Shah (1981) to improve its accuracy in the calculation of the radiative source term. The method is briefly outlined below. For a given control volume, ray-tracing is performed at the center of each control surface (six in three dimensions) along all the directions defined by a T_N quadrature set (Thurgood et al., 1995) to obtain radiation intensities. The net radiative fluxes at these control surface centers were evaluated

Chen, J. C., 1966, "Laminar Heat Transfer in a Tube with Nonlinear Radial Heat-Flux Boundary Conditions," *Int. J. Heat Mass Transfer,* Vol. 9, pp. 433–440.

Cheng, C. H., Weng, C. J., and Aung, W., 1995, "Buoyancy Effect on the Flow Reversal of Three-Dimensional Developing Flow in a Vertical Rectangular Duct—A Parabolic Model Solution," ASME JOURNAL OF HEAT TRANSFER, Vol. 117, pp. 238–241.

Cheng, K. C., and Yuen, F. P., 1985, "Flow Visualization Studies on Secondary Flow Pattern for Mixed Convection in the Entrance Region of Isothermally Heated Inclined Pipes," *Fundamentals of Forced and Mixed Convection,* ASME HTD-Vol. 42, pp. 121–130.

Chou, F. C., and Hwang, G. J., 1987, "Vorticity-Velocity Method for Graetz Problem with the Effect of Natural Convection in a Horizontal Rectangular Channel with Uniform Wall Heat Flux," ASME JOURNAL OF HEAT TRANSFER, Vol. 109, pp. 704–710.

Choudhury, D., and Patankar, S. V., 1988, "Combined Forced and Free Laminar Convection in the Entrance Region of an Inclined Isothermal Tube," ASME JOURNAL OF HEAT TRANSFER, Vol. 110, pp. 901–909.

Fiveland, W. A., 1988, "Three-Dimensional Radiative Heat Transfer Solutions by the Discrete-Ordinates Method," *AIAA J. Thermophysics and Heat Transfer,* Vol. 2, pp. 309–316.

Hishida, M., Nagano, Y., and Montesclaros, M. S., 1982, "Combined Forced and Free Convection in the Entrance Region of an Isothermally Heated Horizontal Pipe," ASME JOURNAL OF HEAT TRANSFER, Vol. 104, pp. 153–159.

Huang, J. M., Lin, J. D., and Chou, F. C., 1990, "Combined Radiation and Laminar Mixed Convection in the Thermal Entrance Region of Horizontal Isothermal Rectangular Channels," *Numer. Heat Transfer,* Part A, Vol. 18, pp. 113–125.

Incropera, F. P., Knox, A. L., and Maughan, J. R., 1988, "Effect of Wall Heat Flux Distribution on Laminar Mixed Convection in the Entry Region of a Horizontal Rectangular Duct," *Numer. Heat Transfer,* Vol. 13, pp. 427–450.

Kim, T. A., and Baek, S. W., 1991, "Analysis of Combined Conductive and Radiative Heat Transfer in a Two-Dimensional Rectangular Enclosure Using the Discrete Ordinates Method," *Int. J. Heat Mass Transfer,* Vol. 34, pp. 2265–2273.

Mahaney, H. V., Incropera, F. P., and Ramadhyani, S., 1987, "Development of Laminar Mixed Convection Flow in a Horizontal Rectangular Duct with Uniform Bottom Heating," *Numer. Heat Transfer,* Vol. 12, pp. 137–155.

Modest, M. F., 1993, *Radiative Heat Transfer,* McGraw-Hill, New York, pp. 541–571.

Morcos, E. M., and Abou-Ellail, M. M. M., 1983, "Buoyancy Effects in the Entrance Region of an Inclined Multirectangular Channel Solar Collector," ASME *Journal of Solar Energy Engineering,* Vol. 105, pp. 157–162.

Morcos, S. M., Hilal, M. M., Kamel, M. M., and Soliman, M. S., 1986, "Experimental Investigation of Mixed Laminar Convection in the Entrance Region of Inclined Rectangular Channels," ASME JOURNAL OF HEAT TRANSFER, Vol. 108, pp. 574–579.

Roache, P. J., 1971, *Computational Fluid Dynamics,* Reinhold, New York, pp. 61–64.

Wassel, A. T., and Edwards, D. K., 1976, "Molecular Radiation in a Laminar or Turbulent Pipe Flow," ASME JOURNAL OF HEAT TRANSFER, Vol. 98, pp. 101–107.

Yan, W. M., 1994, "Mixed Convection Heat and Mass Transfer in Inclined Rectangular Ducts," *Int. J. Heat Mass Transfer,* Vol. 37, pp. 1857–1866.

Yan, W. M., 1995, "Transport Phenomena of Developing Laminar Mixed Convection Heat and Mass Transfer in Inclined Rectangular Ducts," *Int. J. Heat Mass Transfer,* Vol. 38, pp. 2905–2914.

Numerical Solutions of Three-Dimensional Non-Grey Gas Radiative Transfer Using the Statistical Narrow-Band Model

F. Liu[1]

Three-dimensional non-grey gas radiation analyses were conducted using the statistical narrow-band model along with updated band parameters. The exact narrow-band averaged radiative transfer equation was solved using a ray-tracing method. Accurate numerical results were presented for non-grey real gas radiative transfer in a three-dimensional rectangular enclosure containing (i) an isothermal pure water vapor at 1000 K and 1 atm, (ii) an isothermal and inhomogeneous H_2O/N_2 mixture at 1000 K and 1 atm, and (iii) a nonisothermal and homogeneous mixture of $CO_2/H_2O/N_2$ at 1 atm.

1 Introduction

Development of computationally efficient and accurate gas radiative property models for non-grey gas radiation analysis has been an active research subject in recent years. Most of the research attention has been paid to develop absorption coefficient-based models due to its compatibility with the radiative transfer equation (RTE) in standard form. These include the weighted-sum-of-grey-gases models (Hottel and Sarofim, 1967; Denison and Webb, 1993) and the K-distribution method (Goody and Yung, 1989) as well as its variants (Lee et al., 1996; Parthasarathy et al., 1996).

Band models appear to be attractive in terms of efficiency and accuracy based on their principles. However, their applications to multidimensional problems are seriously restricted by the following two factors. First, band models provide band transmissivity rather than the fundamental property, i.e., gas absorption coefficient. As a consequence, most of the solution methods cannot be readily used. Secondly, band averaging of the RTE gives rise to additional source terms which are very difficult to deal with and require much more computing time (Kim et al., 1991; Liu et al., 1997). Despite the difficulties of applying band models to multidimensional problems, results of narrow-band models are often treated as accurate and used as benchmark solution in the evaluation of other approximate models when exact line-by-line (LBL) results are not available (Soufiani and Djavdan, 1994; Parthasarathy et al., 1996; Bedir et al., 1997).

Non-grey gas radiation results reported in the literature are either for *real gases*, i.e., H_2O and CO_2, in one-dimensional parallel-plates geometry; e.g., Kim et al. (1991), Denison and Webb (1993), or for "synthetic gas" with specified gas absorption coefficient in three dimensions, such as those based on Edwards' exponential wide-band model and the Elsasser model for line structure (Tang and Brewster, 1994). Accurate results of three-dimensional non-grey radiation analysis of real gases are typically lacking, primarily due to the unacceptable computing time required by performing LBL calculations in multidimensions. With this situation in mind, the present work aims at reporting accurate numerical results of three-dimensional non-grey gas radiation using the statistical narrow-band (SNB) model in inhomogeneous and nonisothermal media. These results are useful in evaluating the accuracy of other approximate gas radiation models.

2 Numerical Method and the Statistical Narrow-Band Model

The exact narrow-band averaged RTE presented by Kim et al. (1991) was solved using a ray-tracing method in three-dimensional Cartesian coordinates. Interested readers should refer to the papers by Kim et al. (1991) and Liu et al. (1997) for details. The ray-tracing method used in this work is essentially a modified version of the discrete transfer method developed by Lockwood and Shah (1981) to improve its accuracy in the calculation of the radiative source term. The method is briefly outlined below. For a given control volume, ray-tracing is performed at the center of each control surface (six in three dimensions) along all the directions defined by a T_N quadrature set (Thurgood et al., 1995) to obtain radiation intensities. The net radiative fluxes at these control surface centers were evaluated

Copyright © 1999 by ASME

Table 1 Conditions of the three test cases

Case	Temperature distribution	Gas mixture compositions
1	uniform, 1000 K	uniform, pure water vapour
2	uniform, 1000 K	non-uniform H_2O/N_2 mixture
3	non-uniform	uniform, $CO_2/H_2O/N_2$ mixture

from the known radiation intensity and the weight function of the T_N set, a common practice of the discrete-ordinates method. The same procedure is repeated for all the narrow bands. The radiative source term at the control volume under consideration is then found by taking the divergence of the total net heat flux using a straightforward finite difference. This procedure is very time-consuming and is not recommended for other applications. It was developed in this work only for the purpose of obtaining accurate results of the narrow-band averaged RTE in three dimensions.

The SNB model (Ludwig et al., 1973) was used in the present calculations to provide narrow-band gas transmissivity of CO_2 and H_2O. The updated band parameters described by Soufiani and Taine (1997) were employed. For calculations in inhomogeneous and/or nonisothermal media, the Curtis-Godson approximation was used.

3 Description of Test Problems

The geometry of the test problems is a rectangular enclosure of 2 m $\times$ 2 m $\times$ 4 m. All the surrounding walls are black and cold at 300 K. The pressure of the gas mixture in the enclosure is kept at 1 atm for all the cases. Three cases are considered and are summarized in Table 1.

In the second test case, the medium is a nonuniform mixture of H_2O and N_2 with the mole fraction of H_2O specified by $x_{H_2O} = 4(z/L_z)(1 - z/L_z)$, where $L_z = 4$ m. In the third test case, the medium is assumed to be a mixture of $0.1CO_2 + 0.2H_2O + 0.7N_2$ (mole basis). The gas temperature is nonuniform but symmetrical about the centerline of the enclosure and is specified in terms of $T = (T_c - T_e)f(r/R) + T_e$. In this equation, T_c is the gas temperature along the centerline of the enclosure, T_e is the exit temperature at $z = 4$ m. Inside the circular region of the cross section of the enclosure, the variation of gas temperature is defined by $f(r/R) = 1 - 3(r/R)^2 + 2(r/R)^3$, where r is the distance from the enclosure centerline and R is the radius of the circular region ($R = 1$ m). The gas temperature outside the circular region is assumed to be uniform and at the value of the exit temperature. The centerline temperature is assumed to increase linearly from 400 K at the inlet ($z = 0$) to 1800 K at $z = 0.375$ m, then decreases linearly to 800 K at the exit.

4 Results and Discussion

Due to enormous computing time required to carry out the present calculations, numerical results tabulated in this section are obtained using relatively coarse grids and the T_4 quadrature set (128 directions). However, the grid independence of these results were checked by calculating the source term distribution along the centerline of the enclosure using finer grids, since the calculation of source term is more sensitive to grid division than that of heat flux. The effect of angular discretisation on the results was examined in the third case by performing the calculations using the T_4 and the T_6 (288 directions) sets. It was found that the results calculated using the T_4 set differ from those obtained using the T_6 set by only one percent.
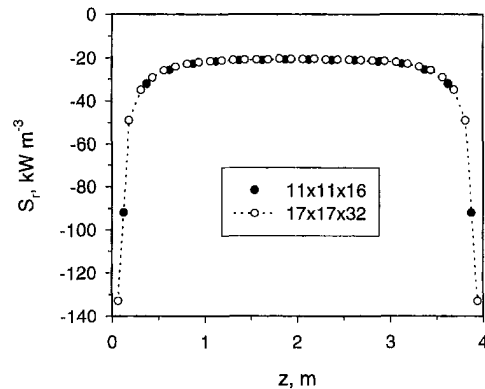
The first case was calculated using a 11 $\times$ 11 $\times$ 16 uniform grid. The calculated radiative source terms along the centerline of the enclosure, (1 m, 1 m, z), and the wall heat flux densities

Table 2 Distributions of radiative source term along the centerline and wall heat flux density along (2 m, 1 m, z) for the first case

z, m	Radiative source, kW m^{-3}	Heat flux density, kW m^{-2}
0.125	−91.962	25.679
0.375	−32.189	28.992
0.625	−25.708	30.047
0.875	−22.708	30.620
1.125	−21.654	30.966
1.375	−21.220	31.103
1.625	−21.043	31.202
1.875	−20.742	31.273

Table 3 Distributions of radiative source along (x, 1 m, 0.375 m) and wall heat flux density along (x, 1 m, 4 m) for the first case

x, m	Radiative source, kW m^{-3}	Heat flux density, kW m^{-2}
0.0909	−115.560	24.953
0.2727	−46.429	28.487
0.4546	−36.741	29.732
0.6364	−34.114	30.324
0.8182	−32.699	30.692
1.0000	−32.189	30.915
1.1819	−32.699	30.692
1.3637	−34.114	30.324
1.5455	−36.741	29.732
1.7274	−46.429	28.487
1.9092	−115.560	24.953

Fig. 1 Comparison of source term distributions along the centerline of the enclosure calculated using two computational grids for the first test case

along (2 m, 1 m, z) are tabulated in Table 2 for half of the enclosure due to the symmetry of this problem. Table 3 displays the radiative source terms along (x, 1 m, 0.375 m) and wall heat flux densities along (x, 1 m, 4 m).

An additional run was carried out in this case using a finer uniform grid, 17 $\times$ 17 $\times$ 32, for source terms along the centerline only in order to confirm that the results shown in Tables 2 and 3 are grid independent. Results obtained using the coarse and the fine grids are compared in Fig. 1. It can be seen that they are almost identical. In addition, the source term distributions shown in Fig. 1 and Table 3 are qualitatively similar to those obtained in one-dimensional parallel-plates enclosure (Kim et al., 1991; Liu et al., 1997).

The second case was calculated using a 11 $\times$ 11 $\times$ 25 uniform grid. Results of the second case are summarized in Tables 4 and 5.

Table 4 Distributions of radiative source term along the centerline and wall heat flux density along (2 m, 1 m, z) for the second case

z, m	Radiative source, kW m^{-3}	Heat flux density, kW m^{-2}
0.08	−23.681	11.942
0.24	−35.010	15.825
0.40	−34.934	19.090
0.56	−32.830	21.617
0.72	−30.425	23.560
0.88	−28.327	25.064
1.04	−26.663	26.236
1.20	−25.416	27.148
1.36	−24.503	27.841
1.52	−23.858	28.351
1.68	−23.443	28.701
1.84	−23.189	28.906
2.00	−23.090	28.973

Table 5 Distributions of radiative source along (x, 1 m, 0.24 m) and wall heat flux density along (x, 1 m, 4 m) for the second case

x, m	Radiative source, kW m^{-3}	Heat flux density, kW m^{-2}
0.0909	−60.316	15.529
0.2727	−41.372	19.275
0.4546	−37.405	20.916
0.6364	−35.918	21.799
0.8182	−35.208	22.380
1.0000	−35.010	22.719
1.1819	−35.208	22.380
1.3637	−35.918	21.799
1.5455	−37.405	20.916
1.7274	−41.372	19.275
1.9092	−60.316	15.529

Table 6 Distributions of radiative source along the centerline and heat flux density along (2 m, 1 m, z) for the third case

z, m	Radiative source, kW m^{-3}	Heat flux, kW m^{-2}
0.040	69.146	11.288
0.115	59.081	13.120
0.190	−11.900	14.644
0.265	−156.04	16.170
0.325	−318.16	16.949
0.375	−531.15	17.529
0.425	−439.46	18.300
0.500	−390.36	19.286
0.600	−354.02	19.901
0.725	−321.33	20.236
0.875	−291.59	20.518
1.025	−267.15	20.614
1.200	−240.06	20.210
1.400	−210.62	19.485
1.600	−184.39	18.620
1.800	−161.07	17.722
2.000	−139.90	16.835
2.250	−112.68	15.762
2.550	−85.092	14.488
2.850	−61.041	13.252
3.125	−43.583	12.136
3.375	−31.102	11.137
3.625	−20.995	10.101
3.875	−25.320	8.483

Fig. 3 Comparison of source term distributions along the centerline of the enclosure calculated using two computational grids for the third test case
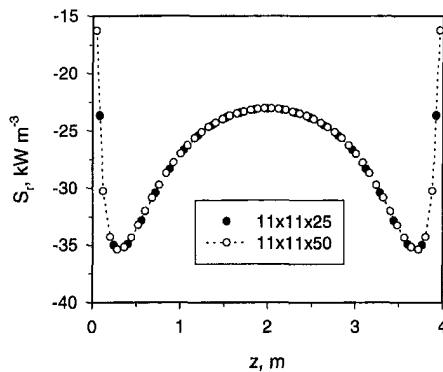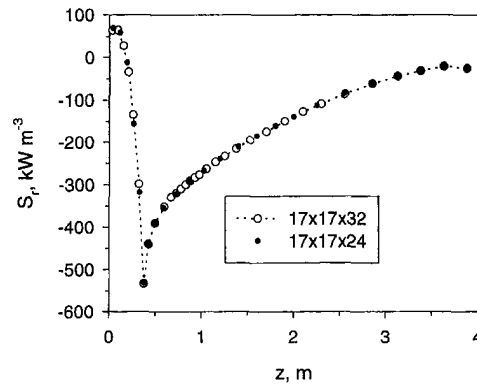

Fig. 2 Comparison of source term distributions along the centerline of the enclosure calculated using two computational grids for the second test case

In order to check the adequacy of the grid division for the results given in Tables 4 and 5, the source terms along the centerline of the enclosure were also calculated using a uniform grid of 11 × 11 × 50. Results obtained using the two grids are compared in Fig. 2. Again, the two grids yield almost identical results. Fig. 2 confirms that the use of the relatively coarse grid of 11 × 11 × 25 is adequate for this case. The W-shaped source term distribution shown in Fig. 2 is similar to that obtained in one-dimensional parallel-plates enclosure (Kim et al., 1991). The left valley of the W-shape occurs at about $z = 0.28$ m.

Calculations of the third case were conducted using a nonuniform grid. The computational grid used was 17 × 17 × 24. Uniform grid division was used in the x and y directions and

the grid division in the z direction was nonuniform with finer grids placed around the peak gas temperature ($z = 0.375$ m). Representative results of this case are tabulated in Table 6.

Grid independence of the results given in Table 6 is demonstrated in Fig. 3 by comparing the results of source term along the centerline calculated using two grids. Once again, the effect of grid size on the results is seen to be negligible. The shape of the source term distribution is expected from the specifications of species and temperature fields. It is interesting to observe that the source term reaches its minimum at the same location as the gas temperature, indicating the dominant influence of local gas emission. However, the wall heat flux density shown in Table 6 peaks further downstream at around $z = 1.025$ m, reflecting the long-distance nature of thermal radiation.

5 Conclusions

Three-dimensional non-grey gas radiation analyses were conducted using the statistical narrow-band model with updated band parameters. The exact narrow-band averaged radiative transfer equation was solved using a ray-tracing technique along with the T_N quadrature set. Accurate numerical results were reported for

non-grey gas radiation in a rectangular enclosure containing three different gas mixtures. These results are valuable for future evaluation of other non-grey gas radiation models.

References

Bedir, H., T'ien, J. S., and Lee, H. S., 1997, "Comparison of Different Radiation Treatments for a One-Dimensional Diffusion Flame," *Combust. Theory Modelling*, Vol. 1, pp. 395–404.

Denison, M. K., and Webb, B. W., 1993, "A Spectral Line-Based Weighted-Sum-of-Gray-Gases Model for Arbitrary RTE Solvers," ASME JOURNAL OF HEAT TRANSFER, Vol. 115, pp. 1004–1011.

Goody, R. M., and Yung, Y. L., 1989, *Atmospheric Radiation*, 2nd Ed. Oxford University Press, Oxford, UK.

Hartmann, J. M., Levi Di Leon, R., and Taine, J., 1984, "Line-by-Line and Narrow-Band Statistical Model Calculation for H₂O," *Journal of Quantitative Spectroscopy and Radiative Transfer*, Vol. 32, No. 2, pp. 119–127.

Hottel, H. C., and Sarofim, A. F., 1967, *Radiative Transfer*, McGraw-Hill, New York.

Kim, T.-K., Menart, J. A., and Lee, H. S., 1991, "Nongray Radiative Gas Analysis Using the S-N Discrete Ordinates Method," ASME JOURNAL OF HEAT TRANSFER, Vol. 113, pp. 946–952.

Lee, P. Y. C., Hollands, K. G. T., and Raithby, G. D., 1996, "Reordering the Absorption Coefficient within the Wide Band for Predicting Gaseous Radiant Exchange," ASME JOURNAL OF HEAT TRANSFER, Vol. 118, pp. 394–400.

Liu, F., Gülder, Ö. L., Smallwood, G. J., and Ju, Y., 1997, "Non-Grey Gas Radiative Transfer Analyses Using the Statistical Narrow-Band Model," *Int. J. Heat Mass Transfer*, to appear.

Lockwood, F. C., and Shah, N. G., 1981, "A New Radiation Solution Method for Incorporation in General Combustion Prediction Procedures," *18th Symposium (International) on Combustion*, The Combustion Institute, pp. 1405–1413.

Ludwig, D. B., Malkmus, W., Reardon, J. E., and Thomson, J. A. L., 1973, "Handbook of Infrared Radiation from Combustion Gases," NASA SP3080.

Parthasarathy, G., Chai, J. C., and Patankar, S. V., 1996, "A Simple Approach to Non-Gray Gas Modeling," *Numerical Heat Transfer*, Part B, Vol. 29, pp. 113–123.

Soufiani, A., and Djavdan, E., 1994, "A Comparison between Weighted Sum of Gray Gases and Statistical Narrow-Band Radiation Models for Combustion Applications," *Combustion and Flame*, Vol. 97, pp. 240–250.

Soufiani, A., and Taine, J., 1997, "High Temperature Gas Radiative Property Parameters of Statistical Narrow-Band Model for H₂O, CO₂ and CO and Correlated-K (CK) Model for H₂O and CO₂," *Int. J. Heat Mass Transfer*, Vol. 40, pp. 987–991.

Tang, K. C., and Brewster, M. Q., 1994, "K-Distribution Analysis of Gas Radiation with Nongray, Emitting, Absorbing, and Anisotropic Scattering Particles," ASME JOURNAL OF HEAT TRANSFER, Vol. 116, pp. 980–985.

Thurgood, C. P., Pollard, A., and Becker, A. B., 1995, "The T_N Quadrature Set for the Discrete Ordinates Method," ASME JOURNAL OF HEAT TRANSFER, Vol. 117, pp. 1068–1070.

Application of Adaptive Quadrature to Fire Radiation Modeling

P. S. Cumber [1]

Nomenclature

E_{bound} = error bound
E_{est} = error estimate
G_1, P_2, P_i = labels for ray orientations
I = spectrally integrated intensity

[1] BG Technology, Gas Research & Technology Centre, Loughborough LE11 3GR, UK. e-mail: peter.cumber@bgtech.co.uk.

I_λ = spectral intensity
N_{bad} = radius of refinement
N_θ, N_φ = number of rays in the θ and φ coordinate directions
q_- = incident flux
s = point vector

Introduction

The accurate modeling of thermal radiation is important in many combusting systems. The radiative flux incident to a point s on a surface or a radiometer can be expressed by the integral

$$q_- = \int_{\Delta\Omega} \int_0^\infty I_\lambda(\Omega, s) \cos\theta d\lambda d\Omega \qquad (1)$$

where I_λ is the spectral intensity, λ denotes wavelength, θ is the angle of incidence, and $\Delta\Omega$ is the field of view of the receiver. Taking scattering to be negligible, the spectral intensity distribution can be calculated, for example, by an exponential wide-band model (e.g., Cumber et al., 1998); alternatively, the spectral integration is avoided and the total intensity is calculated using a more empirical approach, such as a mixed-grey-gas model (e.g., Truelove, 1976).

In this note an adaptive quadrature strategy over a solid-angle implemented as part of the discrete transfer method (Lockwood and Shah, 1981) is presented and evaluated by calculating the received radiation about two natural gas jet fires. The calculation of the external radiation field of a jet fire is a particularly challenging task, as the intensity field is highly anisotropic with a small hot volume of gas dominating the heat transfer external to the flame envelope.

Flame Structure Model

The first jet fire considered is a laboratory scale rim-stabilized axisymmetric methane flame. The flame has a Reynolds number of 8800 based on the bulk velocity at the nozzle exit. The nozzle has a diameter of 8.4 mm. More details of the experiment can be found in Cumber et al. (1998). This flow is computationally inexpensive to calculate, and turbulence-radiation interaction effects have been found to be small (Jeng et al., 1984), making it possible to use a mean flow-field analysis to model the external radiation field. The modeling of the radiation flux requires some representation of the flame structure, which is predicted using a model based on the boundary layer equations, (Spalding, 1977). A detailed description of the model can be found in Cumber et al. (1998).

The sonic natural gas jet fire considered below has a pressure ratio of 1.68 issuing from a stack with a diameter of 385 mm into an atmospheric boundary layer with a wind speed of 6.2 m/s measured at a height of 10 m. The full details of the field scale test and the reacting flow simulation can be found in Cook et al. (1997).

Radiation Modeling

In the discrete transfer method, to evaluate the incident flux integral it is expressed in spherical coordinates and the field of view discretized with a uniform spacing in the angle of rotation (φ) and angle of incidence (θ). For the remainder of this article such a distribution of rays will be described as "uniform." The incident intensity distribution is assumed piecewise constant over the field of view of the receiver. The incident intensity over an element is calculated by tracing the ray with orientation defined by its centroid, through the computational domain, noting the control volumes of the finite volume grid traversed, length of ray segment, and local thermochemical quantities. The ray trace is terminated at the computational boundary. The stored data is then used as an input to a model for participating

non-grey gas radiation in a rectangular enclosure containing three different gas mixtures. These results are valuable for future evaluation of other non-grey gas radiation models.

Acknowledgments

References

Bedir, H., T'ien, J. S., and Lee, H. S., 1997, "Comparison of Different Radiation Treatments for a One-Dimensional Diffusion Flame," *Combust. Theory Modelling*, Vol. 1, pp. 395–404.

Denison, M. K., and Webb, B. W., 1993, "A Spectral Line-Based Weighted-Sum-of-Gray-Gases Model for Arbitrary RTE Solvers," ASME JOURNAL OF HEAT TRANSFER, Vol. 115, pp. 1004–1011.

Goody, R. M., and Yung, Y. L., 1989, *Atmospheric Radiation*, 2nd Ed. Oxford University Press, Oxford, UK.

Hartmann, J. M., Levi Di Leon, R., and Taine, J., 1984, "Line-by-Line and Narrow-Band Statistical Model Calculation for H₂O," *Journal of Quantitative Spectroscopy and Radiative Transfer*, Vol. 32, No. 2, pp. 119–127.

Hottel, H. C., and Sarofim, A. F., 1967, *Radiative Transfer*, McGraw-Hill, New York.

Kim, T.-K., Menart, J. A., and Lee, H. S., 1991, "Nongray Radiative Gas Analysis Using the S-N Discrete Ordinates Method," ASME JOURNAL OF HEAT TRANSFER, Vol. 113, pp. 946–952.

Lee, P. Y. C., Hollands, K. G. T., and Raithby, G. D., 1996, "Reordering the Absorption Coefficient within the Wide Band for Predicting Gaseous Radiant Exchange," ASME JOURNAL OF HEAT TRANSFER, Vol. 118, pp. 394–400.

Liu, F., Gülder, Ö. L., Smallwood, G. J., and Ju, Y., 1997, "Non-Grey Gas Radiative Transfer Analyses Using the Statistical Narrow-Band Model," *Int. J. Heat Mass Transfer*, to appear.

Lockwood, F. C., and Shah, N. G., 1981, "A New Radiation Solution Method for Incorporation in General Combustion Prediction Procedures," *18th Symposium (International) on Combustion*, The Combustion Institute, pp. 1405–1413.

Ludwig, D. B., Malkmus, W., Reardon, J. E., and Thomson, J. A. L., 1973, "Handbook of Infrared Radiation from Combustion Gases," NASA SP3080.

Parthasarathy, G., Chai, J. C., and Patankar, S. V., 1996, "A Simple Approach to Non-Gray Gas Modeling," *Numerical Heat Transfer*, Part B, Vol. 29, pp. 113–123.

Soufiani, A., and Djavdan, E., 1994, "A Comparison between Weighted Sum of Gray Gases and Statistical Narrow-Band Radiation Models for Combustion Applications," *Combustion and Flame*, Vol. 97, pp. 240–250.

Soufiani, A., and Taine, J., 1997, "High Temperature Gas Radiative Property Parameters of Statistical Narrow-Band Model for H₂O, CO₂ and CO and Correlated-*K* (CK) Model for H₂O and CO₂," *Int. J. Heat Mass Transfer*, Vol. 40, pp. 987–991.

Tang, K. C., and Brewster, M. Q., 1994, "*K*-Distribution Analysis of Gas Radiation with Nongray, Emitting, Absorbing, and Anisotropic Scattering Particles," ASME JOURNAL OF HEAT TRANSFER, Vol. 116, pp. 980–985.

Thurgood, C. P., Pollard, A., and Becker, A. B., 1995, "The T_N Quadrature Set for the Discrete Ordinates Method," ASME JOURNAL OF HEAT TRANSFER, Vol. 117, pp. 1068–1070.

Application of Adaptive Quadrature to Fire Radiation Modeling

P. S. Cumber[1]

Nomenclature

E_{bound} = error bound
E_{est} = error estimate
G_1, P_2, P_i = labels for ray orientations
I = spectrally integrated intensity

I_λ = spectral intensity
N_{bad} = radius of refinement
N_θ, N_φ = number of rays in the θ and φ coordinate directions
q_- = incident flux
s = point vector

Introduction

The accurate modeling of thermal radiation is important in many combusting systems. The radiative flux incident to a point s on a surface or a radiometer can be expressed by the integral

$$q_- = \int_{\Delta\Omega} \int_0^\infty I_\lambda(\Omega, s) \cos\theta d\lambda d\Omega \qquad (1)$$

where I_λ is the spectral intensity, λ denotes wavelength, θ is the angle of incidence, and $\Delta\Omega$ is the field of view of the receiver. Taking scattering to be negligible, the spectral intensity distribution can be calculated, for example, by an exponential wide-band model (e.g., Cumber et al., 1998); alternatively, the spectral integration is avoided and the total intensity is calculated using a more empirical approach, such as a mixed-grey-gas model (e.g., Truelove, 1976).

In this note an adaptive quadrature strategy over a solid-angle implemented as part of the discrete transfer method (Lockwood and Shah, 1981) is presented and evaluated by calculating the received radiation about two natural gas jet fires. The calculation of the external radiation field of a jet fire is a particularly challenging task, as the intensity field is highly anisotropic with a small hot volume of gas dominating the heat transfer external to the flame envelope.

Flame Structure Model

The first jet fire considered is a laboratory scale rim-stabilized axisymmetric methane flame. The flame has a Reynolds number of 8800 based on the bulk velocity at the nozzle exit. The nozzle has a diameter of 8.4 mm. More details of the experiment can be found in Cumber et al. (1998). This flow is computationally inexpensive to calculate, and turbulence-radiation interaction effects have been found to be small (Jeng et al., 1984), making it possible to use a mean flow-field analysis to model the external radiation field. The modeling of the radiation flux requires some representation of the flame structure, which is predicted using a model based on the boundary layer equations, (Spalding, 1977). A detailed description of the model can be found in Cumber et al. (1998).

The sonic natural gas jet fire considered below has a pressure ratio of 1.68 issuing from a stack with a diameter of 385 mm into an atmospheric boundary layer with a wind speed of 6.2 m/s measured at a height of 10 m. The full details of the field scale test and the reacting flow simulation can be found in Cook et al. (1997).

Radiation Modeling

In the discrete transfer method, to evaluate the incident flux integral it is expressed in spherical coordinates and the field of view discretized with a uniform spacing in the angle of rotation (φ) and angle of incidence (θ). For the remainder of this article such a distribution of rays will be described as "uniform." The incident intensity distribution is assumed piecewise constant over the field of view of the receiver. The incident intensity over an element is calculated by tracing the ray with orientation defined by its centroid, through the computational domain, noting the control volumes of the finite volume grid traversed, length of ray segment, and local thermochemical quantities. The ray trace is terminated at the computational boundary. The stored data is then used as an input to a model for participating

media which solves the equation of radiative heat transfer. Thus the incident flux is approximated as

$$q_- = \sum_c I(\varphi_c, \theta_c) \tfrac{1}{2} \sin 2\theta_c \sin \Delta\theta \Delta\varphi \tag{2}$$

where the summation is over the field of view of the receiver and (φ_c, θ_c) denotes spherical coordinates on the unit hemisphere. For clarity the λ subscript has been dropped and I denotes the spectrally integrated intensity.

Adaptive Quadrature

An adaptive quadrature algorithm can be divided into three components; a quadrature rule, an initial coarse ray distribution, and an adaption criterion. The quadrature rule used is the piecewise constant quadrature formula, applied on an element-by-element basis. The adaption criterion is based on an extrapolated error estimate. The extrapolation formula, for the quadrature rule, (2) over a single element of the hemispherical mesh can be written,

$$q^c_{-,\mathrm{extrap}} = q^c_{-,fi} \frac{1}{1-\gamma} - q^c_{-,co} \frac{\gamma}{1-\gamma} + O(\Delta\theta^a \Delta\varphi^b),$$

$$\gamma = 0.25, \quad a + b = 3.$$

This is derived by taking a linear combination of a coarse ($q^c_{-,co}$, 1 ray) and fine ($q^c_{-,fi}$, 4 ray) distribution such that the leading term in the truncation error is eliminated, giving a higher order prediction. Taking $q^c_{-,\mathrm{extrap}}$ to be close to the ray converged incident flux, an error estimate can be derived,

$$E^c_{\mathrm{est}} = q^c_{-,\mathrm{extrap}} - q^c_{-,fi}. \tag{3}$$

Elements of the hemispherical mesh are refined if the error estimate exceeds some user-defined tolerance,

$$\frac{|E^c_{\mathrm{est}}|}{q^c_{-,fi}} > \epsilon_{\mathrm{tol}} \Rightarrow \text{Refine Element.} \tag{4}$$

A numerical study revealed the predicted incident flux is relatively insensitive to the adaption tolerance provided it is sufficiently small, i.e., of the order of 0.1. In addition a secondary adaption criteria was implemented such that adapted elements neighboring elements up to a radius of N_{bad} are also refined,

$(\varphi_c, \theta_c) = (\varphi_i, \theta_j)$ is refined $\Rightarrow (\varphi_{i\pm\alpha}, \theta_{j\pm\beta})$ are refined,

$$\alpha + \beta \leq N_{\mathrm{bad}}.$$

For the jet fire, Re = 8800, only three rays $(N_\theta, N_\varphi) = (1, 3)$ in the initial ray distribution with N_{bad} set to one are required to ensure the adaptive quadrature process converges to the ray independent incident flux as more levels of refinement are introduced. The incident flux was calculated at a number of points external to the fire using a mixed-grey-gas model (Truelove, 1976), but for illustrative purposes only one point will be considered at $(r, z) = (0.4 \text{ m}, 0.7 \text{ m})$ in axisymmetric coordinates with the origin located on the jet axis in the plane of the nozzle. The radiometer has a horizontal orientation directed towards the jet axis. Figure 1 shows half the incident intensity distribution with an adaptive ray distribution, taking advantage of the line of symmetry. Five equilogarithmically spaced contours are shown ranging between the ambient intensity and the peak intensity. The incident intensity distribution is significant over a small portion of the field of view, which is reflected in the pattern of adaption. For this receiver five levels of refinement were prescribed, with the first two levels being nonadaptive, i.e., the first two coarsest levels of the grid are full. In all, 396 rays were used to evaluate the incident flux, with an error of less than one percent. If no adaption were used 768 rays would
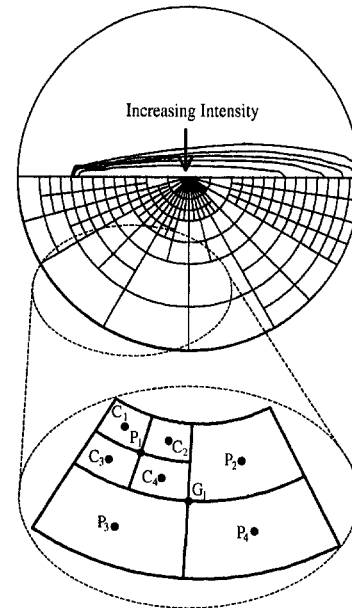

Fig. 1 Incident intensity distribution for the receiver (0.4, 0.7) and an adapted ray distribution with an enlargement of a portion of an adapted ray distribution

be required to give a uniform ray distribution at the finest level of refinement in the adaptive quadrature strategy.

To reduce the need for expensive ray refinement, studies to assess numerical accuracy an error bound can be derived from the extrapolated error estimate (3) by taking the summation of the absolute value of the error estimate applied on an element-by-element basis and correcting for the partially adapted elements similar to that indicated by the dashed ellipse in Fig. 1. As an example of how the error bound is calculated, consider a portion of adapted hemispherical mesh shown in Fig. 1, with the ray orientations labeled as grandparents (G_i), parents (P_i), and children (C_i) appropriate to their level of refinement. The error bound over the portion of adapted mesh can be written

$$E^{G_1}_{\mathrm{bound}} = (1 - \beta)|E^{G_1}_{\mathrm{est}}| + |E^{P_1}_{\mathrm{est}}|, \beta = \frac{|I_{G_1} - I_{P_1}|}{\sum_{i=1}^{4} |I_{G_1} - I_{P_1}|} \tag{5}$$

where β is a correction factor. This is necessary as the error in the quadrature over the element P_1 is included twice otherwise. The form of the correction factor is prescribed by assuming the relative difference in intensity distribution is a good measure of the error distribution in the element G_1. As more levels of refinement are introduced this approximation increases in validity.

Further discussion of the error bound calculated by applying (5) to the whole field of view will be continued below in relation to its application to a field scale sonic natural gas jet fire. The downwind received flux distribution at ground level is calculated using an exponential wide-band model (Cumber et al., 1998). In Figs. 2(a) and 2(b) predictions of incident flux and the error bound (5) using adapted ray distributions with three and four levels of refinement, respectively, are shown together with a ray independent incident flux distribution. For both sets of predicted received flux distributions an initial ray distribution of $(N_\theta, N_\varphi) = (2, 6)$ was used. Each predicted incident flux comparing it to the ray independent prediction is within the error bound.

In Fig. 3 the number of rays necessary to achieve a numerical error of less than five percent in the incident flux for the six receivers using a uniform and adapted ray distribution are shown. Significantly less rays are required to achieve a given
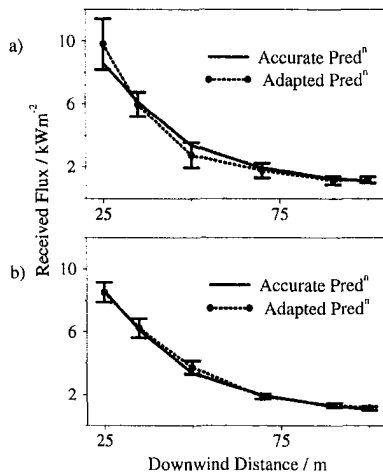
Fig. 2 Incident fluxes downstream of a sonic natural gas jet fire. The ray independent prediction and (a) adapted prediction with error bound (three levels of refinement), and (b) adapted prediction with error bound (four levels of refinement).
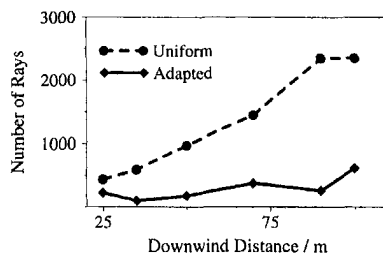

Fig. 3 Number of rays necessary to achieve a numerical error of less than five percent in the incident flux for a sonic natural gas jet fire

accuracy using adaptive quadrature compared to nonadaptive, particularly in the far field of the jet fire. The reduction in the number of rays using adaptive quadrature is due to the small view factor from the fire to the receivers, requiring a fine distribution of rays over a small portion of the field of view of the receivers.

Thus far the number of rays necessary to achieve a given numerical error has been stated to give an indication of the possible gains in efficiency of adaptive over uniform quadrature. However, this is not an ideal measure as there are additional computational overheads with adaptive quadrature associated with calculating the error estimates in the adaption criteria and the data structure used to store the discrete incident intensity distribution is more complex. Comparing the run-time to achieve a given numerical error is also not a good indication of computational cost as in general the numerical error is not available and a ray refinement study is necessary to confirm ray convergence. The run-times to complete a ray refinement study for the receiver 100 meters from the fire source are 563 s and 2813 s for adaptive and uniform quadrature, respectively. Using the uniform quadrature scheme, ray convergence is inferred when doubling the number of rays in each coordinate direction changes the predicted flux by less than five percent. Whereas for the adaptive quadrature scheme ray convergence is inferred when the error bound is less than five percent. The timing data given above was for simulations on a Silicon Graphics R4000 workstation.

Conclusion

An adaptive quadrature strategy applied to jet fire radiation modeling has been presented and analyzed. In the quadrature strategy described, the ray distribution automatically adapts in

response to the variation in the incident intensity distribution. Adaptive quadrature was shown to be successful at reducing the computational cost of calculating the incident flux external to the jet fire. In addition a sharp error bound derived from the extrapolated error formula (3) suitably modified (5) for partially refined hemispherical elements was demonstrated. An error bound reduces the need for expensive ray refinement studies.

The benefits of using adaptive quadrature must be weighed against the additional complexity of implementation, that said, the implementation is a once and for all activity that can be discounted over many years, for a model that is to be applied to many different reacting flows. A further consideration is the adaptive quadrature strategy can more easily be automated, reducing the risk of bogus heat transfer predictions due to poor problem specification by a user not well acquainted with thermal radiation modeling. In this article the focus has been the application of adaptive quadrature to free jet fire simulation; however, it could be applied successfully to other reacting flows where radiative heat transfer is dominated by a small hot emitting volume.

References

Cook D. K., Cumber P. S., Fairweather M., and Shemirani F., 1997, "Modelling free and impacting underexpanded jet fires," *Process Safety—The Future, Hazards XIII,* IChemE, Manchester, UK.

Cumber P. S., Fairweather M., and Ledin S., 1998, "Application of wide band radiation models to non-homogeneous combustion systems," *International Journal of Heat and Mass Transfer,* Vol. 41, pp. 1573–1584.

Jeng S. M., Lai M. C., and Faeth G. M., 1984, "Nonluminous radiation in turbulent buoyant axisymmetric flames," *Combustion Science and Technology,* Vol. 40, pp. 41–53.

Lockwood F. C., and Shah N. G., 1981, "A new radiation solution method for incorporation in general combustion prediction procedures," *Eighteenth Symposium (Int.) on Combustion,* The Combustion Institute, Pittsburgh, pp. 1405–1414.

Spalding D. B., 1977, *GENMIX: A General Computer Program for Two-Dimensional Parabolic Phenomena,* Pergamon Press, UK.

Truelove J. S., 1976, "Mixed grey gas model for flame radiation," AERE R 8494, UKAEA, Harwell, U.K.

Enhanced Cooling via Boiling in Porous Layers: The Effect of Vapor Channels

A. K. Stubos[1] and J.-M. Buchlin[2]

Enhanced heat transfer via boiling in a porous layer covering the heated surface is considered analytically. The effect of vapor channels traversing the porous layer on the power for which a vapor film on the heated surface occurs, is examined by comparing the heat removal capability of the system with and without channels. A significant increase of the attained coolability level is obtained theoretically leading to the possibility of new design configurations for the cooling of intensely heated surfaces.

[1] Ph.D., NCSR Demokritos, 15310 Ag. Paraskevi Attikis, Greece. e-mail: stub-@cyclades.nrcps.ariadne-t.gr. Mem. ASME.

[2] Professor, von Karman Institute, Ch. de Waterloo 72, 1640 Rhode-St.-Genese, belgium. e-mail: buchlin@vki.ac.be
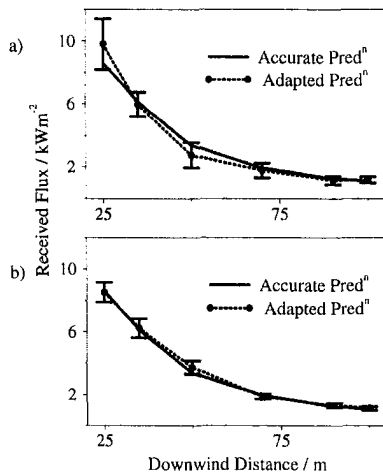
Fig. 2 Incident fluxes downstream of a sonic natural gas jet fire. The ray independent prediction and (*a*) adapted prediction with error bound (three levels of refinement), and (*b*) adapted prediction with error bound (four levels of refinement).
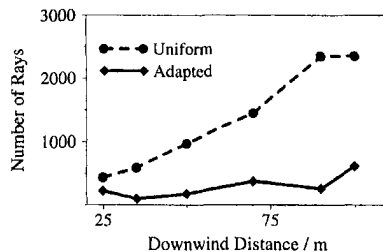

Fig. 3 Number of rays necessary to achieve a numerical error of less than five percent in the incident flux for a sonic natural gas jet fire

accuracy using adaptive quadrature compared to nonadaptive, particularly in the far field of the jet fire. The reduction in the number of rays using adaptive quadrature is due to the small view factor from the fire to the receivers, requiring a fine distribution of rays over a small portion of the field of view of the receivers.

Thus far the number of rays necessary to achieve a given numerical error has been stated to give an indication of the possible gains in efficiency of adaptive over uniform quadrature. However, this is not an ideal measure as there are additional computational overheads with adaptive quadrature associated with calculating the error estimates in the adaption criteria and the data structure used to store the discrete incident intensity distribution is more complex. Comparing the run-time to achieve a given numerical error is also not a good indication of computational cost as in general the numerical error is not available and a ray refinement study is necessary to confirm ray convergence. The run-times to complete a ray refinement study for the receiver 100 meters from the fire source are 563 s and 2813 s for adaptive and uniform quadrature, respectively. Using the uniform quadrature scheme, ray convergence is inferred when doubling the number of rays in each coordinate direction changes the predicted flux by less than five percent. Whereas for the adaptive quadrature scheme ray convergence is inferred when the error bound is less than five percent. The timing data given above was for simulations on a Silicon Graphics R4000 workstation.

Conclusion

An adaptive quadrature strategy applied to jet fire radiation modeling has been presented and analyzed. In the quadrature strategy described, the ray distribution automatically adapts in response to the variation in the incident intensity distribution. Adaptive quadrature was shown to be successful at reducing the computational cost of calculating the incident flux external to the jet fire. In addition a sharp error bound derived from the extrapolated error formula (3) suitably modified (5) for partially refined hemispherical elements was demonstrated. An error bound reduces the need for expensive ray refinement studies.

The benefits of using adaptive quadrature must be weighed against the additional complexity of implementation, that said, the implementation is a once and for all activity that can be discounted over many years, for a model that is to be applied to many different reacting flows. A further consideration is the adaptive quadrature strategy can more easily be automated, reducing the risk of bogus heat transfer predictions due to poor problem specification by a user not well acquainted with thermal radiation modeling. In this article the focus has been the application of adaptive quadrature to free jet fire simulation; however, it could be applied successfully to other reacting flows where radiative heat transfer is dominated by a small hot emitting volume.

References

Cook D. K., Cumber P. S., Fairweather M., and Shemirani F., 1997, "Modelling free and impacting underexpanded jet fires," *Process Safety—The Future, Hazards XIII*, IChemE, Manchester, UK.

Cumber P. S., Fairweather M., and Ledin S., 1998, "Application of wide band radiation models to non-homogeneous combustion systems," *International Journal of Heat and Mass Transfer*, Vol. 41, pp. 1573–1584.

Jeng S. M., Lai M. C., and Faeth G. M., 1984, "Nonluminous radiation in turbulent buoyant axisymmetric flames," *Combustion Science and Technology*, Vol. 40, pp. 41–53.

Lockwood F. C., and Shah N. G., 1981, "A new radiation solution method for incorporation in general combustion prediction procedures," *Eighteenth Symposium (Int.) on Combustion*, The Combustion Institute, Pittsburgh, pp. 1405–1414.

Spalding D. B., 1977, *GENMIX: A General Computer Program for Two-Dimensional Parabolic Phenomena*, Pergamon Press, UK.

Truelove J. S., 1976, "Mixed grey gas model for flame radiation," AERE R 8494, UKAEA, Harwell, U.K.

Enhanced Cooling via Boiling in Porous Layers: The Effect of Vapor Channels

A. K. Stubos[1] and J.-M. Buchlin[2]

Enhanced heat transfer via boiling in a porous layer covering the heated surface is considered analytically. The effect of vapor channels traversing the porous layer on the power for which a vapor film on the heated surface occurs, is examined by comparing the heat removal capability of the system with and without channels. A significant increase of the attained coolability level is obtained theoretically leading to the possibility of new design configurations for the cooling of intensely heated surfaces.

[1] Ph.D., NCSR Demokritos, 15310 Ag. Paraskevi Attikis, Greece. e-mail: stub-@cyclades.nrcps.ariadne-t.gr. Mem. ASME.

[2] Professor, von Karman Institute, Ch. de Waterloo 72, 1640 Rhode-St.-Genese, belgium. e-mail: buchlin@vki.ac.be

Nomenclature

A, B = coefficients (see Tables 1 and 2)
Dc = channel diameter
d_p = particle diameter
F = friction factor
G = gravitational acceleration
H = porous layer height
h_{lv} = latent heat
J = leverett function
Nc = channel population density
P = pressure
Pc = capillary pressure
q = heat flux
γ = kinematic viscosity ratio
ΔP = pressure drop
ΔT = temperature difference
ϵ = porosity
θ = contact angle
κ = permeability
κ_l, κ_v = relative permeabilities
μ = viscosity
ν = kinematic viscosity
ρ = density
σ = surface tension
Q = volumetric heat source
S = saturation (liquid fraction)
T = temperature
T_b = boiling temperature
V = superficial velocity
Vc = vapor velocity in the channels
z = spatial coordinate

Subscripts

l = liquid
v = vapour
w = heated surface

Superscripts

$*$ = Nondimensional quantity

1 Introduction

Enhanced heat transfer via boiling in porous media of variable structure is an efficient method for the intensification of cooling of thermally loaded devices, especially when the temperature of the heat transfer surface is strictly limited. The removal of high heat fluxes can be achieved at relatively small temperature differences. Applications include the cooling of electronic chips, enhanced heat exchange tubes, and boiler surfaces (Incropera, 1988; Thome, 1990; Nakayama, 1991). Heat sink configurations directed at electronic cooling are shown in Fig. 1; they involve ordered or randomized structures with pore sizes of the order of 0.75 mm or more. Such designs offer satisfactory distribution of nucleation sites for the generation and growth of vapor bubbles but do not exploit fully the capillary forces for the achievement of larger heat fluxes. In addition, they use the same pores of the matrix for the counterflow of liquid and vapor thus giving rise to higher pressure losses due to the two-phase conditions inside the pores. Only recently it has been tentatively proposed to separate at a certain extent the flow paths of the two phases in the system in order to obtain more efficient heat transfer (Khrustalev and Faghri, 1995; Mughal and Plumb, 1996). To take advantage of capillary effects, one should use high surface tension liquid and/or decrease the pore size. In this way, the downflow of liquid towards the heated surface may be enhanced (taking in account that with reduced pore size the liquid permeability decreases too) and the formation of vapor film on the heated surface occurs at much higher heat fluxes. To avoid excessive pressure drop in
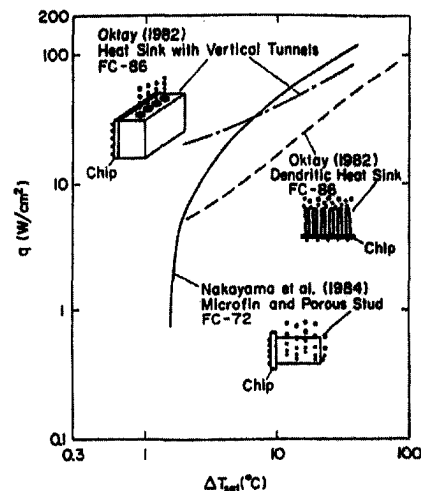

Fig. 1 Pool boiling curve for various heat sink configurations (Incropera, 1988)

the porous structure and promote further the replenishment of the matrix by the liquid flow, some paths, called channels, for the upward escape of the vapor should also be provided. These channels must allow for the separate flow of the two phases (liquid and vapor) in the porous structure. Based on the above arguments, a new heat sink design (Fig. 2) is modeled in the present Note. It consists of a porous layer blanketing the heated surface (e.g., microchip) and characterized by a dual network of passages. The porous structure contains pores with sizes ranging from 5 to 100 μm occupied by the down-coming liquid which evaporates gradually as approaching the heated surface. The structure is periodically traversed by vertical channels of 1 to 2 mm in diameter, which take over the vapor upflow. Horizontal passages of similar sizes (not considered in the present modeling attempt) can be grooved on the heated surface connecting the bases of the vertical channels and driving efficiently the vapour produced on the surface to them. It is expected (as indicated by preliminary tests with rather thick layers) that the achieved heat removal under a specific temperature
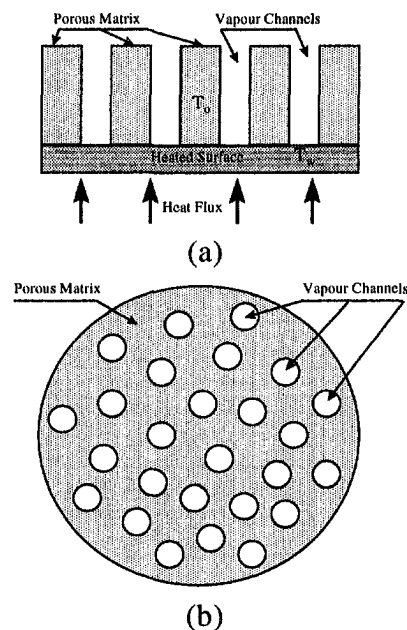

Fig. 2 Channeled porous blanket (a) side view, (b) top view (not to scale)

Table 1 Nondimensional quantities

$$A_1 = \frac{\sigma \cos \theta \sqrt{\epsilon/\kappa}}{\frac{\nu_v H^2 \bar{Q}}{\kappa h_{lv}}} \qquad P^* = \frac{P\kappa h_{lv}}{\nu_v H^2 \bar{Q}} \qquad (\rho g)^* = \frac{\rho g H}{\frac{\nu_v H^2 \bar{Q}}{\kappa h_{lv}}} \qquad z^* = \frac{z}{H}$$

$$A_2 = \frac{\rho_l g H}{\sigma \cos \theta \sqrt{\epsilon/\kappa}} \qquad T^* = \frac{T - T_b}{T_b} \qquad (\rho V)^* = \frac{\rho V h_{lv}}{H\bar{Q}} \qquad \gamma = \frac{\nu_l}{\nu_v}$$

difference $(T_w - T_o)$ will be significantly enhanced using this type of porous coatings. T_w is the heated surface temperature and T_o is the liquid boiling temperature under the prevailing pressure. Smooth transition to film boiling should be exhibited by the corresponding boiling curve as the vapor film formation (inside the porous matrix) is delayed for considerably higher heat fluxes. The calculations reported below are based on previous results from boiling in unconstricted porous layers (Stubos and Buchlin, 1994). The cases of layers without and with channels are considered for the sake of comparison.

2 Vapor-Liquid Counterflow and Limiting Dry-Out Heat Flux in Porous Layers

A one-dimensional approach for the simulation of the steady-state thermohydraulic behavior of a liquid saturated porous layer heated from the bottom or volumetrically is considered. Depending on the boundary conditions, boiling, condensation, subcooled and dryout regimes can be identified along the layer thickness. A thermally homogeneous medium (equal local temperatures for all phases) is assumed due to the small pore size involved (Bird et al., 1960). Without loss of generality, a porous material consisting of a bed of spherical particles is considered for simplicity where ϵ, d_p denote the porosity and the particle diameter, respectively. It is noted that the average pore size associated with a certain particle diameter is of the order of $d_p/6$. The aim is to obtain the limiting dryout heat flux characterized by the formation of a vapor film next to the heated surface. For this purpose, an approximate solution of the counterflow in the boiling zone is sought. The one-dimensional mass and energy balances in the two-phase region of a bed dissipating heat volumetrically may be written in nondimensional form as follows:

$$(\rho_v V_v)^* + (\rho_l V_l)^* = 0 \tag{1}$$

$$\frac{d(\rho_v V_v)^*}{dz^*} = 1 \tag{2}$$

where ρ, V stand for density and superficial velocity and the subscripts l and v refer to the liquid and vapor phases, respectively. The steady-state advective term in the boiling zone is not included since this region is nearly isothermal. Neglecting inertial effects, the extended form of Darcy's law (Fand et al., 1987) expresses the motion of each phase:

$$\frac{dP_i^*}{dz^*} + \frac{(\rho_i V_i)^* \gamma}{\kappa \kappa_i} + (\rho_i g)^* = 0 \tag{3}$$

where γ is the ratio of the liquid to vapor kinematic viscosity ν_l/ν_v and κ_i the relative permeability. The subscript i stands for vapor or liquid while the superscript $*$ denotes nondimensional quantities summarized in Table 1. The system is closed by expressing the relative permeability as function of the liquid fraction (also called saturation) s, $\kappa_l = s^3$ and $\kappa_v = (1 - s)^2$ (Lipinski, 1984; Stubos, 1990).

In high permeability media, one may assume equal pressure gradients for the two fluid phases and obtain from Eq. (3)

$$(\rho_v V_v)^* = [(\rho_l g)^* - (\rho_v g)^*]\left(\frac{1}{\kappa_v} + \frac{\gamma}{\kappa_l}\right)^{-1}. \tag{4}$$

For each value of the liquid fraction between 0 and 1, this algebraic relation provides the corresponding heat flux and implies an almost constant saturation profile $s(z)$ in the boiling zone.

The function $C(s) = (1/\kappa_v + \gamma/\kappa_l)^{-1}$ passes through a maximum as the liquid fraction varies from 0 to 1 (e.g., at $s \approx 0.3$ for water) and thus defines the maximum possible heat flux in the two-phase zone. In the general case, the important driving effect of capillarity, expressed as a pressure differential between the vapor and liquid phases, must be included through the use of the Leverett function $J(s)$ (Lipinski, 1984; Udell, 1985):

$$P_C^* = P_v^* - P_l^* = A_1 J(s) \tag{5}$$

where P_C^* is the capillary pressure, $J(s) = 2.36(s^{-1} - 1)^{0.175}$, and A_1, a coefficient incorporating among others the effects of the surface tension σ and the contact angle θ (see Table 1).

Combining Eqs. (1)–(3) and (5) after neglecting vapor gravity and defining $A_2 = (\rho_l g)^*/A_1$ gives

$$\frac{d\left[A_1 C(s)\left(\frac{dJ}{dz^*} - A_2\right)\right]}{dz^*} = -1. \tag{6}$$

Equation (6) can be linearized to yield

$$A_1 \bar{C}\overline{\left(\frac{dJ}{ds}\right)} \frac{d^2 s}{dz^{*2}} = 1 \tag{7}$$

where $\bar{C}$ and $\overline{(dJ/ds)}$ are average values over the entire saturation range. A_2 denotes the ratio between buoyancy and capillary forces. For fluids like R-11 or water and low permeability media A_2-values range from 0.09 to 6×10^{-4} allowing to neglect the gravity effect (the associated error does not exceed five percent). Then the following boundary conditions apply:

$$s = 1 \text{ at } z^* = 1 \quad \text{and} \quad \frac{ds}{dz^*} = 0 \quad \text{at } z^* = 0.$$

Integrating (7) over the boiling zone (i.e., layer height) and searching for $s = 0$ at $z^* = 0$ gives the following relation for the incipient dryout heat flux:

$$2A_1 \overline{\left(\frac{dJ}{ds}\right)} \bar{C} = -1. \tag{8}$$

In bottom-heated porous layers, the energy balance replacing (2) is simply

$$(\rho_v V_v)^* = 1. \tag{9}$$

In this case we obtain

$$A_1 \frac{dJ}{ds} \frac{ds}{dz^*} + C(s)^{-1} - (\rho_l g)^* = 0 \tag{10}$$

and similarly to Eq. (8),

$$A_1 \bar{C}\left[A_2 - \overline{\left(\frac{dJ}{ds}\right)}\right] = 1. \tag{11}$$

Relationships (8) and (11) provide approximations of the dryout heat flux for volumetrically and bottom-heated low-permeability porous layers, respectively. They can be used for a fast estimation of the heat removal potential of specific porous structures. If subcooling is present at the top, then slight modifications are required to account for the subcooled zone thickness

(Stubos, 1990). In the case of a 8-mm high bed of particles of 0.3 mm in diameter, initially saturated with R-11, the dryout heat flux predictions of the simplified approach are 34.5 kW/m^2 for bottom heating and 52.5 kW/m^2 for volumetric heating. The numerical solution of the full one-dimensional set of equations gives a result close to 42 kW/m^2 (Konstantinou et al., 1997) and the discrepancy is partly due to the fact that the slight top subcooling introduced for stability reasons in the numerical code is not accounted for by the analytical expression. The fin-like effect of the particle layers close to the heated surface in real bottom heating tests should contribute to higher dryout fluxes, as the lower part of the solid matrix operates as if heated volumetrically. In this sense, experimental dryout heat flux data are expected to range between the bottom and volumetric heating results of the computations.

Since the adverse effect of the simultaneous vapor-liquid flow in the pores causes high-pressure drops, modified geometric configurations as shown in Fig. 2 would contribute to an increase of the dryout heat flux by separating the flow paths of the two fluid phases as they move through the porous structure. Such improvements should in principle lead to a significant enhancement of the heat removal rate.

3 The Effect of Vertical Channels on the Limiting Dry-Out Heat Flux

Figure 3(a) presents a processed thermogram of a 10-cm high, unconstricted bed of ferrite particles that are generating heat volumetrically. The unconsolidated porous matrix consists of particles with an average size of 300 microns and was initially saturated with water at atmospheric conditions. The image refers to steady-state reached during the experiment before dryout occurrence in the bed (Stubos, 1990). The colors represent the temperature scale and indicate clearly a nearly isothermal boiling regime in the middle region of the porous layer. An interesting feature is the wavy nature of the temperature contours in the upper half of the porous layer. In fact, as shown in the photograph of Fig. 3(b), the vapor escaping the boiling particulate opens discrete low-resistance paths in the upper part of the matrix. Indeed, a number of channels with diameter approximately one order of magnitude larger than the average particle diameter are seen to traverse the top bed region at locations that correspond to the hot crests of the wavy forms appearing in the thermograms. The vapor in this channeled zone moves through these openings, whereas the downward liquid fills the interstices (pores) of the solid matrix (cool troughs in Fig. 3(a)). It has been observed (Stubos and Buchlin, 1994) that these naturally occurring self-restructuring processes in the unconstricted porous medium result in considerably enhanced bed coolability characterized by significantly higher dryout heat flux. Indeed a more efficient vapor-liquid counterflow structure forms in the channeled zone where the downward liquid flow, in conjunction with the facilitated vapor upflow, replenishes effectively the underlying packed matrix and delays the occurrence of dryout for higher heat fluxes.

Based on the above observations in unconstricted media, it is presently attempted to apply a similar geometric configuration in the much thinner porous coatings described in the previous section for enhanced cooling of intensively heated surfaces. Assuming that the vapor occupies only the channels, the pore space in the matrix is filled completely by the downward-flowing cooler liquid phase. The resulting structured counterflow as visualized in the thermogram of Fig. 3(a) is held to be the main factor responsible for the increased coolability of the system and should be sustained until the vapor pressure at the base of the channels becomes high enough to allow vapor penetration in the porous matrix. This condition can be expressed as follows:
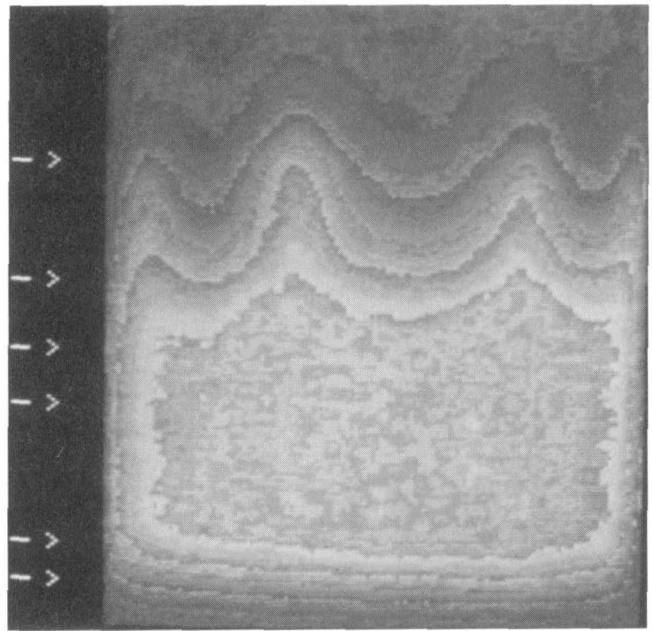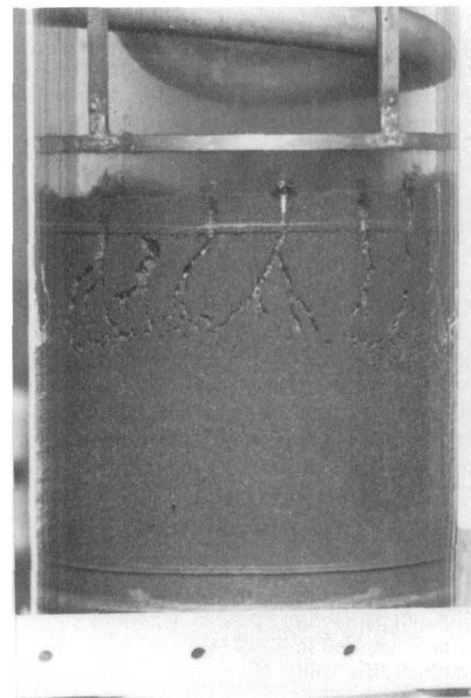

Fig. 3(a)

Fig. 3(b)

Fig. 3 (a) IR thermogram of porous bed, (b) visualization of vapor channels

$$P_{Cb} = P_{Vb} - P_{lb} = \sigma \left(\frac{\epsilon}{\kappa} \right)^{0.5} J_b \qquad (12)$$

where J_b denotes the breakthrough value of the Leverett function (typically 0.4 (Stubos, 1990)). The vapor-liquid pressure difference at the layer bottom is related to the respective pressure drops

$$P_{Cb} = P_{Vo} + \Delta P_V - P_{lo} + \Delta P_l - \rho_l g H. \qquad (13)$$

Combining Eqns. (12) and (13) and assuming equal fluid pressures at the top of the porous layer ($P_{Vo} = P_{lo}$), leads to

Table 2

$$B_1 = 2f\rho_V \frac{H}{Dc}\frac{1}{\left[\frac{\pi D_c^2}{4}h_{IV}\rho_V\right]^2} \qquad B_2 = \frac{\rho_l H}{\eta h_{IV}^2 \rho_{IV}^2}$$

$$B_3 = \frac{\pi D_c^2}{4} \qquad B_4 = \frac{\mu_l H}{\kappa h_{IV}\rho_l} \qquad B_5 = \sigma\cos\theta\sqrt{\frac{\epsilon}{\kappa}}\,J_b + \rho_l g H$$

$$2f\rho_V V_C^2 \frac{H}{D_C} + \mu_l V_l \frac{H}{\kappa} + \rho_l V_l^2 \frac{H}{\eta} = \sigma\left(\frac{\epsilon}{\eta}\right)^{0.5} J_b + \rho_l g H \quad (14)$$

where the vapor and liquid pressure drop terms have been modeled using pipe flow analogy for vapor in the channels and the generalized Ergun equation for flow in the liquid-saturated porous matrix, respectively. V_c, is the vapor velocity in the channels, D_c is the channel diameter and f is the corresponding friction factor; V_l is the superficial liquid velocity and η is the passability of the porous medium. For spherical-particle beds, κ and η are given by Fand et al. (1987)

$$\kappa = \frac{\epsilon^3}{180(1-\epsilon)^2}d_p^2 \quad \text{and} \quad \eta = \frac{\epsilon^3}{1.9(1-\epsilon)}d_p.$$

The inertial term becomes important for values of particle Reynolds number $Re_p = \rho V_l d_p/\mu_l$ larger than about five. For the anticipated range of the channel Reynolds number $10^4 \le Re_c = \rho_V V_c D_c/\mu_V \le 10^5$, a modified form of the Blasius formula is used for the friction factor (Andrianov et al., 1994). In steady-state, V_l and V_C are related to the heat flux, q,

$$q = \rho_l V_l h_{IV}\left[1 - \frac{\pi D_C^2 N_C}{4}\right] = \rho_V V_c h_{IV}\frac{\pi D_C^2 N_C}{4}, \quad (15)$$

where h_{IV} is the latent heat of vaporization. The quantity $1 - \pi D_c^2 N_c/4$ accounts for the reduction of the available area for liquid downflow due to the presence of channels with a population density per unit area N_C. Recasting Eq. (14) and Eq. (15) yields a quadratic equation for q with coefficients depending on N_c:

$$\left(\frac{B_1}{N_C^2} + \frac{B_2}{(1-B_3 N_C)^2}\right)q^2 + \frac{B_4}{(1-B_3 N_C)}q - B_5 = 0 \quad (16)$$

where B_1, B_2, B_3, B_4, and B_5 are functions of the physical properties of the fluids, the porous layer height, the medium permeability and passability, the channel diameter, and the friction factor as expressed in Table 2. Solving Eq. (16) provides the limiting heat flux value above which a dry region (vapour film) is formed on the heated surface for different channel population densities. Evidently, it is possible to maximize q with respect to N_C for each combination of porous medium, fluid, and channel diameter. Furthermore, and after fixing N_C by selecting a value suitable for practical purposes, it is also possible to determine optimal pore size and/or channel diameter values that maximize the limiting heat flux.

On the basis of the above and in order to exemplify the modeling, the 8-mm high bed of consolidated particles of 0.3 mm in diameter is considered again but this time with the presence of vertical channels. The cooling fluid is R-11 and the calculated q versus the channel density is plotted in Fig. 4. The dashed part of the line corresponds to N_c-values which imply that most of the bed cross section is occupied by channels. In this exercise, a channel diameter of 1.5 mm as observed experimentally in unconstricted beds (Stubos and Buchlin, 1994) is chosen. The computations indicate that the limiting dryout heat flux can be higher than the case without channels by almost two orders of magnitude and becomes maximum for
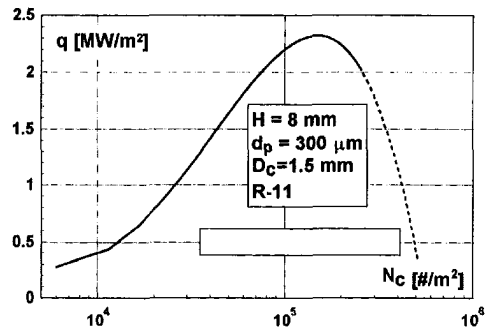

Fig. 4 Dryout heat flux versus channel density. Dashed part of the curve implies that more than 50 percent of the cross section is covered by channels
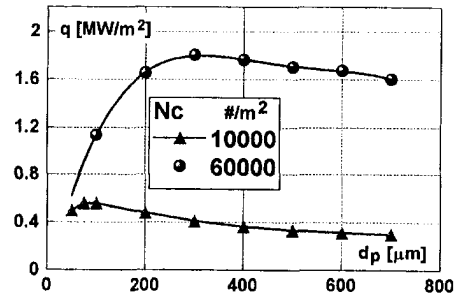

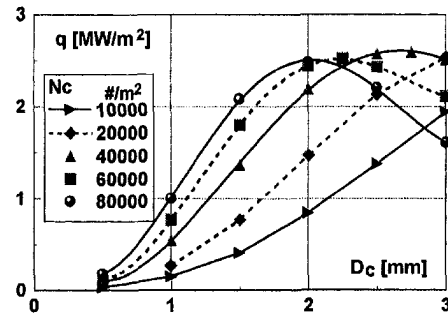**Fig. 5** Dryout heat flux versus particle diameter

Fig. 6 Dryout heat flux versus channel diameter

$N_C = 1.8 \cdot 10^5$ channels/m². Interestingly, this channel density does not differ considerably from the N_c predicted using the relation developed by Stubos and Buchlin (1994) for unconsolidated particle beds on the basis of a modified Taylor instability length. Indeed, that relation gives a channel density of approximately 10^5 channels/m².

The coolability enhancement remains significant even if a practical N_c value ranging between 10^4 and 6×10^4 channels/m² is selected. Then the dryout heat flux varies from 0.415 to 1.78 MW/m² indicating a more than one order of magnitude increase when compared to the case without channels examined in the previous section. On the other hand, by fixing N_C and varying the particle diameter (equivalent to pore size), it is found that the optimal d_p ranges between 0.1 and 0.3 mm (for the N_c values in Fig. 5). Finally, the effect of the channel diameter on q is shown in Fig. 6 for various channel densities. The optimal D_c is seen to decrease with increasing N_c.

4 Concluding Remarks

The dryout heat fluxes for compact and channelled porous matrices have to be compared with those corresponding to porous structures employed in the literature. When no channels exist, the heat

flux attained is lower than the heat removal capabilities exhibited by the different structures shown in Fig. 1. This is expected in view of the larger thickness and smaller pore size of the layers considered presently. It should be noted though that the values presented herein are conservative when compared to those of Fig. 1 in the sense that no external flow of the liquid coolant parallel to the heated surface is considered. In such a case of forced flow evaporative cooling (Wang and Beckermann, 1992), significantly increased coolability should result due to the establishment of subcooled conditions at the top of the bed. On the contrary, when channels are present, it is shown in this work that the expected heat fluxes can be significantly higher than those achieved by structures of Fig. 1. The one-dimensional analysis invoked is obviously limiting the validity of the exact heat flux values as it ignores the boundary effects especially for small surfaces. It is important to mention, however, that the opening of channels in a porous layer has contributed to increased coolability levels in the system of Mughal and Plumb (1996). In addition, the optimum percent vented area predicted in this work (optimum Nc) is consistent with the experimental observations of Abou-Zyan and Plumb (1997) in a slightly different system.

Finally, one should consider the issue of how such increased heat removal capabilities as those predicted by the simplified one-dimensional approach for a vented porous layer can be physically justified (in connection with the critical heat flux for R-11). The simple model proposed herein is essentially assuming a complete separation of the upward vapor flow (through the channels) and the downward liquid flow (through the porous matrix). In this way a well-structured counterflow pattern is obtained in the porous layer whereby the vapor escapes unobstructed upward through the open vents while the liquid takes full advantage of capillarity and gravity for its downflow through the pore space. In this sense the model is expected to (and it actually does) provide quite enhanced values of the dryout heat flux as no instabilities are involved to destroy the counterflow structure. When the vapor-liquid pressure difference at the base of the porous layer becomes so large that the menisci formed at the matrix-vent interface cannot sustain it any more then this counterflow structure ceases to exist and dryout is assumed to occur. Of course the values shown in the figures for the heat flux (reaching 2200 kW/m^2) constitute an upper limit since the presence of some vapour in the matrix (as liquid may boil within it) cannot be excluded. In fact some vapor will eventually be produced within the matrix and will tend to flow towards the neighboring vents (channels) to join the main vapor flow. This means that the assumption of complete separation of the two flows may break down and part of the matrix will experience two-phase flow conditions. To account for this effect one should multiply the permeability and passability appearing in the denominator of the second and third terms of the LHS of Eq. (14) by the corresponding relative permeability and passability which are functions of the saturation (liquid fraction). We performed a rough calculation of the heat flux assuming that half the height of the porous matrix is in two-phase flow condition and that the average saturation there is 0.5. Then the peak in Fig. 5 drops to 800 kW/m^2 a value considerably lower than the upper limit of 2200 kW/m^2 but still high enough to support the main conclusion of the paper, i.e., the existing potential for enhanced heat removal capabilities. Keep also in mind that in Fig. 5 only the Nc values smaller than, say, 8×10^4 may be considered practical. Sustaining the perfect counterflow pattern with many channels distributed across the porous layer is uncertain and definitely needs experimental verification.

One might argue here that the limiting factor in the present (idealized) case of fully separated vapor-liquid counterflow would be stemming from the situation prevailing at the upper surface of the porous layer where the vapor escapes in the form of bubbles from the vents in the overlying liquid pool. Obviously, the conditions there resemble to pool boiling which is in turn limited by the CHF value. In the ''deep'' bed experiments mentioned previously (Stubos, 1990), this situation was avoided by cooling properly the overlying pool such that the

vapor was condensing immediately above the upper porous layer surface. In other applications (Wang and Beckermann, 1992) the continuous flow of coolant parallel to the top surface of the porous layer has assured adequate subcooling of the liquid there. When considering intensively heated surfaces covered by significantly thinner layers, the validity of this assumption has to be carefully checked. Nevertheless, the above outlined configuration offers the possibility of achieving very high heat fluxes with moderate temperature differences and deserves further experimental testing. This is currently under way.

References

Abou-Zyan, H. Z., and Plumb, O. A., 1997, ''Boiling on horizontal surfaces coated with porous metal wicks,'' HTD-Vol. 349, National Heat Transfer Conference, Vol. 11, ASME, New York.

Andrianov, A. B., Zuev, A. V., Levitan, L. L., Malyshenko, S. P., and Orlova, I. A., 1994, ''Hydraulic resistance of two-phase flow in pipes with porous coating,'' High Temperature, Vol. 32, No. 1, pp. 91–96.

Bird, R. B., Stewart, W. E., and Lightfoot, E. N., 1960, Transport Phenomena, John Wiley and Sons, New York.

Fand, R. M., Kim, B. Y. K., Lam, A. C. C., and Phan, R. T., 1987, ''Resistance to the flow of fluids through simple and complex porous media whose matrices are composed of randomly packed spheres,'' J. Fluids Engineering, Vol. 109, p. 268.

Incropera, F. P., 1988, ''Convection Heat Transfer in Electronic Equipment Cooling,'' ASME JOURNAL OF HEAT TRANSFER, Vol. 110, 1097–1111.

Khrustalev, D., and Faghri, A., 1995, ''Heat transfer in the inverted meniscus type evaporator at high heat fluxes,'' Int. J. Heat Mass Transfer, Vol. 38, 3091–3101.

Konstantinou, N. D., Stubos, A. K., Statharas, J. C., Kanellopoulos, N. K., and Papaioannou, A., 1997, ''Enhanced Boiling Heat Transfer in Porous Layers With Application in Electronic Component Cooling,'' Journal of Enhanced Heat Transfer, Vol. 4, pp. 175–186.

Lipinski, R. J., 1984, ''A coolability model for post accident nuclear reactor debris,'' Nuclear Technology, Vol. 65, pp. 53–66.

Mughal, M. P., and Plumb, O. A., 1996, ''An experimental study of boiling on a wicked surface,'' Int. J. Heat Mass Transfer, Vol. 39, pp. 771–777.

Nakayama, W., 1991, ''Porous surface boiling and its application to cooling of microelectronic chips,'' Convective Heat and Mass Transfer in Porous Media, S. Kakac et al., eds., Kluwer Academic Publishers, Dordrecht, The Netherlands, pp. 1007–1030.

Stubos, A. K., 1990, ''Boiling and dryout in unconsolidated particle beds,'' Ph.d. Thesis, Univ. Libre de Bruxelles, von Karman Institute.

Stubos, A. K., and Buchlin, J.-M., 1994, ''Vapour Channels in Boiling, Unconstricted Particle Beds—Effect on the Dryout Heat Flux,'' Int. J. Multiphase Flow, Vol. 20, pp. 131–152.

Thome, J. R., 1990, Enhanced Boiling Heat Transfer, Hemisphere, Washington, DC.

Udell, K. S., 1985, ''Heat transfer in porous media considering phase change and capillarity—The heat pipe effect,'' Int. J. Heat Mass Transfer, Vol. 28, pp. 485–495.

Wang, C. W., and Beckermann, C., 1992, ''A two-phase mixture model of liquid-gas flow and heat transfer in capillary porous media, Part II: Application to pressure driven boiling flow adjacent to a vertical heated plate,'' Int. J. Heat Mass Transfer, Vol. 36, pp. 2759–2768.

Prediction of Pressure Drop in a Boiling Channel

A. S. Fleischer,[1] E. V. McAssey, Jr.,[2,3] and G. F. Jones[2]

Nomenclature

C_p = fluid specific heat at constant pressure, J/kg-K
D = channel diameter, m

[1] Present address: Department of Mechanical Engineering, University of Minnesota.
[2] Department of Mechanical Engineering, Villanova University, 800 Lancaster Avenue, Villanova, PA 19085-1681.
[3] Fellow ASME.

flux attained is lower than the heat removal capabilities exhibited by the different structures shown in Fig. 1. This is expected in view of the larger thickness and smaller pore size of the layers considered presently. It should be noted though that the values presented herein are conservative when compared to those of Fig. 1 in the sense that no external flow of the liquid coolant parallel to the heated surface is considered. In such a case of forced flow evaporative cooling (Wang and Beckermann, 1992), significantly increased coolability should result due to the establishment of subcooled conditions at the top of the bed. On the contrary, when channels are present, it is shown in this work that the expected heat fluxes can be significantly higher than those achieved by structures of Fig. 1. The one-dimensional analysis invoked is obviously limiting the validity of the exact heat flux values as it ignores the boundary effects especially for small surfaces. It is important to mention, however, that the opening of channels in a porous layer has contributed to increased coolability levels in the system of Mughal and Plumb (1996). In addition, the optimum percent vented area predicted in this work (optimum Nc) is consistent with the experimental observations of Abou-Zyan and Plumb (1997) in a slightly different system.

Finally, one should consider the issue of how such increased heat removal capabilities as those predicted by the simplified one-dimensional approach for a vented porous layer can be physically justified (in connection with the critical heat flux for R-11). The simple model proposed herein is essentially assuming a complete separation of the upward vapor flow (through the channels) and the downward liquid flow (through the porous matrix). In this way a well-structured counterflow pattern is obtained in the porous layer whereby the vapor escapes unobstructed upward through the open vents while the liquid takes full advantage of capillarity and gravity for its downflow through the pore space. In this sense the model is expected to (and it actually does) provide quite enhanced values of the dryout heat flux as no instabilities are involved to destroy the counterflow structure. When the vapor-liquid pressure difference at the base of the porous layer becomes so large that the menisci formed at the matrix-vent interface cannot sustain it any more then this counterflow structure ceases to exist and dryout is assumed to occur. Of course the values shown in the figures for the heat flux (reaching 2200 kW/m^2) constitute an upper limit since the presence of some vapour in the matrix (as liquid may boil within it) cannot be excluded. In fact some vapor will eventually be produced within the matrix and will tend to flow towards the neighboring vents (channels) to join the main vapor flow. This means that the assumption of complete separation of the two flows may break down and part of the matrix will experience two-phase flow conditions. To account for this effect one should multiply the permeability and passability appearing in the denominator of the second and third terms of the LHS of Eq. (14) by the corresponding relative permeability and passability which are functions of the saturation (liquid fraction). We performed a rough calculation of the heat flux assuming that half the height of the porous matrix is in two-phase flow condition and that the average saturation there is 0.5. Then the peak in Fig. 5 drops to 800 kW/m^2 a value considerably lower than the upper limit of 2200 kW/m^2 but still high enough to support the main conclusion of the paper, i.e., the existing potential for enhanced heat removal capabilities. Keep also in mind that in Fig. 5 only the Nc values smaller than, say, 8×10^4 may be considered practical. Sustaining the perfect counterflow pattern with many channels distributed across the porous layer is uncertain and definitely needs experimental verification.

One might argue here that the limiting factor in the present (idealized) case of fully separated vapor-liquid counterflow would be stemming from the situation prevailing at the upper surface of the porous layer where the vapor escapes in the form of bubbles from the vents in the overlying liquid pool. Obviously, the conditions there resemble to pool boiling which is in turn limited by the CHF value. In the "deep" bed experiments mentioned previously (Stubos, 1990), this situation was avoided by cooling properly the overlying pool such that the

vapor was condensing immediately above the upper porous layer surface. In other applications (Wang and Beckermann, 1992) the continuous flow of coolant parallel to the top surface of the porous layer has assured adequate subcooling of the liquid there. When considering intensively heated surfaces covered by significantly thinner layers, the validity of this assumption has to be carefully checked. Nevertheless, the above outlined configuration offers the possibility of achieving very high heat fluxes with moderate temperature differences and deserves further experimental testing. This is currently under way.

References

Abou-Zyan, H. Z., and Plumb, O. A., 1997, "Boiling on horizontal surfaces coated with porous metal wicks," HTD-Vol. 349, *National Heat Transfer Conference,* Vol. 11, ASME, New York.

Andrianov, A. B., Zuev, A. V., Levitan, L. L., Malyshenko, S. P., and Orlova, I. A., 1994, "Hydraulic resistance of two-phase flow in pipes with porous coating," *High Temperature,* Vol. 32, No. 1, pp. 91–96.

Bird, R. B., Stewart, W. E., and Lightfoot, E. N., 1960, *Transport Phenomena,* John Wiley and Sons, New York.

Fand, R. M., Kim, B. Y. K., Lam, A. C. C., and Phan, R. T., 1987, "Resistance to the flow of fluids through simple and complex porous media whose matrices are composed of randomly packed spheres," *J. Fluids Engineering,* Vol. 109, p. 268.

Incropera, F. P., 1988, "Convection Heat Transfer in Electronic Equipment Cooling," ASME JOURNAL OF HEAT TRANSFER, Vol. 110, 1097–1111.

Khrustalev, D., and Faghri, A., 1995, "Heat transfer in the inverted meniscus type evaporator at high heat fluxes," *Int. J. Heat Mass Transfer,* Vol. 38, 3091–3101.

Konstantinou, N. D., Stubos, A. K., Statharas, J. C., Kanellopoulos, N. K., and Papaioannou, A., 1997, "Enhanced Boiling Heat Transfer in Porous Layers With Application in Electronic Component Cooling," *Journal of Enhanced Heat Transfer,* Vol. 4, pp. 175–186.

Lipinski, R. J., 1984, "A coolability model for post accident nuclear reactor debris," *Nuclear Technology,* Vol. 65, pp. 53–66.

Mughal, M. P., and Plumb, O. A., 1996, "An experimental study of boiling on a wicked surface," *Int. J. Heat Mass Transfer,* Vol. 39, pp. 771–777.

Nakayama, W., 1991, "Porous surface boiling and its application to cooling of microelectronic chips," *Convective Heat and Mass Transfer in Porous Media,* S. Kakac et al., eds., Kluwer Academic Publishers, Dordrecht, The Netherlands, pp. 1007–1030.

Stubos, A. K., 1990, "Boiling and dryout in unconsolidated particle beds," Ph.d. Thesis, Univ. Libre de Bruxelles, von Karman Institute.

Stubos, A. K., and Buchlin, J.-M., 1994, "Vapour Channels in Boiling, Unconstricted Particle Beds—Effect on the Dryout Heat Flux," *Int. J. Multiphase Flow,* Vol. 20, pp. 131–152.

Thome, J. R., 1990, *Enhanced Boiling Heat Transfer,* Hemisphere, Washington, DC.

Udell, K. S., 1985, "Heat transfer in porous media considering phase change and capillarity—The heat pipe effect," *Int. J. Heat Mass Transfer,* Vol. 28, pp. 485–495.

Wang, C. W., and Beckermann, C., 1992, "A two-phase mixture model of liquid-gas flow and heat transfer in capillary porous media, Part II: Application to pressure driven boiling flow adjacent to a vertical heated plate," *Int. J. Heat Mass Transfer,* Vol. 36, pp. 2759–2768.

Prediction of Pressure Drop in a Boiling Channel

A. S. Fleischer,[1] E. V. McAssey, Jr.,[2,3] and G. F. Jones[2]

Nomenclature

C_p = fluid specific heat at constant pressure, J/kg-K
D = channel diameter, m

[1] Present address: Department of Mechanical Engineering, University of Minnesota.
[2] Department of Mechanical Engineering, Villanova University, 800 Lancaster Avenue, Villanova, PA 19085-1681.
[3] Fellow ASME.

Copyright © 1999 by ASME

h = enthalpy, J/kg
k = thermal conductivity, W/m-K
Nu = Nusselt Number
P = pressure, kPa
St = Stanton number
T = temperature of fluid, K
V = fluid velocity, m/s
X = thermodynamic quality
X_b = thermodynamic quality at onset of significant voiding
X_t = true mass fraction
ϕ = heat flux, W/m^2
ρ = density, kg/m^3
σ = surface tension, N/m

Introduction

The pressure drop in a boiling channel is an important consideration for a number of applications where parallel flow channels exist, e.g., nuclear reactors, and internal combustion engines. The formation of bubbles in a heated channel can have a significant effect on the overall pressure drop along the channel. For fully developed single-phase flow, the pressure drop is comprised primarily of effects due to wall friction, associated with tube surface roughness, which decreases with velocity. For cases where the wall temperature is greater than the saturation temperature of the fluid, as the velocity decreases, the applied heat flux causes the formation of vapor in the fluid. Boiling causes an increase in frictional drag due to the presence of bubbles, and also acts to affect pressure drop through acceleration and buoyancy effects. At some velocity, the increase in pressure drop due to boiling completely offsets the decrease in pressure drop due to channel frictional components. Further velocity reductions cause the pressure drop to rise which results in a minimum point, the onset of flow instability (OFI) point, in the pressure drop versus velocity curve (demand curve). If parallel flow paths exist, this increase in pressure drop in one channel may cause flow to be diverted to alternate channels, destabilizing the system, and resulting in an excursive or Ledinegg instability.

The present study was undertaken to develop a simple model for predicting the pressure drop in a boiling channel which would be applicable from single phase to saturated boiling conditions. The objective was to obtain an accurate simple model that could be used by designers.

Background

Martinelli and Nelson (1948) calculated the two-phase frictional pressure drop for saturated boiling conditions by applying empirical multipliers to the widely accepted methods for calculating single phase pressure drop. Block et al. (1990) collected experimental data identifying OFI for annular geometries and compared that data to an analytical model. The model was based upon three distinct boiling regimes (single phase, nucleate boiling, and fully developed subcooled boiling) as identified by the fluid temperature. This model used the work of Levy (1967) and Saha and Zuber (1974).

Stelling et al. (1996) presented a model for the calculation of pressure drop in a vertical channel which was limited to the downflow of a subcooled boiling fluid. To allow predictions for any channel orientation, a saturated boiling region would have to be included in the model. Dougherty and Yang (1995) developed a nonequilibrium homogenous flow pressure drop model based on a novel rate equation for net steam generation. The method uses a quantity defined as the true mass fraction, which is zero at the onset of significant voiding (OSV) point. Unlike the conventionally defined quality, $(h - h_f)/h_{fg}$, the true mass fraction is always positive. This study seeks to use this earlier work to develop a general pressure drop model which covers the complete range of boiling regimes and flow orientations.

Pressure Drop Models

As a fluid flows through a uniformly heated tube it may pass through four flow regions. Entering as single-phase fluid, the flow progresses along the channel where the heat addition causes nucleate boiling followed by fully developed subcooled boiling, and finally saturated boiling. The transition points between these regions of flow can be identified by the bulk temperature of the fluid. The pressure drop in each region is found by solving a set of equations appropriate for the fluid behavior in that region. The regional pressure drops are then summed to determine the overall pressure drop for the channel.

The partially developed subcooled boiling region (nucleate boiling) is characterized by the presence of small vapor bubbles on the walls of the channel. These bubbles, which do not have enough energy to depart from the channel wall, are formed as the channel wall temperature rises past the saturation temperature. The transition between single-phase flow and partially developed subcooled boiling is referred to as the onset of nucleate boiling (ONB). Fully developed subcooled boiling begins when the bubbles obtain enough energy to detach from the channel wall. This point is known as the onset of significant voiding (OSV). Although the vapor bubbles detach from the channel wall, there is no net vapor generation due to the fact that the bulk of the fluid is still subcooled. However, the bubble presence does introduce a significant acceleration term into the pressure drop model.

The final region of fluid behavior is saturated boiling. This region is reached when the bulk fluid temperature reaches the saturation temperature. The region is characterized by significant net vapor generation. The pressure drop model used in the saturated region must take into account the vapor presence and the pressure drop becomes dependent on the fluid quality.

The two theoretical models presented in this paper treat the fully developed subcooled and saturated boiling regions differently. The first model (Model A) is based on the method proposed by Stelling et al. (1996) for the fully developed subcooled boiling region and is supplemented by the Martinelli and Nelson (1948) method for saturated boiling. The second model (Model B), based on ideas proposed by Dougherty and Yang (1995), does not distinguish between the fully developed subcooled boiling region and the saturated flow region, instead treating the entire region after OSV as a single two-phase region.

For the single-phase and partially developed subcooled boiling regions, both models use the same pressure drop equations as Stelling et al. (1996), but modified to include the effects of flow direction. A detailed description is presented in Fleischer et al. (1997). The present analysis is based upon the standard assumptions of steady state, constant properties evaluated at the average fluid temperature, and a friction factor based upon turbulent flow. The most significant assumption which differentiates models A and B is related to void formation. Model A assumes that no voids are formed until the local fluid temperature reaches the saturation temperature. Model B, however, assumes that void formation begins when the local fluid temperature reaches the OSV temperature. The extent of the single-phase and partially developed subcooled boiling regions can be found by the fluid temperature at the transition points. These are based on the Davis and Anderson (1966) and Saha and Zuber (1974) correlations, respectively.

$$T_{\text{ONB}} = T_{\text{sat}} + \sqrt{\frac{8\sigma\phi T_{\text{sat}}}{h_{fg}k\rho_g}} - \frac{\phi D}{k\,\text{Nu}} \qquad (1)$$

$$T_{\text{OSV}} = T_{\text{SAT}} - \frac{\phi}{\text{St}\,\rho_f C_P V} \qquad (2)$$

With these temperatures, energy balances can be performed to find the length of each region, and the total pressure drop calculated. The pressure drop in the single-phase region is determined
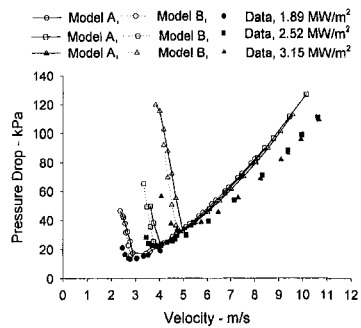
Fig. 1 Downflow in a 15.5-mm diameter tube for an inlet temperature of 25°C, exit pressure of 446 kPa

Fig. 2 Upflow in a 15.5-mm diameter tube for a flux of 1.26 MW/m^2, inlet temperature of 50°C

by a Fanning friction factor, and in the partially developed subcooled region, the friction factor is adjusted for the change in channel roughness caused by the bubbles lining the walls.

For Model A, the pressure gradient in the fully developed subcooled boiling region must account for the vapor present in the flow. A subcooled boiling model developed by Bowring (1962) is used to calculate the vapor mass fraction. The pressure drop in the saturated flow region is calculated according to a model developed by Martinelli and Nelson (1948).

For Model B, the pressure gradient in the two-phase region is calculated according to a nonequilibrium homogenous model proposed by Dougherty and Yang (1995). The key to the method is the calculation of a quantity referred to as true mass fraction, X_t. Unlike conventionally defined quality, which is a function of saturation enthalpy values, true mass fraction is always positive in the regions in which vapor is entrained in the flow. True mass fraction is calculated from Eq. (3).

$$X_b \ln\left(\frac{X - X_t}{X_b}\right) + \ln\left(1 - X + X_b - X_b X_t\right) = 0 \quad (3)$$

Results and Discussion

The pressure drop models are compared to two large experimental data bases for vertical upflow and downflow in uniformly heated tubes. Dougherty et al. (1989, 1990) presented a database for vertical downflow for a wide range of channel diameters and operating conditions. Yang et al. (1993) presented a data set for vertical upflow, limited to one tube diameter, but over a large range of applied flux values. Stelling et al. (1996) presented details describing the experiments used to obtain these data bases. This paper also provides information on measurement uncertainties.

In Fig. 1, we show a comparison of pressure drop predicted by each model versus inlet velocity for downflow conditions in a 15.5-mm tube for a range of surface heat fluxes from 1.89 to 3.15 MW/m^2. For both models, the agreement between the experimental results and the theoretical prediction is very good. It can be seen that the prediction of the minimum point is slightly better with Model B. It is also of interest to note that Model A predicts a maximum point at a velocity below the OFI point (i.e., the minimum in the demand curve).

A comparison of pressure drop versus inlet velocity for upflow conditions is presented at different operating pressures in Fig. 2. An increase in exit pressure suppresses subcooled boiling and reduces the OFI velocity. For both models, the agreement between the experimental results and the theoretical prediction is very good.

Both Model A and Model B will identify operating cases where no minimum point will occur. In Fig. 3 the applied flux was varied and the theoretical demand curve calculated. The theoretical demand curves predict the OFI points for the high flux situations (0.947 MW/m^2), but as the flux is lowered, a
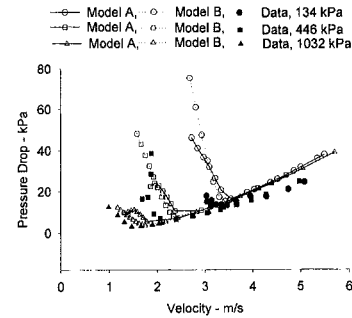
threshold flux is passed and no minimum point occurs. In Fig. 3, the experimental data yielded no minimum point at a flux of 0.437 MW/m^2. At the intermediate flux, the data was unstable and it is not possible to determine if a minimum point occurred. For this case, Model A failed to predict a minimum whereas model B successfully predicted it. Figure 3 emphasizes the difference between the two models. Model A tends to underpredict void generation because it begins generating voids when the fluid temperature reaches the saturation temperature whereas model B initiates void generation at OSV. This effect is not seen at higher velocities because the pressure drop due to convection dominates.

Conclusions

The formation of vapor as a consequence of heating flow through a vertical channel has a significant effect on the overall pressure drop along the channel. Two simple models to predict this effect have been presented. The models can handle flow conditions from single phase through saturated boiling and are valid for any flow orientation. In addition, the models predict a threshold heat flux below which flow instability may not occur for upflow situations.

Comparisons with experimental data for a variety of operating conditions and flow orientations show good agreement with the predicted results. The model provides both qualitative and quantitative pressure drop information. Model B which calculates the pressure gradient in the two phase region as a function of true mass fraction is consistently more accurate at predicting the OFI velocity.

These simple models predict the pressure drop in boiling channels fairly accurately requiring large computer codes. This will be of particular use to designers of systems with multiple flow channels in which boiling can occur in normal operation (i.e., automotive cooling systems).
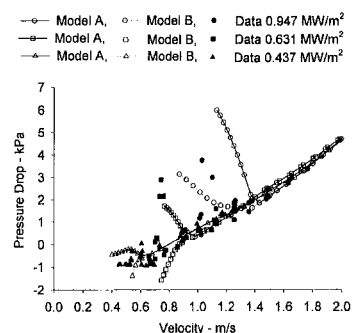
Acknowledgments

Fig. 3 Comparison of model A and B at low flux for a 15.5-mm diameter tube, exit pressure of 1032 kPa, inlet temperature of 50°C

Graduate Research Fellowship. Any opinions, findings, conclusions, or recommendations expressed in this publication are those of the authors and do not necessarily reflect the views of the National Science Foundation.

References

Bowring, R. W., 1962, "Physical Model Based on Bubble Detachment and Calculation of Steam Voidage in the Subcooled Region of a Heated Channel," OECD Halden Reactor Project Report HPR-10.

Davis, E. J., and Anderson, G. H., 1966, "The Incipience of Nucleate Boiling in Forced Convection Flow," *AIChE Journal*, Vol. 12, pp. 774–780.

Dougherty, T., Fighetti, C., McAssey, E., Reddy, G., Yang, B., Chen, K., and Qureshi, Z. C., 1989, "Flow Instability in Vertical Down-Flow at High Heat Fluxes," ASME HTD-Vol. 199, pp. 17–23.

Dougherty, T., Fighetti, C., Reddy, D., Yang, B., Jafri, T., McAssey, E., and Qureshi, Z., 1990, "Flow Boiling in Vertical Downflow," *Proceedings of the Ninth International Heat Transfer Conference*, Vol. 2, Jerusalem, Israel.

Dougherty, T. J., and Yang, B. W., 1995, "Flow Instability and Critical Heat Flux in a Natural Circulation Loop at Low Pressure," *Proceedings of the 1995 ASME National Heat Transfer Conference*, ASME HTD-Vol. 316.

Fleischer, A. S., McAssey, E. V., and Jones, G. F., 1997, "Influence of Bubble Formation on Pressure Drop in a Uniformly Heated Vertical Channel," *ASME Proceedings of the 32nd National Heat Transfer Conference*, ASME HTD-Vol. 342.

Levy, S., 1967, "Forced Convective Subcooled Boiling-Prediction of Vapor Volumetric Fraction," *International Journal of Heat and Mass Transfer*, Vol. 10, pp. 951–965.

Martinelli, R. C., and Nelson, D. B., 1948, "Prediction of Pressure Drop During Forced Circulation Boiling of Water," *Transactions of the ASME*, Vol. 70, p. 695.

Saha, P., and Zuber, N., 1974, "Point of Net Vapor Generation and Vapor Void Fraction in Subcooled Boiling," *Proceedings of the 5th International Heat Transfer Conference*, B4.7, Tokyo, Japan.

Stelling, R., McAssey, E. V., Dougherty, T., Yang, B., 1996, "The Onset of Flow Instability for Downward Flow in Vertical Channels," ASME JOURNAL OF HEAT TRANSFER, Vol. 118, pp. 709–714.

Yang, B. W., Dougherty, T. J., Ouyang, W., McAssey, E. V., Smalec, L., 1993, "Flow Instability in Vertical Upflow Under Low Heat Flux Conditions," *Ninth Proceedings of Nuclear Thermal Hydraulics*, American Nuclear Society Winter Annual Meeting, San Francisco, CA.

Prediction of the Operating Limits of Revolving Helically Grooved Heat Pipes

K. S. Klasing,[1] S. K. Thomas,[2] and K. L. Yerkes[3]

Nomenclature

A_v = cross-sectional area of the vapor space, m
A_w = cross-sectional area of the wick, $\pi h(2r_v + h)$, m²
h_{fg} = heat of vaporization, J/kg
k_l = liquid thermal conductivity, W/(m-K)
k_s = solid wick material thermal conductivity, W/(m-K)
K = permeability, $2\epsilon r_l^2/(f_l \, \text{Re}_l)$, m²
L = distance between grooves, m
L_g = groove length, m

$\dot{m}$ = mass flow rate, kg/s
r_h = radius of the helix, $r_v + h/2$, m
r_i = inner wall radius of the heat pipe, m
r_l = liquid hydraulic radius, $2wh/(2h + w)$, m
r_v = radius of the heat pipe vapor space, m
s = coordinate along the centerline of the helix, m
$V_{l,\text{max}}$ = liquid velocity in the adiabatic section, $Q_g/\rho_l whh_{fg}$, m/s
β = aspect ratio, w/h
ϵ = porosity, whN_g/A_w
μ = absolute viscosity, kg/(m-s)
ρ = density, kg/m³
σ = surface tension, N/m
ϕ = angular parameter, $\phi_0 + 2\pi s/p$, rad

Introduction

Revolving heat pipes have been proposed to be used for electric motor cooling and rotating heat exchangers (Thoren, 1984; Gi and Maezawa, 1990). Revolving heat pipes are defined herein as the case in which the axis of rotation is parallel to (but offset from) the central axis of the heat pipe. A literature survey has shown that most researchers utilized smooth-walled nontapered revolving heat pipes because of their simplicity of manufacture (Thoren, 1984; Gi and Maezawa, 1990; Niekawa et al., 1981; Pokorny et al., 1984; Curtila and Chataing, 1984). However, smooth-walled heat pipes have not proven to be greatly effective because the working fluid is held against the outboard wall of the pipe, leaving a significant portion of the pipe wall dry. A remedy is to have large volumes of working fluid in the heat pipe, which increases the weight of the heat pipe and the potential for imbalance of the rotating system. In addition, it has been found that slight adverse tilt angles between the axis of rotation and horizontal, where the evaporator section is above the condenser section, can severely affect the performance of revolving nontapered heat pipes. Another possibility is to install the heat pipe with a slight tilt (offset of the evaporator section from the axis of rotation is greater than that of the condenser section), such that the working fluid is forced back to the evaporator section due to the favorable body forces. However, this is not always possible due to the design of the machine to be cooled. Yet another alternative is to machine a slight taper on the interior of the pipe wall, but this severely limits the overall heat pipe length due to difficulties encountered in such a machining process. Therefore, a simple mechanism to reliably return the working fluid back to the evaporator section is needed. Recently, an experimental and analytical study was performed in which the capillary limit of a curved helically grooved revolving heat pipe was found to increase with rotational speed (Thomas et al., 1998). This was due to the geometric nature of the helically grooved wick structure. The helically grooved copper tubing was found to be commercially available at a relatively low cost. The results of the aforementioned study (Thomas et al., 1998) has prompted the present analysis to determine the possibility of using helically grooved straight heat pipes for the thermal management of rotating equipment.

Mathematical Model

A mathematical model was formulated to determine the operating limits of revolving helically grooved heat pipes. The capillary limit calculation was complicated by the variation of the body-force field along the length of the groove and around the circumference of the heat pipe. This required an analysis of the total body force imposed on the liquid along the length of the helical grooves. The boiling and entrainment limits were calculated using methods described by Faghri (1995).

Capillary Limitation. As shown in Figs. 1 and 2, the centerline of the heat pipe is parallel to and revolving about the z_1-axis at a radius R_p. The axis of rotation is tilted with respect to

Graduate Research Fellowship. Any opinions, findings, conclusions, or recommendations expressed in this publication are those of the authors and do not necessarily reflect the views of the National Science Foundation.

References

Bowring, R. W., 1962, "Physical Model Based on Bubble Detachment and Calculation of Steam Voidage in the Subcooled Region of a Heated Channel," OECD Halden Reactor Project Report HPR-10.

Davis, E. J., and Anderson, G. H., 1966, "The Incipience of Nucleate Boiling in Forced Convection Flow," *AIChE Journal*, Vol. 12, pp. 774–780.

Dougherty, T., Fighetti, C., McAssey, E., Reddy, G., Yang, B., Chen, K., and Qureshi, Z. C., 1989, "Flow Instability in Vertical Down-Flow at High Heat Fluxes," ASME HTD-Vol. 199, pp. 17–23.

Dougherty, T., Fighetti, C., Reddy, D., Yang, B., Jafri, T., McAssey, E., and Qureshi, Z., 1990, "Flow Boiling in Vertical Downflow," *Proceedings of the Ninth International Heat Transfer Conference*, Vol. 2, Jerusalem, Israel.

Dougherty, T. J., and Yang, B. W., 1995, "Flow Instability and Critical Heat Flux in a Natural Circulation Loop at Low Pressure," *Proceedings of the 1995 ASME National Heat Transfer Conference*, ASME HTD-Vol. 316.

Fleischer, A. S., McAssey, E. V., and Jones, G. F., 1997, "Influence of Bubble Formation on Pressure Drop in a Uniformly Heated Vertical Channel," *ASME Proceedings of the 32nd National Heat Transfer Conference*, ASME HTD-Vol. 342.

Levy, S., 1967, "Forced Convective Subcooled Boiling-Prediction of Vapor Volumetric Fraction," *International Journal of Heat and Mass Transfer*, Vol. 10, pp. 951–965.

Martinelli, R. C., and Nelson, D. B., 1948, "Prediction of Pressure Drop During Forced Circulation Boiling of Water," *Transactions of the ASME*, Vol. 70, p. 695.

Saha, P., and Zuber, N., 1974, "Point of Net Vapor Generation and Vapor Void Fraction in Subcooled Boiling," *Proceedings of the 5th International Heat Transfer Conference*, B4.7, Tokyo, Japan.

Stelling, R., McAssey, E. V., Dougherty, T., Yang, B., 1996, "The Onset of Flow Instability for Downward Flow in Vertical Channels," ASME JOURNAL OF HEAT TRANSFER, Vol. 118, pp. 709–714.

Yang, B. W., Dougherty, T. J., Ouyang, W., McAssey, E. V., Smalec, L., 1993, "Flow Instability in Vertical Upflow Under Low Heat Flux Conditions," *Ninth Proceedings of Nuclear Thermal Hydraulics*, American Nuclear Society Winter Annual Meeting, San Francisco, CA.

Prediction of the Operating Limits of Revolving Helically Grooved Heat Pipes

K. S. Klasing,[1] S. K. Thomas,[2] and K. L. Yerkes[3]

Nomenclature

A_v = cross-sectional area of the vapor space, m
A_w = cross-sectional area of the wick, $\pi h(2r_v + h)$, m^2
h_{fg} = heat of vaporization, J/kg
k_l = liquid thermal conductivity, W/(m-K)
k_s = solid wick material thermal conductivity, W/(m-K)
K = permeability, $2\epsilon r_l^2/(f_l \, Re_l)$, m^2
L = distance between grooves, m
L_g = groove length, m

$\dot{m}$ = mass flow rate, kg/s
r_h = radius of the helix, $r_v + h/2$, m
r_i = inner wall radius of the heat pipe, m
r_l = liquid hydraulic radius, $2wh/(2h + w)$, m
r_v = radius of the heat pipe vapor space, m
s = coordinate along the centerline of the helix, m
$V_{l,\max}$ = liquid velocity in the adiabatic section, $Q_g/\rho_l whh_{fg}$, m/s
β = aspect ratio, w/h
ϵ = porosity, whN_g/A_w
μ = absolute viscosity, kg/(m-s)
ρ = density, kg/m^3
σ = surface tension, N/m
ϕ = angular parameter, $\phi_0 + 2\pi s/p$, rad

Introduction

Revolving heat pipes have been proposed to be used for electric motor cooling and rotating heat exchangers (Thoren, 1984; Gi and Maezawa, 1990). Revolving heat pipes are defined herein as the case in which the axis of rotation is parallel to (but offset from) the central axis of the heat pipe. A literature survey has shown that most researchers utilized smooth-walled nontapered revolving heat pipes because of their simplicity of manufacture (Thoren, 1984; Gi and Maezawa, 1990; Niekawa et al., 1981; Pokorny et al., 1984; Curtila and Chataing, 1984). However, smooth-walled heat pipes have not proven to be greatly effective because the working fluid is held against the outboard wall of the pipe, leaving a significant portion of the pipe wall dry. A remedy is to have large volumes of working fluid in the heat pipe, which increases the weight of the heat pipe and the potential for imbalance of the rotating system. In addition, it has been found that slight adverse tilt angles between the axis of rotation and horizontal, where the evaporator section is above the condenser section, can severely affect the performance of revolving nontapered heat pipes. Another possibility is to install the heat pipe with a slight tilt (offset of the evaporator section from the axis of rotation is greater than that of the condenser section), such that the working fluid is forced back to the evaporator section due to the favorable body forces. However, this is not always possible due to the design of the machine to be cooled. Yet another alternative is to machine a slight taper on the interior of the pipe wall, but this severely limits the overall heat pipe length due to difficulties encountered in such a machining process. Therefore, a simple mechanism to reliably return the working fluid back to the evaporator section is needed. Recently, an experimental and analytical study was performed in which the capillary limit of a curved helically grooved revolving heat pipe was found to increase with rotational speed (Thomas et al., 1998). This was due to the geometric nature of the helically grooved wick structure. The helically grooved copper tubing was found to be commercially available at a relatively low cost. The results of the aforementioned study (Thomas et al., 1998) has prompted the present analysis to determine the possibility of using helically grooved straight heat pipes for the thermal management of rotating equipment.

Mathematical Model

A mathematical model was formulated to determine the operating limits of revolving helically grooved heat pipes. The capillary limit calculation was complicated by the variation of the body-force field along the length of the groove and around the circumference of the heat pipe. This required an analysis of the total body force imposed on the liquid along the length of the helical grooves. The boiling and entrainment limits were calculated using methods described by Faghri (1995).

Capillary Limitation. As shown in Figs. 1 and 2, the centerline of the heat pipe is parallel to and revolving about the z_1-axis at a radius R_p. The axis of rotation is tilted with respect to
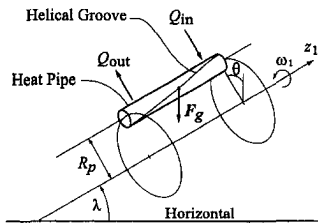
Fig. 1   Schematic of the revolving helically grooved heat pipe

Fig. 3   Geometric considerations: (a) relationship between (x_2, y_2, z_2) and (x_3, y_3, z_3); (b) cross-sectional view of the heat pipe at a particular s location; (c) coordinate system situated in the helical groove

horizontal at an angle λ, where the evaporator is above the condenser. To find the total body force on the liquid, an inertial reference frame (x_1, y_1, z_1) is placed on the axis of rotation (Fig. 2). A noninertial reference (x_2, y_2, z_2) is located at any point on the centerline of the helix. The (x_3, y_3, z_3) coordinate system is in the center of the helical groove at the same s location as the (x_2, y_2, z_2) system (Fig. 3). The x_3 unit vector is directed along the tangent to the helix, z_3 is directed toward the centerline, and y_3 is orthogonal to x_3 and z_3.

With respect to the liquid flow within the helical grooves, the following assumptions are made:

1   The grooves are completely filled along the length of the heat pipe with no puddling or depletion.
2   There is no communication of liquid between the grooves.
3   The liquid velocity vector is directed along the unit vector $\hat{e}_{x_3}$ (tangent to the helical groove).
4   Condensation and evaporation are uniform along the lengths of the condenser and evaporator sections, respectively.

These assumptions result in the following liquid velocity profile along the length of a groove (Silverstein, 1992)

$$\mathbf{V}_l = \begin{cases} \left\{ \left(\dfrac{s}{L_c}\right)V_{l,\max} \right\}\hat{e}_{x_3} & 0 \le s < L_c \\ \{ V_{l,\max} \}\hat{e}_{x_3} & L_c \le s < L_c + L_a \\ \left\{ \left(\dfrac{L_t - s}{L_e}\right)V_{l,\max} \right\}\hat{e}_{x_3} & L_c + L_a \le s < L_t. \end{cases} \quad (1)$$

Note that $V_{l,\max}$ is allowed to vary from one groove to another due to differences in the body forces between grooves. The velocity of the liquid $\mathbf{V}_l$ results in an angular velocity ω_2 of the
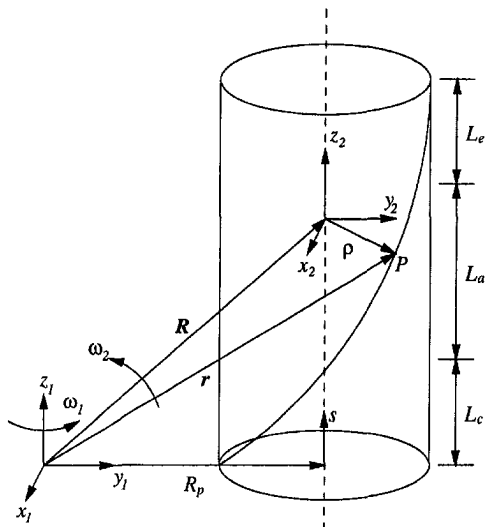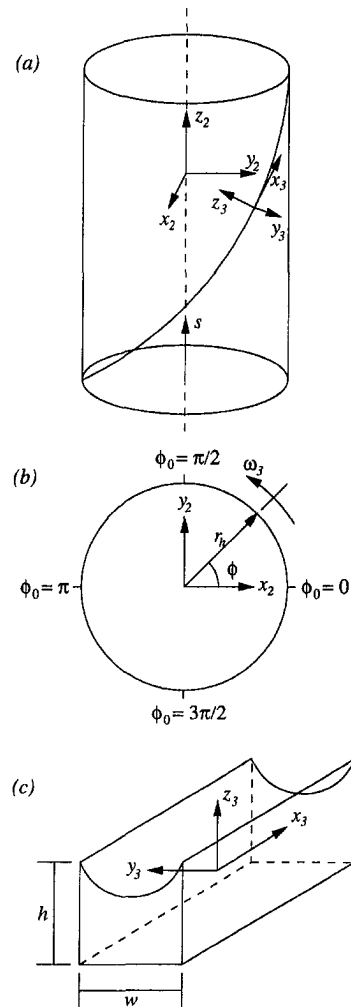

Fig. 2   Relationships between vectors and reference frames

(x_2, y_2, z_2) reference about the x_1-axis (Fig. 2). Since the helix angle α is constant, the angular velocity is

$$\omega_2 = \left\{ \frac{R_p|\mathbf{V}_l|\,\sin\alpha}{R_p^2 + s^2} \right\}\hat{e}_{x_1}. \quad (2)$$

The liquid motion also results in an angular velocity ω_3 around the centerline of the helix, as shown in Fig. 3(b), due to the fluid path around the circumference of the heat pipe.

$$\omega_3 = \left\{ \frac{|\mathbf{V}_l|\,\cos\alpha}{r_h} \right\}\hat{e}_{z_2} \quad (3)$$

The acceleration vector at point P on the helix (Fig. 2) with respect to the inertial reference (x_1, y_1, z_1) is given by (Shames, 1980; Klasing et al., 1998)

$$\mathbf{A} = \left(\frac{d\omega_3}{dt}\right) \times \boldsymbol{\rho} + \omega_3 \times (\omega_3 \times \boldsymbol{\rho}) + \left[\frac{d}{dt}(\omega_1 + \omega_2)\right]$$

$$\times \mathbf{R} + (\omega_1 + \omega_2) \times [(\omega_1 + \omega_2) \times \mathbf{R}] + 2(\omega_1 + \omega_2)$$

$$\times (\omega_3 \times \boldsymbol{\rho}) + \left[\frac{d}{dt}(\omega_1 + \omega_2)\right] \times \boldsymbol{\rho} + (\omega_1 + \omega_2)$$

$$\times [(\omega_1 + \omega_2) \times \boldsymbol{\rho}]. \quad (4)$$

The position vectors $\mathbf{R}$ and $\boldsymbol{\rho}$ for a helical curve rotating about an offset vertical axis are

$$\mathbf{R} = \{R_p\}\hat{e}_{y_1} + \{s\}\hat{e}_{z_1} \tag{5}$$

$$\boldsymbol{\rho} = \{r_h \cos \phi\}\hat{e}_{x_1} + \{r_h \sin \phi\}\hat{e}_{y_1}. \tag{6}$$

A pressure balance within the heat pipe results in the following expression for the capillary limit (Faghri, 1995; Chi, 1976):

$$\Delta P_{\text{cap,max}} \geq \Delta P_v + \Delta P_l + \Delta P_{bf}. \tag{7}$$

The maximum capillary pressure is

$$\Delta P_{\text{cap,max}} = \frac{2\sigma}{r_c} \tag{8}$$

where the capillary radius is equal to the helical groove width $r_c = w$. For a circular cross section of a heat pipe with uniform heat input and output along the lengths of the evaporator and condenser, respectively, the pressure drop in the vapor is

$$\Delta P_v = \frac{4\mu_v Q_t}{\pi \rho_v h_{fg} r_v^4}(L_e + 2L_a + L_c). \tag{9}$$

The liquid pressure drop within a particular groove is (Klasing, 1998)

$$\Delta P_l = \int_0^{L_g} \frac{\mu_l \dot{m}_l}{\rho_l A_w K} dx_3$$

$$= \frac{\mu_l Q_g (f\,\text{Re})_l (L_e + 2L_a + L_c)}{4\rho_l r_l^2 whh_{fg}} \sqrt{\left(\frac{2\pi r_h}{p}\right)^2 + 1}. \tag{10}$$

The coefficient of drag within a rectangular groove is given by (Shah and Bhatti, 1987)

$$(f\,\text{Re})_l = 24(1 - 1.3553\beta + 1.9467\beta^2 - 1.7012\beta^3$$
$$+ 0.9564\beta^4 - 0.2537\beta^5) \tag{11}$$

where the range of the aspect ratio is $0 \leq \beta \leq 1$.

The total body force imposed on the fluid within a particular groove may either aid or hinder the return of the fluid to the evaporator, depending on the groove pitch p, the angle of the starting point of the helix ϕ_0, the rotational speed, and the inclination angle. However, even if the body force hinders the return of the fluid, each groove contributes to the total heat transported. Therefore, the capillary limit equation (Eq. (7)) was first solved for the heat transported by each individual groove Q_g, and the results were summed to determine the total heat transport Q_t. Since the pressure drop in the vapor space was a function of the total heat transported, Eq. (7) was solved iteratively.

For a given tilt angle λ (see Fig. 1), the body force due to gravity in the tangent direction has a changing magnitude as the pipe revolves with constant angular velocity ω_1. Since the objective of this analysis was to find the steady-state capillary limit, it was necessary to find the average value of the body force due to gravity in the tangent direction ($\hat{e}_{x_3}$) for a single revolution. The body forces in the tangent direction due to acceleration (Eq. (4)) and gravity were integrated over the length of the groove to find the average pressure drop due to body forces

$$\Delta P_{bf} = -\rho_l \sqrt{\left(\frac{2\pi r_h}{p}\right)^2 + 1} \left[\int_0^{L_t} \hat{e}_{x_3} \cdot (-\mathbf{A}) ds \right.$$

$$\left. + \frac{1}{2\pi \rho_l} \int_0^{L_t} \int_0^{2\pi} \hat{e}_{x_3} \cdot \mathbf{F}_g d\theta ds \right] \tag{12}$$

where the body force per unit volume due to gravity is

$$\mathbf{F}_g = \{\rho_l g \cos \lambda\}\hat{e}_{y_1} + \{-\rho_l g \sin \lambda\}\hat{e}_{z_1}. \tag{13}$$

The general expression for the maximum capillary limit for a single groove is

$$\frac{2\sigma}{w} \geq \frac{(L_e + 2L_a + L_c)}{h_{fg}}\left\{ \frac{4\mu_v Q_t}{\pi \rho_v r_v^4} + \frac{\mu_l Q_g (f\text{Re})_l}{4\rho_l r_l^2 wh} \sqrt{\left(\frac{2\pi r_h}{p}\right)^2 + 1} \right\}$$

$$- \rho_l \sqrt{\left(\frac{2\pi r_h}{p}\right)^2 + 1} \left[\int_0^{L_t} \hat{e}_{x_3} \cdot (-\mathbf{A}) ds \right.$$

$$\left. + \frac{1}{2\pi \rho_l} \int_0^{L_t} \int_0^{2\pi} \hat{e}_{x_3} \cdot \mathbf{F}_g d\theta ds \right]. \tag{14}$$

This equation was solved for each individual groove. However, the total heat transported Q_t was not known a priori, so an iterative solution procedure was necessary.

To quantify the assumption of no communication of liquid between the grooves, the Bond number was used, which was defined as

$$\text{Bo} = \frac{\rho_l r_l |\mathbf{A}_{\text{res}}|}{2\sigma/w} = \frac{\text{Body Force}}{\text{Surface Tension Force}} \tag{15}$$

where $\mathbf{A}_{\text{res}}$ is the resultant acceleration vector between the y_3 and z_3-directions.

Boiling Limitation. The formation of bubbles (nucleation) within the wick structure of a heat pipe can adversely affect its performance. The growth and motion of bubbles within the wick structure can effectively shut off the liquid return path, causing dryout of the evaporator. The boiling limitation corresponding to a cylindrical heat pipe is (Faghri, 1995)

$$Q_b = \frac{2\pi L_e k_{\text{eff}} \Delta T_{\text{crit}}}{\ln(r_i/r_v)}. \tag{16}$$

The effective thermal conductivity in the evaporator section for grooved heat pipe wick structures is (Chi, 1976)

$$k_{\text{eff}} = \frac{Lk_l k_s h + wk_l(0.185Lk_s + hk_l)}{(w + L)(0.185Lk_s + hk_l)}. \tag{17}$$

The critical temperature difference between the heat pipe wall and the vapor is given by

$$\Delta T_{\text{crit}} = \frac{2\sigma T_a}{h_{fg}\rho_v}\left(\frac{1}{R_b} - \frac{1}{r_c}\right). \tag{18}$$

Since experimental data is not available for axially grooved heat pipes, the value suggested by Faghri (1995) for the nucleation bubble radius was used ($R_b = 10^{-7}$ m).

Entrainment Limitation. The entrainment limit is caused by the viscous interaction of the vapor and liquid flows in the wick structure. Droplets of liquid within the wick structure may be entrained into the counterflowing vapor and carried back to the condenser end cap before reaching the evaporator section, effectively shutting off the liquid flow and drying out the evaporator section. For an axially grooved heat pipe, the entrainment limitation is given by (Faghri, 1995)

$$Q_e = A_v h_{fg}\left(\frac{\sigma \rho_v}{2w}\right)^{1/2}. \tag{19}$$

The temperature dependence of the thermophysical properties was accounted for using the polynomial curve fits (evaluated at the adiabatic temperature) given by Faghri (1995). The heat transfer in the circumferential and axial directions through the pipe wall was neglected in the present model.

Table 1 Heat pipe specifications

Wick structure	Helical grooves
Working fluid	Water
Heat pipe length, L_t	457.2 mm
Evaporator length, L_e	152.4 mm
Adiabatic length, L_a	101.6 mm
Condenser length, L_c	152.4 mm
Vapor core diameter, D_v	13.46 mm
Wall/wick materials	Copper
Helix pitch, p	914.4 mm CW
Groove height, h	0.44 mm
Groove width, w	0.47 mm
Number of grooves, N_g	50

Results and Discussion

The specifications of the heat pipe studied in this analysis are given in Table 1. The heat pipe analyzed was similar to that presented by Thomas et al. (1998), who found that the capillary limit was maximized when $p/L_t = 2$. In the present study, this optimized pitch specification was assumed in the analysis to examine the operating characteristics of straight helically grooved heat pipes. It should be noted that the Bond number was less than unity for all results reported. Water was chosen as the working fluid to accomodate a wide range of temperatures above ambient.

The maximum heat transport versus working (adiabatic) temperature for rotational speeds of 0, 250 and 500 RPM is shown in Fig. 4(a). The boiling limit decreased with temperature, while the entrainment limit increased with temperature. In the present analysis, the boiling and entrainment limits are indepen-

dent of the rotational speed. As can be seen, the capillary limit increased significantly with rotational speed due to the helical geometry of the heat pipe wick structure. It should be noted that the maximum heat transport is defined as the lowest limit value for a given temperature. For instance, for $\omega_1 = 0$, the capillary limit determined the heat pipe performance between $T_a = 100°C$ and approximately $T_a = 133°C$, and the boiling limit was in effect for $T_a > 133°C$. Over the range of temperature examined, the heat pipe was not limited by capillary effects for rotational speeds of $\omega_1 = 500$ RPM for the case shown in Fig. 4(a).

The variation of the maximum heat transport versus tilt angle is shown in Fig. 4(b). For a stationary heat pipe ($\omega_1 = 0$ RPM), the capillary limit decreased from over $Q_{cap} = 1000$ W to zero as the tilt angle ranged from $\lambda = 0$ deg to 4 deg. This type of behavior was observed experimentally by Faghri and Thomas (1989), who studied a stationary axially grooved copper-water heat pipe. In general, the maximum heat transport increased with rotational speed. For $\omega_1 = 500$ and 750 RPM, the heat pipe was restricted by the entrainment limit or capillary limit, depending on the tilt angle.

The variation of the maximum heat transport versus rotational speed is shown in Fig. 4(c). For the horizontal case ($\lambda = 0$ deg), the capillary limit was constant for $\omega_1 < 200$ RPM. For rotational speeds above $\omega_1 = 200$ RPM, the capillary limit increased until the entrainment limit was reached. For $\lambda = 90$ deg, the heat pipe did not operate at all until a rotational speed above approximately $\omega_1 = 700$ RPM was reached. This shows that a minimum value of rotational speed was needed to obtain the benefits of the helical groove geometry. For rotational speeds greater than $\omega_1 \simeq 900$ RPM, the heat pipe was not limited by capillary effects.
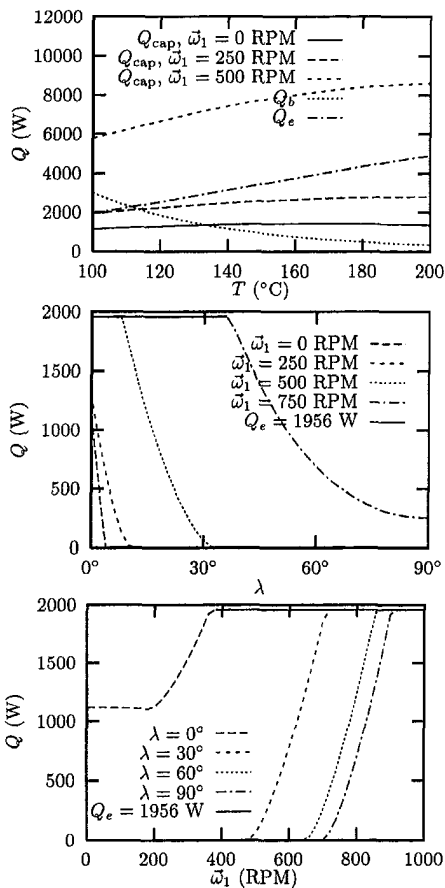
Conclusions

The performance of a helically grooved revolving heat pipe has been examined for various working temperatures, adverse tilt angles, and rotational speeds. It was determined that the capillary limit increased significantly with rotational speed due to the helical geometry of the heat pipe wick structure. A minimum value of rotational speed was required to obtain the benefits of the helical groove geometry when an adverse tilt angle was imposed on the heat pipe. Unlike smooth-walled nontapered revolving heat pipes, the helical groove wick structure allows the present heat pipe to operate when the adverse tilt angle is $\lambda = 90$ deg under certain conditions. While these results are promising in regard to applying helically grooved heat pipes to the thermal management of rotating equipment, experimental data are needed to verify the findings of the model described herein.

Fig. 4 Heat transport limitation versus (a) working temperature ($\lambda = 0$ deg, $R_p = 0.1$ m); (b) tilt angle ($T_a = 100°C$, $R_p = 0.05$ m); (c) rotational speed ($T_a = 100°C$, $R_p = 0.05$ m)

References

Chi, S., 1976, *Heat Pipe Theory and Practice: A Sourcebook*, Hemisphere, Washington, DC.

Curtila, R., and Chataing, T., 1984, "Experimental Study of a Revolving Heat Pipe," *Proceedings of the 5th International Heat Pipe Conference*, Tsukuba, Japan, pp. 268–273.

Faghri, A., 1995, *Heat Pipe Science and Technology*, Taylor and Francis, Washington, DC.

Faghri, A., and Thomas, S., 1989, "Performance Characteristics of a Concentric Annular Heat Pipe: Part I—Experimental Prediction and Analysis of the Capillary Limit," ASME JOURNAL OF HEAT TRANSFER, Vol. 111, pp. 844–850.

Gi, K., and Maezawa, S., 1990, "Heat Transfer Characteristics of a Parallel Rotating Heat Pipe," *Proceedings of the 7th International Heat Pipe Conference*, Minsk, Belarus, pp. 271–283.

Klasing, K. S., 1998, "Performance Characteristics of Revolving Helically-Grooved Heat Pipes," Master's thesis, Wright State University, Dayton, OH.

Klasing, K., Thomas, S., and Yerkes, K., 1998, "Prediction of the Operating Limits of Revolving Helically Grooved Heat Pipes," *Proceedings of the ASME/ AIAA Joint Thermophysics Conference*, HTD-Vol. 357-3, Albuquerque, NM, pp. 117–128.

Niekawa, J., Matsumoto, K., Koizumi, T., Hasegawa, K., Kaneko, H., and Mizoguchi, Y., 1981, "Performance of Revolving Heat Pipes and Application

to a Rotary Heat Exchanger,'' *Proceedings of the 4th International Heat Pipe Conference,* London, pp. 225–234.

Pokorny, B., Polasek, F., Schneller, J., and Stulc, P., 1984, ''Heat Transfer in Co-Axial and Parallel Rotating Heat Pipes,'' *Proceedings of the 5th International Heat Pipe Conference,* Tsukuba, Japan, pp. 259–267.

Shah, R. K., and Bhatti, M. S., 1987, ''Laminar Convective Heat Transfer in Ducts,'' *Handbook of Single-Phase Convective Heat Transfer,* Eds., S. Kakac, R. K. Shah, and W. Aung, eds., John Wiley and Sons, New York.

Shames, I., 1980, *Engineering Mechanics,* 3rd Ed., Prentice-Hall, Englewood Cliffs, NJ.

Silverstein, C., 1992, *Design and Technology of Heat Pipes for Cooling and Heat Exchange,* Taylor & Francis, Washington, DC.

Thomas, S., Klasing, K., and Yerkes, K., 1998, ''The Effects of Transverse Acceleration-Induced Body Forces on the Capillary Limit of Helically Grooved Heat Pipes,'' ASME JOURNAL OF HEAT TRANSFER, Vol. 120, pp. 441–451.

Thoren, F., 1984, ''Heat Pipe Cooled Induction Motors,'' *Proceedings of the 5th International Heat Pipe Conference,* Tsukuba, Japan, pp. 365–371.

Critical Heat Fluxes in Flat Miniature Heat Sinks With Micro Capillary Grooves

R. Hopkins,[1] **A. Faghri,**[1,2] and
D. Khrustalev[1,3]

Nomenclature

A = cross-sectional area (m^2)
D_h = $4A/P$ = hydraulic diameter (m)
G = m/A = mass velocity (kg/m^2s)
h_{fg} = latent heat of vaporization (J/kg)
L = length (m)
m = mass flow rate (kg/s)
p = pressure (N/m^2)
P = perimeter, including grooves (m)
Q = heat load applied to outer wide walls of the heat sinks (W)
Re = axial Reynolds number ($\overline{w}D_h/\nu$)
T = temperature (K)
x = $m_v/(m_v + m_l)$ = equilibrium vapor quality
x_L = $Q/(h_{fg}m)$ = outlet vapor quality
z = axial coordinate

Greek Symbols

ν = kinematic viscosity (m^2/s)
ρ = density (kg/m^3)
σ = surface tension (N/m)

Subscripts

i = inlet
l = liquid
o = outlet
sat = saturated
sub = subcooled
v = vapor

Fig. 1 Schematic of interior capillary groove structure and angle to flat miniature heat sink axis for: (a) FMHS#1, (b) FMHS#2, (c) FMHS#3, (d) FMHS#4 (smooth interior), and (e) angle between groove axis and heat pipe centerline

1 Introduction

Two-phase forced-convection cooling of high-heat-flux/high-power electronic devices is one of the most powerful means of thermal management. This method becomes especially important due to the continuous miniaturization and increase in power dissipation per unit surface area of modern electronic devices that have already reached 300 W/cm² (Jacobs and Hartnett, 1991; Cao et al., 1996). Various two-phase miniature heat sinks have been investigated and presented in the literature to meet this challenging demand (Peng and Wang, 1994; Bowers and Mudawar, 1994; Ravigururajan et al., 1996; Takahashi and Isiikawa, 1995; Khrustalev and Faghri, 1995; Hopkins, 1996).

In this effort, the flat miniature heat sinks enhanced inner surfaces will range from smooth to shallow and wide trapezoidal

to a Rotary Heat Exchanger," *Proceedings of the 4th International Heat Pipe Conference,* London, pp. 225–234.

Pokorny, B., Polasek, F., Schneller, J., and Stulc, P., 1984, "Heat Transfer in Co-Axial and Parallel Rotating Heat Pipes," *Proceedings of the 5th International Heat Pipe Conference,* Tsukuba, Japan, pp. 259–267.

Shah, R. K., and Bhatti, M. S., 1987, "Laminar Convective Heat Transfer in Ducts," *Handbook of Single-Phase Convective Heat Transfer,* Eds., S. Kakac, R. K. Shah, and W. Aung, eds., John Wiley and Sons, New York.

Shames, I., 1980, *Engineering Mechanics,* 3rd Ed., Prentice-Hall, Englewood Cliffs, NJ.

Silverstein, C., 1992, *Design and Technology of Heat Pipes for Cooling and Heat Exchange,* Taylor & Francis, Washington, DC.

Thomas, S., Klasing, K., and Yerkes, K., 1998, "The Effects of Transverse Acceleration-Induced Body Forces on the Capillary Limit of Helically Grooved Heat Pipes," ASME JOURNAL OF HEAT TRANSFER, Vol. 120, pp. 441–451.

Thoren, F., 1984, "Heat Pipe Cooled Induction Motors," *Proceedings of the 5th International Heat Pipe Conference,* Tsukuba, Japan, pp. 365–371.

(a) FMHS#1 $\beta = 4°$

(b) FMHS#2 $\beta = 18°$

(c) FMHS#3 $\beta = 0$
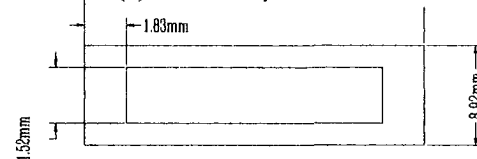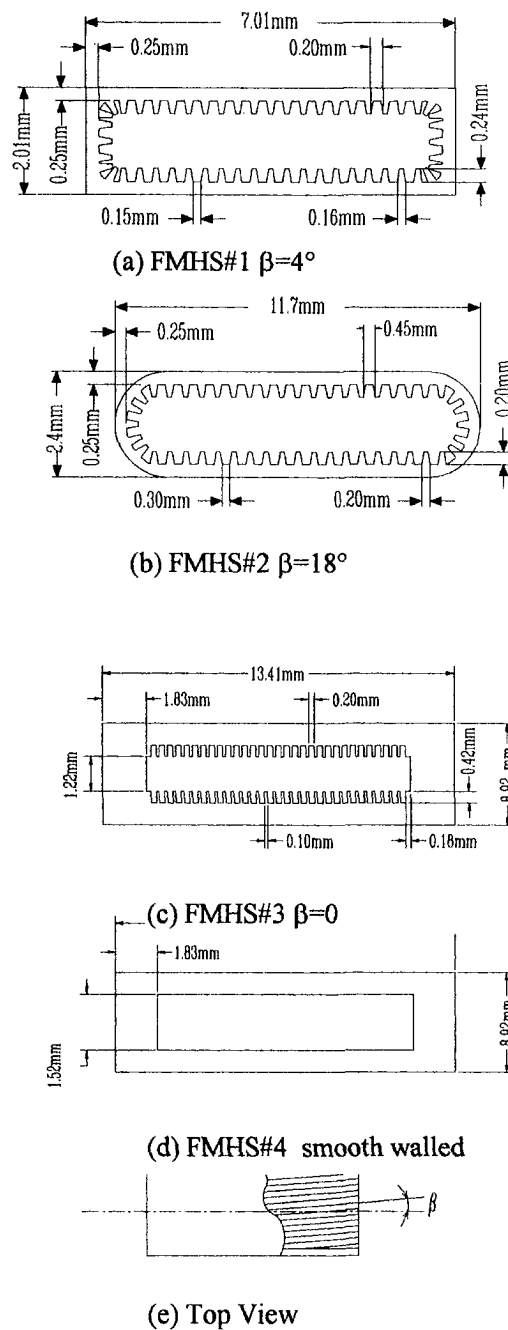
(d) FMHS#4 smooth walled

(e) Top View

Fig. 1 Schematic of interior capillary groove structure and angle to flat miniature heat sink axis for: (a) FMHS#1, (b) FMHS#2, (c) FMHS#3, (d) FMHS#4 (smooth interior), and (e) angle between groove axis and heat pipe centerline

Critical Heat Fluxes in Flat Miniature Heat Sinks With Micro Capillary Grooves

R. Hopkins,[1] A. Faghri,[1,2] and D. Khrustalev[1,3]

Nomenclature

A = cross-sectional area (m^2)
D_h = $4A/P$ = hydraulic diameter (m)
G = m/A = mass velocity (kg/m^{2}s)
h_{fg} = latent heat of vaporization (J/kg)
L = length (m)
m = mass flow rate (kg/s)
p = pressure (N/m^2)
P = perimeter, including grooves (m)
Q = heat load applied to outer wide walls of the heat sinks (W)
Re = axial Reynolds number ($\bar{w}D_h/\nu$)
T = temperature (K)
x = $m_v/(m_v + m_l)$ = equilibrium vapor quality
x_L = $Q/(h_{fg}m)$ = outlet vapor quality
z = axial coordinate

Greek Symbols

ν = kinematic viscosity (m^2/s)
ρ = density (kg/m^3)
σ = surface tension (N/m)

Subscripts

i = inlet
l = liquid
o = outlet
sat = saturated
sub = subcooled
v = vapor

[1] Department of Mechanical Engineering, University of Connecticut, Storrs, CT 06269-3139.
[2] Fellow ASME.
[3] Currently at Thermacore, Inc., Lancaster, PA 17601.

1 Introduction

Two-phase forced-convection cooling of high-heat-flux/high-power electronic devices is one of the most powerful means of thermal management. This method becomes especially important due to the continuous miniaturization and increase in power dissipation per unit surface area of modern electronic devices that have already reached 300 W/cm^2 (Jacobs and Hartnett, 1991; Cao et al., 1996). Various two-phase miniature heat sinks have been investigated and presented in the literature to meet this challenging demand (Peng and Wang, 1994; Bowers and Mudawar, 1994; Ravigururajan et al., 1996; Takahashi and Isiikawa, 1995; Khrustalev and Faghri, 1995; Hopkins, 1996).

In this effort, the flat miniature heat sinks enhanced inner surfaces will range from smooth to shallow and wide trapezoidal

Parameter (mm)	FMHS#1	FMHS#2	FMHS#3	FMHS#4
External width	7.01	11.7	13.41	13.41
External thickness	2.01	2.4	8.92	8.92
Vapor channel width	6.03	10.8	9.75	9.75
Vapor channel thickness	1.03	1.5	1.22	1.52
Number of grooves	52	50	62	-
Groove depth	0.24	0.20	0.42	-
Groove top width	0.20	0.45	0.20	-
Groove bottom width	0.15	0.30	0.20	-
Fin top width	0.16	0.20	0.10	-
Groove angle to heat sink axis	4°	18°	0°	-
Hydraulic diameter	0.87	2.07	1.02	2.63

micro grooves to deep and narrow rectangular grooves. This experimental investigation seeks out the critical heat flux that can be applied uniformly to the two wide evaporator walls for a range of outlet saturation temperature, heated lengths, and total mass flow rates.

2 Experimental Methodology

Experimental Heat Sinks. Four individual copper-water flat miniature heat sinks, with cross sections shown in Fig. 1, were investigated in this effort and relevant geometrical parameters are listed in Table 1. Two of the flat miniature heat sinks (FMHS#1 and #2) contained micro trapezoidal capillary grooves that were at a slight angle to the longitudinal axis of the heat sink and were, respectively, manufactured by The Furukawa Electric Company and Fujikura, Ltd. The capillary groove structure of FMHS#3 consisted of axial rectangular micro capillary grooves produced by a high-speed dicing saw employing a high diamond content carbon blade at the University of Connecticut. A smooth walled flat miniature heat sink, FMHS#4, with the same interior cross-sectional area as FMHS#3 was also produced at the University of Connecticut. The heated length varied from 13 mm to 54 mm. A two-phase flowloop with a liquid pump and a pressure/temperature control reservoir used in this investigation is described in detail in Hopkins et al. (1997).

Experimental Procedure. Four parameters were constantly monitored and adjusted during the experimental investigation of the flat miniature heat sinks critical heat flux. These parameters included: the test section outlet saturation temperature/pressure (40°C/7.39 kPa to 80°C/47.39 kPa), test section inlet subcooled temperature ($\Delta T_{sub,i} = 5°C$), the total liquid mass flow rate (0.25 and 0.50 g/s) and the power applied to the individual resistor pairs. Also, the heated length ranged from one pair of resistors (13.6 mm) to four pairs (54.4 mm). After safe start up of the liquid flow, the flowloop was brought to the desired operating inlet subcooled temperature and outlet saturation pressure and temperature. Inlet subcooling was necessary in order to avoid vapor bubbles at the heat sink inlet and was maintained by adjusting the preheater voltage supply. After all experimental parameters were obtained, an initial heat load, Q, of approximately 20 W/pair was applied.

All experimental results were obtained with a systematic and consistent methodology that is as follows. After all parameters reached steady state, the system was allowed to remain at steady state for 15 minutes. Thirty sets of data were recorded over five minutes and than the applied heat load was increased by 10 Watts/pair (5 Watts/pair as CHF was approached) for five minutes as an intermediate step with no data recorded. This

intermediate step was included in the experimental procedure as a check to help insure that the heat load had sufficient time to uniformly heat the test section surface and also to indicate whether CHF was being approached. Applied heat load was then increased again by an increment of 10 Watts/pair (5 Watts/
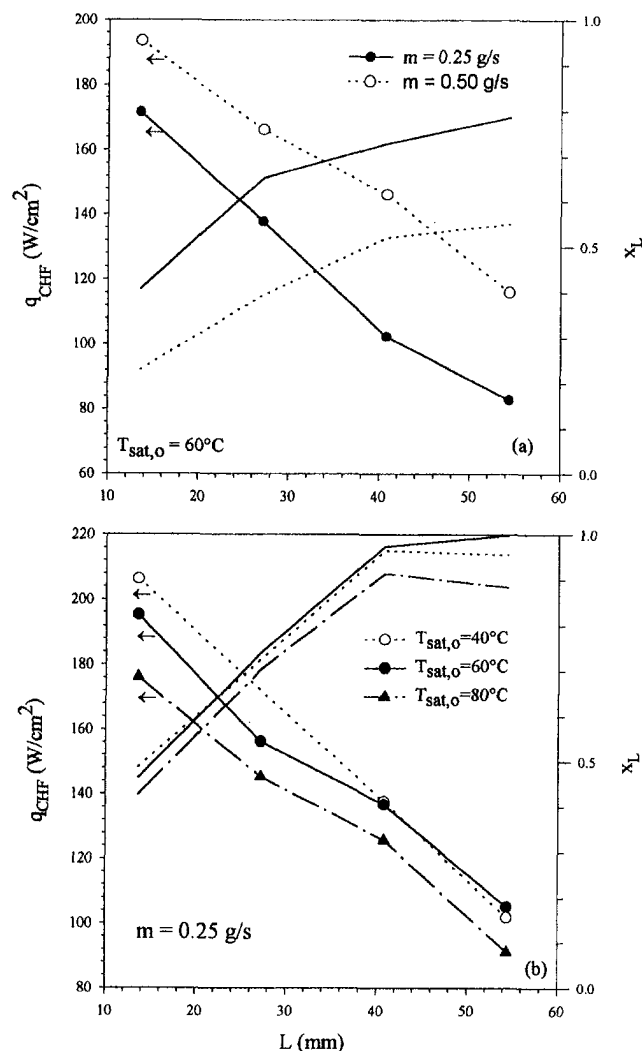

Fig. 2 Experimentally determined critical heat flux (lines with symbols) and outlet vapor quality (lines without symbols) versus heated length for (a) FMHS#1, and (b) FMHS#3

Table 2 Critical heat flux (W/cm²) and outlet vapor quality at critical heat flux (in parenthesis) of various investigated flat miniature heat sinks (N/A–not available)

Operating Conditions	Heated Length	FMHS#1	FMHS#2	FMHS#3	FMHS#4
$\dot{m}=0.25$ g/s $T_{sat}=40°C$	L=13.6 mm	197.1 (0.46)	170.4 (0.40)	209.7 (0.49)	N/A
	L=27.2 mm	164.6 (0.77)	124.4 (0.58)	N/A	N/A
	L=40.8 mm	N/A	N/A	138.2 (0.97)	N/A
	L=54.4 mm	N/A	96.8 (0.90)	102.7 (0.96)	N/A
$\dot{m}=0.25$ g/s $T_{sat}=60°C$	L=13.6 mm	171.6 (0.41)	178.3 (0.42)	195.3 (0.46)	185.8 (0.46)
	L=27.2 mm	137.8 (0.65)	111.2 (0.53)	156.3 (0.74)	171.5 (0.81)
	L=40.8 mm	102.4 (0.73)	96.2 (0.69)	136.8 (0.97)	138.0 (0.98)
	L=54.4 mm	82.9 (0.79)	94.6 (0.90)	105.2 (1.00)	93.5 (0.89)
$\dot{m}=0.25$ g/s $T_{sat}=80°C$	L=13.6 mm	156.1 (0.38)	185.7 (0.45)	176.2 (0.43)	N/A
	L=27.2 mm	117.0 (0.57)	110.3 (0.54)	145.3 (0.71)	N/A
	L=40.8 mm	N/A	N/A	125.8 (0.92)	N/A
	L=54.4 mm	N/A	87.5 (0.85)	91.1 (0.88)	N/A
$\dot{m}=0.50$ g/s $T_{sat}=60°C$	L=13.6 mm	193.5 (0.23)	221.4 (0.26)	206.1 (0.25)	195.7 (0.23)
	L=27.2 mm	166.2 (0.40)	N/A	187.7 (0.45)	168.7 (0.40)
	L=40.8 mm	146.2 (0.52)	N/A	N/A	165.6 (0.59)
	L=54.4 mm	116.1 (0.55)	138.4 (0.66)	154.2 (0.73)	137.2 (0.65)

pair as CHF was approached) and the system was allowed to reach and maintain steady state for 15 minutes before 30 sets of data were recorded as above. This iteration was repeated until CHF was obtained which was characterized by a sudden and sustained increase of the test section temperature at one or more thermocouple locations for longer heated lengths as the outlet equilibrium vapor quality approached unity or by a sudden cracking of a single resistor for shorter heated lengths caused by local dryout. Critical heat flux results obtained were described by an empirical correlation.

3 Results and Discussion

Critical Heat Fluxes. Figure 2 presents a typical portion of the experimentally determined critical heat fluxes, q_{CHF}, and outlet vapor quality values at critical heat flux, x_L, of FMHS#1 and FMHS#3 while all other experimental results are presented in Table 2. CHF's are shown in Fig. 2 for outlet saturation temperatures of $T_{sat,o} = 40°C$, 60°C and 80°C and mass flow rates of $m = 0.25$ g/s and 0.5 g/s as a function of total heated length. All heat fluxes presented have an uncertainty of approximately 2.5 W/cm² which include experimental and equipment error with 95 percent confidence.

Figure 2(a) shows the effect of total mass flow rate on the critical heat flux of FMHS#1 with an outlet saturation temperature of $T_{sat,o} = 60°C$. It is seen that the critical heat flux increases with an increase in total mass flow rate and also appears that the increase in mass flow rate has more of an effect with longer total heated lengths. At the longer heated length of $L = 54.4$ mm, an increase in total mass flow rate from $m = 0.25$ g/s to 0.50 g/s provides an increase in the critical heat flux from 82.9 W/cm² to 116.1 W/cm² or approximately 29 percent. However, at the shortest heated length of $L = 13.6$ mm, the increase in critical heat flux is only approximately 11 percent from 171.6 W/cm² to 193.5 W/cm².

Figure 2(b) presents critical heat flux results obtained for FMHS#3 as a function of heated length and outlet saturation temperatures of $T_{sat,o} = 40°C$, 60°C, and 80°C at a total mass flow rate of $m = 0.25$ g/s. Experimental results for FMHS#3 follow the same general trends as FMHS#1 in that the critical heat flux increases with a decrease in outlet saturation temperature and total heated length. Maximum critical heat flux found for FMHS#3 with a total mass flow rate of $m = 0.25$ g/s was 209.7 W/cm² for an outlet saturation temperature of $T_{sat,o} = 40°C$ and a total heated length of $L = 13.6$ mm.

Influence of mass flow rate on the critical heat flux of the flat miniature heat sinks seems to suggest that two critical heat

flux mechanisms exist dependent on heated length and total mass flow rate. As the heated length becomes longer, for the lower mass flow rate of $m = 0.25$ g/s, it appears that q_{CHF} is restricted by the outlet vapor quality approaching unity. However, as the total mass flow rate is increased to $m = 0.50$ g/s, the outlet vapor quality at critical heat flux dramatically decreases, and therefore, local vapor blanketing is assumed to be the critical heat flux mechanism at higher mass flow rates.

Critical Heat Flux Empirical Correlation. An empirical correlation of the critical heat flux results for all investigated flat miniature heat sinks is developed based on saturated fluid properties and hydrodynamic conditions of the two-phase vapor-liquid flow in a manner consistent with Katto (1978). The empirical correlation is helpful in the design of flat miniature heat sinks with and without micro capillary grooves at the inner surface. All experimental critical heat flux data obtained in this investigation were correlated using a group of dimensionless parameters similar to those chosen by Katto (1978). The final form of the present investigations correlation took the following form:

$$\frac{q_{pred}}{Gh_{fg}} = a\left(\frac{L}{D_h}\right)^b \left(\frac{\rho_v}{\rho_l}\right)^c \left(\frac{G^2 D_h}{\sigma \rho_l}\right)^d \qquad (1)$$

where the coefficients were found to be $a = 0.006154$, $b = -0.29988$, $c = -0.03483$, and $d = -0.3371$. It is noticed that the diameter, D, of Kattos' (1978) correlation was replaced by the hydraulic diameter, $D_h = 4A/P$, of the investigated flat miniature heat sinks taking into account the enhanced surface. The area used for the calculation of the hydraulic diameter was the total area of the vapor channel and grooves while the perimeter included the groove structure. Coefficients were found by the use of the Marquardt-Levenberg nonlinear regression algorithm. In this correlation and Fig. 3, q is calculated using the total heated surface area of the flat miniature heat sink outer wall. This is in contrast to Fig. 2 where it was calculated using the surface area of the heating element. This was done in order to allow direct comparison between the four individual flat miniature heat sinks.

From Fig. 3 it is seen that the correlation predicts the critical heat flux with good accuracy. The majority of the predicted points are within ±20 percent of the experimental results. FMHS#2, however, is slightly overpredicted for most points. This over prediction is explained by the contact resistance at the heating element-wall surface interface.
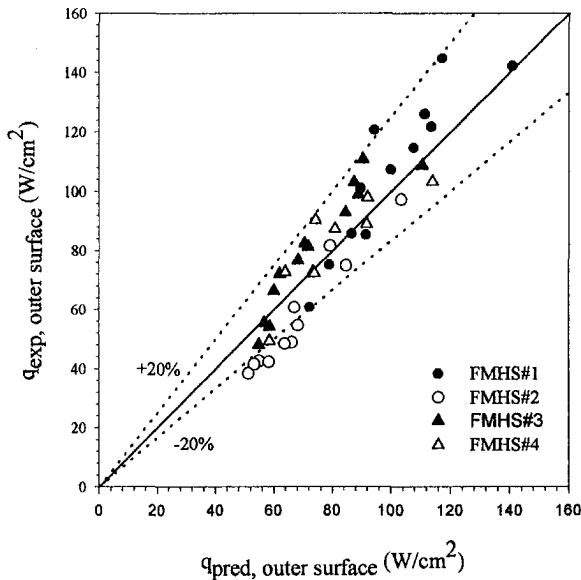
Fig. 3 Experimental CHF of the four heat sinks versus predicted using the empirical correlation

4 Conclusions

Based on the experimental results obtained, the following conclusions are made.

1 All four flat miniature heat sinks achieved very similar trends for critical heat flux for equivalent test parameters. The highest critical heat fluxes were in the area of 200 W/cm² on each of the two sides of miniature heat sinks. It was found that critical heat flux increased with a decrease in heated length and increase in mass flow rate.

2 No significant difference in the critical heat flux was observed between the axial grooved FMHS#3 and the smooth walled FMHS#4 for any test parameter except for a slight difference at the higher mass flow rate.

3 An empirical correlation was developed that generalized experimental CHF's for the four heat sinks with an accuracy of ±20 percent.

Acknowledgments

References

Bowers, M. B., and Mudawar, I., 1994, "High Flux Boiling in Low Flow Rate, Low Pressure Drop Mini-Channel and Micro-Channel Heat Sinks," *International Journal of Heat and Mass Transfer*, Vol. 37, No. 2, pp. 321–332.

Cao, Y., Beam, J. E., and Donovan, B., 1996, "Air-Cooling System for Metal Oxide Semiconductor Controlled Thyristors Employing Miniature Heat Pipes," *Journal of Thermophysics and Heat Transfer*, Vol. 10, No. 3, July–Sept.

Hopkins, R., 1996, "Flat Miniature Heat Sinks and Heat Pipes with Micro Capillary Grooves: Manufacturing, Modeling and Experimental Study," Masters thesis, The University of Connecticut, Storrs, CT.

Hopkins, R., Faghri, A., and Khrustalev, D., 1997, "Critical Heat Fluxes and Pressure Drops in Flat Miniature Heat Sinks with Micro Capillary Grooves," 1997 National Heat Transfer conference, Baltimore, MD, HTD-Vol. 349, pp. 61–70.

Jacobs, H. R., and Hartnett, J. P., 1991, "Thermal Engineering: Emerging Technologies and Critical Phenomena," Workshop Report, NSF Grant No. CTS-91-04006, pp. 139–176.

Katto, Y., 1978, "A Generalized Correlation of Critical Heat Flux for the Forced Convection Boiling in Vertical Uniformly Heated Round Tubes," *Int. J. Heat Mass Transfer*, Vol. 21, pp. 1527–1542.

Khrustalev, D., and Faghri, A., 1995, "Boiling Heat Transfer in the Miniature Axially-Grooved Rectangular Channel with Discrete Heat Sources," *Proceedings of the 30th National Heat Transfer Conference*, HTD-Vol. 305, pp. 165–174.

Peng, X. F., and Wang, B. X., 1994, "Liquid Flow and Heat Transfer in Micro-channels With/Without Phase Change," *Proc. of the 10th International Heat Transfer Conf.*, Brighton, UK, Vol. 1, pp. 159–177.

Ravigururajan, T. S., Cuta, J., McDonald, C. E., and Drost, M. K., 1996, "Effects of Heat Flux on Two-Phase Flow Characteristics of Refrigerant Flows in a Micro-Channel Heat Exchanger," *Proc. of the 31st National Heat Transfer Conference*, Houston, TX, HTD-Vol. 329, Vol. 7, pp. 167–178.

Takahashi, I., and Ishikava, E., 1995. "Microchannel Heat Sink Based on Boiling Heat Transfer," *Journal of the Japan Society of Mechanical Engineers (B)*, Vol. 61, No. 584, pp. 282–293 (in Japanese).

A Model of Bubble Nucleation on a Micro Line Heater

S.-D. Oh[1], S. S. Seung,[2] H. Y. Kwak[3]

The bubble nucleation mechanism on a cavity-free micro line heater surface was studied by using the molecular cluster model. A finite difference numerical scheme for the three-dimensional transient conduction equation for the liquid was employed to estimate the superheated volume where homogeneous bubble nucleation could occur due to heat diffusion from the heater to the liquid. Calculation results revealed that bubble formation on the heater is possible when the temperature at the hottest point in the heater is greater than the superheat limit of the liquid by 6°C–12°C, which is in agreement with the experimental results. Also it was found that the classical bubble nucleation theory breaks down near the critical point where the radius of the critical bubble is below 100 nm.

Nomenclature

d_o = minimum thickness of superheated liquid layer for bubble formation
F_n = free energy needed to form n-mer cluster
J = nucleation rate of bubble per unit volume
J_n = nucleation rate of n-mer cluster per unit volume
k = Boltzmann constant
L = heater length
m = mass of a molecule
n = number of molecules in a cluster
N = number density (molecules/m³)
n_b = number of molecules inside a bubble
P_e = pressure inside bubble
P_v = vapor pressure
P_∞ = ambient pressure
r = radius of bubble
R = gas constant
R_c = the assumed radius of the area covered by vapor on the heater
s = heater thickness
T_c = critical temperature
T_f = melting temperature of liquid

[1] Hyosung Corporation, Seoul 121-020, Korea.
[2] Samchok National University, Samchok City 245-080, Korea.
[3] Department of Mechanical Engineering, Chung-Ang University, 221 Huksuk-Dong, Dongjak-ku, Seoul 156-756, Korea.
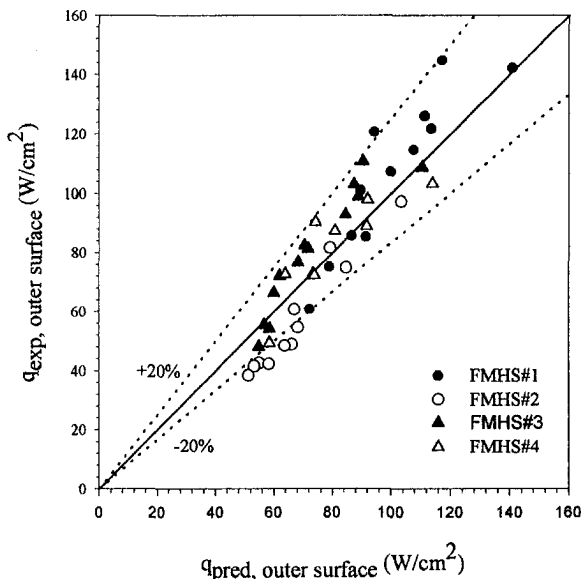
Fig. 3 Experimental CHF of the four heat sinks versus predicted using the empirical correlation

4 Conclusions

Based on the experimental results obtained, the following conclusions are made.

1 All four flat miniature heat sinks achieved very similar trends for critical heat flux for equivalent test parameters. The highest critical heat fluxes were in the area of 200 W/cm^2 on each of the two sides of miniature heat sinks. It was found that critical heat flux increased with a decrease in heated length and increase of mass flow rate.

2 No significant difference in the critical heat flux was observed between the axial grooved FMHS#3 and the smooth walled FMHS#4 for any test parameter except for a slight difference at the higher mass flow rate.

3 An empirical correlation was developed that generalized experimental CHF's for the four heat sinks with an accuracy of ±20 percent.

Acknowledgments

References

Bowers, M. B., and Mudawar, I., 1994, "High Flux Boiling in Low Flow Rate, Low Pressure Drop Mini-Channel and Micro-Channel Heat Sinks," *International Journal of Heat and Mass Transfer*, Vol. 37, No. 2, pp. 321–332.

Cao, Y., Beam, J. E., and Donovan, B., 1996, "Air-Cooling System for Metal Oxide Semiconductor Controlled Thyristors Employing Miniature Heat Pipes," *Journal of Thermophysics and Heat Transfer*, Vol. 10, No. 3, July–Sept.

Hopkins, R., 1996, "Flat Miniature Heat Sinks and Heat Pipes with Micro Capillary Grooves: Manufacturing, Modeling and Experimental Study," Masters thesis, The University of Connecticut, Storrs, CT.

Hopkins, R., Faghri, A., and Khrustalev, D., 1997, "Critical Heat Fluxes and Pressure Drops in Flat Miniature Heat Sinks with Micro Capillary Grooves," 1997 National Heat Transfer conference, Baltimore, MD, HTD-Vol. 349, pp. 61–70.

Jacobs, H. R., and Hartnett, J. P., 1991, "Thermal Engineering: Emerging Technologies and Critical Phenomena," Workshop Report, NSF Grant No. CTS-91-04006, pp. 139–176.

Katto, Y., 1978, "A Generalized Correlation of Critical Heat Flux for the Forced Convection Boiling in Vertical Uniformly Heated Round Tubes," *Int. J. Heat Mass Transfer*, Vol. 21, pp. 1527–1542.

Khrustalev, D., and Faghri, A., 1995, "Boiling Heat Transfer in the Miniature Axially-Grooved Rectangular Channel with Discrete Heat Sources," *Proceedings of the 30th National Heat Transfer Conference*, HTD-Vol. 305, pp. 165–174.

Peng, X. F., and Wang, B. X., 1994, "Liquid Flow and Heat Transfer in Micro-channels With/Without Phase Change," *Proc. of the 10th International Heat Transfer Conf.*, Brighton, UK, Vol. 1, pp. 159–177.

Ravigururajan, T. S., Cuta, J., McDonald, C. E., and Drost, M. K., 1996, "Effects of Heat Flux on Two-Phase Flow Characteristics of Refrigerant Flows in a Micro-Channel Heat Exchanger," *Proc. of the 31st National Heat Transfer Conference*, Houston, TX, HTD-Vol. 329, Vol. 7, pp. 167–178.

Takahashi, I., and Ishikava, E., 1995. "Microchannel Heat Sink Based on Boiling Heat Transfer," *Journal of the Japan Society of Mechanical Engineers (B)*, Vol. 61, No. 584, pp. 282–293 (in Japanese).

A Model of Bubble Nucleation on a Micro Line Heater

S.-D. Oh[1], S. S. Seung,[2] H. Y. Kwak[3]

The bubble nucleation mechanism on a cavity-free micro line heater surface was studied by using the molecular cluster model. A finite difference numerical scheme for the three-dimensional transient conduction equation for the liquid was employed to estimate the superheated volume where homogeneous bubble nucleation could occur due to heat diffusion from the heater to the liquid. Calculation results revealed that bubble formation on the heater is possible when the temperature at the hottest point in the heater is greater than the superheat limit of the liquid by 6°C–12°C, which is in agreement with the experimental results. Also it was found that the classical bubble nucleation theory breaks down near the critical point where the radius of the critical bubble is below 100 nm.

Nomenclature

d_o = minimum thickness of superheated liquid layer for bubble formation
F_n = free energy needed to form n-mer cluster
J = nucleation rate of bubble per unit volume
J_n = nucleation rate of n-mer cluster per unit volume
k = Boltzmann constant
L = heater length
m = mass of a molecule
n = number of molecules in a cluster
N = number density (molecules/m^3)
n_b = number of molecules inside a bubble
P_e = pressure inside bubble
P_v = vapor pressure
P_∞ = ambient pressure
r = radius of bubble
R = gas constant
R_c = the assumed radius of the area covered by vapor on the heater
s = heater thickness
T_c = critical temperature
T_f = melting temperature of liquid

Copyright © 1999 by ASME

T_h = temperature at the hottest point in the heater given input current
T_m = temperature at monitoring point
T_s = superheat limit of liquid
V_m = effective molecular volume of liquid
w = heater width
z_h = thickness of silicon dioxide layer
Z = coordination number
z_s = thickness of the superheated layer

Greek Letters

α_f = heat diffusivity of liquid
β = accommodation coefficient
ΔH_{vap} = enthalpy of evaporation
ΔH_f = enthalpy of fusion
ϵ_m = energy needed to separate a pair of molecules
ρ_g = density of vapor
σ = interfacial tension

Subscript

c = critical cluster or critical size bubble

Introduction

For the initiation of normal boiling or cavitation, the classical theory of bubble nucleation assumes the existence of critical bubbles in a condition of mechanical equilibrium,

$$P_e - P_\infty = \frac{2\sigma}{r_c}. \tag{1}$$

This equation with the Clapeyron equation provides the minimum wall superheat, which is needed to start the growing of the bubble from a cavity. The size of the cavity, which acts as the bubble initiator, is typically in the micron range. This crevice model was very successful in explaining boiling nucleation on metal surfaces that have various sizes of cavities (Griffith and Wallis, 1960). However, it is doubtful whether Eq. (1) is pertinent when r_c approaches molecular dimensions. Recently, modified bubble nucleation models based on molecular interaction have been proposed for homogeneous gas bubble formation (Kwak and Panton, 1983) and vapor bubble formation (Kwak and Panton, 1985).

Very recently, Lin and Pisano (1991) have observed that a bubble forms on a micro line heater made of polysilicon as soon as the highest temperature in the heater reaches the critical temperature of the liquid (fluorocarbons). Also it has been found that ink begins to boil when it is heated close to its superheat limit (about 543K for water-based ink) in a bubble jet printer (Asai et al., 1987). This finding is drastically different from our previous knowledge; the wall superheat needed for boiling nucleation on a metal surface is only 30°C or so, even for subcooled boiling (Judd and Hwang, 1976). This may be due to the use of a cavity-free heater, which is very smooth in the micro range.

In this study, we tried to figure out the bubble nucleation mechanism on a cavity-free micro line heater surface by using the molecular cluster model. A finite difference numerical scheme for the three-dimensional transient conduction equation for the liquid was employed to estimate the superheated volume where homogeneous bubble nucleation could occur due to heat diffusion from the heater to a liquid.

A Vapor Bubble Formation Model Based On Molecular Interactions

The essential element of the molecular cluster model for vapor bubble formation is that the surface energy for the formation of the critical cluster grounded at the molecular level is utilized while keeping the kinetic formalism of the classical theory of nucleation. In this model, it is also assumed that the driving force for the clustering process is the chemical potential difference of liquid molecules between the saturated state and the metastable state.

Employing the assumptions mentioned above, Kwak and Panton (1985) obtained a stability condition of the critical cluster and the corresponding free energy for the bubble formation as

$$-(P_\infty - P_v)n_c^{2/3} = \frac{Z\epsilon_m}{3V_m}, \tag{2.1}$$

$$F_{nc} = \frac{Z\epsilon_m}{6} n_c^{2/3}. \tag{2.2}$$

Using a kinetic theory argument analogous to the condensation case, they also obtained the steady-state nucleation per unit volume. With the minimum free energy for the formation of the critical cluster, Eq. (2.2), the nucleation rate of the critical cluster, J_{nc} (nuclei/m^{3}s), is given by

$$J_{nc} = N\left(\frac{kT}{2\pi m}\right)^{1/2}\left[\frac{Z}{18}\frac{\epsilon_m}{kT}\right]^{1/2}4\left(\frac{3V_m}{4\pi}\right)^{2/3}\beta$$

$$\cdot \exp\left[-\frac{\Delta H_{vap}}{RT} - \frac{\Delta H_f}{RT_f}\right] \cdot N \exp\left[-\frac{Z}{6}\left(\frac{\epsilon_m}{kT}\right)n_c^{2/3}\right]. \tag{3}$$

With a nucleation rate value of $J_{nc} = 10^{16}$ nuclei/m^{3}s this modified cluster model gives a very good prediction of the superheat limit as well as the evaporation speed of a liquid droplet at this limit (Kwak and Lee, 1991).

Critical Cluster and Critical Bubble

One important question to be discussed is how a critical cluster or an aggregate of critical clusters becomes a macroscopic bubble. There are two possible cases for the transition from the cluster state to a macroscopic bubble. For gas bubble formation by dissolved gases in water-gas solutions or in an iron melt where the surface tension $(2\sigma/r)$ is enormous, a critical cluster alone cannot turn into a bubble. Also there is very little chance for the critical clusters to form an aggregate in this case. The only way for a critical cluster to survive is that it grows as a cluster by a kinetic process until it has enough molecules to become a critical bubble (Kwak and Kim, 1998; Kwak and Oh, 1998) which is then governed by the surface tension.

For vapor bubble formation near the superheat limit of a liquid, the situation is very different from the case of a gaseous bubble formation. The critical cluster may choose a way to form an aggregate of the clusters, which easily turns into a macroscopic bubble. The best example is the droplet evaporation at the superheat limit observed by Shepherd and Sturtevant (1982). Their photographic study has revealed that the fully evaporated droplet (an aggregate of a tremendous number of critical clusters) becomes and behaves like a bubble.

Now we have a different case. How does the bubble nucleation process take place on a cavity-free heater, which is initially in contact with a cold liquid? The size of the bubble formed on the heater is certainly dependent on the dimension and the temperature of heater. Before discussing this problem, we need to know how the size of the critical cluster or the critical bubble changes when increasing the temperature of the liquid. Assuming that the vapor in the critical bubble obeys the ideal gas law, one may calculate the number of molecules in the bubble using Eq. (1). That is

$$n_b = \frac{32\pi P_v \sigma^3}{3(P_v - P_\infty)^3 kT}. \tag{4}$$

The corresponding bubble nucleation rate is given by

Table 1 Temperature-dependence of bubble nucleation behavior from the classical bubble nucleation theory and the molecular cluster model for FC-72

Temperature (K)	Classical nucleation theory			Molecular cluster model	
	n_b	r_c (μm)	J (/cm^3 s)	n_c	J_{nc} (/cm^3 s)
405.0	178.6	0.613	4.26×10^{-1}	1698.7	1.02×10^{11}
410.0	81.4	0.4573	3.99×10^{17}	971.4	2.36×10^{15}
415.0	35.1	0.3351	1.99×10^{26}	548.8	2.20×10^{18}
420.0	14.1	0.2403	1.84×10^{30}	306.9	2.26×10^{20}
425.0	5.0	0.1657	8.99×10^{31}	164.3	5.89×10^{21}
430.0	1.5	0.1084	3.63×10^{32}	83.2	5.78×10^{22}
435.0	0.4	0.0652	4.86×10^{32}	38.5	2.94×10^{23}
440.0	0.06	0.0338	4.02×10^{32}	15.1	9.78×10^{23}
445.0	0.003	0.0125	2.44×10^{32}	4.1	2.54×10^{24}
450.0	0.0	0.0009	5.95×10^{31}	0.2	6.49×10^{24}

$$J = N\left(\frac{3\sigma}{\pi m}\right)^{1/2} \cdot \exp\left[-\frac{16\pi\sigma^3}{3kT(P_v - P_\infty)^2}\right]$$

$$\cong N\left(\frac{3\sigma}{\pi m}\right)^{1/2} \cdot \exp\left[-\frac{1}{2} n_b\right]. \qquad (5)$$

As can be clearly seen from Eq. (5), the free energy need to form a critical bubble is proportional to the number of molecules in the bubble. For FC-72, the number of molecules constituting the critical cluster and critical bubble, the corresponding nucleation rates and the radius of the critical bubble are shown in Table 1. As can be seen in Table 1, the radius of the critical bubble rapidly decreases as the temperature of the liquid approaches the critical temperature. Below the bubble size of 100 nm, the macroscopic value of surface tension should not be considered as a measure for the critical bubble, but should be considered as a measure of molecular interactions (Asai, 1989) because there are few molecules in the critical bubble. Thus the classical bubble nucleation theory breaks down near the critical point in the sense that few molecules cannot make an interface. However, the molecular cluster model has no problem in treating the bubble nucleation up to the critical point. Calculation results show that the maximum of the evaporative rate, $J_{nc}n_c$ (Frenkel, 1946) occurs at a temperature of about $0.97T_c$. After that it slows down as the temperature approaches the critical point of equilibrium phase transition.

Bubble Nucleation on a Micro Line Heater

Minimum Thickness of the Superheated Liquid Layer for Bubble Formation. As the current of a micro line heater is turned on, the heater temperature increases very fast and will be in steady state after 12–15 μs. Correspondingly, the temperature of the liquid adjacent to the heater also increases. If the temperature of the liquid layer with thickness of the order of magnitude of the critical cluster diameter reaches the superheat limit, one may expect that the critical clusters form in the layer as a form of linear array. However, the existence of such a thin cluster layer is not a sufficient condition for bubble formation on the heater, especially in the non-uniform thermal layer next to the heater. Since a critical cluster alone cannot become a bubble, as discussed in the previous section, an aggregation of the critical clusters or many layers of the critical clusters is needed for bubble formation on the heater. Thus the maximum temperature of the heater should be greater than the superheat limit of the liquid to obtain a thick superheating layer by heat diffusion.

Even though the evaporated liquid at the superheat limit has high pressure $P_n \approx (Z\epsilon_m/3)/V_m$ (Kwak et al., 1995), it needs enough volume to expand against surrounding liquid. Assume that the potential energy of the evaporated liquid, $\pi d_o^3 P_n/6$, is consumed as the work for the volume to expand with final

pressure of P_∞, that is $4\pi R^2\sigma$. One may then estimate the diameter corresponding to the minimum volume of the superheated liquid for bubble formation. With a relation of $d_o^3 P_n = 8R^3 P_\infty$, one may obtain

$$d_o = 3\left(\frac{P_n}{P_\infty}\right)^{2/3}\left(\frac{2\sigma}{P_n}\right). \qquad (6)$$

The thickness of the superheated liquid layer for bubble formation turns out to be of the order of the critical radius defined in Eq. (1). With an appropriate coefficient other than of 3, this equation may be applied to the formation of bubble with any shape. The surface tension value was evaluated at the ambient temperature which corresponds to P_∞. This diameter may be considered as the minimum thickness of the superheated liquid layer for the bubble formation. The estimated value of the diameter are 0.20–0.30 μm for Fluorinates and methanol. This is why we employed 0.212 μm for the approximate minimum thickness for bubble formation. We have used the following numerical procedure to estimate the time-dependent thickness of the superheated liquid layer (z_s).

Numerical Calculations. A typical configuration of a polysilicon heater fabricated on a silicon dioxide layer is shown in Fig. 1 (Lin and Pisano, 1991). The heater works when a current is applied through the two driving pads, which have much larger volume than that of the heater. The silicon substrate beneath the silicon dioxide layer acts as a heat sink. Applying energy conservation to the differential element in the heater, one may obtain the heat diffusion equation for the heater element considering convection to the liquid. The temperature distribution along the line heater at the steady state was obtained by Lin and Pisano (1991). Also the transient solution can be obtained by separation of variables (Mastrangelo, 1990). These transient and steady-state solutions have been employed as boundary conditions for the three-dimensional heat diffusion equation in the liquid adjacent to the micro line heater:

$$\frac{\partial T}{\partial t} = \alpha_f\left(\frac{\partial^2 T}{\partial x^2} + \frac{\partial^2 T}{\partial y^2} + \frac{\partial^2 T}{\partial z^2}\right). \qquad (7)$$

To solve the above heat diffusion equation numerically, we have used the fully implicit scheme (Roache, 1972). The grid spacings used are 2 μm for Δx, 1 μm for Δy and 0.212 μm for Δz. The numbers of grids used are 18 for the x-direction, 10 for the y-direction and 26 for the z-direction. The numerical calculation region includes a quarter of the micro line heater above the silicon dioxide layer. On the outer boundaries in the y- and x-directions, the ambient temperature was imposed. Adiabatic boundary conditions were employed on the other boundaries. The time interval taken in this numerical calculation is 0.01 μs. In this calculation, we tried to evaluate the time
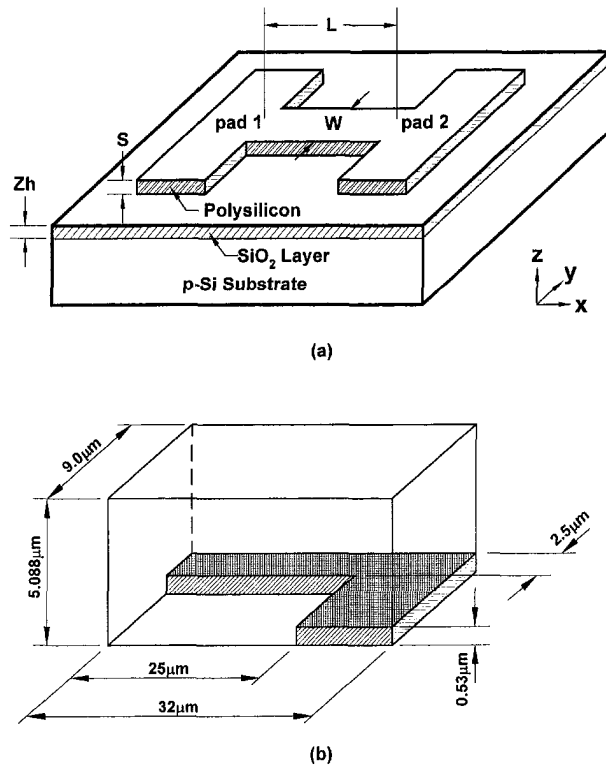
(a)

(b)

Fig. 1 Typical diagram for micro line heater (*a*) from Lin and Pisano and computational domain (*b*)

Fig. 2 Time dependence of liquid temperature at the monitoring point

dependent volume of the superheated liquid as caused by heat diffusion.

Calculation Results and Discussions

The micro line heater dimension used in this numerical calculation is $50 \times 5 \times 0.53$ μm^3. A reason for choosing this size of heater in this study is that the maximum temperature achieved in the steady state is not sensitive to the magnitude of input current. i.e., an increment in the input current of 0.1 mA results in increasing the maximum temperature of the heater by 3°C. On the other hand, for a micro line heater with dimension of $50 \times 1 \times 0.53$ μm^3, the maximum temperature reached at steady state increases as much as 15°C by increasing the input current by the same amount.

The time dependence of the liquid (FC-72) temperature at the point which is located above the center of the heater by one grid spacing (monitoring point) is shown in Fig. 2. The dotted line indicates the case of impulsive heating, i.e., the heater initially has the steady state temperature. The solid line represents the calculation results with the time dependent boundary condition until the heater reaches at the steady state temperature. However the time scale, $(t\text{-}10.)\mu s$ was used in the case of the transient heater temperature because the liquid temperature does not increase very much during the first 10 μs after turning the heater on. As shown in this figure, there is no difference between the two lines after 6 μs. For methanol, the temperature at the monitoring point reaches the steady state more rapidly (about 17 μs) because the thermal diffusivity of methanol is about three times larger than that of Fluorinert.

Assuming that the temperature distribution of the thermal boundary layer above the heater is linear, one can estimate the thickness (z_s) of the superheated liquid layer. That is

$$\frac{z_s(t)}{d_o} = \frac{T_h - T_s}{T_h - T_m(z = d_o)} \qquad (8)$$

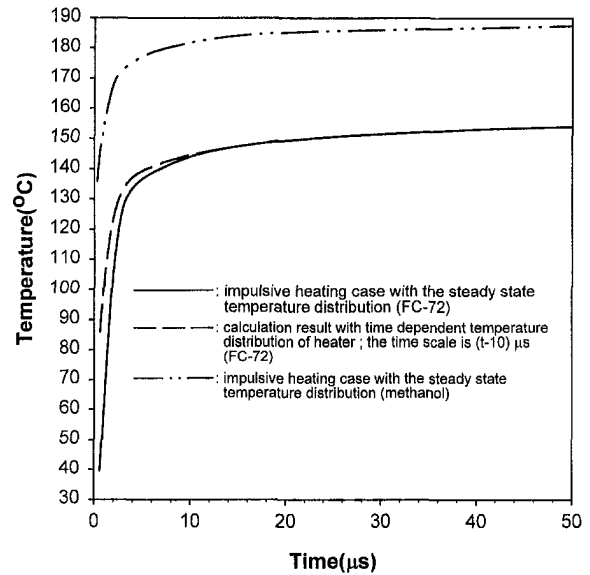The superheated liquid layer is defined as one whose tempera-

ture is greater than the superheat limit of liquid as mentioned before. The liquid temperature at the monitoring point increases as time goes on so that the thickness of the superheated liquid layer increases. The maximum value of superheated layer thickness is determined by the steady state temperature at the monitoring point, which essentially depends on the temperature of the hottest point in the heater. The maximum value of the superheated liquid layer thickness can be used as a criterion for the bubble formation on the heater, i.e., if z_s is less than d_o, no bubble formation results, otherwise bubble formation occurs.

The time dependence of the superheated layer thickness, z_s, determined from Eq. (8), is shown in Fig. 3 for the heater immersed in FC-72. Line (b) is the marginal case in which the steady state temperature of liquid at the monitoring point is the same as the superheat limit. In this case the temperature at the hottest point in the heater is 160.1°C, which is the marginal temperature of the heater for bubble formation. If the temperature of the heater is greater than this value, bubble formation on the heater occurs more easily and rapidly. For a heater tem-
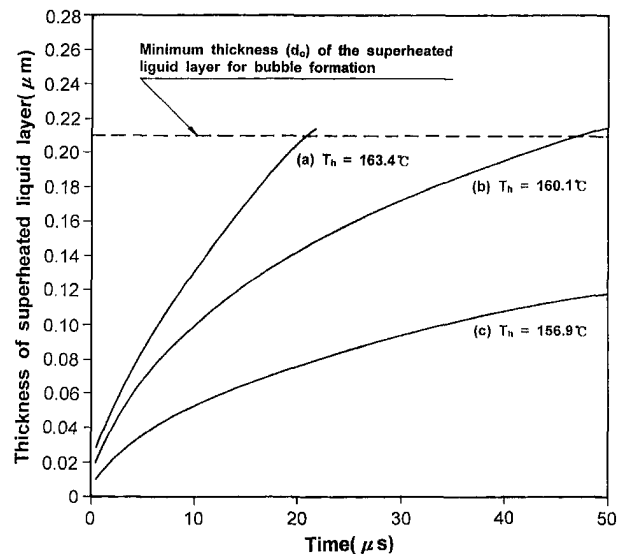

Fig. 3 Time dependence of thickness of the superheated layer depending on the temperature at the hottest point of the heater immersed in FC-72

perature of 163.4°C (line a), bubble formation on the heater could occur at 20 μs after the heater reaches the steady state temperature. For a heater temperature of 156.9°C, no bubble formation may be expected because the liquid temperature at the monitoring point never reaches the superheat limit (line c). As can be seen from this figure, it is reasonable to choose d_o as a criteria for the bubble formation on the heater. A small decrease in the temperature at the hottest point on the heater drastically reduces the thickness of the superheated liquid layer, z_s.

The superheat limit and the calculated values of the temperature at the hottest point on the heater for bubble formation and the corresponding experimental results are shown in Table 2. The superheat limit of liquids is determined with the nucleation rate, $J_{nc} = 10^{16}$ clusters/m^{3}s. A reasonable agreement between experimental and calculation results can be seen in this Table. As shown in Table 2, the reduced superheat limits (T_s/T_c) for Fluorinerts are much greater than those for methanol and other hydrocarbons (Blanders and Katz, 1975). This is due to the extraordinarily low value of the critical pressure for Fluorinerts. In the range of temperature concerned, the value of accommodation coefficient is very crucial for determining the superheat limit of liquid as well as the temperature at the hottest point of heater. For example, if one takes the accommodation coefficient of FC-72 as 0.1, the superheat limit evaluated with the nucleation rate of $J_{nc} = 10^{16}$ clusters/m^{3}s is about 158°C, which is higher than the value in Table 2 by 4.5°C (see Table 1). Correspondingly, the temperature at the hottest point in the heater for bubble formation in FC-72 is about 164.6°C, which is in good agreement with experimental result.

As can clearly be seen in Table 2, the temperature at the hottest point of the micro line heater is much greater than the superheat limit of the liquid, the maximum temperature at which the liquid boils explosively. This may be due to the presence of the steep temperature gradient near the heater wall. It is well known that non-uniform temperature on the liquid-vapor interface of the bubble puts a limit on the growth of the bubble. If one applies the bubble growth condition for the cavity-based bubble nucleus (Madejski, 1965) to this case by assuming that the fictitious cavity radius of the area covered by vapor on the heater is R_c, one finds

$$T_h - T_s = \frac{2\sigma T_s}{\Delta H_{vap}\rho_g \delta}\left(\frac{\delta}{R_c}\right)f\left(\frac{R_c}{\delta}\right) \qquad (9)$$

With a choice of the limiting value of R_c with the dimensionless temperature gradient, R_c/δ of 3.0 (Madejski, 1966), Eq. (9) may be written as

$$T_h - T_s = 1.55\left(\frac{2\sigma T_s}{\Delta H_{vap}\rho_g R_c}\right) \qquad (10)$$

In this case the shape of nucleus is a typical flattened spheroid.

Table 2 The temperature at the hottest point of the heater for bubble formation (from Asai*, 1991); the other experimental results were taken from Lin and Pisano (1991)

Liquid	T_s (°C) (T_s/T_c)	T_h (°C) (Calculation)	T_h (°C) (Experiment)	T_h(calculation)- T_s
FC-72	153.5 (0.946)	160.1	165.8	6.6
FC-75	210.0 (0.966)	220.0	215.0†	10.0
FC-43	280.0 (0.975)	292.0	292.1†	12.0
Methanol	184.0 (0.892)	190.0	195.0*	6.0

† Data obtained by private communication with Lin (1992).
* A. Asai, 1991, ASME/JSME Thermal Engineering Proceedings, Vol. 2, pp. 269–274.
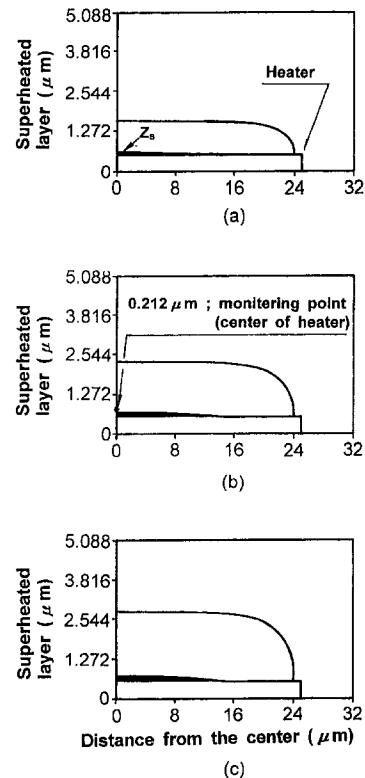

Fig. 4 Time-dependent evolution of the superheated liquid volume for the impulsive heating case with the heater immersed in FC-72; (a) 10 μs, (b) 30 μs, (c) 50 μs

With the property values evaluated at the superheat limit, the magnitude of $T_h - T_s$ for bubble formation in FC-72 is about 10.4, which is close to the value given in Table 2. The above argument shows that the activation of the nucleus on the micro line heater is governed by the superheat at $z = d_o$ in the nonuniform temperature distribution case, which is very similar to the growth condition for the cavity base bubble.

In Fig. 4, the evolution of the superheated liquid volume (dark area) is shown for the case when the temperature at the hottest point of heater immersed in FC-72 is 160.1°C. Certainly, the temperature distribution of the heater determines the volume of the superheated liquid region or the size of bubble formed on the heater. The solid line above the superheated region denotes the isotherm at the boiling point of the liquid (56°C). For the case with non-uniform geometry as shown in Fig. 1, three-dimensional simulation is essential for evaluating the volume of the superheated liquid. Note that random generation of a bubble on the heater surface was observed for the two-dimensional case (Asai, 1989) so that the model presented in this study cannot be applied.

Acknowledgment

References

Asai, A., Hara, T., and Endo, I., 1987, "One-Dimensional Model of Bubble Growth and Liquid Flow in Bubble Jet Printers," *Jpn. J. Appl. Phys.*, Vol. 26, pp. 1794–1801.

Asai, A., 1989, "Application of the Nucleation Theory to the Design of Bubble Jet Printers," *Jpn. J. Appl. Phys.*, Vol. 28, pp. 909–915.

Asai, A., 1991, "Bubble Dynamics in Boiling under High Heat Flux Pulse Heating," *ASME/JSME Thermal Engineering Proceedings*, Vol. 2, pp. 269–274.

Blander, M., and Katz, J. L., 1975, "Bubble Nucleation in Liquids," *AIChE J.*, Vol. 21, pp. 833–848.

Frenkel, J., 1946, *Kinetic Theory of Liquids*, Oxford University Press, Oxford, UK, p. 392.

Griffith, P., and Wallis, J. D., 1960, "The Role of Surface Conditions in Nucleate Boiling," *CEP Symp. Ser.*, Vol. 56, pp. 49–63.

Judd, R. L., and Hwang, K. S., 1976, "A Comprehensive Model for Nucleate Pool Boiling Heat Transfer Including Microlayer Evaporation," ASME JOURNAL OF HEAT TRANSFER, Vol. 98, pp. 623–629.

Kwak, H., and Panton, R. L., 1983, "Gas Bubble Formation in Nonequilibrium Water-Gas Solutions," *J. Chem. Phys.*, Vol. 78, pp. 5795–5799.

Kwak, H., and Panton, R. L., 1985, "Tensile Strength of Simple Liquids Predicted by a Model of Molecular Interactions," *J. Phys., D: Appl. Phys.*, Vol. 18, pp. 647–659.

Kwak, H., and Kim, W., 1998, "Homogeneous Nucleation and Macroscopic Growth of Gas Bubble in Organic Solutions," *International J. Heat Mass Transfer*, Vol. 41, pp. 757–767.

Kwak, H., and Lee, S., 1991, "Homogeneous Bubble Nucleation Predicted by a Molecular Interaction Model," ASME JOURNAL OF HEAT TRANSFER, Vol. 113, pp. 714–721.

Kwak, H., and Oh, S., 1998, "A Model of Homogeneous Bubble Nucleation of CO Bubbles in Fe–C–O Melts," *J. Colloid and Interface Sci.*, Vol. 198, pp. 113–118.

Kwak, H., Oh, S., and Park, C., 1995, "Bubble Dynamics on the Evolving Bubble Formed From the Droplet at the Superheat Limit," *Int. J. Heat Mass Transfer*, Vol. 38, pp. 1709–1718.

Lin, L., and Pisano, A. P., 1991, "Bubble Forming on a Micro Line Heater," *Micromechanical Sensors, Actuators, and Systems*, DSC-Vol. 32, ASME, New York, pp. 147–163.

Madejski, J., 1965, "Activation of Nucleation Cavities on a Heating Surface with Temperature Gradient in Superheated Liquid," *Int. J. Heat Mass Transfer*, Vol. 9, pp. 295–300.

Mastrangelo, C. H., 1990, "Thermal Applications of Microbridge," Ph.D. thesis, University of California, Berkeley, CA.

Roache, P. J., 1972, *Computational Fluid Dynamics*, Hermosa Publishers, Albuquerque, NM.

Shepherd, J. E., and Sturtevant, B., 1982, "Rapid Evaporation at the Superheat Limit," *J. Fluid Mech.*, Vol. 121, pp. 379–402.

The Influence of Particulates on CaCO₃ Scale Formation

N. Andritsos[1] and A. J. Karabelas[1]

Introduction

In many industrial heat exchanger systems, as in cooling water circuits, particulate matter is almost always present in the process streams, even if side-stream filtration takes place. The presence of suspended particles may not only affect the rate of precipitation fouling (due to dissolved inorganic solids), but may also drastically modify the compactness and the rest of the physical properties of the deposit layer. A considerable part of the particulate matter is of colloidal dimensions, which can easily pass through a filter. These colloidal particles may be indigenous (through bulk precipitation and silica polymerization or from removal of deposits) or may enter the process streams with the make-up water. There is experimental evidence in the literature that the presence of particulates tends to increase the fouling resistance. Using river clay as suspended solids, at a concentration of 25 mg/L, Lee and Knudsen (1978) found a significant increase of the fouling resistance. Similarly, Watkinson (1983) reported that particulates contributed significantly to enhance deposition even at low concentrations; the presence of ~250 mg/L particulates (apparently resulting from bulk pre-

cipitation in the system) gave deposition rates almost two orders of magnitude greater than the rates calculated using the wall crystallization model of Hasson et al. (1978). Bramson et al. (1995) examined the effect of calcium sulfate particle addition on scaling of a heated metal surface covered by a falling film. Using a relatively high particle concentration (2.5 g/L) they obtained a considerable enhancement of CaSO₄ deposition rate. Additionally, they reported that coprecipitation of CaCO₃ led to more adherent and tenacious scales as compared to a pure CaSO₄ scale layer. Recently, Bansal et al. (1997) studying CaSO₄ crystallization fouling in a plate heat exchanger reported that the effect of particles on crystallization depended on their nature; the presence of CaSO₄ particles significantly increased the crystallization rate, while noncrystalline alumina particles reduced crystal growth rate. The latter is attributed to higher removal rates associated with the reduction of deposit strength.

Calcium carbonate is one of the dominant scale-forming species in heat exchangers and similar equipment, and its deposition has already been studied in this laboratory (Andritsos et al., 1996, 1997). The work reported here is based on an experimental investigation of the effect of well-defined commercial calcium carbonate particles and silica nanoparticles on the deposition rate and morphology of deposits, formed during the flow of a solution supersaturated with respect to CaCO₃. The term *combined* shall be used for such runs. The effect of the above particles on the spontaneous precipitation in a supersaturated calcium carbonate solution is also examined. Isothermal conditions are maintained in all the tests.

Experimental Work

The experimental set-up and the measurement procedure are described in Andritsos et al. (1996). The tap water used in the experiments contains approximately 80 mg/L Ca, 20 mg/L Mg, and 360 mg/L HCO_3^-. A complete analysis of the water is given in the aforementioned paper. A metering piston pump is used to feed the suspension from a stirred tank into the tubular test section. The pump was calibrated volumetrically. The progress of bulk precipitation with or without particles can be monitored through periodic sample withdrawal, either by light absorbance measurements (in a HITACHI 3000 spectrophotometer) or by recording the pH change (in runs with pH < 9.5).

A Ludox® (Dupont) suspension was used as the source of silica particles. The size of these colloidal silica particles was almost uniform with a mean diameter 21 nm, and under the experimental conditions used the particles bear a negative charge. Particle concentration in all the tests was 100 mg/L. The commercial CaCO₃ (Solvay 90A) particles were assayed by X-ray analysis (in a Siemens D500 diffractometer) and by chemical analysis (ICP 40, Perkin-Elmer). The XRD pattern exhibited peaks characteristic of both calcite and aragonite. The particles were pure CaCO₃ with less than 0.2 percent w/w magnesium. The morphology of the particles was examined by SEM (in a JEOL, JSM-840A unit); they appeared to be agglomerates consisting of small needle-like particles with dimensions approximately $1 \times 0.2 \ \mu m^2$. The size distribution of suspended particles in tap and in demineralized water was determined by a 2600 Malvern particle sizer; the mean particle size was in the range 5–10 μm. The zeta-potential of these particles at pH 9.5 was −26 mV (Thonon et al., 1996).

Results and Discussion

(a) **Effect of Calcium Carbonate Particles.** All experiments were conducted in duplicate at 25°C, with a particle concentration 40(±5) mg/L. The flow velocity was varied between 0.43 and 1.5 m/s. Runs were carried out at two pH values, namely 8.8 and 10. In the absence of particles, there is nearly zero deposition rate at pH 8.8, while at pH 10 a considerable

Frenkel, J., 1946, *Kinetic Theory of Liquids,* Oxford University Press, Oxford, UK, p. 392.

Griffith, P., and Wallis, J. D., 1960, "The Role of Surface Conditions in Nucleate Boiling," *CEP Symp. Ser.,* Vol. 56, pp. 49–63.

Judd, R. L., and Hwang, K. S., 1976, "A Comprehensive Model for Nucleate Pool Boiling Heat Transfer Including Microlayer Evaporation," ASME JOURNAL OF HEAT TRANSFER, Vol. 98, pp. 623–629.

Kwak, H., and Panton, R. L., 1983, "Gas Bubble Formation in Nonequilibrium Water-Gas Solutions," *J. Chem. Phys.,* Vol. 78, pp. 5795–5799.

Kwak, H., and Panton, R. L., 1985, "Tensile Strength of Simple Liquids Predicted by a Model of Molecular Interactions," *J. Phys., D: Appl. Phys.,* Vol. 18, pp. 647–659.

Kwak, H., and Kim, W., 1998, "Homogeneous Nucleation and Macroscopic Growth of Gas Bubble in Organic Solutions," *International J. Heat Mass Transfer,* Vol. 41, pp. 757–767.

Kwak, H., and Lee, S., 1991, "Homogeneous Bubble Nucleation Predicted by a Molecular Interaction Model," ASME JOURNAL OF HEAT TRANSFER, Vol. 113, pp. 714–721.

Kwak, H., and Oh, S., 1998, "A Model of Homogeneous Bubble Nucleation of CO Bubbles in Fe–C–O Melts," *J. Colloid and Interface Sci.,* Vol. 198, pp. 113–118.

Kwak, H., Oh, S., and Park, C., 1995, "Bubble Dynamics on the Evolving Bubble Formed From the Droplet at the Superheat Limit," *Int. J. Heat Mass Transfer,* Vol. 38, pp. 1709–1718.

Lin, L., and Pisano, A. P., 1991, "Bubble Forming on a Micro Line Heater," *Micromechanical Sensors, Actuators, and Systems,* DSC-Vol. 32, ASME, New York, pp. 147–163.

Madejski, J., 1965, "Activation of Nucleation Cavities on a Heating Surface with Temperature Gradient in Superheated Liquid," *Int. J. Heat Mass Transfer,* Vol. 9, pp. 295–300.

Mastrangelo, C. H., 1990, "Thermal Applications of Microbridge," Ph.D. thesis, University of California, Berkeley, CA.

Roache, P. J., 1972, *Computational Fluid Dynamics,* Hermosa Publishers, Albuquerque, NM.

Shepherd, J. E., and Sturtevant, B., 1982, "Rapid Evaporation at the Superheat Limit," *J. Fluid Mech.,* Vol. 121, pp. 379–402.

The Influence of Particulates on CaCO3 Scale Formation

N. Andritsos[1] and A. J. Karabelas[1]

Introduction

In many industrial heat exchanger systems, as in cooling water circuits, particulate matter is almost always present in the process streams, even if side-stream filtration takes place. The presence of suspended particles may not only affect the rate of precipitation fouling (due to dissolved inorganic solids), but may also drastically modify the compactness and the rest of the physical properties of the deposit layer. A considerable part of the particulate matter is of colloidal dimensions, which can easily pass through a filter. These colloidal particles may be indigenous (through bulk precipitation and silica polymerization or from removal of deposits) or may enter the process streams with the make-up water. There is experimental evidence in the literature that the presence of particulates tends to increase the fouling resistance. Using river clay as suspended solids, at a concentration of 25 mg/L, Lee and Knudsen (1978) found a significant increase of the fouling resistance. Similarly, Watkinson (1983) reported that particulates contributed significantly to enhance deposition even at low concentrations; the presence of ~250 mg/L particulates (apparently resulting from bulk pre-

[1] Chemical Process Engineering Research Institute and Department of Chemical Engineering, Aristotle University of Thessaloniki, P.O. Box 1517, GR 540 06 Thessaloniki, Greece.

cipitation in the system) gave deposition rates almost two orders of magnitude greater than the rates calculated using the wall crystallization model of Hasson et al. (1978). Bramson et al. (1995) examined the effect of calcium sulfate particle addition on scaling of a heated metal surface covered by a falling film. Using a relatively high particle concentration (2.5 g/L) they obtained a considerable enhancement of CaSO4 deposition rate. Additionally, they reported that coprecipitation of CaCO3 led to more adherent and tenacious scales as compared to a pure CaSO4 scale layer. Recently, Bansal et al. (1997) studying CaSO4 crystallization fouling in a plate heat exchanger reported that the effect of particles on crystallization depended on their nature; the presence of CaSO4 particles significantly increased the crystallization rate, while noncrystalline alumina particles reduced crystal growth rate. The latter is attributed to higher removal rates associated with the reduction of deposit strength.

Calcium carbonate is one of the dominant scale-forming species in heat exchangers and similar equipment, and its deposition has already been studied in this laboratory (Andritsos et al., 1996, 1997). The work reported here is based on an experimental investigation of the effect of well-defined commercial calcium carbonate particles and silica nanoparticles on the deposition rate and morphology of deposits, formed during the flow of a solution supersaturated with respect to CaCO3. The term *combined* shall be used for such runs. The effect of the above particles on the spontaneous precipitation in a supersaturated calcium carbonate solution is also examined. Isothermal conditions are maintained in all the tests.

Experimental Work

The experimental set-up and the measurement procedure are described in Andritsos et al. (1996). The tap water used in the experiments contains approximately 80 mg/L Ca, 20 mg/L Mg, and 360 mg/L HCO_3^-. A complete analysis of the water is given in the aforementioned paper. A metering piston pump is used to feed the suspension from a stirred tank into the tubular test section. The pump was calibrated volumetrically. The progress of bulk precipitation with or without particles can be monitored through periodic sample withdrawal, either by light absorbance measurements (in a HITACHI 3000 spectrophotometer) or by recording the pH change (in runs with pH < 9.5).

A Ludox® (Dupont) suspension was used as the source of silica particles. The size of these colloidal silica particles was almost uniform with a mean diameter 21 nm, and under the experimental conditions used the particles bear a negative charge. Particle concentration in all the tests was 100 mg/L. The commercial CaCO3 (Solvay 90A) particles were assayed by X-ray analysis (in a Siemens D500 diffractometer) and by chemical analysis (ICP 40, Perkin-Elmer). The XRD pattern exhibited peaks characteristic of both calcite and aragonite. The particles were pure CaCO3 with less than 0.2 percent w/w magnesium. The morphology of the particles was examined by SEM (in a JEOL, JSM-840A unit); they appeared to be agglomerates consisting of small needle-like particles with dimensions approximately $1 \times 0.2 \ \mu m^2$. The size distribution of suspended particles in tap and in demineralized water was determined by a 2600 Malvern particle sizer; the mean particle size was in the range 5–10 μm. The zeta-potential of these particles at pH 9.5 was −26 mV (Thonon et al., 1996).

Results and Discussion

(a) **Effect of Calcium Carbonate Particles.** All experiments were conducted in duplicate at 25°C, with a particle concentration 40(±5) mg/L. The flow velocity was varied between 0.43 and 1.5 m/s. Runs were carried out at two pH values, namely 8.8 and 10. In the absence of particles, there is nearly zero deposition rate at pH 8.8, while at pH 10 a considerable
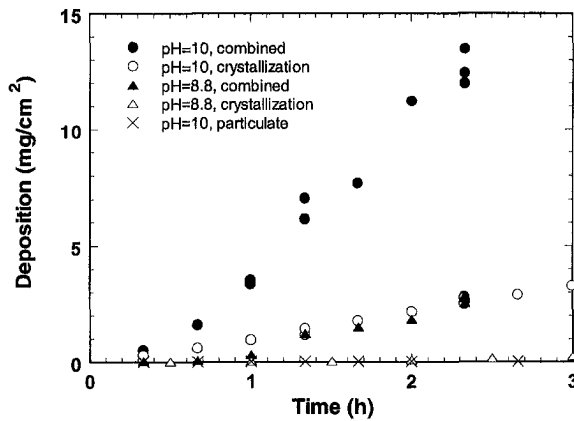
Fig. 1 Effect of particulates on deposit formation with tap water at pH 10 and 8.8 and with demineralized water at pH 10 (particle concentration ~40 mg/L)

Fig. 3 Effect of flow velocity on the combined deposit formation (particle concentration ~40 mg/L, pH = 10)

mass of deposits is formed (Andritsos et al., 1996) and a marked effect of flow velocity is observed.

Figure 1 shows the temporal evolution of deposit mass per unit area at pH 10 and 8.8 for a flow velocity of 0.43 m/s. The mass of deposits formed under the same conditions depicted with no addition of particles (*crystallization* runs) is also, as well as the mass of deposits obtained with demineralized water at pH 10 with 40 mg/L of particulates (*particulate* runs). A six to eightfold increase of the deposition rate is observed at pH 10, while at the lower pH a substantial deposition rate is obtained in the presence of particles compared with the nearly zero deposition rate in the crystallization run. As expected, only a scanty mass of deposits was obtained in the particulate run; i.e., orders of magnitude smaller than that obtained in the combined runs. Very similar results were obtained in a run with particulates at the pH of tap water (7.4).

In all combined runs, after a short time from start, the scale has a rippled appearance (transverse to the flow direction) with ridges and valleys, as depicted in the pictures (Fig. 2). The thickness of the scale did not vary along the 0.6-m long horizontal test section. For runs at pH 10 rippled deposits first appear at the bottom of the pipe, while a layer of relatively hard deposits forms uniformly around the pipe circumference. With time the rippled deposits cover the entire pipe circumference, but in the lower part there is a greater mass. These rippled deposits can be physically removed with ease, when they are
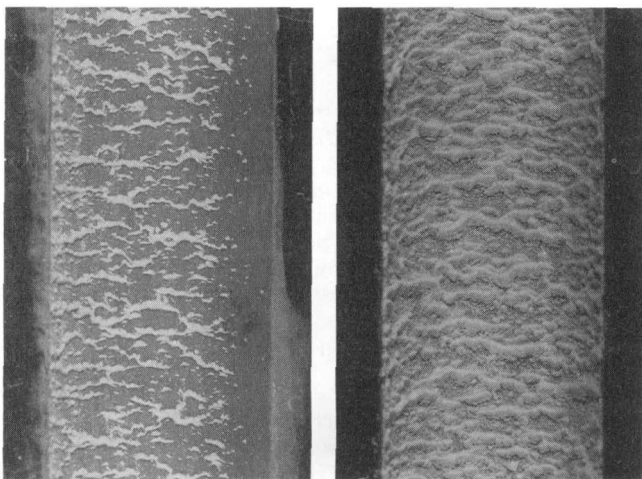

Fig. 2 Pictures of dry deposit obtained after a 1-h run, left, and after a 3.5-h run, right. (Conditions: V = 0.69 m/s, pH = 10 and part. conc. = 40 mg/L.)
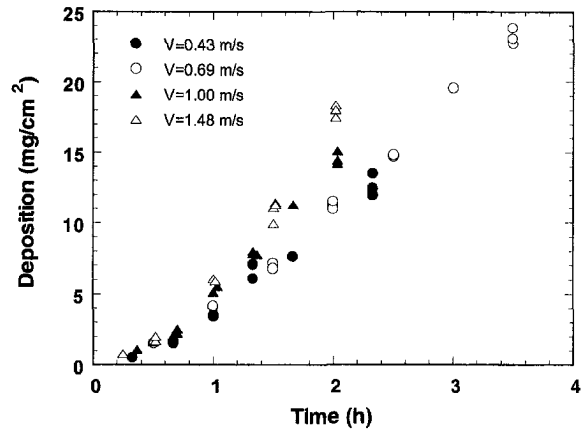
dry, uncovering a uniform layer of hard scale (right on the surface), familiar from runs with no addition of particulates. The mass of these hard deposits compares well with crystallization-only results under the same conditions.

Microscopically, the particulate deposits appear to be agglomerates of small needle-like particles, while the deposits from combined tests consist of calcite and aragonite particles and of the added particulates. The presence of these particulates seems to promote the simultaneous formation of calcite and aragonite deposits, while under similar conditions in crystallization runs mostly calcite deposits are observed. SEM examination of deposit ridges shows that they are comprised of aggregates of calcite particles (of the order of 10 μm), while the deposits at the valleys contain aragonite clusters and isolated calcite particles. The XRD pattern of deposits from the combined runs at pH 10 is distinctly different from that of particulates, showing peaks characteristic only to calcite. The XRD analysis and the SEM observations, in connection with results of particulate-only runs, point to the preliminary conclusion that the increased mass deposited in the combined runs is not due to particulate deposition, but rather to an enhanced wall crystallization rate induced by the presence of the particulates.

A similar physical description applies to the deposition results of the runs at pH 8.8. The height and the distance of ridges are smaller than those observed in deposits obtained at pH 10. Most of the deposited mass is in the form of large interpenetrated calcite crystals up to 50 μm in size. Particulates and small aragonite particles can also be observed on the substrate, but their contribution to the total mass of deposits seems negligible. Similar interpenetrated calcite crystals (but of smaller dimensions) are observed in a run at pH 8.6. Figure 1 clearly shows the great increase of the mass of deposits (more than 20 times), promoted by the presence of particulates. It should be also noted that, although tap water at 25°C is a stable supersaturated solution at pH 8.8, the addition of particulates quickly induces bulk precipitation.

The effect of flow velocity (V) on the net deposition rate in the case of particle addition is illustrated in Fig. 3. A 3.5-fold increase of the flow velocity results in a 60 percent increase of the mass of deposits obtained for the same run duration. On the other hand, the deposition rate scales with $V^{0.85}$ in pure crystallization runs (Andritsos et al., 1996), resulting in a three-fold increase of the deposited mass for the same velocity increase. Thus, the relative enhancement of the mass of deposits obtained in the presence of particles tends to decrease with increasing flow velocity. This trend may be attributed to a removal rate increasing the velocity. Furthermore, although the velocity increase does not change the macroscopic appearance of the rippled deposits, it is observed that at higher velocities

the deposits are more compact and they can be removed with more difficulty than those formed at lower velocities.

(b) Silica Particles. Only a few runs were carried out (25°C, flow velocity: 0.43 m/s, particle concentration: 100 mg/L), since it was found that the presence of the colloidal silica does not affect the initial deposition rate. Morphologically, however, it seems that addition of particles leads to a reduction of the mean calcite crystal size, crystallized on the metal substrate. Furthermore, calculations for particle deposition suggest that the contribution of particulate silica deposition to the total deposited mass is very small and could not have been detected if it were acting alone under the conditions used in the present experiments. Regarding bulk precipitation experiments, no detectable effect on the induction period is observed with the silica seed addition. This means that the silica particles do not have any nucleation capability, which may be attributed to the noncrystalline nature of the Ludox® particles. Another reason may be the small size of the particles; Walton (1967) and others report that the particles promoting nucleation are of a size greater than 100 nm.

Concluding Remarks

The greatest enhancement of deposition rate due to $CaCO_3$ particle addition was obtained at the smallest velocity (0.43 m/s), with a tendency to diminish at higher flow rates. Although conditions were not exactly the same, enhancement at low velocity (in the presence of particles) was also reported by Watkinson (1983) for $CaCO_3$ deposition, and by Bansal et al. (1997) for $CaSO_4$ scaling.

At present, there is no obvious explanation for the observed synergistic effect of the added crystalline particles on the $CaCO_3$ deposition rate. However, there are strong indications that the extra deposits result from augmented wall crystallization and are not due to an enhanced particulate deposition. This is also in line with the suggestion of Bramson et al. (1995) regarding the mechanism of $CaCO_3$ scaling. On the basis of all the evidence available, one might offer the following tentative explanation for the effect of particles: The surface roughness created by the initial deposition of some particles tends to significantly increase the mass transfer rate enhancing the crystallization rate. Obviously, more data are needed to elucidate this phenomenon. Nevertheless, the results presented here clearly demonstrate what has been found in practice and in the laboratory so far; i.e., filtering out of particles and (in the presence of particles) avoiding low velocity regions are measures for controlling scale deposition.

Acknowledgments

References

Andritsos, N., Kontopoulou, M., Karabelas, A. J., and Koutsoukos, P. G., 1996, "CaCO₃ scale layers formed under isothermal flow conditions," *Can. J. Chem. Eng.*, Vol. 74, pp. 911–919.

Andritsos, N., Karabelas, A. J., and Koutsoukos, P. G., 1997, "Morphology and Structure of CaCO₃ deposit formation under isothermal conditions," *Langmuir*, Vol. 13, pp. 2873–1879.

Bansal, B., Müller-Steinhagen, H., and Chen, X. D., 1997, "Effect of Suspended Particles on Crystallization Fouling in Plate Heat Exchangers," ASME JOURNAL OF HEAT TRANSFER, Vol. 119, pp. 568–574.

Bramson, D., Hasson, D., and Semiat, R., 1995, "The roles of gas bubbling, wall crystallization and particulate deposition in CaSO₄ scale formation," *Desalination*, Vol. 100, pp. 105–113.

Hasson, D., Sherman, H., and Biton, M., 1978, "Prediction of CaCO₃ scaling rates," *6th Int. Symposium Fresh Water from the Sea*, pp. 193–199.

Lee, S. H., and Knudsen, J. G., 1979, "Scaling Characteristics of Cooling Tower Water," *ASHRAE Transactions*, Vol. 85, Part I, pp. 81–302.

Thonon, B., Grillot, J. M., and Vidil, R., 1996, "Liquid side fouling of plate heat exchangers," *Fouling Mitigation of Industrial Heat-Exchange Equipment*, C. B. Panchal, ed., pp. 537–548, Begell House, New York, pp. 537–548.

Walton, A. G., 1967, *The Formation and Properties of Precipitates*, Krieger, Huntington, NY.

Watkinson, A. P., 1983, "Water quality effects on fouling from hard waters," *Heat Exchangers Theory and Practice*, J. Taborek et al., eds., Hemisphere, Washington DC, pp. 853–861.

Fin (on a Pipe) Effectiveness: One Dimensional and Two Dimensional

D. C. Look, Jr.[1]

Nomenclature

Bi = Biot number = hL/k
Bi^* = Biot number = $h_e L/k$
h = convection coefficient of the lateral surfaces of the fin
h_e = convection coefficient of the fin tip
I_0, I_1 = modified Bessel functions of the first kind of order $n = 0, 1$
k = thermal conductivity
K_0, K_1 = modified Bessel functions of the second kind of order $n = 0, 1$
L = half-thickness of fin
$Q(\text{fin})$ = the heat lost by a fin
$Q(\text{no fin})$ = the heat lost by a surface the size of the fin base
r = radial independent variable of the fin analysis $(r_1 \leq r \leq r_2)$
R = effectiveness = $Q(\text{fin})/Q(\text{no fin})$
T = temperature within the fin
T_w = fin root temperature
T_∞ = ambient temperature

Greek Symbols

β = r_2/r_1
Γ = r_1/L
θ = $(T - T_\infty)/(T_w - T_\infty)$
λ_n = determined from solutions of transcendental Eq. (8e)
ν = z/L $(-1 \leq \nu \leq 1)$
ξ = r/r_1 $(1 \leq \xi \leq \beta)$

Introduction

Historically, the fin, spline, or extended surface has been used by engineers as a means of controlling the temperature of a piece of equipment. In order to analyze the fin and its effect, a one-dimensional approach generally has proved to be sufficient (Murray, 1938). That is, according to this approach, the physical parameters are of such a magnitude that only the temperature variation from the fin root to tip is considered. This is, of course, a convenience because the mathematics involved is not difficult and is widely accepted in both the academic and industrial communities. The assumptions upon which this one-dimen-

the deposits are more compact and they can be removed with more difficulty than those formed at lower velocities.

(b) Silica Particles. Only a few runs were carried out (25°C, flow velocity: 0.43 m/s, particle concentration: 100 mg/L), since it was found that the presence of the colloidal silica does not affect the initial deposition rate. Morphologically, however, it seems that addition of particles leads to a reduction of the mean calcite crystal size, crystallized on the metal substrate. Furthermore, calculations for particle deposition suggest that the contribution of particulate silica deposition to the total deposited mass is very small and could not have been detected if it were acting alone under the conditions used in the present experiments. Regarding bulk precipitation experiments, no detectable effect on the induction period is observed with the silica seed addition. This means that the silica particles do not have any nucleation capability, which may be attributed to the noncrystalline nature of the Ludox® particles. Another reason may be the small size of the particles; Walton (1967) and others report that the particles promoting nucleation are of a size greater than 100 nm.

Concluding Remarks

The greatest enhancement of deposition rate due to $CaCO_3$ particle addition was obtained at the smallest velocity (0.43 m/s), with a tendency to diminish at higher flow rates. Although conditions were not exactly the same, enhancement at low velocity (in the presence of particles) was also reported by Watkinson (1983) for $CaCO_3$ deposition, and by Bansal et al. (1997) for $CaSO_4$ scaling.

At present, there is no obvious explanation for the observed synergistic effect of the added crystalline particles on the $CaCO_3$ deposition rate. However, there are strong indications that the extra deposits result from augmented wall crystallization and are not due to an enhanced particulate deposition. This is also in line with the suggestion of Bramson et al. (1995) regarding the mechanism of $CaCO_3$ scaling. On the basis of all the evidence available, one might offer the following tentative explanation for the effect of particles: The surface roughness created by the initial deposition of some particles tends to significantly increase the mass transfer rate enhancing the crystallization rate. Obviously, more data are needed to elucidate this phenomenon. Nevertheless, the results presented here clearly demonstrate what has been found in practice and in the laboratory so far; i.e., filtering out of particles and (in the presence of particles) avoiding low velocity regions are measures for controlling scale deposition.

Acknowledgments

References

Andritsos, N., Kontopoulou, M., Karabelas, A. J., and Koutsoukos, P. G., 1996, "$CaCO_3$ scale layers formed under isothermal flow conditions," *Can. J. Chem. Eng.*, Vol. 74, pp. 911–919.

Andritsos, N., Karabelas, A. J., and Koutsoukos, P. G., 1997, "Morphology and Structure of $CaCO_3$ deposit formation under isothermal conditions," *Langmuir*, Vol. 13, pp. 2873–1879.

Bansal, B., Müller-Steinhagen, H., and Chen, X. D., 1997, "Effect of Suspended Particles on Crystallization Fouling in Plate Heat Exchangers," ASME JOURNAL OF HEAT TRANSFER, Vol. 119, pp. 568–574.

Bramson, D., Hasson, D., and Semiat, R., 1995, "The roles of gas bubbling, wall crystallization and particulate deposition in $CaSO_4$ scale formation," *Desalination*, Vol. 100, pp. 105–113.

Hasson, D., Sherman, H., and Biton, M., 1978, "Prediction of $CaCO_3$ scaling rates," *6th Int. Symposium Fresh Water from the Sea*, pp. 193–199.

Lee, S. H., and Knudsen, J. G., 1979, "Scaling Characteristics of Cooling Tower Water," *ASHRAE Transactions*, Vol. 85, Part I, pp. 81–302.

Thonon, B., Grillot, J. M., and Vidil, R., 1996, "Liquid side fouling of plate heat exchangers," *Fouling Mitigation of Industrial Heat-Exchange Equipment*, C. B. Panchal, ed., pp. 537–548, Begell House, New York, pp. 537–548.

Walton, A. G., 1967, *The Formation and Properties of Precipitates*, Krieger, Huntington, NY.

Watkinson, A. P., 1983, "Water quality effects on fouling from hard waters," *Heat Exchangers Theory and Practice*, J. Taborek et al., eds., Hemisphere, Washington DC, pp. 853–861.

Fin (on a Pipe) Effectiveness: One Dimensional and Two Dimensional

D. C. Look, Jr.[1]

Nomenclature

Bi = Biot number = hL/k

Bi* = Biot number = $h_e L/k$

h = convection coefficient of the lateral surfaces of the fin

h_e = convection coefficient of the fin tip

I_0, I_1 = modified Bessel functions of the first kind of order $n = 0, 1$

k = thermal conductivity

K_0, K_1 = modified Bessel functions of the second kind of order $n = 0, 1$

L = half-thickness of fin

$Q(\text{fin})$ = the heat lost by a fin

$Q(\text{no fin})$ = the heat lost by a surface the size of the fin base

r = radial independent variable of the fin analysis ($r_1 \leq r \leq r_2$)

R = effectiveness = $Q(\text{fin})/Q(\text{no fin})$

T = temperature within the fin

T_w = fin root temperature

T_∞ = ambient temperature

Greek Symbols

β = r_2/r_1

Γ = r_1/L

θ = $(T - T_\infty)/(T_w - T_\infty)$

λ_n = determined from solutions of transcendental Eq. (8e)

ν = z/L ($-1 \leq \nu \leq 1$)

ξ = r/r_1 ($1 \leq \xi \leq \beta$)

Introduction

Historically, the fin, spline, or extended surface has been used by engineers as a means of controlling the temperature of a piece of equipment. In order to analyze the fin and its effect, a one-dimensional approach generally has proved to be sufficient (Murray, 1938). That is, according to this approach, the physical parameters are of such a magnitude that only the temperature variation from the fin root to tip is considered. This is, of course, a convenience because the mathematics involved is not difficult and is widely accepted in both the academic and industrial communities. The assumptions upon which this one-dimen-

sional analysis is usually based are constant thermophysical properties and negligible heat transfer from the tip (insulated) (Gardner, 1945). This last assumption is not strictly true, since under certain conditions (e.g., large convection coefficients) non-negligible quantities of energy may be lost from the fin tip. A two-dimensional analysis, including fin tip effects, is a more difficult approach but could produce an understanding of fins which has been glossed over in the marginal cases, including an expanded number of fin materials and fin shapes which could possibly produce adequate thermal control at a reduced cost.

The validity of the one-dimensional approach has been the subject of many investigations. Some papers (Avrami and Little, 1942; Burmeister, 1979; Crank and Parker, 1966; Keller and Somers, 1959; Irey, 1975; Lau and Tan, 1973; Levitky, 1972; Snider and Kraus, 1983; Unal, 1988) have shown that the one-dimensional fin approach, although convenient, may be in error under certain conditions. For constant convection coefficients (h) and thermal conductivity (k), the criterion for the validity of the one-dimensional assumption is that the Biot number, based on the fin root half-thickness, must be less than 0.1 regardless of any parameter magnitude. Other papers (Hrymk et al., 1985; Snider and Kraus, 1981; Eslinger and Chung, 1979) present finite difference or finite element methods to solve problems involving nonstandard geometry and nonconstant physical properties. These methods produce accurate results because they are a direct application of the first law but require simultaneous solutions of nodal equations at each and every point of interest on, and within, the boundary of the domain (Reiser and Apple, 1974; Cengel, 1998). Of course, h and k are dependent upon temperature and are thus variable throughout the fin. The effect of assuming these to be constant (Stachiewicz, 1969; Razelos and Imre, 1980) and the effect of the insulated tip (Avrami and Little, 1942; Burmeister, 1979; Hrymk, et al., 1985) have also been presented in the literature.

There are papers (Buccini and Soliman, 1986; Crank and Parker, 1966; Hrymk, et al., 1985; Irey, 1975; Ju, et al., 1989; Juca' and Prata, 1993; Kang and Look, 1993; Look, 1988 and 1989; Look and Kang, 1991 and 1992; Ma, et al., 1991; Razelos and Georgiou, 1992) which present analyses of fins as a two-dimensional heat transfer mechanism. While these analyses appear to be somewhat more involved, the results are somewhat more realistic. The purpose of this paper is to demonstrate two-dimensional effects by comparing the results of one and two-dimensional analyses of a rectangular fin on a pipe with convection from the tip as a function of the Biot number and the relative fin size. That is, the difference in the two results will be pointed out through a comparison of heat transfer situations using the fin effectiveness versus the Biot number.

Analysis

Consider the annular fin on a pipe illustrated in Fig. 1. To formulate the problem, assume the surface at $r = r_2$ is convecting heat to the ambient at T_∞ through a convection coefficient, h_e and $\nu = 0$ is the plane at the center of the fin.

One-Dimensional Case. Based on the usual one-dimensional first-law analysis for constant thermophysical properties, the temperature profile is

$$\theta = C_1 I_o(\Gamma \xi \sqrt{Bi}) + C_2 K_o(\Gamma \xi \sqrt{Bi}) \qquad (1a)$$

$$C_1 = [\sqrt{Bi} K_1(\Gamma \beta \sqrt{Bi}) - B_i^* K_0(\Gamma \beta \sqrt{Bi})]/D \quad \text{and}$$

$$C_2 = [\sqrt{B_i} I_1(\Gamma \beta \sqrt{Bi}) + B_i^* I_0(\Gamma \beta \sqrt{Bi})]/D \qquad (1b)$$

and

$$D = \sqrt{B_i}[I_1(\Gamma \beta \sqrt{Bi})K_0(\Gamma \sqrt{Bi}) + I_o(\Gamma \sqrt{Bi})K_1(\Gamma \beta \sqrt{Bi})]$$

$$+ B_i^*[I_0(\Gamma \beta \sqrt{Bi})K_0(\Gamma \sqrt{Bi}) - I_0(\Gamma \sqrt{Bi})K_0(\Gamma \beta \sqrt{Bi})], \qquad (1c)$$
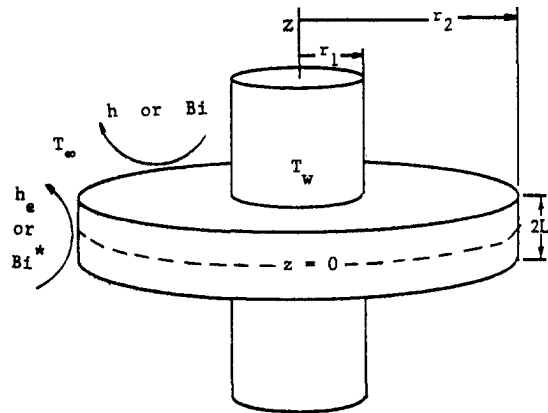

Fig. 1 Geometric schematic of a fin on a pipe

where $1 \leq \xi \leq \beta$. For this problem, the boundary conditions are

$$\xi = 1, \quad \theta_w = 1 \quad \text{and} \quad \xi = \beta, \quad \frac{d\theta}{d\xi} + Bi^*\Gamma = 0. \quad (2)$$

Notice that the convection coefficient at the tip of the fin, $h_e(Bi^*)$, may be unequal to the corresponding convection coefficients, $h(Bi)$, of the top and bottom (lateral) surfaces of the fin. The power lost by the fin is

$$Q(\text{fin}) = \int_{-L}^{L} \left(-k \frac{dT}{dr}\Big|_{r=r_1} \right) dA$$

$$= 4\pi r_1 \sqrt{hLk}(T_w - T_\infty)[C_1 I_1(\Gamma \sqrt{Bi})$$

$$- C_2 K_1(\Gamma \beta \sqrt{Bi})]. \quad (3)$$

Finally, the power lost by the pipe surface if there were no fin attached is

$$Q(\text{no fin}) = 4\pi r_1 Lh(T_w - T_\infty). \qquad (4)$$

Thus a convenient parameter, the fin effectiveness (Cengel, 1998) is

$$R = Q(\text{fin})/Q(\text{no fin})$$

$$= [C_1 I_1(\Gamma \sqrt{Bi}) - C_2 K_1(\Gamma \sqrt{Bi})]/\sqrt{Bi}. \qquad (5)$$

Two-Dimensional Case. Again, based upon a first-law analysis, but for conduction within the fin in both the r and z directions, the temperature profile is

$$\theta = \sum_{n=1}^{\infty} [C_{1_n} I_o(\lambda_n L\Gamma \xi) + C_{2_n} K_o(\lambda_n L\Gamma \xi)] \cos(\lambda_n L\nu) \quad (6a)$$

where

$$C_{1_n} = C_n[\sqrt{Bi} K_1(\lambda_n L\Gamma \beta) - B_i^* K_0(\lambda_n L\Gamma \beta)]/D \qquad (6b)$$

$$C_{2_n} = C_n[\sqrt{Bi} I_1(\lambda_n L\Gamma \beta) + B_i^* I_0(\lambda_n L\Gamma \beta]/D \qquad (6c)$$

$$C_n = 2 \sin(\lambda_n L)/[\cos(\lambda_n L) \sin(\lambda_n L) + \lambda_n L] \qquad (6d)$$

$$D_n = \sqrt{Bi}[I_o(\lambda_n L\Gamma)K_1(\lambda_n L\Gamma \beta) + K_o(\lambda_n L\Gamma)I_1(\lambda_n L\Gamma \beta)]$$

$$- B_i^*[I_0(\lambda_n L\Gamma)K_0(\lambda_n L\Gamma \beta) - K_0(\lambda_n L\Gamma)I_0(\lambda_n L\Gamma \beta)] \qquad (6e)$$

and

$$\lambda_n L = Bi \cot(\lambda_n L) \qquad (6f)$$

where $1 \leq \xi \leq \beta$ and $-1 \leq \nu \leq 1$. In this case the boundary conditions are

$$\xi = 1 \theta = 1; \quad \xi = \beta \; \frac{\partial \theta}{\partial \xi} + Bi^* \Gamma \theta = 0 \qquad (7a)$$

and

$$\nu = 0 \; \frac{\partial T}{\partial \nu} = 0; \quad \nu = 1 \; \frac{\partial \theta}{\partial \nu} + Bi \Gamma \theta = 0. \qquad (7b)$$

The corresponding expression for the fin effectiveness is

$$R = Q(\text{fin})/Q(\text{no fin}) = \sum_{n=1}^{\infty} [C_{1_n} I_1 (\lambda_n L \Gamma)$$

$$- C_{2_n} K_1 (\lambda_n L \Gamma)] \; \text{Sin} \; (\lambda_n L)/Bi. \qquad (8)$$

Results

In order to present some results, h_e was set equal to h (i.e., $Bi = Bi^*$). Although this is not strictly true, it is a convenient approximation which allows a representative amount of data to be made available for presentation as results.

Figure 2 presents information concerning the effectiveness of fins presented as Eqs. (5) and (8). For this demonstration, $R = 1$ will be the lowest possible acceptable fin performance. Note, in practice, this ratio should have a magnitude of 3 or more before a fin is considered to be enhancing the heat transfer regardless of the analysis. In fact, for R in the order of 10, the one-dimensional and two-dimensional analyses will produce identical results because Bi is small regardless of the magnitude of β. However, depending on the application, the effectiveness of a fin is judged by several analyses (not only heat transfer, but economic and so on). Under that minimum acceptable proviso, Fig. 2 indicates that in the case of a two-dimensional thick fin ($r_1 = L$), the minimum dividing line between a fin being useful or unnecessary is not sharp (see region A) as expected from the one-dimensional analysis. It depends upon a relationship between Bi and the β ratio for $\Gamma = 1$. That is, for $\Gamma = 1$, the effectiveness increases as β increases for a given Bi.

Figure 3 presents the same information as Fig. 2, but for a relatively thinner fin ($r_1 = 5L$). It is easily seen from this figure that the spread of the effectiveness is reduced as a function of the size ratio for a given Bi. Further, at the transition line, the transition points occur at approximately the same value of Bi for all size ratios. However, for selection of an effectiveness of a magnitude of 3, the size ratio of 3 would be in the "use fin" region for Bi < 0.2. Thus, it is seen that similar effectiveness relationships exists for the one-dimensional and two-dimen-
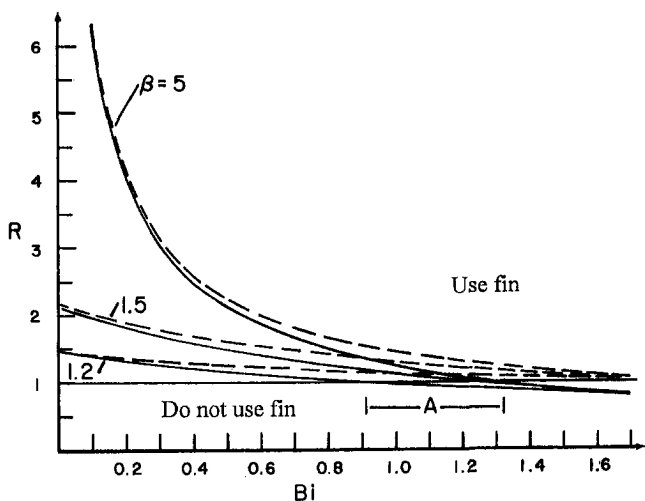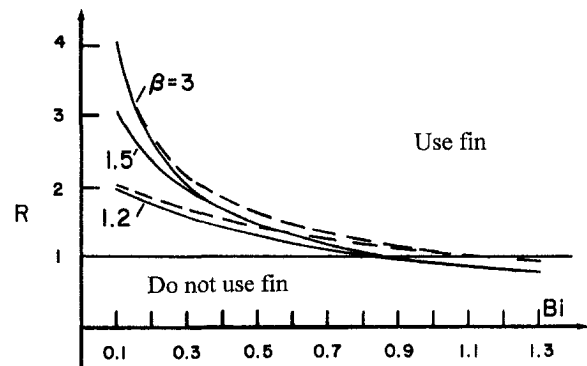

Fig. 3   Effectiveness as a function of Bi for Γ = 5 when the size ratio, β has values of 3.0, 1.5, and 1.2 (——, two dimensional; -----, one dimensional)

sional analyses; the major difference is that the one dimensional is less restrictive.

Acknowledgment

References

Avrami, M., and Little, J. B., 1942, "Diffusion of Heat Through a Rectangular Bar and the Cooling and Insulating Effect of Fins," *J. Appl. Phy.*, Vol. 13, pp. 225–264.

Buccini, A., and Soliman, H. M., 1986, "Optimum Dimensions of Annular Fin Assemblies," ASME JOURNAL OF HEAT TRANSFER, Vol. 108, No. 2, pp. 459–462.

Burmeister, L. C., 1979, "Triangular Fin Performance by the Heat Balance Integral Method," ASME JOURNAL OF HEAT TRANSFER, Vol. 101, pp. 565–564.

Cengel, Y. A., 1998, *Heat Transfer: A Practical Approach*, WCB McGraw-Hill, Boston, MA.

Crank, J., and Parker, I. B., 1966, "Approximate Methods for Two-Dimensional Problems in Heat Flow," *Q. J. of Mech. and Appl. Math.*, Vol. 19, Part 2, pp. 167–181.

Eslinger, R. G., and Chung, B. T. F., 1979, "Periodic Heat Transfer in Radiating and Convecting Fins and Fin Arrays," *AIAA J.*, Vol. 17, No. 10, pp. 1134–1140.

Gardner, K. A., 1945, "Efficiency of Extended Surfaces," *ASME Trans.*, Vol. 67, pp. 621–631.

Hrymk, A. N., McRae, G. J., and Westerberg, A. W., 1985, "Combined Analysis and Optimization of Extended Heat Transfer Surfaces," ASME JOURNAL OF HEAT TRANSFER, Vol. 107, pp. 527–532.

Irey, R. K., 1975, "Errors in One-Dimensional Fin Solution," ASME JOURNAL OF HEAT TRANSFER, Vol. 97, pp. 175–176.

Ju, Y-H., Chou, Y., and Hsiao, C. C., 1989, "A New Approach to Transient Conduction In a 2-D Rectangular Fin," *Int. J. Heat Mass Trans.*, Vol. 32, No. 9 pp. 1657–1661.

Juca, P. C. S., and Prata, A. T., 1993, "Two-dimensional Fins Attached to a Thick Wall-Effect of Non-uniform Root Temperature," *Int. J. Heat Mass Trans.*, Vol. 36, No. 1, pp. 233–236.

Kang, H. S., and Look, D. C., Jr., 1993, "A Forced Analytical Scheme Applied to A 2-D Fin: An Unsuccessful Venture," presented at the AIAA 28th Thermophysics Conference, Paper No. 93-2854.

Keller, H. H., and Somers, E. V., 1959, "Heat Transfer from an Annular Fin of Constant Thickness," ASME JOURNAL OF HEAT TRANSFER, Vol. 81, pp. 151–156.

Lau, W., and Tan, C. W., 1973, "Errors in One-Dimensional Heat Transfer Analysis in Straight and Annular Fins," ASME JOURNAL OF HEAT TRANSFER, Vol. 95, pp. 549–551.

Levitky, M., 1972, "The Criterion for Validity of the Fin Approximation," *Int. J. Heat and Mass Trans.*, Vol. 15, pp. 1960–1963.

Look, D. C., Jr., 1988, "Two Dimensional Fin Performance: Bi (top surface) ≥ Bi (bottom surface)," ASME JOURNAL OF HEAT TRANSFER, Vol. 110, pp. 780–782.

Look, D. C., Jr., 1989, "Two Dimensional Fin with Non-Constant Root Temperature," *Int. J. Heat Mass Trans.*, Vol. 32, No. 5, pp. 977–980.

Look, D. C., Jr., and Kang, H. S., 1991, "Effects of Variation In Root Temperature on Heat Lost From a Thermally Non-Symmetric Fin," *Int. J. Heat Mass Trans.*, Vol. 34, No. 5, pp. 1059–1065.

Look, D. C., Jr., and Kang, H. S., 1992, "Optimization of a Thermally Non-Symmetric Fin: Preliminary Evaluation," *Int. J. Heat Mass Trans.*, Vol. 35, No. 8, pp. 2057–2060.

Fig. 2   Effectiveness as a function of Bi for Γ = 1.0 where the size ratio, β has values of 5, 1.5, and 1.2 (——, two dimensional; ----, one dimensional)

Look, D. C., Jr., 1995, "Fin on a Pipe (Insulated Tip): Minimum Conditions for Fin to be Beneficial," *Heat Trans. Engr.,* Vol. 16, No. 3, pp. 65–75.

Ma, S. W., Behbahani, A. I., and Tsuei, Y. G., 1991, "Two-dimensional Rectangular Fin with Variable Heat Transfer Coefficient," *Int. J. Heat Mass Trans.,* Vol. 34, No. 1, pp. 79–85.

Murray, W. M., 1938, "Heat Transfer Through an Annular Disk or Fin of Uniform Thickness," ASME *Journal of Applied Mechanics,* Vol. 60, pp. A78–A80.

Razelos, P., and Imre, K., 1980, "The Optimum Dimensions of Circular Fins with Variable Thermal Parameters," ASME JOURNAL OF HEAT TRANSFER, Vol. 102, pp. 420–425.

Razelos, P., and Georgiou, E., 1992, "Two Dimensional Effects and Design Criteria for Convective Extended Surfaces," *Heat Trans. Engr.,* Vol. 13, pp. 38–48.

Reiser, M. J., and Apple, J. F., 1974, "A Numerical Method for Heat Conduction Problems," ASME JOURNAL OF HEAT TRANSFER, pp. 307–312.

Snider, A. D., and Kraus, A. D., 1981, "A General Extended Surface Analysis Method," ASME JOURNAL OF HEAT TRANSFER, Vol. 103, No. 4, pp. 699–704.

Snider, A. D., and Kraus, A. D., 1983, "Recent Developments in the Analyses and Design of Extended Surfaces," ASME JOURNAL OF HEAT TRANSFER, Vol. 105, pp. 302–306.

Stachiewicz, J. W., 1969, "Effect of Variation of Local Film Coefficient on Fin Performance," ASME JOURNAL OF HEAT TRANSFER, Vol. 91, pp. 21–26.

Unal, H. C., 1988, "The Effect of the Boundary Condition at a Fin Tip on the Performance of the Fin With and Without Internal Heat Generation," *Int. J. Heat Mass Trans.,* Vol. 31, No. 7, pp. 1483–1496.
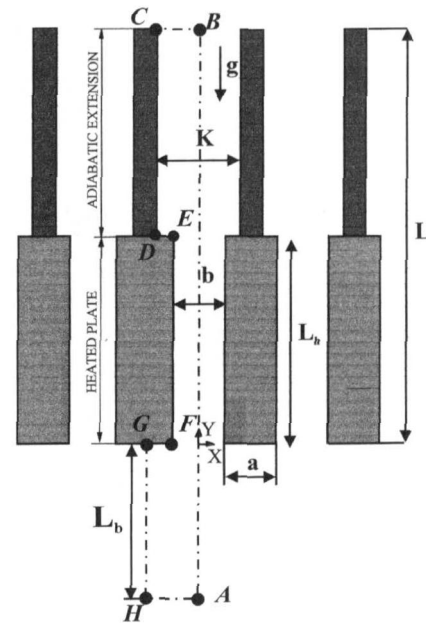
Fig. 1 Sketch of the heat transfer system

Heat Transfer Enhancement Generated by the Chimney Effect in Systems of Vertical Channels

G. A. Shahin[1,3] and J. M. Floryan[2,3]

Introduction

Passive character of cooling by natural convection makes it very attractive for applications in electronic devices. Ever-increasing cooling requirements necessitate, however, the search for methods of intensification of natural convection, especially in geometries found in electronic devices. Cooling of computer boards can be studied by idealizing them as forming vertical channels. Evaluation of increase of heat transfer induced by the chimney effect in such geometries is the objective of the present study.

Bodoia and Osterle (1962) were the first to consider heat transfer in a single channel. Naylor et al. (1991) provided correct description of the entrance effects. Floryan and Novak (1995) considered systems consisting of two, three, and an infinite number of channels. They found that channels interact with each other and that the heat transfer can be significantly increased by placing channels sufficiently close to each other. They showed that the overall heat transfer can be increased by up to 18 percent; if only the entrance zone is considered (defined as ten percent of the total channel length) the mean Nusselt number may increase by up to 48 percent. Haaland and Sparrow (1983) investigated chimney effect in a channel with a heat source. Straatman et al. (1993) investigated a similar effect in a single heated channel. They considered adiabatic extensions (straight chimneys) of lengths from 1.5 to 4 times the channel length and reported an increase of heat transfer from 10 percent

to 30 percent. Use of an expanded extension offered enhancements from 30 percent to 250 percent.

The objective of the present study is to evaluate the increase of the heat transfer in systems of channels with adiabatic chimneys (extensions). Since the interaction between the channels induces higher flow rates, the associated chimney effect is expected to be stronger permitting use of shorter chimneys. The presented results should complement the available heat transfer correlations, such as those given by Bar-Cohen and Rohsenow (1984).

Problem Formulation

Figure 1 shows the geometry of the flow system. Fluid flows by natural convection between parallel plates arranged periodically in the horizontal directions. The plates have length L_h, thickness a, spacing b, and are kept at a constant temperature T_w. The bottom and top of the plates are insulated. Each plate has an adiabatic wall attached centrally to its top. These walls form chimneys of length $(L - L_h)$ and thickness K. The fluid below the channels, at a sufficient distance L_b, is at ambient temperature T_0 and the flow is uniform and directed upward. The flow is fully developed at the exits from the chimneys.

The motion of the fluid is described by the two-dimensional incompressible continuity, Navier-Stokes and energy equations. All fluid properties are constant with the exception of density in the buoyancy term in the y-momentum equation, which is approximated using the Boussinesq assumption. The problem was solved in dimensionless form using the following scaling: $U = u/U_{ref}$, $V = v/U_{ref}$, $X = x/b$, $Y = y/b$, $\theta = (T - T_0)/(T_w - T_0)$, $P = pb/\mu U_{ref}$ where $U_{ref} = \alpha$ Pr $Gr^{1/2}/b$ and $Gr = g\beta(T_w - T_0)b^3/\nu^2$. The (u, v) denote the velocity components in the (x, y) directions, p stands for the pressure, g represents the gravitational acceleration, μ denotes the dynamic viscosity, ν stands for the kinematic viscosity, β denotes the volumetric expansion coefficient, $Pr = \nu/\alpha$ is the Prandtl number, α represents the thermal diffusivity, and Gr stands for the Grashof number.

The solution domain has been reduced to area ABCDEFGH in Fig. 1 due to various symmetries present in the problem. The boundary conditions take the following form: $\partial\theta/\partial x = \partial V/\partial X = U = 0$ along the line (AB); $\partial\theta/\partial X = \partial V/\partial Y = 0$ along the line (BC); $\partial\theta/\partial X = U = V = 0$ along the line (CD); $\partial\theta/\partial Y$

Look, D. C., Jr., 1995, "Fin on a Pipe (Insulated Tip): Minimum Conditions for Fin to be Beneficial," *Heat Trans. Engr.*, Vol. 16, No. 3, pp. 65–75.

Ma, S. W., Behbahani, A. I., and Tsuei, Y. G., 1991, "Two-dimensional Rectangular Fin with Variable Heat Transfer Coefficient," *Int. J. Heat Mass Trans.*, Vol. 34, No. 1, pp. 79–85.

Murray, W. M., 1938, "Heat Transfer Through an Annular Disk or Fin of Uniform Thickness," ASME *Journal of Applied Mechanics*, Vol. 60, pp. A78–A80.

Razelos, P., and Imre, K., 1980, "The Optimum Dimensions of Circular Fins with Variable Thermal Parameters," ASME JOURNAL OF HEAT TRANSFER, Vol. 102, pp. 420–425.

Razelos, P., and Georgiou, E., 1992, "Two Dimensional Effects and Design Criteria for Convective Extended Surfaces," *Heat Trans. Engr.*, Vol. 13, pp. 38–48.

Reiser, M. J., and Apple, J. F., 1974, "A Numerical Method for Heat Conduction Problems," ASME JOURNAL OF HEAT TRANSFER, pp. 307–312.

Snider, A. D., and Kraus, A. D., 1981, "A General Extended Surface Analysis Method," ASME JOURNAL OF HEAT TRANSFER, Vol. 103, No. 4, pp. 699–704.

Snider, A. D., and Kraus, A. D., 1983, "Recent Developments in the Analyses and Design of Extended Surfaces," ASME JOURNAL OF HEAT TRANSFER, Vol. 105, pp. 302–306.

Stachiewicz, J. W., 1969, "Effect of Variation of Local Film Coefficient on Fin Performance," ASME JOURNAL OF HEAT TRANSFER, Vol. 91, pp. 21–26.

Unal, H. C., 1988, "The Effect of the Boundary Condition at a Fin Tip on the Performance of the Fin With and Without Internal Heat Generation," *Int. J. Heat Mass Trans.*, Vol. 31, No. 7, pp. 1483–1496.
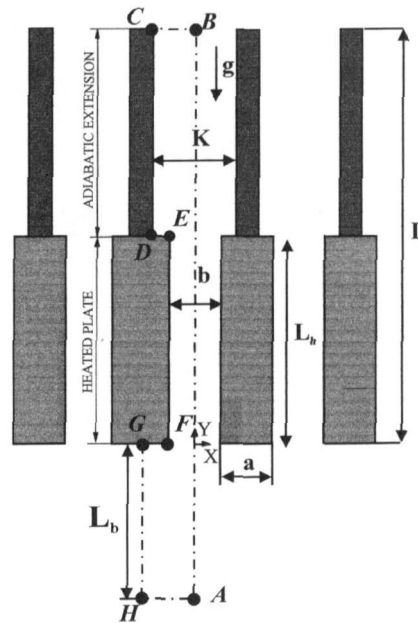
Fig. 1 Sketch of the heat transfer system

Heat Transfer Enhancement Generated by the Chimney Effect in Systems of Vertical Channels

G. A. Shahin[1,3] and J. M. Floryan[2,3]

Introduction

Passive character of cooling by natural convection makes it very attractive for applications in electronic devices. Ever-increasing cooling requirements necessitate, however, the search for methods of intensification of natural convection, especially in geometries found in electronic devices. Cooling of computer boards can be studied by idealizing them as forming vertical channels. Evaluation of increase of heat transfer induced by the chimney effect in such geometries is the objective of the present study.

Bodoia and Osterle (1962) were the first to consider heat transfer in a single channel. Naylor et al. (1991) provided correct description of the entrance effects. Floryan and Novak (1995) considered systems consisting of two, three, and an infinite number of channels. They found that channels interact with each other and that the heat transfer can be significantly increased by placing channels sufficiently close to each other. They showed that the overall heat transfer can be increased by up to 18 percent; if only the entrance zone is considered (defined as ten percent of the total channel length) the mean Nusselt number may increase by up to 48 percent. Haaland and Sparrow (1983) investigated chimney effect in a channel with a heat source. Straatman et al. (1993) investigated a similar effect in a single heated channel. They considered adiabatic extensions (straight chimneys) of lengths from 1.5 to 4 times the channel length and reported an increase of heat transfer from 10 percent

[1] Graduate Student.
[2] Professor. Mem. ASME.
[3] Department of Mechanical Materials and Engineering, The University of Western Ontario, London, Ontario N6A 5B9, Canada.

to 30 percent. Use of an expanded extension offered enhancements from 30 percent to 250 percent.

The objective of the present study is to evaluate the increase of the heat transfer in systems of channels with adiabatic chimneys (extensions). Since the interaction between the channels induces higher flow rates, the associated chimney effect is expected to be stronger permitting use of shorter chimneys. The presented results should complement the available heat transfer correlations, such as those given by Bar-Cohen and Rohsenow (1984).

Problem Formulation

Figure 1 shows the geometry of the flow system. Fluid flows by natural convection between parallel plates arranged periodically in the horizontal directions. The plates have length L_h, thickness a, spacing b, and are kept at a constant temperature T_w. The bottom and top of the plates are insulated. Each plate has an adiabatic wall attached centrally to its top. These walls form chimneys of length $(L - L_h)$ and thickness K. The fluid below the channels, at a sufficient distance L_b, is at ambient temperature T_0 and the flow is uniform and directed upward. The flow is fully developed at the exits from the chimneys.

The motion of the fluid is described by the two-dimensional incompressible continuity, Navier-Stokes and energy equations. All fluid properties are constant with the exception of density in the buoyancy term in the y-momentum equation, which is approximated using the Boussinesq assumption. The problem was solved in dimensionless form using the following scaling: $U = u/U_{ref}$, $V = v/U_{ref}$, $X = x/b$, $Y = y/b$, $\theta = (T - T_0)/(T_w - T_0)$, $P = pb/\mu U_{ref}$ where $U_{ref} = \alpha$ Pr $Gr^{1/2}/b$ and $Gr = g\beta(T_w - T_0)b^3/\nu^2$. The (u, v) denote the velocity components in the (x, y) directions, p stands for the pressure, g represents the gravitational acceleration, μ denotes the dynamic viscosity, ν stands for the kinematic viscosity, β denotes the volumetric expansion coefficient, Pr $= \nu/\alpha$ is the Prandtl number, α represents the thermal diffusivity, and Gr stands for the Grashof number.

The solution domain has been reduced to area ABCDEFGH in Fig. 1 due to various symmetries present in the problem. The boundary conditions take the following form: $\partial\theta/\partial x = \partial V/\partial X = U = 0$ along the line (AB); $\partial\theta/\partial X = \partial V/\partial Y = 0$ along the line (BC); $\partial\theta/\partial X = U = V = 0$ along the line (CD); $\partial\theta/\partial Y$

Fig. 2 Mean Nusselt number as a function of the distance a/b between channels for $\widetilde{\mathrm{Gr}} = \mathrm{Gr}\, b/L_h = 2000$. (*i*) periodic channels without chimneys; (*ii*) periodic channels with straight chimneys ($K/b = 1$) of length $L/L_h = 2$; (*iii*) periodic channels with expanded chimneys ($K/b = 2$) of length $L/L_h = 2$.

Fig. 3 Distribution of the local Nusselt number Nu_l on the channel wall for $\widetilde{\mathrm{Gr}} = \mathrm{Gr}\, b/L_h = 2000$, $a/b = 2.5$. (*i*) no chimney $L = L_h$; (*ii*) straight chimney ($K/b = 1$) of length $L/L_h = 2$; (*iii*) expanded chimney ($K/b = 2$) of length $L/L_h = 2$.

$= U = V = 0$ along the line (DE); $\theta = 1$, $U = V = 0$ along the line (EF); $\partial\theta/\partial Y = U = V = 0$ along the line (FG); $\partial\theta/\partial X = \partial V/\partial X = U = 0$ along the line (GH) and $\theta = \partial V/\partial Y = U = 0$ along the line (HA).

Local (Nu_l) and mean (Nu_m) Nusselt numbers are defined by the following relations:

$$N_l = \frac{h_l b}{k} = -\left.\frac{\partial\theta}{\partial X}\right|_{X=1}, \quad N_m = \frac{h_m b}{K} = -\frac{b}{L_h}\int_0^{L_h/b}\left.\frac{\partial\theta}{\partial X}\right|_{X=1} dY$$

where h_l, h_m denote the local and the mean heat transfer coefficients, and k stands for the thermal conductivity.

Solution Methodology

The governing equations were discretized using the finite element method. As a benchmark, the experimentally verified results of Naylor et al. (1991) and Straatman et al. (1993) and theoretical results of Floryan and Novak (1995) were first replicated. A 14,621 node mesh with a higher density around the channel entrance was used. In all cases, Prandtl number Pr $= 0.7$, channel aspect ratio $L_h/b = 17$, chimney length $L/L_h = 2$, and length of the inlet zone $L_b/b = 7$ were used. L_b was selected on the basis of numerical experiments, where the calculations were repeated with the increasing values of L_b until L_b was large enough so that its further increase would affect the results below the accepted level of numerical error. Nine-node quadrilateral elements having quadratic interpolation functions for both velocity and temperature were utilized. The penalty formulation was employed for pressure and calculations were made to four decimal places. Grid convergence experiments based upon the mean Nusselt number indicated accuracies of better than one percent.

Results and Discussion

Results displayed in Fig. 2 show that addition of adiabatic extensions (chimneys) enhances the heat transfer from periodic isothermal channels for all configurations considered. Addition of a straight extension ($K/b = 1$) increases the mean Nusselt number Nu_m by about ten percent; addition of an expanded extension ($K/b = 2$) increases Nu_m by another ten percent. The interaction between the channels is negligible if the spacing between them is $a/b > 2$ (see Fig. 1). This interaction rapidly increases as a/b decreases and adds about five percent to the value of Nu_m for the smallest spacing ($a/b = 0.5$) considered.
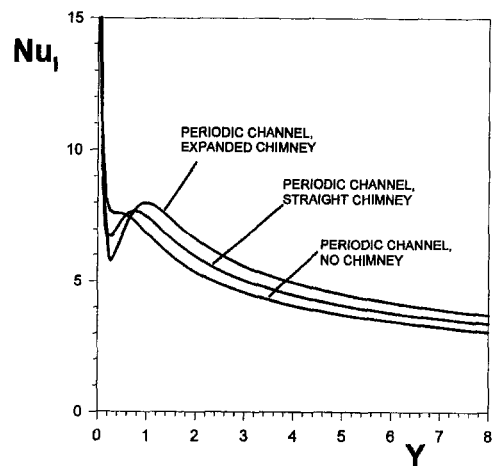
The interaction as measured by Nu_m, is about 30 percent stronger in the case of an expanded channel as compared to other configurations.

Figure 3 displays the distribution of the local Nusselt number Nu_l for three geometrical configurations. The local reduction of Nu_l in the entrance zone is associated with flow separation phenomenon (see Naylor et al., 1991). Addition of a straight chimney induces higher flow rate and increases the size of the separation zone. The local Nusselt number has a more pronounced minimum at the entrance zone but considerably higher values in the rest of the channel. Addition of an expanded channel amplifies the same effect, i.e., the induced flow rate is much higher, the separation zone is bigger, there is a more pronounced drop of Nu_l in the entrance zone and there are much higher values of Nu_l in the rest of the channel.

Figure 4 displays the mean Nusselt number as a function of the modified Grashof number $\widetilde{\mathrm{Gr}} = \mathrm{Gr}\, b/L_h$. The global effect of the presence of straight extensions is an increase of the magnitude of the Nu_m by about 0.2 over a wide range of $\widetilde{\mathrm{Gr}}$. Expanded channel is more effective and it increases Nu_m by about 0.5. The chimney effect is relatively stronger for small
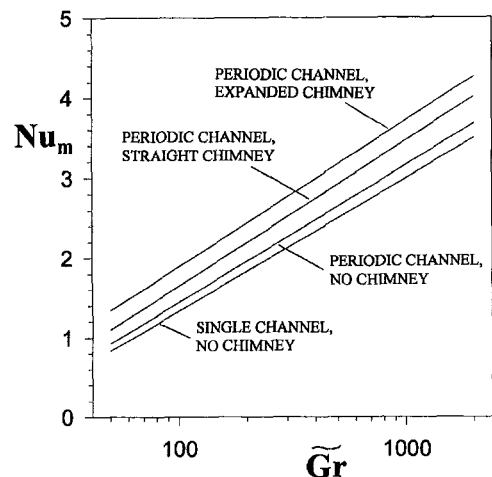
Fig. 4 Mean Nusselt number as a function of the modified Grashof number $\widetilde{\mathrm{Gr}} = \mathrm{Gr}\, b/L_h$. (*i*) single channel without chimney; (*ii*) periodic channels without chimneys ($a/b = 2.5$); (*iii*) periodic channels with straight chimneys ($K/b = 1$, $a/b = 2.5$, $L/L_h = 2$); (*iv*) periodic channels with expanded chimneys ($K/b = 2$, $a/b = 2.5$, $L/L_h = 2$).

values of $\tilde{G}r$ where it increases Nu_m by about 15 percent for straight extensions ($K/b = 1$) and by about 40 percent for expanded extensions ($K/b = 2$), as compared to channels without any extensions.

An additional improvement in heat transfer can be expected from elimination of the flow separation in the entrance zone (and the associated local minimum of Nu_l—Fig. 3) through rounding off the entrance zone corners, Roberts and Floryan (1996). This effect is yet to be precisely quantified, however, the large local decrease of Nu_l in the entrance zone (Fig. 3) demonstrates its potential importance, especially for higher induced flow rates associated with the chimney effect.

Acknowledgments

References

Bar-Cohen, A., and Rohsenow, W. M., 1984, "Thermally Optimum Spacing of Vertical, Natural Convection Cooled, Parallel Plates," ASME JOURNAL OF HEAT TRANSFER, Vol. 106, pp. 116–123.

Bodoia, J. R., and Osterle, J. F., 1962, "The Development of Free Convection Between Heated, Vertical Plates," ASME JOURNAL OF HEAT TRANSFER, Vol. 84, pp. 40–44.

Haaland, S. E., and Sparrow, E. M., 1983, "Solutions for the Channel Plume and the Parallel-Walled Chimney," Numerical Heat Transfer, Vol. 6, pp. 155–172.

Floryan, J. M., and Novak, M., 1995, "Free Convection Heat Transfer in Multiple Vertical Channels," Int. J. Heat and Fluid Flow, Vol. 16, pp. 244–253.

Naylor, D., Floryan, J. M., and Tarasuk, J. D., 1991, "A Numerical Study of Developing Free Convection between Isothermal Vertical Plates," ASME JOURNAL OF HEAT TRANSFER, Vol. 113, pp. 620–626.

Roberts, D. A., and Floryan, J. M., 1998, "Heat Transfer Enhancement in the Entrance Zone of a Vertical Channel," ASME JOURNAL OF HEAT TRANSFER, Vol. 120, pp. 290–291.

Straatman, A. G., Tarasuk, J. D., and Floryan, J. M., 1993, "Heat Transfer Enhancement from a Vertical, Isothermal Channel Generated by the Chimney Effect," ASME JOURNAL OF HEAT TRANSFER, Vol. 115, pp. 395–402.

An Experimental Study of Heat Transfer in Reciprocating Square Duct Fitted With Ribs Skewed to the Flow

S. W. Chang,[1] L. M. Su,[1] T. L. Yang,[2] and C. C. Hwang[2]

Introduction

The fuel economy plays the most important requirement for a marine propulsion plant as it has the decisive influence on the operating cost of a ship. In general the improvements of the propulsive and engine efficiencies could reduce the fuel consumption. Therefore, for a marine main diesel engine, the substantial increase of stroke/bore ratio, so that the engine speed can be significantly reduced in order to increase the propulsive

[1] Department of Marine Engineering, National Kaosiung Institute of Marine Engineering, National Kaohsiung Institute of Marine Technology, Taiwan, R.O.C.

[2] Department of Naval Architecture and Marine Engineering, National Cheng Kung University, Tainan, Taiwan, R.O.C.

efficiency, is observed as a common trend of development in the industry of marine engineering. Along with the efforts in reducing the speed of a propulsive engine, the continuous increases of maximum cycle pressure and temperature of the engine in order to increase the engine efficiency has proceeded in the last decade. As a result, one of the main assemblies of a combustion chamber, the piston, experiences a more difficult working environment. To compensate for the increasing thermal and mechanical loads experienced by a piston, the designs of the piston crown and its cooling system have to be modified. However, due to the reciprocating nature of the piston, the coolant flow circulating within these cooling passages is subjected to an additional time-varied periodical body force induced by reciprocation (Chang and Su, 1997). Therefore the influences of reciprocating force on the flow field and its cooling performance cannot be ignored if the optimum design of such a cooling system is to be achieved.

In the open literature, although the needs for further improvement of cooling performance underneath the piston crown with marine application are obvious, very few studies investigate the effects of reciprocating force on the heat transfer, especially when the flow is turbulent. In summary, for the smooth-walled cooling passage, the influences of reciprocation on heat transfer become minimum and are significantly enhanced if the transverse ribs are fitted on the surfaces of the coolant passages (Chang and Su, 1997; Chang and Su, 1996). One of the main flow physics those facilitate such heat transfer modification from the nonreciprocating situation inside the rib-roughened duct is the combinative influence of rib-associated flows and reciprocating force on the flow field near the duct wall. As a result, the fluid mixing in the radial direction of duct can be considerable enhanced leading to the heat transfer enhancement (Roberts and Mackley, 1996). In this respect, the researches of oscillatory and pulsating flows revealed clearly the flow physics for various cooling geometry (Ralph, 1986; Ghaddar et al., 1986; Nishimura et al., 1987; Greiner, 1991), although there are fundamental differences between the reciprocating and oscillatory/pulsating flows (Chang and Su, 1997). In general when the oscillatory/pulsating flow was superimposed on the flow mainstream, the periodically time-varied eddy motions near the roughened walls were observed when the baffled fins were attached on the duct walls or when the duct was a sinusoidal wavy-walled or grooved channel (Ralph, 1986; Ghaddar et al., 1986; Nishimura et al., 1987; Greiner, 1991; Roberts and Mackley, 1996). Thus considerable enhanced mixing within these channels resulted which led to better heat transfer. For reciprocating duct flow in which the reciprocating force was present, the use of rib-roughened surface might induce similar flow behavior so that heat transfer could be further improved. However, as the artificial roughness using transverse ribs with 90-deg of angle-of-attack for nonreciprocating ducted flow showed less heat transfer enhancement than the skewed ribs with 45-deg of angle-of-attack (Han et al., 1985, 1991; Park et al., 1992; Fann et al., 1994), this study investigated the cooling performance of skewed ribs in the reciprocating duct.

Heat Transfer Test Module

To perform reciprocating experiments, the heat transfer test module shown in Fig. 1 was installed onto a reciprocating facility that created the reciprocating motion of test module. Schematics of the reciprocating facility have been previously reported (Chang and Su, 1997). As shown in Fig. 1, the square-sectioned test duct (1) fitted with ten pairs of square skewed ribs at a regular downstream interval was made of bronze copper having a thermal conductivity of 50 W/mK at temperature 20°C. Only two opposite sides of the duct were rib-roughened. The skewed ribs with angle-of-attack of 45 deg were arranged in the opposite manner. The length and width of this test duct was 165 and 15 mm, respectively, with wall thickness of 1.5 mm.

values of $\tilde{Gr}$ where it increases Nu_m by about 15 percent for straight extensions ($K/b = 1$) and by about 40 percent for expanded extensions ($K/b = 2$), as compared to channels without any extensions.

An additional improvement in heat transfer can be expected from elimination of the flow separation in the entrance zone (and the associated local minimum of Nu_l—Fig. 3) through rounding off the entrance zone corners, Roberts and Floryan (1996). This effect is yet to be precisely quantified, however, the large local decrease of Nu_l in the entrance zone (Fig. 3) demonstrates its potential importance, especially for higher induced flow rates associated with the chimney effect.

Acknowledgments

References

Bar-Cohen, A., and Rohsenow, W. M., 1984, "Thermally Optimum Spacing of Vertical, Natural Convection Cooled, Parallel Plates," ASME JOURNAL OF HEAT TRANSFER, Vol. 106, pp. 116–123.

Bodoia, J. R., and Osterle, J. F., 1962, "The Development of Free Convection Between Heated, Vertical Plates," ASME JOURNAL OF HEAT TRANSFER, Vol. 84, pp. 40–44.

Haaland, S. E., and Sparrow, E. M., 1983, "Solutions for the Channel Plume and the Parallel-Walled Chimney," Numerical Heat Transfer, Vol. 6, pp. 155–172.

Floryan, J. M., and Novak, M., 1995, "Free Convection Heat Transfer in Multiple Vertical Channels," Int. J. Heat and Fluid Flow, Vol. 16, pp. 244–253.

Naylor, D., Floryan, J. M., and Tarasuk, J. D., 1991, "A Numerical Study of Developing Free Convection between Isothermal Vertical Plates," ASME JOURNAL OF HEAT TRANSFER, Vol. 113, pp. 620–626.

Roberts, D. A., and Floryan, J. M., 1998, "Heat Transfer Enhancement in the Entrance Zone of a Vertical Channel," ASME JOURNAL OF HEAT TRANSFER, Vol. 120, pp. 290–291.

Straatman, A. G., Tarasuk, J. D., and Floryan, J. M., 1993, "Heat Transfer Enhancement from a Vertical, Isothermal Channel Generated by the Chimney Effect," ASME JOURNAL OF HEAT TRANSFER, Vol. 115, pp. 395–402.

An Experimental Study of Heat Transfer in Reciprocating Square Duct Fitted With Ribs Skewed to the Flow

S. W. Chang,[1] L. M. Su,[1] T. L. Yang,[2] and C. C. Hwang[2]

Introduction

The fuel economy plays the most important requirement for a marine propulsion plant as it has the decisive influence on the operating cost of a ship. In general the improvements of the propulsive and engine efficiencies could reduce the fuel consumption. Therefore, for a marine main diesel engine, the substantial increase of stroke/bore ratio, so that the engine speed can be significantly reduced in order to increase the propulsive

[1] Department of Marine Engineering, National Kaosiung Institute of Marine Engineering, National Kaohsiung Institute of Marine Technology, Taiwan, R.O.C.

[2] Department of Naval Architecture and Marine Engineering, National Cheng Kung University, Tainan, Taiwan, R.O.C.

efficiency, is observed as a common trend of development in the industry of marine engineering. Along with the efforts in reducing the speed of a propulsive engine, the continuous increases of maximum cycle pressure and temperature of the engine in order to increase the engine efficiency has proceeded in the last decade. As a result, one of the main assemblies of a combustion chamber, the piston, experiences a more difficult working environment. To compensate for the increasing thermal and mechanical loads experienced by a piston, the designs of the piston crown and its cooling system have to be modified. However, due to the reciprocating nature of the piston, the coolant flow circulating within these cooling passages is subjected to an additional time-varied periodical body force induced by reciprocation (Chang and Su, 1997). Therefore the influences of reciprocating force on the flow field and its cooling performance cannot be ignored if the optimum design of such a cooling system is to be achieved.

In the open literature, although the needs for further improvement of cooling performance underneath the piston crown with marine application are obvious, very few studies investigate the effects of reciprocating force on the heat transfer, especially when the flow is turbulent. In summary, for the smooth-walled cooling passage, the influences of reciprocation on heat transfer become minimum and are significantly enhanced if the transverse ribs are fitted on the surfaces of the coolant passages (Chang and Su, 1997; Chang and Su, 1996). One of the main flow physics those facilitate such heat transfer modification from the nonreciprocating situation inside the rib-roughened duct is the combinative influence of rib-associated flows and reciprocating force on the flow field near the duct wall. As a result, the fluid mixing in the radial direction of duct can be considerable enhanced leading to the heat transfer enhancement (Roberts and Mackley, 1996). In this respect, the researches of oscillatory and pulsating flows revealed clearly the flow physics for various cooling geometry (Ralph, 1986; Ghaddar et al., 1986; Nishimura et al., 1987; Greiner, 1991), although there are fundamental differences between the reciprocating and oscillatory/pulsating flows (Chang and Su, 1997). In general when the oscillatory/pulsating flow was superimposed on the flow mainstream, the periodically time-varied eddy motions near the roughened walls were observed when the baffled fins were attached on the duct walls or when the duct was a sinusoidal wavy-walled or grooved channel (Ralph, 1986; Ghaddar et al., 1986; Nishimura et al., 1987; Greiner, 1991; Roberts and Mackley, 1996). Thus considerable enhanced mixing within these channels resulted which led to better heat transfer. For reciprocating duct flow in which the reciprocating force was present, the use of rib-roughened surface might induce similar flow behavior so that heat transfer could be further improved. However, as the artificial roughness using transverse ribs with 90-deg of angle-of-attack for nonreciprocating ducted flow showed less heat transfer enhancement than the skewed ribs with 45-deg of angle-of-attack (Han et al., 1985, 1991; Park et al., 1992; Fann et al., 1994), this study investigated the cooling performance of skewed ribs in the reciprocating duct.

Heat Transfer Test Module

To perform reciprocating experiments, the heat transfer test module shown in Fig. 1 was installed onto a reciprocating facility that created the reciprocating motion of test module. Schematics of the reciprocating facility have been previously reported (Chang and Su, 1997). As shown in Fig. 1, the square-sectioned test duct (1) fitted with ten pairs of square skewed ribs at a regular downstream interval was made of bronze copper having a thermal conductivity of 50 W/mK at temperature 20°C. Only two opposite sides of the duct were rib-roughened. The skewed ribs with angle-of-attack of 45 deg were arranged in the opposite manner. The length and width of this test duct was 165 and 15 mm, respectively, with wall thickness of 1.5 mm.
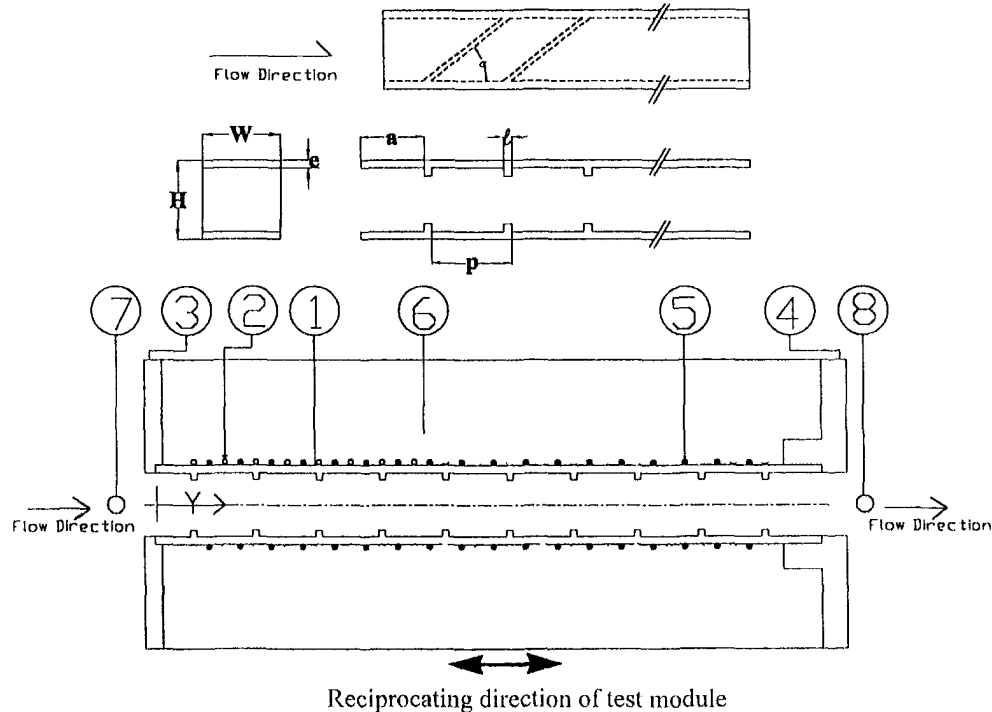
Copyright © 1999 by ASME

$$a/e = 10 \qquad e/d = 0.1$$
$$P/e = 10.0 \qquad H/W = 1.0$$
$$\ell/e = 1.0$$

$$\alpha \quad \text{(angle of attack)} = 45°$$

d : equivalent diameter of square duct = 15 mm

Reciprocating direction of test module

(1) Test duct
(2) Thermocouple for wall temperature
(3) Inlet cover
(4) Exit cover
(5) Ni/Cr resistance wire
(6) Thermal insulation
(7) Thermocouple for flow temperature at entrance
(8) Thermocouple for flow temperature at exit

Fig. 1 Constructional details of heat transfer test module

Geometric specifications of the test section are described in terms of five nondimensional groups defined in Fig. 1 as

smooth entry length/rib height (a/e) = 10.0
pitch/rib height ratio (P/e) = 10.0
rib height/hydraulic diameter ratio (e/d) = 0.1
land/rib height (l/e) = 1.0
aspect ratio (H/W) = 1.0

On a rib-roughened surface, eight type K thermocouples (2) with equal intervals were embedded with a 1 mm depth into the wall. The actual distance between each thermocouple and the fluid/wall interface was controlled at 0.5 mm. Test section unit, (1), was held by two end-covers, (3)(4), made of thermal insulation material, on both ends. For heating purposes, Ni/Cr resistance wire, (5), was spirally wound with a pitch of 2 mm on the outer surface of the test duct, (1). This arrangement created a basically uniform heat flux heating condition. To minimize the external heat loss, thermal insulation material, (6), was wrapped around the heated test section. Two additional

thermocouples, (7) (8), were located in the flow entrance and exit, respectively, in order to access the fluid temperature rise. All the instant temperature measurement signals were transferred to a DX 33 PC through a Fluke Hydra 2620A-100 data logger. The selected data were stored on the hard disk of a PC for subsequent data processing.

Experimental Details

To define the nondimensional groups that controlled the flow physics in a reciprocating duct, one feasible approach is to describe the flow equations relative to a reciprocating reference frame. For piston cooling application, the motion of the reciprocating frame of reference can be related to a position vector of the crank arm, $\mathbf{r}$, and the angular velocity vector of engine's shaft, $\boldsymbol{\omega}$, as $\boldsymbol{\omega} \times \mathbf{r}$, so that the reciprocation of piston motion could be simulated. The detailed derivation of the flow momentum equation using this approach can be referred to in Chang and Su (1997). As long as the fluid motion was referred to such a reciprocating reference frame, an additional body force

term induced by reciprocation arose naturally which affected the balance of fluid momentum and was responsible for the time-dependent heat transfer variation observed in the reciprocating ducted flow. In general, based on the aforementioned geometric and thermal boundary conditions described in Fig. 1, and if the temperature variation of coolant did not make a considerable change of coolant's Prandtl number, the nondimensional heat transfer relationship for forced convection in the reciprocating test duct was an equation of

$$\text{Nu} = \{\text{Re, Pu, }Y\}, \tag{1}$$

in which

$$\text{Nu} = q_f d/k_f \{T_w - T_f\} \quad \text{Nusselt number} \tag{2}$$

$$\text{Re} = W_m d/v \quad \text{Reynolds number} \tag{3}$$

$$\text{Pu} = \omega r/W_m \quad \text{pulsating number.} \tag{4}$$

In the equations above, q_f, d, k_f, W_m, and v represent the convective heat flux, hydraulic diameter of test duct, thermal conductivity of coolant, mean through flow velocity, and fluid kinematic viscosity, respectively. T_w and T_f, respectively, stand for wall and flow bulk temperatures.

It may be worth noting that, for such reciprocating flow, the pulsating number, Pu, defined in Eq. (4), provides an indication of the time-averaged force ratio between the reciprocating and convective inertial forces. As the effective reciprocating force periodically varies with time, the possible chaotic behavior of fluid motion and its consequent effect on heat transfer in a surface-roughened duct have been observed (Roberts and Mackley, 1996). Nevertheless, for the stationary forced convective tests, the pulsating number becomes zero, representing zero reciprocating effect. Although the Dittus-Boelter correlation (Dittus and Boelter, 1930) may not be perfectly valid for the Reynolds numbers tested by the present study, we normalize the reciprocating heat transfer results by the Dittus-Boelter correlation for convenient comparison and to realize the approximate beneficial cooling effect of a skewed rib for reciprocating duct flow. The Dittus-Boelter correlation reads

$$\text{Nu}_\infty = 0.023\text{Pr}^{0.4}\,\text{Re}^{0.8}. \tag{5}$$

The heat transfer tests were initially performed at nonreciprocating states with through flow Reynolds numbers varying from 2300–7270. It was consequently followed by the reciprocating tests. At each selected Reynolds number, the test module was reciprocated at four different frequencies, namely 0.42, 0.83, 1.25, and 1.66 Hz. For each individual test, the flow and heating level were fixed for about 30 min. in order to assure the flow reached an equilibrium state. Once such flow state was reached, the on-line data acquisition system would collect and store the instant data for a period of ten seconds. These data were subsequently processed into the dimensionless groups defined in Eq. (2).

An uncertainty approximation of the data reduction was conducted using the method described in JHT (1993). As the local properties of the coolant showing in Eqs. (2)–(4) were estimated from the fluid bulk temperature, one of the major sources to attribute uncertainty was the temperature measurement and the uncertainty in temperature measurement estimated to be $\pm 1°C$. The maximum percentages of error for the coolant's specific heat, mass flow rate and thermal conductivity, the temperature difference of wall-to-fluid, the hydraulic diameter of the test duct, and the heating area were estimated as ± 0.8 percent, ± 7 percent, ± 0.6 percent, ± 8 percent, ± 0.6 percent, and ± 1.5 percent, respectively. With the temperature difference between wall and fluid varied from 12 to 56°C, the maximum uncertainty for the Nusselt number was about 21 percent. For the Reynolds and pulsating numbers, their maximum uncertainties were estimated as 6 percent and 2 percent, respectively.

Results and Discussion

Stationary Results. A series of nonreciprocating heat transfer experiments were undertaken for benchmark validation of test section construction, instrumentation, and data processing methods. Figure 2 shows the normalized axial Nusselt number variations along the rib-roughened wall with which relevant available data from Park et al. (1992) and Fann et al. (1994) are compared for validation. General good agreement among the compared data is observed. As shown, for each axial station, the data collapse for the rib-roughened duct appears as a systematically downward data-spread when the Reynolds number is increased, indicating that the exponential relationship between the Nusselt and Reynolds numbers is no longer and less than 0.8 for the angled-rib flow (Han and Park, 1986). However, slight differences among the compared data are observed and attributed to the differences in the rib heights and the imperfect installation of thermocouples and heating elements. As the 45-deg angled ribs induce the secondary flows between ribs and break the laminar sublayer and enhance turbulence (Park et al., 1992; Fann et al., 1994), about a threefold improvement of heat transfer relative to the smooth-walled duct flow level can be achieved.

Reciprocating Results. Typical axial Nusselt number distributions along the test duct at nominal Reynolds numbers of 2400, 3725, 5250, 6250, and 7270, when the test duct reciprocates at frequency of 1.25, are shown in Fig. 3. With the reciprocating frequency fixed at 1.25 Hz, increasing the Reynolds number systematically results in a corresponding reduction of pulsating number. Thus the relative strength of reciprocating force involved gradually reduces from Fig. 3(a) to 3(e). When the reciprocating force was induced, the periodically time-dependent heat transfer variation at each measured spot was observed and the amplitude of such time-varied "oscillatory" Nusselt number values at each thermocouple station was plotted as a data bar with the time-averaged value to be marked as shown in Fig. 3. In each plot, the time-dependent Nusselt number ratio periodically varied at each measurement spot with relatively large variation span occurring at locations where the time-averaged heat transfer levels were relatively high. It was speculated that such an "oscillatory" reciprocating Nusselt number was a result of the chaotic advection for which the rib-associated eddies in the ribbing area were varied in a chaotic manner due to the addition of the periodical reciprocating force. As a result of such additional chaotic mixing, the transfer rates of flow momentum and heat near the wall could be further enhanced and, as a consequent effect, the larger variation span emerged at locations where the time-averaged heat transfer was relatively high due to strong chaotic advection. With Reynolds and pulsating numbers of 7270 and 3.99, respectively, the influence of reciprocation on heat transfer is not obvious when Fig. 2 and Fig. 3(e) are compared, although the temporal Nusselt number variations appear at several axial locations. Nevertheless, at $Y = 2.5$, Fig. 3 shows a locally high Nusselt number and this peak is also observed in stationary data shown in Fig. 2. Previously, Han et al. (1991) has reported this heat transfer increase due to the development of secondary flow caused by the angled ribs. When ribbed duct reciprocates, this peak does not diminish and shows to gradually increase with the pulsating number if Figs. 3(e) to 3(a) are compared. Therefore, this observation suggests that the co-existence of secondary flow and reciprocation could further enhance fluid mixing and heat transfer. However, with the pulsating number increased by reducing the Reynolds number at a fixed reciprocating frequency, the influence of reciprocation on heat transfer gradually emerges if Figs. 3(e) to 3(a) are examined. As an overall tendency, the time-averaged Nusselt number ratios increase with the increase of a pulsating number as shown in Fig. 3. Therefore, with the possible improvement in fluid mixing due to the increasing
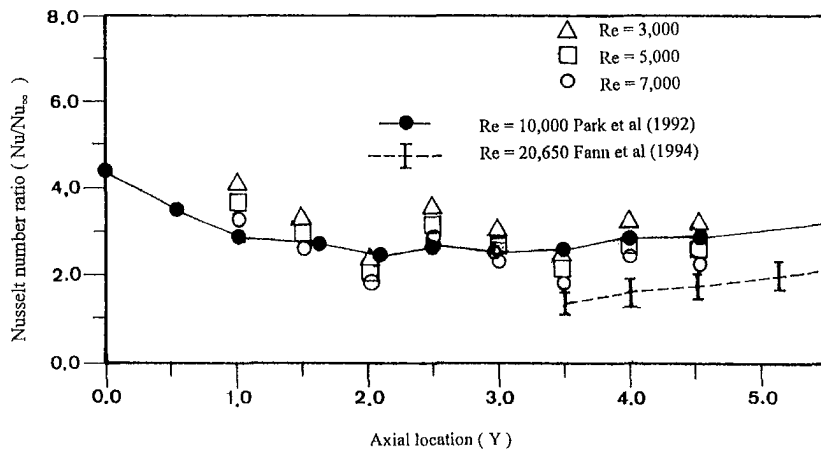
Fig. 2 Local Nusselt number ratios in the two-sided ribbed square channel with 45-deg angle of attack for ribs

strength of chaotic eddies created within the ribbing area, the Nusselt number ratios in a reciprocating ribbed duct increase.

Figure 2 suggests that the functional relationship between the Nusselt and Reynolds numbers may take an exponential relationship when the power index of the Reynolds number is less than 0.8. The increase of the reciprocating Nusselt number ratio, Nu/Nu_∞, shown in Fig. 3 due to the decrease of the Reynolds number at a fixed reciprocating frequency may partly result from the effect of the Reynolds number variation because the power index of the Reynolds number for Nu_∞ is 0.8. In

order to clarify the individual reciprocating effect on heat transfer, several tests were performed at a fixed Reynolds number while the reciprocating frequencies were systematically increased in order to increase the pulsating number. The net results of increasing the pulsating number with the Reynolds numbers controlled at 3725 and 6250 are shown in Figs. 4(a) and 4(b), respectively. In each plot, the axial distributions of time-averaged Nusselt number ratios are plotted for three different pulsating numbers. As shown in Figs. 4(a) and 4(b), for each fixed Reynolds number, a systematic heat transfer increment due to the increase of the pulsating number is observed. The axially averaged reciprocating Nusselt number shown in Fig. 4(a) could reach about four times the Dittus-Boelter correlation value. Such heat transfer enhancement could be attributed to the effects of reciprocation on the flow field near the wall which improve the fluid mixing via the chaotic eddies formulated around the ribs (Roberts and Mackley, 1996). However, the overall patterns of axial distributions of the Nusselt number ratio in these plots do not vary. Therefore the increasing strength of the reciprocating force may not alter the dominant flow physics that facilitate heat convection and can further enhance heat transfer. Comparison with Figs. 4(a) and 4(b) suggests that the higher Nusselt number ratios in terms of Nu/Nu_∞ occur when the Reynolds number is relatively low. Thus the influence
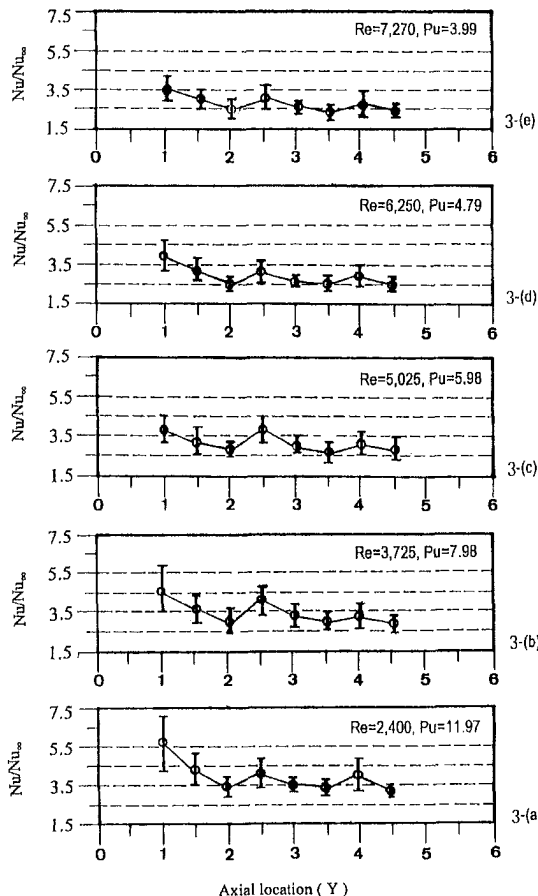

Fig. 3 Typically axial distributions of Nusselt number ratio at reciprocating frequency of 1.25 Hz
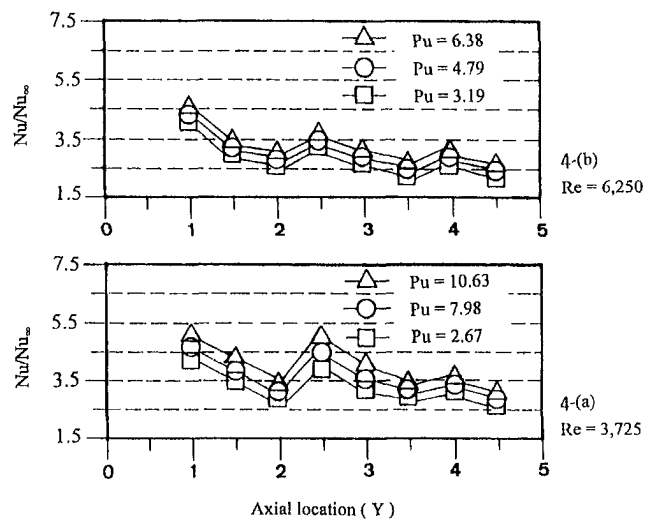

Fig. 4 Axial distributions of time-averaged Nusselt number ratio for Reynolds numbers of 6250 and 3725 with different pulsating numbers

Journal of Heat Transfer

of reciprocation on heat transfer is Reynolds number dependent and there are considerable coupling effects between the Reynolds and pulsating numbers on heat transfer. Nevertheless, as the heat transfer is improved by this artificial rib roughness and can be further enhanced when the duct reciprocates, the use of skewed ribs within the cooling passages of a reciprocating piston could be an effective way for heat transfer enhancement.

Conclusion

The skewed ribs with 45 deg of angle-of-attack result in significant heat transfer enhancement due to their influences on the flow field near the wall. For a stationary duct fitted with the skewed ribs, the Nusselt numbers could be increased up to about three times that of the smooth-walled values. When the rib-roughened duct was reciprocating, the periodically time-varied Nusselt number was found at each axial spot. The larger variation spans occur at locations where the time-averaged Nusselt numbers are relatively high. This particular reciprocating result suggests the possible chaotic advection for the flow field among the ribbing area. The heat transfer rates were increased with the increases of a pulsating number for flows with a fixed Reynolds number. However, the influences of reciprocating force on heat transfer revealed by the variations of pulsating numbers depend on the value of Reynolds number so that the coupling effects of convective inertial and reciprocating forces on heat transfer are demonstrated. With the addition of the beneficial effect of chaotic advection on heat transfer within this rib-roughened reciprocating duct, the adoption of roughened coolant passages fitted with skewed ribs can be a feasible approach for heat transfer enhancement within a piston.

References

Chang, S. W., and Su, L. M., 1996, "Heat transfer of pulsating flow with application of piston cooling for marine diesel engine," *Proceedings of 9th conference on naval architects and marine engineering,* Taipei, Taiwan, R.O.C., Nov. 22–23, pp. 344–351.

Chang, S. W., and Su, L. M., 1997, "Influence of reciprocating motion on heat transfer inside ribbed duct with application to piston cooling in marine diesel engine," *Journal of Ship Research,* Vol. 41, No. 4, pp. 332–339.

Dittus, F. W., and Boelter, L. M. K., 1930; *Calif. Pubs., Engng.,* Vol. 2, p. 443.

Fann, S., Yang, W. J., and Zhang, N., 1994, "Local heat transfer in a rotating serpentine passage with rib-roughened surfaces," *Int. J. Heat Mass Transfer,* Vol. 37, No. 2, pp. 217–228.

Ghaddar, N. K., Magen, M., Mikic, B. B., and Patera, A. T., 1986, "Numerical investigation of incompressible flow in grooved channels. Part 2. Resonance and oscillatory heat-transfer enhancement," *J. Fluid Mech.,* Vol. 168, pp. 541–567.

Greiner, M., 1991, "An experimental investigation of resonant heat transfer enhancement in grooved channels," *Int. J. Heat Mass Transfer,* Vol. 34, No. 6, pp. 1383–1391.

Han, J. C., Park, J. S., and Lei, C. K., 1985, "Heat Transfer Enhancement in Channels With Rib Turbulence Promoter," ASME *Journal of Engineering for Gas Turbine and Power,* Vol. 107, pp. 629–635.

Han, J. C., and Park, J. S., 1986, "Measurement of heat transfer and pressure drop in rectangular channels with turbulence promoters," NASA contract report 4015.

Han, J. C., Zhang, Y. M., and Lee, C. P., 1991, "Augmented Heat Transfer in Square Channels With Parallel, Crossed, and V-Shaped Angle Ribs," ASME JOURNAL OF HEAT TRANSFER, Vol. 113, pp. 590–596.

JHT Editorial Board of ASME J. Heat Transfer, 1993, "Journal of Heat Transfer Policy on Reporting Uncertainties in Experimental Measurements and Results," ASME JOURNAL OF HEAT TRANSFER, Vol. 115, pp. 5–6.

Nishimura, T., Taurmoto, A., and Kawamura, Y., 1987, "Flow and mass transfer characteristics in wavy channels for oscillatory flow," *Int. J. Heat Mass Transfer,* Vol. 30, pp. 1007–1015.

Park, J. S., Han, J. C., Hung, Y., and Ou, S., 1992, "Heat transfer performance comparisons of five different rectangular channels with parallel angled ribs," *Int. J. Heat Mass Transfer,* Vol. 35, No. 11, pp. 2891–2903.

Ralph, M. E., 1986, "Oscillatory flows in wavy-walled tubes," *J. Fluid Mech.,* Vol. 168, pp. 515–540.

Roberts, E. P. L., and Mackley, M. R., 1996, "The development of asymmetry and period coupling for oscillatory flow in baffled channels," *J. Fluid Mech.,* Vol. 328, pp. 19–48.

Correlation of Fully Developed Heat Transfer and Pressure Drop in a Symmetrically Grooved Channel

R. A. Wirtz,[1] F. Huang,[2] and M. Greiner[2]

Nomenclature

a = groove depth
D_h = minimum hydraulic diameter
f_G, f_F = grooved and flat channel friction factor
H = channel height
j_G, j_F = grooved and flat channel Colburn j-factor
$\dot{m}$ = mass flow rate
$\underline{\text{Nu}}$ = local Nusselt number, Eq. (2)
$\overline{\text{Nu}}$ = groove-average Nusselt number
Pr = Prandtl number
∇p = pressure gradient
Re = Reynolds number
T_c = channel centerline temperature
T_s = surface temperature
∇T = temperature gradient $\perp$ to surface
V = fluid velocity
W = channel width
x = groove wall coordinate
μ = viscosity
ρ = density

Introduction

Compact heat exchangers invariably incorporate heat transfer augmentation technology at the fluid-solid interface. Geometric modification of the passage walls can be used to modify the core flow and give rise to an increase in surface conductance. Spatially periodic disturbance promoters, such as a series of transverse grooves cut into a channel wall, destabilize Tolmein-Schlichting waves, leading to a self-sustained two-dimensional oscillatory flow at a Reynolds number of approximately 350. A subsequent transition to three-dimensional unsteady flow at Reynolds numbers greater than 700, accompanied by an increase in both the surface conductance and the pressure drop, has been demonstrated by Greiner et al. (1997).

The present investigation is concerned with symmetrically heated parallel-plate channels having a series of transverse V-grooves formed in both walls. Pressure drop and local heat flux measurements are reported for fully developed flow in a channel having an aspect ratio of 20.4:1 for the Reynolds number range: $800 \leq Re \leq 5000$. Grooved-channel performance characteristics are compared to equivalent measurements made in fully developed flow in a flat channel having the same hydraulic diameter. A more detailed description of test apparatus, measurement procedures, error analysis, and results described in this note is found in Wirtz et al. (1997).

of reciprocation on heat transfer is Reynolds number dependent and there are considerable coupling effects between the Reynolds and pulsating numbers on heat transfer. Nevertheless, as the heat transfer is improved by this artificial rib roughness and can be further enhanced when the duct reciprocates, the use of skewed ribs within the cooling passages of a reciprocating piston could be an effective way for heat transfer enhancement.

Conclusion

The skewed ribs with 45 deg of angle-of-attack result in significant heat transfer enhancement due to their influences on the flow field near the wall. For a stationary duct fitted with the skewed ribs, the Nusselt numbers could be increased up to about three times that of the smooth-walled values. When the rib-roughened duct was reciprocating, the periodically time-varied Nusselt number was found at each axial spot. The larger variation spans occur at locations where the time-averaged Nusselt numbers are relatively high. This particular reciprocating result suggests the possible chaotic advection for the flow field among the ribbing area. The heat transfer rates were increased with the increases of a pulsating number for flows with a fixed Reynolds number. However, the influences of reciprocating force on heat transfer revealed by the variations of pulsating numbers depend on the value of Reynolds number so that the coupling effects of convective inertial and reciprocating forces on heat transfer are demonstrated. With the addition of the beneficial effect of chaotic advection on heat transfer within this rib-roughened reciprocating duct, the adoption of roughened coolant passages fitted with skewed ribs can be a feasible approach for heat transfer enhancement within a piston.

References

Chang, S. W., and Su, L. M., 1996, "Heat transfer of pulsating flow with application of piston cooling for marine diesel engine," *Proceedings of 9th conference on naval architects and marine engineering,* Taipei, Taiwan, R.O.C., Nov. 22–23, pp. 344–351.

Chang, S. W., and Su, L. M., 1997, "Influence of reciprocating motion on heat transfer inside ribbed duct with application to piston cooling in marine diesel engine," *Journal of Ship Research,* Vol. 41, No. 4, pp. 332–339.

Dittus, F. W., and Boelter, L. M. K., 1930; *Calif. Pubs., Engng.,* Vol. 2, p. 443.

Fann, S., Yang, W. J., and Zhang, N., 1994, "Local heat transfer in a rotating serpentine passage with rib-roughened surfaces," *Int. J. Heat Mass Transfer,* Vol. 37, No. 2, pp. 217–228.

Ghaddar, N. K., Magen, M., Mikic, B. B., and Patera, A. T., 1986, "Numerical investigation of incompressible flow in grooved channels. Part 2. Resonance and oscillatory heat-transfer enhancement," *J. Fluid Mech.,* Vol. 168, pp. 541–567.

Greiner, M., 1991, "An experimental investigation of resonant heat transfer enhancement in grooved channels," *Int. J. Heat Mass Transfer,* Vol. 34, No. 6, pp. 1383–1391.

Han, J. C., Park, J. S., and Lei, C. K., 1985, "Heat Transfer Enhancement in Channels With Rib Turbulence Promoter," ASME *Journal of Engineering for Gas Turbine and Power,* Vol. 107, pp. 629–635.

Han, J. C., and Park, J. S., 1986, "Measurement of heat transfer and pressure drop in rectangular channels with turbulence promoters," NASA contract report 4015.

Han, J. C., Zhang, Y. M., and Lee, C. P., 1991, "Augmented Heat Transfer in Square Channels With Parallel, Crossed, and V-Shaped Angle Ribs," ASME JOURNAL OF HEAT TRANSFER, Vol. 113, pp. 590–596.

JHT Editorial Board of ASME J. Heat Transfer, 1993, "Journal of Heat Transfer Policy on Reporting Uncertainties in Experimental Measurements and Results," ASME JOURNAL OF HEAT TRANSFER, Vol. 115, pp. 5–6.

Nishimura, T., Taurmoto, A., and Kawamura, Y., 1987, "Flow and mass transfer characteristics in wavy channels for oscillatory flow," *Int. J. Heat Mass Transfer,* Vol. 30, pp. 1007–1015.

Park, J. S., Han, J. C., Hung, Y., and Ou, S., 1992, "Heat transfer performance comparisons of five different rectangular channels with parallel angled ribs," *Int. J. Heat Mass Transfer,* Vol. 35, No. 11, pp. 2891–2903.

Ralph, M. E., 1986, "Oscillatory flows in wavy-walled tubes," *J. Fluid Mech.,* Vol. 168, pp. 515–540.

Roberts, E. P. L., and Mackley, M. R., 1996, "The development of asymmetry and period coupling for oscillatory flow in baffled channels," *J. Fluid Mech.,* Vol. 328, pp. 19–48.

Correlation of Fully Developed Heat Transfer and Pressure Drop in a Symmetrically Grooved Channel

R. A. Wirtz,[1] F. Huang,[2] and M. Greiner[2]

Nomenclature

a = groove depth
D_h = minimum hydraulic diameter
f_G, f_F = grooved and flat channel friction factor
H = channel height
j_G, j_F = grooved and flat channel Colburn j-factor
$\dot{m}$ = mass flow rate
Nu = local Nusselt number, Eq. (2)
$\overline{\mathrm{Nu}}$ = groove-average Nusselt number
Pr = Prandtl number
∇p = pressure gradient
Re = Reynolds number
T_c = channel centerline temperature
T_s = surface temperature
∇T = temperature gradient $\perp$ to surface
V = fluid velocity
W = channel width
x = groove wall coordinate
μ = viscosity
ρ = density

Introduction

Compact heat exchangers invariably incorporate heat transfer augmentation technology at the fluid-solid interface. Geometric modification of the passage walls can be used to modify the core flow and give rise to an increase in surface conductance. Spatially periodic disturbance promoters, such as a series of transverse grooves cut into a channel wall, destabilize Tolmein-Schlichting waves, leading to a self-sustained two-dimensional oscillatory flow at a Reynolds number of approximately 350. A subsequent transition to three-dimensional unsteady flow at Reynolds numbers greater than 700, accompanied by an increase in both the surface conductance and the pressure drop, has been demonstrated by Greiner et al. (1997).

The present investigation is concerned with symmetrically heated parallel-plate channels having a series of transverse V-grooves formed in both walls. Pressure drop and local heat flux measurements are reported for fully developed flow in a channel having an aspect ratio of 20.4:1 for the Reynolds number range: $800 \leq \mathrm{Re} \leq 5000$. Grooved-channel performance characteristics are compared to equivalent measurements made in fully developed flow in a flat channel having the same hydraulic diameter. A more detailed description of test apparatus, measurement procedures, error analysis, and results described in this note is found in Wirtz et al. (1997).
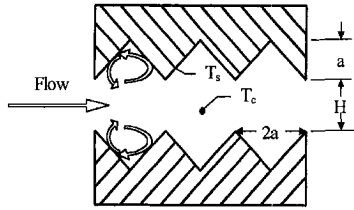
Fig. 1 Grooved channel geometry

Grooved-Channel Characterization

The groove-channel geometry under consideration is shown in Fig. 1. Grooves are symmetrically placed in the channel walls and they span the width of the channel. Each groove is right-triangular with depth, a, and opening $2a$. The channel wall-to-wall spacing is H, and the channel width (perpendicular to the plane of the figure) is W. The channel walls are symmetrically heated to a uniform temperature T_s, and T_c is the temperature at the centerline of the channel, opposite the vertices of two opposing grooves. This work is concerned with flow sufficiently far from the channel entrance or exit that the convection processes are fully developed in a groove-periodic sense. The flow rate in the channel is characterized in terms of channel Reynolds number

$$\text{Re} = \frac{\rho V D_h}{\mu} = \frac{2\dot{m}}{\mu(H + W)}, \tag{1}$$

where $D_h = 2HW/(H + W)$ is the minimum hydraulic diameter of the grooved channel, $V = \dot{m}/(\rho HW)$, and ρ, μ are the fluid density and viscosity, respectively. All properties are evaluated at the channel inlet condition.

Experiments were conducted in two open-circuit flow channels. Each channel consists of a grooved section followed by a long flat-walled section. Measurements were made in both sections so that grooved-channel performance could be compared to flat-channel performance at the same flow conditions. The larger channel ($a = 12.0 \pm 0.1$ mm, $H = 10.0 \pm 0.3$ mm, $W/H = 20.4$ mm), with seven V-grooves located in each wall, was used for heat transfer measurements. Arrays of individually powered microfoil heaters maintained each wall of the channel isothermal to within $\pm 0.4°C$. Fluid temperature measurements were made with a holographic interferometer operated in real-time mode (Vest, 1979). Measurements were made with the optical axis of the device aligned transverse to the mean flow giving rise to cross-span average values. Data was collected at the sixth groove, and in the flat-walled section 52 D_h downstream from the end of the grooved section. Interferograms were captured with a 600-line video camera and frame-grabber and analyzed using an image processing system (McAuliffe and Wirtz, 1991). The local temperature gradient perpendicular to each groove face, $\nabla T(0)$, was estimated using a second-order finite-difference approximation. The local Nusselt number based on wall-to-centerline temperature difference was then computed as

$$\text{Nu} = \frac{-\nabla T(0)D_h}{T_s - T_c}. \tag{2}$$

The Colburn j-factor in the flat-walled section is then given as

$$j_F = \frac{\text{Nu}}{\text{Re Pr}^{1/3}}. \tag{3}$$

The average Nusselt number along the groove faces, $\overline{\text{Nu}}$, was calculated by trapezoid rule integration. Then the Colburn j-factor for each groove, *based on* $(T_s - T_c)$ *and the projected area of the groove opening* $(2aW)$ is

$$j_G = \sqrt{2} \frac{\overline{\text{Nu}}}{\text{Re Pr}^{1/3}}. \tag{4}$$

The small test channel, which is used for pressure drop measurements, is $\frac{1}{4}$th scale of the large unit. It has 13 groove pairs in the grooved section. Pressure taps located along the centerline of one wall are used to measure the pressure gradient. A least-squares fit of the linear part of the pressure distribution gives the fully developed pressure gradient, $\nabla p|_{f.d.}$, and the grooved channel friction factor is computed as

$$f_G = \frac{-\nabla p|_{f.d.}D_h}{2\rho V^2}. \tag{5}$$

A similar analysis of the pressure gradient in the flat-walled section of the channel gives f_F.

A Monte Carlo technique was used to assess experimental error (Huang, 1998). The analysis shows that the 99 percent confidence level expected error in reported Reynolds numbers is less than 7.1 percent at the lowest flow rates; and these values decrease to less than one percent at Re > 2400. The error for the Colburn j-factor is less than seven percent for Re > 1000; it equals 15 percent at Re = 800. The error in friction factor ranges from approximately 15 percent at the lowest flow rates to less than five percent at high Reynolds numbers.

Results

Measured values of f_G and f_F as a function of Re are plotted in Fig. 2. The measured results (filled and open circles) are compared to the laminar result for flow between parallel plates, and a turbulent correlation for flow in a tube having the same hydraulic diameter (solid lines) (Kakac et al., 1987).

$$f_F = \frac{24}{\text{Re}} \tag{6}$$

$$f_F = 0.00128 + 0.1143 \, \text{Re}^{-0.311} \tag{7}$$

For the purposes of comparison, these two correlations have each been extended to their intersection point, which occurs at Re = 1914. Also shown in the figure are recent computational results for the same grooved-channel geometry (Greiner et al., 1997, open diamond symbols).

The flat-channel experimental results are in reasonable agreement with Eqs. (6) and (7). These measurements lay approximately ten percent above the correlations. This may be due to experimental offset error, or it may be due to residual mixing in the flow from the (upstream) grooved section.
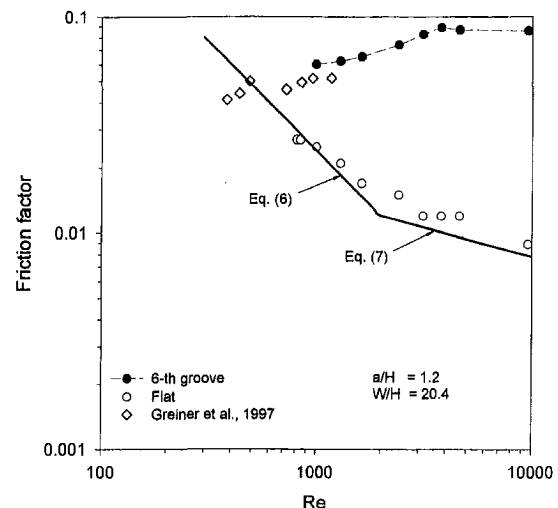

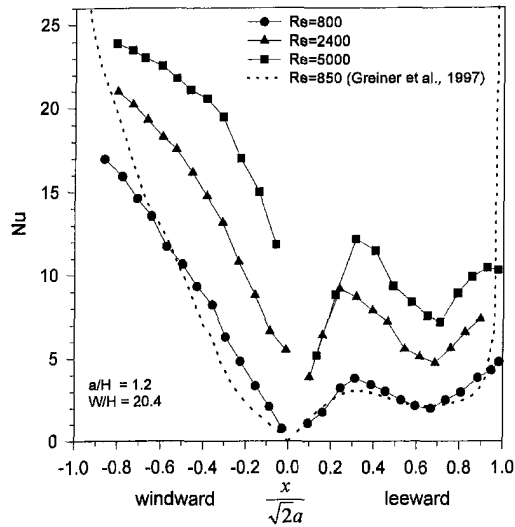**Fig. 2 Grooved and flat-channel friction factor**

Fig. 3 Local Nusselt number on grooved surface

Fig. 4 Grooved and flat-channel Colburn j-factor

Where results overlap, the grooved section measurements are about 15 percent higher then the direct numerical simulation results. This may be due to the above mentioned potential offset error, or differences between the conditions of the experiment and the simulations. For example, the simulation imposes a constant pressure gradient across a single groove pair, resulting in a time-varying channel Reynolds number. On the other hand, the experimental facility (consisting of a 1-meter long channel, blower and duct work) is observed to have a steady mean flow. Figure 2 shows that the measured grooved-channel friction factor increases to a maximum value at Re $\approx$ 3800, and then it decreases slightly as Re $\to 10^4$.

The local groove surface Nusselt number for Re = 800, 2400, and 4800 is shown in Fig. 3. Nu is plotted versus nondimensional position measured from the vertex of the groove, $x/\sqrt{2}a$. Also shown in the figure is a computational result for Re = 850 (Greiner et al., 1997, dashed line). The local Nusselt number on the windward groove face ($x/\sqrt{2}a < 0$) is seen to be minimum near the vertex of the groove and increase towards the groove opening. The heat flux along the leeward groove face is considerably smaller than that observed along the windward face. It is minimum near the groove vertex and increases to a local maximum at $x/\sqrt{2}a \approx 0.3$. This is due to a second impingement of flow as it recirculates within the groove (see sketch of fluid path lines in Fig. 1). The heat flux then passes through another local minimum and increases again near $x/\sqrt{2}a = +1$.

The measurements at Re = 800 are in reasonably good agreement with the numerical simulation (Re = 850) except near the groove-tips where the data generally levels off as $x/\sqrt{2}a \to \pm1$ whereas the numerical simulation predicts Nu(±1) $\to \infty$. As a consequence, experimentally determined estimates of overall heat transfer coefficient will be lower than those predicted by the numerical code.

Measured fully developed grooved and flat-channel Colburn j-factors (j_G and j_F, respectively) are compared in Fig. 4. The flat-channel measurements are obtained 52 D_h downstream from the grooved section where it is thought that groove-induced mixing has dissipated. Also shown in the figure are computational results of Greiner et al. (1997), and the laminar result for flow between parallel plates,

$$j_F = \frac{5.86}{\text{Re Pr}^{1/3}} \cdot \qquad (8)$$
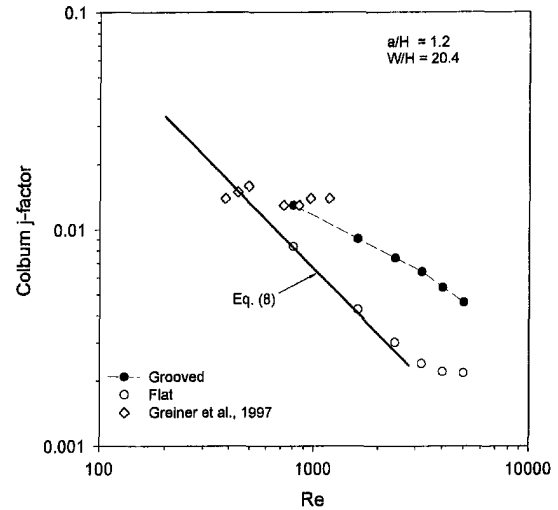
Note in Eq. (8), the coefficient is 5.86 instead of the expected

value, 7.54, since j_F is based on the temperature difference ($T_s - T_c$), rather than the wall surface-to-bulk fluid temperature difference.

The flat-channel measurements are in almost identical agreement with Eq. (8) at Re = 800, and they reside increasingly above Eq. (8) as the Reynolds number increases toward the transition point. This may be due to residual grooved-induced mixing in the flow. At Re > 2400, there is a transition in j_F which is suggestive of transition toward turbulence.

The groove-section measurements at Re = 800 are in good agreement with the simulation results of Greiner et al. This may be somewhat coincidental since our pressure profile measurements indicate that at this Reynolds number, the flow is probably not fully developed. However, it is not known whether this would result in an increase or decrease in measured j-factor. Extrapolation of the present experimental result suggests that j_G is greater than j_F for Re $\gtrsim$ 450, in agreement with the simulation. There is a continuous decrease in j_G as Re increases, and it appears that j_G will approach j_F (resulting in no heat transfer augmentation) as Re increases beyond a value of about 10,000.

Table 1 summarizes measured values of f_G and j_G. Note, the second reported j-factor value at Re = 2400 is measured in the 5th groove. The close agreement with the 6th groove value and pressure profile measurements at Re = 1294 (reported in Wirtz et al., 1997) tend to confirm that the flow at Re $\geq$ 1300 is fully developed.

Conclusions

Air flows at Re $\geq$ 1300 in symmetrically V-grooved channels become fully developed, in a groove-periodic sense, after roughly four groove-pairs, and the fully developed character of the flow maintains to the last groove-pair in the series. Thin

Table 1   Summary of f_G and j_G at sixth groove-pair

Reynolds No., Re	Friction factor, f	Reynolds No., Re	Colburn j-factor, j_G
996	0.060	800	0.0130
1294	0.062		
1625	0.065	1600	0.0091
2411	0.074	2400	0.0074
		2400	$0.0071_{5\text{-th}}$
3134	0.083	3200	0.0064
3814	0.089	4000	0.0054
4627	0.087	5000	0.0046
9991	0.086		

thermal boundary layers form adjacent to groove faces, and the heat flux distribution is nonuniform with a minimum at the vertex of each groove. The Nusselt number of the windward face is approximately twice that of the leeward face. The fully developed j-factor, j_G, becomes greater than equivalent flat channel values when $Re > 450$, and it appears that heat transfer augmentation is maintained to $Re \approx 10^4$.

References

Greiner, M., Faulkner, R. J., Fischer, P. F., and Wirtz, R. A., 1997, "Direct Numerical Simulation Of Three-Dimensional Flow And Heat Transfer In A Symmetrically Grooved Channel With Constant Temperature Walls," ASME-HTD Vol. 353-3, pp. 269–276.

Huang, F., 1998, "Experimental Investigation of Fully-Developed Augmented Convection in a Symmetrically Grooved Channel," M.S. thesis, Mechanical Engineering Department, University of Nevada, Reno, NV.

Kakac, S., Shah, R. K., and Aung, W., 1987, Handbook of Single Phase Heat Transfer, John Wiley and Sons, New York.

McAuliffe, W., and Wirtz, R. A., 1991, "Application of On-Line Image Analysis to Local Heat Transfer Measurements," Fundamental Experimental Measurements in Heat Transfer, ASME HTD-Vol. 179, pp. 1–7.

Vest, C. M., 1979, Holographic Interferometry, John Wiley and Sons, New York.

Wirtz, R. A., Huang, F., and Greiner, M., 1997, "Measurements of Fully-Developed Augmented Convection in a Symmetrically Grooved Channel," ASME-HTD Vol. 353-3, pp. 29–35.

Radiation Heat Transfer in Multitube, Alkali-Metal Thermal-to-Electric Converter

J.-M. P. Tournier[1] and M. S. El-Genk[1,2]

Introduction

Vapor anode, multitube Alkali-Metal Thermal-to-Electric Converters (AMTECs) are being considered for a number of space missions, such as the NASA Pluto/Express (PX) and Europa missions, scheduled for the years 2004 and 2005, respectively. These static converters can achieve a high fraction of Carnot efficiency at relatively low operating temperatures. An optimized cell can potentially provide a conversion efficiency between 20 and 30 percent, when operated at a hot-side temperature of 1000–1200 K and a cold-side temperature of 550–650 K. A comprehensive modeling and testing program of vapor anode, multitube AMTEC cells has been underway for more than three years at the Air Force Research Laboratory's Power and Thermal Group (AFRL/VSDVP), jointly with the University of New Mexico's Institute for Space and Nuclear Power Studies. The objective of this program is to demonstrate the readiness of AMTECs for flight on future U.S. Air Force space missions.

[1] Institute for Space and Nuclear Power Studies, Department of Chemical and Nuclear Engineering, University of New Mexico, Albuquerque, NM 87131.

[2] Mem. ASME. To whom all correspondence should be addressed. e-mail: mgenk@unm.edu.

Nomenclature

A_{bk} = radiative back face of solid element k
A_{fk} = radiative front face of solid element k
F_{kp} = radiation view factor between surfaces A_k and A_p
I = total cell electrical current (A)
N = number of axial sections along BASE tubes
N_c = number of axial sections along standoff
N_R = total number of radiant surface areas
N_S = total number of solid elements (nodes)
N_{sh} = number of axial sections along shield
N_w = number of axial sections along artery
P_e = cell electrical power output (W_e)
q = heat flux (W/m^2)
Q = heat flow (W)
R_L = external load resistance (Ω)
R_w = inner radius of cell (m)
T = temperature (K)
T' = temperature correction vector (K)
T^* = best estimate of temperatures (K)

Greek

β_k = flag, $\beta_k = 1$ if element k has a radiative back face, $\beta_k = 0$ otherwise
δ_{kp} = Kronecker delta, $\delta_{kp} = 1$ if $k = p$, $\delta_{kp} = 0$ otherwise
ϵ_k = total emissivity of surface A_k
σ = Stefan-Boltzmann constant, $\sigma = 5.67 \times 10^{-8}$ W/m$^2 \cdot$K^4
φ_k = flag, $\varphi_k = 1$ if element k has a radiative front face, $\varphi_k = 0$ otherwise

Subscripts and Superscripts

air = air calorimeter
cond = condenser
hot = hot end
in = incident/input
loss = net radiant loss
out = outgoing
rods = alumina rods supporting the cell's cold plate

A fast, integrated AMTEC Performance and Evaluation Analysis Model (APEAM) has been developed to support ongoing vacuum tests at AFRL and perform analyses and investigate potential design changes to improve the PX-cell performance. This model consists of three major components (Tournier and El-Genk 1998a, b): (a) a sodium vapor pressure loss model, which describes continuum, transition and free-molecule flow regimes in the low-pressure cavity of the cell; (b) an electrochemical and electrical circuit model; and (c) a radiation/conduction heat transfer model, for calculating parasitic heat losses. This Technical Note describes the methodology used to calculate the radiation view factors within the enclosure of the PX-cells (Fig. 1), and the numerical procedure developed in this work to determine the radiation heat transport and temperatures within the cell cavity.

Description of PX-Series, Vapor Anode, Multitube AMTEC Cell

A vapor anode, multitube AMTEC (Fig. 1) is a regenerative concentration cell, in which sodium vapor expansion through the Beta"-Alumina Solid Electrolyte (BASE) is directly converted into electricity. The BASE, whose ionic conductivity is much larger than its electronic conductivity, separates the hot (high sodium vapor pressure) region from the colder (low sodium vapor pressure) region. The PX cells had either 5, 6, or 7 BASE tubes each. The BASE tubes, connected electrically in series, are brazed to a stainless steel support plate. Their low-pressure (cathode) and high-pressure (anode) sides are covered with TiN porous electrodes and molybdenum mesh current collectors. Sodium vapor ions diffuse through the BASE, while

thermal boundary layers form adjacent to groove faces, and the heat flux distribution is nonuniform with a minimum at the vertex of each groove. The Nusselt number of the windward face is approximately twice that of the leeward face. The fully developed j-factor, j_G, becomes greater than equivalent flat channel values when Re > 450, and it appears that heat transfer augmentation is maintained to Re $\approx 10^4$.

References

Greiner, M., Faulkner, R. J., Fischer, P. F., and Wirtz, R. A., 1997, "Direct Numerical Simulation Of Three-Dimensional Flow And Heat Transfer In A Symmetrically Grooved Channel With Constant Temperature Walls," ASME-HTD Vol. 353-3, pp. 269–276.

Huang, F., 1998, "Experimental Investigation of Fully-Developed Augmented Convection in a Symmetrically Grooved Channel," M.S. thesis, Mechanical Engineering Department, University of Nevada, Reno, NV.

Kakac, S., Shah, R. K., and Aung, W., 1987, Handbook of Single Phase Heat Transfer, John Wiley and Sons, New York.

McAuliffe, W., and Wirtz, R. A., 1991, "Application of On-Line Image Analysis to Local Heat Transfer Measurements," Fundamental Experimental Measurements in Heat Transfer, ASME HTD-Vol. 179, pp. 1–7.

Vest, C. M., 1979, Holographic Interferometry, John Wiley and Sons, New York.

Wirtz, R. A., Huang, F., and Greiner, M., 1997, "Measurements of Fully-Developed Augmented Convection in a Symmetrically Grooved Channel," ASME-HTD Vol. 353-3, pp. 29–35.

Radiation Heat Transfer in Multitube, Alkali-Metal Thermal-to-Electric Converter

J.-M. P. Tournier[1] and M. S. El-Genk[1,2]

Introduction

Vapor anode, multitube Alkali-Metal Thermal-to-Electric Converters (AMTECs) are being considered for a number of space missions, such as the NASA Pluto/Express (PX) and Europa missions, scheduled for the years 2004 and 2005, respectively. These static converters can achieve a high fraction of Carnot efficiency at relatively low operating temperatures. An optimized cell can potentially provide a conversion efficiency between 20 and 30 percent, when operated at a hot-side temperature of 1000–1200 K and a cold-side temperature of 550–650 K. A comprehensive modeling and testing program of vapor anode, multitube AMTEC cells has been underway for more than three years at the Air Force Research Laboratory's Power and Thermal Group (AFRL/VSDVP), jointly with the University of New Mexico's Institute for Space and Nuclear Power Studies. The objective of this program is to demonstrate the readiness of AMTECs for flight on future U.S. Air Force space missions.

[1] Institute for Space and Nuclear Power Studies, Department of Chemical and Nuclear Engineering, University of New Mexico, Albuquerque, NM 87131.

[2] Mem. ASME. To whom all correspondence should be addressed. e-mail: mgenk@unm.edu.

Nomenclature

A_{bk} = radiative back face of solid element k
A_{fk} = radiative front face of solid element k
F_{kp} = radiation view factor between surfaces A_k and A_p
I = total cell electrical current (A)
N = number of axial sections along BASE tubes
N_c = number of axial sections along standoff
N_R = total number of radiant surface areas
N_S = total number of solid elements (nodes)
N_{sh} = number of axial sections along shield
N_w = number of axial sections along artery
P_e = cell electrical power output (W_e)
q = heat flux (W/m^2)
Q = heat flow (W)
R_L = external load resistance (Ω)
R_w = inner radius of cell (m)
T = temperature (K)
T' = temperature correction vector (K)
T^* = best estimate of temperatures (K)

Greek

β_k = flag, $\beta_k = 1$ if element k has a radiative back face, $\beta_k = 0$ otherwise
δ_{kp} = Kronecker delta, $\delta_{kp} = 1$ if $k = p$, $\delta_{kp} = 0$ otherwise
ϵ_k = total emissivity of surface A_k
σ = Stefan-Boltzmann constant, $\sigma = 5.67 \times 10^{-8}$ W/$m^2 \cdot K^4$
φ_k = flag, $\varphi_k = 1$ if element k has a radiative front face, $\varphi_k = 0$ otherwise

Subscripts and Superscripts

air = air calorimeter
cond = condenser
hot = hot end
in = incident/input
loss = net radiant loss
out = outgoing
rods = alumina rods supporting the cell's cold plate

A fast, integrated AMTEC Performance and Evaluation Analysis Model (APEAM) has been developed to support ongoing vacuum tests at AFRL and perform analyses and investigate potential design changes to improve the PX-cell performance. This model consists of three major components (Tournier and El-Genk 1998a, b): (a) a sodium vapor pressure loss model, which describes continuum, transition and free-molecule flow regimes in the low-pressure cavity of the cell; (b) an electro-chemical and electrical circuit model; and (c) a radiation/conduction heat transfer model, for calculating parasitic heat losses. This Technical Note describes the methodology used to calculate the radiation view factors within the enclosure of the PX-cells (Fig. 1), and the numerical procedure developed in this work to determine the radiation heat transport and temperatures within the cell cavity.

Description of PX-Series, Vapor Anode, Multitube AMTEC Cell

A vapor anode, multitube AMTEC (Fig. 1) is a regenerative concentration cell, in which sodium vapor expansion through the Beta"-Alumina Solid Electrolyte (BASE) is directly converted into electricity. The BASE, whose ionic conductivity is much larger than its electronic conductivity, separates the hot (high sodium vapor pressure) region from the colder (low sodium vapor pressure) region. The PX cells had either 5, 6, or 7 BASE tubes each. The BASE tubes, connected electrically in series, are brazed to a stainless steel support plate. Their low-pressure (cathode) and high-pressure (anode) sides are covered with TiN porous electrodes and molybdenum mesh current collectors. Sodium vapor ions diffuse through the BASE, while

Fig. 1(a)

Fig. 1(b)

Fig. 1 A schematic of vapor anode, multitube AMTEC cell (not to scale); (a) elevation; (b) plan view

the electrons circulate through the external load, then return to recombine with sodium ions at the BASE/cathode electrode interface (Fig. 1). The neutral sodium atoms then diffuse through the cathode electrode and traverse the vapor space to the remote condenser. Liquid sodium is then circulated back to the cell evaporator by the capillary action of the wick structure. The cell conical evaporator provides a larger surface area for evaporation of liquid sodium.

The heat input, Q_{in}, is transported by conduction and radiation from the cell's hot plate to the BASE tubes and to the evaporator structure. The circumferential radiation shield, placed in the cavity above the BASE tubes, reduces parasitic heat losses to the side wall. The metal stud improves heat conduction from the hot end to the support plate, which helps achieve higher evaporator and BASE temperatures (Fig. 1). To prevent condensation of sodium vapor and electrical shorting of the BASE tubes in the cell, the BASE temperature is kept slightly higher (20–50 K) than that of the evaporator.

Modeling radiation heat transfer in the enclosure of an AMTEC cell is a challenging task because of its complex geometry. Only a few investigators have attempted to tackle this difficult problem. Schock and Or (1997) and Hendricks et al. (1998) have developed comprehensive thermal models for PX-type cells, based on the SINDA Thermal Analyzer software. Shock and Or (1997) used the ITAS Radiation Interchange package to calculate all radiation view factors within the cell cavity.

Hendricks et al. (1998) used the RadCAD thermal radiation analysis software, based on Monte Carlo ray-tracing, to evaluate all radiation view factors in the cell. They reported their calculations of PX-type cells using 170 temperature nodes and assuming an adiabatic cell wall. Only 12 and 5 nodes were used along the cell wall and BASE tubes, respectively. By contrast, the evaporator standoff, BASE tubes support plate, conduction stud, and thermal heat shields were finely discretized. Results of their model compared well with experimental data. However, calculating the radiation view factors using numerical contour integration or Monte Carlo calculation methods is very CPU intensive. Furthermore, large thermal analyzer codes such as SINDA/FLUINT are not particularly suitable or easily amenable to handling the strong couplings between the many physical processes occurring in an AMTEC cell, resulting in a relatively slow convergence.

Model Description

The present radiation/conduction thermal model was developed to calculate internal parasitic heat losses and temperatures within the cell enclosure (Fig. 1). All surfaces that exchange radiant energy in the interior of the cell were assumed gray and diffuse. The hemispherical total absorptivity and emissivity of the surfaces were assumed equal, and depended only on temperature (Siegel and Howell, 1981). Even though this condition is achieved only by a limited number of real materials, it is often the most reasonable approach, for two reasons. First, the radiative properties are usually not known to high accuracy, especially their dependence on wavelength and direction. Second, in many cases of practical interest, the gray-diffuse approach is accurate enough, even in enclosures involving specular surfaces, or surfaces with both diffuse and specular components (Schornhorst and Viskanta, 1968). Two additional assumptions were made: (a) the reflected energy is diffuse, and (b) the reflected energy is uniform over each surface element.

The present model can easily handle 100–200 temperature nodes in the cell. The surface emissivities and all thermophysical properties of structural materials and sodium are temperature dependent. At the temperatures of interest (<1200 K), the low pressure (<1 atm), monoatomic sodium vapor is essentially transparent to radiation. Because of the very small density and thermal capacity of sodium vapor, heat transport by convection is negligible compared to that due to radiation and conduction.

Radiation View Factors. In this work, a radiation view factors database was developed for the various surface elements in the complex cavity of PX-type cells (Fig. 1). This database has taken advantage of the extensive tabulations of view factor formulas available in the literature for simple geometries (Siegel and Howell, 1981; Howell, 1982). Figure 2 shows the numerical mesh used to calculate the heat transfer in a cell without a thermal shield nor a conduction metal stud. The mesh generator discretized the BASE tubes bundle into N sections of identical height, and the coaxial cylindrical cavity above the BASE tubes into N_w identical axial sections. The evaporator standoff was discretized into N_c identical axial sections, while the wick of the evaporator was discretized into $N_{ev} = (N - N_c)$ axial sections of equal height. Only one axial node was used in the hot plenum wall, since the height of the plenum was very small, typically <2 mm.

As shown in Fig. 2, there are two separate enclosures for radiation heat transfer within the cell, the high and the low-vapor pressure cavities. For the purpose of calculating the radiation view factors, the cell cavity was divided into several, radiatively coupled, elementary or subcavities (Fig. 2): (a) the hot plenum baffle; (b) the evaporator standoff; (c) the inside of BASE tubes; (d) the BASE tubes/standoff bundle; (e) the coaxial cylindrical cavity above the BASE tubes; and (f) the annular space between the circumferential shield and the cell wall. The
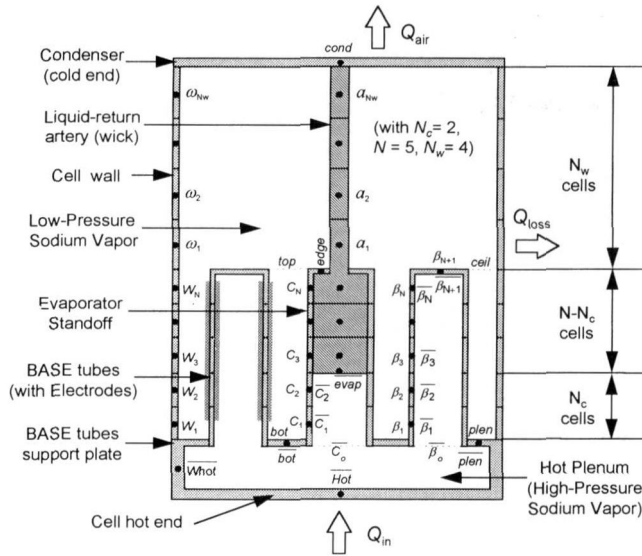
Fig. 2 Numerical grid layout of multitube AMTEC cell, without thermal shield or conduction stud

surfaces $\overline{\beta_o}$, $\overline{C_o}$, *top*, and *ceil* are fictitious boundaries through which radiative coupling between subcavities occurs (Fig. 2). The radiation view factors for each of the subcavities were calculated using an approximate analytical approach. In the artery cylindrical subcavity, the N_β BASE tube tops were approximated by an equivalent thick-circular ring of identical surface area (Fig. 1(b)). Similarly, in the hot plenum subcavity, the N_β BASE tube openings were approximated by an equivalent thick-circular ring. Using these approximations, all view factors in the subcavities (a), (b), (c), (e), and (f) were determined analytically using closed-form algebraic relations and elementary flux algebra (Siegel and Howell, 1981; Howell, 1982).

Because of the complex geometry of the BASE tubes/standoff bundle cavity, approximate relations of the view factors were derived, that ensured that all reciprocity ($A_k F_{kp} = A_p F_{pk}$) and enclosure relations ($\sum\limits_{k=1}^{N_R} F_{pk} = 1$) were satisfied. The reciprocity and enclosure relations were accounted for explicitly when computing the view factors in all the cell subcavities. The complete set of linear view factor relationships was solved using Gauss elimination. A complete description of the view factor relations developed in this work cannot be included here due to length limitation, a few examples, however, are given below.

Hottel's crossed-string analytical method (Siegel and Howell, 1981) was used, in conjunction with the approximate cavity model of Juul (1982), to estimate the view factors between the evaporator standoff and the BASE tubes, and between the different BASE tubes, that were partially obstructed by the evaporator standoff or by another BASE tube (Fig. 1(b)). Using the crossed-string method, the view factor between infinite, vertical cylinders 1 and 2 was obtained as (Fig. 3(a)):

$$F_{12}^{\infty} = \frac{1}{2\pi R} \left\{ (1 + R)\sin^{-1}\frac{1 + R}{X} - (1 - R)\sin^{-1}\frac{1 - R}{X} \right.$$
$$\left. + \sqrt{X^2 - (1 + R)^2} - \sqrt{X^2 - (1 - R)^2} \right\}, \quad (1)$$

where

$$R = \frac{R_1}{R_2}$$

and

$$X = \frac{a}{R_2}.$$

When the cylinders have identical radii ($R = 1$), Eq. (1) reduces to

$$F_{12}^{\infty} = F_{21}^{\infty} = \frac{1}{\pi}\left\{ \sin^{-1}\frac{1}{H} + \sqrt{H^2 - 1} - H \right\}, \quad (2)$$

where $H = X/2 = a/2R_1$, which is identical to that given by Siegel and Howell (1981).

The view factor between two infinitely long, vertical cylinders A_1 and A_1' of radii R_1, partially obstructed by another vertical cylinder A_2 of radius R_2, was also calculated using the crossed-string method. For small obstruction, $\beta < \varphi$ (Fig. 3(b)), one obtained

$$F_{A_1 \to A_1'} = \frac{1}{\pi}\left\{ \sin^{-1}\frac{1}{X} + \sqrt{X^2 - 1} - X \right\}$$

$$+ \frac{1}{2\pi}\left\{ (\sigma - \theta) - R\beta + X - \sqrt{X^2 + (H + R)^2 - (1 - R)^2} \right\},$$

where

$$\sigma = \tan^{-1}\frac{H + R}{X}, \quad \theta = \sin^{-1}\frac{1 + R}{\sqrt{X^2 + (H + R)^2}},$$

$$\omega = \tan^{-1}\frac{X}{H + R},$$

$$R = \frac{R_2}{R_1}, \quad X = \frac{a}{2R_1}, \quad H = \frac{d - R_2}{R_1} = \frac{h}{R_1},$$

$$\text{and } \beta = \omega + \theta - \frac{\pi}{2} \quad (\beta < \varphi, 0 < H < 1). \quad (3)$$

When $h = R_1$, then $H = 1$, $\beta = 0$, $\gamma = \varphi$, and $\sigma = \theta$. In that case, the second bracket in Eq. (3) equals zero and the view factor reduces to that between two unobstructed vertical cylinders of identical radii, Eq. (2). For large obstruction, ($\beta > \varphi$), the view factor between A_1 and A_1' has the expression (Fig. 3(c)):

$$F_{A_1 \to A_1'} = \frac{1}{2\pi}\left\{ (1 - R)(\sigma - \alpha) \right.$$

$$\left. + \sqrt{X^2(H + R)^2 - (1 - R)^2} - X \right\},$$

where

$$\sigma = \tan^{-1}\frac{H + R}{X} \text{ and } \alpha = \sin^{-1}\frac{R - 1}{\sqrt{X^2 + (H + R)^2}} \quad (H < 0).$$

$$(4)$$

When $d = R_2 - R_1$, then $H = -1$, and consideration of the rectangular triangle of sides X and $|R - 1|$ shows that $F_{A_1 \to A_1'}$ reduces to zero; the view between cylinders A_1 and A_1' is completely obstructed by cylinder A_2. Although it is not directly apparent, both Eqs. (3) and (4) give identical results when $\beta = \varphi$, that is when the cylinder A_2 is in contact with the cross strings $\overline{bd}$ and $\overline{d'b'}$ between the two identical cylinders ($\gamma = o$, and $\delta = \varphi$, see Figs. 3(b) and 3(c)). This is because, for these view factors derived from the crossed-string method, the length of the strings used in the two equations is identical when $\beta = \varphi$.

Juul (1982) has developed an approximate analytical expression for the view factor between two opposed (vertical) cylinders of finite and equal length. In the arrangement where cylinder 1 is completely surrounded by n identical (vertical) cylin-
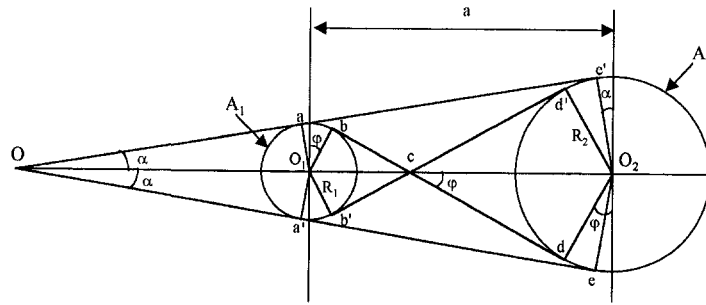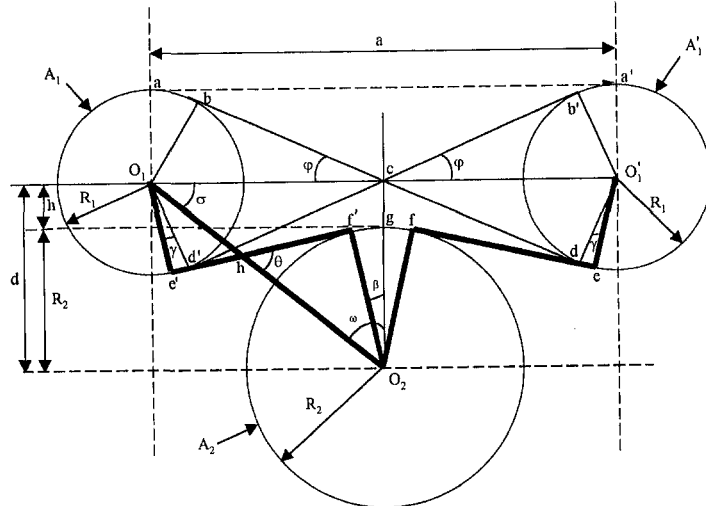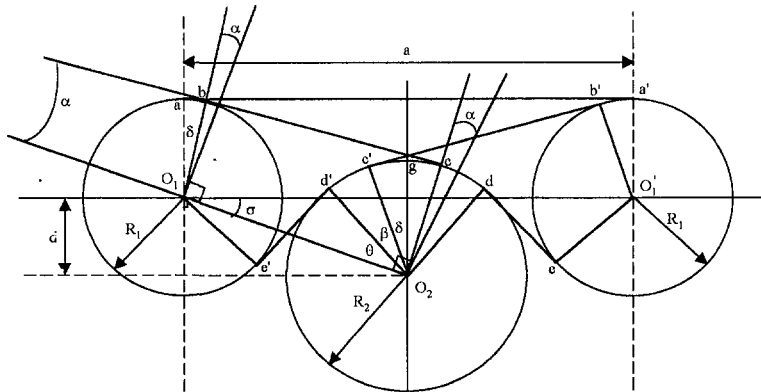
Fig. 3(a)

Fig. 3(b)

Fig. 3(c)

Fig. 3 Calculation of view factors between infinitely long parallel cylinders partially obstructed by another parallel cylinder, using Hottel's crossed-string method; (a) no obstruction; (b) small, partial obstruction ($\beta \leq \varphi, H \leq 1$); (c) large, partial obstruction ($\beta \geq \varphi, H \geq -1, X > R + 1$)

ders of radius R_2, and whose axes lie on a concentric circle having a radius equal to the spacing a between cylinders 1 and 2, the view factor between cylinders 1 and 2 can be approximated by (Juul 1982)

$$F_{12} \cong F_{12}^\infty (1 - 2F_{13'}) = F_{12}^\infty \times F_{10}, \qquad (5)$$

where F_{12}^∞ is the view factor between infinitely long cylinders 1 and 2, given by Eq. (1). F_{10} is the view factor between cylinder 1 and the inner surface of an opposed and concentric cylinder having a radius R_o given by

$$\left(\frac{R_o}{R_2} \right)^2 = 1 + \left[\sqrt{\left(\frac{a}{R_2} \right)^2 - 1} - \frac{\pi}{2} \right] \times \left[\sin^{-1} \frac{R_2}{a} \right]. \quad (6)$$

Juul (1982) has compared the results of this approximate method

with that obtained by numerical integration and showed Eq. (5) to be very accurate; the difference was less than one percent when $R_1 \leq R_2$ and $3 < h/R_2 < 10$. For all cases of practical interest, the error in the view factor calculated using Eq. (5) was less than three percent. The approximate method of Juul was extended to the case where the finite cylinders 1 and 2 are separated by a height c: $F_{12} \cong F_{12}^\infty \times F_{10}$, where A_o is the inner surface of a cylinder having a radius R_o, concentric with the cylinder 1, and at the level of cylinder 2 with a height h_2.

The present model has made extensive use of reciprocity, symmetry, and fractional analysis to reduce the number of approximate factor relationships to a strict minimum and insure satisfaction of all reciprocity and enclosure relations. For example, the view factors between the bottom ring and BASE tube sections are simply obtained by symmetry: $F_{\text{bot} \to \beta_k} =$

$F_{\text{top}\to\beta_{N+1-k}}$. The view factors between the first evaporator stand-off section C_1 and the surfaces W_k, *ceil* and *plen*, were calculated using fractional analysis, assuming that the fractions of rays emitted by C_1 and reaching these other surfaces are unchanged, with or without the BASE tubes present (Fig. 2). These fractions are obtained using the calculated view factors G in the annular cavity obtained when the BASE tubes were removed. The fraction of rays leaking through the open spacings between BASE tubes (Fig. 1) was then calculated as

$$F_{C_1\to\text{leak}} = 1 - F_{C_1\to\text{top}} - F_{C_1\to\text{bot}} - \sum_{k=1}^{N} F_{C_1\to\beta_k}. \qquad (7)$$

If we define

$$G_{C_1\to\text{leak}} = G_{C_1\to\text{ceil}} + G_{C_1\to\text{plen}} + \sum_{k=1}^{N} G_{C_1\to W_k}, \qquad (8)$$

then

$$F_{C_1\to\text{ceil}} = \frac{G_{C_1\to\text{ceil}}}{G_{C_1\to\text{leak}}} \times F_{C_1\to\text{leak}},$$

$$F_{C_1\to\text{plen}} = \frac{G_{C_1\to\text{plen}}}{G_{C_1\to\text{leak}}} \times F_{C_1\to\text{leak}},$$

and

$$F_{C_1\to W_k} = \frac{G_{C_1\to W_k}}{G_{C_1\to\text{leak}}} \times F_{C_1\to\text{leak}}, \quad k = 1 \text{ to } N. \qquad (9)$$

Note that the use of fractional view factors insures that the enclosure relation is satisfied for C_1. The factors $F_{C_1\to W_k}$ can then be used to deduce all factors $F_{C_p\to W_k}$. By symmetry,

$$F_{C_p\to W_k} = F_{C_1\to W_{|p-k|+1}}. \qquad (10)$$

The calculated view factors of the cell's subcavities were modified to account for the radiative coupling between them, through the fictitious boundaries $\overline{\beta}_o$, $\overline{C}_o$, *top*, and *ceil*, which were eliminated. As an illustration, let us consider the simpler case of the radiative coupling between the hot baffle and evaporator standoff. Since the inside height of the hot baffle is much smaller than both its diameter and the height of the first standoff axial section $\overline{C}_1$, all radiation emitted by the surface $\overline{W}$hot, streaming through surface $\overline{C}_o$, will end into surface $\overline{C}_1$ (Fig. 2). Therefore

$$F_{\overline{W\text{hot}}\to\overline{C}_1} = F_{\overline{W\text{hot}}\to\overline{C}_o}, F_{\overline{W\text{hot}}\to\overline{C}_k} = 0 \text{ for } k > 1,$$

and

$$F_{\overline{W\text{hot}}\to\overline{\text{evap}}} = 0. \qquad (11)$$

$F_{\overline{C}_1\to\overline{W\text{hot}}}$ is calculated by reciprocity, and since surface $\overline{C}_1$ sees only $\overline{W}$hot and $\overline{\text{Hot}}$ through $\overline{C}_o$, we have $F_{\overline{C}_1\to\overline{\text{Hot}}} = F_{\overline{C}_1\to\overline{C}_o} - F_{\overline{C}_1\to\overline{W\text{hot}}}$. Finally, all other surfaces inside the evaporator casing see only the hot plate through $\overline{C}_o$, so that

$$F_{\overline{C}_k\to\overline{\text{Hot}}} = F_{\overline{C}_k\to\overline{C}_o} \text{ for } k > 1,$$

and

$$F_{\overline{\text{evap}}\to\overline{\text{Hot}}} = F_{\overline{\text{evap}}\to\overline{C}_o}. \qquad (12)$$

All other factors between the hot baffle and evaporator standoff casing can be obtained by reciprocity, or are nul.

A similar treatment is applied to the radiative coupling between the inside surfaces of the BASE tubes and surfaces $\overline{W}$hot and $\overline{\text{Hot}}$ of the high-pressure baffle. The only difference from the previous treatment is that the surface areas inside a BASE tube must be multiplied by the number of tubes in the cell, N_β, before performing the radiative coupling treatment. In the end, all view factors involving surfaces $\overline{C}_o$ and $\overline{\beta}_o$ were set equal to zero.

The coupling between the tubes bundle's subcavity and the artery cylindrical subcavity above was the most challenging. Because of their complex geometry, in addition to the reciprocity and enclosure relations, it was necessary to develop other approximate relations to calculate all the radiation view factors in the cell. Again, the present model made extensive use of reciprocity, symmetry, and fractional analysis to reduce the number of unknown factors to a strict minimum and insure satisfaction of all reciprocity and enclosure relations. However, such details are beyond the scope of this Technical Note.

The heat shield (Fig. 1(a)) was modeled as a thin cylindrical metallic shell of radius R_{sh}, placed close to the cell wall, ($R_w - R_{sh}$) $\ll R_w$. It was divided into N_{sh} identical axial sections. The view factors for the annulus between the cell wall and the radiation shield were easily calculated using closed-form algebraic relations. The top and bottom rings of this annular cavity were assumed to be perfect reflectors. The top ring saw a portion of the Creare condenser surface, which was highly reflective ($\epsilon \sim 0.05$, Tournier and El-Genk 1998a).

Numerical Solution Methodology. The energy balance and associated boundary conditions were discretized on a staggered grid using the well-known control-volume approach proposed by Patankar (1980). The solution obtained using this approach satisfies global conservation, even on a nonuniform grid. The multitube AMTEC cell was discretized into N_S ($N_S = 4N + 2N_w - N_c + 8$) solid elements (Fig. 2). There were $N + N_w + 1$ wall sections, $N + 1$ BASE tube elements, N evaporator tube sections, $N_w + N - N_c$ artery and evaporator wick sections, one each for the hot end plate, condenser, standoff annular edge, and the evaporator surface, and two ring elements for the support plate.

Most solid elements k exchanged radiant energy through their front area A_{fk}, only ($fk = 1$ to N_S). Some elements k exchanged radiant energy in both the high-pressure, hot plenum cavity, and the low-pressure enclosure above the BASE tubes, through both their front face, A_{fk}, and back face, A_{bk} ($bk = N_S + 1$ to N_R). These elements were the BASE tubes support plate nodes, *bot* and *plen*, the BASE tubes nodes, β_1 to β_{N+1}, and the evaporator standoff nodes, C_1 to C_{Nc} (Fig. 2). There were a total of N_R ($N_R = N_S + 2N_c + 3$) surface elements, which exchanged radiant energy within the cell cavities. N_R is equal to the number of solid elements, N_S, minus the number of elements that did not communicate with the vapor space, and therefore, did not exchange heat by radiation ($N - N_c$ evaporator wick nodes), plus the number of solid elements which also have a back face in contact with sodium vapor ($N + 1$ BASE tube elements, N_c evaporator standoff sections, and two ring elements for the support plate). The energy balance for an element k was written as

$$\sum_{p=1}^{N_S} \Lambda_{kp} T_p - S_k = -\varphi_k Q_{fk}^{\text{loss}} - \beta_k Q_{bk}^{\text{loss}}. \qquad (13)$$

The terms on the left-hand side of Eq. (13) arose from the well-known control-volume discretization method (Patankar 1980), and include heat storage enthalpies, heat conduction between node k and adjacent elements, convection due to liquid sodium flow in the wicks, and source/sink terms due to condensation and evaporation of sodium at the condenser and evaporator nodes, respectively. These terms also include the fraction of heat converted to electrical energy in the BASE tube nodes, and heat input and losses at the outer boundaries of the cell (hot end, side wall, and condenser).

The electric current density along the BASE TiN electrodes and the total electrical current, calculated by the cell electrical model (Tournier and El-Genk, 1998a, b), were used in the input to the present radiation/conduction model. All radiant

heat exchange terms were collected on the right-hand side of Eq. (13). After the temperatures of all nodes in the cell were obtained, Eq. (13) was used to evaluate the heat input at the hot end and the heat removed at the cold end of the cell (condenser). In Eq. (13), the matrix coefficients, Λ_{kp}, the source terms, S_k, and the net radiant energy loss terms, Q^{loss}, were all functions of temperature, through the temperature-dependent properties.

In the AMTEC cell, the mass flow rate of sodium is proportional to the cell electrical current. However, since the heat of vaporization/condensation constitutes a large fraction of the total heat input to the cell, it significantly affects the evaporator and condenser temperatures. Therefore, the partial derivatives of the cell current in terms of the evaporator, BASE tubes, and condenser temperatures were obtained from the cell electrical model (Tournier and El-Genk, 1998b). These derivatives were used to linearize the dependence of the sodium flow rate on temperature in the energy balance equations of the condenser and evaporator nodes. Results from numerical experiments showed that this linearization was a key to obtaining an efficient, fast-converging solution algorithm (Tournier and El-Genk, 1998a).

To solve the energy balance, Eq. (13), for the solid node temperatures, the net radiant energy loss terms, Q^{loss}, were expressed as functions of temperatures. First, the net radiant energy losses were expressed in terms of the rates of outgoing radiant energy (Siegel and Howell 1981),

$$q_k^{loss} = q_k^{out} - \sum_{p=1}^{N_R} F_{kp} q_p^{out}, \text{ for } k = 1 \text{ to } N_R, \quad (14)$$

or in matrix notation: $[q^{loss}] = \{\mathfrak{T} - \mathbf{F}\}[q^{out}]$. Then, the radiant energy balance for the surface A_k was expressed as (Siegel and Howell, 1981)

$$q_k^{out} - (1 - \epsilon_k) \sum_{p=1}^{N_R} F_{kp} q_p^{out} = \epsilon_k \sigma T_k^4. \quad (15)$$

Equation (15) represents an $N_R \times N_R$ linear system of equations, which relates the rates of outgoing radiant energy in the cell enclosure to the surface temperatures, as

$$\{\mathbf{R}\}[q^{out}] = [\epsilon_k \sigma T_k^4],$$

where

$$R_{kp} = \delta_{kp} - (1 - \epsilon_k) F_{kp}, \quad k, p = 1 \text{ to } N_R. \quad (16)$$

A solution routine was developed and tested to inverse the radiation matrix $\{\mathbf{R}\}$ using the Gauss-Jordan elimination algorithm. Once the radiation matrix was inverted, the net radiant energy loss terms were expressed explicitly in terms of the node temperatures, as

$$[q^{loss}] = \{\mathfrak{T} - \mathbf{F}\}[q^{out}] = \{\mathfrak{T} - \mathbf{F}\}\{\mathbf{R}\}^{-1}[\epsilon_k \sigma T_k^4], \text{ or}$$

$$[Q^{loss}] = \{\mathbf{M}\}[\sigma T_k^4], \quad (17)$$

where

$$M_{kp} = A_k \epsilon_p \left(R_{kp}^{-1} - \sum_{m=1}^{N_R} F_{km} R_{mp}^{-1} \right), \quad k, p = 1 \text{ to } N_R.$$

The energy balance for the solid element k in the cell could then be written as

$$\sum_{p=1}^{N_S} \Lambda_{kp} T_p - S_k + \sigma \sum_{m=1}^{N_R} (\varphi_k M_{fk,m} + \beta_k M_{bk,m}) T_m^4 = 0,$$

$$k = 1 \text{ to } N_S. \quad (18)$$

The temperatures of the back faces of the solid nodes, exchanging radiant energy through both their front and back faces, were taken equal to that of the front faces of the elements,

$$T_{bk} = T_{fk}, \quad bk = N_S + 1 \text{ to } N_R. \quad (19)$$

The matrices $\{\Lambda\}$ and $\{\mathbf{M}\}$, and source term $[S]$ in Eq. (18) were evaluated explicitly using the best estimate of the temperatures $[T^*]$ in the cell (they depend on the values of the temperature-dependent, thermophysical, and radiative properties). One seeks a temperature correction vector $[T']$, such that the vector $[T] = [T^*] + [T']$ satisfies the energy balance Eqs. (18)–(19). To resolve the strong nonlinearity of radiant energy fluxes, the fourth power of the temperature was linearized using the first two terms of the Taylor series, as

$$T_m^4 = (T_m^* + T_m')^4 \cong (T_m^*)^4 + 4(T_m^*)^3 T_m'$$

$$= (T_m^*)^3 [T_m^* + 4T_m']. \quad (20)$$

The linearized energy balance Eq. (18) had the final form:

$$\sum_{p=1}^{N_S} \Lambda_{kp}^* T_p' + 4\sigma \sum_{m=1}^{N_R} (\varphi_k M_{fk,m}^* + \beta_k M_{bk,m}^*)(T_m^*)^3 T_m' = \hat{S}_k,$$

where

$$\hat{S}_k = S_k^* - \sum_{p=1}^{N_S} \Lambda_{kp}^* T_p^* - \varphi_k (Q_{fk}^{loss})^* - \beta_k (Q_{bk}^{loss})^*,$$

$$k = 1 \text{ to } N_S. \quad (21)$$

The linearized energy balance equations were solved for the temperature corrections $[T']$, using Gauss elimination method with row normalization and partial pivoting. After the temperatures in the cell cavity were corrected, an energy balance for the cell was performed again. The solution was iterated until temperatures satisfied the convergence criterion (when the magnitude of temperature correction vector <0.2 K) and the cell energy balance was satisfied (within <0.1 percent). Only two to four iterations were needed to resolve the strong nonlinearity of the radiant energy fluxes.

Calculated Performance of PX-5A Cell

The present radiation/conduction model was coupled to a vapor pressure loss and an AMTEC cell electrochemical and electrical circuit models, using an efficient iterative solution procedure to resolve the strong couplings between various physical processes in the cell (Tournier and El-Genk, 1998a). The fully integrated cell model (APEAM) was used to simulate the experimental setup of PX-series AMTEC cells at AFRL. The model results were compared with experimental measurements of a number of PX-series cells (El-Genk and Tournier, 1998). The PX-cell tests were performed in vacuum at 5×10^{-6} torr (0.7 mPa). The radiation/conduction thermal model in APEAM was modified to account for axial and radial conduction in the Min-K insulation surrounding the cell in the vacuum tests. The test data were obtained at fixed hot and cold end temperatures.

As an illustration, the predicted heat transfer and temperatures in the PX-5A cell, near its peak conversion efficiency, are presented. This calculation was performed with $N_c = 4$, $N = 10$, $N_w = 12$, and $N_{sh} = 11$. The resulting mesh had 79 temperature nodes and 100 surfaces exchanging radiant energy within the cell cavity. An additional 48 temperature nodes were used in the surrounding insulation in the test. The calculation took less than 10 s on a Pentium 200-MHz PC; about a fourth of this time was used to calculate the view factors in the cell.

The PX-5A cell was 38 mm in diameter, and made entirely of stainless steel. It had six 40-mm long BASE tubes, a conical evaporator, a circumferential molybdenum shield above the BASE tubes, a conduction stud, 100 mm² in cross-section area, and four 2.5-mm thick stainless steel rings around the evaporator standoff to enhance conduction. The PX-5A cell used a Creare condenser (Tournier and El-Genk, 1998a), whose effective emissivity was taken equal to 0.05.
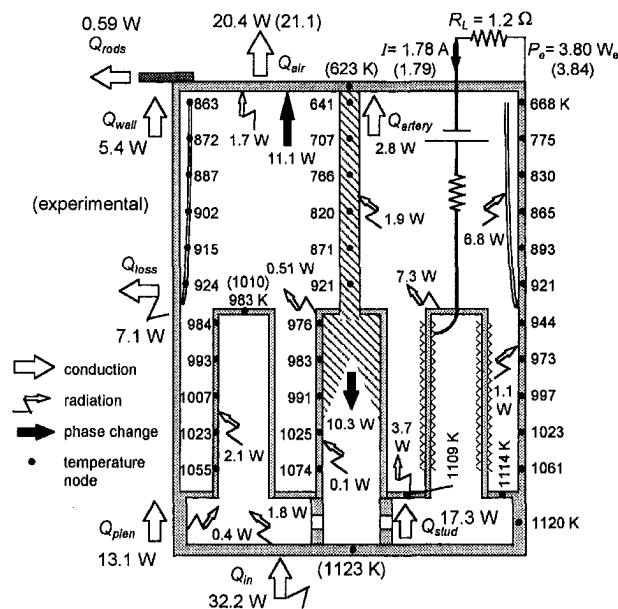
Fig. 4 Predicted heat transfer and temperatures in PX-5A AMTEC cell, at the peak conversion efficiency

ture near the condenser was 623 K. As a result, the radiation shield significantly reduced the parasitic heat losses through the cell wall. The PX-5A cell delivered 3.8 W_e at a peak conversion efficiency of 11.8 percent, and an average electrodes power density of 0.104 W_e/cm^2. The predicted heat losses through the cell wall were 7.1 W, or 22 percent of the heat input to the cell. As shown in Fig. 4, the predicted heat removal at the condenser end, BASE tubes cold end temperature and cell electrical power output were in good agreement with experimental data. Such good agreement gave confidence in the soundness of the modeling approach and the accuracy of the radiation/conduction model.

Acknowledgments

References

El-Genk, M. S., and Tournier, J.-M., 1998, "Recent Advances in Vapor-Anode, Multi-Tube, Alkali-Metal Thermal-to-Electric Conversion Cells for Space Power," *Proc. of the 5th European Space Power Conference,* SP-416, Paper No. 1046, European Space Agency.

Hendricks, T. J., Borkowski, C. A., and Huang, C., 1998, "Development and Experimental Validation of a SINDA/FLUINT Thermal/Fluid/Electrical Model of a Multi-Tube AMTEC Cell," *Proc. Space Technology and Applications Int. Forum,* CONF-980103, M. S. El-Genk, ed., American Institute of Physics, New York, AIP CP No. 420, Vol. 3, pp. 1491–1501.

Howell, J. R., 1982, *A Catalog of Radiation Configuration Factors,* McGraw-Hill, New York.

Juul, N. H., 1982, "View Factors in Radiation Between Two Parallel Oriented Cylinders of Finite Lengths," ASME JOURNAL OF HEAT TRANSFER, Vol. 104, pp. 384–388.

Patankar, S. V., 1980, *Numerical Heat Transfer and Fluid Flow,* Hemisphere, Washington, DC.

Schock, A., and Or, C., 1997, "Coupled Thermal, Electrical, and Fluid Flow Analyses of AMTEC Multi-tube Cell with Adiabatic Cell Wall," *Proc. Space Technology and Applications International Forum,* CONF-970115, M. S. El-Genk, ed., American Institute of Physics, New York, AIP CP No. 387, Vol. 3, pp. 1381–1394.

Schornhorst, J. R., and Viskanta, R., 1968, "An Experimental Examination of the Validity of the Commonly Used Methods of Radiant Heat Transfer Analysis," ASME JOURNAL OF HEAT TRANSFER, Vol. 90, No. 4, pp. 429–436.

Siegel, R., and Howell, J. R., 1981, *Thermal Radiation Heat Transfer,* 2nd Ed., Hemisphere, New York, Section 9.3, pp. 283–292.

Tournier, J.-M., and El-Genk, M. S., 1998a, "AMTEC Performance and Evaluation Analysis Model (APEAM): Comparison with Test Results of PX-4C, PX-5A, and PX-3A," *Proc. Space Technology and Applications Int. Forum,* CONF-980103, M. S. El-Genk, ed., American Institute of Physics, New York, AIP CP No. 420, Vol. 3, pp. 1576–1585.

Tournier, J.-M., and El-Genk, M. S., 1998b, "An Electrical Model of Vapor Anode, Multi-tube AMTEC Cells," *Proc. 33rd Intersociety Energy Conversion Engineering Conference,* Paper No. 98056, American Nuclear Society, Chicago, IL.

Figure 4 shows the predicted heat transport and thermal energy exchange in the PX-5A cell, at hot and cold end temperatures of 1123 K and 623 K, respectively. The conduction stud transported 17.3 W (about 54 percent), and the plenum wall conducted 13.1 W (about 41 percent) of the heat input to the cell, Q_{in} = 32.2 W, to the support plate. Only 1.8 W were radiated out from the hot end (five percent). The temperature of the support plate was only 14 K lower than the cell's hot end temperature. About 60 percent of the heat conducted by the stud was consumed in the evaporation of liquid sodium in the evaporator wick (10.3 W).

A total of 21 W = Q_{air} + Q_{rods} was removed at the cell condenser, which comprised (a) the sodium latent heat of condensation (11.1 W); (b) heat conduction up the side wall of the cell (5.4 W); (c) parasitic radiation losses to the condenser surface (1.7 W); and (d) heat conduction up the liquid sodium return artery (2.8 W). In the low-sodium pressure cavity, the hot support plate lost 3.7 W by radiation, and the 6 BASE tubes lost 7.3 W by radiation to the cooler surfaces in the cavity. The far end of the BASE tubes was 126 K cooler than the support plate.

The temperature of the stainless steel (SS) radiation shield varied between 863 K and 924 K, while the cell wall tempera-

Consecutive-Photo Method to Measure Vapor Volume Flow Rate During Boiling From a Wire Immersed in Saturated Liquid[1]

J. R. Thome[2]. The consecutive-photo method presented by the authors is not a new technique as claimed but actually dates back quite awhile. The only difference is that Ammerman and You have used a relatively low-speed digital camera (240 frames/s) rather than a true high-speed cine camera (speeds of 4000 frames/s or more). Numerous researchers utilized high-speed cine cameras to obtain bubble growth data for isolated bubbles in the 1960s and 1970s, e.g., refer to the two-volume book *Boiling Phenomena* by van Stralen and Cole published in 1979. In particular with respect to the consecutive-photo method, Thome and co-workers (Preston et al., 1979; Thome and Davey, 1981) presented a detailed description of how they applied a computerized image analysis system to measure of a large number of consecutive bubbles departing from the same boiling site (up to 30 bubble growth cycles per cine film with each bubble image divided into numerous segments to determine its profile with departure frequencies up to 120 bubbles/s) and thus compiled an extensive database with both individual and statistically averaged bubble growth rates, bubble departure diameters and bubble departure frequencies for liquid nitrogen, liquid argon, and also their mixtures at a variety of wall superheats. The corresponding volumetric vapor flow rates were later published in the ASME *Journal of Heat Transfer* (Thome, 1982) together with analysis of their influence on the bubble evaporation and cyclic thermal boundary layer stripping heat transfer mechanisms, work which lead to an analytical model of bubble growth and departure in a mass transfer model for predicting pool boiling coefficients in mixtures (Thome, 1981; Thome and Shock, 1984). Thus, while I am pleased to see renewed interest in the fundamentals of nucleate pool boiling, let's not neglect the past work of others.

References

Preston, G., Thome, J. R., Bald, W. B., and Davey, G., 1979, "The Measurement of Growing Bubbles on a Heated Surface Using a Computerized Image Analysis System," *International Journal of Heat and Mass Transfer*, Vol. 22, pp. 1457–1459.

Thome, J. R., 1981, "Nucleate Pool Boiling of Binary Mixtures: An Analytical Equation," *AIChE Symposium Series*, Vol. 77, No. 208, pp. 238–250.

Thome, J. R., 1982, "Latent and Sensible Heat Transport Rates in the Boiling of Binary Mixtures," ASME JOURNAL OF HEAT TRANSFER, Vol. 104, pp. 474–478.

Thome, J. R., and Davey, G., 1981, "Bubble Growth Rates in Liquid Nitrogen, Argon and Their Mixtures," *International Journal of Heat and Mass Transfer*, Vol. 24, pp. 89–97.

[1] by C. N. Ammerman and S. M. You and published in the Aug. 1998 issue of the ASME JOURNAL OF HEAT TRANSFER, Vol. 120, pp. 561–567.

[2] Departement de Genie Mecanique, Laboratoire de Transfert de Chaleur et de Masse, DGM-ME Ecublens, CH-1015 Lausanne, Switzerland.

Thome, J. R., and Shock, R. A. W., 1984, "Boiling of Multicomponent Mixtures," *Advances in Heat Transfer*, Vol. 16, J. P. Hartnett and T. J. Irvine, Jr., eds., Academic Press, New York, pp. 59–156.

Authors' Closure[3]

As early as the 1930s, Jakob and Linke (1933) used high-speed photography (500 fps) to study the fundamental aspects of boiling, including bubble departure diameter and frequency from a single nucleation site. By the 1950's, Westwater and his co-workers (1955, 1960) were examining single-site departure diameter and frequency as well as nucleation site density using film speeds of up to 5000 fps. Throughout this period in history, it was generally believed that latent heat removal in boiling contributed insignificantly to the total heat flux. In 1964, however, Rallis and Jawurek were among the first to recognize the importance of the latent heat contribution. They used single-site bubble frequency and departure diameter measurements along with nucleation site densities to calculate vapor volume flow rate departing from a wire for various heat fluxes. These vapor flow rates resulted in latent heat contributions as high as 80 percent of the total nucleate boiling heat flux. During the 1960s and 1970s, numerous researchers used high-speed photography to measure single-site bubble departure diameter and frequency, as well as bubble growth rates.

Around 1980, Thome also was using high-speed photography (up to 4000 fps) to measure single-site, boiling bubble growth rates, departure diameters, and departure frequencies. At this time, the current method of obtaining bubble diameter was to manually measure bubble chord lengths in each successive photographic frame. Thome and his co-workers (Preston et al., 1979; Thome and Davey, 1981) introduced a computer-aided method for measuring these bubble chord lengths which automated the previous manual measurement technique. This time-saving method enabled the analysis of up to 800 frames per hour. In 1982, Thome went on to publish the vapor volume flow rate data resulting from these measurements. With these data, he was able to calculate a single-bubble latent heat contribution. He then used a semi-empirical method to estimate the per-bubble sensible heat contribution and compared it with the latent heat value.

In 1998, the present authors introduced a consecutive-photo method for measuring the vapor volume flow rate departing from a wire during boiling. Instead of examining characteristics of a single nucleation site, this method measures the vapor volume flow rate from all nucleation sites simultaneously. Because this method does not focus on a single site, it also enables the experimental evaluation of the sensible energy contribution in nucleate boiling.

[3] C. N. Ammerman and S. M. You, Dr. Ammerman's current address is Los Alamos National Laboratory, ESA-DE, P.O. Box 1663, MS H821, Los Alamos, NM 87545.

ERRATUM

Paper entitled "Local and Global Simulations of Bridgman and Liquid-Encapsulated Czochralski Crystal Growth" by H. Zhang, L. L. Zheng, V. Prasad and D. J. Larson, Jr., pp. 865–873, November 1998.
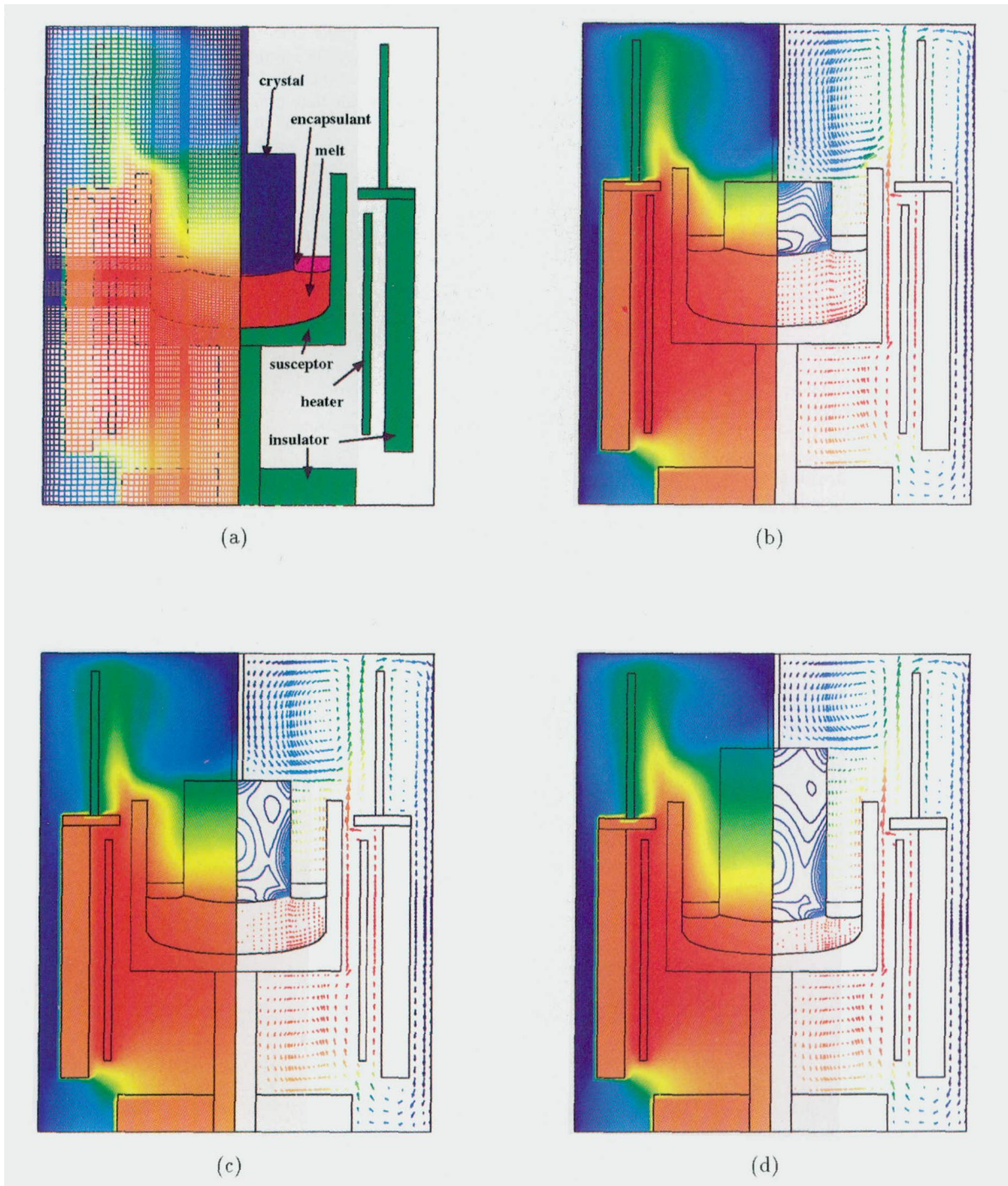 Figure 7 of this paper is reproduced here in color to show the details of the temperature and flow fields.

Fig. 7 Velocity, temperature, and von Mises stress fields in the crystal for a global simulation of GaAs growth with $Gr_g = 10^{10}$ and $Gr_l = 10^7$: (a) schematic and grid distribution, and represented for different crystal heights (b) 50 mm, (c) 80 mm, and (d) 110 mm

Copyright © 1999 by ASME